

Pertanika Journal of
**SCIENCE &
TECHNOLOGY**

JST

VOL. 32 (6) OCT. 2024



PERTANIKA
JOURNALS

A scientific journal published by Universiti Putra Malaysia Press

PERTANIKA JOURNAL OF SCIENCE & TECHNOLOGY

About the Journal

Overview

Pertanika Journal of Science & Technology is an official journal of Universiti Putra Malaysia. It is an open-access online scientific journal. It publishes original scientific outputs. It neither accepts nor commissions third party content.

Recognised internationally as the leading peer-reviewed interdisciplinary journal devoted to the publication of original papers, it serves as a forum for practical approaches to improve quality on issues pertaining to science and engineering and its related fields.

Pertanika Journal of Science & Technology currently publishes 6 issues a year (*January, March, April, July, August, and October*). It is considered for publication of original articles as per its scope. The journal publishes in **English** and it is open for submission by authors from all over the world.

The journal is available world-wide.

Aims and scope

Pertanika Journal of Science & Technology aims to provide a forum for high quality research related to science and engineering research. Areas relevant to the scope of the journal include: bioinformatics, bioscience, biotechnology and bio-molecular sciences, chemistry, computer science, ecology, engineering, engineering design, environmental control and management, mathematics and statistics, medicine and health sciences, nanotechnology, physics, safety and emergency management, and related fields of study.

History

Pertanika Journal of Science & Technology was founded in 1993 and focuses on research in science and engineering and its related fields.

Vision

To publish a journal of international repute.

Mission

Our goal is to bring the highest quality research to the widest possible audience.

Quality

We aim for excellence, sustained by a responsible and professional approach to journal publishing. Submissions can expect to receive a decision within 90 days. The elapsed time from submission to publication for the articles averages 180 days. We are working towards decreasing the processing time with the help of our editors and the reviewers.

Abstracting and indexing of Pertanika

Pertanika Journal of Science & Technology is now over 27 years old; this accumulated knowledge and experience has resulted the journal being abstracted and indexed in SCOPUS (Elsevier), Clarivate Web of Science (ESCI), EBSCO, ASEAN CITATION INDEX, Microsoft Academic, Google Scholar, and MyCite.

Citing journal articles

The abbreviation for Pertanika Journal of Science & Technology is *Pertanika J. Sci. & Technol.*

Publication policy

Pertanika policy prohibits an author from submitting the same manuscript for concurrent consideration by two or more publications. It prohibits as well publication of any manuscript that has already been published either in whole or substantial part elsewhere. It also does not permit publication of manuscript that has been published in full in proceedings.

Code of Ethics

The *Pertanika* journals and Universiti Putra Malaysia take seriously the responsibility of all of its journal publications to reflect the highest in publication ethics. Thus, all journals and journal editors are expected to abide by the journal's codes of ethics. Refer to *Pertanika's Code of Ethics* for full details, or visit the journal's web link at http://www.pertanika.upm.edu.my/code_of_ethics.php

Originality

The author must ensure that when a manuscript is submitted to *Pertanika*, the manuscript must be an original work. The author should check the manuscript for any possible plagiarism using any program such as Turn-It-In or any other software before submitting the manuscripts to the *Pertanika* Editorial Office, Journal Division.

All submitted manuscripts must be in the journal's acceptable similarity index range:
≤ 20% – PASS; > 20% – REJECT.

International Standard Serial Number (ISSN)

An ISSN is an 8-digit code used to identify periodicals such as journals of all kinds and on all media—print and electronic.

Pertanika Journal of Science & Technology: e-ISSN 2231-8526 (Online).

Lag time

A decision on acceptance or rejection of a manuscript is reached in 90 days (average). The elapsed time from submission to publication for the articles averages 180 days.

Authorship

Authors are not permitted to add or remove any names from the authorship provided at the time of initial submission without the consent of the journal's Chief Executive Editor.

Manuscript preparation

For manuscript preparation, authors may refer to *Pertanika*'s **INSTRUCTION TO AUTHORS**, available on the official website of *Pertanika*.

Editorial process

Authors who complete any submission are notified with an acknowledgement containing a manuscript ID on receipt of a manuscript, and upon the editorial decision regarding publication.

Pertanika follows a **double-blind peer-review** process. Manuscripts deemed suitable for publication are sent to reviewers. Authors are encouraged to suggest names of at least 3 potential reviewers at the time of submission of their manuscripts to *Pertanika*, but the editors will make the final selection and are not, however, bound by these suggestions.

Notification of the editorial decision is usually provided within 90 days from the receipt of manuscript. Publication of solicited manuscripts is not guaranteed. In most cases, manuscripts are accepted conditionally, pending an author's revision of the material.

The journal's peer review

In the peer-review process, 2 to 3 referees independently evaluate the scientific quality of the submitted manuscripts. At least 2 referee reports are required to help make a decision.

Peer reviewers are experts chosen by journal editors to provide written assessment of the **strengths** and **weaknesses** of written research, with the aim of improving the reporting of research and identifying the most appropriate and highest quality material for the journal.

Operating and review process

What happens to a manuscript once it is submitted to *Pertanika*? Typically, there are 7 steps to the editorial review process:

1. The journal's Chief Executive Editor and the Editor-in-Chief examine the paper to determine whether it is relevance to journal needs in terms of novelty, impact, design, procedure, language as well as presentation and allow it to proceed to the reviewing process. If not appropriate, the manuscript is rejected outright and the author is informed.
2. The Chief Executive Editor sends the article-identifying information having been removed, to 2 to 3 reviewers. They are specialists in the subject matter of the article. The Chief Executive Editor requests that they complete the review within 3 weeks.

Comments to authors are about the appropriateness and adequacy of the theoretical or conceptual framework, literature review, method, results and discussion, and conclusions. Reviewers often include suggestions for strengthening of the manuscript. Comments to the editor are in the nature of the significance of the work and its potential contribution to the research field.

3. The Editor-in-Chief examines the review reports and decides whether to accept or reject the manuscript, invite the authors to revise and resubmit the manuscript, or seek additional review reports. In rare instances, the manuscript is accepted with almost no revision. Almost without exception, reviewers' comments (to the authors) are forwarded to the authors. If a revision is indicated, the editor provides guidelines for attending to the reviewers' suggestions and perhaps additional advice about revising the manuscript.
4. The authors decide whether and how to address the reviewers' comments and criticisms and the editor's concerns. The authors return a revised version of the paper to the Chief Executive Editor along with specific information describing how they have addressed the concerns of the reviewers and the editor, usually in a tabular form. The authors may also submit a rebuttal if there is a need especially when the authors disagree with certain comments provided by reviewers.
5. The Chief Executive Editor sends the revised manuscript out for re-review. Typically, at least 1 of the original reviewers will be asked to examine the article.
6. When the reviewers have completed their work, the Editor-in-Chief examines their comments and decides whether the manuscript is ready to be published, needs another round of revisions, or should be rejected. If the decision is to accept, the Chief Executive Editor is notified.
7. The Chief Executive Editor reserves the final right to accept or reject any material for publication, if the processing of a particular manuscript is deemed not to be in compliance with the S.O.P. of *Pertanika*. An acceptance letter is sent to all the authors.

The editorial office ensures that the manuscript adheres to the correct style (in-text citations, the reference list, and tables are typical areas of concern, clarity, and grammar). The authors are asked to respond to any minor queries by the editorial office. Following these corrections, page proofs are mailed to the corresponding authors for their final approval. At this point, **only essential changes are accepted**. Finally, the manuscript appears in the pages of the journal and is posted on-line.

Pertanika Journal of
**SCIENCE
& TECHNOLOGY**

Vol. 32 (6) Oct. 2024



A scientific journal published by Universiti Putra Malaysia Press

EDITOR-IN-CHIEF

Luqman Chuah Abdullah
Chemical Engineering

CHIEF EXECUTIVE EDITOR

Mohd Sapuan Salit

UNIVERSITY PUBLICATIONS COMMITTEE

CHAIRMAN

Zamberi Sekawi

EDITORIAL STAFF

Journal Officers:

Ellyianur Puteri Zainal
Kanagamalar Silvarajoo
Siti Zuhaila Abd Wahid
Tee Syin Ying

Editorial Assistants:

Ku Ida Mastura Ku Baharom
Siti Juridah Mat Arip
Zulinaardawati Kamarudin

English Editor:

Norhanizah Ismail

PRODUCTION STAFF

Pre-press Officers:

Nur Farrah Dila Ismail
Wong Lih Jiun

WEBMASTER

IT Officer:

Illi Najwa Mohamad Sakri

EDITORIAL OFFICE

JOURNAL DIVISION

Putra Science Park
1st Floor, IDEA Tower II
UPM-IMTDC Technology Centre
Universiti Putra Malaysia
43400 Serdang, Selangor Malaysia.

General Enquiry

Tel. No: +603 9769 1622 | 1616

E-mail:

executive_editor.pertanika@upm.edu.my

URL: www.journals-jd.upm.edu.my

PUBLISHER

UPM Press

Universiti Putra Malaysia
43400 UPM, Serdang, Selangor, Malaysia.
Tel: +603 9769 8851
E-mail: penerbit@putra.upm.edu.my
URL: <http://penerbit.upm.edu.my>



ASSOCIATE EDITOR

2023-2024

Adem Kilicman

Mathematical Sciences
Universiti Putra Malaysia, Malaysia

Miss Laiha Mat Kiah

Security Services Sn: Digital Forensic,
Steganography, Network Security,
Information Security, Communication
Protocols, Security Protocols
Universiti Malaya, Malaysia

Saidur Rahman

Renewable Energy, Nanofluids, Energy
Efficiency, Heat Transfer, Energy Policy
Sunway University, Malaysia

EDITORIAL BOARD

2022-2024

Abdul Latif Ahmad

Chemical Engineering
Universiti Sains Malaysia, Malaysia

Ho Yuh-Shan

Water research, Chemical Engineering
and Environmental Studies
Asia University, Taiwan

Mohd Zulkifly Abdullah

Fluid Mechanics, Heat Transfer,
Computational Fluid Dynamics (CFD)
Universiti Sains Malaysia, Malaysia

Ahmad Zaharin Aris

Hydrochemistry, Environmental
Chemistry, Environmental Forensics,
Heavy Metals
Universiti Putra Malaysia, Malaysia

Hsiu-Po Kuo

Chemical Engineering
National Taiwan University, Taiwan

Mohd. Ali Hassan

Bioprocess Engineering, Environmental
Biotechnology
Universiti Putra Malaysia, Malaysia

Azlina Harun@Kamaruddin

Enzyme Technology, Fermentation
Technology
Universiti Sains Malaysia, Malaysia

Ivan D. Rukhlenko

Nonlinear Optics, Silicon Photonics,
Plasmonics and Nanotechnology
The University of Sydney, Australia

Nor Azah Yusof

Biosensors, Chemical Sensor, Functional
Material
Universiti Putra Malaysia, Malaysia

Bassim H. Hameed

Chemical Engineering: Reaction
Engineering, Environmental Catalysis &
Adsorption
Qatar University, Qatar

Lee Keat Teong

Energy Environment, Reaction
Engineering, Waste Utilization,
Renewable Energy
Universiti Sains Malaysia, Malaysia

Norbahiah Misran

Communication Engineering
Universiti Kebangsaan Malaysia,
Malaysia

Biswajeet Pradhan

Digital image processing, Geographical
Information System (GIS), Remote
Sensing
University of Technology Sydney,
Australia

Mohamed Othman

Communication Technology and
Network, Scientific Computing
Universiti Putra Malaysia, Malaysia

Roslan Abd-Shukur

Physics & Materials Physics,
Superconducting Materials
Universiti Kebangsaan Malaysia,
Malaysia

Daud Ahmad Israf Ali

Cell Biology, Biochemical, Pharmacology
Universiti Putra Malaysia, Malaysia

Mohd Shukry Abdul Majid

Polymer Composites, Composite
Pipes, Natural Fibre Composites,
Biodegradable Composites, Bio-
Composites
Universiti Malaysia Perlis, Malaysia

Wing Keong Ng

Aquaculture, Aquatic Animal Nutrition,
Aqua Feed Technology
Universiti Sains Malaysia, Malaysia

INTERNATIONAL ADVISORY BOARD

2021-2024

CHUNG, Neal Tai-Shung

Polymer Science, Composite and
Materials Science
National University of Singapore,
Singapore

Mohamed Pourkashanian

Mechanical Engineering, Energy, CFD
and Combustion Processes
Sheffield University, United Kingdom

Yulong Ding

Particle Science & Thermal Engineering
University of Birmingham, United
Kingdom

Hiroshi Uyama

Polymer Chemistry, Organic
Compounds, Coating, Chemical
Engineering
Osaka University, Japan

Mohini Sain

Material Science, Biocomposites,
Biomaterials
University of Toronto, Canada

ABSTRACTING AND INDEXING OF PERTANIKA JOURNALS

The journal is indexed in SCOPUS (Elsevier), Clarivate-Emerging Sources Citation Index (ESCI), BIOSIS, National Agricultural Science (NAL), Google Scholar, MyCite, ISC. In addition, Pertanika JSSH is recipient of "CREAM" Award conferred by Ministry of Higher Education (MoHE), Malaysia.

The publisher of Pertanika will not be responsible for the statements made by the authors in any articles published in the journal. Under no circumstances will the publisher of this publication be liable for any loss or damage caused by your reliance on the advice, opinion or information obtained either explicitly or implied through the contents of this publication.

All rights of reproduction are reserved in respect of all papers, articles, illustrations, etc., published in Pertanika. Pertanika provides free access to the full text of research articles for anyone, web-wide. It does not charge either its authors or author-institution for refereeing/publishing outgoing articles or user-institution for accessing incoming articles.

No material published in Pertanika may be reproduced or stored on microfilm or in electronic, optical or magnetic form without the written authorization of the Publisher.

Copyright © 2021 Universiti Putra Malaysia Press. All Rights Reserved.

Pertanika Journal of Science & Technology
Vol. 32 (6) Oct. 2024

Contents

Foreword <i>Mohd Sapuan Salit</i>	i
Performance Comparison of Seed Generation Techniques of Stimulated Brillouin Scattering-based Microwave Photonics Amplifier and Filter <i>Shahad Khudhair Abbas, Noran Azizan Cholan, Mohd Saiful Dzulkefly Zan, Mohd Adzir Mahdi, Makhfudzah Mokhtar and Zuraidah Zan</i>	2405
Bernoulli Distillation System (BDS) for Bioethanol Sorghum Stalk Purification <i>Djoko Wahyudi, Wignyanto, Yusuf Hendrawan and Nurkholis Hamidi</i>	2421
Spectroscopic Analysis of Chrysotile Asbestos and its Environmental Resistance in Asbestos Cement Waste Products <i>Gergely Zoltán Macher, Fanni Károly, Christopher Teh Boon Sung, Dóra Beke, András Torma and Szilveszter Gergely</i>	2441
<i>Review Article</i>	
State-of-the-Art Probabilistic Solar Power Forecasting: A Structured Review <i>Noor Hasliza Abdul Rahman, Shahril Irwan Sulaiman, Mohamad Zhafran Hussin, Muhammad Asraf Hairuddin, Ezril Hisham Mat Saat and Nur Dalila Khirul Ashar</i>	2459
Prediction of Temperature Variability on Power Transmission Line Parameters Using Intelligent Approaches <i>Ashfaq Ahmad, Iqra Javed, Changan Zhu, Muhammad Babar Rasheed, Muhammad Waqar Akram, Muhammad Wisal Khan, Umair Ghazanfar, Waseem Nazar, Syed Baqar Hussain and Amber Sultan</i>	2489
Isolation and Screening of Indigenous Filamentous Fungi Producing Ligninolytic, Cellulolytic and Hemicellulolytic Enzymes from Decomposed Oil Palm Frond <i>Ahmad Fariz Nicholas, Hasliza Abu Hassim, Mohd Huzairi Mohd Zainudin, Zunita Zakaria, Mohd Termizi Yusof, Mohd Nazri Md Nayan and Amirul Faiz Mohd Azmi</i>	2511
Chemical Composition of Acid Soluble Collagen (ASC) Isolated from Indonesia Local “Kacang” Goat Skin (<i>Capra aegagrus hocus</i>) <i>Dita Prameswari Trenggono Putri, Rina Wahyuningsih, Rusman, Nurliyani and Yuny Erwanto</i>	2541

Low-temperature Deposited Highly Sensitive Integrated All-solid Electrodes for Electrochemical pH Detection <i>Norhidayatul Hikmee Mahzan, Shaiful Bakhtiar Hashim, Rosalena Irma Alip, Zuhani Ismail Khan and Sukreen Hana Herman</i>	2561
Design an Agricultural Soil and Environment Monitoring System Based on IoT <i>Bayu Rima Aditya, Elis Hernawati, Tedi Gunawan and Pramuko Aji</i>	2575
Analysis of Soil Viability Monitoring System for In-house Plantation Growth Using an Internet of Things Approach <i>Spoorthi Singh, Utkarsh Ojha, Prashant M Prabhu, Poothi Rohan Reddi and Shivashankar Hiremath</i>	2591
Evaluating Convolutional Neural Network Architecture for Historical Topographic Hardcopy Maps Analysis: A Study on Training and Validation Accuracy Variation <i>Saiful Anuar Jaafar, Abdul Rauf Abdul Rasam and Norizan Mat Diah</i>	2609
A Comprehensive Analysis of a Framework for Rebalancing Imbalanced Medical Data Using an Ensemble-based Classifier <i>Jafhate Edward, Marshima Mohd Rosli and Ali Seman</i>	2631
Improved Early Detection of Tube Leaks Faults in Pulverised Coal-fired Boiler Using Deep Feed Forward Neural Network <i>Abdul Munir Abdul Karim, Yasir Mohd Mustafah and Zainol Arifin Zainal Abidin</i>	2655
A Framework for Prioritising the Performance Criteria of Natural Fibre Composite Materials: Incorporation of CRITIC-TOPSIS Method <i>Mohd Hidayat Ab Rahman, Siti Mariam Abdul Rahman, Ridhwan Jumaidin and Jamaluddin Mahmud</i>	2679
Machine Learning and Remote Sensing Applications for Assessing Land Use and Land Cover Changes for Under-monitored Basin <i>Muhammad Amiruddin Zulkifli, Jacqueline Isabella Anak Gisen, Syarifuddin Misbari, Shairul Rohaziawati Samat and Qian Yu</i>	2699
Variation and Forecasting of Land Surface Temperature in Malaysia <i>Munawar Munawar, Rhysa McNeil, Rohana Jani, Edwar M Nur and Don McNeil</i>	2723
The Application of Smart Drip Irrigation System for Precision Farming <i>Suhardi, Bambang Marhaenanto and Bayu Taruna Widjaja Putra</i>	2737

Assessment of Nitrate Reduction by Microbes in Artificial Groundwater Medium <i>Preeti Thakur and Pammi Gauba</i>	2753
<i>Review Article</i>	
A Comprehensive Review of State-of-the-art Optical Methods for Methane Gas Detection <i>Sayma Khandaker, Nurulain Shaipuzaman, Md Mahmudul Hasan, Mohd Amir Shahlan Mohd Aspar and Hadi Manap</i>	2769
<i>Case Study</i>	
Carbon Emission from Transportation in Higher Learning Institutions: A Case Study at Universiti Tun Hussein Onn Malaysia <i>Khairunmarhanis Zekefli, Aeslina Abdul Kadir, Amir Detho and Mohd Ikhmal Haqem Hassan</i>	2797
Physiological Behavior of Rubber Plants (<i>Hevea Brasiliensis</i>) to Different Soil Moisture Conditions <i>Rohaizad Mislan, Zulkefly Sulaiman, Siti Nor Akmar Abdullah, Mohd Razi Ismail, Sarker Mohammad Rezaul Karim, Mohd Aswad Abdul Wahab and Aizat Shamin Noran</i>	2807
Dehydrated Food Waste and Leftover for Trench Composting <i>Khalida Aziz, Naweedullah Amin, Vinod Kumar Nathan, Mami Irie, Irwan Syah Md. Yusoff, Luqman Chuah Abdullah, Amirrudin Azmi and Muhammad Heikal Ismail</i>	2827
<i>Review Article</i>	
A Systematic Review of Aquatic Organism Antimicrobial Peptides <i>Li Ting Lee, Arnold Ang, Ibrahim Mahmood, Ahmed AbdulKareem Najm, Adura Mohd Adnan, Shazrul Fazry and Douglas Law</i>	2847
Application of GIS for Monitoring Firefly Population Abundance (<i>Pteroptyx tener</i>) and the Influence of Abiotic Factors <i>Nurhafizul Abu Seri and Azimah Abd Rahman</i>	2873
Secure Data Aggregation and Transmission System for Wireless Body Area Networks Using Twofish Symmetric Key Generation <i>Insozhan Nagasundharamoorthi, Prabhu Venkatesan and Parthasarathy Velusamy</i>	2903

Foreword

Welcome to the sixth issue of 2024 for the *Pertanika Journal of Science and Technology (PJST)*!

PJST is an open-access journal for studies in Science and Technology published by Universiti Putra Malaysia Press. It is independently owned and managed by the university for the benefit of the world-wide science community.

This issue contains 25 articles: three review articles; one case study; and the rest are regular articles. The authors of these articles come from different countries namely Afghanistan, Brazil, China, Hungary, India, Indonesia, Iraq, Malaysia, Pakistan, South Korea and Thailand.

A regular article titled “Machine Learning and Remote Sensing Applications for Assessing Land Use and Land Cover (LULC) Changes for Under-Monitored Basin” was presented by Muhammad Amiruddin Zulkifli and co-researchers from Malaysia and China. A quantitative assessment of image classification schemes was examined using 2022 Sentinel-2 satellite imagery to measure its performance. Kappa coefficient and overall accuracy were used to determine the classification accuracy. Then, 32 years of LULC changes in Kuantan were investigated using Landsat 5 TM, Landsat 8 OLI, and Sentinel-2 based on the best classifier. Random forest classification outperformed maximum likelihood classification with an overall accuracy of 85% compared to 92.8%. The findings also revealed that urbanization is the main factor contributing to land changes in Kuantan, with a 32% increase in the build-up region and 32% in forest degradation. The detailed information of this study is available on page 2699.

An application of the Geographic Information System for monitoring firefly population abundance (*Pteroptyx tener*) and the influence of abiotic factors was studied by Nurhafizul Abu Seri and Azimah Abd Rahman from Universiti Sains Malaysia. The study was conducted from November 2021 to April 2022, utilizing GIS software to apply hotspot mapping and Inverse Distance Weighting analysis to elucidate the spatial distribution of firefly populations. A total of 111,615 individuals were recorded, with a particular focus on this firefly species' presence on their display trees. Hotspot analysis showed that Station 6, located at the mouth of a river with dense mangroves, hosted 55,723 fireflies (50.01%). In contrast, Stations 9 and 10, near ponds and shrimp settlements, recorded 517–723 fireflies (0.65% and 0.46%). Pearson's correlation coefficient (r) unveiled a statistically significant positive correlation ($r = 0.88$, $p < 0.05$) between wind speed and the abundance of firefly populations within the Sepetang River. However, no statistically significant correlation ($p > 0.05$) was found between firefly abundance and other abiotic parameters, including relative humidity, air temperature, tide level, pH, electrical conductivity, salinity, total dissolved solids, and water clarity. Thus, the results revealed the preference for fireflies due to the availability of vegetation, wind speed and minimal disturbance in this area. The detailed information of this study is available on page 2873.

Another article on secure data aggregation and transmission systems for wireless body area networks using Twofish symmetric key generation by Insozhan Nagasundharamoorthi et al. from India. The Twofish technique is animatedly employed to make the secure symmetric keys chosen for its robust encryption capabilities. These keys are used to encrypt and decrypt aggregated health data through transmission. The proposed TFSKG-SDA method implements effective algorithms for aggregating data to safeguard end-to-end privacy and preserve data accuracy while reducing bandwidth consumption. Thus, for improved performance, an innovative genetic algorithm for data security is presented in this study. This paper introduces TFSKG-SDA, a system that, by employing rigorous simulation testing, enhances security protocols, resistance against recognized threats, and data transmission efficacy in resource-constrained WBANs. We assess the encryption strength, computational cost, and communication efficiency of the TFSKG- SDA method to prove its significance to real-world healthcare applications. Further details of the investigation can be found on page 2903.

In the last 12 months, of all the manuscripts peer-reviewed, 29.4% were accepted. This seems to be the trend in PJST.

We anticipate that you will find the evidence presented in this issue to be intriguing, thought-provoking and useful in reaching new milestones in your own research. Please recommend the journal to your colleagues and students to make this endeavour meaningful.

All the papers published in this edition underwent Pertanika's stringent peer-review process involving a minimum of two reviewers comprising internal as well as external referees. This was to ensure that the quality of the papers justified the high ranking of the journal, which is renowned as a heavily-cited journal not only by authors and researchers in Malaysia but by those in other countries around the world as well.

We would also like to express our gratitude to all the contributors, namely the authors, reviewers, Editor-in-Chief and Editorial Board Members of PJST, who have made this issue possible.

PJST is currently accepting manuscripts for upcoming issues based on original qualitative or quantitative research that opens new areas of inquiry and investigation.

Chief Executive Editor

Mohd Sapuan Salit

executive_editor.pertanika@upm.edu.my

Performance Comparison of Seed Generation Techniques of Stimulated Brillouin Scattering-based Microwave Photonics Amplifier and Filter

Shahad Khudhair Abbas¹, Noran Azizan Cholan², Mohd Saiful Dzulkefly Zan³,
Mohd Adzir Mahdi^{1,4}, Makhfudzah Mokhtar^{1,4} and Zuraidah Zan^{1,4*}

¹Department of Computer and Communication Systems Engineering, Faculty of Engineering, Universiti Putra Malaysia, 43400 Serdang, Selangor, Malaysia

²Faculty of Electrical and Electronics Engineering, Universiti Tun Hussein Onn Malaysia (UTHM), 86400 Parit Raja, Batu Pahat, Johor, Malaysia

³Department of Electrical, Electronic & Systems Engineering, Faculty of Engineering & Built Environment, Universiti Kebangsaan Malaysia, Selangor 43600, Malaysia

⁴Wireless and Photonics Networks (WiPNET) Research Center, Faculty of Engineering, Universiti Putra Malaysia, 43400 Serdang, Selangor, Malaysia

ABSTRACT

This work presents a Brillouin amplification performance comparison of seed generation techniques using double-sideband suppressed carrier (DSB-SC) and single-sideband suppressed carrier (SSB-SC) modulations. The SSB-SC is obtained using an optical bandpass filter (OBPF) and in-phase and quadrature Mach-Zehnder modulator (IQ-MZM). All three techniques provide high amplification performance with optical signal-to-noise ratio (OSNR) enhancement of 37.47 dB, 33.14 dB, and 32.67 dB using DSB-SC, SSB-SC/OBPF, and SSB-SC/IQ-MZM, respectively. The best seed generation technique is using the DSB with a signal amplification of 62.47 dB. The technique presents ~4 dB higher OSNR enhancement due to the dual-energy transfer obtained from the beating process of the DSB

than SSB. A ~3 dB OSNR reduction is found when pump linewidth (LW) was changed from 1kHz to 50 MHz, which suggests using a low-cost pump source whenever the OSNR reduction is not critical. The work also shows that the three techniques required 10 dBm stimulated Brillouin scattering threshold (SBST) to stimulate the process. An additional analysis of DSB-SC shows that a high-carrier suppression during the

ARTICLE INFO

Article history:

Received: 29 August 2023

Accepted: 25 March 2024

Published: 09 October 2024

DOI: <https://doi.org/10.47836/pjst.32.6.01>

E-mail addresses:

shahadkhudhair92@gmail.com (Shahad Khudair Abbas)

noran@uthm.edu.my (Noran Azizan Cholan)

saifuldzul@ukm.edu.my (Mohd Saiful Dzulkefly Zan)

mam@upm.edu.my (Mohd Adzir Mahdi)

fudzah@upm.edu.my (Makhfudzah Mokhtar)

zuraidahz@upm.edu.my (Zuraidah Zan)

* Corresponding author

seed generation technique using MZMs is insignificant to the amplification performance. The high-carrier suppression produces a high seed signal power that distorts the Brillouin gain spectrum (BGS) and the pump depletion region, hence reducing the Brillouin gain (BG). Since carrier suppression is not a primary consideration, a cost-effective MZM with a modest extinction ratio requirement is allowed. The relaxed requirement of the pump's linewidth and MZM's extinction ratio suggest a cost-effective development of the SBS-based optical amplifier with narrow filter bandwidth.

Keywords: Brillouin amplifier, double-sideband, noise ratio enhancement, optical signal, single-sideband

INTRODUCTION

Microwave photonic filters based on stimulated Brillouin scattering (SBS) have become a promising alternative for ultra-narrow passband filters with noise suppression and amplification within the filter bandwidth (Pang et al., 2022; Zhang et al., 2022). With the SBS-based amplification, a narrow gain bandwidth between 10 to 100 MHz can be obtained with a lower pump power than using a Raman-based (Qi et al., 2022). The pump operated at a specific power is required to reach a Brillouin threshold and produce an SBS process where most of the incident power is reflected and produces an amplification. A Stokes signal at around 11 GHz from the laser pump's center frequency is obtained with more than 20-dB Brillouin gain (BG) at the pump power that exceeds the SBS threshold (SBST). SBS is known for its amplification with a high selectivity filtering owing to its high selectivity amplification and becomes a promising approach to enhancing a transmission system's optical signal-to-noise ratio (OSNR).

In Marhic and Cholan (2014), signal amplification with a narrow bandwidth was shown to provide noise suppression with 27-dB OSNR enhancement. It is supported by Nieves et al. (2021), where noise suppression can be obtained with combinations of waveguide properties, pump power, Stokes field, pulse durations, and interaction time. The SBS-based amplification needs a frequency-locking or beating between the optical signal (required to be amplified) with the backward-generated Stokes within a Brillouin-gain-bandwidth (BGBW). The signal required to be amplified is a probe or seed signal in the SBS-based amplification. Techniques to generate and beat the seed signal with Brillouin's Stokes can be done using a single or two independent laser pumps (Gertler et al., 2022; Marhic & Cholan, 2014).

A recent study utilizing two laser pumps was presented by Gertler et al. (2022) with two free-running laser sources around 1550 nm wavelength with a narrow linewidth (LW). In this study, the seed generation was done using two laser pumps to modulate the intensity of a wideband RF signal and produce a double sideband-suppressed carrier (DSB-SC) of several RF tones with a fully suppressed carrier (Ali et al., 2022; Gertler et

al., 2022). It requires a special device, a multi-port photonic-phononic emitter-receiver (PPER), fabricated using phononic crystals. The seed generation was done within these special waveguides that can generate and tune the seed at the expense of complexity and implementation costs. Another study reported using a single laser as the pump source but, however, required three phase-modulators for the seed generations using DSB, where at the final stage of the generation, the optical carrier was also suppressed using an optical filter (Du et al., 2023). The study focused on beating the generated seeds for the application of spectral measurement without emphasizing the modulation techniques used. Meanwhile, a study utilizing a single sideband modulation with the suppressed carrier (SSB-SC), which utilized the SBS effect in fiber to obtain the gain spectrum, was reported by Bhogal and Sindhvani (2022). The study, however, focuses on frequency shifting and a high carrier suppressed with the effect of Brillouin gain. In Marhic and Cholan (2014), an SBS experiment demonstrated 27-dB OSNR signal enhancement using a continuous-wave pump. A narrow linewidth (LW) laser pump with 30 dBm output power has been used with an intensity modulator focusing on a DSB modulation for the seed signal generation. The work has yet to explain the condition of the seed signal generation in terms of its modulation type, carrier suppression requirement, pump power, and interaction within a BGBW.

In this manuscript, the performance of the seed generation techniques comparing the DSB and SSB modulations is presented to obtain a high-gain SBS-based amplifier with a narrow band associated with the Brillouin gain bandwidth. Typical DSB modulation with carrier suppression adjusted using voltage biasing is obtained using a single-armed Mach Zehnder modulator (MZM), while two techniques are used for the SSB modulation. The first one is done by adding an optical bandpass (OBP) filter to remove an upper sideband, and the second is utilizing a costly optical modulator to generate the SSB directly after the modulator's output with the use of in-phase and quadrature MZM (IQ-MZM). The carrier suppression is also tuned with the biasing voltage supplied to the MZM's arms without any biasing control circuit. The proposed setups are more straightforward and cost-effective than the technique used by Gertler et al. (2022) and Ali et al. (2022), which requires a PPER device to perform sideband filtering and carrier suppression.

On the other hand, Du et al. (2023) performed the SBS generation using the DSB modulation but with cascaded phase modulations (PM) and OBP filters. Two free-running laser diodes and optical modulators were utilized by Ali et al. (2022) to perform the microwave filtering based on SBS, which again incurred additional cost and phase noise due to the free-running lasers, as opposed to a single laser diode with single MZM to perform the SBS seed generations in our proposed work. The single laser diode produces a strong phase correlation between the laser and the generated seed, reducing the phase noise impact on the system (Mandalawi et al., 2019). The work also highlights the requirement of the suppressed carrier for the modulation, which can be used to identify the MZM

specifications, specifically the required extinction ratio. With the narrow bandwidth, a high selectivity of 50 MHz optical bandwidth can be obtained with a high OSNR, indicating noise suppression. It can be another option for a high selectivity optical amplification as opposed to the typical Erbium-doped fiber-based amplifier with a wide bandwidth of 35 nm where a predominant amplified spontaneous emission (ASE) noise is imposed within the amplified signal. Investigations have been carried out in this work using VPItransmissionMaker™, a well-known simulator that industries and academics use to mimic expensive optical systems. The performance comparison between the SBS and DSB modulations shows that DSB provides the best seed generation technique to obtain a high gain. OSNR is the DSB modulation technique with a relaxed carrier suppression requirement. The technique provides a signal amplification of 62.47 dB with an OSNR enhancement of 37.47 dB. The results suggested using a cost-effective MZM with a modest extinction ratio requirement.

METHODOLOGY

Seed Generation Techniques

A single pump source at a frequency, f_o , generates the seed signal and the SBS process. The pump signal, f_o , is amplified by an erbium-doped fiber amplifier (EDFA) to satisfy the SBST required to stimulate the Brillouin process and generate BGBW. Figure 1 illustrates the spectrum modulation and its interaction with BG and BGBW.

The induced soundwave signal has an acoustic velocity, V_a , to generate the Stokes signal at a BFS of ν_B given by $\nu_B = \frac{2nV_a}{\lambda}$, where n is the optical fiber refractive index, and λ is the pump-signal wavelength (Ali et al., 2022; Du et al., 2023). The signal that must be enhanced or amplified needs to be injected with the same frequency and direction of the BFS aligned within the BGBW. In this case, a seed signal is backward injected into the optical fiber, beaten with the pump signal, and an amplified signal is produced at $-f_m$. The pump signal, f_o , is modulated with an RF signal, f_m , tuned to ν_B , as shown in Figure 1(b). The MZM is DC-biased at a null point with respect to the MZM's transfer function, as shown in Figure 1(b)(iii); according to Figure 1(b)(i), the generation of the SSB-SC seed signal using an OBPF after the MZM lets the lower-sideband signal interact within BGBW and filter out the upper-sideband. Meanwhile, Figure 1(b)(ii) shows the SSB-SC seed signal generated using an IQ-MZM. This technique requires a local oscillator tuned to f_m where one of the RF signals is 90° phase-shifted from the other inputs to produce in-phase and quadrature RF signal components. These signals drive the IQ-MZM to produce a seed signal at ν_B . The IQ-MZM is biased at the quadrature point of the transfer function, as illustrated in Figure 1(b)(iii). The theoretical mathematical models to explain Brillouin's Stokes amplification and the seed generations have been reported by Gökhan et al. (2018), Loayssa et al. (2004) and Qing et al. (2016).

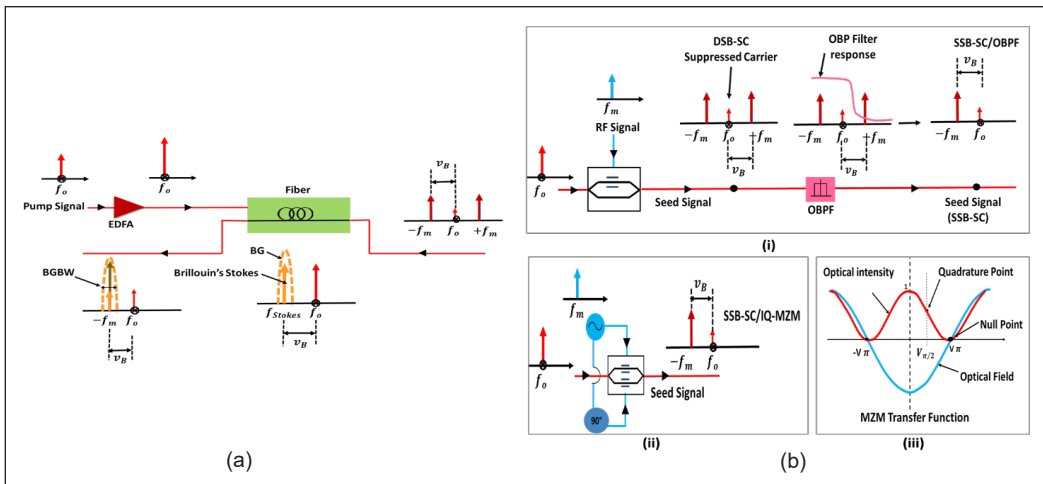


Figure 1. Illustration of (a) Brillouin's Stokes with BG generation and seed interaction within BGBW and (b) seed signal generations using MZMs to generate (i) DSB-SC and SSB-SC using an optical bandpass filter (OBPF), (ii) SSB-SC using in-phase and quadrature Mach-Zehnder modulator (IQ-MZM) with biasing voltages with respect to (iii) MZM's transfer function

Simulation Setup

The simulation setup of SBS-based optical amplification with signals before the interaction/ beating processes using (a) DSB-SC, (b) SSB- SC/OBPF, and (c) SSB-SC/IQ-MZM of seed signal generation blocks illustrated by the inset diagrams of Figure 2. A CW-laser with a center frequency of 193.1 THz (corresponding to 1552.52 nm of wavelength), an output power of 6 dBm, and a linewidth (LW) of 1 MHz is used as the pump source for this system. The CW-laser light is split by 50/50 Coupler 2, and the outputs are used for the pump source and to drive the MZM denoted as a carrier signal in the seed generation block. The MZM is used to generate the BFS light, in which an RF signal generator tunes the amount of the frequency shift. The optical MZM's extinction ratio is set to a typical value of 30 dB for all configurations, indicating the MZM's carrier-suppression ratio. The carrier suppression is obtained by biasing the MZM near the null region of its transfer function curve.

The output light of the CW-laser is added with an amplified-spontaneous emission (ASE) noise source to provide a constant white noise and a gain-controlled EDFA to vary the level of a noise- floor for OSNR and gain analyses. The combined CW-light and the ASE noise signal are fed onto an OBPF with a rectangular transfer function to limit the signal bandwidth (BW). At Point 1, the CW-light power is maintained at 3 dBm with an OSNR of 25 dB. The pump source at Output 1 of Coupler 2 is amplified to 30 dBm using a power-controlled EDFA and connected to a polarization controller (PC1) before the light is injected into a bidirectional optical fiber to stimulate a Brillouin process. PC1 is

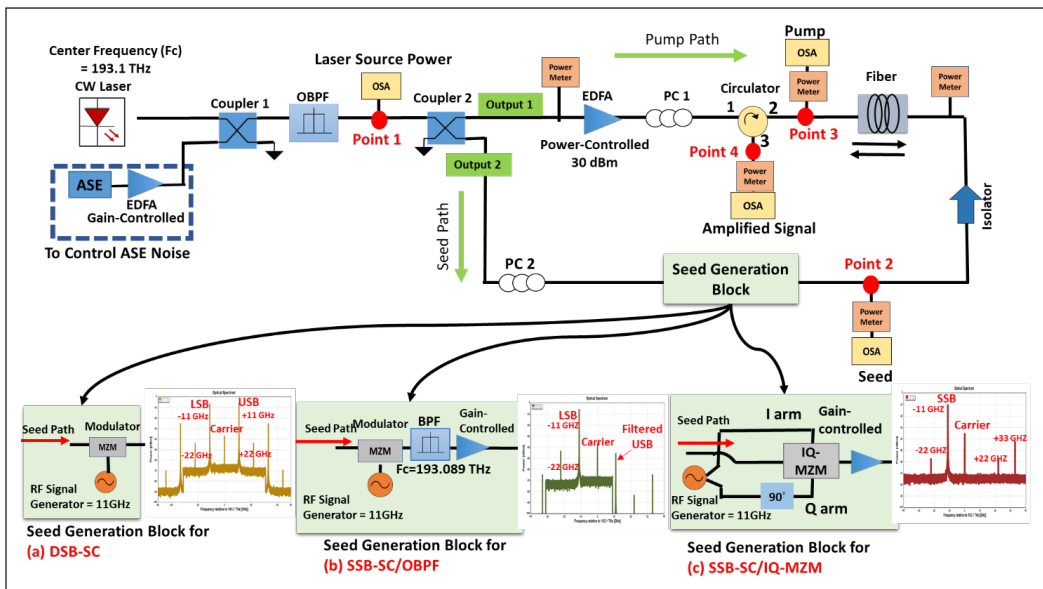


Figure 2. Simulation setups of SBS-based optical amplification using (a) DSB-SC, (b) SSB-SC/OBPF and (c) SSB-SC/IQ-MZM seed generation blocks

required before the fiber because the EDFA changes the signal’s state of polarization (Ali et al., 2023; Du et al., 2023).

The fiber parameters set are 14 km in length, 0.2 dB/km of attenuation, effective core area, A_{eff} of $8 \times 10^{-10} \text{ m}^2$, Brillouin gain coefficient, g_0 of $4.6 \times 10^{-11} \text{ m/W}$, intrinsic Brillouin bandwidth (BBW) of 50 MHz, Brillouin frequency shift, ν_B 11 GHz, and a nonlinear index of $26 \times 10^{-21} \text{ m}^2/\text{W}$. The CW-light at Output, 2 of Coupler 2, is linearly polarized before it is used to drive the MZM in the seed generation block. The pump and seed signals must be polarized because the SBS is a polarizer-dependence process (Deventer & Boot, 1994). The respective modulation techniques of DSB-SC, SSB-SC/OBPF and SSB-SC/IQ-MZM are shown in the inset diagrams of Figure 2(a), (b) and (c), respectively.

Every modulation technique is modulated with an RF signal from a local oscillator to generate side tones at a frequency equal to ν_B . The DSB-SC is constructed using a single RF-drive MZM with the biasing voltage set to 1 V to obtain carrier suppression. A complete null carrier-suppression cannot be obtained with the supplied biasing voltage due to the low 30-dB extinction ratio of the MZM. Thus, a carrier leakage of 3 dB, shown by the inset spectrum of Figure 2(a), is produced. The modulated signal also produced harmonic components at ± 22 and ± 33 GHz. The SSB-SC/OBPF technique is the same as the DSB-SC design but uses an OBPF of 60 GHz BW, 40 dB stop-band centered at 193.089 THz with a rectangular transfer function. It filters out the USB and passes the LSB part of the seed signal. The LSB at 193.089 THz is obtained with respect to the difference between the center frequency, f_0 and ν_B . The seed signal spectrum of the SSB-SC/OBPF with 3-dB

carrier leakage and the harmonic component at -22 GHz can be shown in Figure 2(b). Figure 2(c) shows the SSB-SC/IQ-MZM design, constructed using an IQ-MZM with an RF signal generator connected to a power splitter to provide the in-phase signal. In contrast, the quadrature signal component is produced after the 90°-phase shift. The I- and Q-arms are biased at 0.5 V. The output signal is the SSB at ν_B with 4 dB carrier leakage, and 23.3-dB carrier suppression is obtained with the harmonic components at ± 22 and +33 GHz. The seed signal power at Point 2 is -2 dBm for the three designs. The insertion losses of the components used in the SSB-SC/OBPF and SSB-SC/IQ-MZM seed generation block are compensated using an EDFA. The output of the seed generation block is injected through an isolator to prevent a back-reflection, fed into the bidirectional universal fiber and then extracted through Port 3 of the circulator as the amplified signal denoted as Point 4.

RESULTS AND DISCUSSION

SBS-based signal amplification is taken at Point 4 of the circulator's output. The spectra are analyzed to identify the gain and the OSNR enhancement obtained by comparing the SBS amplified signal to the pump source at the output at Point 1 of Figure 3.

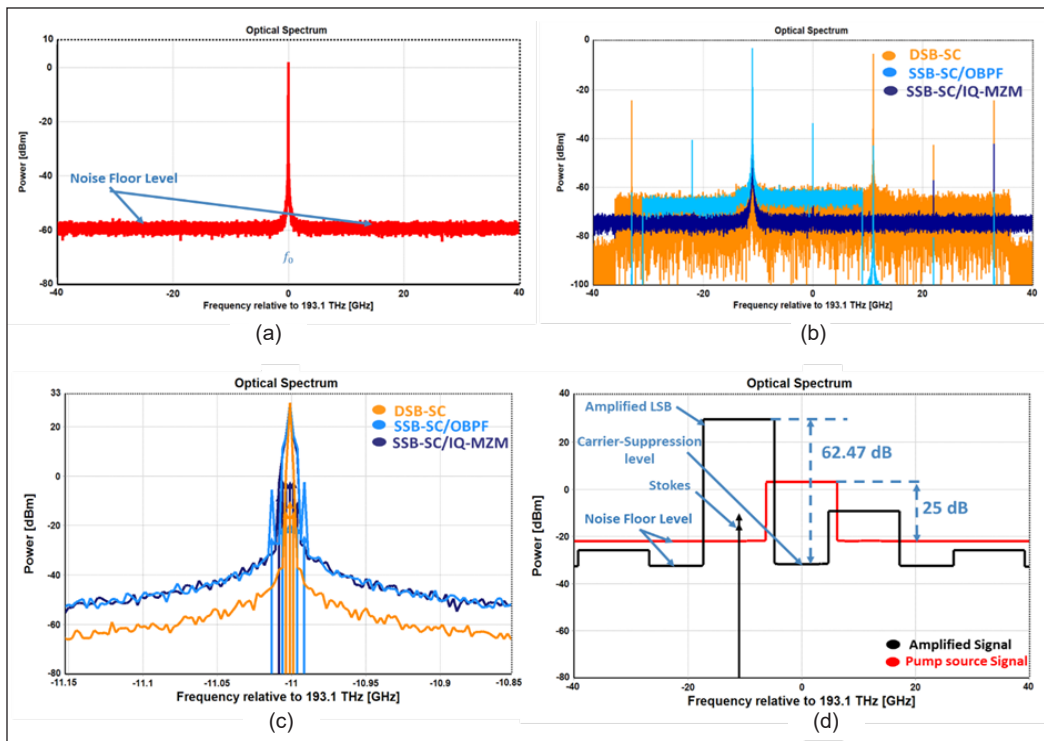


Figure 3. Spectra of (a) laser source signal at Point 1, (b) seed signal generation before the interaction at Point 2 for DSB-SC, SSB-SC/OBPF and SSB-SC/IQ-MZM, (c) aligned Stokes with the amplified signals of DSB-SC and SSB-SC at 2 MHz resolution bandwidth (RBW) and (d) amplified signal at Point 4 using DSB-SC seed generation with its pump source signal at Point 1 with RBW of 12.5 GHz

The 0.1 nm RBW is a standard OSNR measurement using a typical OSA (Ali et al., 2022). The spectrum has been magnified from a Lorentzian-shaped spectrum to present the Stokes signal at -11 GHz, where the simulator represents the Stokes signal using the arrows. The Stokes produces a Lorentzian-shaped BG with a narrow BGBW, whereas the gain will amplify the seed signal injected backward within the interaction area. In contrast, the signal and noise outside the BGBW are not affected. It produced a much narrower amplifier BW than an EDFA, amplified all the signals within a wide BW, and added an ASE noise onto the amplified signal (Ali et al., 2022). The Stokes signal is produced when part of the pump signal is back-scattered due to the periodical modulation of the refractive index when it interacts with the fiber medium. Stokes signal is considered a noise if there is no backward seed signal. The refractive index modulation obtains an exponentially increased back-scattered pump power signal, similar to a Bragg condition. The power is then transferred to the seed signal and amplified (Ali et al., 2022).

The Stokes wave power is higher in the DSB-SC than in the SSB-SCs due to the higher transferred power of the DSB to the pump, which leads to a more back-scattered pump power (Ali et al., 2022; Preussler & Schneider, 2015). The measurement of the OSNR enhancement is shown by taking the difference between the OSNR of the amplified signal with respect to its noise floor (black line) and the pump source signal with its respective noise floor (red line), as shown in Figure 3(d) (Marhic & Cholan, 2014). The noise floor of the amplified signal is represented by the carrier-suppression level of the seed generation technique, which is, in this case, the DSB-SC. The OSNR enhancement obtained is 37.47 dB, resulting from the subtraction between 62.47 dB and 25 dB, as shown in Figure 3(d).

Figure 4(a) shows the harmonic frequency components at multiple $\pm f_m$ for the DSB-SC and at multiple $-f_m$ for the SSB-SC from the laser pump's center frequency at 193.089 THz, where each component is separated at ν_B of 11 GHz. When the Stokes signal is aligned, the LSB signal at -11 GHz away from the laser pump's center frequency is amplified to a peak power of 30 dBm. When the LSB frequency does not match the BFS, no power transfer process between the seed and pump signals will occur. These indicate that the signals are unaligned; hence, the seed signal (LSB) will not be amplified. In this simulation, the Stokes signal is fixed to ν_B with a constant phase. The pump power used is 30 dBm. The OSNRs are 62.47 dB, 58.14 dB and 57.67 dB for the DSB-SC, SSB-SC/OBPF, and SSB-SC/IQ-MZM seed generation techniques, respectively. Measured BGs with respect to the unamplified (unaligned seed signal within BGBW) are 38.4 dB, 34.08 dB and 33.6 dB for the DSB-SC, SSB-SC/OBPF and SSB-SC/IQ-MZM, respectively.

A BGBW is obtained by taking a full-wave half maximum (FWHM) measurement of the amplified spectrum. The amplified optical power obtained at Point 4 is similar to the pump power at Point 3 due to the total power reflection from the saturated pump signal (Aoki et al., 1988; Ravet et al., 2008). The obtained OSNR enhancements of 37.47 dB,

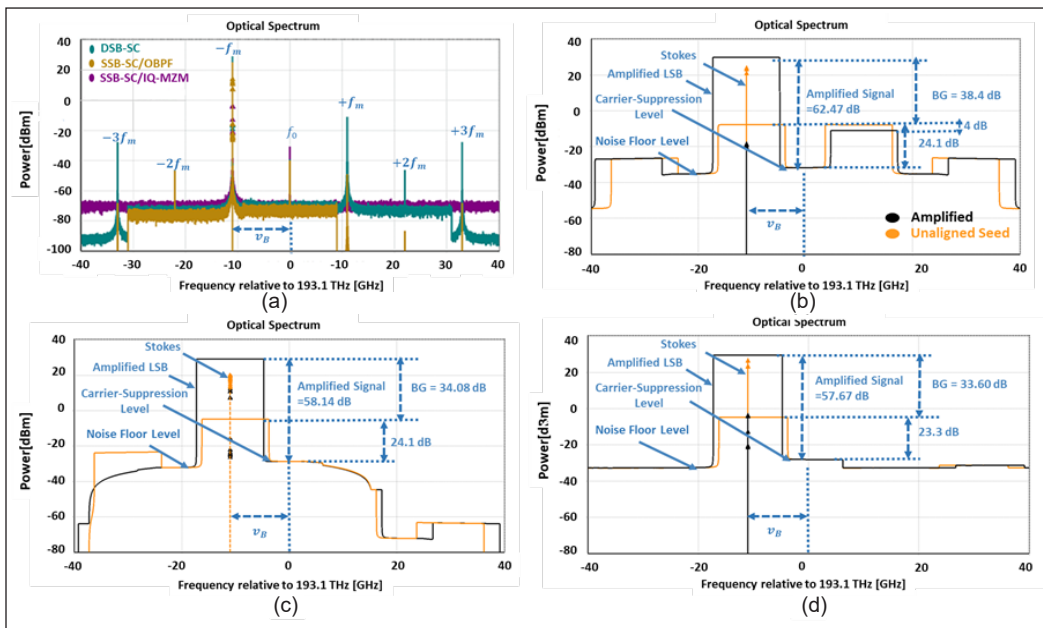


Figure 4. Spectra of the aligned and unaligned seed with Stokes signals obtained at Point 4 for (a) all seed generation techniques at 2 MHz RBW, (b) DSB-SC, (c) SSB-SC/OBPF and (d) SSB-SC/IQ-MZM seed generation techniques at 12.5 GHz RBW

33.14 dB and 32.67 dB for the DSB-SC, SSB-SC/OBPF and SSB-SC/IQ-MZM seed signal generation techniques, respectively. 4-dB higher OSNR enhancement is obtained using the DSB- SC than the SSB-SCs due to the higher power transferred from the USB at $+f_m$ and carrier at f_0 to the LSB at $-f_m$. It is shown in Figure 4(b), where the amplified USB power (black line) is reduced by 4 dB compared to the unamplified USB (orange line) when no alignment occurred. It confirmed the result obtained in Marhic & Cholan (2014) with slightly higher OSNR enhancement due to the circulator’s low insertion loss and high isolation.

Figure 5 analyzes the noise power level before and after the interaction and shows additional noise from the Brillouin amplifier. The DSB-SC amplification signal is compared since the noise floor level is identical to the SSB-SCs. It shows a ~ 24 dB additional noise power compared to the pump source signal. It is due to the characteristic of EDFA that amplifies the whole signal band, including the noise. The amplified signal noise level decreased by 9 dB due to component power loss (coupler, polarizer and MZM). Hence, the Brillouin amplifier added negligible noise to the signal, in agreement with Souidi et al. (2016). The Brillouin amplifier added low noise compared to EDFA due to Brillouin’s narrow gain bandwidth.

In this simulation, the injected seed signal power into the fiber is fixed at -2 dBm to compare the seed generation techniques. The Stokes signal peak power is obtained by the

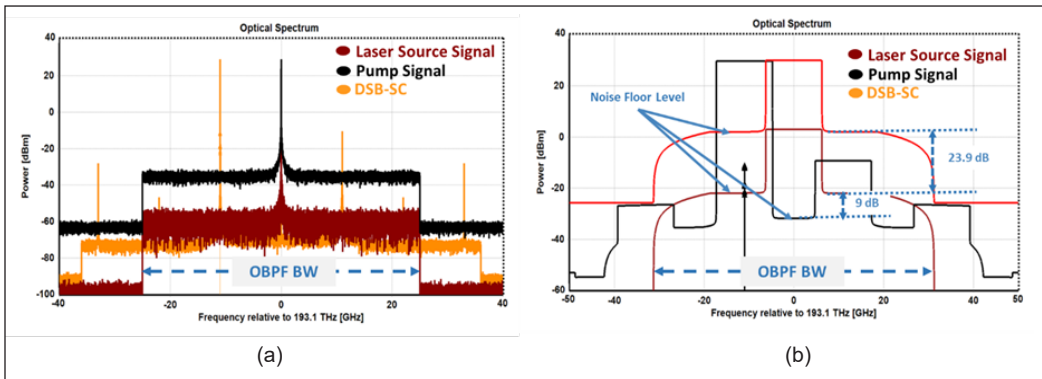


Figure 5. Spectra of the laser source signal, Pump signal, and amplified signal of DSB-SC at (a) 2 MHz RBW and (b) 12.5 MHz RBW

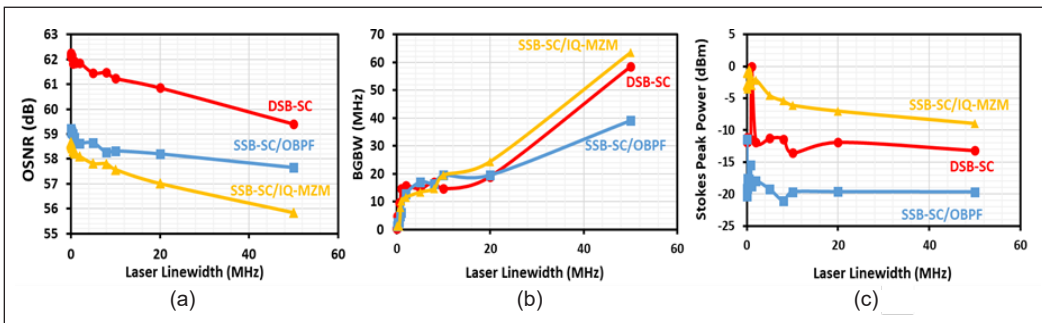


Figure 6. Pump source phase noise effect to (a) amplified signal OSNR, (b) BGBW and (c) Stokes's peak power using DSB-SC, SSB-SC/OBPF and SSB-SC/IQ-MZM seed generation techniques

highest arrow peak power value, which indicates the Stokes signal. Figure 6(a) shows that the highest OSNR is obtained with the narrowest LW and fluctuates when the LW is broadened for the three modulations. It is expected that the pump LW is narrower than the intrinsic Brillouin bandwidth. All three seed generation techniques require a coherence source for the highest amplification. When the pump source with a high phase noise or an insufficient coherence pump source is used, the phase noise becomes the dominant factor that reduces the obtained gain and induces the Brillouin gain fluctuations. It can be associated with the obtained fluctuated OSNR when the LW is broadened. However, the fluctuations amount is negligible and considered stable due to the frequency-locking approach that makes the generated Stokes wave follow the pump signal frequency, consequently canceling gain fluctuations and providing a stable amplification as explained in Figure 6(a) (Souidi et al., 2016).

The results agreed well with the BGBW, as shown in Figure 6(b). To obtain the maximum gain, the pump LW must be much narrower than the intrinsic Brillouin bandwidth of 50 MHz in the simulation setup. The BGBW is relatively broadened and fluctuates

when the pump LW is increased, which agrees with its respective amount of gain shown in Figure 6(a). The broadened pump LW also affects the threshold power required to produce the stimulated Brillouin effect. Consequently, reducing the SBST will reduce the gain amplification produced by the SBS (Ali et al., 2022; Du et al., 2023; Harish & Nilsson, 2019). Figure 6(c) shows that the narrower the pump LW than the Brillouin bandwidth, the stronger the Stokes signal is obtained, resulting in the highest gain. Figure 6 shows that the DSB-SC provides better overall performance than the SSB-SC/IQ-MZM and SSB-SC/OBPF due to the double-energy transfer processes, as explained in Figure 4 (Frederic et al., 2013). It is shown by the significantly high Stokes's peak power in Figure 6(c) for the narrowest LW pump. When the pump LW is broadened, the Stokes power is reduced as the phase noise dominates.

The obtained OSNR is reduced at around 1 dB when the LW is broadened from 1 kHz to 20 MHz and around ~ 2.6 -dB reduction when the LW is broadened to 50 MHz, equal to the intrinsic Brillouin bandwidth. At 50 MHz pump LW, the obtained BGBW is ~ 60 MHz for the DSB-SC and SSB-SC/IQ-MZM, while ~ 40 MHz for the SSB-SC/OBPF. The BGBW will increase proportionally with the increase of pump LW through the relationship between Brillouin LW parameter, Γ and BGBW, Δv_B given by $\Delta v_B \alpha \Gamma / 2\pi$, where Γ is also related to the pump LW, Δv_p by $\Gamma = f(T_B, \Delta v_B)$ where T_B is phonon lifetime (Zhao et al., 2020). Nevertheless, the results suggest a low-cost distributed feedback laser (DFB) can generate the 50 MHz pump LW. Thus, a low-cost laser source could be used as the pump source.

Figure 7 shows the effect of the pump power on the (a) BG, (b) amplified seed signal power, and (c) amplified seed signal OSNR obtained at Point 4 of Figure 2 using DSB-SC, SSB-SC/OBPF and SSB-SC/IQ-MZM seed generation techniques. The OSNR is obtained using an OSA with respect to 0.1 nm (~ 12.5 GHz), a typical OSA RBW, and the signal power is measured using a power meter. It is to analyze the SBST for the three designs. The laser time trace is assumed to be stable throughout the loop for Figure 2(a), (b), and (c) without phase mismatch. Figure 7(a) shows that the BG increased linearly with the pump power, and at 10 dBm, it started to increase rapidly. It indicates that a stimulated Brillouin process has taken place, and a pump depletion occurs when the pump power is transferred to the seed signal. It gives the SBST value relatively the same for all three techniques. At the pump power higher than the SBST, most of the power is transferred to the seed signal, resulting in the signal amplification at the Brillouin frequency, v_B , away from f_o and saturating the power of f_o . The BG starts to saturate after 30 dBm of pump power. Figure 7(b) confirms that the f_o power is transferred to the seed signal at $-f_m$ saturates after 30 dBm. Figure 7(c) presents that after 15 dBm peak power, the OSNR of the amplified seed signal using DSB-SC provides a 3-dB better OSNR than the SSB-SC. It confirms the double energy transfer processes between the pump and the USB and LSB of the DSB-SC. The OSNR continues to improve exponentially with the increase of the pump power until at 30

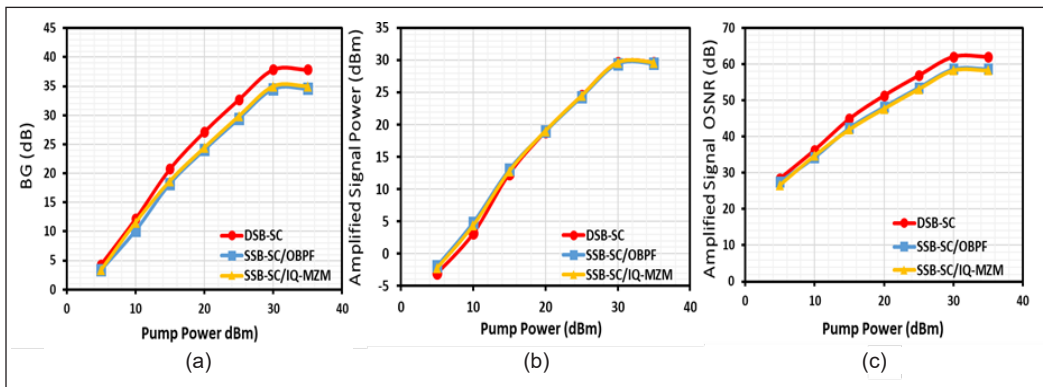


Figure 7. Pump-power effect on (a) BG, (b) amplified signal power, and (c) amplified signal OSNR at Point 4 using DSB-SC, SSB- SC/OBPF and SSB-SC/IQ-MZM seed generation techniques

dBm when it starts to saturate. The highest OSNR obtained is 62.47 dB for the DSB-SC and 58 dB for the SSB-SC. An OSNR enhancement of 37.47 dB is obtained compared to the 25-dB OSNR of the laser source taken at Point 1 of Figure 2 of the DSB-SC.

Figure 8 shows the effect of the MZM biasing voltage concerning the amplified signal OSNR and the seed power. The varying MZM biasing voltages will produce a respective carrier suppression at 193.1 THz laser-pump frequency based on the MZM’s transfer function curve and extinction ratio value. The biasing voltages of 0.1 V, 0.5 V, 1 V and 1.6 V produced carrier suppression of 8.1 dB, 20.2 dB, 24.1 dB and 31 dB, respectively. The spectra of Figure 8(a) show that the carrier is suppressed down to the noise floor when the MZM is biased at 1.6 V and a small suppression at 0.1 V. When the carrier is suppressed, the carrier power is distributed to the sidebands or the seed signal at $\pm f_m$ hence producing a high-power seed signal at -6 dBm. When the carrier suppression is small, for example, at 8.1 dB, the power of the seed signal is low at -21 dBm when the MZM is biased at 0.1 V, where a considerably high carrier signal can be seen in the spectrum. High carrier suppression is desired for a coherent transmission system. However, generating the seed signal for an SBS-based amplifier is unnecessary, as shown in Figure 8(b). The lowest carrier suppression of 8.1 dB with its respective seed signal power of -21 dBm of Figure 8(c) provides the best-amplified signal OSNR of ~80 dB. It satisfies the required backward interacting light-wave signal power of tens of microwatts (Du et al., 2023; Marhic & Cholan, 2014; Zan et al., 2013). Moreover, the high carrier in the generated seed signal provides an extended energy transfer between the pump, f_o and $+f_m$ into $-f_m$. When the carrier suppression level is increased, for example, at 20.2 dB, the OSNR of the amplified signal is reduced by close to 14 dB. At a high carrier suppression level of 24.1 dB and 31 dB, when the MZM is biased close to or at the null point of the MZM’s transfer function, the produced seed signal power is -2 dBm and -6 dBm, respectively. At this seed signal power, the OSNR becomes saturated. It agreed that the seed signal power should not

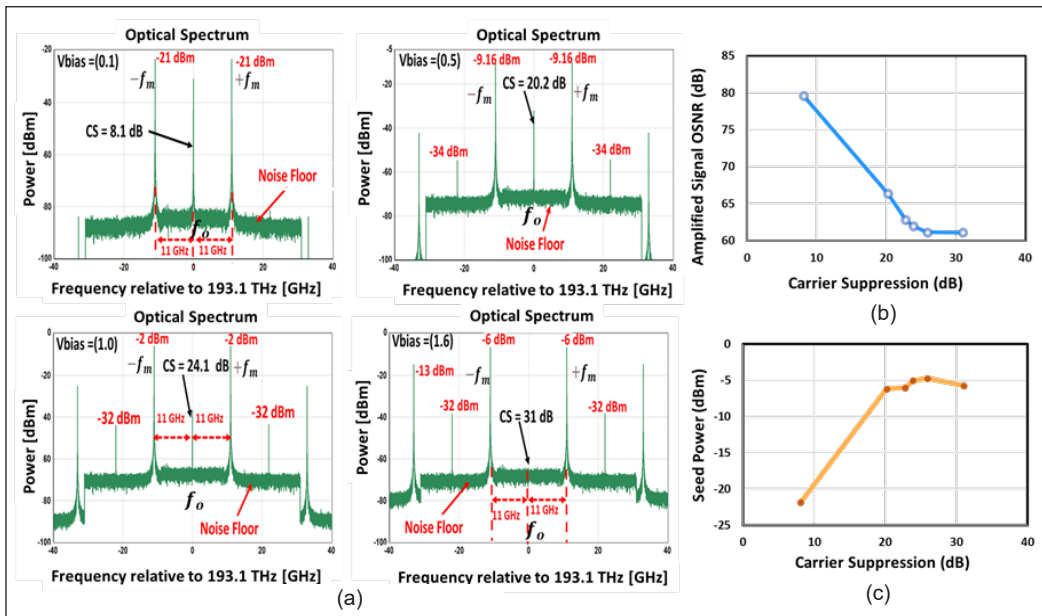


Figure 8. MZM biasing voltage effect with the resulting (a) seed spectra, (b) amplified signal OSNR at Point 4, and (c) seed power at Point 2 using a DSB-SC seed signal generation design

exceed $10 \mu\text{W}$ to prevent BGS distortion. The high seed signal power will strongly beat within BGBW, and the gain is decreased because the pump-depletion region is prominent at the peak of the BGS.

Furthermore, the carrier suppressed at 24.1 dB and 31 dB will produce high-order harmonics of the carrier and sidebands. It can induce intermodulation distortion between the harmonics and the signal sidebands when this amplifier is used for a transmission system. The obtained results can be used as a guide to tune the optimum biasing point for seed generation with respect to the carrier suppression required. A typical commercially available IQ-MZM requires a biasing point higher than the quadrature to produce the small carrier suppression to meet the seed signal power requirement. Since the carrier suppression is insignificant in producing a high Brillouin gain, a cheap MZM with a low extinction ratio can be used for the seed signal generation. The requirement of SSB-SC/IQ-MZM can be relaxed as DSB-SC without a stringent carrier suppression requirement is shown to perform well. Furthermore, an EDFA to compensate for the insertion loss of the MZM is also not required for the seed generation block.

CONCLUSION

This work investigated the amplification performance of modulation techniques to generate a seed signal using DSB-SC, SSB-SC/OBPF and SSB-SC/IQ-MZM driven by a single CW laser pump using simulation. The three techniques used an MZM to generate the

seed signal at a BFS of 11 GHz, where the SSB is obtained using an OBPF and IQ-MZM. The produced seed will beat within a BGBW to obtain the amplified signal. The OSNR enhancements achieved are 37.47 dB, 33.14 dB and 32.67 dB using DSB-SC, SSB-SC/OBPF and SSB-SC/IQ-MZM, respectively. It is found that the DSB-SC seed generation modulation technique performed the best with the highest amplified seed signal of 62.47 dB compared to 58.14 dB and 57.67 dB obtained with SSB SC/OBPF and SSBSC/ IQ-MZM. The dual-energy transfer occurs through the beating process involving the USB and LSB instead of the single-energy transfer in the SSB-SCs. Laser pump phase noise represented by the LW is also a limiting factor for the BG as it reduces the gain and induces fluctuations. However, the BG performance tolerates the LW of 50 MHz with a slight OSNR reduction of ~3-dB measured from the resulting amplified seed signal for all generation techniques. It suggests that a low-cost laser source, such as a DFB laser, can be used as a pump source if the OSNR requirement is not critical. Also, the carrier suppression ratio of the resulting DSB and SSB modulation signals is less significant. The seed signal power must be as low as tens of microwatt to prevent the distortion of the BGS and pump depletion. It permits using a low-cost MZM with a low extinction ratio value.

ACKNOWLEDGEMENTS

This work was supported by the Fundamental Research Grant Scheme (FRGS), Ministry of Higher Education, Malaysia, No. FRGS/1/2019/TK04/UPM/02/8 and 6300294/UPM/ National Instruments Research Grant.

REFERENCES

- Ali, M., Haxha, S., & Flint, I. (2022). Tuneable microwave photonics filter based on stimulated Brillouin scattering with enhanced gain and bandwidth control. *Journal of Lightwave Technology*, 40(2), 423-431. <https://doi.org/10.1109/JLT.2021.311831>
- Aoki, Y., Tajima, K., & Mito, I. (1988). Input power limits of single-mode optical fibers due to stimulated Brillouin scattering in optical communication systems. *Journal of Lightwave Technology*, 6(5), 710-719. <https://doi.org/10.1109/50.4057>
- Bhogal, R. K., & Sindhvani, M. (2022). Generation of single sideband-suppressed carrier (SSB-SC) signal based on stimulated Brillouin scattering. *Journal of Physics: Conference Series* 2327(1), Article 012025. <https://doi.org/10.1088/1742-6596/2327/1/012025>
- Deventer, M. O. V., & Boot, A. J. (1994). Polarization properties of stimulated Brillouin scattering in single-mode fibers. *Journal of Lightwave Technology*, 12(4), 585-590. <https://doi.org/10.1109/50.285349>
- Du, S., Liu, X., Du, P., Wang, D., Ma, B., Li, D., Wang, Y., Zhang, J., Wang, Y., & Wang, A. (2023). Broadband microwave photonic frequency measurement based on optical spectrum manipulation and stimulated Brillouin scattering. *IEEE Photonics Journal*, 15(2), Article 5500708. <https://doi.org/10.1109/JPHOT.2023.3251974>

- Frederic, A., Veronique, Q., Mikael, G., Andre, P., & Yves, A. (2013). A low-consumption electronic system developed for a 10 km long all-optical extension dedicated to sea floor observatories using power-over-fiber technology and SPI protocol. *Microwave and Optical Technology Letters*, 55(11), 2562-2568. <https://doi.org/10.1002/mop.27916>
- Gertler, S., Otterstrom, N. T., Gehl, M., Starbuck, A. L., Dallo, C. M., Pomerene, A. T., Trotter, D. C., Lentine, A. L., & Rakich, P. T. (2022). Narrowband microwave-photonic notch filters using Brillouin-based signal transduction in silicon. *Nature Communications*, 13(1), Article 1947. <https://doi.org/10.1038/s41467-022-29590-0>
- Gökhan, F. S., Göktaş, H., & Sorger, V. J. (2018). Analytical approach of Brillouin amplification over threshold. *Applied Optics*, 57(4), 607-611. <https://doi.org/10.1364/AO.57.000607>
- Harish, A. V., & Nilsson, J. (2019). Suppression of stimulated Brillouin scattering in single-frequency fiber Raman amplifier through pump modulation. *Journal of Lightwave Technology*, 37(13), 3280-3289. <https://doi.org/10.1109/JLT.2019.2914081>
- Loayssa, A., Hernández, R., Benito, D., & Galech, S. (2004). Characterization of stimulated Brillouin scattering spectra by use of optical single-sideband modulation. *Optics Letters*, 29(6), 638-640. <https://doi.org/10.1364/OL.29.000638>
- Mandalawi, Y. N. A., Yaakob, S., Adnan, W. A. W., Yaacob, M. H., & Zan, Z. (2019). Laser phase noise effect and reduction in self-homodyne optical OFDM transmission system. *Optics Letters*, 44(2), 307-310. <https://doi.org/10.1364/OL.44.000307>
- Marhic, M. E., & Cholan, N. A. (2014, June 8-13). *Improvement of optical signal-to-noise ratio of a high-power pump by stimulated brillouin scattering in an optical fiber*. [Paper Presentation]. Conference on Lasers and Electro-Optics (CLEO), San Jose, USA. https://doi.org/10.1364/CLEO_SI.2014.SM4N.6
- Nieves, O. A., Arnold, M. D., Steel, M. J., Schmidt, M. K., & Poulton, C. G. (2021). Noise and pulse dynamics in backward stimulated Brillouin scattering. *Optics Express*, 29(3), 3132-3146. <https://doi.org/10.1364/OE.414420>
- Pan, J., Richter, T., & Tibuleac, S. (2018, March 11-15). *OSNR Measurement comparison in systems with ROADM filtering for flexible grid networks*. [Paper presentation]. Optical Fiber Communications Conference and Exposition (OFC), San Diego, California.
- Pang, Y., Xu, Y., Zhao, X., Qin, Z. & Liu, Z. (2022). Stabilized narrow-linewidth brillouin random fiber laser with a double-coupler fiber ring resonator. *Journal of Lightwave Technology*, 40(9), 2988–2995. <https://doi.org/10.1109/jlt.2022.3148118>
- Preussler, S., & Schneider, T. (2016). Stimulated Brillouin scattering gain bandwidth reduction and applications in microwave photonics and optical signal processing. *Optical Engineering*, 55(3), Article 031110. <https://doi.org/10.1117/1.OE.55.3.031110>
- Qi, T., Li, D., Wang, Z., Wang, L., Yu, W., Yan, P., Gong, M., & Xiao, Q., (2022). 6.85 KW ytterbium-raman fiber amplifier based on adjustable raman threshold method. *Journal of Lightwave Technology*, 40(12), 3907-3915. <https://doi.org/10.1109/JLT.2022.3151489>
- Qing, T., Li, S., Xue, M., & Pan, S. (2016). Optical vector analysis based on double-sideband modulation and stimulated Brillouin scattering. *Optics Letters*, 41(15), 3671-3674. <https://doi.org/10.1364/OL.41.003671>

- Ravet, F., Snoddy, J., Bao, X., & Chen, L. (2008). Power thresholds and pump depletion in Brillouin fiber amplifiers. *The Open Optics Journal*, 2(1), 1-5. <https://doi.org/10.2174/1874328500802010001>
- Souidi, Y., Taleb, F., Zheng, J., Lee, M. W., Du Burck, F., & Roncin, V. (2016). Low-noise and high-gain Brillouin optical amplifier for narrowband active optical filtering based on a pump-to-signal optoelectronic tracking. *Applied Optics*, 55(2), 248–253. <https://doi.org/10.1364/AO.55.000248>
- Zan, M. S. D. B., Tsumuraya, T., & Horiguchi, T. (2013). The use of Walsh code in modulating the pump light of high spatial resolution phase-shift-pulse Brillouin optical time domain analysis with non-return-to-zero pulses. *Measurement Science and Technology*, 24(9), Article 094025. <https://doi.org/10.1088/0957-0233/24/9/094025>
- Zhang, Q., Han, X., Shao, X., Wang, Y., Jiang, H., Dong, W., & Zhang, X. (2022). Stimulated Brillouin scattering-based microwave photonic filter with a narrow and high selective passband. *IEEE Photonics Journal*, 14(4), Article 5537507. <https://doi.org/10.1109/JPHOT.2022.3184761>
- Zhao, J., Yang, F., Wei, F., Zhang, X., Ding, Z., Wu, R., & Cai, H. (2020). Effect of linewidth on intensity noise induced by stimulated Brillouin scattering in single-mode fibers. *Optics Express*, 28(10), 15025–15034. <https://doi.org/10.1364/OE.393239>

Bernoulli Distillation System (BDS) for Bioethanol Sorghum Stalk Purification

Djoko Wahyudi^{1*}, Wignyanto², Yusuf Hendrawan³ and Nurkholis Hamidi⁴

¹Department of Mechanical Engineering, Faculty of Engineering and Informatics, Panca Marga University, Yos Sudarso 107 Dringu, Probolinggo, East Java, Indonesia

²Department of Agro Industry Engineering, Faculty of Agricultural Technology, Brawijaya University, Veteran St, Malang, East Java, ZIP 65145, Indonesia

³Department of Biosystem Engineering, Faculty of Agricultural Technology, Brawijaya University, Veteran St, Malang, East Java, ZIP 65145, Indonesia

⁴Department of Mechanical Engineering, Faculty of Engineering, Brawijaya University, Veteran St, Malang, East Java, ZIP 65145, Indonesia

ABSTRACT

Sorghum is a plant that produces syrup, forage and animal feed silage. The utilization of sorghum stalk as fuel oil (bioethanol) is an energy increasingly needed by the depletion of deposits of fossil fuel oil. Thus, tools and methods are needed to produce sorghum stem bioethanol, which has a certain purity level. This study aims to increase the purity of bioethanol from sorghum stems using the Bernoulli Distillation System (BDS) by experimentally testing the purification of sorghum stem bioethanol. In the bioethanol purification stage, heat transfer in the reactor and condenser was analyzed, and the performance of the ejector was analyzed with a vacuum pressure (-55 cmHg), temperature 71°C, test time of 1800, 3600, 5400 and 7200 seconds with a test material of 28% capacity 20 liters. The results of the analysis of the highest conduction heat transfer on the water jacket wall are 14757.72 Joules, the reactor tank is 962.1 Joules, the bottom of the reactor

tank is 765.05 Joules and convection in the reactor fluid is 2.09 Joules. The highest heat transfer energy in the condenser is 72683.1 Joules. While the efficiency of the water jet ejector is 65.4%, the highest increase in bioethanol content is 51% in 3600 seconds, as much as 745 ml. The characteristics of the bioethanol obtained included a calorific value test of 1389.48 cal/gram, a viscosity of 1.02044, a flash point of 32.5°C, and a

ARTICLE INFO

Article history:

Received: 03 September 2023

Accepted: 12 April 2024

Published: 09 October 2024

DOI: <https://doi.org/10.47836/pjst.32.6.02>

E-mail addresses:

djokowahyudi@gmail.com (Djoko Wahyudi)

wignyanto@ub.ac.id (Wignyanto)

yusufhendrawan@gmail.com (Yusuf Hendrawan)

hamidi@ub.ac.id (Nurkholis Hamidi)

* Corresponding author

density of 0.934 g/cm³. Thus, the Bernoulli Distillation System's purification process can increase bioethanol levels effectively and efficiently.

Keywords: Bioethanol purification, heat transfer energy, sorghum stalk

INTRODUCTION

Bioethanol is a type of alternative energy that can be used in engines as a source of heat energy. Bioethanol raw materials can be obtained from plants. One of the plants that has the potential to be processed into bioethanol is sorghum (Malherbe et al., 2023). In Indonesia, sorghum can be found on Java, Kalimantan, Sulawesi, and Nusa Tenggara islands. Sorghum contains relatively high glucose and has a much higher biomass production when compared to sugar cane (Ndapamuri et al., 2021). If viewed from the harvest cycle, sorghum can be harvested earlier than sugarcane. The harvest cycle of sorghum is around 4 months, while that of sugar cane is 7 months. In terms of physical properties, sorghum has a glucose content of 11%–16% and 10%–14.4% sucrose, while sugarcane contains 10%–18% and 9%–17% sucrose. The glucose content is quite high in sorghum, so sorghum has the potential to be developed as a bioethanol product (Suryaningsih & Irhas, 2014).

Processing is required to convert sorghum into bioethanol. Generally, sorghum processing into bioethanol can be carried out through separation and purification (Kartawiria et al., 2015). It is done to produce optimal bioethanol products. The optimal product can be seen from the resulting bioethanol product's yield and physical and chemical properties (Nnaemeka et al., 2021). Separating and purifying raw materials into bioethanol is carried out during the distillation stage (Chen & Fu, 2016). However, the distillation stage requires concrete and renewable innovation because the bioethanol products are still average and have low alcohol content, causing high production costs. Therefore, it is necessary to research the bioethanol production process. Bioethanol production is still being done using a simple distillation system. The simple distillation process produces bioethanol products that are low in yield and alcohol content. Therefore, further research is needed to increase the yield and alcohol content. One way that can be done is by using a vacuum distillation system.

Vacuum distillation has the advantage of being able to separate two or more fluid components based on differences in their boiling points (Luyben, 2022). The boiling liquid converts to vapor. Steam is flowed into the condensate to be cold-treated so that it becomes a liquid fluid. However, liquid fluids that have lower boiling points will evaporate first. The boiling point of pure ethanol is 78°C, and water's is 100°C (standard conditions). At 78°C, ethanol evaporates first, followed by water. Vacuum distillation reduces the air pressure in the distillation so that the boiling point of the separated compounds is lower than the boiling point at normal atmospheric pressure (Benedetto et al., 2018; Sippola & Taskinen, 2018). Thus, these compounds can be separated more easily. Bioethanol production is processed using vacuum distillation using a vacuum system reactor. A vacuum distillation reactor functions

to convert xylose compounds or glucose into bioethanol (Aditiya et al., 2016). However, the vacuum distillation process cannot be separated from the heat transfer scheme. Heat transfer in the reactor will determine the resulting bioethanol product (Almeida et al., 2021). Heat transfer is a form of energy transfer that moves from a system to the environment or the surrounding system. So, heat can move across the boundary of one system to another. Heat transfer occurs due to the difference in temperature between the system and its surroundings (Jiaqiang et al., 2018). Research is needed on the heat rate that has reacted with the material used to determine the heat transfer. Two factors, namely the material and the rate of heat transfer, determine the resulting bioethanol product (Zabed et al., 2017).

Quality bioethanol can be produced through the right process by calculating convection heat transfer. Proper thermal energy is needed to convert glucose into bioethanol products (Chandan et al., 2022). If the thermal treatment is less than or exceeds the limit, it will change the structure of glucose so that the resulting bioethanol product does not comply with established standards. Changing the glucose structure damages the carbon chains, so the resulting calorific value becomes low. The heat transfer rate can be calculated by calculating the total heat transfer in the surface area subject to heat (Allan et al., 2022). Data on the temperature of the incoming and outgoing fluids, the total heat transfer coefficient, the total heat transfer rate, and other supporting data are needed to obtain data on the total heat transfer rate. This data can be known by calculating the energy balance between hot and cold fluids, ignoring heat transfer that occurs to the environment and changes in kinetic and potential energy.

Similar research was conducted by Li et al. (2023). The research examined optimizing heat transfer and temperature control of battery thermal management systems based on composite phase change materials. The results of the study stated that if two objects with different temperatures are placed in contact with each other, heat will flow from the object with a higher temperature to the object with a lower temperature. This instantaneous heat transfer is always in the direction that tends to equalize the temperature. If this is allowed, the temperatures of the two will be the same, and both are said to be in a state of thermal equilibrium, meaning no heat transfer occurs between the two.

Xiao et al. (2023), in their research entitled "Effects of circumferential heat conduction on heat transfer characteristics of supercritical R134a in horizontal tubes," simulated supercritical heat transfer of R134a in horizontal tubes in order to study the effect of circular heat conduction on heat transfer damage, and the phenomenon of abnormal temperature distribution that is higher than the flow non-gravitational supercritical is described. The results show that heat transfer deterioration is due to specific heat disturbance and heat conduction in the boundary layer. In contrast, heat transfer is due to increased thermal conduction and turbulent convection after recovery. A dimensionless parameter Biot number is defined to characterize the thermal resistance ratio of a differential conductive environment to convective heat transfer. The redistribution of wall temperature due to

conduction entails circumferential influences supercritical convection in the horizontal tube. Non-gravitational supercritical flow may have higher wall temperatures when the Bi number is small. Top surface damage can be significantly reduced in tubes with greater wall thickness or thermal conductivity.

Murshed presents a cutting-edge review of the research and development of the conduction (thermal conductivity) and convection heat transfer characteristics of ethylene glycol-based nanofluids. Methods of preparation and stabilization of nanofluids are summarized and discussed. The effects of nanoparticle type, size and concentration, as well as temperature, on the thermal conductivity of nanofluids based on available ethylene glycol and ethylene glycol/water mixtures have been analyzed and discussed critically and individually. Studies on convective heat transfer of these nanofluids have also been reviewed, and results from different studies have been compared. The review clearly shows that this nanofluid has much higher thermal conductivity and convective heat transfer characteristics compared to its base fluid, i.e., ethylene glycol and aqueous mixtures. The thermal features of these nanofluids are a key factor for their performance in thermal management and energy applications. With their enhanced thermal conductivity and convective heat transfer coefficient, nanofluids offer great potential in energy harvesting and storage as well as for advanced cooling applications (Murshed & Castro, 2016).

Effendy et al. (2013) conducted a study entitled “Effect of mesh topologies on wall heat transfer and pressure loss prediction of a blade coolant passage.” The results showed that the manufacture of grid mesh greatly influenced the heat transfer coefficient and pressure loss. In addition, according to Manente et al. (2022), wasted heat energy can be reduced by placing heat insulation around the reactor.

Gholinia et al. (2018) researched the water jacket to find the temperature on the water jacket wall. The results showed that the temperature of the water jacket along the height of the combustion chamber wall increased until it reached its boiling point. However, the temperature gradient decreases when the water jacket flow is higher. Further research is necessary based on the description above and the research done. This study analyzes the heat transfer energy in the reactor and condenser and the effectiveness of the ejector in bioethanol purification to increase bioethanol content. Further research was conducted to optimize the production of bioethanol from sorghum stems. The research was carried out using thermal energy transfer testing. The research results analyze the thermal energy in the reactor and condenser. This study will discuss and analyze the scope of the research, including the reactor’s and condenser’s thermal energy for sorghum stalk bioethanol purification with a vacuum distillation system. The vacuum distillation system is used by applying the Bernoulli system so that the vacuum process does not use a vacuum pump. Thus, the tool designed is named the Bernoulli Distillation System (BDS). Applying the Bernoulli system in the form of a water ejector makes the bioethanol purification process maximally efficient and produces an increasing number of purified bioethanol products.

MATERIALS AND METHODS

The material used during the test was sorghum stalk bioethanol. However, before becoming bioethanol, treatment is required so that it goes through a fermentation process. The process of processing sorghum into bioethanol begins with the selection of quality sorghum materials. Quality sorghum is selected so that the resulting sap is optimal. Sorghum is pressed on the stem using a sugar press. The process of taking sorghum sap is shown in Figure 1. The result of pressing is sorghum sap. Then, the sorghum sap is continued with the fermentation process. The treatment used in this process is the Batch system.

Making sorghum bioethanol begins with heating the nira at 40°C for 10 minutes. After the heating process, *Saccharomyces cerevisiae* (yeast), NPK (Nitrogen, Phosphorus and Kalium), and Urea were added. *Saccharomyces cerevisiae* was added to 2% of the total mass of nira (m/m), 0.5% NPK (m/m), and 0.2% urea (m/m). Then, after adding it, it was stirred until evenly distributed. The nira and the mixture are placed in a container and fermented for seven days. In the fermentation process, carbohydrate feed was added so that the microbes grow and develop. After seven days, the distillation process is continued at 70°C. The resulting bioethanol product will be measured for its bioethanol content using an alcohol meter so that the value of the bioethanol content is known before the purification process is carried out. Figure 2 shows the scheme for making sorghum bioethanol.

The design of the bioethanol purification process tool in this study is one of the most important parts (Amornraksa et al., 2020). Success in testing is highly dependent on



Figure 1. A taking of sorghum stalk nira

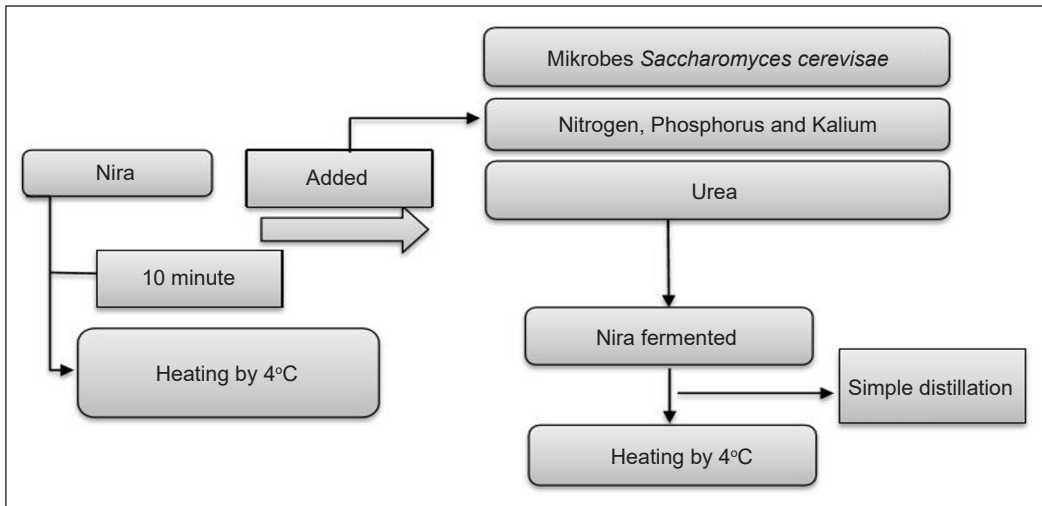


Figure 2. Bioethanol production process

how the initial design was planned for the tool to be made (Sivamani & Baskar, 2018). The specifications for the bioethanol purification tool designed are Double Jacket tubes with a 20-liter capacity and AISI 304 Stainless Steel (Stainless Steel has excellent corrosion resistance, making it suitable for use in environmental conditions containing hazardous chemicals and very high temperatures) (Yu et al., 2017). Meanwhile, the chemical composition of stainless steel 304 can be seen in Table 1.

Table 1
Chemical composition of stainless steel 304 (Fu et al., 2021)

Element	C	Mn	p	S	Si	Cr	Ni	N
Wt%	≤ 0.08	≤ 2.00	≤ 0.045	≤ 0.030	≤ 1.00	18.0-20.0	8.0–11.0	≤ 0.10

The research process requires selecting the appropriate method, collecting data, and processing and analyzing the data so that it becomes a conclusion that gives birth to new ideas. In this study, the research method was carried out experimentally. The experimental method is that the test is carried out by direct observation to identify a cause-and-effect relationship using several treatments. The test scheme can be observed in Figure 3.

The process of purifying bioethanol from sorghum stalks in this study used a device designed as shown in Figure 4. A vacuum distillation system is designed by applying the Bernoulli principle to the ejector so that the device does not use a vacuum pump; therefore, this tool is called the Bernoulli Distillation System (BDS). A double jacket in a reactor combines methods used in separation processes and chemical reactions involving low pressure. Adding a double jacket to the reactor aims to provide better temperature control for the ongoing chemical reactions. This method allows for more efficient separation of

requirements for heating. In addition, better temperature control in the reactor can also optimize energy use in chemical reactions.

Primary data from the test results was collected using a data logger. The data logger is a temperature control device with several components, including the Arduino Mega 2560, SD Card, Max 6675 Module, and Type K Thermocouple channel (Spinelli et al., 2019).

RESULTS AND DISCUSSION

Refining bioethanol from sorghum stalks showed maximum results, from 1800 seconds to 7200 seconds. Increased levels of bioethanol indicate that the tool is designed to function properly and efficiently. The material used in the purification process with a content of 28% bioethanol is 20 liters and has increased bioethanol levels as shown in Table 2, where the test for 1800 seconds showed that bioethanol content increased to 48% by 245 ml for 3600 seconds to 51% by 745 ml, for 5400% to 50% as much as 1245 ml, and 7200 seconds to 49% as much as 1645 ml.

Table 2
Heat transfer energy and levels of purified bioethanol

Time Test (second)	Conduction Heat Transfer Energy			Convection Heat Transfer Energy		Produced Bioethanol (ml)	Levels of Purified Bioethanol (%)
	Water Jacket Wall	Reactor Tank	Reactor Tank Base	Reactor Fluid	Condenser		
	(Joule)	(Joule)	(Joule)	(Joule)	(Joule)		
1800	-27407.20	663.51	700.70	1.94	33988.50	245	48
3600	-9487.10	962.10	765.05	2.09	66931.20	745	51
5400	8433.00	763.04	722.15	2.00	72683.10	1245	50
7200	14757.72	696.69	707.85	1.96	71637.30	1645	49

Heat Transfer Energy in Reactor

The results of the tests that have been carried out produce data on the values of the wall thermal resistance, the outer wall temperature value, and the inner wall temperature value of the water jacket, reactor tank, and reactor tank bottom. The resulting values are used to obtain conduction heat transfer energy values for the water jacket walls, reactor walls, and reactor wall base, carried out in 1800, 3600, 5400, and 7200 seconds.

Conduction Heat Transfer on the Water Jacket Wall: It is known that the highest temperature on the outer wall is 72°C at 5400 seconds, the highest temperature on the inner wall is 75.25°C at 7200 seconds, and the highest value of conduction heat transfer energy occurred at 7200 seconds with a value of 14757.72 J.

The highest temperature of conduction heat transfer in the reactor tank is known: the outer wall's highest temperature is 81.25°C, the inner wall's highest temperature is

81.04°C at 7200 seconds, and the highest conduction heat transfer energy value occurs at 3600 seconds, rated at 962.1 J.

The highest temperature on the outer wall is 77.98°C, and the highest on the inner wall is 76.97°C at 5400 seconds. The highest conduction heat transfer energy value occurs at 3600 seconds with a value of 765.05 J.

Figure 5 shows the conduction heat transfer on the water jacket wall; the outer wall temperature is 59°C, and the inner wall temperature is 52.5°C at 1800 seconds. From the calculation results, the energy value is (-27407.2) J. The same thing also occurs in the 3600-second conduction heat transfer, which produces an energy value of (-9487.1) J. In the heat transfer test on the energy-water jacket, a negative value means energy loss during the heat transfer (energy losses). The causes of negative energy can involve several factors, including heat radiation, unwanted thermal conduction, and inefficient convection (Vrugt, 2021).

At 5400 and 7200 seconds, the energy values resulting from the calculations show positive values, namely 5400 seconds of 8433 J and 7200 seconds of 14757.72 J. It indicates an energy or energy receipt increase during the heat transfer process. Factors for increasing energy include the addition of external energy and higher heat transfer efficiency (Bezaatpour & Rostamzadeh, 2020).

Figure 6, conduction heat transfer in the reactor tank, shows that the temperature of the reactor tank's outer wall and inner wall from 1800 seconds to 7200 seconds has almost the same increase. The temperature change that occurs at the same time between the outer wall and the inner wall is very small. Some things cause small changes in temperature, including:

1. Wall thickness

The thicker the wall, the greater the distance heat must travel and the smaller the temperature change. With thinner walls, the temperature change between the outer and inner walls will be more significant (Rakvin et al., 2014).

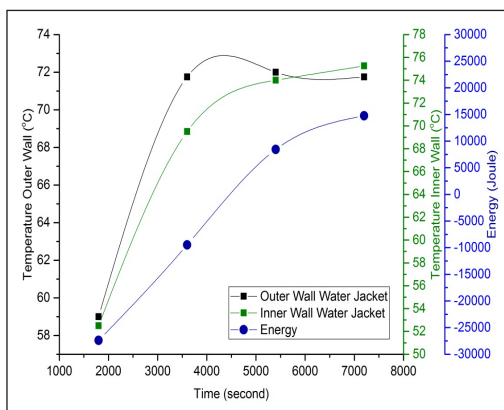


Figure 5. Conduction heat transfer on the water jacket wall

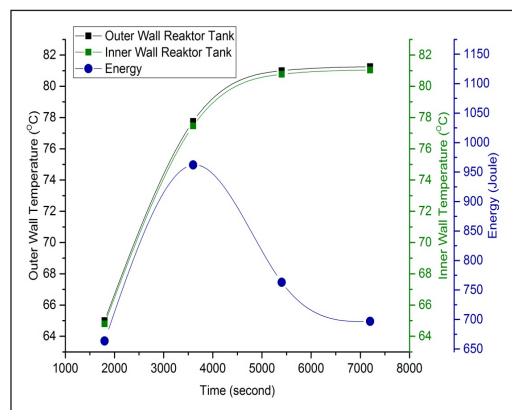


Figure 6. Conduction heat transfer in reactor tanks

2. Initial temperature difference

The initial temperature difference between the outer and inner walls of the reactor tank will also affect the temperature changes that occur in conduction heat transfer. If the initial temperature is close to equilibrium, the temperature change between the outer and inner walls will be very small.

3. Heat transfer coefficient

The heat transfer coefficient is a measure of the efficiency of heat transfer between two surfaces. The higher the heat transfer coefficient, the faster heat can be conducted and the smaller the temperature change. Factors such as surface conditions, fluid flow around the surface, and the fluid's thermal conductivity can affect the heat transfer coefficient (Dongliang et al., 2023).

Meanwhile, the energy generated from the calculation process is known to increase from 1800 to 3600 seconds by 298.59 J. The increase in energy is due to the difference in temperature between two objects that are interconnected. Suppose there is an increase in one of the objects. In that case, heat energy will flow from the object with a higher temperature to the object with a lower temperature, causing an increase in energy for the cooler object (Hu et al., 2023). Furthermore, at 5400 seconds, the energy decreased by 199.06 J; at 7200 seconds, the energy also decreased due to the shrinking temperature difference. The temperature difference between these objects is smaller, so the transfer of heat energy by conduction will be slower, and the energy transferred will be reduced.

Figure 7 shows the conduction heat transfer process on the outer wall of the reactor tank base, which shows an increase in temperature from 1800 seconds to 3600 seconds at 11.34°C. At the same time, a temperature rise of 11.25°C also occurred on the inner wall of the reactor tank base. In the next second, the temperature increase is 2.19°C on the outer wall and 2.25°C on the inner wall. However, at 7200 seconds, the temperature of the outer and inner walls decreased. Temperature rises due to temperature differences and materials' thermal conductivity. The increase and decrease in temperature is a form of thermal equilibrium between two objects that experience a difference in temperature (Wang et al., 2023).

From the results of the calculation analysis, it is known that the value of the heat transfer energy conduction at the base of the reactor tank for 1800 seconds is 700.70 J, 3600 seconds is 765.05 J, 5400 seconds is 722.15 J, and 7200 seconds is

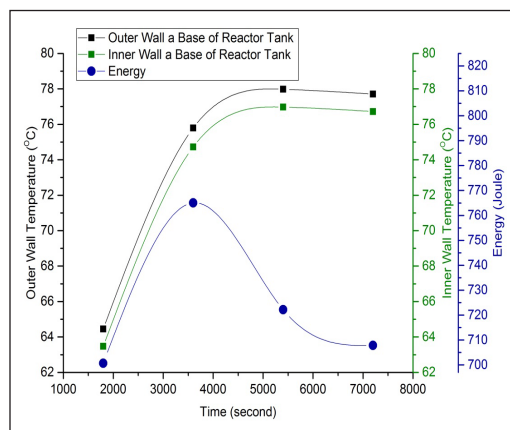


Figure 7. Conduction heat transfer at the base of the reactor tank

707.85 J. At 1800 seconds, 3600 experienced an increase of 64.35 Joules. The increase in energy is caused by a temperature difference between two interconnected objects. Suppose there is an increase in one object. In that case, heat energy will flow from the object with a higher temperature to the object with a lower temperature, causing an increase in energy in the cooler object (Murshed & Castro, 2016). Furthermore, at 5400 seconds and 7200 seconds, the energy produced tends to decrease due to a shrinking temperature difference. The temperature difference between these objects is smaller, so the transfer of heat energy by conduction will be slower, and the energy transferred will be reduced (Ellzey et al., 2019).

The results of the tests that have been carried out produce data on the values of the wall thermal resistance, the reactor wall temperature, and the reactor fluid temperature. The resulting value is used to obtain the energy value of convection heat transfer in the reactor fluid, carried out at 1800, 3600, 5400, and 7200 seconds.

From Table 3, convection heat transfer in the reactor fluid, it is known that the highest temperature on the reactor wall is 76.97°C, the highest temperature in the reactor fluid is 75.74°C at 5400 seconds, and the highest convection heat transfer energy value occurs at 600 seconds with a value of 2.09 J.

Figure 8 shows that the temperature of the inner wall of the reactor increased at 3600 seconds and 5400 seconds and decreased at 7200 seconds. The temperature of the walls in the reactor from 1800 seconds to 3600 seconds increased by 11.25°C; from 3600 seconds to 5400 seconds, it increased by 2.25°C; and from 5400 seconds to 7200 seconds, the temperature dropped by 0.25°C. The temperature rise is due to differences in temperature and materials' thermal conductivity (Anh & Pásztor, 2021). The increase and decrease in temperature is a form of thermal equilibrium between two objects (the outer wall and inner wall) of the reactor tank that experience a temperature difference, which is a conduction heat transfer process (Scotch et al., 2021).

Meanwhile, the temperature of the fluid also increases and decreases, as does the temperature of the reactor wall. The temperature of the reactor fluid from 1800 seconds to 3600 seconds increased by 11.16°C; from 3600 seconds to 5400

Table 3
Convection heat transfer in reactor fluids

Time (second)	Temperature (°C)		Energy (J)
	Reactor Wall	Reactor Fluids	
1800	63.47	62.27	1.94
3600	74.72	73.43	2.09
5400	76.97	75.74	2.00
7200	76.72	75.51	1.96

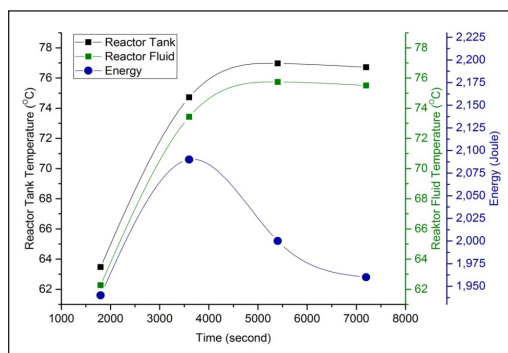


Figure 8. Convection heat transfer in reactor fluids

seconds, it increased by 2.31°C; and from 5400 seconds to 7200 seconds, the temperature decreased by 0.23°C. The temperature increase in the bioethanol fluid can occur due to convection heat transfer from the wall to the reactor fluid. The higher the reactor wall temperature and the higher the temperature difference between the wall and the fluid, the greater the convection heat transfer rate. Reducing the temperature of the reactor wall against the bioethanol fluid can occur by cooling or heat release from the reactor wall to the bioethanol fluid. If the temperature of the reactor wall is higher than the temperature of the bioethanol fluid, heat will flow from the reactor wall to the bioethanol fluid (Morales et al., 2021).

Furthermore, from the results of the calculation of the convection heat transfer energy between the inner wall of the reactor tank and the bioethanol fluid, at 1800 seconds, it was 1.94 Joules. At 3600 seconds, it was 2.09 joules, which experienced an increase in energy of 0.19 Joules. The increase in energy can be affected by temperature differences, as seen in Table 3. Then, at 5400 seconds and 7200 seconds, the energy decreased by 2.00 Joules and 1.96 joules, respectively. Changes in fluid properties can cause energy reduction in convection heat transfer. Fluid properties such as viscosity, thermal conductivity, or density can change with temperature, pressure, or composition changes. This change can affect the efficiency of convection heat transfer so that the energy transferred by convection can be reduced (Yang et al., 2023).

Heat Transfer Energy in the Condenser

The vapor fluid resulting from the distillation process in the reactor tube will then undergo condensation in the condenser tube. This phenomenon is a heat transfer process using the forced convection method (Wang et al., 2022) between the water fluid that touches the condenser pipe wall and bioethanol vapor. Forced convection heat transfer occurs in the condenser at 1800, 3600, 5400, and 7200 seconds.

Table 4 shows the convection heat transfer in the condenser: the highest inlet steam fluid temperature is 60°C, the highest inlet cooling water temperature is 25.25°C, and the highest energy is 72683.1 Joules at 5400 seconds.

Figure 9 shows the temperature of the steam fluid entering the condenser from the test results at 1800 seconds of 41.00°C, 3600 seconds of 55.25°C, 5400 seconds of 60.00°C, and 7200 seconds of 59.00°C. As previously described, the steam fluid obtained from the reactor produces fluids with different temperatures. The temperature

Table 4
Convection heat transfer in condensers

Time (second)	Temperature (°C)		Energy (J)
	Inlet Vapor Fluid	Incoming Cooling Water	
1800	41.00	24.75	33988.5
3600	55.25	23.25	66931.2
5400	60.00	25.25	72683.1
7200	59.00	24.75	71637.3

difference in the vapor fluid is caused by an energy balance process between the reactor's inner wall and the bioethanol fluid in the reactor during the bioethanol purification process.

The temperature of the cooling water entering the condenser from the test results at 1800 seconds was 24.75°C, 3600 seconds was 23.25°C, 5400 seconds was 25.25°C, and 7200 seconds was 24.75°C. The temperature of the cooling water entering the condenser increases and decreases due to variations in the cooling load. Changes

in the cooling load in the cooling system can cause fluctuations in the cooling water temperature in the condenser. If the cooling load increases, for example, due to an increase in cooling temperature requirements, the cooling water temperature tends to rise because it has to absorb more heat from the condenser. Conversely, the cooling water temperature decreases if the cooling load decreases. Meanwhile, the heat energy in the condenser from the calculation results is known at the 1800th second as 33988.5 Joules, the 3600th second as 66931.2 Joules, the 5400th second as 72683.1 Joules, and the 7200th second as 71637.3 Joules. The energy generated in 1800, 3600, and 5400 seconds has increased, while at 7200 seconds, it has decreased. Variations in the inlet steam temperature affect the increase and decrease in energy. If the temperature of the steam entering the condenser rises, the energy carried by the steam will also increase. It will cause an increase in energy in the condenser. Conversely, if the temperature of the inlet steam drops, the energy carried by the steam will decrease, causing a decrease in energy in the condenser. By using a data logger, it is known that the test results every second for 7200 seconds show that the forced convection heat transfer energy that occurs in the condenser is increasing.

Figure 10 shows the forced convection heat transfer energy in the condenser. Testing for 1800 seconds, the forced convection heat transfer energy at the beginning of the process experienced a decrease in energy from 25000 to 15000 Joules in the 300th second, then experienced an energy increase of 15000 to 42000 Joules in the 1350th second. Likewise, the energy value has increased and decreased in the following seconds, namely for 3600, 5400, and 7200 seconds. Variations influence the increase and decrease in energy in the inlet steam temperature. If the temperature of the steam entering the condenser rises, the energy carried by the steam will also increase. It will cause an increase in energy in the condenser. Conversely, if the temperature of the inlet steam drops, the energy carried by the steam will decrease, causing a decrease in energy in the condenser.

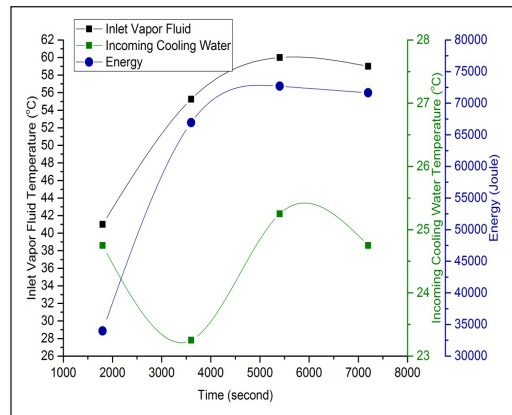


Figure 9. Forced convection heat transfer energy in the condenser

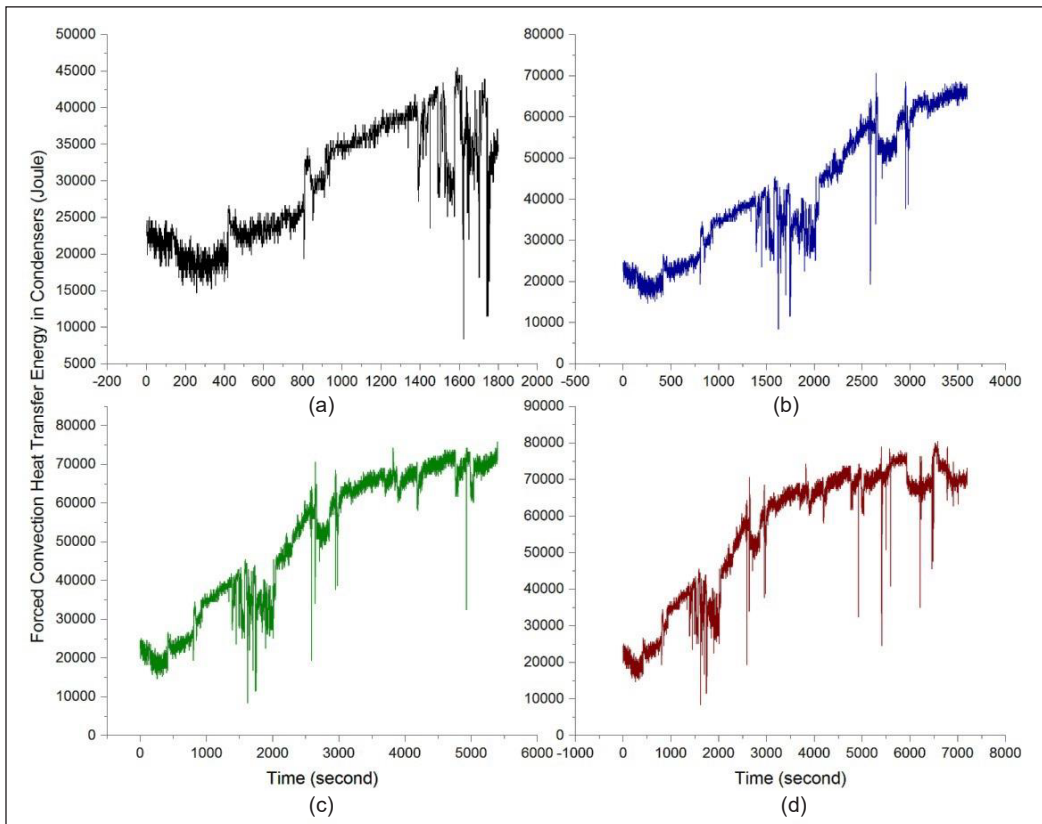


Figure 10. Forced convection heat transfer energy in the condenser: (a) Test for 1800 seconds; (b) Test for 3600 seconds; (c) Test for 5400 seconds; and (d) Test for 7200 seconds

Water Jet Ejector Efficiency

The results of the analysis of the performance of the ejector at a content of 28% bioethanol material show that the Mach Number is the same as 2.75 according to the classification as Compressible Supersonic Flow. In this case, water is included in the supersonic compressible fluid category, which means that it can be compressed and has the ability to flow at speeds that exceed the speed of sound (Dai et al., 2023). In supersonic conditions, the airflow around objects will experience complex changes and cause different aerodynamic effects compared to airflow at subsonic speeds. In supersonic conditions, the air stream is significantly compressed because its pressure increases with speed (Kong & Kim, 2016).

In this case, the water ejector performance efficiency value of 65.4% means that the ejector can produce around 65.4% of the theoretical maximum work that can be achieved under ideal conditions. High-performance efficiency in the water ejector is very important to ensure effective and efficient performance in sucking gas or steam from the surrounding space. The higher the performance efficiency value, the greater the ability of the ejector to

produce maximum and effective work. Several factors affect the performance efficiency of a water ejector, including ejector design, operating fluid pressure, characteristics of the gas or vapor being sucked, and pressure losses in pipes and other components. The performance efficiency of the water jet ejector can produce maximum and effective work in the bioethanol purification process, one of which can be identified by knowing the products produced by the system. After testing the purified bioethanol product, the levels of bioethanol increased.

From Figure 11, it is known that the bioethanol produced always experiences an increase in volume. At 1800 seconds, it was 245 ml; at 3600 seconds, it was 745 ml; at 5400 seconds, it was 1245 ml; and at 7200 seconds, it was 1645 ml. It shows that the bioethanol purification production process went well and efficiently. Meanwhile, the bioethanol content increased from 1800 to 3600 seconds by 48% and 51%, respectively. However, in the next second, the value of the bioethanol content decreased until the end of the purification process.

The increase and decrease in levels of purified bioethanol can be seen from the composition of the raw materials (initial bioethanol) used in the production of bioethanol, which can vary from time to time (Loh et al., 2023). If the raw material composition changes, this can affect the purification process for a predetermined time and temperature and produce different levels of bioethanol. Even though the volume of bioethanol increases, the value of the ethanol content can fluctuate.

Sorghum bioethanol was purified for 2700 seconds, then tested at the Motor Fuel Laboratory, Brawijaya University, Malang, to determine the characteristics of the bioethanol obtained, including the calorific value (cal/gram), viscosity, flash point ($^{\circ}\text{C}$), and density (g/cm^3).

The resulting calorific value of 1389.48 cal/gram in bioethanol will affect the combustion process and the energy efficiency produced from this fuel (Table 5).

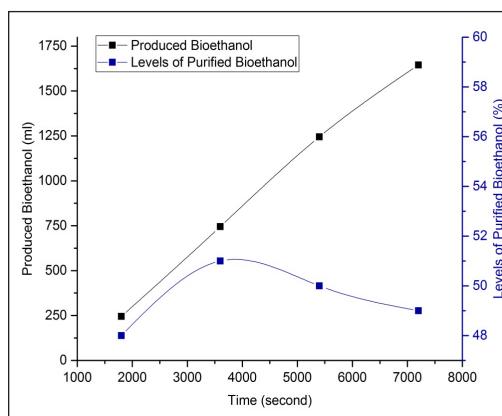


Figure 11. Levels of purified bioethanol

Table 5

Physical properties of bioethanol

No	Standard Bioethanol	Calorific Value (cal/gram)	Viscosity	Flash Point ($^{\circ}\text{C}$)	Density (g/cm^3)	Reference
1	ASTM D8406	7092.1	1.2–1.5	12	0.7805	Sebayang et al., 2016; Yusuf & Inambao, 2019
2	SNI	6380	1.525	12	0.7890	ESDM RI, 2008
3	Purification Results Bioethanol	1389.48	1.02	32.5	0.9340	This Paper

When bioethanol is burned with oxygen in the combustion process, a chemical reaction produces heat and gases such as carbon dioxide and water vapor. The high calorific value indicates that bioethanol will release more energy per gram during combustion. Bioethanol with a viscosity of 1.02044 shows the level of viscosity of the liquid. The effect of viscosity on the combustion process can affect several aspects, although not as much as the effect of the heating value. The flash point is the minimum temperature at which a fuel, such as bioethanol, will produce enough vapor to form an air-fuel mixture that can temporarily ignite if exposed to flame but does not continue to burn after the flame is removed. In the case of bioethanol, the flash point of 32.5°C indicates that at that temperature, bioethanol will give off steam, which can form a flammable mixture if there is a heat source or fire nearby. Density is a measure of mass per unit volume of a material. Bioethanol with a density of 0.934 g/cm³ shows a weight of 0.934 grams of bioethanol contained in every cubic centimeter (cm³) of volume.

CONCLUSION

This research used the Bernoulli Distillation System (BDS) to increase bioethanol levels by analyzing heat transfer energy in the reactor and condenser and the ejector jet's performance efficiency. Based on research results and analysis of heat transfer energy, the Bernoulli Distillation System for 4 times the test time showed an increase in the percentage value of bioethanol content, namely 48%, 51%, 50% and 49%. The highest percentage value of bioethanol content, namely 51%, was obtained in 3600 seconds, the conduction heat transfer energy on the water jacket wall was (-9487.10) J, the reactor tank was 962.10 J, the reactor tank bottom was 765.05 J, the transfer energy the convection heat in the reactor fluid was 2.09 J and the condenser was 66931.20 J. In addition, according to the test results for 2700 seconds, the physical properties of bioethanol were produced, namely a heating value of 1389.48 (cal/gram), viscosity of 1.02, flash point of 32.5 (°C) and density of 0.934 (g/cm³). Therefore, this bioethanol purification tool is the right tool and has the potential to be developed and further used for other bioethanol purification.

ACKNOWLEDGEMENTS

The authors thank those who have contributed and supported them throughout their journey of completing the study. The authors would also like to extend their gratitude to Universiti Brawijaya, Indonesia, for providing the research facilities.

REFERENCES

- Aditiya, H. B., Mahlia, T. M. I., Chong, W. T., Nur, H., & Sebayang, A. H. (2016). Second generation bioethanol production: A critical review. *Renewable and Sustainable Energy Reviews*, 66, 631–653. <https://doi.org/10.1016/j.rser.2016.07.015>

- Allan, J., Croce, L., Dott, R., Georges, G., & Heer, P. (2022). Calculating the heat loss coefficients for performance modelling of seasonal ice thermal storage. *Journal of Energy Storage*, 52(PA), Article 104528. <https://doi.org/10.1016/j.est.2022.104528>
- Almeida, L. P., Silva, C. R., Martins, T. B., Pereira, R. D., Esperança, M. N., Cruz, A. J. G., & Badino, A. C. (2021). Heat transfer evaluation for conventional and extractive ethanol fermentations: Saving cooling water. *Journal of Cleaner Production*, 304, Article 127063. <https://doi.org/10.1016/j.jclepro.2021.127063>
- Amornraksa, S., Subsaipin, I., Simasatitkul, L., & Assabumrungrat, S. (2020). Systematic design of separation process for bioethanol production from corn stover. *BMC Chemical Engineering*, 2(1), Article 10. <https://doi.org/10.1186/s42480-020-00033-1>
- Anh, L. D. H., & Pásztor, Z. (2021). An overview of factors influencing thermal conductivity of building insulation materials. *Journal of Building Engineering*, 44, Article 102604. <https://doi.org/10.1016/j.job.2021.102604>
- Benedetto, A. D., Sanchirico, R., & Sarli, V. D. (2018). Effect of pressure on the flash point of various fuels and their binary mixtures. *Process Safety and Environmental Protection*, 116, 615–620. <https://doi.org/10.1016/j.psep.2018.03.022>
- Bezaatpour, M., & Rostamzadeh, H. (2020). Heat transfer enhancement of a fin-and-tube compact heat exchanger by employing magnetite ferrofluid flow and an external magnetic field. *Applied Thermal Engineering*, 164, Article 114462. <https://doi.org/10.1016/j.applthermaleng.2019.114462>
- Chandan, R. R., Aditya, C. R., Elankeerthana, R., Anitha, K., Sabitha, R., Sathyamurthy, R., Mohanavel, V., & Sudhakar, M. (2022). Machine learning technique for improving the stability of thermal energy storage. *Energy Reports*, 8, 897–907. <https://doi.org/10.1016/j.egy.2022.09.205>
- Chen, H., & Fu, X. (2016). Industrial technologies for bioethanol production from lignocellulosic biomass. *Renewable and Sustainable Energy Reviews*, 57, 468–478. <https://doi.org/10.1016/j.rser.2015.12.069>
- Dai, C., Sun, B., Yue, L., Zhou, S., Zhuo, C., Zhou, C., & Yu, J. (2023). Thermochemical non-equilibrium flow characteristics of high Mach number inlet in a wide operation range. *Chinese Journal of Aeronautics*, 36(12), 164–184. <https://doi.org/10.1016/j.cja.2023.07.033>
- Dongliang, M., Yi, L., Tao, Z., & Yanping, H. (2023). Research on prediction and analysis of supercritical water heat transfer coefficient based on support vector machine. *Nuclear Engineering and Technology*, 55(11), 4102–4111. <https://doi.org/10.1016/j.net.2023.07.030>
- Effendy, M., Yao, Y., & Yao, J. (2013). Effect of mesh topologies on wall heat transfer and pressure loss prediction of a blade coolant passage. *Applied Mechanics and Materials*, 315, 216–220. <https://doi.org/10.4028/www.scientific.net/AMM.315.216>
- Ellzey, J. L., Belmont, E. L., & Smith, C. H. (2019). Heat recirculating reactors: Fundamental research and applications. *Progress in Energy and Combustion Science*, 72, 32–58. <https://doi.org/10.1016/j.pecs.2018.12.001>
- ESDM RI. (2008). *Keputusan Direktur Jenderal Minyak dan Gas Bumi* [Decision of the Director General of Oil and Gas]. (Report no. 23204.K/10/DJM.S/2008). Ministry of Energy and Mineral Resources Republic of Indonesia.

- Fu, P., Hu, B., Lan, X., Yu, J., & Ye, J. (2021). Simulation and quantitative study of cracks in 304 stainless steel under natural magnetization field. *NDT and E International*, *119*, Article 102419. <https://doi.org/10.1016/j.ndteint.2021.102419>
- Gholinia, M., Pourfallah, M., & Chamani, H. R. (2018). Numerical investigation of heat transfers in the water jacket of heavy duty diesel engine by considering boiling phenomenon. *Case Studies in Thermal Engineering*, *12*, 497–509. <https://doi.org/10.1016/j.csite.2018.07.003>
- Hu, J., Guo, L., Yang, H., He, X., & Luo, Y. (2023). Improvement methods for thermal backflow phenomenon in engine compartment blow-type air cooler module. *Case Studies in Thermal Engineering*, *49*, Article 103182. <https://doi.org/10.1016/j.csite.2023.103182>
- Jiaqiang, E., Zhang, Z., Tu, Z., Zuo, W., Hu, W., Han, D., & Jin, Y. (2018). Effect analysis on flow and boiling heat transfer performance of cooling water-jacket of bearing in the gasoline engine turbocharger. *Applied Thermal Engineering*, *130*, 754–766. <https://doi.org/10.1016/j.applthermaleng.2017.11.070>
- Kartawiria, I. S., Syamsu, K., Noor, E., & Sa'Id, E. G. (2015). Sorghum stalk juice pre-treatment method for bioethanol fermentation process. *Energy Procedia*, *65*, 140–145. <https://doi.org/10.1016/j.egypro.2015.01.047>
- Kong, F., & Kim, H. D. (2016). Optimization study of a two-stage ejector-diffuser system. *International Journal of Heat and Mass Transfer*, *101*, 1151–1162. <https://doi.org/10.1016/j.ijheatmasstransfer.2016.05.129>
- Li, Z., Liang, Z., Wang, C., & Wu, T. (2023). Optimization of heat transfer and temperature control of battery thermal management system based on composite phase change materials. *Surfaces and Interfaces*, *36*, Article 102621. <https://doi.org/10.1016/j.surfin.2022.102621>
- Loh, S. R., Tan, I. S., Foo, H. C. Y., Tan, Y. H., Lam, M. K., & Lim, S. (2023). Exergy analysis of a holistic zero waste macroalgae-based third-generation bioethanol biorefinery approach: Biowaste to bioenergy. *Environmental Technology and Innovation*, *30*, Article 103089. <https://doi.org/10.1016/j.eti.2023.103089>
- Luyben, W. L. (2022). Optimum vacuum distillation pressure. *Chemical Engineering and Processing - Process Intensification*, *171*, Article 108630. <https://doi.org/10.1016/j.cep.2021.108630>
- Malherbe, S. J. M., Cripwell, R. A., Favaro, L., Zyl, W. H. V., & Viljoen-Bloom, M. (2023). Triticale and sorghum as feedstock for bioethanol production via consolidated bioprocessing. *Renewable Energy*, *206*, 498–505. <https://doi.org/10.1016/j.renene.2023.02.047>
- Manente, G., Ding, Y., & Sciacovelli, A. (2022). A structured procedure for the selection of thermal energy storage options for utilization and conversion of industrial waste heat. *Journal of Energy Storage*, *51*, Article 104411. <https://doi.org/10.1016/j.est.2022.104411>
- Morales, M., Arvesen, A., & Cherubini, F. (2021). Integrated process simulation for bioethanol production: Effects of varying lignocellulosic feedstocks on technical performance. *Bioresource Technology*, *328*, Article 124833. <https://doi.org/10.1016/j.biortech.2021.124833>
- Murshed, S. M. S., & Castro, C. A. N. D. (2016). Conduction and convection heat transfer characteristics of ethylene glycol based nanofluids – A review. *Applied Energy*, *184*, 681–695. <https://doi.org/10.1016/j.apenergy.2016.11.017>

- Ndapamuri, M. H., Herawati, M. M., & Meitiniarti, V. I. (2021). Production of sugar from sweet sorghum stems with hydrolysis method using *trichoderma viride*. *Biosaintifika*, *13*(1), 121–127. <https://doi.org/10.15294/biosaintifika.v13i1.25954>
- Nnaemeka, I. C., Egbuna Samuel, O., Onoh Maxwell, I., Christain, A. O., & Chinelo S, O. (2021). Optimization and kinetic studies for enzymatic hydrolysis and fermentation of *colocynthis vulgaris* Shrad seeds shell for bioethanol production. *Journal of Bioresources and Bioproducts*, *6*(1), 45–64. <https://doi.org/10.1016/j.jobab.2021.02.004>
- Rakvin, M., Markučić, D., & Hižman, B. (2014). Evaluation of pipe wall thickness based on contrast measurement using Computed Radiography (CR). *Procedia Engineering*, *69*, 1216–1224. <https://doi.org/10.1016/j.proeng.2014.03.112>
- Scotch, C. G., Murgulet, D., & Constantz, J. (2021). Time-series temperature analyses indicate conduction and diffusion are dominant heat-transfer processes in fine sediment, low-flow streams. *Science of the Total Environment*, *768*, Article 144367. <https://doi.org/10.1016/j.scitotenv.2020.144367>
- Sebayang, A. H., Masjuki, H. H., Ong, H. C., Dharma, S., Silitonga, A. S., Mahlia, T. M. I., & Aditiya, H. B. (2016). A perspective on bioethanol production from biomass as alternative fuel for spark ignition engine. *RSC Advances*, *6*(18), 14964–14992. <https://doi.org/10.1039/c5ra24983j>
- Sippola, H., & Taskinen, P. (2018). Activity of supercooled water on the ice curve and other thermodynamic properties of liquid water up to the boiling point at standard pressure. *Journal of Chemical and Engineering Data*, *63*(8), 2986–2998. <https://doi.org/10.1021/acs.jced.8b00251>
- Sivamani, S., & Baskar, R. (2018). Process design and optimization of bioethanol production from cassava bagasse using statistical design and genetic algorithm. *Preparative Biochemistry and Biotechnology*, *48*(9), 834–841. <https://doi.org/10.1080/10826068.2018.1514512>
- Spinelli, G. M., Gottesman, Z. L., & Deenik, J. (2019). A low-cost arduino-based datalogger with cellular modem and FTP communication for irrigation water use monitoring to enable access to CropManage. *HardwareX*, *6*, Article e00066. <https://doi.org/10.1016/j.ohx.2019.e00066>
- Suryaningsih, R., & Irhas. (2014). Bioenergy plants in indonesia: Sorghum for producing bioethanol as an alternative energy substitute of fossil fuels. *Energy Procedia*, *47*, 211–216. <https://doi.org/10.1016/j.egypro.2014.01.216>
- Vrugt, M. T. (2021). The mereology of thermodynamic equilibrium. *Synthese*, *199*(5–6), 12891–12921. <https://doi.org/10.1007/s11229-021-03359-2>
- Wang, C. H., Liu, Z. Y., Jiang, Z. Y., & Zhang, X. X. (2022). Numerical investigations of convection heat transfer in a thermal source-embedded porous medium via a lattice Boltzmann method. *Case Studies in Thermal Engineering*, *30*, Article 101758. <https://doi.org/10.1016/j.csite.2022.101758>
- Wang, M., Bu, S., Zhou, B., Li, Z., & Chen, D. (2023). Multi-scale heat conduction models with improved equivalent thermal conductivity of TRISO fuel particles for FCM fuel. *Nuclear Engineering and Technology*, *55*(3), 1140–1151. <https://doi.org/10.1016/j.net.2022.12.001>
- Xiao, R., Zhang, Y., Chen, L., Wang, J., Chen, S., & Hou, Y. (2023). Effects of circumferential heat conduction on heat transfer characteristics of supercritical R134a in horizontal tubes. *International Journal of Thermal Sciences*, *183*, Article 107884. <https://doi.org/10.1016/j.ijthermalsci.2022.107884>

- Yang, Y., AL-Khafaji, M. O., Fazilati, M. A., Hassan Saeed, S., Salman, N. A., Abdulkadhim, A. H., Shaghnab, M. L., Gatea, M. A., Jawad, A. J. M., & Toghraie, D. (2023). Energy and exergy analysis of a liquid desiccant heat and mass transfer loop with natural convection: The effect of heat sink and heat source temperature. *Case Studies in Thermal Engineering*, 45, Article 102833. <https://doi.org/10.1016/j.csite.2023.102833>
- Yu, J., Ji, G., Liu, Q., Zhang, J., & Shi, Z. (2017). Effect of sol-gel ZrO₂ films on corrosion behavior of the 304 stainless steel in coal-gases environment at high temperature. *Surface and Coatings Technology*, 331, 21–26. <https://doi.org/10.1016/j.surfcoat.2017.10.037>
- Yusuf, A. A., & Inambao, F. L. (2019). Bioethanol production from different Matooke peels species: A surprising source for alternative fuel. *Case Studies in Thermal Engineering*, 13, Article 100357. <https://doi.org/10.1016/j.csite.2018.11.008>
- Zabed, H., Sahu, J. N., Suely, A., Boyce, A. N., & Faruq, G. (2017). Bioethanol production from renewable sources: Current perspectives and technological progress. *Renewable and Sustainable Energy Reviews*, 71, 475–501. <https://doi.org/10.1016/j.rser.2016.12.076>

Spectroscopic Analysis of Chrysotile Asbestos and its Environmental Resistance in Asbestos Cement Waste Products

Gergely Zoltán Macher^{1*}, Fanni Károly², Christopher Teh Boon Sung^{3,4}, Dóra Beke⁴, András Torma¹ and Szilveszter Gergely⁵

¹*Department of Applied Sustainability, Széchenyi István University, Hungary*

²*Faculty of Engineering, University of Pannonia, Hungary*

³*Department of Land Management, Faculty of Agriculture, Universiti Putra Malaysia, 43400 UPM, Serdang, Selangor, Malaysia*

⁴*Department of Plant Sciences, Széchenyi István University, Hungary*

⁵*Department of Applied Biotechnology and Food Science, Budapest University of Technology and Economics, Hungary*

ABSTRACT

Most asbestos-related studies have focused on asbestos exposure risks, their associated health implications, and waste management issues. Our research introduced a unique perspective that has rarely been explored: the impact of environmental factors on asbestos cement products. The novelty of the study is that, in contrast to previous research, in addition to determining the material quality of asbestos, it analyses the trace materials, additives and the emissive nature of chrysotile fibers. This study aims to identify the chrysotile-asbestos content in three common asbestos cement products found in Hungary, with regard to the release of their fibers upon exposure to the environment and to identify trace elements that could be used to identify the origin and function of each of these products. Our analyses revealed the presence of chrysotile in each tested sample, with spectral matches ranging

from 59.6% to 86.7%. Asbestos cement products exposed to various environmental influences for long periods showed a greater chrysotile emission capacity than those unexposed or hermetically sealed ones. Additionally, we established that all asbestos cement products contained glass fibers, with an average spectral match of 62.1%. We further identified polysilicate in the materials with an average spectral match of 66.0%, as it was included in asbestos cement

ARTICLE INFO

Article history:

Received: 08 September 2023

Accepted: 17 January 2024

Published: 09 October 2024

DOI: <https://doi.org/10.47836/pjst.32.6.03>

E-mail addresses:

macher.gergely.zoltan@sze.hu (Gergely Zoltán Macher)

ka.fanka1313@gmail.com (Fanni Károly)

chris@upm.edu.my (Christopher Teh Boon Sung)

beke.dora@sze.hu (Dóra Beke)

torma@ga.sze.hu (András Torma)

gergely.szilveszteredu@bme.hu (Szilveszter Gergely)

* Corresponding author

products to enhance their heat resistance. Our results pave the way for a new methodology for assessing asbestos cement products with regard to the implementation of their trace element level assessments.

Keywords: Asbestos, chrysotile asbestos, environmental resistance, FTIR, glass fiber, polysilicate

INTRODUCTION

Asbestos is a commercial term for a set of naturally occurring minerals with unique chemical and physical properties (Kusiorowski et al., 2023; Misseri, 2023). These minerals, including chrysotile, amosite, crocidolite, actinolite, tremolite, and anthophyllite, have fibrous appearances and are known as silicate minerals (Tóth & Weiszburg, 2011). They can be classified into two categories: serpentines (sheet silicates) and amphiboles (chain silicates) (Ristić et al., 2011). The term ‘asbestiform’ is often used to describe their fibrous morphology (Zholobenko et al., 2021). These minerals are characterized by their ability to be separated into long, silky fibers resistant to traction and heat and almost chemically inert (Malinconico et al., 2022).

Asbestos use can be traced back to ancient times (Lavento & Hornytkyj, 1995; Virta, 2005), but the understanding of the elemental compositions and crystal structures of amphibole and serpentine minerals has only spanned since the 19th century (Ross et al., 2008). Asbestos comprises hydrated silicates of magnesium, iron, calcium, and sodium. The chemical composition of amphibole asbestos (except chrysotile) is $M_7Si_8O_{22}(OH)_2$, with the “M” representing metal cations such as calcium, iron, magnesium, or sodium. Chrysotile, a serpentine mineral, has a distinctive $Mg_3Si_2O_5(OH)_4$ composition (Ross et al., 2008; Speil & Leineweber, 1969; Zholobenko et al., 2021). Serpentine minerals, including chrysotile, are characterized by their curved shape under a microscope, whereas amphiboles exhibit a straight and rigid morphology (Castro et al., 2003). Chrysotile comprises octahedral Mg and tetrahedral Si layers that bundle together to form a fiber with the outermost layer of Mg hydroxide (Bales & Morgan, 1985; Walter et al., 2022). This natural magnesia-silicate clay mineral has a distinct fibrous or tubular nanostructure comprising silica oxide tetrahedral sheets and brucite octahedral sheets in a 1:1 stoichiometric ratio. However, the lattice sizes of these two sheets differ, resulting in curly and fibrous structures that allow for lattice matching (Dubin et al., 2013; Liu et al., 2020). Chrysotile asbestos has exceptional splitting properties, allowing it to be separated into filaments with diameters as small as 1 to 2 μm (Wang et al., 2019).

Asbestos has been used in ancient times as a fire-resistant material (Røe & Stella, 2015). Its usage has become widespread during the industrial age (Janela & Pereira, 2016), particularly in chrysotile and crocidolite forms. The valuable properties of asbestos, such as high tensile strength, heat and fire resistance, electrical insulation, and chemical inertness

(Zholobenko et al., 2021), make it ideal for use as products in construction materials, automotive components, and fireproof textiles (Bartrip, 2004; Dodson &, 2011; Hassanpour et al., 2012). Asbestos production peaked in 1977, with around 4.8 million tons produced in 25 countries (Park et al., 2012). Between 1900 and 2015, approximately 210 million tons of asbestos were extracted globally. It has been used in over 3000 different products (Harris & Kahwa, 2003; Szeszenia-Dąbrowska, 2004), including sealants, brake pads, membranes, pipes, facade panels, roof coverings, filters, clothing, and fire retardant fabrics (Iwaszko et al., 2018). Asbestos-cement products have been used in Hungary since the 1940s, predominantly as roofing sheets and pipes. The compositions of these products vary internationally. For instance, Poland classifies them as soft (containing over 20% asbestos) or hard (< 20% asbestos) (Dyczek, 2007).

In Hungary, low binder asbestos products such as blown insulation contain 95% to 97% asbestos and 3% to 5% binder. Applications with a high binder content, such as asbestos-cement flat slate, corrugated slate, and water pipes, have 8% to 10% asbestos and 90% to 92% cement binder (Tóth & Weiszburg, 2011). Table 1 summarizes the general properties and characteristics of the asbestos-cement roofing elements widely used in Hungary and prepared according to Hungarian methodologies. Asbestos-cement products in Hungary typically use various tracers and additives, typically various polysilicates and glass fiber, to improve the final physical properties of the final product. Differences between countries

Table 1
General characteristics of small and large asbestos cement roofing elements

Main properties	Small asbestos cement roofing elements	Large asbestos cement roofing elements
Asbestos content (%)	8–10	8–10
Cement content (%)	90%–92%	90%–92%
Thickness (mm)	4	5
Length (cm)	30–40	160–250
Width (cm)	30–40	93
Weight (kg/m ²)	7,6	11,7
Flexural strength (MPa)	31	170
Heat resistance (°C)	200	200
Resistance to frost (°C)	-20	-20
Water absorption (%)	15	15–25
Resistance to dilute acids	No	No
Resistance to dilute brine	No	No
Resistance to oil	No	No
Resistance to petrol	No	No
Resistance to weak alkali	Yes	Yes
Thermal conductivity (W/mK)	0,65	0,651

Source: Székely et al., 1972

are clear, as Poland has asbestos fiber contents ranging from 10% to 11% for pressed flat panels, 10%–14% in corrugated sheets, and 14%–18% in asbestos-cement pipes (Dyczek, 2007; Raczko et al., 2022). Asbestos-based cement composites were installed globally in water mains, still forming a significant part of water distribution networks (Bahadori, 2016; Brandt et al., 2017; Zavašnik et al., 2022). Health concerns related to asbestos emerged in the early 20th century (Doll, 1993) and have led to its ban in many countries (Korda et al., 2017) due to associated health risks from inhaling asbestos fibers.

These risks include lung cancer, mesothelioma (Azuma et al., 2009; Currie et al., 2009; Goldberg & Luce, 2009; Zha et al., 2019), and asbestosis, with increasing related deaths (Harremoës et al., 2001; Murayama et al., 2006). The WHO (1986) defines asbestos fibers as having a length greater than 5 μm , a diameter less than 3 μm , and an aspect ratio of at least 3:1. Many health agencies have adopted this definition for asbestos fiber size (Thives et al., 2022). Asbestos materials' harmfulness and disposal challenges are now globally recognized, with over 75 countries banning their use owing to their carcinogenic potential (Santana et al., 2023; Stayner et al., 2013). Asbestos-related diseases cause around 100,000 deaths annually, including 15,000 in Europe and 12,000 in the United States (Iwaszko et al., 2018).

Despite this, asbestos-cement roofing components and artifacts remain in many buildings or are improperly disposed of in landfills (Carneiro et al., 2021). The lifespan of asbestos cement products is estimated at 30 to 40 years, though it varies due to differences in material and quality composition between countries. Punurai & Davis (2017) estimated a 70-year lifespan for asbestos-cement pipes, though, in Hungary, it is approximately 40 years, evidenced by increasing failures and pipe breaks. Scientific research on asbestos is extensive and is divided into various interdisciplinary fields, such as medicine and engineering (Thives et al., 2022). Despite the ubiquity of asbestos pollution as an environmental concern, the scientific literature remains scarce (Lisco et al., 2023). Asbestos-cement wastes pose a significant environmental challenge owing to the pathogenic properties of asbestos and the proliferation of products containing asbestos fibers (Iwaszko et al., 2018). More detailed information on fiber size and type in the environments is necessary to aid epidemiological studies. Developing and enhancing exposure metrics is crucial for accurately predicting asbestos-related disease risks (Berman & Crump, 2003). Ervik et al. (2021) analyzed asbestos fibers from a 60-year-old corrugated cement roof in Southern Norway. They discovered that numerous fibers in runoff water and weathered roof debris samples were prone to be carried away by the wind into the air and soil or washed out by rainwater (Thives et al., 2022).

Despite these findings, the number of asbestos tests conducted for environmental monitoring remains limited, with measurements primarily focused on air detection. The weathering of an asbestos cement sheet primarily depends on its main component (90%

cement), whereas the more resistant asbestos is increasingly exposed as the cement matrix wears away. As a result, weathered asbestos cement often has a higher potential to release fibers than unweathered cement, as more loosely bound fibers are exposed on the surface. In extreme cases, weathering may cause the surface to flake or crack, thereby increasing the area from which asbestos can be released into the air (Burdett, 2006). The resistance of chrysotile to acids is limited. Both the sulfuric acid in acid rain and the organic acids produced by molds, mosses, and lichens (Favero-Longo et al., 2005) interact with exposed chrysotile asbestos. Over time, these reactions progressively strip magnesium hydroxide from the chrysotile structure (Burdett, 2006; Hodgson & Darnton, 2000).

Consequently, the primary objectives of this study were (1) to determine the chrysotile content, which is a prevalent asbestos mineral (Landrigan, 1998), in several selected Hungarian-manufactured asbestos cement products, (2) to identify the trace elements present in these products, and (3) to analyze the differences in these products when exposed to or protected from environmental factors. The novelty of this research is underlined by the fact that most previous research has focused only on the qualitative characterization of asbestos (Malinconico et al., 2022; Rolfe et al., 2024; Tabata et al., 2022; Zholobenko et al., 2021). Typically, the role of trace elements, origin-specific analysis and environmental effects have been neglected segments. To achieve these goals, we employed Fourier transformation infrared (FTIR) and transmission electron microscopy (TEM) techniques on a pair of samples from each of three product groups: asbestos-cement pipes, flat slates, and corrugated slates, subjecting them to either direct environmental exposure for at least one year or hermetically sealing them to prevent exposure to the environment. We hypothesized that chrysotiles could be detected in all the asbestos cement samples, and the chrysotiles from samples exposed to environmental effects would be more easily detected because of their structural erosion. In addition, traces of specific additives were also searched, which have not been investigated by any research until now (Károly, 2022).

METHODOLOGY

Experimental Materials

Three product groups were used: (1) asbestos-cement pipes, (2) flat slates, and (3) corrugated slates. We took a pair of samples from each group, resulting in six samples. For each product group, the first sample was subjected to environmental exposure (e.g., rain and wind) for at least one year. In contrast, the second sample was hermetically sealed and protected from external influences. This approach allowed us to compare the effects of environmental exposure on each product group with their respective sealed counterparts.

The first pair of samples, an asbestos cement corrugated plate (ACCP-1 and ACCP-2), was approximately 30 years old and originated in a cement factory in Hungary. The plates exhibited typical erosion and damage.

The second pair of samples were asbestos cement slates (ACF-1 and ACF-2), both approximately 20 to 25 years old, eroded and damaged by surface corrosion.

The third pair of samples, ACP-1 and ACP-2, were unassembled and unused products aged 30 to 40. They also originated from a cement factory in Hungary. Both the ACP-1 and ACP-2 pipes were physically well-structured, without extensive cracks and corroded, eroded surfaces.

Before each analysis, all three pairs of samples were thoroughly cleaned with distilled water and isopropyl to remove contaminants that could bias the results. The samples were then cut to similar sizes and densities, and each piece was cast with multi-component epoxy resin and polished into disks of the same size. All samples are shown in Figure 1. The main characteristics of the tested samples are summarized in Table 2.

All asbestos shows intense absorption in the 1200–900 cm^{-1} range and 600–300 cm^{-1} . Recording the spectrum up to 200 cm^{-1} provides all the necessary information for qualitative

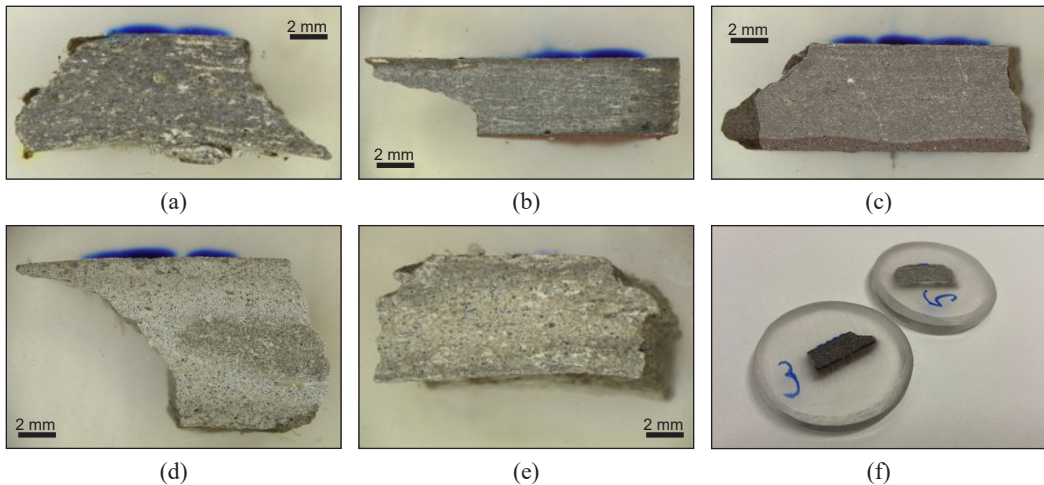


Figure 1. Asbestos cement waste samples. From left to right, beginning from the top: (a) ACCP-1 asbestos cement corrugated plate; (b) ACF-1 asbestos cement slate (isolated); (c) ACF-2 asbestos cement slate (exposed); (d) ACP-1 asbestos cement pipe (isolated); (e) ACP-2 asbestos cement pipe (exposed); (f) prepared samples.

Table 2

Characteristics of the analyzed samples

ID	Product type	Product age	Exposed or Isolated
ACCP-1	Asbestos cement corrugated plate	30 years old	Isolated
ACCP-2	Asbestos cement corrugated plate	30 years old	Exposed
ACF-1	Asbestos cement slate	20 to 25 years old	Isolated
ACF-2	Asbestos cement slate	20 to 25 years old	Exposed
ACP-1	Asbestos cement pipe	30 to 40 years old	Isolated
ACP-2	Asbestos cement pipe	30 to 40 years old	Exposed

identification of the asbestos type. Chrysotile differs significantly from amphiboles in that it shows intense double hydroxyl groups at 3693 cm^{-1} and 3648 cm^{-1} , formed between layers of hydroxyl groups located between the main silicate layers of the lattice. Chrysotile can be quantified from its absorption at 3690 cm^{-1} in the absence of anthophyllite (Károly, 2022).

Sample Preparation and the Used Instrument

Macro measurements were performed using a PerkinElmer Spotlight 400 (PerkinElmer, MA, US) device. For such an examination, the samples were carefully prepared, and broken pieces of asbestos-cement products were poured into an epoxy resin solution for preparation and then polished to make their cross-section easier to examine. The samples were cleaned with distilled water treatment; the treatment itself would have distorted the investigation of the role of environmental effects. Pouring with epoxy resin uses a mold according to the specified dimensions. The discs were ground with a grinder to achieve a disc range of $30 \times 5\text{ mm}$. The resulting $30 \times 5\text{ mm}$ discs were placed on the slide of the instrument, where the material could be examined with a 0.3-mm germanium crystal facing downwards so that the selected area of the sample could be scanned with infrared rays, resulting in the creation of an absorption map of the material. From this map, different spectra are marked with different colors, which point to specific materials in the spectrum library, thus making the components identifiable.

The PerkinElmer Spectrum 400 (PerkinElmer, MA, U.S.) machine was used to perform the microscopic measurements. For these measurements, we took samples from broken sections of asbestos cement products and collected scrap samples from the matrix material to analyze their composition, particularly for additives. Subsequently, these materials were then positioned on the object table of the spectroscope, specifically on a 0.3-mm diamond crystal facing upwards. A force of approximately 100 N was then applied to secure the materials for the analysis. These tests were sensitive to moisture and carbon dioxide; therefore, before each measurement, the spectrum of the environmental background had to be recorded first so that the instrument could distinguish between the true and background spectrum of the sample.

RESULTS AND DISCUSSION

Therefore, in our research, we conducted targeted analyses to verify the chrysotile content of asbestos-cement products and the role of environmental exposure in influencing emissions. In addition to chrysotile content, we looked for trace elements such as glass fiber and polysilicate content, which were typically the main excipients of products manufactured in Hungary.

Therefore, we are looking for answers to two main questions: (1) Can the role of environmental impact be demonstrated by infrared technology? And (2) Is it possible to perform an origin-specific analysis of these products using infrared technology?

Detection of Chrysotile Asbestos

All asbestos exhibits intense absorption in the 1200–900 cm^{-1} and 600–300 cm^{-1} range. Weaker characteristic bands were also observed between 850–600 cm^{-1} . All information for qualitative identification of the asbestos type can be obtained by recording the spectrum up to 200 cm^{-1} . A slight absorption was observed around 3700–3200 cm^{-1} and 1700–1400 cm^{-1} . Chrysotile differs markedly from amphiboles because it shows intense double hydroxyl groups at 3693–3648 cm^{-1} , formed between layers of hydroxyl groups between the main silicate layers of the lattice. This band characterized and quantified fibers in liquid samples saturated with dust or asbestos fibers.

The band is sensitive to interference from other silicate minerals, such as talc, kaolinite, and montmorillonite, which are widely used in industry. The forms of chrysotile, amosite, anthophyllite and crocidolite can be identified separately by infrared spectroscopy. Chrysotile was quantified by its absorbance at 3690 cm^{-1} in the absence of anthophyllite. Anthophyllite was detected at 670 cm^{-1} in the absence of talc. The amosite, crocidolite, and anthophyllite absorption bands at 775 cm^{-1} could be used for quantitative analysis.

Detection of Chrysotile from Asbestos Cement Corrugated Plates

The corrugated asbestos cement plate is a high-binder asbestos-cement product; thus, its asbestos content was close to 8%–10%, with a corresponding cement content above 90%. The corrugated sheet (ACCP-1) under investigation had been exposed to environmental influences originating from construction and demolition activities, but the structure did not appear to have been extensively damaged by weathering. Its surface was rough, similar to cement, and its color was greyish brown. The sample structure was robust and hard, with asbestos fibers clearly visible, arranged in thin bundles, such as individual fibers, intermingled with the cement mixture. The fibers could only be pulled out along the fracture. Table 3 contains the results obtained from the instrument's spectral library supplemented with asbestos spectra.

Table 3

Concordance rates for chrysotile from asbestos cement corrugated plates

Range	Search Reference	Search Reference Spectrum Description	Match
Full range	RESTAURO- ID0344	IMP00280.SP IMP00280 CHRYSOTILE, SI-NMNH, #107853, PMA, TRAN	68.4%
	PERKIN~1- PO0265	GOMMA NBR + PVC + PLASTIFICANTE	66.1%
	PERKIN~4- GS0005	ACRILONITRILE	64.8%
1800-650 cm^{-1}	RESTAURO- ID0344	IMP00280.SP IMP00280 CHRYSOTILE, SI-NMNH, #107853, PMA, TRAN	71.5%
	PERKIN~1- PO0265	GOMMA NBR + PVC + PLASTIFICANTE	70.9%
	PERKIN~1- PO0264	GOMMA NBR + PVC + PLASTIFICANTE + TALCO	67.7%

Determining chrysotile asbestos in practice can be very challenging; therefore, even a hit rate above 50%–60% is decisive enough to be accepted as identification. The chrysotile was identified with 68.41% certainty over the whole range (Table 1). There was a lower probability of plastic derivatives and nitrile compounds being found, which could have been absorbed from the matrix material into the fibers. In the 1800–650 cm⁻¹ band, the third hit was asbestos derivatives with 65.79% certainty, but the results also included plasticizers and talc. Based on these values, it can be stated that chrysotile was clearly detectable in the corrugated plate.

Detection of Chrysotile from Asbestos Cement Flats

The test samples for flat shale analysis included (1) from an environmentally exposed shale (ACF-1) and (2) from a preserved shale (ACF-2). It was assumed that asbestos fibers would be more securely incorporated into the matrix material of the preserved product, making them more difficult to detect. In contrast, owing to structural degradation, we anticipated more easily detectable results from the eroded asbestos slate.

The first flat shale sample was an environmentally exposed asbestos product, with its characteristic layered shape clearly visible owing to the manufacturing processes. A staggered detachment pattern emerged when broken, which could be attributed to weathering delamination, causing the plates to separate slightly. The surface was smooth, firm to touch, and harder than the other samples, and the shale contained coarser fragments scattered throughout its non-homogeneous structure. Asbestos fibers in the sample were clearly visible as thinner bundles, with individual fibers being less discernible or not visible at all. Here, asbestos was removed using tweezers, and the fibers were not easily separated from the binder. The search results of the obtained spectra are listed in Table 4.

These results were similar to those of the corrugated plate measurement (Table 1) but with a higher degree of agreement, as chrysotile had a 70% greater probability of being the first hit in both instances. The second asbestos mound tested, which was not affected

Table 4
Concordance rates for chrysotile from asbestos cement flats

Range	Search Reference	Search Reference Spectrum Description	Match
Full range	RESTAURO- ID0344	IMP00280.SP IMP00280 CHRYSOTILE, SI-NMNH, #107853, PMA, TRAN	74.0%
	PERKIN~4- GS0005	ACRILONITRILE	69.5%
	PERKIN~1- PO0264	GOMMA NBR + PVC + PLASTIFICANTE + TALCO	61.3%
1800-650 cm ⁻¹	RESTAURO- ID0344	IMP00280.SP IMP00280 CHRYSOTILE, SI-NMNH, #107853, PMA, TRAN	73.2%
	PERKIN~1- PO0264	GOMMA NBR + PVC + PLASTIFICANTE + TALCO	65.6%
	PERKIN~1- PO0265	GOMMA NBR + PVC + PLASTIFICANTE	65.1%

by environmental influences over the years, was denser, had a higher amount of matrix material, and featured a harder texture compared to the other material.

The asbestos fibers in the sample appear arranged individually rather than as bundles, giving it an almost hair-like appearance. Despite the large number of fibers, their distribution was homogeneous. These fibers were firmly embedded in the mixture, making them difficult to extract as they either broke or slipped out of the tweezers during preparation. Due to these factors, chrysotile was not detected in Sample 3.

Detection of Chrysotile from Asbestos Cement Pipes

Similar to the artificial shale, two samples of asbestos-cement pipes were tested to analyze the effect of environmental exposure on the structure. The first test pipe, a large cross-section asbestos cement pipe (ACP-1), was exposed to environmental effects. Its structure was not homogeneous, but it had smaller and darker to lighter grains appearing in the light-base color of the matrix material. The asbestos fibers were well-defined, arranged in islands, dense bundles, and were clearly visible in their bright white color. They were the easiest samples to cut out and handle and tended to splinter rather than tear. The spectral library hits for these samples are listed in Tables 5 and 6.

Based on the results, the most reliable evidence for the presence of chrysotile was 86.7% and 89.88%, respectively. The plastic derivative, previously detected, was also present, as was polysilicate, a type of sodium silicate found in cements and refractories. This substance could be explained by the fact that, during production, the compound was absorbed into the porous fibers of the asbestos or the fiber bundles. With a smaller cross-section, the second pipe was an asbestos product protected from environmental influences. Its fracture was staggered, similar to that of shale stored under similar conditions, with layers of delamination observed. The texture was similar to textiles; it was rough, highly textured, and much lighter in color than the other test materials.

This tube was the most heterogeneous of the samples, with various darker to lighter patches mixed with the binder. The asbestos bundles were clearly visible, but the number

Table 5
Concordance rates for chrysotile from asbestos cement pipe (ACP-1)

Range	Search Reference	Search Reference Spectrum Description	Match
Full range	RESTAURO- ID0344	IMP00280.SP IMP00280 CHRYSOTILE, SI-NMNH, #107853, PMA, TRAN	86.7%
	PERKIN~1- PO0265	GOMMA NBR + PVC + PLASTIFICANTE	74.4%
1800-650 cm ⁻¹	POLYMER - HU1137	POLYSILICATE 1.7/250MG KBR 0-00-0	71.1%
	RESTAURO- ID0344	IMP00280.SP IMP00280 CHRYSOTILE, SI-NMNH, #107853, PMA, TRAN	89.9%
	PERKIN~1- PO0265	GOMMA NBR + PVC + PLASTIFICANTE	80.9%
	TRANSM~1- HU1137	POLYSILICATE 1.7/250MG KBR 0-00-0	77.5%

Table 6

Concordance rates for chrysotile from asbestos cement pipe (ACP-2)

Range	Search Reference	Search Reference Spectrum Description	Match	
Full range	RESTAURO- ID0344	IMP00280.SP IMP00280 CHRYSOTILE, SI-NMNH, #107853, PMA, TRAN	59.6%	
	PERKIN~4- GS0005	ACRILONITRILE	66.3%	
	PERKIN~3- IN0016	FIBRA DI VETRO STRAND G	63.5%	
	RESTAURO- ID0365	IMP00301.SP IMP00301 CHROME YELLOW, PBS04 + PB CR04, FORBES, SCC, TRAN	63.3%	
	PERKIN~3- IN0028	VETRO - ATR DI GERMANIO	63.1%	
	PERKIN~1- PO0265	GOMMA NBR + PVC + PLASTIFICANTE	60.5%	
	1800-650 cm ⁻¹	TRANSM~1- GS0017	C2H4-4 100% ETHEN; D=10CM; NACL	69.8%
		PERKIN~3- IN0028	VETRO - ATR DI GERMANIO	69.4%
		RESTAURO- ID0221	IMP00157.SP IMP00157 CHROME GREEN, FORBES: ROWNEY, PMA# I-40, PMA, TRAN	67.6%
		TRANSM~1- GS0018	C2H4-5 100 % ETHEN; D=2CM; BAF2	66.1%
	PERKIN~3- IN0016	FIBRA DI VETRO STRAND G	66.0%	

of asbestos bundles appeared to be smaller than in the previously tested samples. The fine particles were scattered. The fibers were easily held with tweezers; however, extraction was not as easy as before, and they were torn along the fracture line, as in the large pipe, with the mineral fibers fluffed up. Although asbestos fibers were not difficult to extract from the fifth sample, chrysotile came in a mere sixth of the hit list, with only 59.61%. No results were obtained from the characteristic peak band, but both yielded a higher probability of glass fiber.

Acrylonitrile, fiberglass, and plastic derivatives, which had previously been found, appeared in the full range, with yellow pigment material as an additional element on the list. In addition, several hits that did not appear in the previously analyzed hits, such as ethene, whose origin was unknown. It may have been deposited over the years.

Detection of Glass Fibers

In manufacturing these products, a mixture of 20% to 30% by weight of expanded perlite with a grain size of 0.5 mm and 20% to 80% by weight of silica fume is suspended. Spongy silica is sometimes used instead of hard earth, where at least 98% by weight of material with a grain size of up to 0.2 mm is used. The mixture also contains preferably 1.3% to 1.5% by weight of cellulose (Lejsek et al., 1976).

Glass fiber was detected in several samples of asbestos fibers and scrapings. It was found in the corrugated slate, the first environmentally exposed flat slate, and the small cross-section asbestos cement tube (Table 7). The upper half of Table 7 displays the spectral analysis of the asbestos fibers, whereas the lower half shows the glass fiber detected in the matrix material sample. In all cases, the agreement was above 55.0%.

There are several possible explanations for its presence. The use of asbestos-cement products led to increasing demands in terms of fire resistance and structural performance. In 1976, a new patent was granted to address these needs. The proposed technology involved sifting well-known asbestos cement containing up to 55 wt% (weight percent) asbestos through a sieve with a mesh size of 1.35 mm to obtain a residue of at least 40 wt%. Then, a quartz content of 3–50 wt%, consisting of expanded perlite and silica fume, was added. Lastly, 3 wt% of inorganic fibrous material, an asbestos-glass fiber suspension, was included, with the glass fiber length preferably being 10 mm. Additionally, 1.3–1.5 wt% cellulose might be required (Lejsek et al., 1976).

The advantage of altering the composition was achieving the desired strength while maintaining a low bulk density and high porosity. It was accomplished by reducing the amount of cement binder and increasing the filler. Table 8 compares the bending tests of two previously manufactured, unnamed asbestos-cement formulations and the new formulation (Lejsek et al., 1976). The test was used to determine the maximum stress and load capacity. Based on the data, it can be concluded that the glass fiber-reinforced product had a much lower bulk density compared to its predecessors. However, its relative bending strength parallel and perpendicular to the fibers was more favorable, making the material more robust. In accordance with the standards for asbestos cement, eight random samples

Table 7
Concordance rates for glass fibers from asbestos cement wastes

Range	Sample	Search Reference	Search Reference Spectrum Description	Match
Full range	ACP-2- asbestos	PERKIN~3- IN0016	FIBRA DI VETRO STRAND G	63.5%
	ACF-1 - asbestos	PERKIN~3- IN0016	FIBRA DI VETRO STRAND G	59.9%
1800-650 cm ⁻¹	ACP-2 - asbestos	PERKIN~3- IN0016	FIBRA DI VETRO STRAND G	66.0%
	ACF-1 - asbestos	PERKIN~3- IN0016	FIBRA DI VETRO STRAND G	61.7%
	ACCP-1 - asbestos	PERKIN~3- IN0016	FIBRA DI VETRO STRAND G	57.1%
Full range	ACF-1 - cement	PERKIN~3- IN0016	FIBRA DI VETRO STRAND G	63.2%
	ACF-1 – cement	PERKIN~3- IN0016	FIBRA DI VETRO STRAND G	63.5%

Table 8
Flexural strength testing of asbestos cement products enriched with glass fibers (Lejsek et al., 1976)

Property	Asbestos cement containing glass fiber	Previously used asbestos cement	
Volumetric weight (kPa m ⁻³)	650	796	741
Flexural strength parallel to the elementary fibers (kp cm ⁻²)	105	92.2	113.7
Flexural strength perpendicular to the elementary fibers (kp cm ⁻²)	65–70	72.9	104.9

were taken from every 50,000 pieces produced and tested. For the flexural strength test, 22 cm long, 10 cm wide rectangular elements were prepared, and both perpendicular and parallel samples were tested. The analysis was preceded by 28 days of air-dry confinement (Fügedi, 1986).

Detection of Polysilicate (Water Glass)

Sodium silicate, commonly known as water glass, exists in ortho-, meta-, poly-, and pyrosilicate forms. When mixed with cement, sodium silicate enhances thermal resistance, and when added to adhesives, it improves the thermal resistance of the bonding surface. Another benefit of its use is that it can prevent water infiltration into the material by blocking moisture from entering the pores when used as a surface treatment agent. It also has flame-retardant and fire-resistant properties, as it releases water when heated, which cools the surface. All these characteristics have made it a popular additive in the fire protection, woodworking, and construction industries (Grote, 1897).

The first mention of the role of polysilicates in asbestos production dates to 1896 in a patent by Lajos Grote. In his patent, he described a manufacturing process for asbestos products where the fibers were impregnated with a mixture of water glass, glue and formaldehyde solution. The process involved dissolving one part of glue in 12 parts of boiling water, mixing the cooled solution with six parts of water glass solution, and finally adding 7–9 parts of 40% formaldehyde. The asbestos fibers were soaked in this mixture until they saturated sufficiently. The resulting asbestos products dried and hardened in about 12 hours, after which they were ready for machining (Grote, 1897).

The results obtained for the asbestos cement corrugated plates, flat slates, and pipes consistently showed the presence of polysilicate, or water glass, in both ranges. In all measurements, the extracted asbestos fibers indicated the presence of the compound, which could be due to the absorption of material into porous fibers. The spectral agreement was above 60.0% in all cases except one. The pipe measured the highest values, while the lowest was obtained in the slate. The detailed results can be seen in Table 9.

Table 9
Concordance rates for polysilicate from asbestos cement wastes

Range	Sample	Search Reference Spectrum Description	Match
Overlap	ACCP-1	POLYSILICATE 1.7/250MG KBR 0-00-0	60.2%
	ACF-1	POLYSILICATE 1.7/250MG KBR 0-00-0	57.8%
	ACP-1 -asbestos	POLYSILICATE 1.7/250MG KBR 0-00-0	66.6%
	ACP-2 -asbestos	POLYSILICATE 1.7/250MG KBR 0-00-0	67.2%
1800-650 cm ⁻¹	ACCP-1 - asbestos	POLYSILICATE 1.7/250MG KBR 0-00-0	60.5%
	ACP-1 - asbestos	POLYSILICATE 1.7/250MG KBR 0-00-0	74.4%
	ACP-2 - asbestos	POLYSILICATE 1.7/250MG KBR 0-00-0	75.6%

CONCLUSION

Chrysotile asbestos (white asbestos) was detected in all the tested product-waste groups with a relatively high hit rate and agreement—the presence of chrysotile in each sample tested, with spectral matches ranging from 59.6% to 86.7%. A particularly significant finding was that removing asbestos from asbestos-cement products exposed to environmental influences was easier, and the degree of agreement between the results was higher than that for products sealed off from such effects. The presence of chrysotile was much easier to detect for the environmentally exposed AC pipe compared with the sealed samples. However, contrary to expectations, a higher degree of agreement with chrysotile was demonstrated when examining the AC pipes than when measuring the flat or corrugated shale slate samples. The match rate with the chrysotile spectrum ranged from 86.7 to 89.9% for the AC pipe exposed to the environment. This compares to 59.6% for all samples that were isolated and spared from environmental influence.

Additionally, we established that all asbestos cement products contained glass fibers, with an average spectral match of 62.1%. Our analysis showed an average spectral match of 66.0% in the case of polysilicates, which were classified as very typical additives in Hungary during the production period of the products. Overall, using infrared technology principles, chrysotile (white asbestos) was detected in all examined products and waste groups. A key implication of this research is that environmental influences make white asbestos fibers easier to detect and separate than sealed-off products. Another important implication is that FT-IR technology can also be used to determine the inherent specific character of these products. However, the lack of a uniform patent and methodology, as well as the difficulty of testing asbestos-cement products, are major limitation factors to research. Our analyses were based on samples currently common in Hungary, but the work can be adapted to other countries. We aim to broaden the spectrum of this research in the future, carry out comparative studies by testing products manufactured abroad, and develop a methodology.

ACKNOWLEDGEMENT

This research is supported by the Publication Support Programme of Széchenyi István University, Hungary.

REFERENCES

- Azuma, K., Uchiyama, I., Chiba, Y., & Okumura, J. (2009). Mesothelioma risk and environmental exposure to asbestos: Past and future trends in Japan. *International Journal of Occupational and Environmental Health*, 15(2), 166–172. <https://doi.org/10.1179/oeh.2009.15.2.166>
- Bahadori, A. (2016). Chapter 8 - Water supply and distribution systems. In A. Bahadori (Ed.), *Essentials of Oil and Gas Utilities* (pp. 225–328). Elsevier. <https://doi.org/10.1016/B978-0-12-803088-2.00008-0>

- Bales, R. C., & Morgan, J. J. (1985). Dissolution kinetics of chrysotile at pH 7 to 10. *Geochimica et Cosmochimica Acta*, 49(11), 2281–2288. [https://doi.org/10.1016/0016-7037\(85\)90228-5](https://doi.org/10.1016/0016-7037(85)90228-5)
- Bartrip, P. W. J. (2004). History of asbestos related disease. *Postgraduate Medical Journal*, 80(940), 72–76. <https://doi.org/10.1136/pmj.2003.012526>
- Berman, D., & Crump, K. (2003). *Technical Support Document for a Protocol to Assess Asbestos-related Risk*. U.S. Environmental Protection Agency.
- Brandt, M. J., Johnson, K. M., Elphinston, A. J., & Ratnayaka, D. D. (2017). Chapter 7 - Chemistry, microbiology and biology of water. In M. J. Brandt, K. M. Johnson, A. J. Elphinston & D. D. Ratnayaka (Eds.), *Twort's Water Supply* (pp. 235–321). Elsevier. <https://doi.org/10.1016/B978-0-08-100025-0.00007-7>
- Burdett, G. (2006). *Investigation of the Chrysotile Fibres in an Asbestos Cement Sample*. Health & Safety Laboratory.
- Carneiro, G. O., Santos, T. A., Simonelli, G., Ribeiro, D. V., Cilla, M. S., & Dias, C. M. R. (2021). Thermal treatment optimization of asbestos cement waste (ACW) potentializing its use as alternative binder. *Journal of Cleaner Production*, 320, Article 128801. <https://doi.org/10.1016/j.jclepro.2021.128801>
- Castro, H., Giannasi, F., & Novello, C. (2003). A luta pelo banimento do amianto nas Américas: Uma questão de saúde pública [The struggle to ban asbestos in the Americas: A public health issue]. *Ciência & Saúde Coletiva*, 8(4), 903–911. <https://doi.org/10.1590/S1413-81232003000400013>
- Currie, G. P., Watt, S. J., & Maskell, N. A. (2009). An overview of how asbestos exposure affects the lung. *BMJ*, 339, Article b3209. <https://doi.org/10.1136/bmj.b3209>
- Dodson, R. F., & Hammar, S. P. (2011). *Asbestos - Risk assessment, epidemiology, and health effects* (2nd ed.). CRC Press. <https://doi.org/10.1201/b10958>
- Doll, R. (1993). Mortality from lung cancer in asbestos workers 1955. *Occupational and Environmental Medicine*, 50(6), 485–490. <https://doi.org/10.1136/oem.50.6.485>
- Dubin, H., Xi, C., & Xiu-yun, C. (2013). Structure performance and application research of natural nanotubular chrysotile. *Journal of Functional Biomaterials*, 44(14), 1984–1989. <https://doi.org/10.3969/j.issn.1001-9731.2013.14.002>
- Dyczek, J. (2007). *Bezpieczne postępowanie z azbestem i materiałami zawierającymi azbest : Szkoła "Azbest - bezpieczne postępowanie"* [Safe Handling of Asbestos and Materials Containing Asbestos: School of "Asbestos - safe handling"]. Wydawnictwo Naukowe.
- Ervik, T., Hammer, S. E., & Graff, P. (2021). Mobilization of asbestos fibers by weathering of a corrugated asbestos cement roof. *Journal of Occupational and Environmental Hygiene*, 18(3), 110–117. <https://doi.org/10.1080/15459624.2020.1867730>
- Favero-Longo, S. E., Turci, F., Tomatis, M., Castelli, D., Bonfante, P., Hochella, M. F., Piervittori, R., & Fubini, B. (2005). Chrysotile asbestos is progressively converted into a non-fibrous amorphous material by the chelating action of lichen metabolites. *Journal of Environmental Monitoring*, 7(8), 764–766. <https://doi.org/10.1039/b507569f>
- Goldberg, M., & Luce, D. (2009). The health impact of nonoccupational exposure to asbestos: What do we know? *European Journal of Cancer Prevention*, 18(6), 489–503. <https://doi.org/10.1097/CEJ.0b013e32832f9bee>

- Grote, L. (1897). *Eljárás plasztikus testeknek azbesztrostokból vagy azbesztgyártmányokból való előállítására* [Process for the production of plastic bodies from asbestos fibers or asbestos products] (Patent 8094). Magyar Királyi Szabadalmi Hivatal.
- Harremoës, P., Gee, D., MacGarvin, M., Stirling, A., Keys, J., Wynne, B., & Guedes, V. S. (2001). *Late lessons from early warnings: The precautionary principle 1896-2000* (Report No. 22 Environment Issue). European Environment Agency.
- Harris, L., & Kahwa, I. (2003). Asbestos: Old foe in 21st century developing countries. *The Science of The Total Environment*, 307(1–3), 1–9. [https://doi.org/10.1016/S0048-9697\(02\)00504-1](https://doi.org/10.1016/S0048-9697(02)00504-1)
- Hassanpour, M., Shafigh, P., & Mahmud, H. Bin. (2012). Lightweight aggregate concrete fiber reinforcement – A review. *Construction and Building Materials*, 37, 452–461. <https://doi.org/10.1016/j.conbuildmat.2012.07.071>
- Hodgson, J. T., & Darnton, A. (2000). The quantitative risks of mesothelioma and lung cancer in relation to asbestos exposure. *The Annals of Occupational Hygiene*, 44(8), 565–601. <https://doi.org/10.1093/annhyg/44.8.565>
- Iwaszko, J., Zawada, A., Przerada, I., & Lubas, M. (2018). Structural and microstructural aspects of asbestos-cement waste vitrification. *Spectrochimica Acta Part A: Molecular and Biomolecular Spectroscopy*, 195, 95–102. <https://doi.org/10.1016/j.saa.2018.01.053>
- Janela, J. M. E. M., & Pereira, P. J. S. (2016). História do amianto no mundo e em Portugal [History of asbestos in the world and in Portugal]. *CEM Cultura, Espaço & Memória*, 7, 93–206.
- Korda, R. J., Clements, M. S., Armstrong, B. K., Law, H. Di, Guiver, T., Anderson, P. R., Trevenar, S. M., & Kirk, M. D. (2017). Risk of cancer associated with residential exposure to asbestos insulation: A whole-population cohort study. *The Lancet Public Health*, 2(11), e522–e528. [https://doi.org/10.1016/S2468-2667\(17\)30192-5](https://doi.org/10.1016/S2468-2667(17)30192-5)
- Kusiorowski, R., Lipowska, B., Kujawa, M., & Gerle, A. (2023). Problem of asbestos-containing wastes in Poland. *Cleaner Waste Systems*, 4, Article 100085. <https://doi.org/10.1016/j.clwas.2023.100085>
- Landrigan, P. J. (1998). Asbestos — Still a carcinogen. *The New England Journal of Medicine*, 338(22), 1618–1619. <https://doi.org/10.1056/NEJM199805283382209>
- Lavento, M., & Hornytzkjy, S. (1995). On asbestos used as temper in Finnish subneolithic, neolithic and early metal period pottery. *Fennoscandia Archaeologica*, 12, 71–75.
- Lejsek, L., Vichta, A., Zboril, F., Kovar, J., Fridal, J., Franc, V., & Knezek, J. (1976). *Eljárás tűzálló, állandó térfogatú azbesztcementelemek előállítására* [Process for the production of refractory, constant volume asbestos cement elements] (Patent 170236). Magyar Népköztársaság Országos Találmányi Hivatal.
- Lisco, S., Lapietra, I., Laviano, R., Mastronuzzi, G., Fracchiolla, T., & Moretti, M. (2023). Sedimentological features of asbestos cement fragments in coastal environments (Taranto, southern Italy). *Marine Pollution Bulletin*, 187, Article 114469. <https://doi.org/10.1016/j.marpolbul.2022.114469>
- Liu, Q., Peng, H., Tian, X., & Guo, J. (2020). Synthesis of chrysotile based nanocomposites for tuning band gap and photocatalytic property. *Applied Clay Science*, 199, Article 105885. <https://doi.org/10.1016/j.clay.2020.105885>

- Malinconico, S., Paglietti, F., Serranti, S., Bonifazi, G., & Lonigro, I. (2022). Asbestos in soil and water: A review of analytical techniques and methods. *Journal of Hazardous Materials*, 436, Article 129083. <https://doi.org/10.1016/j.jhazmat.2022.129083>
- Misseri, M. (2023). Nucleation of naturally occurring calcic amphibole asbestos. *Environmental Research*, 230, Article 114940. <https://doi.org/10.1016/j.envres.2022.114940>
- Murayama, T., Takahashi, K., Natori, Y., & Kurumatani, N. (2006). Estimation of future mortality from pleural malignant mesothelioma in Japan based on an age-cohort model. *American Journal of Industrial Medicine*, 49(1), 1–7. <https://doi.org/10.1002/ajim.20246>
- Park, E. K., Takahashi, K., Jiang, Y., Movahed, M., & Kameda, T. (2012). Elimination of asbestos use and asbestos-related diseases: An unfinished story. *Cancer Science*, 103(10), 1751–1755. <https://doi.org/10.1111/j.1349-7006.2012.02366.x>
- Punurai, W., & Davis, P. (2017). Prediction of asbestos cement water pipe aging and pipe prioritization using monte Carlo simulation. *Engineering Journal*, 21(2), 1–13. <https://doi.org/10.4186/ej.2017.21.2.1>
- Raczko, E., Krówczyńska, M., & Wilk, E. (2022). Asbestos roofing recognition by use of convolutional neural networks and high-resolution aerial imagery. Testing different scenarios. *Building and Environment*, 217, Article 109092. <https://doi.org/10.1016/j.buildenv.2022.109092>
- Ristić, M., Czako-Nagy, I., Musić, S., & Vértés, A. (2011). Spectroscopic characterization of chrysotile asbestos from different regions. *Journal of Molecular Structure*, 993(1–3), 120–126. <https://doi.org/10.1016/j.molstruc.2010.10.005>
- Røe, O. D., & Stella, G. M. (2015). Malignant pleural mesothelioma: History, controversy and future of a manmade epidemic. *European Respiratory Review*, 24(135), 115–131. <https://doi.org/10.1183/09059180.00007014>
- Rolfé, M., Hayes, S., Smith, M., Owen, M., Spruth, M., McCarthy, C., Forkan, A., Banerjee, A., & Hocking, R. K. (2024). An AI based smart-phone system for asbestos identification. *Journal of Hazardous Materials*, 463, Article 132853. <https://doi.org/10.1016/j.jhazmat.2023.132853>
- Ross, M., Langer, A. M., Nord, G. L., Nolan, R. P., Lee, R. J., Van Orden, D., & Addison, J. (2008). The mineral nature of asbestos. *Regulatory Toxicology and Pharmacology*, 52(1), S26–S30. <https://doi.org/10.1016/j.yrtph.2007.09.008>
- Santana, H. A., Júnior, N. S. A., Carneiro, G. O., Ribeiro, D. V., Cilla, M. S., & Dias, C. M. R. (2023). Asbestos-cement wastes as supplementary precursors of NaOH-activated binders. *Construction and Building Materials*, 364, Article 129921. <https://doi.org/10.1016/j.conbuildmat.2022.129921>
- Speil, S., & Leineweber, J. P. (1969). Asbestos minerals in modern technology. *Environmental Research*, 2(3), 166–208. [https://doi.org/10.1016/0013-9351\(69\)90036-X](https://doi.org/10.1016/0013-9351(69)90036-X)
- Stayner, L., Welch, L. S., & Lemen, R. (2013). The worldwide pandemic of asbestos-related diseases. *Annual Review of Public Health*, 34(1), 205–216. <https://doi.org/10.1146/annurev-publhealth-031811-124704>
- Szeszenia-Dąbrowska, N. (2004). *Azbest - ekspozycja zawodowa i środowiskowa - skutki, profilaktyka* [Asbestos - Occupational and environmental exposure - Effects, prevention]. Oficyna Wydawnicza Instytut Medycyny.

- Székely, L., Scharle, Gy., Betlehem, A. (1972). *Segédlet a szakipari munkák tervezéséhez és kivitelezéséhez* [Guide to planning and carrying out specialist works]. Építésügyi Tájékoztatói Központ.
- Tabata, M., Fukuyama, M., Yada, M., & Toshimitsu, F. (2022). On-site detection of asbestos at the surface of building materials wasted at disaster sites by staining. *Waste Management*, 138, 180–188. <https://doi.org/10.1016/j.wasman.2021.11.039>
- Thives, L. P., Ghisi, E., Thives Júnior, J. J., & Vieira, A. S. (2022). Is asbestos still a problem in the world? A current review. *Journal of Environmental Management*, 319, Article 115716. <https://doi.org/10.1016/j.jenvman.2022.115716>
- Tóth, E., & Weiszburg, T. (2011). *Környezeti ásványtan [Environmental Mineralogy]*. Typotex Kiadó.
- Virta, R. L. (2005). *Mineral commodity profiles-asbestos: U.S. geological survey circular 1255-KK*. USGS Science for a Changing World. <http://www.usgs.gov/pubprod>
- Walter, M., Geroldinger, G., Gille, L., Kraemer, S. M., & Schenkeveld, W. D. C. (2022). Soil-pH and cement influence the weathering kinetics of chrysotile asbestos in soils and its hydroxyl radical yield. *Journal of Hazardous Materials*, 431, Article 128068. <https://doi.org/10.1016/j.jhazmat.2021.128068>
- Wang, Y., Huo, T., Feng, C., Zeng, Y., Yang, J., Zhang, X., Dong, F., & Deng, J. (2019). Chrysotile asbestos induces apoptosis via activation of the p53-regulated mitochondrial pathway mediated by ROS in A549 cells. *Applied Clay Science*, 182, Article 105245. <https://doi.org/10.1016/j.clay.2019.105245>
- WHO (1986). *Asbestos and other natural mineral fibres*. World Health Organization. <https://apps.who.int/iris/handle/10665/37190>
- Zavašnik, J., Šestan, A., & Škapin, S. (2022). Degradation of asbestos – Reinforced water supply cement pipes after a long-term operation. *Chemosphere*, 287, Article 131977. <https://doi.org/10.1016/j.chemosphere.2021.131977>
- Zha, L., Kitamura, Y., Kitamura, T., Liu, R., Shima, M., Kurumatani, N., Nakaya, T., Goji, J., & Sobue, T. (2019). Population-based cohort study on health effects of asbestos exposure in Japan. *Cancer Science*, 110(3), 1076-1084. <https://doi.org/10.1111/cas.13930>
- Zholobenko, V., Rutten, F., Zholobenko, A., & Holmes, A. (2021). In situ spectroscopic identification of the six types of asbestos. *Journal of Hazardous Materials*, 403, Article 123951. <https://doi.org/10.1016/j.jhazmat.2020.123951>

Review Article

State-of-the-Art Probabilistic Solar Power Forecasting: A Structured Review

Noor Hasliza Abdul Rahman^{1,2}, Shahril Irwan Sulaiman^{3,4}, Mohamad Zhafran Hussin^{1,4*}, Muhammad Asraf Hairuddin^{1,5}, Ezril Hisham Mat Saat¹ and Nur Dalila Khirul Ashar^{1,6}

¹*School of Electrical Engineering, College of Engineering, Universiti Teknologi MARA, Cawangan Johor, Kampus Pasir Gudang, 81750 Masai, Johor, Malaysia*

²*School of Electrical Engineering, College of Engineering, Universiti Teknologi MARA, 40450 Shah Alam, Selangor, Malaysia*

³*Green Energy Research Centre, Universiti Teknologi MARA, 40450 Shah Alam, Selangor, Malaysia*

⁴*SPECTRA Research Group, Faculty of Applied Sciences, Universiti Teknologi MARA, 40450, Shah Alam, Selangor, Malaysia*

⁵*Institute for Big Data Analytics and Artificial Intelligence (IBDAAI), Universiti Teknologi MARA, Shah Alam, Selangor, Malaysia*

⁶*Department of Computer and Communication Systems, Faculty of Engineering, Universiti Putra Malaysia, 43400 Serdang, Selangor, Malaysia*

ABSTRACT

In recent years, the installed capacity increment with regard to solar power generation has been highlighted as a crucial role played by Photovoltaic (PV) generation forecasting in integrating a growing number of distributed PV sites into power systems. Nevertheless, because of the PV generation's unpredictable nature, deterministic point forecast methods struggle to accurately assess the uncertainties associated with PV generation. This paper presents a detailed structured review of the state-of-the-art concerning Probabilistic Solar

Power Forecasting (PSPF), which covers forecasting methods, model comparison, forecasting horizon and quantification metrics. Our review methodology leverages the Preferred Reporting Items for Systematic Reviews and Meta-Analyses (PRISMA) approach to systematically identify primary data sources, focusing on keywords such as probabilistic forecasting, Deep Learning (DL), and Machine learning (ML). Through

ARTICLE INFO

Article history:

Received: 11 October 2023

Accepted: 16 April 2024

Published: 09 October 2024

DOI: <https://doi.org/10.47836/pjst.32.6.04>

E-mail addresses:

noorhasliza@uitm.edu.my (Noor Hasliza Abdul Rahman)

shahril_irwan2004@yahoo.com (Shahril Irwan Sulaiman)

mzhafran@uitm.edu.my (Mohamad Zhafran Hussin)

masraf@uitm.edu.my (Muhammad Asraf Hairuddin)

ezril@uitm.edu.my (Ezril Hisham Mat Saat)

nurdalila306@uitm.edu.my (Nur Dalila Khirul Ashar)

* Corresponding author

an extensive and rigorous search of renowned databases such as SCOPUS and Web of Science (WoS), we identified 36 relevant studies (n=36). Consequently, expert scholars decided to develop three themes: (1) Conventional PSPF, (2) PSPF utilizing ML, and (3) PSPF using DL. Probabilistic forecasting is an invaluable tool concerning power systems, especially regarding the rising proportion of renewable energy sources in the energy mix. We tackle the inherent uncertainty of renewable generation, maintain grid stability, and promote efficient energy management and planning. In the end, this research contributes to the development of a power system that is more resilient, reliable, and sustainable.

Keywords: Deep learning, machine learning, photovoltaic, probabilistic forecast, solar power

INTRODUCTION

Solar power has emerged as a highly promising and environmentally sustainable renewable energy source. It holds the potential to address escalating global energy demands while simultaneously mitigating the negative impacts of greenhouse gas emissions (Panagiotopoulou et al., 2022; Shafiullah et al., 2022). Due to the high solar radiation, global Photovoltaic (PV) development has been increasing and is expected to reach 4,500 GW by 2050 (Chowdhury et al., 2020). Global photovoltaic (PV) capacity experienced substantial growth in 2022, reaching a cumulative capacity of 1,185 GW, as reported by the International Energy Agency (IEA) (International Energy Agency, 2023). However, integrating solar energy into the grid system presents a few challenges, primarily due to its intermittent and unpredictable nature (Zafar et al., 2022). The intermittency stems from several factors, such as the diurnal sunlight cycle, cloud cover, and weather conditions. Conventional fossil fuel power plants generate a consistent and manageable output, while solar power generation fluctuates throughout the day and halts during nighttime. Moreover, the variability poses significant challenges for grid operators and energy planners tasked with ensuring a reliable power supply.

Traditional forecasting methods typically utilize deterministic approaches, providing a single-point forecast of expected solar generation (Maraggi et al., 2021). However, the application of Artificial Intelligence (AI) methods, particularly Machine Learning (ML), has garnered widespread attention in a multitude of recent research (Mellit et al., 2020; Pazikadin et al., 2020). In the current status quo, the ML method has become a focal point for numerous researchers. ML-based models leverage their ability to predict PV power with precision dependent on the volume and quality of data and the selected learning algorithm. Random Forest (RF), Support Vector Regression (SVR), Support Vector Machine (SVM), and Artificial Neural Network (ANN) are also some of the prominent ML models with regard to forecasting in the PV system application.

Nevertheless, conventional ML model learning typically offers limited depth for long-term sequence data (Wang et al., 2019). Since ML models learn from input data,

they struggle to familiarize themselves with environmental changes. Other than that, the complexity with regard to weather conditions as well as the massive input data required with respect to large-scale solar applications. It indicates that shallow models may not fully capture the corresponding deep non-linear characteristics as well as time-series dynamic characteristics regarding the dataset (Yu et al., 2020).

Deep Learning (DL) refers to a subset of machine models. It attracted significant attention because of its capability to tackle complex problems with massive as well as unstructured data volumes utilizing deep neural networks (Chen et al., 2019). Compared to ML, DL adapts to environmental changes by continuously receiving input and improving its models. Note that the main application scenario for DL models is sequential or time-series data. These comprise Recurrent Neural Networks (RNN), Long Short-Term Memory (LSTM), Gated Recurrent Units (GRU), and Convolutional Neural Networks (CNN). The hierarchical relationship between AI, ML, and DL is illustrated in Figure 1.

Recently, there have been significant advancements in solar power forecasting. It marks a notable shift towards improving the accuracy and dependability of forecasting regarding solar power generation (Li et al., 2022; Thaker & Höller, 2022). This progress stems from acknowledging that traditional deterministic forecasts are inadequate for the modern energy landscape. It is defined by the unpredictable and intermittent nature of solar power generation since traditional deterministic methods forecast the power generation future relying on a single value without considering the associated uncertainty.

Probabilistic Solar Power Forecasting (PSPF) utilizes advanced techniques to generate forecasts that predict the most probable future solar power output and quantify the associated uncertainties (Abuella & Chowdhury, 2019; Wen et al., 2020). This approach is especially critical in variable solar generation, as it enables decision-makers to make well-informed choices based on a comprehensive understanding of the projected outputs and the inherent risks involved. By assigning probabilities to different scenarios, this method fosters a deeper understanding of the potential range of outcomes and their associated uncertainties. Hence, this information is invaluable for decision-makers, enabling them to assess the risks and make well-informed choices considering the likelihood of various outcomes.

Note that a significant number of research papers have reviewed the deterministic solar power forecast in ML and DL methods. The research on ML and DL models in PSPF

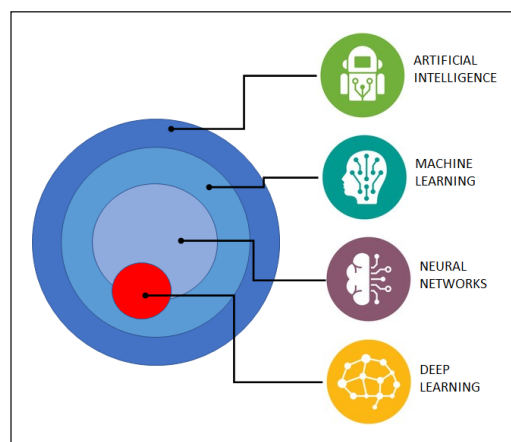


Figure 1. The relationship exists between ML, AI, Neural Networks (NN), and DL

may be established new as well as lacking in comparison to deterministic forecasting (Ahmed et al., 2020; Chu et al., 2021; Devaraj et al., 2021; Feng et al., 2021; Kumari & Toshniwal, 2021; Mittal et al., 2022; Rajagukguk et al., 2020; Wang et al., 2019). PSPF has not yet been broadly adopted in PV fields. Nonetheless, its applications are progressively applied to other decision-making challenges under uncertainty. For instance, PSPF techniques are utilized in wind forecasting (Bazionis & Georgilakis, 2021) and domains beyond energy forecasting. It includes weather predictions (Kirkwood et al., 2021) and applications in economics and finance (Salisu et al., 2021). Solar power forecasting may benefit advancements in wind forecasting. However, it has challenges, such as high weather variability and increased penetration of PV systems into the grid.

Considering these developments, this structured review aims to furnish a comprehensive overview of the state-of-the-art in PSPF. One notable exclusion from the present literature is adopting the ML and DL models in probabilistic forecasting. It encourages us to examine cutting-edge forecasting approaches in their entirety, as well as the most current advancements in the PSPF field.

This research's contributions are given below:

- A comprehensive review of the impact of forecasting horizon and model performances.
- A comparative evaluation of ML and DL in probabilistic forecasting model advancement.
- A comprehensive review of uncertainty quantification metric.

MATERIAL AND METHODS

Identification

The structured review consists of three key stages in choosing pertinent articles for this research. Note that the first stage involves recognizing keywords and searching for related terms utilizing thesauruses, previous research, encyclopedias, and dictionaries. Once all the relevant keywords were decided, search strings were generated regarding the SCOPUS and Web of Science (WoS) databases (Table 1). Before the structured review process's initial phase, this study project acquired 165 papers from both databases.

Screening

As part of the screening process, extensive measures are needed to ensure the utmost accuracy and reliability of findings. In the initial stage of the study, 39 articles were meticulously screened using the scholars' inclusion and exclusion criteria. The main focus was on literature, specifically research articles and conference papers, as they are the primary sources. Only publications in the English language were reviewed to ensure

Table 1
The search string

Database	Descriptions
Scopus	<p>TITLE-ABS-KEY (("probabilistic forecast*" AND ("deep learning" OR "deep neural network" OR deep OR "machine learning" OR "artificial intelligence") AND ("solar power" OR photovoltaic OR pv OR "large scale solar" OR "utility-scale")) AND PUBYEAR > 2019 AND PUBYEAR < 2025 AND (LIMIT-TO (DOCTYPE , "ar") OR LIMIT-TO (DOCTYPE , "cp")) AND (LIMIT-TO (LANGUAGE , "english")))</p> <p>Access Date: 12 March 2024</p>
WoS	<p>"probabilistic forecast*" AND ("deep learning" OR "deep neural network" OR deep OR "machine learning" OR "artificial intelligence") AND ("solar power" OR photovoltaic OR pv OR "large scale solar" OR "utility-scale") (Topic) and 2024 or 2023 or 2022 or 2021 or 2020 (Publication Years) and Article or Proceeding Paper (Document Types) and English (Languages)</p> <p>Access Date: 12 March 2024</p> <p>"probabilistic forecast*" AND ("deep learning" OR "deep neural network" OR deep OR "machine learning" OR "artificial intelligence") AND ("solar power" OR photovoltaic OR pv OR "large scale solar" OR "utility-scale") (Title) and 2023 or 2022 or 2020 (Publication Years) and Article or Proceeding Paper (Document Types) and English (Languages)</p> <p>Access Date: 12 March 2024</p>

consistency and clarity in findings. Consequently, it is important to note that the study focused on the past six years (2019–2024). For the second round, 39 articles were rejected to eliminate any duplicates. In total, 88 publications were eliminated based on our rigorous selection criteria.

Eligibility

The third phase resembled the eligibility assessment. A total of 77 articles were compiled. During this stage, a comprehensive evaluation of both article titles and essential content was conducted to verify their adherence to the inclusion criteria and alignment with the current research objectives of the study. Consequently, 41 reports were deemed ineligible for being outside the scope, featuring irrelevant titles, having abstracts unrelated to the study's objectives, or full text not being accessible. Finally, 36 articles were deemed eligible for review, as tabulated in Table 2.

Table 2
Searching selection criterion

Criterion	Inclusion	Exclusion
Language	English	Non-English
Timeline	2019–2024	<2019
Literature type	Journal article and conference proceeding	Book chapter, review, data paper

Data Abstraction and Analysis

As a part of this study, an integrative analysis was utilized to assess a range of research designs, including quantitative, qualitative, and mixed methods. The study aimed to identify relevant topics and subtopics by utilizing a meticulous approach that commenced with data collection. Figure 2 illustrates the analysis of 36 articles to extract information related to the study’s topics. Correspondingly, the studies related to probabilistic forecasting were assessed, carefully considering each study’s research methods and findings. Subsequently, the authors collaborated to develop themes based on the evidence presented in the study’s context. A comprehensive log was diligently maintained throughout the entirety of the data analysis process, meticulously documenting all pertinent analyses and perspectives relevant to the interpretation of the data. Once the themes were developed, the authors compared them to ensure consistency. The produced themes were then fine-tuned to establish consistency. In securing the findings’ validity, two experts were interviewed, one having expertise in solar power forecasting as well as statistical analysis. These experts reviewed each sub-theme to ensure its clarity, importance, and adequacy by determining domain validity. Consequently, the author adjusted corresponding to the feedback and comments by experts.

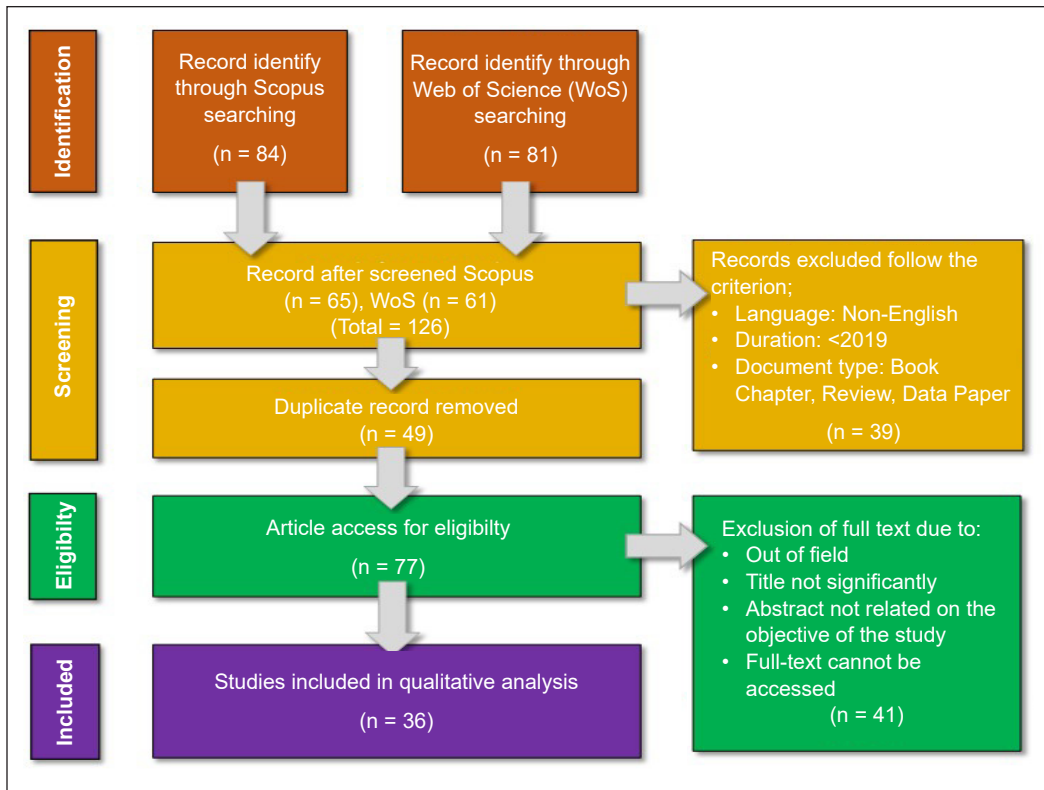


Figure 2. Flow diagram of the proposed search study (Mustafa, 2022)

RESULTS AND DISCUSSION

Accurate forecasts of solar power generation are vital for effective grid management and integrating renewable energy sources. Researchers have developed various solar power forecasting techniques, including probabilistic approaches, ML, and DL.

Throughout the most recent six years, the total number of publications per year from 2019 to 2024 is illustrated in Figure 3. The development of the PSPF study that is being presented demonstrates a steady rise in the number of publications for the WoS and SCOPUS databases. By 2020, there were twice as many documents available as in 2019. Note that a total of 12 documents were published. The years 2022 and 2023 saw the highest peak publishing numbers, with 36 papers published annually overall. Whether they are small- or large-scale solar systems, this spike probably reflects the increased interest in grid-connected PV systems. However, with just seven papers produced in 2024, there was a noticeable decline in the overall number of publications. Instead of a true decline in interest, this decline could be attributed to missing data or database updates. The data that has been presented indicates a distinct preference for publishing in the SCOPUS database over WoS. This preference could result from factors including citation metrics evaluation or accessibility. Other than that, these publications demonstrate the increasing interest in and significance of precise PSPF in renewable energy published in several scholarly journals and conference proceedings.

An extensive literature review was conducted, and 36 relevant articles were analyzed. It categorized them into three themes: probabilistic forecasting (eight articles) in Table 3, PSPF with ML (9 articles) in Table 4, and PSPF with DL (19 articles) in Table 5. The analysis has covered a significant state-of-the-art trend, providing a comprehensive overview of the

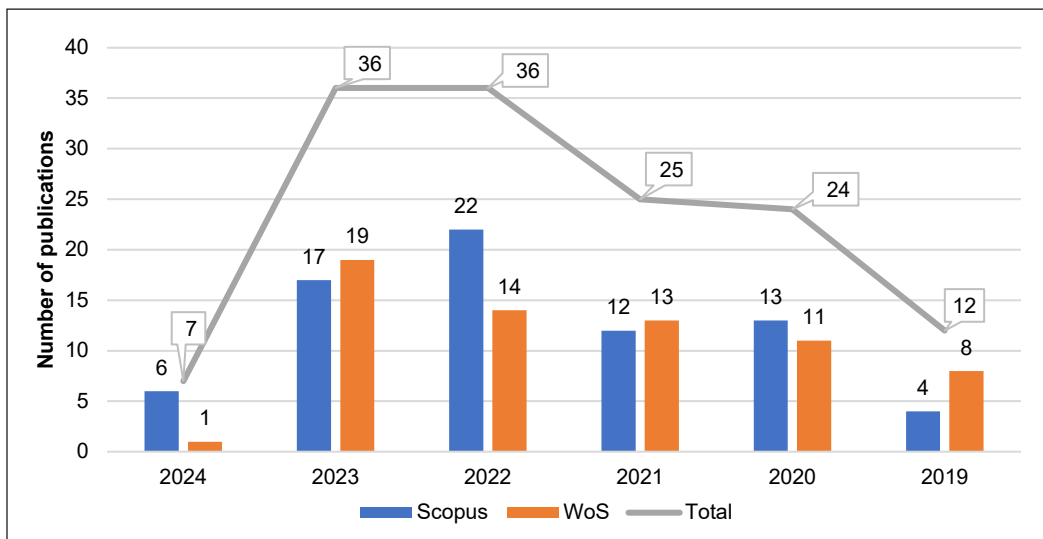


Figure 3. Publication trend analysis of PSPF

present research status of PSPF, as exhibited in Tables 3 to 5. Moreover, the analysis has disclosed the existence of forecasting models based on day-ahead and hour-ahead forecasting horizons, as depicted in Figure 4. The term day ahead resembles a forecasting horizon enveloping the next day (Andrade et al., 2017). Conversely, an hour ahead generally pertains to the formulation of forecasting that covers the next hour from the current moment (Wang et al., 2020). The number of articles published on hour-ahead forecasting in 2022 has significantly increased compared to prior years. It indicates an increasing attraction to this field of study. Conversely, the number of articles published on day-ahead forecasting peaked in 2020 and has relatively maintained over the following four years.

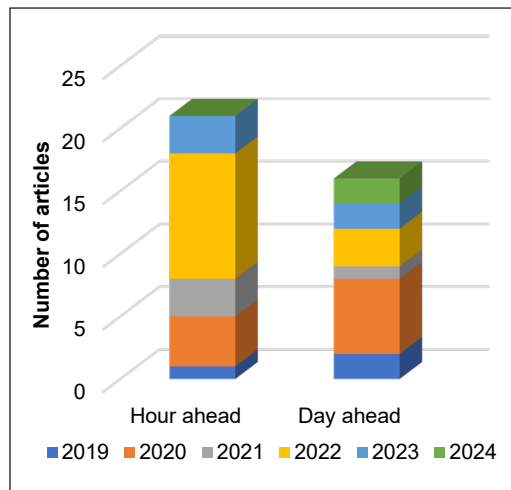


Figure 4. The probabilistic forecasting is based on the forecasting horizon from 2019 to 2024

Impact of Forecasting Horizon and Model Performances

The accuracy and reliability of PV power forecasting are achieved for a limited period called forecasting horizon. The selection of appropriate time horizons allows grid operators, utility companies, and energy managers to effectively strategize and enhance the operation of the grid and balance the supply and demand while maintaining the accuracy of forecasting output (Ahmed et al., 2020). Depending on the application for which forecasting is employed, the classification can vary significantly, involving very short, short-term, medium-term, or long-term horizons. However, there is no standard on horizon classifications, and the categories may overlap in some applications. Table 6 shows the type of forecasting horizon for the application in PV fields.

Based on the results from Tables 3 to 5, the majority of papers address short-term forecasting, focusing on horizons ranging from intra-day (hour ahead to day-ahead) (Bai et al., 2023; Mitrentsis & Lens, 2022; Phan et al., 2024). According to Mpfumali et al. (2019), “day ahead” pertains to a forecasting horizon that spans the entirety of the subsequent day. On the other hand, the term “hour ahead” typically refers to the development of a forecast that encompasses the subsequent hour from the present moment (Wang et al., 2020).

The field of probabilistic forecasting has yielded significant insight. Research reveals that forecasting models display varying performance levels based on the evaluation time horizon. Moreover, recent research has demonstrated the significance of employing short-term (hour ahead) forecasting methodologies when integrating PV power generation into

Table 3
Conventional Probabilistic Solar Power Forecasting (PSPF)

Authors	Title	Source Title	Method	Forecasting Horizon	Dataset & Case Study Location	Results
Bai M., Zhou Z., Chen Y., Liu J., Yu D. (Bai et al., 2023)	Accurate four-hour-ahead probabilistic forecast of PV power generation based on multiple meteorological variables-aided intelligent optimization of numeric weather prediction data.	Earth Science Informatics	NWP and Kernel Density	4 hours ahead	3 years, Brussels	MAE ranging from: 25.04% to 48.12% for 1-4 steps 14.80% to 21.27% for 5-8 steps 6.40% to 11.10% for 9-12 steps 2.18% to 4.45% for 13-16 step
Doelle O., Klinkenberg N., Amthor A., Ament C. (Doelle et al., 2023)	Probabilistic Intraday PV Power Forecast Utilizing Ensembles of Deep Gaussian Mixture Density Networks	Energies	Gaussian mixture density networks	Intra-day	20 months, Germany	Multiple Gaussian Distribution Skill score= 20.5% Ensembles Gaussian Distribution Skill score= 19.5%
Zhou N., Xu X., Yan Z., Shahidepour M. (Zhou et al., 2022)	Spatio-Temporal Probabilistic Forecasting of PV Power Based on Monotone Broad Learning System and Copula Theory	IEEE Transactions on Sustainable Energy	Quantile Regression Monotone broad Learning System (QRMBLS) and Copula theory.	Hour ahead	Australia and USA	Pinball Loss (kW) 5 min = 1.7640 1 h = 2.7674 Wrinkle Score (kW) 5 min = 25.7535 1 h = 39.3493
Van Der Meer D., Camal S., Kariniotakis G. (Meer et al., 2022)	Generalizing Renewable Energy Forecasting Utilizing Automatic Feature Selection and Combination	2022 17th International Conference on Probabilistic Methods Applied to Power Systems, PMAFS 2022	Analogue Ensemble (AnEn)	7 hours ahead	21 months	Mean \pm Standard Deviation = 0.274 \pm 0.06, 0.277 \pm 0.065 and 0.227 \pm 0.032

Table 3 (continue)

Authors	Title	Source Title	Method	Forecasting Horizon	Dataset & Case Study Location	Results
Wang W. T., Yang D. Z., Hong T., Kleissl J. (Wang et al., 2022)	An archived dataset from the ECMWF Ensemble Prediction System for probabilistic solar power forecasting	Solar Energy	NWP model (model chain)	90 hours ahead	4 years, Europe and North America	MAE = 1.27 RMSE = 2.24
Yagli G. M., Yang D., Srinivasan D. (Yagli et al., 2020)	Reconciling solar forecasts: Probabilistic forecasting with homoscedastic Gaussian errors on a geographical hierarchy	Solar Energy	Hierarchical forecasting and reconciliation	Day ahead and hour ahead	California and Arizona	PINAW = 93.10 CRPSSS = 61.55% PICP = 44.03
Alessandri S., McCandless T. (Alessandri & McCandless, 2020)	The Schaake Shuffle technique combines solar and wind power probabilistic forecasting	Energies	Analogue Ensemble (AnEn) + Schaake Shuffle (SS)	Hour ahead	26 months, Kuwait	CRPS = 182 Reliability = 8.74
Mpfumali P., Sigauke C., Bere A., Mulaudzi S. (Mpfumali et al., 2019)	Day ahead hourly global horizontal irradiance forecasting—application to South African data	Energies	Quantile Regression	Day ahead	South Africa (August 2009–April 2010)	CRPS = 151.57 Pinball loss = 8.82 PICP = 98.82%

Table 4
Probabilistic Solar Power Forecasting with regard to ML

Authors	Title	Source Title	Method	Forecasting Horizon	Dataset & Case Study Location	Results
Polo J., Martín-Chivelet N., Alonso-Abella M., Sanz-Saiz C., Cuenca J., de la Cruz M. (Polo et al., 2023)	Exploring the PV Power Forecasting at Building Façades Using Gradient Boosting Methods	Energies	Deterministic: XGBoost + Random Forest. Probabilistic: XGBoost + Bootstrap	Hour ahead	2 years, BIPV Spain	MAE: 40% (south array) MAE: 30% (East array)

Table 4 (continue)

Authors	Title	Source Title	Method	Forecasting Horizon	Dataset & Case Study Location	Results
Thaker J., Höllner R. (Thaker & Höllner, 2022)	A Comparative Study of Time Series Forecasting of Solar Energy Based on Irradiance Classification	Energies	Ensemble ML	72 hours ahead	9 months	rMAE = 20.9% rRMSE 32.4% skill score = 0.48
Mitrentsis G., Lens H. (Mitrentsis & Lens, 2022)	An interpretable probabilistic model for short-term solar power forecasting utilizing natural gradient boosting	Applied Energy	NGBoost	Hour ahead	20 months, Southern Germany	MAE (pu) = 0.0367 RMSE (pu) = 0.0617 MBE (pu) = -0.0007 PICP (-) = 0.8882 PINAW (pu) = 0.1732 CRPS (pu) = 0.0274
Cui W., Wan C., Song Y. (Cui et al., 2022)	Hybrid Probabilistic Forecasting of PV Power Generation Considering Weather Conditions	IEEE Power and Energy Society General Meeting	Extreme learning machine-based quantile regression, as well as the Hidden Markov Model (HMEQR)	3 hours ahead	-	Skill score = -0.0258 Average Coverage Deviation (ACD) 90% = -1.48 80% = 0.33
Mitrentsis G., Liu M., Lens H. (Mitrentsis et al., 2022)	Open-Source Tool for Probabilistic Short-Term PV and Wind Power Forecasting	2022 17th International Conference on Probabilistic Methods Applied to Power Systems, PMAPS 2022	NGBoost	Day ahead	-	Spring CRPS (pu) = 0.03 RMSE (pu) = 0.07 Summer CRPS (pu) = 0.02 RMSE (pu) = 0.05 Autumn CRPS (pu) = 0.01 RMSE (pu) = 0.03 Winter CRPS (pu) = 0.01 RMSE (pu) = 0.02

Table 4 (continue)

Authors	Title	Source Title	Method	Forecasting Horizon	Dataset & Case Study Location	Results
Bhavsar S., Pitchumani R., Ortega-Vazquez M. A. (Bhavsar et al., 2021)	ML-enabled reduced-order scenario generation for stochastic analysis of solar power forecasts	Applied Energy	Clustering-based ML	Hour ahead	California ISO	Reduced uncertainty estimation 2-4.5%
Qiao J., Pu T. J., Wang X. Y. (Qiao et al., 2021)	Renewable Scenario Generation Using Controllable Generative Adversarial Networks with Transparent Latent Space	IEEE	Generative Adversarial Networks	Hour ahead	-	-
Liu W., Xu Y. (Liu & Xu, 2020)	Randomized learning-based hybrid ensemble model for probabilistic forecasting of PV power generation	IET Generation, Transmission and Distribution	Randomized Learning-based Hybrid Ensemble (RLHE)	Day ahead	2 years, Australia	RMSE = 10.03% MAE = 6.19%
Lauret P., David M., Pinson P. (Lauret et al., 2019)	Verification of solar irradiance probabilistic forecasts	Solar Energy	Quantile Regression Forest Gradient Boosting	Hour ahead	United States and La Réunion Island	USA, CRPS = 6.97% Reunion Island, CRPS = 23.1%

Table 5
 Probabilistic Solar Power Forecasting with regard to DL

Authors	Title	Source Title	Method	Forecasting Horizon	Dataset & Case Study Location	Results
Phan Q. T., Wu Y. K., Phan Q. D. (Phan et al., 2024)	Enhancing One-Day-Ahead Probabilistic Solar Power Forecast With a Hybrid Transformer-LUBE Model and Missing Data Imputation	IEEE Transactions on Industry Applications	Transformer-LUBE	Day ahead	Taiwan	PI 90%: PINAW = 10.93 PI 80%: PINAW = 8.57 PI 70%: PINAW = 7.01
Bai M., Zhou Z., Li J., Chen Y., Liu J., Zhao X., Yu D. (Bai et al., 2024)	Deep graph gated recurrent unit network-based spatial-temporal multi-task learning for intelligent information fusion of multiple sites with application in the short-term spatial-temporal probabilistic forecast of photovoltaic power	Expert Systems with Applications	Gated Recurrent Unit (GRU) – Kernel Density Estimation (KDE)	Day ahead	Belgium and China	PI 90%: PINAW = 93.3% PI 80%: PINAW = 87.6% PI 70%: PINAW = 83.8%
Liu Y., Liu Y., Cai H., Zhang J. (Liu et al., 2023)	An innovative short-term multi-horizon PV power output forecasting method based on variational mode decomposition and a capsule convolutional neural network	Applied Energy	Two-stage hybrid Variational Mode Decomposition (VMD) as well as Innovative Capsule CNN (ACNet)	Day ahead	DKASC Australia	Highest Coefficient of Determination (R^2) values for the six forecast horizons 5 min = 0.9640 15 min = 0.9647 30 min = 0.9655 1 h = 0.9607 6 h = 0.9637 1 d = 0.9617

Table 5 (continue)

Authors	Title	Source Title	Method	Forecasting Horizon	Dataset & Case Study Location	Results
Jonler J. F., Brunolottrup F., Berg B., Zhang D., Chen K. (Jonler et al., 2023)	Probabilistic Forecasts of Global Horizontal Irradiance for Solar Systems	IEEE Sensors Letters	Transformer model	Hour ahead	Groningen (Netherlands) Brighton (United Kingdom)	MASE Netherlands = 0.846 United Kingdom = 0.807
Shi J., Wang Y., Zhou Y., Ma Y., Gao J., Wang S., Fu Z. (Shi et al., 2023)	Bayesian Optimization - LSTM Modeling and Time-Frequency Correlation Mapping Based Probabilistic Forecasting of Ultra-short-term Photovoltaic Power Outputs	IEEE Transactions on Industry Applications	Bayesian-LSTM		North China	PI 80% = 0.08 PI 90% = 0.10 PI 95% = 0.13
Sansine, V Ortega, P Hissel, D Hopare, M (Sansine et al., 2022)	Solar Irradiance Probabilistic Forecasting Using Machine Learning, Metaheuristic Models and Numerical Weather Predictions	Sustainability	PSO-LSTM-Gaussian PSO-LSTM-Laplacian	Day ahead	Tahiti	PI 38%: CWC = 6.3% PI 68%: CWC = 14.68% PI 95%: CWC = 59.13% PI 99%: CWC = 40.1%
Lin F., Zhang Y., Wang K., Wang J., Zhu M. (Lin et al., 2022)	Parametric Probabilistic Forecasting of Solar Power with Fat-Tailed Distributions and Deep Neural Networks	IEEE Transactions on Sustainable Energy	Laplace and DeepAR (LSTM)	Hour ahead	10 months	Sharpness = 0.2147 CRPS = 0.0523
Sun M., He L., Zhang J. (Sun et al., 2022)	DL-based probabilistic anomaly detection for solar forecasting under cyberattacks	International Journal of Electrical Power and Energy Systems	Convolution Neural Network - LSTM -Gaussian CNN-LSTM-Gaussian	Hour ahead	4 years, Texas	True Positive Rate (TPR) = 0.94 False Positive Rate (FPR) = 0.21 F-1 Score = 0.86

Table 5 (continue)

Authors	Title	Source Title	Method	Forecasting Horizon	Dataset & Case Study Location	Results
Afrasiabi S., Allahmoradi S., Salimi M., Liang X., Chung C.Y. (Afrasiabi et al., 2022)	Nonparametric Maximum Likelihood Probabilistic PV Power Generation Forecasting based on Spatial-Temporal DL	Canadian Conference on Electrical and Computer Engineering	CNN – Gated Recurrent Unit - Nonparametric Smooth Band Limit Maximum Likelihood CNN-GRU-NSBML	Hour ahead	-	CRPS = 1.0963 MAPE = 2.4634 CE = 0.0357 NRMSE = 0.0633
Dumas J., Wehenkel A., Lanaspeze D., Cornélusse B., Sutura A. (Dumas et al., 2022)	A deep generative model for probabilistic energy forecasting in power systems: normalizing flows	Applied Energy	Variational AutoEncoders (VAE), Generative Adversarial Networks (GAN), and Normalizing Flow (NF)	Hour ahead	Global Energy Forecasting Competition 2014	NF outperformed GAN and VAE CRPS = 2.35 QS = 1.19 MAE-r = 2.66 AUC = 0.950 ES = 23.08 VS = 4.68
Cheng L. L., Zang H. X., Wei Z. N., Zhang F. C., Sun G. Q., (Cheng et al., 2022)	Evaluation of opaque DL solar power forecast models toward power-grid applications	Renewable Energy	LSTM - Analogue Ensemble LSTM-AE	Day ahead	2 years, GEFCOM 2014	MAE = 0.050 ± 0.002 RMSE = 0.098 ± 0.003
Kodaira D., Tsukazaki K., Kure T., Kondoh J. (Kodaira et al., 2021)	Improving forecast reliability for geographically distributed PV generations	Energies	Neural Network-Native Bayes Classifier - LSTM	Day ahead	1 year, Japan	Cover Rate = 87% - 98.1% PI Width = 0.78kW - 4.051kW MAPE = 12.1% - 81.6% RMSE = 0.113kW - 0.939kW
Lin Y., Koprinska I., Rana M. (Lin et al., 2021)	Temporal Convolutional Attention Neural Networks for Time Series Forecasting	Proceedings of the International Joint Conference on Neural Networks	Temporal Convolutional Attention Neural Network (TCAN)	Hour ahead	6 years, Australia	MAPE = 0.062 - 0.068 MAE = 0.031 - 0.035

Table 5 (continue)

Authors	Title	Source Title	Method	Forecasting Horizon	Dataset & Case Study Location	Results
Dumas J., Coainte C., Fettweis X., Cornelusse B. (Dumas et al., 2021)	DL-based multi-output quantile forecasting of PV generation	2021 IEEE Madrid PowerTech, PowerTech 2021 - Conference Proceedings	MLP, LSTM, Encoder-Decoder (ED), Gradient Boosting Regression (GBR)	Day ahead and intra-day	5 months, Belgium	NMAE MLP= 7.9 LSTM = 7.7 GBR = 9.0 NRMSE MLP= 9.7 LSTM = 9.4 GBR = 10.9 CRPS MLP= 6.2 LSTM = 4.4 GBR = 6.3
Mashlakov A., Kuronen T., Lensu L., Kaarna A., Honkapuro S. (Mashlakov et al., 2021)	Assessing the performance of deep learning models for multivariate probabilistic energy forecasting	Applied Energy	DeepAR (LSTM), DeepTCN, LSTNet (GRU), and DSANet	-	2 years	Error Sensitivity DeepAR = 0.24 ± 0.099 DeepTCN = 0.32 ± 0.281 LSTNet = 0.33 ± 0.141 DSANet = 0.16 ± 0.070
Huang Q., Wei S. (Huang & Wei, 2020)	Improved quantile CNN with two-stage training for daily-ahead probabilistic forecasting of PV power	Energy Conversion and Management	Quantile CNN (QCNN)	Day ahead	Australia	Quantile 0.05 RMSE = 0.43kW MAPE = 19% Quantile 0.95 RMSE = 0.49kW MAPE = 23.9%
Kharlova E., May D., Musilek P. (Kharlova et al., 2020)	Forecasting PV Power Production using a DL Sequence to Sequence Model with Attention	Proceedings of the International Joint Conference on Neural Networks	LSTM Sequence to Sequence	Day ahead	-	Skill scores = 42.5-46%

Table 5 (continue)

Authors	Title	Source Title	Method	Forecasting Horizon	Dataset & Case Study Location	Results
Zang H., Cheng L., Ding T., Cheung K. W., Wei Z., Sun G. (Zang et al., 2020)	Day-ahead PV power forecasting approach based on deep CNN and meta-learning	International Journal of Electrical Power and Energy Systems	Novel CNN - Residual network (ResNet) and dense convolutional network (DenseNet)	Day ahead	10 years, DKASC Australia	MAEs ResNet = 0.152kW DenseNet = 0.180 kW Coverage error = 1% - 5%
Park S., Park S., Hwang E. (Park et al., 2020)	Normalized residue analysis for DL-based probabilistic forecasting of PV generations	Proceedings - 2020 IEEE International Conference on Big Data and Smart Computing, BigComp 2020	Auto-regressive recurrent neural network (DeepAR)	Hour ahead	2 years, Korea	RMSE = 50.7338 MAE = 37.8768
Toubeau J. F., Botticau J., Váalle F., De Greve Z., (Toubeau et al., 2019)	Deep Learning-Based Multivariate Probabilistic Forecasting for Short-Term Scheduling in Power Markets	IEEE TRANSACTIONS ON POWER SYSTEMS	Bi-LSTM-Gaussian Bi-LSTM-Quantile	Day ahead		Quantile Loss Bi-LSTM-Gaussian = 42MW Bi-LSTM-Quantile = 41MW

Table 6

Solar Power Forecasting horizon classification and application (Mishra et al., 2020; Perera et al., 2022)

Forecasting Classification	Horizon	Horizon Range	Application
Very-short term	Intra hour	1 min–30 min	Real-time control, ramp rate control, variability management
Short-term	Intra day	1–24 h	Demand response scheduling, grid operation
Medium-term	Intra week	1–7 days	Transmission scheduling and maintenance, economic dispatch
Long-term	Intra month	1 month–1 year	Energy procurement, economic feasibility, optimal design of renewable power plant

the electricity grid. Shi et al. (2023) have proposed an innovative method for predicting PV power outputs in the short term, focusing on time intervals ranging from minutes to hours. The researchers employ LSTM networks in combination with Bayesian optimization to provide probabilistic predictions. These predictions have prediction ranges of 80%, 90%, and 95%, resulting in accuracies of 0.08, 0.10, and 0.13, respectively. Jonler et al. (2023) have proposed a methodology that utilizes ensemble modeling and QR techniques to generate probabilistic predictions of Global Horizontal Irradiance (GHI) within a short-term horizon. The proposed approach provides probabilistic predictions encompassing the whole spectrum of conceivable GHI values, resulting in a predicted Mean Absolute Scaled Error (MASE) as minimal as 0.807.

Accuracy is of utmost importance in short-term forecasting when the level of uncertainty is comparatively smaller than that of longer forecasting horizons. Although advanced forecasting approaches are valuable, conventional XGBoost (Polo et al., 2023) may also be enough for short-term forecasting. The utilization of advanced forecasting methodologies is paramount in successfully integrating solar PV power generation into the power grid, guaranteeing efficient and dependable management of energy resources.

In solar power forecasting, day-ahead forecasting is significant for power system planning and market operations. The research conducted by Dumas et al. (2022; Zang et al., 2020) demonstrates the significance of day-ahead forecasting in these scenarios. Consequently, their study's findings indicate that this method improves forecasting precision while maintaining computing efficiency. It presents it as appropriate for incorporation into intraday decision-making tools for effective optimization. Other researchers, Huang and Wei (2020) and Kharlova et al. (2020), also explore day-ahead forecasting but propose innovative approaches to improve precision and reliability. The proposed techniques achieved skill scores ranging from 42.5% to 46% utilizing normalized root mean square error (RMSE) based on forecast skill records as a performance metric. However, challenges escalate with increasing uncertainty over longer forecasting horizons (Liu et al., 2023).

As the forecasting horizon increases, there is an increasing demand for complex models that can effectively manage increased levels of uncertainty. PSPF is preferable for longer-term horizons since it provides a more reliable representation of possible solar power generation. Furthermore, the increasing length of the forecasting horizon highlights the need for reliable probabilistic forecasting methods, such as advanced DL models, to enable efficient decision-making in power systems, given the inherent uncertainty associated with solar power generation. The latest research by Bai et al. (2024) and Phan et al. (2024) employs the DL method for day-ahead forecasts. The advancement of AI techniques, specifically DL algorithms, has shown significant effectiveness in PSPF.

The significance of the forecasting horizon is apparent in numerous aspects of power system operations, market dynamics, and the incorporation of renewable energy sources. Day-ahead and hour-ahead forecasting are vital to decision-making since they serve different purposes regarding planning horizons and operational requirements. The accuracy level generally tends to decrease as the duration of the forecasting period increases. Nevertheless, selecting these forecasting horizons depends on the distinct requirements and objectives. The adaptability of forecasting approaches to correspond with expected forecasting timeframes is crucial to ensure accurate, reliable, and effective decision-making in power system management and planning.

Comparative Evaluation of Machine Learning and Deep Learning in Probabilistic Model Advancement

Two methods can be used to create a probabilistic forecast: (1) parametric, calculating the parameters of the prediction distribution, and (2) nonparametric, which requires developing a predictive distribution with a limited amount of data observations. Many scholars prefer the parametric approach, a straightforward technique for creating predictive distributions that is well-known for its simplicity and low computational cost. After comparing probabilistic predictions made with parametric and nonparametric methods, Bakker et al. (2019) discovered that the nonparametric approaches perform significantly. The use of parametrics in the probabilistic forecast is restricted since they are the least dependable compared to nonparametric methods.

With the nonparametric method, the distribution is created using a variety of observable models rather than assuming its shape. One significant benefit of the nonparametric method is its flexibility. The input data are used to directly compute the output value distribution, reducing the number of estimating errors brought on by false assumptions concerning a specific distribution.

Initially, parametric and nonparametric methods were considered conventional probabilistic methods. These conventional methods traditionally relied on statistical approaches such as Autoregressive Moving Averages (ARMA), Autoregressive Integrated Moving Averages (ARIMA), Bayesian, Gaussian Distribution (Doelle et al., 2023), Quantile Regression (QR) (Zhou et al., 2022) (Mpfumali et al., 2019), Kernel Density Estimation (KDE) (Bai et al., 2023) and bootstrapping. The straightforward conventional modeling approaches that require fewer computational resources and expertise give an advantage to this method. Due to this, conventional probabilistic forecasting methods frequently offer interpretable models, facilitating comprehension of the fundamental assumption (Doelle et al., 2023). However, conventional probabilistic forecasting might encounter difficulties when dealing with big datasets based on multiple meteorological variables (Bai et al., 2023). Conventional probabilistic forecasting techniques, QR, Bayesian models, and Gaussian

methods frequently encounter difficulties in effectively capturing the associated complexity. Handling a massive dataset may require significant resources and time to train the model and tune complexity, thus making it unfeasible for certain applications.

In recent years, a significant increase in research has highlighted the ML models' incorporation within the domain of PSPF. The increasing interest in ML models arises from recognizing their enhanced efficacy in handling the inherent complexities of solar power forecasting, exceeding conventional approaches (Liu et al., 2023; Polo et al., 2023; Qiao et al., 2021). Their proficiency in employing advanced algorithms and computational techniques enables them to discern complex patterns, enhancing forecasting accuracy. Implementing ML, particularly decision tree-based methods such as XGBoost and Random Forest, allows the inclusion of exogenous parameters, leading to improved forecasting accuracy. This flexibility enables the model to capture additional information that may influence solar power generation (Polo et al., 2023). Besides that, the availability of implementation tools, such as the forecast library in Python, facilitates the implementation of different deterministic and probabilistic forecasting schemes by using ML models. These transparency implementation tools enable reproducibility and accelerate experimentation with different methodologies (Mitrentsis et al., 2022).

Hybrid ensemble models, which integrate multiple ML algorithms, exhibit the potential to enhance the accuracy of PSPF by offering enhanced prediction intervals essential for capturing the inherent uncertainty in solar power output (Liu & Xu, 2020). According to Bhavsar et al. (2021), ML techniques effectively handle uncertainty, decreasing the number of scenarios needed for analysis and simplifying the forecasting process. Mitrentsis and Lens (2022) proposed an advanced study that researched a two-stage probabilistic forecasting framework for PV power forecasting. It utilizes Natural Gradient Boosting (NGBoost) and Shapley additive explanation. Compared to state-of-the-art algorithms, the framework improved performance and accuracy, allowing for detailed analysis of complex non-linear relationships and interaction effects.

Since ML methods learn from the input data, they struggle to adapt to environmental changes. It could potentially lead to the models not fully capturing the corresponding deep non-linear characteristics under varying environmental conditions. On top of that, ML methods may encounter scalability issues that require extensive computational resources for data training, especially when dealing with time series utility-scale PV system applications (Mitrentsis & Lens, 2022).

In the age of computer hardware, software, and big data technology advancements, a notable and expanding emphasis exists on DL networks. It draws inspiration from the human brain's functions and structure. These networks have evolved into a vital component of contemporary AI and ML owing to their remarkable capacity to autonomously identify and grasp intricate patterns and representations from extensive datasets. Among DL-based models, LSTM is widely used in PSPF due to its ability to model time series data and

capture long-term temporal dependencies (Sun et al., 2022). (Sansine et al., 2022; Shi et al., 2023) evaluated various DL models based on LSTM and emphasized that the LSTM model is the most reliable in terms of its practicality for applications inside the energy market.

Notably, a two-stage hybrid approach combining Variational Mode Decomposition (VMD) and Innovative Capsule CNN (ACCNet) achieves high Coefficient of Determination (R^2) values for different forecast horizons, indicating strong predictive performance (Liu et al., 2023). Other models, such as Laplace and DeepAR (LSTM) (Lin et al., 2022), demonstrate good calibration and accuracy, while CNN-LSTM-Gaussian showcases robust binary classification performance. Normalizing Flow (NF), Generative Adversarial Networks (GAN), as well as Variational AutoEncoders (VAE), reveal that NF outperforms others in probabilistic forecasting (Dumas et al., 2022). LSTM-AE excels in point forecasting with low MAE and RMSE, while DSANet exhibits low error sensitivity (Mashlakov et al., 2021). However, some methods show room for improvement, such as the Auto-regressive recurrent neural network (DeepAR) (Park et al., 2020), which yields relatively high RMSE and MAE. These findings offer a detailed analysis of DL methods with regard to solar power forecasting, assisting in selecting appropriate models based on specific forecasting requirements.

The present study on Transformer architectures for probabilistic DL forecasting has revealed higher accuracy than alternative AI models. Transformers utilize parallel processing capabilities and excel over traditional methods in dynamic forecasting contexts (Phan et al., 2024). DL algorithms greatly improve the accuracy and efficiency of PSPF, providing scalable and flexible solutions for dynamic situations. Note that probabilistic DL techniques have the advantage of being extremely scalable due to their ability to leverage the parallel processing capabilities of Graphics Processing Units (GPUs) as well as Tensor Processing Units (TPUs). Other than that, they adapt to diverse data sources and changing conditions, making them more flexible in dynamic forecasting environments.

Nevertheless, the development and implementation of DL models inherently incur costs associated with hardware resources like GPUs and TPUs. DL models also need sufficient data to train for accurate probabilistic forecasting (Jonler et al., 2023). Compared to conventional probabilistic forecasting methods, pre-processing and data imputation need to be implemented in the DL model to help improve convergence, prevent vanishing or exploding gradients, and enhance the model's ability to learn relevant patterns from the data (Phan et al., 2024).

Table 7 summarizes PSPF's strengths and weaknesses. However, the advancement of ML and DL models holds great promise for enhancing the accuracy and reliability of probabilistic solar power forecasting in the future, thereby facilitating the integration of solar energy into the power grid and supporting the transition to renewable energy sources. As a result, probabilistic ML and DL techniques are advantageous in improving forecasting performance compared to conventional methods.

Table 7
Strengths and weaknesses of the PSPF Model

Model category	Strength	Weakness
Conventional PSPF	<ul style="list-style-type: none"> • Simplicity modeling approaches • Low computational cost 	<ul style="list-style-type: none"> • Difficulties in capturing the complexity associated. • Requires significant resources and time to train and tune the model. • Not feasible in handling massive datasets and complex application
ML PSPF	<ul style="list-style-type: none"> • Ability to adapt to dynamic and uncertain environments. • Availability of open-source tools. • Allows the inclusion of exogenous parameters. 	<ul style="list-style-type: none"> • Difficulty in capturing long-term temporal dependencies. • Requiring extensive computational resources • Require a large dataset.
DL PSPF	<ul style="list-style-type: none"> • Ability to capture long-term temporal dependencies. • Adapt to diverse data sources and uncertain environments. • Ability to leverage parallel processing capabilities. 	<ul style="list-style-type: none"> • High cost associated (GPU and TPU) • Requiring extensive computational resources • Require a large dataset.

Uncertainty Quantification Metric

Probabilistic forecasts, frequently depicted as interval or scenario predictions, present further complexity in contrast to deterministic forecasts due to incorporating a range of possible outcomes compared to a single-point prediction. The measurement of uncertainty in PSPF implies assessing the reliability and sharpness of these forecasts. Note that reliability is related to the probabilistic calculation, the forecasting model’s accuracy that aligns with the actual probabilities. At the same time, sharpness quantifies the dispersion of the predicted distributions and evaluates the forecasts independently, indicating the forecast model’s usefulness (Doubleday et al., 2020).

The utilization of metrics to assess reliability and sharpness offers valuable insights into the quality and accuracy of forecasting. Prediction Interval Coverage Probability (PICP) and Average Coverage Error (ACE) are often utilized reliability metrics that assess the extent to which prediction intervals correspond to observed data. Lower ACE values indicate better reliability, as the prediction intervals are closer to the desired coverage probability. An elevated PICP, as illustrated by (Mpfumali et al., 2019) attaining 98.82%, indicates superior reliability, whereas reduced ACE values indicate enhanced reliability.

The optimization of sharpness while maintaining reliability is crucial in probabilistic forecasting since it helps to reduce uncertainty. Sharpness analysis often uses metrics such as Coverage Width-based Criterion (CWC), Prediction Interval Normalized Average Width (PINAW), and CRPS. The PINAW metric evaluates the mean width of prediction intervals concerning the variability observed in the data, where smaller values

indicate more precise forecasts. Nevertheless, the capability to compare studies may be constrained when employing distinct metrics, as outlined by Phan et al. (2024) and Bai et al. (2024). The CWC technique assesses the difference between predicted and observed cumulative distribution functions, where lower values indicate superior performance. It is demonstrated by the research undertaken by Sansine et al. (2022) with 38%, 68%, 95%, and 99% with regard to prediction interval. CWC values are 6.3, 14.68, 59.13, and 40.1, respectively.

CRPS is a robust metric that combines reliability and sharpness evaluation. The key advantage of this approach is its ability to facilitate the comparison between probabilistic and point forecasts. Consequently, it has the potential to establish itself as an established method for validating probabilistic forecasts, as proposed by Lauret et al. (2019). CRPS has become popular in academic research because it maintains unit consistency with the projected variable. Studies conducted by Yang (2020), Alessandrini and McCandless (2020), Mpfumali et al. (2019) and Lin et al. (2022) have consistently shown that lower scores are indicative of higher accuracy. For example, Dumas et al. (2021) compared CRPS values among several forecasting models. LSTM had the lowest CRPS of 4.4, lower than MLP and GBR. Furthermore, a study conducted by Mitrentsis et al. (2022) examined the CRPS across various seasons, revealing that the winter season exhibited the lowest CRPS value of 0.01. The investigation of spatial distribution in the United States and Reunion Island revealed disparate values of CRPS, with the United States exhibiting lower scores in comparison to Reunion Island, with 6.97 and 23.1, respectively.

ML and DL models routinely demonstrate superior performance compared to conventional methods. Mitrentsis et al. (2022) demonstrated that the ML model attained a CRPS value of 0.01, whereas Lin et al. (2022) reported that the DL model achieved a CRPS value of 0.0523. As Yagli et al. (2020) described, the conventional approach exhibited a CRPS value 0.615. Furthermore, significant research highlights the effectiveness of ML methods in enhancing solar power forecasting accuracy. ML methodologies have exhibited a capacity to adjust to changing circumstances, providing precision of solar power (Bai et al., 2024; Jonler et al., 2023; Sansine et al., 2022). Additionally, ML-based offers probabilistic forecasts and prediction intervals, which hold significant value in the context of grid management and decision-making procedures.

Beyond the CRPS method, the pinball loss function and the Winkler score account for reliability and sharpness, making them particularly suitable for quantile forecasting. A low pinball score and Winkler score signify an accurate probabilistic prediction. Zhou et al. (2022) conducted an assessment 5 minutes ahead; forecasting indicates a minimum Pinball loss of 1.76kW in contrast to 2.767kW observed 1 hour ahead. For the Winkler score, the lowest 25.75kW was observed 5 minutes ahead of forecasting compared to 39.94kW obtained 1 hour ahead of forecasting. Overall, these uncertainty quantification

metrics serve a valuable role in optimizing the use of PSPF to evaluate accuracy and reliability, facilitating informed decisions regarding integrating renewable energy and managing power grids.

CONCLUSION

In conclusion, integrating ML and DL methods has resulted in remarkable advancements in PSPF. Researchers have explored various models and evaluation metrics to improve PSPF reliability and accuracy. Note that forecasting horizons significantly impact the performance of solar power forecasting models. The increasing length of the forecasting horizon highlights the need for reliable probabilistic forecasting methods such as the ML and DL models. Day-ahead and hour-ahead forecasting are both vital components of the decision-making process since they serve different purposes in terms of planning horizons and operational requirements. ML ensemble and hybrid models show promise in improving the accuracy of PSPF by providing improved prediction intervals with low relative MAE and RMSE values and high accuracy scores. The advancement of the latest DL Transformer architecture, leveraging their ability to discover intricate patterns in large datasets, has revealed higher accuracy. The uncertainty quantification metric, CRPS's robust metric that combines reliability and sharpness evaluation, assists in selecting the best probabilistic forecasts due to its ability to maintain unit consistency with the projected variable. These research findings provide valuable insights for stakeholders in solar power generation, enabling informed choices about forecasting methods, horizons, and uncertainty metrics. As the field evolves, integrating the ML and DL methods is crucial in improving efficiency and reliability regarding solar power forecasting, ultimately contributing to the growth and sustainability of renewable energy sources. Future work could extend a comprehensive review of a hybrid probabilistic model method for utility-scale PV systems known as large-scale solar.

ACKNOWLEDGEMENT

The authors extend their gratitude to Universiti Teknologi MARA, Malaysia, for facilitating the Strategic Research Partnership: UiTM-Universitas Indonesia Bilateral Strategic Alliance (UiTM-UI BISA) Matching Grant (UiTM Project Number: 100-RMC 5/3/SRP (051/2021) and UI Project Number: No: NKB-671/UN2.RST/HKP.05.00/2021).

REFERENCES

- Abuella, M., & Chowdhury, B. (2019). Forecasting of solar power ramp events: A post-processing approach. *Renewable Energy*, 133, 1380-1392. <https://doi.org/10.1016/j.renene.2018.09.005>
- Afrasiabi, S., Allahmoradi, S., Salimi, M., Liang, X., & Chung, C. Y. Y. (2022, September 18-20). *Nonparametric maximum likelihood probabilistic photovoltaic power generation forecasting based on spatial-temporal deep learning*. [Paper presentation]. IEEE Canadian Conference

- on Electrical and Computer Engineering(CCECE), Halifax, Canada. <https://doi.org/10.1109/CCECE49351.2022.9918338>
- Ahmed, R., Sreeram, V., Mishra, Y., & Arif, M. D. (2020). A review and evaluation of the state-of-the-art in PV solar power forecasting: Techniques and optimization. *Renewable and Sustainable Energy Reviews*, *124*, Article 109792. <https://doi.org/10.1016/j.rser.2020.109792>
- Alessandrini, S., & McCandless, T. (2020). The schaaake shuffle technique to combine solar and wind power probabilistic forecasting. *Energies*, *13*(10), Article 2503. <https://doi.org/10.3390/en13102503>
- Andrade, J. R., Filipe, J., Reis, M., & Bessa, R. J. (2017). Probabilistic price forecasting for day-ahead and intraday markets: Beyond the statistical model. *Sustainability*, *9*(11), Article 1990. <https://doi.org/10.3390/su9111990>
- Bai, M., Zhou, Z., Chen, Y., Liu, J., & Yu, D. (2023). Accurate four-hour-ahead probabilistic forecast of photovoltaic power generation based on multiple meteorological variables-aided intelligent optimization of numeric weather prediction data. *Earth Science Informatics*, *16*(3), 2741–2766. <https://doi.org/10.1007/s12145-023-01066-9>
- Bai, M., Zhou, Z., Li, J., Chen, Y., Liu, J., Zhao, X., & Yu, D. (2024). Deep graph gated recurrent unit network-based spatial-temporal multi-task learning for intelligent information fusion of multiple sites with application in short-term spatial-temporal probabilistic forecast of photovoltaic power. *Expert Systems with Applications*, *240*, Article 122072. <https://doi.org/10.1016/j.eswa.2023.122072>
- Bakker, K., Whan, K., Knap, W., & Schmeits, M. (2019). Comparison of statistical post-processing methods for probabilistic NWP forecasts of solar radiation. *Solar Energy*, *191*, 138-150. <https://doi.org/10.1016/j.solener.2019.08.044>
- Bazionis, I. K., & Georgilakis, P. S. (2021). Review of deterministic and probabilistic wind power forecasting: Models, methods, and future research. *Electricity*, *2*(1), 13-47. <https://doi.org/10.3390/electricity2010002>
- Bhavsar, S., Pitchumani, R., & Ortega-Vazquez, M. A. (2021). Machine learning enabled reduced-order scenario generation for stochastic analysis of solar power forecasts. *Applied Energy*, *293*, Article 116964. <https://doi.org/10.1016/j.apenergy.2021.116964>
- Chen, Z., Chen, Y., Wu, L., Cheng, S., Lin, P., & You, L. (2019). Accurate modeling of photovoltaic modules using a 1-D deep residual network based on I-V characteristics. *Energy Conversion and Management*, *186*, 168-187. <https://doi.org/10.1016/j.enconman.2019.02.032>
- Cheng, L. L., Zang, H. X., Wei, Z. N., Zhang, F. C., & Sun, G. Q. (2022). Evaluation of opaque deep-learning solar power forecast models towards power-grid applications. *Renewable Energy*, *198*, 960-972. <https://doi.org/10.1016/j.renene.2022.08.054>
- Chowdhury, M. S., Rahman, K. S., Chowdhury, T., Nuthammachot, N., Techato, K., Akhtaruzzaman, M., Tiong, S. K., Sopian, K., & Amin, N. (2020). An overview of solar photovoltaic panels' end-of-life material recycling. *Energy Strategy Reviews*, *27*, Article 100431. <https://doi.org/10.1016/j.esr.2019.100431>
- Chu, Y., Li, M., Coimbra, C. F. M., Feng, D., & Wang, H. (2021). Intra-hour irradiance forecasting techniques for solar power integration: A review. *IScience*, *24*(10), Article 103136. <https://doi.org/10.1016/j.isci.2021.103136>

- Cui, W., Wan, C., & Song, Y. (2022, July 17-21). *Hybrid probabilistic forecasting of photovoltaic power generation considering weather conditions*. [Paper presentation]. IEEE Power and Energy Society General Meeting (PESGM), Denver, USA. <https://doi.org/10.1109/PESGM48719.2022.9917228>
- Devaraj, J., Elavarasan, R. M., Shafiullah, G. M., Jamal, T., Khan, I., Elavarasan, R. M., Shafiullah, G. M., Jamal, T., & Khan, I. (2021). A holistic review on energy forecasting using big data and deep learning models. *International Journal of Energy Research*, 45(9), 13489-13530. <https://doi.org/10.1002/er.6679>
- Doelle, O., Klinkenberg, N., Amthor, A., & Ament, C. (2023). Probabilistic intraday PV power forecast using ensembles of deep gaussian mixture density networks. *Energies*, 16(2), Article 646. <https://doi.org/10.3390/en16020646>
- Doubleday, K., Van Scyoc Hernandez, V., & Hodge, B. M. (2020). Benchmark probabilistic solar forecasts: Characteristics and recommendations. *Solar Energy*, 206, 52-67. <https://doi.org/10.1016/j.solener.2020.05.051>
- Dumas, J., Cointe, C., Fettweis, X., & Cornélusse, B. (2021, June 28- July 2). *Deep learning-based multi-output quantile forecasting of PV generation*. [Paper presentation]. IEEE Madrid PowerTech, Madrid, Spain. <https://doi.org/10.1109/PowerTech46648.2021.9494976>
- Dumas, J., Wehenkel, A., Lanaspéze, D., Cornélusse, B., & Sutura, A. (2022). A deep generative model for probabilistic energy forecasting in power systems: Normalizing flows. *Applied Energy*, 305, Article 117871. <https://doi.org/10.1016/j.apenergy.2021.117871>
- Feng, C., Liu, Y., & Zhang, J. (2021). A taxonomical review on recent artificial intelligence applications to PV integration into power grids. *International Journal of Electrical Power and Energy Systems*, 132, Article 107176. <https://doi.org/10.1016/j.ijepes.2021.107176>
- Huang, Q., & Wei, S. (2020). Improved quantile convolutional neural network with two-stage training for daily-ahead probabilistic forecasting of photovoltaic power. *Energy Conversion and Management*, 220, Article 113085. <https://doi.org/10.1016/j.enconman.2020.113085>
- International Energy Agency. (2023). *Snapshot of global PV markets 2023* (Report No. IEA-PVPS T1-44:2023). International Energy Agency. chrome-extension://efaidnbmnnnnibpcajpcggleclfindmkaj/https://iea-pvps.org/wp-content/uploads/2023/04/IEA_PVPS_Snapshot_2023.pdf
- Jonler, J. F. F., Brunolottrup, F., Berg, B., Zhang, D., & Chen, K. (2023). Probabilistic forecasts of global horizontal irradiance for solar systems. *IEEE Sensors Letters*, 7(1), Article 7000104. <https://doi.org/10.1109/LSENS.2022.3228783>
- Kharlova, E., May, D., & Musilek, P. (2020, July 19-24). *Forecasting photovoltaic power production using a deep learning sequence to sequence model with attention*. [Paper presentation]. International Joint Conference on Neural Networks (IJCNN), Glasgow, United Kingdom. <https://doi.org/10.1109/IJCNN48605.2020.9207573>
- Kirkwood, C., Economou, T., Odbert, H., & Pugeault, N. (2021). A framework for probabilistic weather forecast post-processing across models and lead times using machine learning. *Philosophical Transactions of the Royal Society A*, 379(2194), Article 20200099. <https://doi.org/10.1098/rsta.2020.0099>
- Kodaira, D., Tsukazaki, K., Kure, T., & Kondoh, J. (2021). Improving forecast reliability for geographically distributed photovoltaic generations. *Energies*, 14(21), Article 7340. <https://doi.org/10.3390/en14217340>

- Kumari, P., & Toshniwal, D. (2021). Deep learning models for solar irradiance forecasting: A comprehensive review. *Journal of Cleaner Production*, 318, Article 128566. <https://doi.org/10.1016/j.jclepro.2021.128566>
- Lauret, P., David, M., & Pinson, P. (2019). Verification of solar irradiance probabilistic forecasts. *Solar Energy*, 194, 254-271. <https://doi.org/10.1016/j.solener.2019.10.041>
- Li, Q., Xu, Y., Chew, B. S. H., Ding, H., & Zhao, G. (2022). An integrated missing-data tolerant model for probabilistic PV power generation forecasting. *IEEE Transactions on Power Systems*, 37(6), 4447-4459. <https://doi.org/10.1109/TPWRS.2022.3146982>
- Lin, F., Zhang, Y., Wang, K., Wang, J., & Zhu, M. (2022). Parametric probabilistic forecasting of solar power with fat-tailed distributions and deep neural networks. *IEEE Transactions on Sustainable Energy*, 13(4), 2133-2147. <https://doi.org/10.1109/TSTE.2022.3186517>
- Lin, Y., Koprinska, I., & Rana, M. (2021, July 18-22). *Temporal convolutional attention neural networks for time series forecasting*. [Paper presentation]. International Joint Conference on Neural Networks (IJCNN), Shenzhen, China. <https://doi.org/10.1109/IJCNN52387.2021.9534351>
- Liu, W., & Xu, Y. (2020). Randomised learning-based hybrid ensemble model for probabilistic forecasting of PV power generation. *IET Generation, Transmission and Distribution*, 14(24), 5816-5822. <https://doi.org/10.1049/iet-gtd.2020.0625>
- Liu, Y., Liu, Y., Cai, H., & Zhang, J. (2023). An innovative short-term multihorizon photovoltaic power output forecasting method based on variational mode decomposition and a capsule convolutional neural network. *Applied Energy*, 343, Article 121139. <https://doi.org/10.1016/j.apenergy.2023.121139>
- Maraggi, L. M. R., Lake, L. W., & Walsh, M. P. (2021, October 18-21). *Bayesian predictive performance assessment of rate-time models for unconventional production forecasting*. [Paper presentation]. SPE Europec Featured at 82nd EAGE Conference and Exhibition, Amsterdam, The Netherlands. <https://doi.org/10.2118/205151-ms>
- Mashlakov, A., Kuronen, T., Lensu, L., Kaarna, A., & Honkapuro, S. (2021). Assessing the performance of deep learning models for multivariate probabilistic energy forecasting. *Applied Energy*, 285, Article 116405. <https://doi.org/10.1016/j.apenergy.2020.116405>
- Mellit, A., Massi Pavan, A., Ogliari, E., Leva, S., & Lughi, V. (2020). Advanced methods for photovoltaic output power forecasting: A review. *Applied Sciences*, 10(2), Article 487.
- Mishra, M., Dash, P. B., Nayak, J., Naik, B., & Swain, S. K. (2020). Deep learning and wavelet transform integrated approach for short-term solar PV power prediction. *Measurement: Journal of the International Measurement Confederation*, 166, Article 108250. <https://doi.org/10.1016/j.measurement.2020.108250>
- Mitrentsis, G., & Lens, H. (2022). An interpretable probabilistic model for short-term solar power forecasting using natural gradient boosting. *Applied Energy*, 309, Article 118473. <https://doi.org/10.1016/j.apenergy.2021.118473>
- Mitrentsis, G., Liu, M., & Lens, H. (2022, June 12-15). *Open source tool for probabilistic short-term pv and wind power forecasting*. [Paper presentation]. 17th International Conference on Probabilistic Methods Applied to Power Systems (PMAPS), Manchester, United Kingdom. <https://doi.org/10.1109/PMAPS53380.2022.9810561>

- Mittal, A. K., Mathur, K., & Mittal, S. (2022). A review on forecasting the photovoltaic power using machine learning. *Journal of Physics: Conference Series*, 2286(1), Article 012010. <https://doi.org/10.1088/1742-6596/2286/1/012010>
- Mpfumali, P., Sigauke, C., Bere, A., & Mulaudzi, S. (2019). Day ahead hourly global horizontal irradiance forecasting—Application to South African data. *Energies*, 12(18), Article 3569. <https://doi.org/10.3390/en12183569>
- Mustafa, W. A. (2022). Cervical cancer situation in Malaysia: A systematic literature review. *BIOCELL*, 46(2), 367–381. <https://doi.org/10.32604/biocell.2022.016814>
- Panagiotopoulou, V. C., Stavropoulos, P., & Chryssoulouris, G. (2022). A critical review on the environmental impact of manufacturing: A holistic perspective. *International Journal of Advanced Manufacturing Technology*, 118(1–2), 603–625. <https://doi.org/10.1007/s00170-021-07980-w>
- Park, S., Park, S., & Hwang, E. (2020, February 19–22). *Normalized residue analysis for deep learning based probabilistic forecasting of photovoltaic generations*. [Paper presentation]. IEEE International Conference on Big Data and Smart Computing (BigComp), Busan, Korea. <https://doi.org/10.1109/BigComp48618.2020.00-20>
- Pazikadin, A. R., Rifai, D., Ali, K., Malik, M. Z., Abdalla, A. N., & Faraj, M. A. (2020). Solar irradiance measurement instrumentation and power solar generation forecasting based on Artificial Neural Networks (ANN): A review of five years research trend. *Science of the Total Environment*, 715, Article 136848. <https://doi.org/10.1016/j.scitotenv.2020.136848>
- Perera, M., De Hoog, J., Bandara, K., & Halgamuge, S. (2022). Multi-resolution, multi-horizon distributed solar PV power forecasting with forecast combinations. *Expert Systems with Applications*, 205, Article 117690. <https://doi.org/10.1016/j.eswa.2022.117690>
- Phan, Q. T. Q. D., Wu, Y. K., & Phan, Q. T. Q. D. (2024). Enhancing one-day-ahead probabilistic solar power forecast with a hybrid transformer-LUBE model and missing data imputation. *IEEE Transactions on Industry Applications*, 60(1), 1396–1408. <https://doi.org/10.1109/TIA.2023.3325798>
- Polo, J., Martín-Chivelet, N., Alonso-Abella, M., Sanz-Saiz, C., Cuenca, J., & Cruz, M. D. L. (2023). Exploring the PV power forecasting at building façades using gradient boosting methods. *Energies*, 16(3), Article 1495. <https://doi.org/10.3390/en16031495>
- Qiao, J., Pu, T. J., & Wang, X. Y. (2021). Renewable scenario generation using controllable generative adversarial networks with transparent latent space. *CSEE Journal of Power and Energy Systems*, 7(1), 66–77. <https://doi.org/10.17775/CSEEJPES.2020.00700>
- Rajagukguk, R. A., Ramadhan, R. A. A., & Lee, H. J. (2020). A review on deep learning models for forecasting time series data of solar irradiance and photovoltaic power. *Energies*, 13(24), Article 6623. <https://doi.org/10.3390/en13246623>
- Salisu, A. A., Gupta, R., & Ogbonna, A. E. (2021). Point and density forecasting of macroeconomic and financial uncertainties of the USA. *Journal of Forecasting*, 40(4), 700–707. <https://doi.org/10.1002/for.2740>
- Sansine, V., Ortega, P., Hissel, D., & Hopuare, M. (2022). Solar irradiance probabilistic forecasting using machine learning, metaheuristic models and numerical weather predictions. *Sustainability*, 14(22), Article 15260. <https://doi.org/10.3390/su142215260>

- Shafiullah, M., Ahmed, S. D., & Al-Sulaiman, F. A. (2022). Grid integration challenges and solution strategies for solar PV systems: A review. *IEEE Access*, *10*, 52233-52257. <https://doi.org/10.1109/ACCESS.2022.3174555>
- Shi, J., Wang, Y., Zhou, Y., Ma, Y., Gao, J., Wang, S., & Fu, Z. (2023). Bayesian optimization - LSTM modeling and time frequency correlation mapping based probabilistic forecasting of ultra-short-term photovoltaic power outputs. *IEEE Transactions on Industry Applications*, *60*(2), 2422-2430. <https://doi.org/10.1109/TIA.2023.3334700>
- Sun, M., He, L., & Zhang, J. (2022). Deep learning-based probabilistic anomaly detection for solar forecasting under cyberattacks. *International Journal of Electrical Power and Energy Systems*, *137*, Article 107752. <https://doi.org/10.1016/j.ijepes.2021.107752>
- Thaker, J., & Höller, R. (2022). A comparative study of time series forecasting of solar energy based on irradiance classification. *Energies*, *15*(8), Article 2837. <https://doi.org/10.3390/en15082837>
- Toubeau, J. F., Botticau, J., Vallee, F., & De Greve, Z. (2019). Deep learning-based multivariate probabilistic forecasting for short-term scheduling in power markets. *IEEE Transactions on Power Systems*, *34*(2), 1203-1215. <https://doi.org/10.1109/TPWRS.2018.2870041>
- Wang, H., Lei, Z., Zhang, X., Zhou, B., & Peng, J. (2019). A review of deep learning for renewable energy forecasting. *Energy Conversion and Management*, *198*, Article 111799. <https://doi.org/10.1016/j.enconman.2019.111799>
- Wang, J., Qian, Z., Wang, J., & Pei, Y. (2020). Hour-ahead photovoltaic power forecasting using an analog plus neural network ensemble method. *Energies*, *13*(12), Article 3259. <https://doi.org/10.3390/en13123259>
- Wang, W., Yang, D., Hong, T., & Kleissl, J. (2022). An archived dataset from the ECMWF ensemble prediction system for probabilistic solar power forecasting. *Solar Energy*, *248*, 64–75. <https://doi.org/10.1016/j.solener.2022.10.062>
- Wen, Y., AlHakeem, D., Mandal, P., Chakraborty, S., Wu, Y. K., Senjyu, T., Paudyal, S., & Tseng, T. L. (2020). Performance evaluation of probabilistic methods based on bootstrap and quantile regression to quantify PV power point forecast uncertainty. *IEEE transactions on neural networks and learning systems*, *31*(4), 1134-1144. <https://doi.org/10.1109/TNNLS.2019.2918795>
- Yagli, G. M., Yang, D., & Srinivasan, D. (2020). Reconciling solar forecasts: Probabilistic forecasting with homoscedastic Gaussian errors on a geographical hierarchy. *Solar Energy*, *210*, 59–67. <https://doi.org/10.1016/j.solener.2020.06.005>
- Yang, D. (2020). Reconciling solar forecasts: Probabilistic forecast reconciliation in a nonparametric framework. *Solar Energy*, *210*, 49-58. <https://doi.org/10.1016/j.solener.2020.03.095>
- Yu, W., Liu, G., Zhu, L., & Yu, W. (2020). Convolutional neural network with feature reconstruction for monitoring mismatched photovoltaic systems. *Solar Energy*, *212*, 169-177. <https://doi.org/10.1016/j.solener.2020.09.026>
- Zafar, M. H., Khan, N. M., Mansoor, M., Mirza, A. F., Moosavi, S. K. R., Sanfilippo, F., Zafar, M. H., Khan, N. M., Mansoor, M., Mirza, A. F., Moosavi, S. K. R., & Sanfilippo, F. (2022). Adaptive ML-based technique for renewable energy system power forecasting in hybrid PV-Wind farms power conversion systems. *Energy Conversion and Management*, *258*, Article 115564. <https://doi.org/10.1016/j.enconman.2022.115564>

Zang, H., Cheng, L., Ding, T., Cheung, K. W., Wei, Z., & Sun, G. (2020). Day-ahead photovoltaic power forecasting approach based on deep convolutional neural networks and meta learning. *International Journal of Electrical Power and Energy Systems*, 118, Article 105790. <https://doi.org/10.1016/j.ijepes.2019.105790>

Zhou, N., Xu, X., Yan, Z., & Shahidehpour, M. (2022). Spatio-temporal probabilistic forecasting of photovoltaic power based on monotone broad learning system and copula theory. *IEEE Transactions on Sustainable Energy*, 13(4), 1874–1885. <https://doi.org/10.1109/TSTE.2022.3174012>

Prediction of Temperature Variability on Power Transmission Line Parameters Using Intelligent Approaches

Ashfaq Ahmad^{1,2*}, Iqra Javed³, Changan Zhu², Muhammad Babar Rasheed⁴, Muhammad Waqar Akram^{2,5}, Muhammad Wisal Khan⁶, Umair Ghazanfar⁷, Waseem Nazar⁸, Syed Baqar Hussain³ and Amber Sultan⁸

¹Department of Artificial Intelligence, School of Systems and Technology, University of Management and Technology, Lahore, Pakistan

²Department of Precision Machinery & Instrumentation, University of Science and Technology of China, Hefei, China

³Department of Computer Science, School of Systems and Technology, University of Management and Technology, Lahore, Pakistan

⁴Department of Electronics & Electrical Systems, University of Lahore, Lahore, Pakistan

⁵Department of Farm Machinery & Power, University of Agriculture, Faisalabad, Pakistan

⁶Department of Intelligent Systems, University of Lahore, Lahore, Pakistan

⁷Department of Informatics and Systems, School of Systems and Technology, University of Management and Technology, Lahore, Pakistan

⁸Department of Technology, University of Lahore, Lahore, Pakistan

ABSTRACT

Due to changes in meteorological factors, the instability in the power at the end of the transmission system demands considerable attention. The temperature of the transmission line varies, which has a significant impact on the line parameters. An accurate prediction of line parameters behaviour is necessary to ensure system reliability. The present study is a step towards predicting variations in line parameters with respect to temperature

variation. In addition, power loss and voltage drop due to variations in resistance are also predicted. Support Vector Machine (SVM) and ElasticNet, a machine learning algorithm, predict line parameters such as resistance, inductance, capacitance, voltage drop, and power losses. Furthermore, different seasons-based SVM and ElasticNet models for these parameters are considered. Seasons-based models are divided into two types, namely, summer and winter. 220-Kilovolt transmission data and weather

ARTICLE INFO

Article history:

Received: 25 October 2023

Accepted: 12 April 2024

Published: 09 October 2024

DOI: <https://doi.org/10.47836/pjst.32.6.05>

E-mail addresses:

ashfaqahmad83@hotmail.com (Ashfaq Ahmad)

iqrajaved_07@yahoo.com (Iqra Javed)

electricalengineer9313@gmail.com (Changan Zhu)

babargmeher@gmail.com (Muhammad Babar Rasheed)

mwaqar13@mail.ustc.edu.cn (Muhammad Waqar Akram)

muhammad.wasil@es.uol.edu.pk (Muhammad Wisal Khan)

umair.ghazanfar@umt.edu.pk (Umair Ghazanfar)

waseem.nazar@es.uol.edu.pk (Waseem Nazar)

baqar.hussain@es.uol.edu.pk (Syed Baqar Hussain)

amber.sultan.ahmed@gmail.com (Amber Sultan)

* Corresponding author

information are used as model inputs. Predicted results of transmission line parameters are described in the form of RMSE and MRE. Moreover, the performance results of SVM and ElasticNet are also compared to show better prediction results. The result shows that the minimum prediction error of line parameters are 0.0511, 0.301, 0.426, 0.913, and 0.1501 in RMSE and 4.212, 0.518, 2.888, 0.097, and 0.615 percentages in MRE. This research work may provide technical guidance to transmission line engineers on enhancing the performance of transmission systems.

Keywords: ElasticNet, line voltage drop, power losses, power transmission line parameters, support vector machine, temperature variation effects

INTRODUCTION

The electrical overhead transmission line is vital to the power system, conveying electricity from the power generating stations to the consumer. During the transmission, they are affected by various environmental conditions, such as temperature, lightning, and wind (Campbell, 2012; Yao et al., 2016). The temperature variation is responsible for variations in transmission line parameters like resistance, inductance, and capacitance, which leads to power losses and voltage drop (Farzaneh et al., 2013). The temperature of a high-voltage transmission line conductor is fixed by its current carrying capacity and meteorological atmosphere conditions (Reddy & Chatterjee, 2016). The variation in line current capacity and meteorological atmosphere conditions cause variations in transmission line temperature (Cecchi et al., 2011). According to a study by IEEE Std 738 – 2006 (2007), environmental factors such as environmental temperature, speed of air and its direction, and solar radiation are responsible for variations in conductor temperature.

Chakraborty et al. (2009) conducted a study based on voltage control equipment, such as a static var compensator and a synchronous condenser, to investigate the variation of transmission line reactance. Fan (2015) estimated the synchronous generator's parameters based on two estimation methods, least-square error and Kalman-based estimation, using Phasor Measurement Unit (PMU) data. Chavan et al. (2017) conducted a study based on the Phasor Measurement Unit (PMU) to investigate the transmission line inter-area impedances, Thevenin's reactance, rotational inertia, and damping of the aggregated generators. Ahmad et al. (2020) conducted a study to develop a transmission line model to investigate line segments where high tension is generated under symmetrical and unsymmetrical spacing using the finite element method. In another research conducted, Kirschen et al. (1997) found line losses in power transmission lines due to shunt conductance. The conductance between the line-to-line and a line-to-ground occurs due to current leakage and is responsible for losses. In addition, the conductor's resistance is also responsible for power losses and voltage drops in transmission lines (Ajenikoko & Adeleke, 2017). Moreover, the electricity

requirement is increasing daily (Nedic et al., 2006). It requires a situational understanding of power transmission lines under varying environmental circumstances (Diao et al., 2010). Particularly, it is important to consider temperature variations in transmission lines to limit the power losses and voltage drop.

A few studies have investigated the effect of temperature on transmission line parameters. Bockarjova and Andersson (2007) have developed a two-stage state estimation algorithm to study the variations in the behaviour of a transmission line resistance due to temperature changes and utilised estimated current for resistance correction. Fu et al. (2011) have proposed a dynamic line rating method to measure peak current flow within the steady-state temperature limit. However, the dynamic line rating method did not consider the unsteady-state temperature. Indulkar and Ramalingam (2008) conducted a study to assess the transmission line parameters at starting and receiving ends using the power, voltage, and current magnitude. Du and Liao (2012) employed line voltage and current phasors to assess the positive phase sequence transmission line parameters. However, these studies have considered the single-temperature profile impact on transmission line conductors and have not considered the impact of the multi-temperature profile. Duta et al. (2020) conducted a study using Variance-based re-weighted nonlinear least squares to estimate the three-phase untransposed scheme-based distribution lines parameter and obtained RMS of 10% and 30.7%. Morteza et al. (2023) conducted a study for dynamic line rating (DLR) forecasting, which reliably predicted the overall current carrying potential of overhead transmission lines using support vector machines (SVM), random forest (RF), and multi-layer perceptron (MLP) and achieved an average prediction accuracy of 6.7%, 9.4% and 3.4%. Wei and Goa (2021) developed a model to predict the transmission line galloping using machine learning algorithms GA-BP, SVM and GA-BP-SVM. Their research achieved a combined model accuracy of 95.5% and an F1 score of 0.938. Ghiasi et al. (2019) proposed a study to identify transmission line parameters by considering measured data from one side of the transmission line using the least squares estimation method. They achieved relative error (RE) of 0.054%, 1.078%, 0.209% and 1.121%. In Bendjabeur et al. (2020), the authors conducted a study based on the Galerkin method using Synchronised time-domain data to identify the transmission line parameters. They obtained absolute relative errors of 7.55%–2.45%, 8.36%–0.25% and 3.35%–0.02%. However, in the studies mentioned above, the percentage error of the model could still be improved.

The effect of temperature variation on power transmission line parameters is very important for the effective influence of power transmission line operation. High variation in the temperature causes high variation in transmission line parameters, resulting in less precision on parameter values, which affects the output power at the receiving station. The literature review shows that different machine-learning approaches have been applied for transmission line parameters estimation and classification and are successfully used in

other power systems fields. Moreover, various numerical methods have also been applied to analyse the effects of temperature on the power system and some of the line parameters. Based on the successful application of machine learning algorithms in other fields, it is presumed that a machine learning method can also be used to accurately predict the effects of temperature on transmission line parameters. In this regard, a study using intelligent machine learning approaches is needed to predict the effect of temperature variation on power transmission line parameters such as resistance, inductance, and shunt capacitance. In addition, power loss and voltage drop due to variations in resistance also need to be predicted.

In this context, the present study aims to efficiently predict the temperature variation effect on transmission line parameters that affect the transmission system output power. Based on the aim, the objectives of the present study are: First, to efficiently predict the variation of transmission line parameters like resistance, inductance, capacitance, power losses, and voltage drop due to temperature by considering the effect of the polynomial kernel and radial-based kernels of Support Vector Machine and ElasticNet. Second, to predict transmission line parameters using a multi-temperature profile (-10°C to 50°C). Third, the seasonal SVM and ElasticNet models should be considered to predict the transmission line parameters and, in the end, to compare the obtained results with the Poly kernel, RBF kernels, and ElasticNet.

METHODOLOGY

Basic Theory of Transmission Line Current-temperature Relationship and Machine Learning

Transmission Line Current Relationship with Temperature

The carrying capacity of the transmission current and environmental weather conditions affect the transmission line temperature. The main factors affecting the temperature of the transmission line include the heat created due to the current that passes from the transmission line and the heat absorbed by solar rays. The line temperature is determined by equating the total input heat to the total output heat (House & Tuttle, 1958). As there is a difference in the ambient temperature and the conductor temperature, the transmission conductor output heat is in the form of convection heat and radiant heat. The power transmission line heat balance equation is presented in Equation 1, as indicated in Yan et al. (2017).

$$q_1 + q_s = q_c + q_r \quad [1]$$

In Equation 2, $q_1 = I^2R$ then, the Equation 2 becomes:

$$I^2R + Q_{Solar} = Q_{Convection} + Q_{Radiation} \quad [2]$$

In Equation 2, the heat gain is I^2R because of the current flowing in the conductor of the transmission line, and R is transmission line resistance and is a function of temperature; heat gain is Q_{Solar} due to solar radiation received on the transmission line, heat loss is $Q_{Convection}$, which is due to the ambient temperature, transmission line conductor temperature and wind speed and heat radiation is $Q_{Radiation}$, which is due to the temperature difference. Then, the current capacity of the high-voltage transmission line conductor can be calculated, as shown in Equation 3.

$$I = \sqrt{\frac{Q_{Convection} + Q_{Radiation} - Q_{Solar}}{R}} \tag{3}$$

Basic Theory of Machine Learning

SVM Theory. SVM is the most popular, powerful, and versatile tool for machine learning. The SVM algorithm is used to solve linear or nonlinear classification and regression problems. SVMs are particularly fit for small or medium-sized complex datasets. It gives low false positives under small or medium datasets (Géron, 2017). A high-dimensional feature space is used in SVM for nonlinear mapping of the input vectors. Finding the minimum validation error is the key feature of the SVM, and for this purpose, the margin parameter γ is used (Brownlee, 2016; Chang & Lin, 2011).

SVR Theory. The key concept of prediction with SVR is expressed as suppose that the training data set is $(x_i, y_i)(i = 1, 2, \dots \dots n)$, whereby the input vector with n -dimensions is $x_i \in R^n$; $y_i \in R$ pertained to the required output data of (Bhavsar & Ganatra, 2012; Vapnik, 1999). In Support Vector Regression, it aims to finds a function $f(x)$ that is commonly divergent ϵ from abs. y_i targets are achieved for all the data sets used for training. The Support Vector Regression algorithm defines function $f(x)$, as shown in Equation 4 (Chang & Lin, 2002; Scholkopf et al., 2000).

$$f(x) = \langle w, x \rangle + b \quad \text{with } w \in x, b \in \mathfrak{R} \tag{4}$$

Whereas “comma (,)” implies the dot product in x and from the x_i input space x as a nonlinear feature mapped, the vector weight is w , and to ensure function flatness, f, b is a constant. The normal weight shall be reduced as in Equation 5.

$$\begin{aligned} & \text{Minimise } \frac{1}{2} \|w\|^2 \\ & \text{Subject to } \begin{cases} y_i - \langle w, x_i \rangle - b \leq \epsilon \\ \langle w, x_i \rangle + b - y_i \leq \epsilon \end{cases} \end{aligned} \tag{5}$$

Setup of ξ_i, ξ_i^* is presented in Equations 6 and 7.

$$\text{Minimize } \frac{1}{2} \|w^2\| + C \sum_{i=1}^l (\xi_i + \xi_i^*) \quad [6]$$

$$\text{Subject to } \begin{cases} y_i - \langle w, x_i \rangle - b \leq \varepsilon + \xi_i \\ \langle w, x_i \rangle + b - y_i \leq \varepsilon + \xi_i^* \\ \xi_i, \xi_i^* \geq 0 \end{cases} \quad [7]$$

Where the constant is C , which has a value above zero, that decides the compromise between 'f' flatness and the quantity by which deviations are greater than ε . It accepts that with an ε -unresponsive loss function $|\xi|_\varepsilon$ is presented in Equation 8.

$$|\xi|_\varepsilon : \begin{cases} 0 & \text{if } |\xi| \leq \varepsilon \\ |\xi| - \varepsilon & \text{otherwise} \end{cases} \quad [8]$$

The main concept is to create a Lagrange function with the objective function. Equation 9 illustrates the problem of twofold optimisation.

$$\text{Maximize } \begin{cases} -\frac{1}{2} \sum_{i,j=1}^l (\alpha_i - \alpha_i^*)(\alpha_j - \alpha_j^*) \cdot k(x_i, x_j) \\ -\varepsilon \sum_{i=1}^l (\alpha_i + \alpha_i^*) + \sum y_i (\alpha_i - \alpha_i^*) \end{cases}$$

$$\text{subject to } \sum_{i=1}^l (\alpha_i - \alpha_i^*) = 0 \text{ and } \alpha_i, \alpha_i^* \in [0, C] \quad [9]$$

The weights of the models are determined by Equation 10.

$$w = \sum_{i=1}^l (\alpha_i - \alpha_i^*) x_i \quad [10]$$

Finally, the model can be written as Equation 11:

$$f(x) = \sum_{i=1}^l y_i (\alpha_i - \alpha_i^*) k(x_i, x) + b \quad [11]$$

Where the linear relationship of x_i training samples can be represented by w and by considering the conditions of Karush Kuhn Tucker (KKT), the parameter b can be evaluated (Steidl et al., 2005). The kernel function is represented with k ; the kernel functions which are commonly used for SVM are described as Equation 12:

$$\begin{aligned}
 \text{Linear: } k(x, x') &= x, x' \\
 \text{Polynomial: } k(x, x') &= (\gamma x, x' + c)^d. \\
 \text{Sigmoidal: } k(x, x') &= \tanh(\gamma x, x' + c). \\
 \text{RBF: } k(x, x') &= \exp\left(\frac{-\|x, x'\|^2}{2\sigma^2}\right) \quad [12]
 \end{aligned}$$

Where γ, c and d are kernel parameters

ElasticNet Theory. Elastic net is a popular machine learning algorithm used to solve regression problems. ElasticNet regression is a regularisation regression algorithm combining the power of ridge regression and lasso regression into a single algorithm. It implies that the ElasticNet algorithm can control the mix ratio x . When $x = 0$, the ElasticNet algorithm is equivalent to the ridge regression, and when $x = 1$, the ElasticNet algorithm is equivalent to the lasso regression. The elastic net algorithm is best for reducing the regression model’s complexity, magnitude, and number of regression coefficients. It uses the L2-norm (sum squared coefficient values) and the L1-norm (sum absolute coefficient values). The elastic net algorithm is very suitable for conditions where the dimensional data is greater than the number of samples. The key features of the elastic net algorithm are groupings and variable selection. The cost function of the ElasticNet algorithm is presented in Equation 13.

$$f(\phi) = MSE(\phi) + x\alpha \sum_{i=1}^n |\phi_i| + \frac{1-x}{2}\alpha \sum_{i=1}^n \phi_i^2 \quad [13]$$

Season-based Prediction Model of Transmission Line Parameters

This research paper uses a Support Vector Machine for transmission line model prediction. Following transmission line parameters such as resistance ($R_{(T)}$), inductance ($L_{(T)}$), capacitance ($C_{(T)}$), voltage drop ($V.D_{(T)}$), and power losses ($P.L_{(T)}$) are considered for prediction. There are various factors which affect the parameters of the transmission line. It is hard to figure out the relationship of the transmission line model with a single weather. The transmission line parameter models have been divided into two weather-based groups, summer and winter, according to the weather variability and the factors influencing the line parameters.

Line Parameters Relationship with Temperature

A transmission line usually has three components: resistance (R), inductance (L), and capacitance (C). They are distributed uniformly over the line length and affect the

transmission power from the sending to the receiving end. The resistance and inductance of transmission line conductors are the series components, and capacitance is the shunt component (Mellit & Pavan, 2010). The transmission resistance is the most significant cause of power loss in a transmission line. The electric, magnetic and material characteristics of the conductors mainly determine these parameters. Temperature-based relationships of transmission line parameters are shown in the equations below (Rashid et al., 2005).

The resistance as a function of temperature can be calculated using Equation 14.

$$R_{(T)} = R_{(T_0)} * [1 + TC_1 * (T - T_0) + TC_2 * (T - T_0)^2] \quad [14]$$

The inductance as a temperature and current dependence function can be calculated using Equation [15].

$$L_{(T)} = L_{(T_0)} * (1 + IL_1 * I + IL_2 * I^2) * [1 + TC_1 * (T - T_0) + TC_2 * (T - T_0)^2] \quad [15]$$

The capacitance as a function of temperature and voltage-dependent can be calculated using Equation [16].

$$C_{(T)} = C_{(T_0)} * (1 + VC_1 * V + VC_2 * V^2) * [1 + TC_1 * (T - T_0) + TC_2 * (T - T_0)^2] \quad [16]$$

where $R_{(T_0)}$, $L_{(T_0)}$, and $C_{(T_0)}$ are the reference temperature parameters, T , T_0 is the reference and actual conductor temperature, I , V is the voltage and current, TC_1 , TC_2 , IL_1 , IL_2 , and VC_1 , VC_2 are linear and quadratic temperature, current and voltage coefficients.

Support Vector Machine Implementation

In defining the procedure for training the SVM algorithm, first, a transmission line and weather dataset are available with several instances categorised by several features. The data is saved to the machine using Comma Separated Values (CSV) in a specified readable format. The following steps are used in the initial procedure to train the SVR and ElasticNet algorithms.

Step 1: In this step, the CSV format transmission line and weather dataset are loaded into the machine.

Step 2: In this step, the dataset is divided into input and output features.

Step 3: This step involves splitting our dataset into training data and test data.

Step 4: Finally, the SVR and ElasticNet models were applied for prediction.

The model parameters are optimised to achieve the best performance of the SVR and ElasticNet model. During the parameter's optimisation procedure, the following steps are used: SVR parameter's optimisation step:

Step 1: In the parameter optimisation step, we first select the kernel in our study: a polynomial or RBF kernel.

Step 2: In this step, the procedure of step 1 is repeated by varying the kernel function parameter ε to find the lowest selected error, i.e. RMSE, MRE for selected iterations.

Step 3: In this step, steps 1 and 2 are repeated by varying the capacity parameter C to find the lowest selected error, i.e. RMSE and MRE for selected iterations.

Step 4: In the final step, the above procedures are repeated by varying the kernel parameter γ to find the lowest selected error, i.e. RMSE, MRE for selected iterations.

The following steps are used for the training algorithm, the prediction from data, and the evaluation of the algorithm. ElasticNet parameter's optimisation step:

Step 1: The elastic net tuning parameters alpha and l_1_ratio are selected in the parameter's optimisation step.

Step 2: In this step, the procedure is repeated by varying the elastic net tuning parameters alpha to find the lowest selected error, i.e., RMSE and MRE for selected iterations.

Step 3: In the final step, the above procedures are repeated by varying the elastic net tuning parameters $l_1-ratio$ to find the lowest selected error, i.e., RMSE and MRE for selected iterations.

The following steps are used for the training algorithm, the prediction from data, and the algorithm's evaluation.

Step 1: After selecting the best optimisation parameters, the fit command of SVR and ElasticNet is separately called to train the algorithm on the training data, which is passed as a parameter to the fit method.

Step 2: After algorithm training, the SVR and ElasticNet predict command is used for prediction.

Step 3: Once the prediction is done, the last step of the learning algorithm is to make evaluations. In our study, RMSE and MRE are considered for evaluation. Finally, the findings are presented graphically for every parameter.

All steps are repeated in the development of each model. The pseudocode of the prediction algorithm is shown below.

Algorithm Prediction of Temperature Variation in Transmission Line Parameters

Start

1: Require:

2: Datafile: [Loaded input and output features in CSV format]

3: Labels: [Loaded all parameter labels]

4: Dataset = Read all instances and features with a label from steps 1 and 2 using
[read_csv (Datafile, Labels = Labels)]

5: Data = Load numerical values without labels [Dataset.values]

6: Input: Feature of any line parameter such as R_T from Dataset $[[=data[:, 0:F_T], X_i, \dots, X_n]$

7: Output: Feature of any line parameter such as R_T from Dataset $[y_{out}=data[:, F_T], Y_i, \dots, Y_n]$

Data splitting into training data and test data

8: Input: 90% input data for training $[x_{train}=x_{in}[0:l_{T90}:]]$

9: Test Input: 10% input data for test $[x_{test}=x_{in}[l_{T90}:l_T:]]$

10: Output: 90% output data for training $[y_{train}=Y_{out}[0:l_{T90}]]$

11: Test Output: 10% output data for test $[y_{test}=Y_{out}[l_{T90}:l_T:]]$

12: Processing: StandardScaler function used for data pre-processing $[sc=StandardScaler()]$

13: Model: SVR and ElasticNet models are applied for prediction $[reg = svm.SVR(, , , \dots)]$ and $[reg = ElasticNet(, , , \dots)]$

Selection of Kernel, C, gamma, and epsilon parameters

14: Kernel: In the present study, polynomial / BRF kernel was considered $[reg=svm.SVR(kernel='poly')]$

15: SVR Parameters Selection: for parameter selection grid search function used $[gs=GridSearchCV(cv=10, estimator=reg, param_grid= [{"C": C, "gamma": gamma, "epsilon": epsilon}], scoring=scoring)]$

15: ElasticNet Parameters Selection: for parameter selection grid search function used $[gs=GridSearchCV(cv=10, estimator=reg, param_grid= [{"alpha": alpha, "l1_ratio": l1_ratio}], scoring=scoring)]$

Training, prediction, and evaluation of model

16: Training: fit command is used to train the model $reg.fit(x \text{ training instances}, y \text{ training instances})$

17: Prediction: y_{pre} is the predicted result of test instances x , for prediction the predict command is used $[y_{pre}=reg.predict(x \text{ test instances})]$

18: Evaluation: Results are presented in the form of the RMSE and MRE $[final=(rmse(y_{pre}, test \text{ output}))]$

Graphical Representation of Model

19: Finally, line parameters predicted error results are presented graphically.

20: End

Data Description and Machine Learning Models

In order to predict the temperature effect on line parameters, 220-Kv transmission line data and weather data are used as model input. The transmission line data used in our study are described below: Line length is 675.9 km (420 miles), type of transmission conductor is

Falcon with delta configuration. The following of the characteristics of transmission line conductor at a standard temperature of 20°C and a frequency of 60 Hz; $r(T_0)$ is 0.0985 ohm per kilometre (0.0612 ohms per mile), $X_L(T_0)$ is 0.9786 ohms per kilometre (0.6081 ohms per miles), $X_C(T_0)$ is 0.2290 mega ohm per kilometre (0.1423 mega ohms per miles), the resistance temperature coefficient, α_1 is 0.003(1/°C). The reactance temperature coefficient, α_2 is 0.005(1/°C). On the other hand, the meteorological temperature data for the summer and winter seasons and a conductor temperature based on the relationship of current and meteorological circumstances around the line are considered.

The time interval between data is 30 minutes. In the present work, 4368 sample datasets are used, which is further distributed into two subsets: for the training of the model, 3931 samples are used, and for validation of the model, 437 samples are utilised. Moreover, the 3931 training samples are further split into two subsets according to the selected weather: 1987 samples are utilised in the summer transmission line model, and in the winter transmission line model, 1944 samples are used. The validation data sample set 437 is divided into two transmission line models. Two hundred twenty-one samples are utilised in the transmission summer model, and for the transmission line winter model, 216 samples are used.

Furthermore, to achieve the most proficient model, the dataset was pre-processed. As indicated in Rashid et al. (2005), the relationship of pre-processing is provided in Equation [17].

$$x'_i = \frac{x_i - x_{min}}{x_{max} - x_{min}} \tag{17}$$

Where x'_i and x_i are the processed and original input data values, x_{min} and x_{max} are the minimum and maximum data values.

The present study uses Python libraries such as Python sklearn, pandas, and NumPy to develop the transmission line parameters' summer and winter models. Figure 1 shows the steps involved in the development of these models. Individual hyperparameters have been chosen to develop these models.

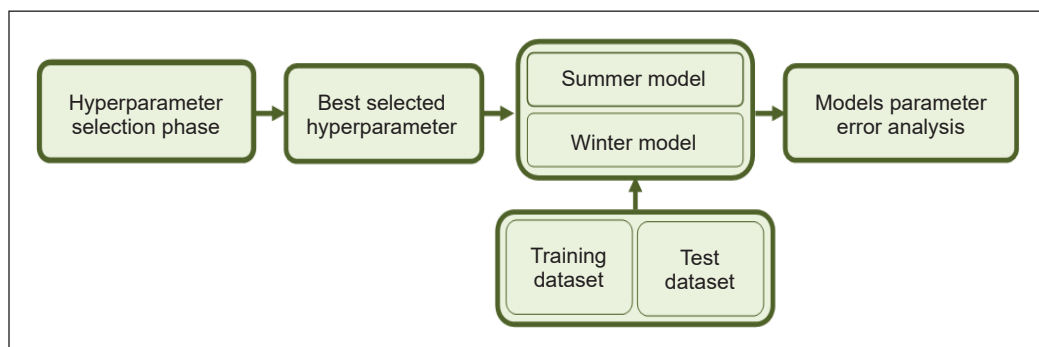


Figure 1. Flow chart of power transmission line parameter prediction

Parameters Selection. In machine learning, hyperparameters affect the precision of the model. Every machine learning algorithm has its hyperparameters, which are used to optimise the model’s performance. In the present study, two machine learning algorithms, such as SVM and ElasticNet, are considered for prediction. The commonly used SVM kernel parameters are gamma (γ), the insensitive loss (ϵ) and the upper bound (C). On the other hand, the ElasticNet algorithm hyperparameters are alpha and l1_ratio. Hence, a suitable range for these hyperparameters is necessary. The setting of this hyperparameter is based on the real training set of data. Furthermore, two SVM kernel functions, poly, radial-based function (RBF), and ElasticNet algorithm, are examined in the present work. Both kernel functions are classical and perform well in many cases (Changsong et al., 2009). According to Huang et al. (2006), when the data is normally distributed, it is suggested that the Radial Based Function (RBF) or the Polynomial (Poly) kernel be used. Finally, the findings are compared with these two kernels’ functions and ElasticNet. As previously mentioned, various combinations of SVM parameters C , d , ϵ and γ and ElasticNet parameters such as (alpha, l1_ratio) are chosen to optimise the seasonal transmission line models for both kernel functions such as poly, RBF and ElasticNet. The description of optimisation parameters is illustrated in Table 1 (Ali & Smith, 2003).

Table 1
Hyperparameters of season-based models of transmission line with poly, RBF kernel and ElasticNet

Models	Parameters of Poly kernels Model				Parameters of RBF kernels Model				Parameters ElasticNet Model	
	C	d	ϵ	γ	C	d	ϵ	γ	alpha	l1_ratio
$R(T)$										
Summer	1000	3	0.10	0.1	1000	3	0.1	10	1.5	0.09
Winter	1000	3	0.10	2.5	1000	3	0.1	9	1.6	0.09
$L(T)$										
Summer	1000	3	0.10	0.9	1000	3	1.5	5	0.05	0.09
Winter	1000	3	0.5	1.5	1000	3	0.5	10	0.001	0.38
$C(T)$										
Summer	1000	3	0.8	0.9	1000	3	0.5	0.8	1.5	0.009
Winter	1000	3	0.9	0.9	1000	3	0.9	1.5	1.8	0.009
$VD(T)$										
Summer	1000	3	0.25	0.1	1000	3	0.05	2	0.55	0.9
Winter	1000	3	0.1	0.4	1000	3	0.06	2.5	0.555	0.99
$PL(T)$										
Summer	1000	2.9	0.05	9	4000	3	0.05	6	1.3	0.33
Winter	1000	2.9	0.05	17	5000	3	0.05	0.2	2.5	0.22

Evaluation Criteria. Mean Relative Error (MRE) and Root Mean Square Error (RMSE) have been used to assess the accuracy of the transmission line model prediction. The relationships of these errors are given in Equations 18 and 19, respectively.

$$RMSE = \sqrt{\frac{\sum_{i=1}^n (P_i - a_i)^2}{n}} \tag{18}$$

$$MRE = \frac{1}{n} \sum_{i=1}^n \left(\frac{P_i - a_i}{a_T} \right) * 100 \tag{19}$$

Where the predicted value is P_i , the actual value is a_i , the total parameter measured value is a_T , and the total sample is n .

RESULTS AND DISCUSSION

This discussion presents the prediction error results of transmission line parameter models, such as resistance ($R_{(T)}$), inductance ($L_{(T)}$), capacitance ($C_{(T)}$), voltage drop ($V.D_{(T)}$), and power losses ($P.L_{(T)}$). The prediction models are trained for each transmission line parameter to attain the best prediction result. The input data in these SVM and ElasticNet models includes weather and transmission line parameter data.

Transmission Line Resistance Model (R_T)

Figure 2 shows the retrieved prediction results of the summer and winter models for the transmission line resistance. The value of optimisation parameters is selected for both SVM kernels and ElasticNet. The line resistance models are trained for 100 different iterations. It is concluded that the MRE was reduced to approximately 4.2115% for the SVM poly kernel after 48 iterations. In contrast, the MRE reduced to 6.734% for the SVM RBF kernel after 30 iterations, while for the ElasticNet, it reduced to 9.254% after 32 iterations.

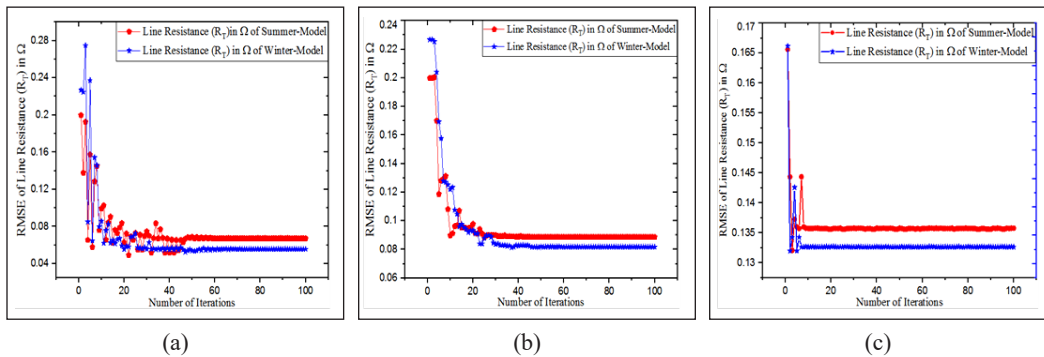


Figure 2. Prediction of R_T with SVM and ElasticNet: (a) SVM poly kernel; (b) SVM RBF kernel; and (c) ElasticNet

Table 2 compares the results of the $R_{(T)}$ transmission line resistance model for SVM poly, RBF kernel, and ElasticNet. Mean Relative and Root Mean Square Error have been chosen for the model evaluations. The polynomial kernel models perform better than ElasticNet and RBF kernel models.

Table 2

Comparison of transmission line resistance (R_T) poly SVM model, RBF SVM model and Elastic Net model (accuracy measurement with RMSE and MRE)

Support Vector Machine and ElasticNet Models	Samples Tested	RMSE and MRE of Line Inductance (R_T)					
		Kernel (poly)		Kernel (RBF)		Elastic Net	
		RMSE (Ω)	MRE (%)	RMSE (Ω)	MRE (%)	RMSE (Ω)	MRE (%)
Model-1 (Summer)	2208	0.0494	7.659	0.0884	12.12	0.1321	9.136
Model-2 (Winter)	2160	0.0527	0.764	0.0815	1.351	0.1645	9.372
Average Value	4368	0.0511	4.212	0.0850	6.734	0.1483	9.254

Transmission Line Inductance Model (L_T)

The extracted prediction results of the developed seasons-based models for the transmission line inductance are shown in Figure 3. The value of optimisation parameters is selected for both SVM kernels and ElasticNet. The line inductance models are trained for 100 different iterations. It is concluded that the MRE reduced to 0.5195% for the SVM poly kernel approximately after 15 iterations. In contrast, the MRE reduced to 0.609% for the SVM RBF kernel after 28 iterations, while for the ElasticNet, it reduced to 3.266% after 60 iterations of the summer model and 90 iterations of the winter model.

Table 3 compares the results of the transmission line inductance $L_{(T)}$ model for SVM poly, RBF kernel and ElasticNet. MRE and RMSE were selected for the model evaluations. The poly kernel models perform much better than RBF kernel models and ElasticNet.

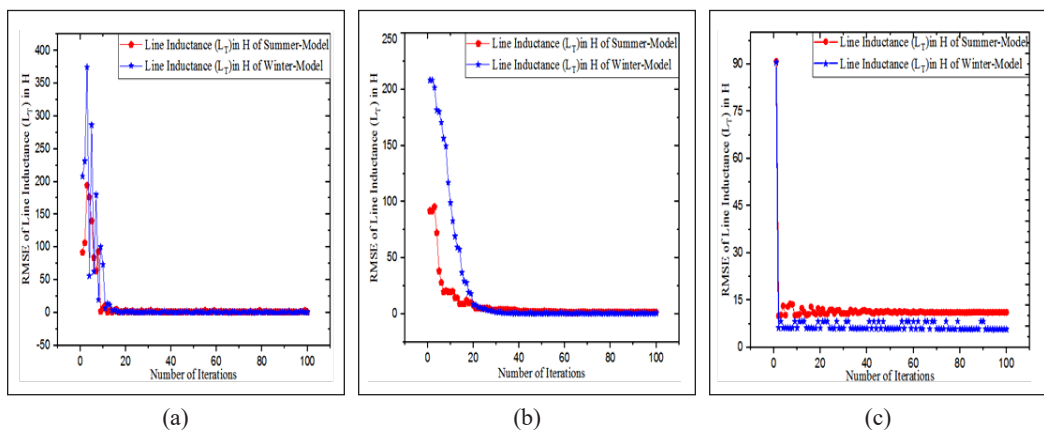


Figure 3. Prediction of transmission line inductance L_T with SVM and ElasticNet: (a) SVM poly kernel; (b) SVM RBF kernel; and (c) ElasticNet

Table 3

Comparison of transmission line inductance (L_T) poly SVM model, RBF SVM model and ElasticNet model (accuracy measurement with RMSE and MRE)

Support Vector Machine and ElasticNet Models	Samples Tested	RMSE and MRE of Line Inductance (L_T)					
		Kernel (poly)		Kernel (RBF)		Elastic Net	
		RMSE (H)	MRE (%)	RMSE (H)	MRE (%)	RMSE (H)	MRE (%)
Model-1 (Summer)	2208	0.369	0.364	1.412	0.810	10.04	0.964
Model-2 (Winter)	2160	0.232	0.675	0.480	0.387	12.85	5.569
Average Value	4368	0.301	0.518	0.946	0.609	11.45	3.266

Transmission Line Capacitance Model (C_T)

The retrieved prediction results of the summer and winter models for the transmission line capacitance are shown in Figure 4. The value of optimisation parameters is selected for both SVM kernels and ElasticNet. The line capacitance models are trained for 100 different iterations. It is concluded that the MRE reduced to 3.021% for the SVM poly kernel approximately after 60 iterations. In contrast, the MRE was reduced to 2.888% for the SVM RBF kernel after 32 iterations. For ElasticNet, it was reduced to 6.088% after 60 iterations of the summer model and 12 iterations of the winter model.

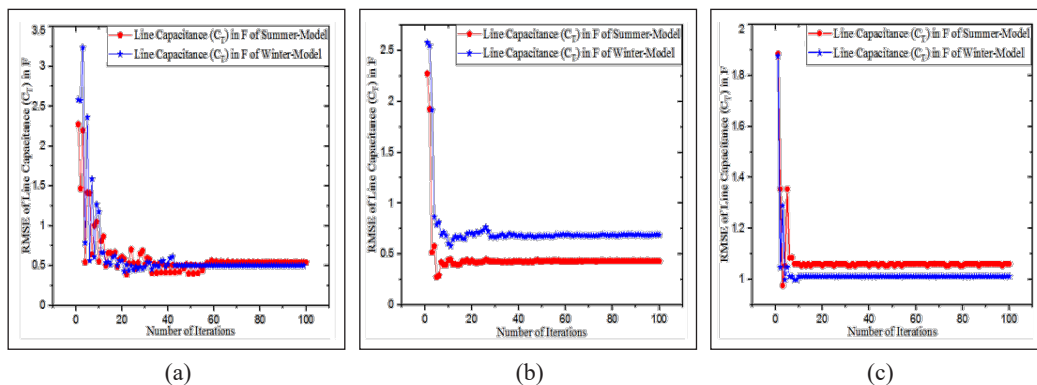


Figure 4. Prediction of transmission line capacitance C_T with SVM and ElasticNet: (a) SVM poly kernel; (b) SVM RBF kernel; and (c) ElasticNet

Table 4

Comparison of transmission line capacitance (C_T) poly SVM model, RBF SVM model and ElasticNet model (accuracy measurement with RMSE and MRE)

Support Vector Machine and ElasticNet Models	Samples Tested	RMSE and MRE of Line Capacitance (C_T)					
		Kernel (poly)		Kernel (RBF)		Elastic Net	
		RMSE (F)	MRE (%)	RMSE (F)	MRE (%)	RMSE (F)	MRE (%)
Model-1 (Summer)	2208	0.390	5.4	0.273	5.075	0.977	5.578
Model-2 (Winter)	2160	0.428	0.642	0.579	0.701	1.262	6.597
Average Value	4368	0.409	3.021	0.426	2.888	1.119	6.088

Table 4 compares the results of the transmission line capacitance $C_{(T)}$ model for SVM Poly, RBF kernels and ElasticNet. MRE and RMSE were chosen for the model evaluations. The efficiency of SVM models is different for both summer and winter models. The RBF kernel performs better for the summer model, whereas the Poly kernel performs better for the winter model.

Transmission Line Voltage Drop Model ($V.D_T$)

The extracted prediction results of transmission line voltage drop developed seasons-based models are shown in Figure 5. The value of optimisation parameters is selected for both SVM kernels and ElasticNet. The line voltage drop models of SVM and ElasticNet are trained for 100 different iterations. It is concluded that the MRE reduced to 0.798% for the SVM poly kernel approximately after 30 iterations. In contrast, the MRE was reduced to 0.097% for the SVM RBF kernel after 40 iterations and errors of ElasticNet models were reduced to 3.247% after 35 iterations of the summer model and 90 iterations of the winter model.

Table 5 compares the transmission line voltage drop $V.D_{(T)}$ model's results for SVM poly, RBF kernel and ElasticNet. MRE and RMSE were chosen for the model's evaluation.

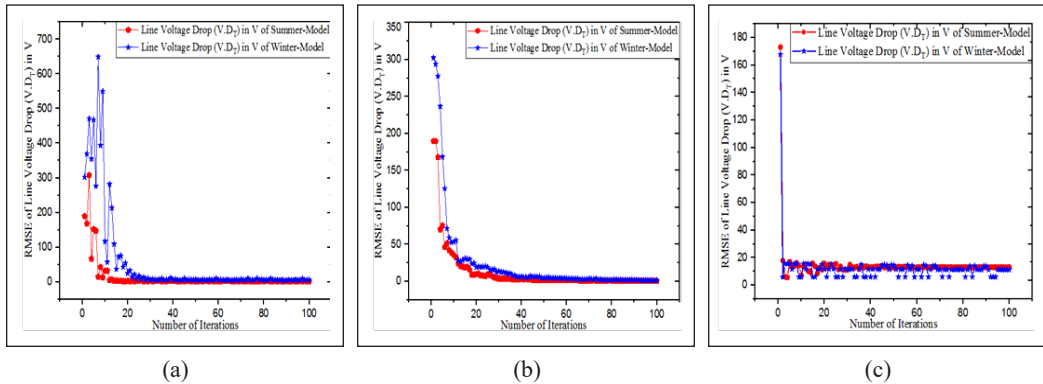


Figure 5. Prediction of transmission line voltage drop $V.D$ with SVM and ElasticNet : (a) SVM poly kernel; (b) SVM RBF kernel; and (c) ElasticNet

Table 5

Comparison of transmission line voltage drop ($V.D_T$) poly SVM model and RBF SVM model (accuracy measurement with RMSE and MRE)

Support Vector Machine and ElasticNet Models	Samples Tested	RMSE and MRE of Line Voltage Drop ($V.D_T$)					
		Kernel (poly)		Kernel (RBF)		Elastic Net	
		RMSE (V)	MRE (%)	RMSE (V)	MRE (%)	RMSE (V)	MRE (%)
Model-1 (Summer)	2208	0.840	0.408	0.548	0.070	5.639	0.531
Model-2 (Winter)	2160	3.818	1.188	1.277	0.124	5.056	5.962
Average Value	4368	2.329	0.798	0.913	0.097	5.347	3.247

The errors from RBF kernel models are much less than those from Poly kernel and ElasticNet models.

Transmission Line Power Losses Model (P.L_T)

The extracted prediction results of transmission line power losses developed seasons-based models are shown in Figure 6. The value of optimisation parameters is selected for both SVM kernels and ElasticNet. The line power loss models of SVM and ElasticNet are trained for 100 different iterations. It is concluded that the MRE reduced to 1.1765% for the SVM poly kernel, approximately after 30 iterations of the summer model and 60 iterations of the winter model. In contrast, the MRE was reduced to 0.6156% for the SVM RBF kernel after 45 iterations for the summer model and 75 iterations for the winter model. In contrast, the ElasticNet reduces to 8.448% after 7 iterations of the summer model and 15 iterations of the winter model.

Table 6 compares transmission line power losses P.L_(T) model results for SVM poly, RBF kernel and ElasticNet. MRE and RMSE have been used to evaluate the models. The performance of SVM models is different for both summer and winter models. The Poly kernel performs better for the summer model, whereas the RBF kernel performs better for the winter model.

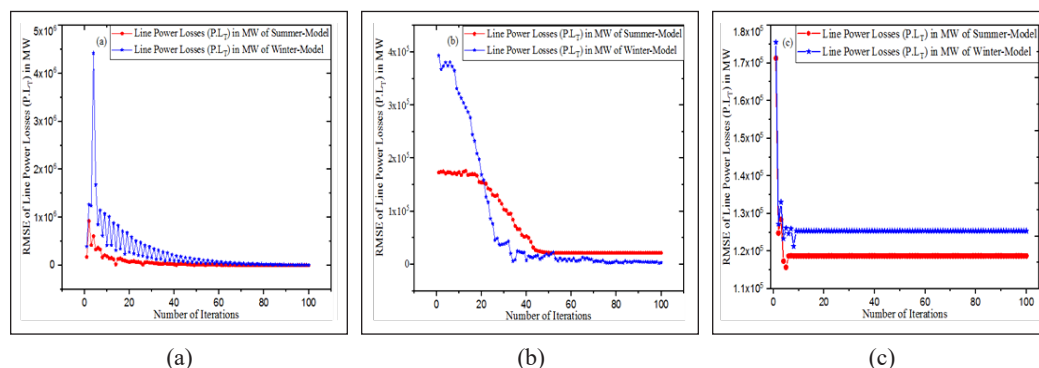


Figure 6. Prediction of transmission line power losses P.L_T with SVM and ElasticNet: (a) SVM poly kernel; (b) SVM RBF kernel; and (c) ElasticNet

Table 6

Comparison of transmission line power losses (P.L_T) poly SVM model and RBF-SVM model (accuracy measurement with RMSE and MRE)

Support Vector Machine and ElasticNet Models	Samples Tested	RMSE and MRE of Line Power Losses (P.L _T)					
		Kernel (poly)		Kernel (RBF)		Elastic Net	
		RMSE (MW)	MRE (%)	RMSE (MW)	MRE (%)	RMSE (MW)	MRE (%)
Model-1 (Summer)	2208	0.4128	0.201	0.0215	1.087	0.1257	9.345
Model-2 (Winter)	2160	0.3817	2.152	0.2786	0.144	0.1904	7.551
Average Value	4368	0.3972	1.177	0.1501	0.615	0.1581	8.448

Comparison

The comparison of the resulting error is shown in Table 7. Bockarjova and Andersson (2007) used a state estimation accuracy tool to estimate the power losses by considering the effect of temperature on line resistance. They divided the model into correct line resistance and uncorrected line resistance, and estimated power losses were inaccurate in the case of the uncorrected line resistance model. They obtained the best results using Monte Carlo Simulations and achieved the best relative error of 20%. The total value for the whole system is approaching 15%, respectively. The power loss error determined zero in the case of correct line resistance. Another study Wang et al. (2018) used time-space variation for power flow analysis in transmission systems to investigate the power losses based on the relationship between temperature and transmission line parameters. For that, they have considered five cases in case 1 and case 2, where temperatures are 70°C and -10°C, respectively. In case 3, the average temperature is considered -20°C; in case 4, the weight average temperatures -28°C and -34°C are taken. In case 5, the temperature threshold of 6°C is taken. They concluded that in case 1 and base case, the power loss was 26.14%, and in case 1 and case 2, the power loss was 14.09%. In case 3, case 4, and case 5, the difference in power losses is 19.71%. The existing studies worked on power losses. However, our study predicts all transmission line parameters, power losses and voltage

Table 7
Comparison of proposed study prediction results with poly-SVM, RBF-SVM and ElasticNet

Studies	Prediction-Method	Predicted Parameters	Error
Bockarjova & Andersson, 2007	State Estimation Accuracy	P.L _(T) (Uncorrected model)	20 % and for the whole system 15 % (RE)
		P.L _(T) (Correct model)	Zero (error)
Wang et al., 2018	Time-Space Variation	P.L _(T) (Case 1 and base case)	26.14 %
		P.L _(T) (Case 1 and Case 2)	14.09 %
		P.L _(T) (Case 3, 4 and 5)	19.71 %
	ElasticNet	R _(T)	0.1483 (RMSE), 9.254 (% MRE)
		L _(T)	11.451 (RMSE), 3.266 (% MRE)
		C _(T)	1.119 (RMSE), 6.088 (% MRE)
		V _(T)	5.347 (RMSE), 3.247 (% MRE)
Our Study	Support Vector Regression Poly and RBF Kernel	P.L _(T)	0.1581 (RMSE), 8.448 (% MRE)
		P.L _(T)	0.0511, 0.0850 (RMSE), 4.212, 6.734 (% MRE)
		L _(T)	0.301, 0.946 (RMSE), 0.518, 0.609 (% MRE)
		C _(T)	0.409, 0.426 (RMSE), 3.021, 2.888 (% MRE)
		V.D _(T)	2.329, 0.913 (RMSE), 0.798, 0.097 (% MRE)
		P.L _(T)	0.3972, 0.1501 (RMSE), 1.177, 0.615(% MRE)

drop based on the relationship between temperature and line parameters. It can be clearly observed that our SVM models show less error.

CONCLUSION AND FUTURE WORK

Transmission lines are a pillar of electrical power transmission systems that need to be protected on a priority basis. The impact of changes in transmission line parameters due to temperature variations cannot be neglected. This research developed the prediction models for transmission line parameters using Support Vector Machines and the ElasticNet modelling approach. For each line parameter, two seasons-based models were established. The transmission line's parameters and weather data were used as model inputs. The polynomial, RBF kernel and ElasticNet results have also been compared to express the predicted results' better performance.

The predicted results showed that in transmission line resistance and inductance models, the poly-SVM kernel performed better than the RBF-SVM kernel for both season models. The average minimum prediction errors in line resistance and inductance were 0.0511 Ω , 0.301 H in RMSE and 4.212, 0.518% in MRE, respectively. Furthermore, the predicted results of the transmission line capacitance model showed that the performance of the polynomial kernel was better than RBF for a winter model. Meanwhile, the summer-model RBF-SVM kernel performed better than the poly-SVM. The average minimum prediction error in line capacitance with RBF kernel was 0.426 F in RMSE and 2.888% in MRE. Moreover, the performance of transmission line voltage drops ($V.D_T$) and power losses ($P.L_T$) were better with the RBF kernel than the polynomial kernel for both seasonal models. The average prediction error of voltage drop was 0.913 V in RMSE and 0.097% in MRE, while the average prediction error in power losses was 0.1501 MW in RMSE and 0.6156% in MRE. On the other hand, the average prediction errors in the line resistance, inductance, capacitance, voltage drop and power losses with ElasticNet algorithm are 0.1483 Ω , 11.451 H, 1.119 F, 5.347 V, 0.1581 MW in RMSE and 9.254, 3.266, 6.088, 3.247, 8.448% in MRE, respectively.

In the future, the seasons-based predicted models of transmission line parameters can be further divided into four seasons based on the availability of large training data. In addition, the hybrid algorithm machine learning approach can also be used to achieve good performance for predicting transmission line parameters and losses. That can be used to improve the transmission line output without affecting the secure operation of the transmission line.

ACKNOWLEDGEMENT

The authors thank everyone involved for their invaluable contributions, insightful discussions and constructive feedback. Their collaboration was essential in refining the ideas presented in this paper.

REFERENCES

- Ahmad, A., Jin, Y., Zhu, C., Javed, I., & Akram, M. W. (2020). Electrical power and energy systems investigating tension in overhead high voltage power transmission line using finite element method. *Electrical Power and Energy Systems*, 114, Article 105418. <https://doi.org/10.1016/j.ijepes.2019.105418>
- Ajenikoko, G., & Adeleke, B. S. (2017). Effect of temperature change on the resistance of transmission line losses in electrical power network. *International Journal of Renewable Energy Technology Research*, 6(1), 1–8.
- Ali, S., & Smith, K. A. (2003, October 27-29). *Automatic parameter selection for polynomial kernel*. [Paper presentation]. Proceedings Fifth IEEE Workshop on Mobile Computing Systems and Applications, Las Vegas, USA. <https://doi.org/10.1109/IRI.2003.1251420>
- Bendjabeur, A., Kouadri, A., & Mekhilef, S. (2020). Novel technique for transmission line parameters estimation using synchronised sampled data. *IET Generation, Transmission and Distribution*, 14(3), 506–515. <https://doi.org/10.1049/iet-gtd.2019.0702>
- Bhavsar, H., & Ganatra, A. (2012). A comparative study of training algorithms for supervised machine learning. *International Journal of Soft Computing and Engineering*, 2(4), 74–81. <https://doi.org/10.1.1.492.6088>
- Bockarjova, M., & Andersson, G. (2007, July 1-5). *Transmission line conductor temperature impact on state estimation accuracy*. [Paper presentation]. IEEE Lausanne Power Tech, Lausanne, Switzerland. <https://doi.org/10.1109/PCT.2007.4538401>
- Brownlee, J. (2016). *Master Machine Learning Algorithms*. MachineLearningMastery
- Campbell, R. J. (2012). *Weather-related power outages and electric system resiliency* (Report No. 7-5700). CRS Report. <chrome-extension://efaidnbmninnibpcapjcgiclfndmkaj/https://www.ourenergypolicy.org/wp-content/uploads/2016/02/R42696.pdf>
- Cecchi, V., Miu, K., Leger, A. S., & Nwankpa, C. (2011, July 24-28). *Study of the impacts of ambient temperature variations along a transmission line using temperature-dependent line models*. [Paper presentation]. IEEE Power and Energy Society General Meeting, Detroit, USA. <https://doi.org/10.1109/PES.2011.6039110>
- Chakraborty, A., Chow, J. H., & Salazar, A. (2009). Interarea model estimation for radial power system transfer paths with intermediate voltage control using synchronized phasor measurements. *IEEE Transactions on Power Systems*, 24(3), 1318-1326. <https://doi.org/10.1109/TPWRS.2009.2022995>
- Changsong, C., Shaxu, D., & Jinjun, Y. (2009). Design of photovoltaic array power forecasting model based on neutral network. *Transactions of China Electrotechnical Society*, 24(9), 153–158. <https://doi.org/10.19595/j.cnki.1000-6753.tces.2009.09.023>
- Chang, C. C., & Lin, C. J. (2002). Training v-support vector regression: Theory and algorithms. *Neural Computation*, 14(8), 1959–1977. <https://doi.org/10.1162/089976602760128081>
- Chang, C. C., & Lin, C. J. (2011). LIBSVM: A Library for support vector machines. *ACM Transactions on Intelligent Systems and Technology*, 2(3), Article 27. <https://doi.org/10.1145/1961189.1961199>
- Chavan, G., Weiss, M., Chakraborty, A., Bhattacharya, S., Salazar, A., & Ashrafi, F. H. (2017). Identification and predictive analysis of a multi-area WECC power system model using synchrophasors. *IEEE Transactions on Smart Grid*, 8(4), 1977–1986. <https://doi.org/10.1109/TSG.2016.2531637>

- Diao, R., Vittal, V., & Logic, N. (2010). Design of a real-time security assessment tool for situational awareness enhancement in modern power systems. *IEEE Transactions on Power Systems*, 25(2), 957–965. <https://doi.org/10.1109/TPWRS.2009.2035507>
- Du, Y., & Liao, Y. (2012). On-line estimation of transmission line parameters, temperature and sag using PMU measurements. *Electric Power Systems Research*, 93, 39–45. <https://doi.org/10.1016/j.epsr.2012.07.007>
- Dutta, R., Member, S., Patel, V., Chakrabarti, S., Member, S., Sharma, A., Das, R. K., & Mondal, S. (2020). Parameter estimation of distribution lines using SCADA measurements. *IEEE Transactions on Instrumentation and Measurement*, 70 Article 9000411. <https://doi.org/10.1109/TIM.2020.3026116>
- Fan, L. (2015, July 26-30). *Least squares estimation and kalman filter based dynamic state and parameter estimation*. [Paper presentation]. IEEE Power & Energy Society General Meeting, Denver, USA.
- Farzaneh, M., Farokhi, S., & Chisholm, W. A. (2013). *Electrical design of overhead power transmission lines*. McGraw-Hill Education.
- Fu, J., Morrow, D. J., Abdelkader, S., & Fox, B. (2011, September 5-8). *Impact of dynamic line rating on power systems*. [Paper presentation]. International Universities' Power Engineering Conference (UPEC), Soest, Germany.
- Géron, A. (2017). *Hands-on machine learning with Scikit-learn and TensorFlow*. O'Reilly Media.
- Ghiasi, S. M. S., Abedi, M., & Hosseinian, S. H. (2019). Mutually coupled transmission line parameter estimation and voltage profile calculation using one terminal data sampling and virtual black-box. *IEEE Access*, 7, 106805–106812. <https://doi.org/10.1109/ACCESS.2019.2901813>
- House, H. E., & Tuttle, P. D. (1958). Current-carrying capacity of ACSR. *Transactions of the American Institute of Electrical Engineers. Part III: Power Apparatus and Systems*, 77(3), 1169–1173. <https://doi.org/10.1109/AIEEPAS.1958.4500119>
- Huang, T. M., Kecman, V., & Kopriva, I. (2006). *Kernel based algorithms for mining huge data sets*. Springer.
- IEEE Std 738 - 2006. (2007). *Standard for Calculating the Current-Temperature of Bare Overhead Conductors*. IEEE. <https://doi.org/10.1109/IEEESTD.2007.301349>
- Indulkar, C. S., & Ramalingam, K. (2008). Estimation of transmission line parameters from measurements. *International Journal of Electrical Power & Energy Systems*, 30(5), 337–342. <https://doi.org/10.1016/j.ijepes.2007.08.003>
- Kirschen, D., Allan, R., & Strbac, G. (1997). Contributions of individual generators to loads and flows. *IEEE Transactions on power systems*, 12(1), 52–60. <https://doi.org/10.1109/59.574923>
- Mellit, A., & Pavan, A. M. (2010). A 24-h forecast of solar irradiance using artificial neural network: Application for performance prediction of a grid-connected PV plant at Trieste, Italy. *Solar Energy*, 84(5), 807–821. <https://doi.org/10.1016/j.solener.2010.02.006>
- Morteza, A., Sadipour, M., Fard, R. S., Taheri, S., & Ahmadi, A. (2023). A dagging-based deep learning framework for transmission line flexibility assessment. *IET Renewable Power Generation*, 17(5), 1092–1105. <https://doi.org/10.1049/rpg2.12663>

- Nedic, D. P., Dobson, I., Kirschen, D. S., Carreras, B. A., & Lynch, V. E. (2006). Criticality in a cascading failure blackout model. *International Journal of Electrical Power and Energy Systems*, 28(9), 627–633. <https://doi.org/10.1016/j.ijepes.2006.03.006>
- Rashid, M. H., Rashid, M. H., & Rashid, M. H. (2005). *SPICE for power electronics and electric power*. CRC Press. <https://doi.org/10.1201/9781420026429>
- Reddy, B. S., & Chatterjee, D. (2016). Performance evaluation of high temperature high current conductors. *IEEE Transactions on Dielectrics and Electrical Insulation*, 23(3), 1570–1579. <https://doi.org/10.1109/TDEI.2016.005529>
- Scholkopf, B., Smola, A. J., Williamson, R. C., & Bartlett, P. L. (2000). New support vector algorithms. *Neural Computation*, 12(5), 1207–1245. <https://doi.org/10.1162/089976600300015565>
- Steidl, G., Didas, S., & Neumann, J. (2005). Relations between higher order TV regularization and support vector regression. In R. Kimmel, N. A. Sochen & J. Weickert (Eds.) *Lecture Notes in Computer Science* (pp. 515–527). Springer. https://doi.org/10.1007/11408031_44
- Vapnik, V. N. (1999). *The nature of statistical learning theory*. Springer.
- Wang, Y., Mo, Y., Wang, M., Zhou, X., Liang, L., & Zhang, P. (2018). Impact of conductor temperature time-space variation on the power system operational state. *Energies*, 11(4), Article 760. <https://doi.org/10.3390/en11040760>
- Wei, Y., & Gao, X. (2021). Transmission line galloping prediction based on GA-BP-SVM combined method. *IEEE Access*, 9, 107680–107687. <https://doi.org/10.1109/ACCESS.2021.3100345>
- Yan, Z., Wang, Y., & Liang, L. (2017). Analysis on ampacity of overhead transmission lines being operated. *Journal of Information Processing Systems*, 13(5), 1358–1371. <https://doi.org/10.3745/JIPS.04.0044>
- Yao, R., Huang, S., Sun, K., Liu, F., Zhang, X., & Mei, S. (2016). A multi-timescale quasi-dynamic model for simulation of cascading outages. *IEEE Transactions on Power Systems*, 31(4), 3189–3201. <https://doi.org/10.1109/TPWRS.2015.2466116>

Isolation and Screening of Indigenous Filamentous Fungi Producing Ligninolytic, Cellulolytic and Hemicellulolytic Enzymes from Decomposed Oil Palm Frond

Ahmad Fariz Nicholas¹, Hasliza Abu Hassim^{1,2*}, Mohd Huzairi Mohd Zainudin², Zunita Zakaria¹, Mohd Termizi Yusof³, Mohd Nazri Md Nayan⁴ and Amirul Faiz Mohd Azmi⁵

¹Department of Veterinary Preclinical Sciences, Faculty of Veterinary Medicine, Universiti Putra Malaysia, 43400 UPM, Serdang, Selangor, Malaysia

²Laboratory of Sustainable Animal Production and Biodiversity, Institute of Tropical Agriculture and Food Security, Universiti Putra Malaysia, 4300 UPM, Serdang, Selangor, Malaysia

³Department of Microbiology, Faculty of Biotechnology and Biomolecular Sciences, Universiti Putra Malaysia, 43400 UPM, Serdang, Selangor, Malaysia

⁴Department of Animal Science, Universiti Putra Malaysia, 43400 UPM, Serdang, Selangor, Malaysia

⁵Department of Veterinary Preclinical Sciences, Faculty of Veterinary Medicine, Universiti Malaysia Kelantan, 16100 Kota Bharu, Kelantan, Malaysia

ABSTRACT

Oil palm frond (OPF) is a palm oil plantation by-product commonly used in animal feeding in Malaysia. The large production, availability, and nutrient content make OPF the best candidate for utilization as animal feed. However, OPF contains high lignin bonds to cellulose and hemicellulose that further limit the digestibility of rumen microbes to produce volatile fatty acids as an energy source for ruminants. This study aims to identify and determine the enzyme activity (ligninolytic, cellulolytic, and hemicellulolytic) of enzymes extracted from filamentous fungi in the pre-treatment of OPF using the

solid-state fermentation (SSF) technique. The enzyme extracted from SSF was determined by its enzyme activity (laccase, lignin peroxidase, manganese peroxidase, carboxymethylcellulose, avicelase, and xylanase). Eight fungi were successfully identified to produce enzymes determined in this experiment. *Phanerina mellea* showed the highest average ligninolytic enzyme activity with a value of 0.37 U/mL and an average cellulolytic + hemicellulolytic of

ARTICLE INFO

Article history:

Received: 31 October 2023

Accepted: 01 February 2024

Published: 09 October 2024

DOI: <https://doi.org/10.47836/pjst.32.6.06>

E-mail addresses:

ahmadfariznicholas@yahoo.com (Ahmad Fariz Nicholas)

haslizaabu@upm.edu.my (Hasliza Abu Hassim)

mohdhuzairi@upm.edu.my (Mohd Huzairi Mohd Zainudin)

Zunita@upm.edu.my (Zunita Zakaria)

mohdtermizi@upm.edu.my (Mohd Termizi Yusof)

nazri.nayan@upm.edu.my (Mohd Nazri Md Nayan)

amirul.ma@umk.edu.my (Amirul Faiz Mohd Azmi)

* Corresponding author

0.18 U/mL. In this experiment, *P. mellea* was the most desired fungi for the pre-treatment of OPF. The optimum ligninolytic enzyme production time of OPF pre-treatment is 10 days of SSF.

Keywords: Animal feed, biological pre-treatment, enzyme activity, lignin, oil palm frond, white rot fungi

INTRODUCTION

The abundant lignocellulosic materials from either agriculture or forestry wastes triggered various applications to utilize and turn scraps into valuable products (Manavalan et al., 2015). In Malaysia, oil palm plantations represent 60% of total agricultural land, contributing to high lignocellulosic waste materials (Ghani et al., 2017). The planted area of palm oil trees in Malaysia for 2022 is 5.67 million hectares, which is 1.1% lower compared to 5.74 million hectares in 2021 (Parveez et al., 2022). However, the reduced planted area is caused by the replanting of the trees, and the numbers will be increased, directly increasing the amount of OPF production in Malaysia. The valorization of lignocellulosic waste materials becomes the subject of intense study since they are potentially harmful to the environment.

Lignocellulosic material like oil palm frond (OPF) is a carbohydrate-rich residue containing significant cellulose, hemicellulose and lignin (Sukri et al., 2014). OPF contains 22% soluble carbohydrate and 70% fiber on a dry matter (DM) basis (Saminathan et al., 2012). According to Islam et al. (2000), the nutritional composition of OPF is 439, 926, 698, 501, 168, 196, 748, and 52 (g/kg) of DM, organic matter (OM), neutral detergent fiber (NDF), acid detergent fiber (ADF), cellulose, hemicellulose, total carbohydrate (TC), and non-fiber carbohydrate (NFC), respectively for leaflet parts of the OPF. At the same time, the petiole contains lower ($p < 0.01$) DM, CP and EE than the leaflet (Islam et al., 2000).

As a substitute for grasses or roughages, OPF is commonly used as ruminant feed, especially during the short feed supply (Rusli et al., 2019). The potential of OPF to be livestock feed is hindered by the high neutral detergent fiber (NDF) and lignin contents of the OPF itself (Rahman et al., 2011), making it difficult to be degraded by ruminant digestive systems. To overcome this problem, various pre-treatment methods, such as enzymatic treatment, have been used to improve the digestibility of lignocellulose materials in ruminant feed.

White rot fungi (WRF) is a decaying wood fungus in agricultural residues. It can leave a remarkable reaction by leaving a bleached on the attacked wood by lignin degradation (Asgher et al., 2008). The valuable enzyme system of WRF and its effectiveness in degrading lignocellulosic biomasses attracted considerable research interest in different fields of study (Manavalan et al., 2015). The lignin-degrading capabilities of WRF inspired studies to deepen the knowledge of its enzyme activity for various importances. Many species have been studied, including *Ceriporiopsis subvermispora* (Rahman et al., 2011), *Pleurotus ostreatus* (Tuyen et al., 2013), and *Lentinussajor-caju* (Chanjula et al.,

2017). However, less than 20 species out of 1500 different species of WRF were applied in biological pre-treatment. There are possibilities that the potential WRF can be found in nature (Tian et al., 2012).

Three major enzymes that are working in the degradation of lignin produced by WRF are laccase, lignin peroxidase (LiP), and manganese peroxidase (MnP) (Robinson et al., 2001). These ligninolytic enzymes mineralize the lignin into carbon dioxide (CO₂) and water. These enzymes were used in various applications, for example, bleaching and wastewater treatment for laccase enzyme (Madhavi & Lele, 2009), coal depolymerization and skin lightening by melanin oxidation for LiP enzyme (Falade et al., 2017), and juice extract clarification and biofuel production for MnP enzyme (Kumar & Arora, 2022). The delignification of the lignocellulosic biomasses will allow more cellulose and hemicellulose release for rumen microbial activity. Accessing rumen microbes to cellulose and hemicellulose is the key to improving rumen degradability (Rusli et al., 2021).

The study on the effect of pre-treated OPF feeding on meat quality and animal performance is minimal. A study reported by Azmi et al. (2019) showed that the nutritional value of OPF can be improved by pre-treating it with ligninolytic enzyme extract. Another study reported by Hamchara et al. (2018) showed that the feeding of OPF pre-treated with *L. sajor-ceju* to 16-month-old crossbred male goats improved the estimated energy intakes (ME Mcal/DM/d) by up to 53 %. The pre-treatment of OPF by WRF is promising in improving the low nutritional value of OPF. This study aims to identify and determine the enzyme activity of enzyme extract from filamentous fungi collected from Palm oil tree plantations in Taman Pertanian Universiti, Universiti Putra Malaysia (TPU, UPM).

MATERIALS AND METHODS

Fungi Culture and Isolation

The fungi were collected at the Palm oil tree plantations in University Agricultural Park, Universiti Putra Malaysia (UAP, UPM) (2.983592895423529, 101.71000476197045). The fungi were collected from rotten oil palm fronds, placed in paper bags, and taken to the FAMTEC laboratory in the Faculty of Biotechnology UPM (Azmi et al., 2019). The collected samples were cultured on potato dextrose agar (PDA) (Bacton, Dickinson and Company, USA) containing streptomycin and penicillin antibiotics. The sub-culturing process was repeated until the pure culture was obtained. Stocks of isolated fungi were prepared using the filter paper method and agar slant.

Morphological Identification

The isolated fungi were cultured on PDA (OXOID CM0139) agar for seven days before being used for microscopic observation and identification. First, the morphology of the

fungi on the agar plate was observed. The culture's texture, structure, edge, and elevation were also observed.

Molecular Identification

The DNA extracted from the isolated fungi underwent a polymerase chain reaction (PCR) using Bio-Rad T100 PCR Thermal Cycler with primer internal transcribed spacer, ITS1 (5'-TCCGTAGGTGAACCTGCGG-3') and ITS4 (5'-TCCTCCGCTTATTGATATGC-3'). ITS1 and ITS4 acted as forward and reversed primers, respectively. The amplified DNA was run on gel electrophoresis and viewed under UV light with the range size of 600 and 700 base pairs (bp). The sequencing was done, and the Apical Scientific (1st Base) result was processed with Chromas and MEGA7 software. The aligned sequence was compared with the sequence in GenBank using the Basic Local Alignment Search Tool (BLAST), NCBI, and the fungal species were determined. The phylogenetic tree was constructed using NCBI taxonomy and MEGA7 software.

Microscopic Observation

The fungi were placed onto a glass slide covered with a cover slip and pressed to get a good separation of the hyphae. A methylene blue solution was used for staining. The fungi characteristics were then observed using a compound microscope (Olympus BX53M, Japan) with a digital camera. The morphological structure of the fungi was compared with the previous studies and determined based on fungi characteristics stated by Galal et al. (2017). The characteristics involve branching, hyphae, conidiospores and spores (Galal et al., 2017).

Solid-state Fermentation

The OPF was collected from Taman Pertanian Universiti, Universiti Putra Malaysia. Then, the OPF was chopped into a smaller size. In the Erlenmeyer flask, 15 g of chopped OPF was added. Then, 0.05% of glucose and 2.4 mM of nitrogen source, ammonium sulfate ((NH₄)₂SO₄), were added to 45 mL of distilled water. The flasks were then covered with cotton plugs and aluminum foil. It was autoclaved to remove any existing microorganisms. Each flask was added with three 3–10 mm agar plugs from each fungi culture. The flasks were incubated in the oven incubator at 28°C for 10, 20, and 30 days (Azmi et al., 2019).

Enzyme Extraction

Enzyme extraction begins once the fermentation period ends. Each flask received 150 mL of distilled water, and the flasks were shaken for 3 hours. The mixture was then filtered

using six layers of wound gauze. The filtrate was mixed with polyvinylpolypyrrolidone (PVPP) to remove tannins (Toth & Pavia, 2000). The amount of PVPP added is 0.5% of the total filtrate. The mix of the filtrate and PVPP was centrifuged (Avanti J-26S XP1, High-Performance Centrifuge, Beckman Coulter, USA) at 12,000 g for 10 minutes. The temperature during the centrifuging process was 4°C. The supernatant was then collected and stored for enzyme activity determination (Azmi et al., 2019).

Ligninolytic Enzyme Activity Determinations

Laccase enzyme activity determination used citrate-phosphate buffer and 2,2'-azino-bis(3-ethylbenzothiazoline-6-sulphonic (ABTS) acid substrate in the experiment. To prepare citrate-phosphate buffer (50 mM), 1.921 g of citric acid, $C_6H_8O_7$, was added into 100 ml distilled water and the pH was calibrated to pH 5.0 and labeled as solution A. Then, 3.581 g of sodium phosphate dibasic, Na_2HPO_4 , was added into 100 mL distilled water and labeled solution B. The substrate was prepared with 0.165 g of ABTS added into 10 mL of distilled water. The substrate was then transferred to an Eppendorf tube. The blank solution was prepared before reading at 420 nm light absorbance of spectrophotometer nanodrop (Tecan Infinite M200 Pro™, Switzerland) against blank. All enzyme activity values were represented in unit concentration, U/mL (unit/milliliter), with three replicates (Azmi et al., 2019). The calculation for laccase enzyme activity determination was done using Equation 1.

$$\text{Concentration} \left(\frac{U}{ml} \right) = \frac{A}{\Sigma mM^{-1}cm^{-1}} \times \frac{1500 \text{ ul}}{100 \text{ ul}} \quad [1]$$

Where A = Absorbance; total volume in cuvette = 1500 ul; total volume of enzyme in cuvette = 100 ul; and light absorbance at 420 nm = $\Sigma mM^{-1} cm^{-1}$

Lignin peroxidase enzyme activity was determined with acid tartrate buffer, substrate, and hydrogen peroxide, H_2O_2 used in the experiment. The buffer was prepared with 3.752 g of acid tartrate, $C_4H_6O_6$ was added to 250 mL of distilled water, and the pH was calibrated to pH 3.0 with HCL before being kept at 4°C. Substrate preparation was done with 0.105 mL of veratryl alcohol (3, 4-Dimethoxybenzyl alcohol) added to 25 mL of distilled water and stored at 4°C in an Eppendorf tube. Then, the hydrogen peroxide, H_2O_2 , was prepared according to the manufacturer's specifications. After that, the mixture tube was prepared by adding 2570 μ L of acid tartrate buffer, 200 μ L veratryl alcohols, 30 μ L hydrogen peroxide, and 200 μ L of enzyme extract. The blank prepared with 2570 μ L of acid tartrate buffer was added to 200 μ L veratryl alcohol and 30 μ L hydrogen peroxide. Finally, the mixture tubes were read at 310 nm light absorbance of spectrophotometer nanodrop (Tecan Infinite M200 Pro™, Switzerland) against blank. The calculation for LiP enzyme activity determination was done using Equation 2.

$$\text{Concentration} \left(\frac{\text{U}}{\text{ml}} \right) = \frac{A}{\Sigma \text{mM}^{-1} \text{cm}^{-1}} \times \frac{3000 \text{ ul}}{200 \text{ ul}} \quad [2]$$

Where: A = Absorbance; total volume in cuvette = 1500 uL; total volume of enzyme in cuvette = 100 uL; light absorbance at 310 nm = $\Sigma \text{mM}^{-1} \text{cm}^{-1}$

Manganese peroxidase was determined by preparing a sodium tartrate buffer with 5.752 g of sodium tartrate added to 250 mL of distilled water. The solution was adjusted to pH 5.0 using HCL or NaOH and kept at 4°C. The substrate was prepared by adding 0.254 g of manganese sulfate to 50 ml of distilled water and stored at 4°C. The H₂O₂ was prepared according to the manufacturer's specifications. After that, the mixture tube was prepared by adding 2550 µL of sodium tartrate buffer mixed with 200 µL manganese sulfate, 30 µL H₂O₂, and 200 µL of enzyme extract. The blank was prepared by 2550 µL sodium tartrate buffer added to 200 µL manganese sulfate and 30 µL H₂O₂. The mixture tubes were read at 238 nm light absorbance of spectrophotometer nanodrop (Tecan Infinite M200 Pro™, Switzerland) against blank. The calculation for MnP enzyme activity determination was done using Equation 3.

$$\text{Concentration} \left(\frac{\text{U}}{\text{ml}} \right) = \frac{A}{\Sigma \text{mM}^{-1} \text{cm}^{-1}} \times \frac{3000 \text{ ul}}{200 \text{ ul}} \quad [3]$$

Where: A = Absorbance; total volume in cuvette = 1500 uL; total volume of enzyme in cuvette = 100 uL; light absorbance at 238 nm = $\Sigma \text{mM}^{-1} \text{cm}^{-1}$

Cellulolytic Enzyme Activity Determination

Substrate and citrate buffers were prepared to screen carboxymethylcellulase (CMCase) enzyme activity. The substrate was prepared with 1 g of carboxymethylcellulose and added to 100 mL of distilled water in a 250 mL Erlenmeyer flask. The solution was then stirred until homogeneous and stored at 4°C. For the citrate buffer, 0.1 M citrate buffer was prepared by adding 0.1 mol of citric acid to 0.1 mol of sodium citrate adjusted to pH 4.8 using HCl or NaOH. After that, the mixture tube was prepared by adding 0.5 mL substrate and 0.5 mL enzyme. Three control tubes were prepared: buffer control tube, enzyme control tube, and substrate control tube. For the buffer control tube, 1 mL citrate buffer in a tube was prepared. For the enzyme control tube, 0.5 ml of the enzyme was added to 0.5 mL citrate buffer and 0.5 mL of the substrate was added to 0.5 mL citrate buffer to prepare the substrate control tube. The tubes were then incubated in a water bath at 50°C for 30 min (Dinis et al., 2009). The reaction was stopped by adding 3 mL of dinitrosalicylic (DNS) acid to each tube. The mixture, buffer control, enzyme control and substrate control tubes were then placed in boiling water for 10 min. The tubes were then read at 575 nm light absorbance of spectrophotometer nanodrop (Tecan Infinite M200 Pro™, Switzerland) against blank. The glucose solution was prepared in 6 different concentrations (100 mg, 300 mg, 600 mg,

900 mg, 1200 mg, and 1500 mg) with distilled water dilution as the standard. The enzyme activity was eventually measured in unit U/mL (unit/milliliter)

Avicelase enzyme activity was determined using an avicel microcrystalline substrate and citrate buffer. Substrate of 1 g of avicel microcrystalline was used and added to 100 mL distilled water in a 250 mL Erlenmeyer flask. The solution was then stirred until homogeneous. The citrate buffer was prepared by adding 0.1 mol of citric acid with 0.1 mol of sodium citrate to get 0.1 M of citrate buffer at pH adjusted to pH 4.8, either HCl or NaOH. The mixture tube was prepared by adding 0.5 mL enzyme and 1.0 mL substrate. For the buffer control tube, 1.5 mL of citrate buffer was prepared. For the enzyme control tube, 0.5 mL of the enzyme was added to 1.0 mL citrate buffer in the tube, and for the substrate control tube, 1.0 mL substrate was added to 0.5 mL citrate buffer. The tubes were then incubated in a water bath at 50°C for 30 min (Dinis et al., 2009). The reaction was stopped by adding 3 mL of dinitrosalicylic (DNS) acid to each tube. All tubes were then placed in boiling water for 10 min. The tubes were then read at 575 nm light absorbance of spectrophotometer nanodrop (Tecan Infinite M200 Pro™, Switzerland) against blank. The glucose solution was prepared in six different concentrations (100 mg, 300 mg, 600 mg, 900 mg, 1200 mg, and 1500 mg) with distilled water dilution as the standard. The enzyme activity was eventually measured in unit U/mL (unit/milliliter)

Hemicellulolytic Enzymes Activity Determinations

This experiment added 0.25 g xylan from beechwood to 100 mL distilled water as the substrate. The solution was then heated at 70°C with continuous shaking. The citrate buffer was prepared by adding 0.1 mol of citric acid with 0.1 mol of sodium citrate to get 0.1 M of citrate buffer at pH adjusted to pH 4.8, either HCl or NaOH. The mixture tube was prepared by adding 0.5 mL enzyme to 0.5 mL substrate. The buffer control tube was prepared with only 1.0 mL citrate buffer. For the enzyme control tube, 0.5 mL enzyme was added to 0.5 mL citrate buffer and the substrate control tube was prepared by adding 0.5 mL substrate to 0.5 mL citrate buffer. The tubes were then incubated in a water bath at 50°C for 30 min (Dinis et al., 2009). The reaction was stopped by adding 3 mL of dinitrosalicylic (DNS) acid to each tube. All tubes were then placed in boiling water for 10 min. The tubes were then read at 575 nm light absorbance of spectrophotometer nanodrop (Tecan Infinite M200 Pro™, Switzerland) against blank. The xylose solution was prepared in six different concentrations (100 mg, 300 mg, 600 mg, 900 mg, 1200 mg and 1500 mg) with citrate buffer dilution as the standard.

Fungi Selection with Optimum Enzyme Activity and Pre-treatment Time

The enzyme activity determination results data were used to select fungi with the most optimum ligninolytic enzyme activity. A scatterplot graph consists of the y-axis representing

the average of total ligninolytic activity while the x-axis represents the constructed cellulolytic and hemicellulolytic average enzyme activity. The fungi that produced the high ligninolytic enzyme (laccase, LiP, and MnP) activity with low cellulolytic (CMCase and avicelase) and hemicellulolytic (xylanase) enzyme activity were selected. The optimum pre-treatment time of OPF was determined based on enzyme activity results on days 10, 20, and 30 of solid-state fermentation.

Statistical Analysis

IBM SPSS statistics 27 was used in this study and presented as mean \pm SEM (standard error of the mean). Analysis of variance (ANOVA) was applied to compare the significant difference of each pre-treatment time with a significant difference of $p < 0.05$, followed by Tukey's test.

RESULTS

Morphological Selection

In this experiment, 79 fungi isolates were identified and labeled as F01 until F79. The isolates were classified into eight groups based on their morphology on the PDA agar. One isolate was selected from each group, which is F14, F03, F32, F39, F49, F65, F77, and F02 (Figure 1). All fungi were selected from the filamentous structures on the PDA agar. The fungi colony showed in white concentric rings for F14, F39, F49, and F02. The colony for F03 and F32 were green in color. F65 was brownish peach cottony, and F77

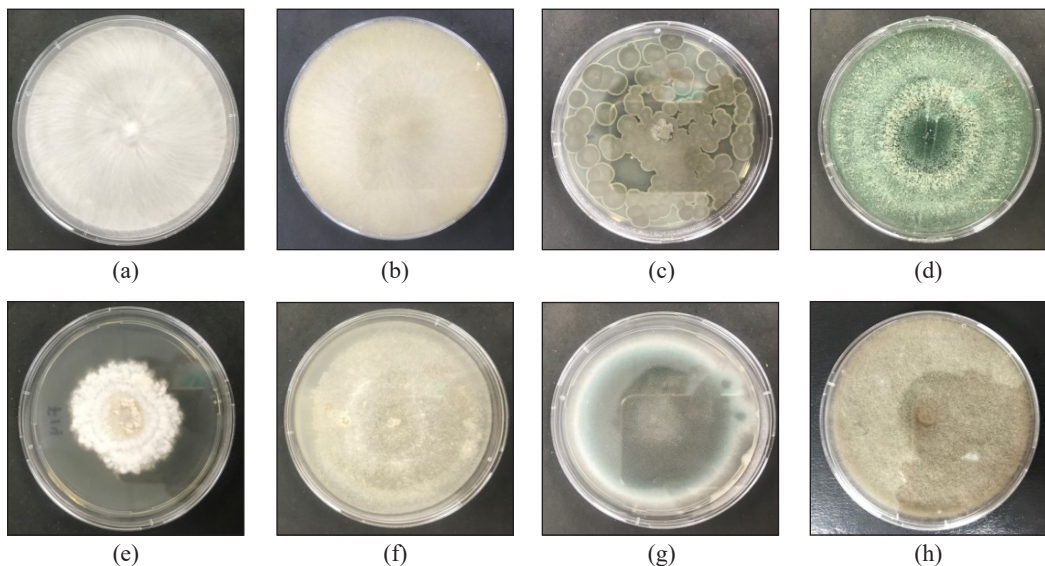


Figure 1. Selected fungi culture from eight different groups: (a) F49; (b) F02; (c) F77; (d) F32; (e) F14; (f) F39; (g) F03; and (h) F6

showed multiple scattered colonies with grey-green color rings. The fungi were also in an augmented raised cottony structure with abundant aerial mycelium grown on PDA agar (Table S1).

Molecular Observation

After a series of DNA extraction, amplification, and sequencing, the phylogenetic tree showed that the fungi were identified as F49 (*Marasmius palmivorus* MN871732), F02 (*Mucor fusiformis* KY560315), F77 (*Penicillium citrinum* MK312421), F32 (*Trichoderma asperellum* MK928414), F14 (*Schizophyllum commune* MN856258), F39 (*Phanerina mellea* or *Ceriporia mellea* MK432982), F03 (*Aspergillus ellipticus* MG596660) and F65 (*Syncephalastrum racemosum* MH857909) (Table S2).

Microscopic Observation

Figure 2 shows the morphology of each selected fungus under microscopic observation. The microscopic observation was based on branching, hyphae, conidiospores and spores, following Galal et al. (2017). The structures were compared with those of previous studies, as shown in Tables S3 to S10.

Schizophyllum commune showed the appearance of hyphae, and these fungi formed a clamp connection at the septa (Sigler et al., 1999). The hyphae also formed a thread-like branching and septate. However, the conidiophores and spores could not be seen. For *A. ellipticus*, it was confusing to differentiate from other *Aspergillus* sp. as the shapes were almost the same. However, *A. ellipticus* conidia were elliptical (Mahmood & Azhar, 2017). *A. ellipticus* cannot be seen clearly under the compound microscope, but the multiple conidia showed that the fungi were *Aspergillus* sp.

Trichoderma asperellum showed a branch structure with septate hypha. The conidia could be seen near the conidiophores at the tip of the hyphae. The structure was similar to that of *T. asperellum* observed by Podder and Ghosh (2019). *Phanerina mellea* hyphae structure was monomitic, brunching with a sharp angle and simple septa (Miettinen et al., 2016). The conidiophores could not be seen, and the fungi formed no clamp.

Marasmius palmivorus showed hypha with a thread-like structure under x1000 magnification of a compound microscope. The image by Tamur et al. (2019) in Table S7 showed the septal wall of fungal hyphae with the clamp connection between hyphae, which was also shown by the microscopic observation of *M. palmivorus*. The branched rough hypha structure was absent of conidiophores. *S. racemosum* could be seen, and the structure was very similar to the image shown by Raju et al. (2020) in Table S8. The conidiophores were shown in sporangiophores, and the hyphae were shown in broad aseptate.

Penicillium citrinum showed a microscopic structure similar to the image shown by Saif et al. (2020). Like other *Penicillium* sp., *P. citrinum* contained highly branched

septate hyphae. At the tip of the hyphae, there were branches of conidiophores, the main dispersal route for the fungi. The sporangiospores structure of *M. fusiformis* could be seen under the compound microscope. However, the conidiophores could be seen clearly like the image shown by Walther et al. (2013), which was viewed using a scanning electron microscope (SEM). *Mucor fusiformis*, also known as *Zygorhynchus psychrophilus*, is in a *Mucor* group with a sporangiospores structure that is poorly sympodially branched tall with small sporangia (Walther et al., 2013).

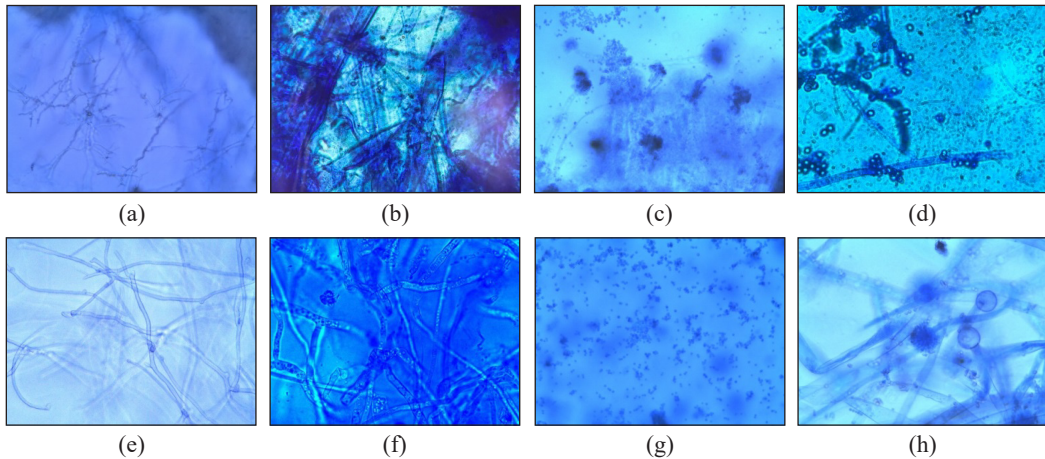


Figure 2. Microscopic morphology of eight different fungi identified: (a) *Marasmius palmivorus* (MP), (b) *Mucor fusiformis* (MF), (c) *Penicillium citrinum* (PC), (d) *Trichoderma asperellum* (TA), (e) *Schizophyllum commune* (SC), (f) *Phanerina mellea* (PM), (g) *Aspergillus ellipticus* (AE), and (h) *Syncephalastrum racemosum* (SR)

Enzyme Activity Determination

The enzyme activity determination experiment showed that all eight species of fungi identified were successfully detected to produce the enzyme analyzed in this experiment. Only *M. fusiformis* (MF) and *A. ellipticus* (AE) showed no laccase enzyme activity production.

The laccase enzyme activity of *P. mellea* (PM) showed significantly ($p < 0.05$) higher average enzyme activity compared to the other fungi (Figure 3). The laccase enzyme activity of *P. mellea* increased from 0.28 U/mL on day 10 to 0.53 U/mL on day 20 of SSF. On day 30, the laccase enzyme activity of *P. mellea* decreased to 0.24 U/mL. It is followed by *M. palmivorus* (MP), *S. commune* (SC), *P. citrinum* (PC), *T. asperellum* (TA), and *S. racemosum* (SR). Most fungi, such as PM, MP, SC, PC, and TA, generally showed the highest laccase enzyme activity on day 20 of SSF.

All fungi produced lignin peroxidase (LiP) enzyme activity (Figure 4). The LiP enzyme activity of PM showed the highest value, which is 0.90 U/mL, on day 10 of SSF, compared to the other fungi. The LiP enzyme activity was then reduced to 0.34 U/mL and

0.08 U/mL on days 20 and 30 of SSF, respectively. AE, SC, SR, PC, MF, TA, and MP follow the same trend. Most fungi showed the highest LiP enzyme activity on day 10 of SSF, including PM, AE, SC, SR and PC. MF, TA, and MP showed the highest LiP enzyme activity on day 20 of SSF.

All fungi are shown to produce manganese peroxidase (MnP) enzyme activity (Figure 5). The MnP enzyme activity of SC is 0.58 U/mL on day 10 of SSF, showing the highest value, followed by AE, PM, MF, PC, TA, SR and MP. The SC MnP enzyme activity shows a decrease of 0.03 U/mL on day 20 with a value of 0.55 U/mL and decreased again to 0.39 U/mL on day 30 of SSF. Most fungi were shown to produce the highest MnP enzyme activity on day 10 of SSF except for AE and SR, which produced the highest on day 20 of SSF.

The carboxymethylcellulose (CMCase) enzyme activity for all fungi showed a similar pattern as the activity increased from day 10 to 20, setting the highest activity before reducing on day 30 of SSF (Figure 6). The CMCase enzyme activities for all fungi are the highest on day 20 of SSF compared to days 10 and 30. MF shows the highest value, 0.20 U/mL, and PC shows the lowest value, 0.02 U/mL, on day 30 of SSF.

The avicelase enzyme activity was produced by all fungi, with most fungi having the highest activity on day 20 of SSF (Figure 7). Each fungus can see no obvious comparison in a similar pattern to CMCase enzyme activity. The highest avicelase enzyme activity is shown by TA, with a value of 0.38 U/mL on day 20 of SSF, and the lowest is by AE, with a value of 0.15 U/mL on day 10 of SSF.

Xylanase enzyme activity is similar for each fungus, where the highest activity is shown on day 10 before it is reduced on days 20 and 30 of SSF (Figure 8). All fungi show a similar pattern of xylanase enzyme activity, where TA shows the highest value on day 10 with a value of 0.27 U/mL.

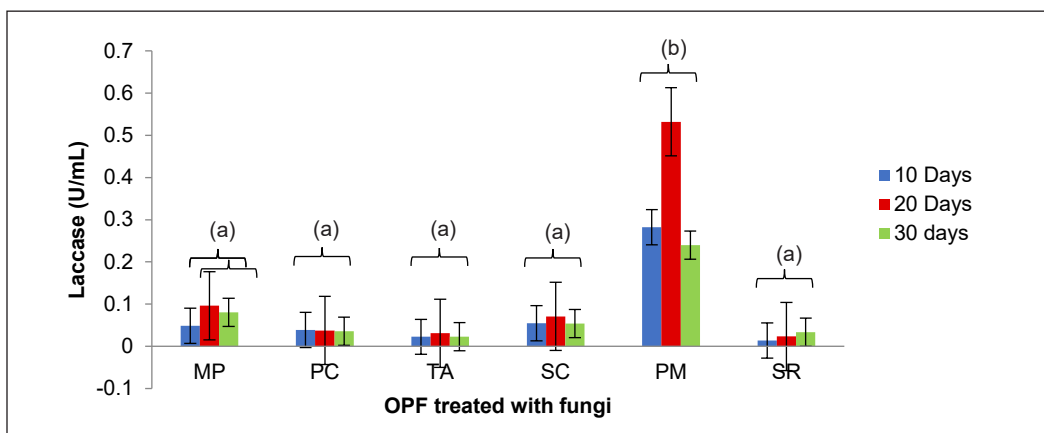


Figure 3. Laccase activity of enzyme extract after OPF pre-treatment with different fungi at 10, 20 and 30 days of incubation

Note. MP = *Marasmius palmivorus*; PC = *Penicillium citrinum*; TA = *Trichoderma asperellum*; SC = *Schizophyllum commune*; PM = *Phanerina mellea*; SR = *Syncephalastrum racemosum*

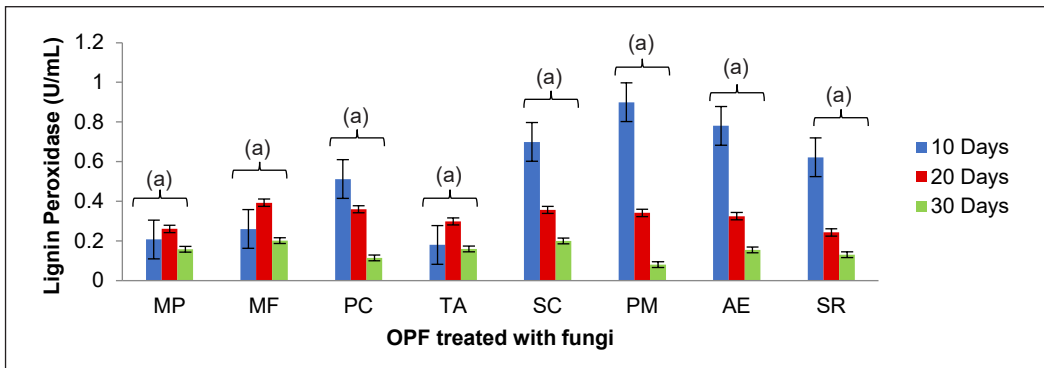


Figure 4. Lignin peroxidase activity of enzyme extract after OPF pre-treatment with different fungi at 10, 20 and 30 days of incubation (MP = *Marasmius palmivorus*; MF = *Mucor fusiformis*; PC = *Penicillium citrinum*; TA = *Trichoderma asperellum*; SC = *Schizophyllum commune*; PM = *Phanerina mellea*; AE = *Aspergillus ellipticus*; SR = *Syncephalastrum racemosum*)

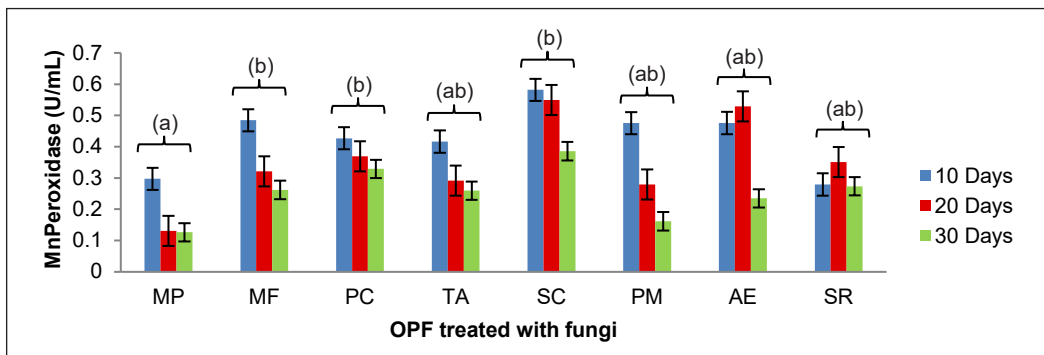


Figure 5. Manganese peroxidase activity of enzyme extract after OPF pre-treatment with different fungi at 10, 20 and 30 days of incubation (Note. MP = *Marasmius palmivorus*; MF = *Mucor fusiformis*; PC = *Penicillium citrinum*; TA = *Trichoderma asperellum*; SC = *Schizophyllum commune*; PM = *Phanerina mellea*; AE = *Aspergillus ellipticus*; SR = *Syncephalastrum racemosum*)

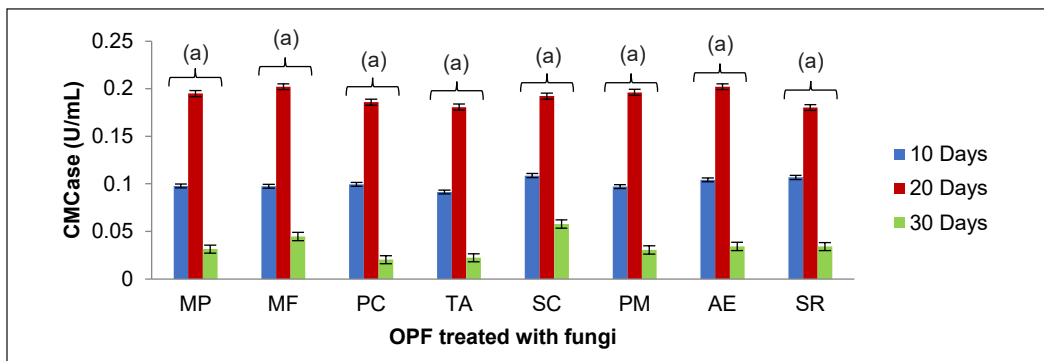


Figure 6. CMCase activity of enzyme extract after OPF pre-treatment with different fungi at 10, 20 and 30 days of incubation (MP = *Marasmius palmivorus*; MF = *Mucor fusiformis*; PC = *Penicillium citrinum*; TA = *Trichoderma asperellum*; SC = *Schizophyllum commune*; PM = *Phanerina mellea*; AE = *Aspergillus ellipticus*; SR = *Syncephalastrum racemosum*)

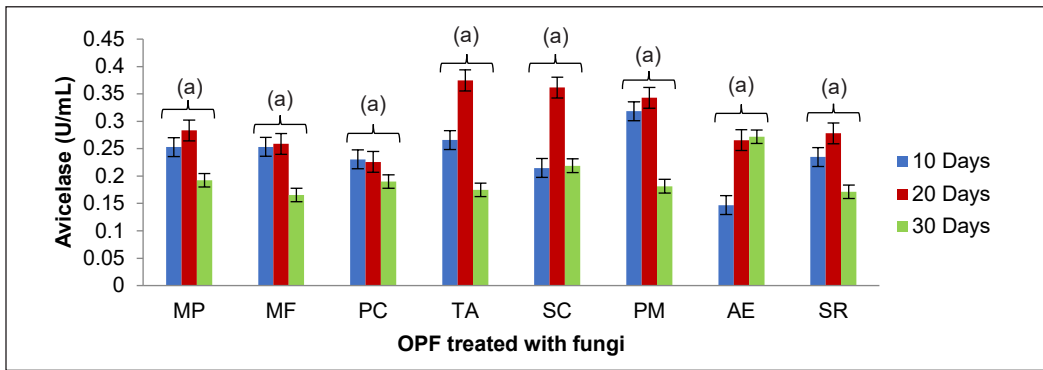


Figure 7. Avicelase activity of enzyme extract after OPF pre-treatment with different fungi at 10, 20 and 30 days of incubation (MP = *Marasmius palmivorus*; MF = *Mucor fusiformis*; PC = *Penicillium citrinum*; TA = *Trichoderma asperellum*; SC = *Schizophyllum commune*; PM = *Phanerina mellea*; AE = *Aspergillus ellipticus*; SR = *Syncephalastrum racemosum*)

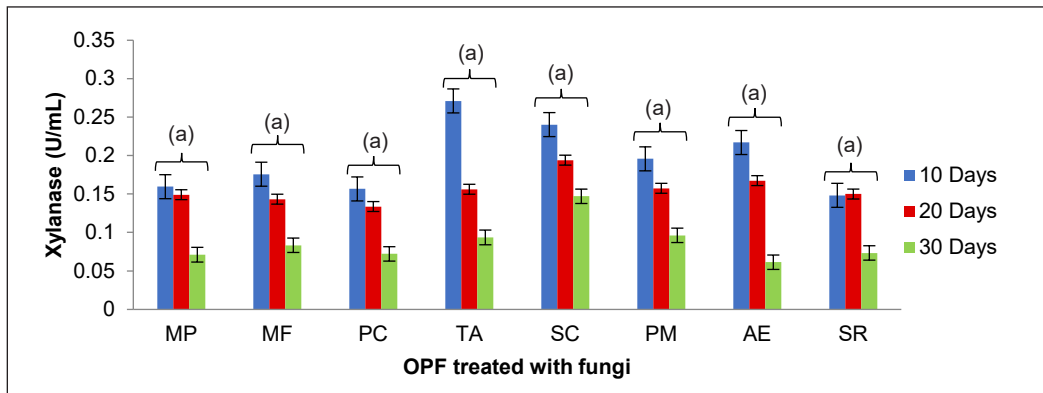


Figure 8. Xylanase activity of enzyme extract after OPF pre-treatment with different fungi at 10, 20 and 30 days of incubation (MP = *Marasmius palmivorus*; MF = *Mucor fusiformis*; PC = *Penicillium citrinum*; TA = *Trichoderma asperellum*; SC = *Schizophyllum commune*; PM = *Phanerina mellea*; AE = *Aspergillus ellipticus*; SR = *Syncephalastrum racemosum*)

Selection of Fungi

The selection of the most favorable fungi for pre-treatment of OPF was based on the average enzyme activity determination results. Figure 9 shows a scatterplot graph of the average ligninolytic enzyme activity against the total cellulolytic + hemicellulolytic enzyme activity. From the graph, *P. mellea* is plotted at the top of the graph (red circle), which shows that the fungi have the highest ligninolytic enzyme activity with low cellulolytic and hemicellulolytic enzyme activity. The ratio between ligninolytic enzyme, which is the desired enzyme, and cellulolytic + hemicellulolytic are best shown by *P. mellea*. It is followed by *S. commune*, located lower than *P. mellea*. *Phanerina mellea* shows the highest average ligninolytic enzyme activity with a value of 0.37 U/mL and an average cellulolytic + hemicellulolytic of 0.18 U/mL. It is followed by *S. commune*, the average ligninolytic

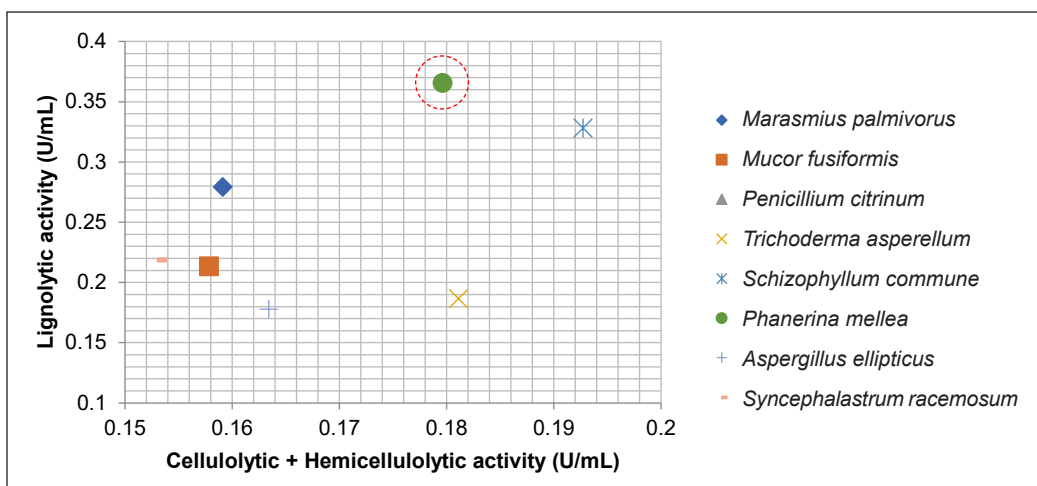


Figure 9. Graph of average ligninolytic enzyme activity against total average cellulolytic and hemicellulolytic enzyme activity of fungi. Note. The red circle shows *Phanerina mellea* is plotted at the top of the graph

enzyme activity is 0.33 U/mL, and the average cellulolytic + hemicellulolytic is 0.19 U/mL. In this experiment, *P. mellea* was the most desired fungi for the pre-treatment of OPF.

Selection of the Optimal Ligninolytic Enzyme Activity Production Time

Table 1 shows the average enzyme activity of fungi at different treatment times based on the type of enzyme that was experimented with. The average laccase enzyme activity shows that day 20 has the highest enzyme activity compared to days 10 and 30 of SSF. However, there is no significant difference among days 10, 20, and 30 of SSF ($p>0.05$). For average LiP and MnP enzyme activity, day 10 shows the highest activity, followed by days 20 and 30. However, no significant difference ($p>0.05$) exists between days 10 and 20. It also shows no significant difference between days 20 and 30. However, day 10 is significantly different from day 30 of SSF.

The mean CMCCase enzyme activity of day 20 shows the highest activity, followed by days 10 and 30. Days 10, 20, and 30 significantly differ ($p<0.05$) between each treatment time. Like CMCCase, average avicelase enzyme activity also shows that day 20 has the highest activity compared to days 10 and 30. There is no significant difference ($p>0.05$) between days 20 and 30 of SSF. However, day 10 significantly differs ($p<0.05$) from days 20 and 30. The mean xylanase enzyme activity of day 10 shows the highest activity, followed by days 20 and 30. The variance analysis shows that day 10 has no significant difference ($p>0.05$) from day 20. However, day 30 significantly differs ($p<0.05$) from days 10 and 20 of SSF.

On average, ligninolytic and hemicellulolytic enzyme activity showed the highest activity on day 10 of SSF, while cellulolytic enzyme activity showed the highest activity

on day 20 of SSF. This study needed ligninolytic enzymes for lignin degradation with minimum cellulolytic and hemicellulolytic enzymes. Therefore, the optimum OPF pre-treatment time is day 10 of SSF.

Table 1
Average enzyme activity of fungi identified on days 10, 20 and 30 of solid-state fermentation

Treatment time (Days)	Average enzyme activity (U/mL)					
	Laccase	LiP	MnP	CMCase	Avicelase	Xylanase
10	0.06 ^a	0.52 ^b	0.43 ^b	0.10 ^b	0.24 ^a	0.20 ^b
20	0.10 ^a	0.32 ^{ab}	0.35 ^{ab}	0.19 ^c	0.30 ^b	0.16 ^b
30	0.06 ^a	0.15 ^a	0.25 ^a	0.03 ^a	0.20 ^a	0.09 ^a
SEM	0.01	0.09	0.04	0.04	0.02	0.09
<i>p</i> -Value	0.75	<0.001	0.01	<0.001	<0.001	<0.001

Note: Means that do not share a letter are significantly different, where ($P < 0.05$) is considered a significant value

DISCUSSION

The different coloration and colony structure indicated the differences between each fungus. Some fungi can easily be noticed based on their morphological structure in nature. For example, the fungi filamentous structure is shown in the cottony fibrous structure of hyphae with cellulose-enriched materials (Mäkelä et al., 2020). The white concentric rings of F14, F39, and F49 are synonymous with WRF (Abdel-Hamid et al., 2013). F03, F32, F77, F65, and F02 are brown or soft rot fungi.

Each species identified in this study has its specialties. Some fungi species are used in commercial industries, and some are still under investigation. For example, *M. palmivorus* pre-treatment on empty fruit bunches (EFB) and palm kernel meal (PKM) did not improve the growth of larvae of the Black Soldier Fly (BSF) (Colombatto et al., 2003). *Mucor fusiformis* or *Zygorhynchus psychrophilus* is a fungus usually used in food manufacturing, such as cheese and tofu. However, it is infectious and dangerous to human health (Walther et al., 2013). *Penicillium citrinum* is used in β -mannanase enzyme production and industrial applications, including animal feed production (Lima et al., 2021). *Schizophyllum commune* is used in rice straw fermentation to produce high levels of xylanase enzyme under the state fermentation method for the pre-bleaching of ethanol-soda pulp (Gautam et al., 2018).

Phanerina mellea is also a WRF commonly called *Ceriporia mellea* (Miettinen et al., 2016). The information on this fungus is limited, and its enzyme activity production and application have never been investigated. *Aspergillus ellipticus* is a well-known wood-decaying fungus, and various studies have used this fungus in cellulose production studies. This fungus is usually used in pharmaceuticals, food ingredients and enzyme production (Gupte & Madamwar, 1997).

In this enzyme activity determination study, some fungi lacked laccase enzyme activities as some physiological fungi groups were never reported to produce laccase enzyme, such as *zygomycetes*, which is the division of *M. fusiformis* (Mäkelä et al., 2020). Gupte et al. (2007) reported no laccase activity in *P. chrysosporium*. *Fusarium verticillioides* and *Aspergillus niger* secreted no laccase enzyme activity in the study reported by Pant and Adholeya (2007). Enzyme production by fungi can be classified into three categories which are fungi that secrete laccase and two peroxidases (MnP, LiP), laccase and one peroxidase, and laccase or peroxidase only (Wang et al., 2019). *Mucor fusiformis* and *A. elepticus* are classified into fungi that secrete laccase and one peroxidase.

Lignin peroxidase resulted in the highest enzyme activity in the 0.08 – 0.90 U/mL range, with the highest recorded by *P. mellea* on day 10 of SSF. It is lower compared to LiP enzyme activity produced by *P. chrysosporium* with 14.25 U/mL on day 10 of SSF with wheat straw as the substrate, as reported by Gupte et al. (2007). The difference in LiP enzyme activity production between these two studies could be caused by the different substrates, nutrient supplementation and even the inoculation number used. In this study, three inoculums were used, but they used five inoculums in their SSF.

In general, most of the fungi identified in this study produced higher MnP enzyme activity than laccase and lower than LiP enzyme. The low supplementation of manganese (II) ion, which is highly reactive and was used to avoid MnP, hindered LiP enzyme production (Hofrichter, 2002).

Cellulolytic enzyme activity showed a similar value and trend for all fungi identified with day 20 showed the highest activity compared to days 10 and 30 of SSF. The peak time production of cellulolytic enzyme was delayed compared to ligninolytic enzyme. The physiological structure of the OPF, which is covered with the cell wall structure, induces the production of ligninolytic enzymes first before WRF produces cellulolytic and hemicellulolytic enzymes. The WRF colonized the cell lumina of the OPF before the fungal mycelia propagated the cell wall structure by the Fenton reaction. This event caused the fungi to produce ligninolytic enzyme first before cellulolytic enzyme (Dong et al., 2013; Ji et al., 2014; Rouches et al., 2016). It was also shown by Rahman et al. (2011) that *P. chrysosporium* secretes the ligninolytic enzyme before the cellulolytic enzyme, resulting in lower sugar production compared to *A. terreus*. The activity decreased on day 30 as the cellulolytic enzyme activity was suppressed, and delignification happened, producing water.

In the selection of fungi, filamentous fungi that produced high ligninolytic enzymes with low cellulolytic + hemicellulolytic enzyme activity will be selected for further study. Ligninolytic enzymes are responsible for delignification (Saha et al., 2016). Narayanazwamy et al. (2013) reported that lignin degradation involves extracellular enzymes (LiP, MnP and laccase). The lignin degradation ability of filamentous fungi is

the critical factor in the pre-treatment. However, cellulose recovery to conserve the total availability of glucose used by animals will determine the fungi's actual potential ability (Tian et al., 2012). *Phanerina mellea* showed the highest ligninolytic enzyme activity with low cellulolytic and hemicellulolytic enzyme activity.

The optimal ligninolytic enzyme production time was determined based on the average enzyme activity of fungi identified on days 10, 20 and 30 of SSF. In this study, each fungus showed various laccase enzyme activities. The production of laccase enzyme activity is different for different fungi strains. Isroi et al. (2011) stated that one of the factors that influenced the production of ligninolytic enzyme production was the fungi strain. The study by Gupte et al. (2007) also reported that the production of enzyme activity by *T.versicolor*, *P.cryosporium*, *P.ostreatus*, and *I. lateus* on wheat straw showed the highest on day 10 of SSF. Akpinar and Urek (2012) also reported that the highest laccase enzyme production time by *Pleurotus eryngii* is on day 10 of SSF.

CONCLUSION

WRF has the potential to be used in the biological pre-treatment of lignocellulosic materials. With the SSF technique, the enzyme activity of WRF was successfully detected and analyzed, as well as their ability to degrade lignin in OPF. The average ligninolytic enzyme activity was higher than the average cellulolytic + hemicellulolytic enzyme activity. *P. mellea* best showed the enzyme activity production of the desired enzyme. *P. mellea* showed an average ligninolytic enzyme activity value of 0.37 U/mL; the average cellulolytic + hemicellulolytic is 0.18 U/ml. *P. mellea* can be further used for pre-treatment OPF in animal feed production. The optimal pre-treatment time of OPF was also successfully analyzed. Day 10 of SSF showed the best pre-treatment time for producing high ligninolytic enzyme activity.

ACKNOWLEDGEMENTS

The authors would like to acknowledge the Ministry of Higher Education (MOHE) Malaysia through the Fundamental Research Grant Scheme (FRGS/1/2017/WAB01/UPM/02/18) with grant number 5540032 for the financial support for this project. The completion of this study could not have been possible without the participation of many people whose names may not be enumerated. We are grateful to all the authors and the staff who took part in this study.

REFERENCES

- Abdel-Hamid, A. M., Solbiati, J. O., & Cann, I. K. (2013). Insights into lignin degradation and its potential industrial applications. *Advances in Applied Microbiology*, 82, 1–28. <https://doi.org/10.1016/B978-0-12-407679-2.00001-6>

- Akpinar, M., & Urek, R. O. (2012). Production of ligninolytic enzymes by solid-state fermentation using *Pleurotus eryngii*. *Preparative Biochemistry and Biotechnology*, 42(6), 582–597. <https://doi.org/10.1080/10826068.2012.673528>
- Asgher, M., Bhatti, H. N., Ashraf, M., & Legge, R. L. (2008). Recent developments in biodegradation of industrial pollutants by white rot fungi and their enzyme system. *Biodegradation*, 19(6), 771-783. <https://doi.org/10.1007/s10532-008-9185-3>
- Azmi, M. A., Yusof, M. T., Zunita, Z., & Hassim, H. A. (2019). Enhancing the utilization of oil palm fronds as livestock feed using biological pre-treatment method. *IOP Conference Series: Earth and Environmental Science*, 230(1), Article 12077. <https://doi.org/10.1088/1755-1315/230/1/012077>
- Buayairaksa, M., Kanokmedhakul, S., Kanokmedhakul, K., Moosophon, P., Hahnvajjanawong, C., & Soyong, K. (2011). Cytotoxic lasiodiplodin derivatives from the fungus *Syncephalastrum racemosum*. *Archives of Pharmacal Research*, 34(12), 2037–2041. <https://doi.org/10.1007/s12272-011-1205-x>
- Chanjula, P., Petcharat, V., & Cherdthong, A. (2017). Effects of fungal (Lentinussajor-caju) treated oil palm frond on performance and carcass characteristics in finishing goats. *Asian-Australasian Journal of Animal Sciences*, 30(6), Article 811. <https://doi.org/10.5713/ajas.16.0704>
- Chandran, B., & Nigam, P. (2001). Studies on the production of enzymes by white-rot fungi for the decolourisation of textile dyes. *Enzyme and Microbial Technology*, 29(8-9), 575–579. [https://doi.org/10.1016/S0141-0229\(01\)00430-6](https://doi.org/10.1016/S0141-0229(01)00430-6)
- Colombatto, D., Morgavi, D. P., Furtado, A. F., & Beauchemin, K. A. (2003). Screening of exogenous enzymes for ruminant diets: Relationship between biochemical characteristics and in vitro ruminal degradation. *Journal of Animal Science*, 81(10), 2628–2638. <https://doi.org/10.2527/2003.81102628x>
- Dinis, M. J., Bezerra, R. M. F., Nunes, F., Dias, A. A., Guedes, C. V, Ferreira, L. M. M., Cone, J. W., Marques, G. S. M., Barros, A. R. N., & Rodrigues, M. A. M. (2009). Bioresource Technology Modification of wheat straw lignin by solid state fermentation with white-rot fungi. *Bioresource Technology*, 100(20), 4829–4835. <https://doi.org/10.1016/j.biortech.2009.04.036>
- Dong, X. Q., Yang, J. S., Zhu, N., Wang, E. T., & Yuan, H. L. (2013). Sugarcane bagasse degradation and characterization of three white-rot fungi. *Bioresource Technology*, 131, 443–451. <https://doi.org/10.1016/j.biortech.2012.12.182>
- Falade, A. O., Nwodo, U. U., Iweriebor, B. C., Green, E., Mabinya, L. V., & Okoh, A. I. (2017). Lignin peroxidase functionalities and prospective applications. *MicrobiologyOpen*, 6(1), Article e00394. <https://doi.org/10.1002/mbo3.394>
- Galal, F. H., AbuElnasr, A., Abdallah, I., Zaki, O., & Seufi, A. M. (2017). Culex (Culex) pipiens mosquitoes carry and harbor pathogenic fungi during their developmental stages. *Journal of Clinical Practice and Research*, 39(1), 1-6. <https://doi.org/10.5152/etd.2017.16067>
- Gautam, A., Kumar, A., Bharti, A. K., & Dutt, D. (2018). Rice straw fermentation by *Schizophyllum commune* ARC-11 to produce high level of xylanase for its application in pre-bleaching. *Journal of Genetic Engineering and Biotechnology*, 16(2), 693–701. <https://doi.org/10.1016/j.jgeb.2018.02.006>
- Ghani, A. A. A., Rusli, N. D., Shahudin, M. S., Goh, Y. M., Zamri-Saad, M., Hafandi, A., & Hassim, H. A. (2017). Utilisation of oil palm fronds as ruminant feed and its effect on fatty acid metabolism. *Pertanika Journal of Tropical Agricultural Science*, 40(2), 215-224.

- Gupte, A., & Madamwar, D. (1997). Production of cellulolytic enzymes by coculturing of *Aspergillus ellipticus* and *Aspergillus fumigatus* grown on bagasse under solid state fermentation. *Applied Biochemistry and Biotechnology*, 62, 267–274. <https://doi.org/10.1007/BF02788002>
- Gupte, A., Gupte, S., & Patel, H. (2007). Ligninolytic enzyme production under solid-state fermentation by white rot fungi. *Journal of Scientific and Industrial Research* 66(08), 611–14.
- Hofrichter, M. (2002). Lignin conversion by manganese peroxidase (MnP). *Enzyme and Microbial Technology*, 30(4), 454–466. [https://doi.org/10.1016/S0141-0229\(01\)00528-2](https://doi.org/10.1016/S0141-0229(01)00528-2)
- Hu, H. L., Brink, J. Van Den, Gruben, B. S., Wösten, H. A. B., Gu, J., & Vries, R. P. De. (2011). International biodeterioration & biodegradation improved enzyme production by co-cultivation of *Aspergillus niger* and *Aspergillus oryzae* and with other fungi. *International Biodeterioration & Biodegradation*, 65(1), 248–252. <https://doi.org/10.1016/j.ibiod.2010.11.008>
- Islam, M., Dahlan, I., Rajion, M. A., & Jelan, Z. A. (2000). Productivity and nutritive values of different fractions of oil palm (*Elaeis guineensis*) frond. *Asian-Australasian Journal of Animal Sciences*, 13(8), 1113–1120. <https://doi.org/10.5713/ajas.2000.1113>
- Isroi, I., Millati, R., Niklasson, C., Cayanto, C., Taherzadeh, M. J., & Lundquist, K. (2011). Biological treatment of lignocelluloses with white-rot fungi and its applications. *BioResources*, 6(4), 5224–5259.
- Ji, L., Yang, J., Fan, H., Yang, Y., Li, B., Yu, X., Zhu, N., & Yuan, H. (2014). Synergy of crude enzyme cocktail from cold-adapted *Cladosporium cladosporioides* Ch2-2 with commercial xylanase achieving high sugars yield at low cost. *Biotechnology for Biofuels*, 7(1), Article 130. <https://doi.org/10.1186/s13068-014-0130-x>
- Khan, S. A., Hamayun, M., Yoon, H., Kim, H. Y., Suh, S. J., Hwang, S. K., Kim, J. M., Lee, I. J., Choo, Y. S., Yoon, U. H., Kong, W. S., Lee, B. M., & Kong, W. S. (2008). Plant growth promotion and *Penicillium citrinum*. *BMC Microbiology*, 8(1), Article 231. <https://doi.org/10.1186/1471-2180-8-231>
- Kumar, A., & Arora, P. K. (2022). Biotechnological applications of manganese peroxidases for sustainable management. *Frontiers in Environmental Science*, 10, Article 875157. <https://doi.org/10.3389/fenvs.2022.875157>
- Lima, A. C., Silva, D., Silva, V., Godoy, M., Cammarota, M., & Gutarra, M. (2021). β -Mannanase production by *Penicillium citrinum* through solid-state fermentation using açai residual biomass (*Euterpe oleracea*). *Journal of Chemical Technology & Biotechnology*, 96(10), 2744–2754. <https://doi.org/10.1002/jctb.6818>
- Madhavi, V., & Lele, S. S. (2009). Laccase: Properties and applications. *BioResources*, 4(4), 1-24.
- Mäkelä, M. R., Hildén, K. S., & Kuuskeri, J. (2020). Fungal lignin-modifying peroxidases and H₂O₂-producing enzymes. In O. Zaragoza & A. Casdevall (Eds.) *Encyclopedia of Mycology* (pp. 247-259). Elsevier.
- Manavalan, T., Manavalan, A., & Heese, K. (2015). Characterization of lignocellulolytic enzymes from white-rot fungi. *Current Microbiology*, 70(4), 485–498. <https://doi.org/10.1007/s00284-014-0743-0>
- Mahmood, Z. A., & Azhar, I. (2017). Detection of aflatoxins and use of scanning electron microscope for the identification of fungal species in some commonly used spices. *Asian Journal of Plant Science and Research*, 7(5), 64–73. Miettinen, O., Spirin, V., Vlasák, J., Rivoire, B., Stenroos, S., & Hibbett, D. (2016).

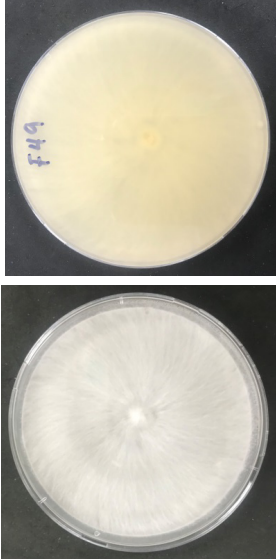
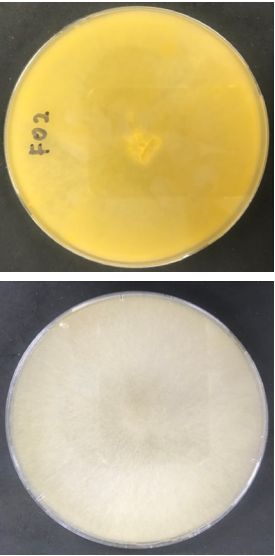
- Polypores and genus concepts in Phanerochaetaceae (Polyporales, Basidiomycota). *MycKeys*, 17, 1-46. <https://doi.org/10.3897/mycokeys.17.10153>
- Pant, D., & Adholeya, A. (2017). Enhanced production of ligninolytic enzymes and decolorization of molasses distillery wastewater by fungi under solid-state fermentation. *Biodegradation*, 18, 647–659. <https://doi.org/10.1007/s10532-006-9097-z>
- Ohm, R. A., Jong, J. F. De, Lugones, L. G., Aerts, A., Kothe, E., Stajich, J. E., de Vries, R. P., Record, E., Levasseur, A., Baker, S. E., Bartholomew, K. A., Coutinho, P. M., Erdmann, S., Fowler, T. J., Gathman, A. C., Lombard, V., Henrissat, B., Knabe, N., Kües, U., ... & Wösten, H. A. B. (2010). Genome sequence of the model mushroom *Schizophyllum commune*. *Nature Biotechnology*, 28(9), 957-963. <https://doi.org/10.1038/nbt.1643>
- Parveez, G. K. A., Kamil, N. N., Zawawi, N. Z., Ong-Abdullah, M., Rasuddin, R., Loh, S. H., Selvadaray, K. R., Hoong, S. S., & Idris, Z. (2022). Oil palm economic performance in Malaysia and R&D progress in 2021. *Journal of Oil Palm Research*, 34(2), 185–218. <https://doi.org/10.21894/jopr.2022.0036>
- Pham, M. T., Huang, C. M., & Kirschner, R. (2019). First report of the oil palm disease fungus *Marasmius palmivorus* from Taiwan causing stem rot disease on native Formosa palm *Arenga engleri* as new host. *Letters in Applied Microbiology*, 70(3), 143-150. <https://doi.org/10.1111/lam.13257>
- Podder, D., & Ghosh, S. K. (2019). A new application of *Trichoderma asperellum* as an *Anopheline* larvicide for eco friendly management in medical science. *Scientific Reports*, 9(1), Article 1108. <https://doi.org/10.1038/s41598-018-37108-2>
- Rahman, M. M., Lourenço, M., Hassim, H. A., Baars, J. J., Sonnenberg, A. S., Cone, J. W., Boever, J. D., & Fievez, V. (2011). Improving ruminal degradability of oil palm fronds using white rot fungi. *Animal Feed Science and Technology*, 169(3-4), 157–166. <https://doi.org/10.1016/j.anifeeds.2011.06.014>
- Raju, B., Santhanakumar, K. S., & Kesavachandran, U. (2020). Gastrointestinal involvement of unusual *Mucormycete*, *Syncephalastrum racemosum* in a diabetic patient with adenocarcinoma: Rare case presentation with review of literature. *Infection*, 48, 791–797. <https://doi.org/10.1007/s15010-020-01455-y>
- Rouches, E., Herpoël-Gimbert, I., Steyer, J. P., & Carrere, H. (2016). Improvement of anaerobic degradation by white-rot fungi pretreatment of lignocellulosic biomass: A review. *Renewable and Sustainable Energy Reviews*, 59, 179–198. <https://doi.org/10.1016/j.rser.2015.12.317>
- Rusli, N. D., Azmi, M. A., Mat, K., Hasnita, C. H., Wan-Zahari, M., Azhar, K., Zamri-Saad, M., & Hassim, H. A. (2019). The effect of physical and biological pre-treatments of oil palm fronds on in vitro ruminal degradability. *Pertanika Journal of Tropical Agricultural Science*, 42(2), 791-805.
- Rusli, N. D., Ghani, A. A. A., Mat, K., Yusof, M. T., Zamri-Saad, M., & Hassim, H. A. (2021). The potential of pretreated oil palm frond in enhancing rumen degradability and growth performance: A review. *Advances in Animal and Veterinary Sciences*, 9(6), 811–822. <http://dx.doi.org/10.17582/journal.aavs/2021/9.6.811.822>
- Saha, B. C., Qureshi, N., Kennedy, G. J., & Cotta, M. A. (2016). Biological pretreatment of corn stover with white-rot fungus for improved enzymatic hydrolysis. *International Biodeterioration & Biodegradation*, 109, 29–35. <https://doi.org/10.1016/j.ibiod.2015.12.020>

- Saif, F. A., Yaseen, S. A., Alameen, A. S., Mane, S. B., & Undre, P. B. (2020). Identification of *Penicillium* species of fruits using morphology and spectroscopic methods. In *Journal of Physics: Conference Series*, 1644, Article 12019. <https://doi.org/10.1088/1742-6596/1644/1/012019>
- Saminathan, M., Mohamed, W. N. W., Noh, A. M., Ibrahim, N. A., Fuat, M. A., Ramiah, S. K., Chung, E. L. T., & Dian, N. L. H. M. (2012). Treated oil palm frond and its utilisation as an improved feedstuff for ruminants-An overview. *Journal of Oil Palm Research*, 34(4), 591–607. <https://doi.org/10.21894/jopr.2021.0041>
- Sigler, L., Bartley, J. R., Parr, D. H., & Morris, A. J. (1999). Maxillary Sinusitis Caused by Medusoid Form of *Schizophyllum commune*. *Journal of Clinical Microbiology*, 37(10), 3395–3398.
- Sukri, S. M., Rahman, R. A., Illias, R. M., & Yaakob, H. (2014). Optimization of alkaline pretreatment conditions of oil palm fronds in improving the lignocelluloses contents for reducing sugar production. *Biotechnology Letter*, 19(1), 9006–9018.
- Tamur, H. A., Al-Janabi, H. J., Al-Janabi, J. K. A., Mohsin, L. Y., & Al-Yassiry, Z. A. N. (2019). Characterization and antagonistic activity of new causal agent of wilt disease in *Imperata cylindrica* (*Marasmius palmivorus*). *Journal of Pure and Applied Microbiology*, 13(3), 1525–1536. <https://doi.org/10.22207/JPAM.13.3.24>
- Tian, X. F., Fang, Z., & Guo, F. (2012). Impact and prospective of fungal pre-treatment of lignocellulosic biomass for enzymatic hydrolysis. *Biofuels, Bioproducts and Biorefining*, 6(3), 335–350. <https://doi.org/10.1002/bbb.346>
- Toth, G. B., & Pavia, H. (2000). Removal of dissolved brown algal phlorotannins using insoluble polyvinylpyrrolidone (PVPP). *Journal of Chemical Ecology*, 27, 1899–1910. <https://doi.org/10.1023/A:1010421128190>
- Tuyen, D. V., Phuong, H. N., Cone, J. W., Baars, J. J. P., Sonnenberg, A. S. M., & Hendriks, W. H. (2013). Effect of fungal treatments of fibrous agricultural by-products on chemical composition and in vitro rumen fermentation and methane production. *Bioresource Technology*, 129, 256–263. <https://doi.org/10.1016/j.biortech.2012.10.128>
- Verma, M., Brar, S. K., Tyagi, R. D., Surampalli, R. Y., & Val, J. R. (2007). Antagonistic fungi, *Trichoderma spp.* *Panoply of Biological Control*, 37, 1–20. <https://doi.org/10.1016/j.bej.2007.05.012>
- Walther, G., Pawłowska, J., Alastruey-Izquierdo, A., Wrzosek, M., Rodriguez-Tudela, J. L., Dolatabadi, S., Chakrabarti, A., & Hoog, G. S. D. (2013). DNA barcoding in Mucorales: An inventory of biodiversity. *Persoonia: Molecular Phylogeny and Evolution of Fungi*, 30(1), 11–47. <https://doi.org/10.3767/003158513X665070>
- Wang, F., Xu, L., Zhao, L., Ding, Z., Ma, H., & Terry, N. (2019). Fungal laccase production from lignocellulosic agricultural wastes by solid-state fermentation: A review. *Microorganisms*, 7(12), Article 665. <https://doi.org/10.3390/microorganisms7120665>
- Zafar, A. M., Najma, S., Farhana, T., Shahlla, I., Safia, A., Iqbal, A. (2017). Detection of aflatoxins and use of scanning electron microscope for the identification of fungal species in some commonly used spices. *Asian Journal of Plant Science and Research*, 7(5), 64–73.

APPENDICES

Supplementary Tables

Table S1
Fungi identified species with the characteristics

No	Sample Name	Scientific Name	Characteristics
1	F49	<i>Marasmius palmivorus</i>	<ul style="list-style-type: none"> • Mushroom-forming fungi • Division: <i>Basidiomycota</i> • Causing white rot • Mainly in monocots and particularly oil and coconut palms • Produced disease symptoms and death of non-wounded Formosa palm tree (Pham et al., 2019)
			
2	F02	<i>Mucor fusiformis</i>	<ul style="list-style-type: none"> • Epithet: Fusiformis • Other name: <i>Zygorhynchus psychrophilus</i>. • Division: <i>Zygomycota</i>. • Filamentous fungi. • Saprotroph organisms inhabiting dead plant material, soil and dung. • Used in the fermentation of tempeh or tofu. • Used in the production of several cheeses. • Responsible for spoiling fresh and manufactured food. • Involved in human infection (Walther et al., 2013)
			

3 F77

Penicillium citrinum



Front

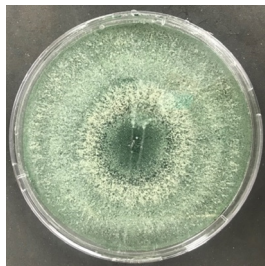


Back

- Division: *Ascomycota*
- Common Endophytic fungus of cereal plants.
- Benefits to the host plant include increased tolerance to herbivory, disease, heat, salt, and drought, as well as increased below and above-ground biomass (Khan et al., 2008)

4 F32

Trichoderma asperellum



Front

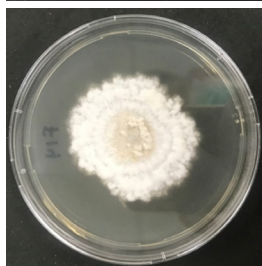


Back

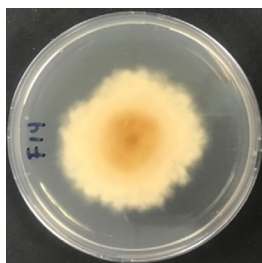
- Division: *Ascomycota*.
- Causing soft-rot.
- Used commercially and experimentally as a biopesticide and biocontrol agent.
- Well known as rivalry for several soil phytopathogens, including other fungi, bacteria and invertebrates.
- Help with other plant growth (domestic and greenhouse plants and crops) (Verma et al., 2007)

5 F14

Schizophyllum commune



Front



Back

- Other Name: Split gill Fungus
- Division: *Basidiomycota*.
- Causing white rot.
- Found on every continent except Antarctica.
- The gills function to produce basidiospores.
- Can be found on fallen branches and timber of deciduous trees. (Ohm et al., 2010)

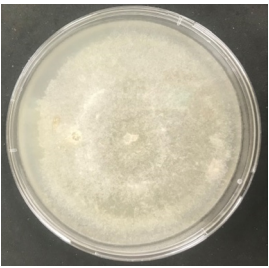
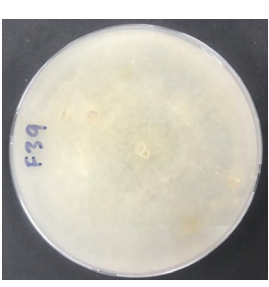
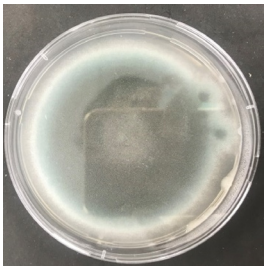
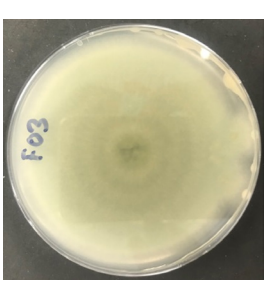
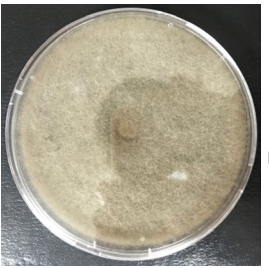
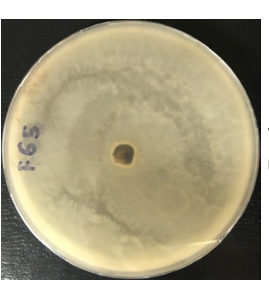
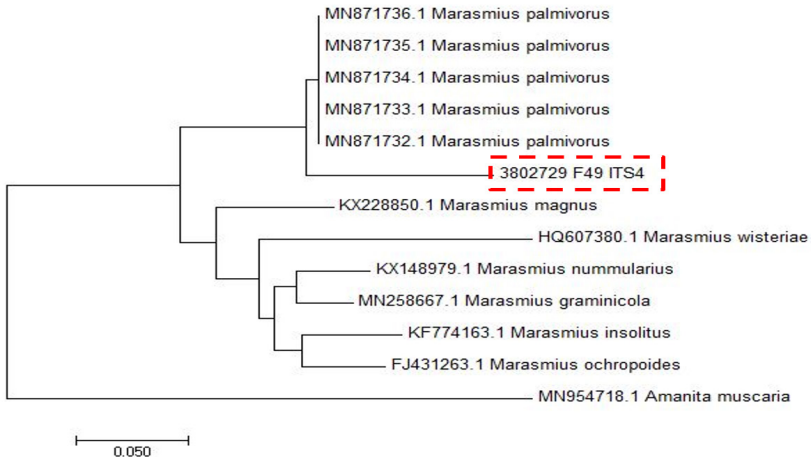
6	F39	<i>Phanerina mellea</i>	 <p>Front</p>  <p>Back</p>	<ul style="list-style-type: none"> • Other Name: <i>Polyporus melleus</i>, <i>Poria mellea</i>, <i>Ceriporia mellea</i>, <i>Gloeoporus melleus</i>. • Division: <i>Basidiomycota</i> • Causing white rot • Genus: <i>Phanerochaete</i> • Miettinen et al., 2016
7	F03	<i>Aspergillus ellipticus</i>	 <p>Front</p>  <p>Back</p>	<ul style="list-style-type: none"> • Divisions: <i>Ascomycota</i> • Other name: <i>Aspergillus helicothrix</i>. • Used for pharmaceuticals, food ingredients and enzymes (Hu et al., 2011) • Show a high degree of β-glucosidase activity. • Wood decaying fungi • Synergism between <i>Aspergillus ellipticus</i> and <i>Aspergillus fumigatus</i> improves hydrolytic and β-glucosidase activity (Gupte & Madamwar, 1997)
8	F65	<i>Syncephalastrum racemosum</i>	 <p>Front</p>  <p>Back</p>	<ul style="list-style-type: none"> • Other name: <i>Syncephalastraceae</i> • Filamentous fungi • Can cause nail disease • Isolated fungal species of soil in tropical and subtropical regions. • Produce the highest DNase activity. • Used in microbial transformation for hydroxylation of steroids, olivetol, milbemycins, and cinobufagin (Buayairaksa et al., 2011)

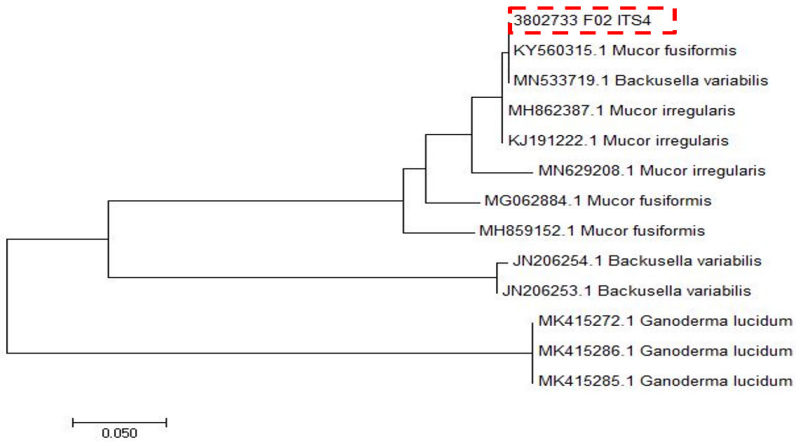
Table S2

Phylogenetic tree of isolated fungi from OPF sample

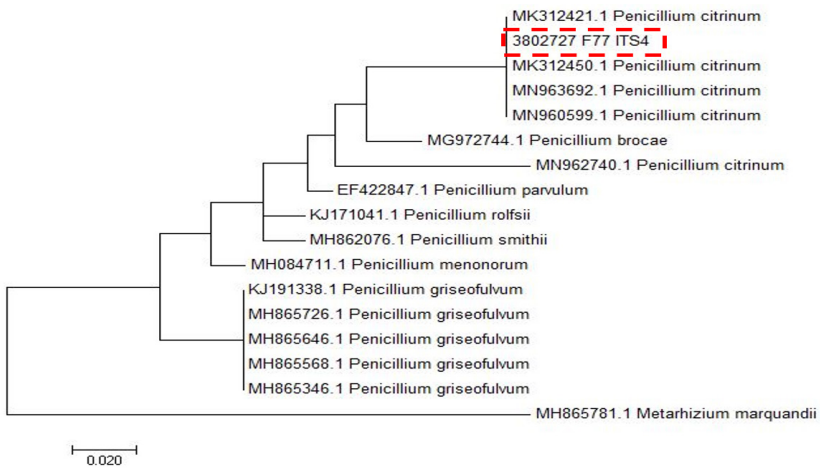
F49



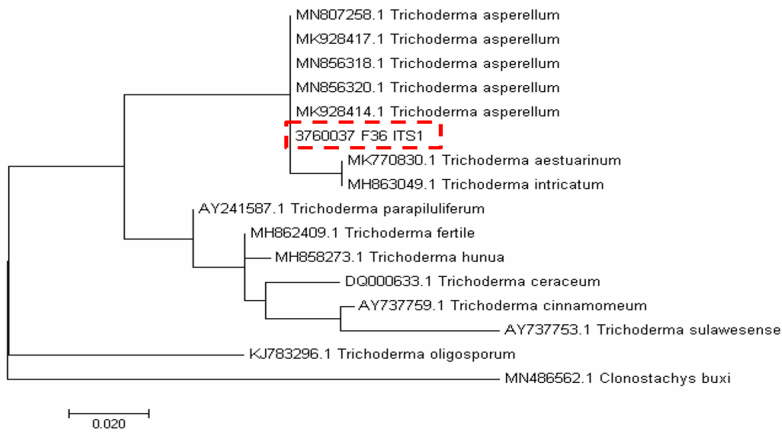
F02



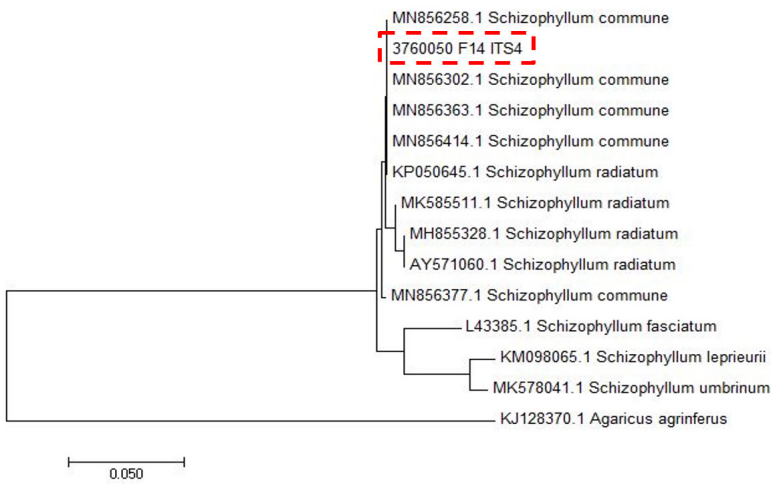
F77



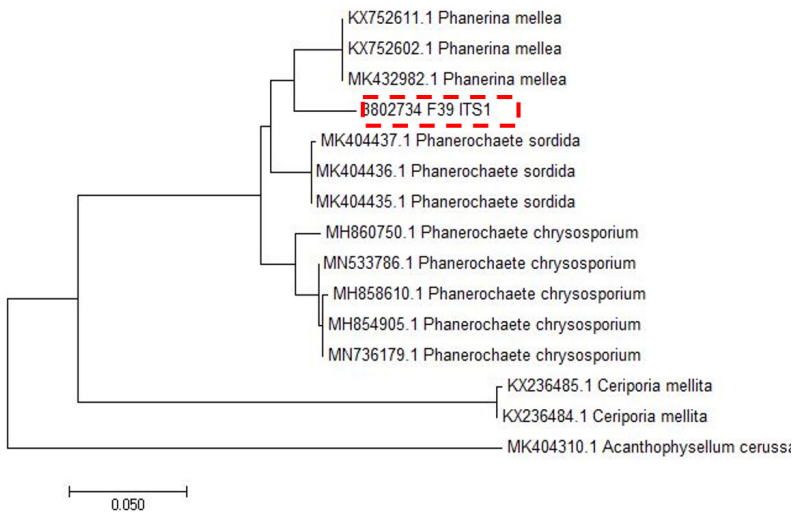
F32



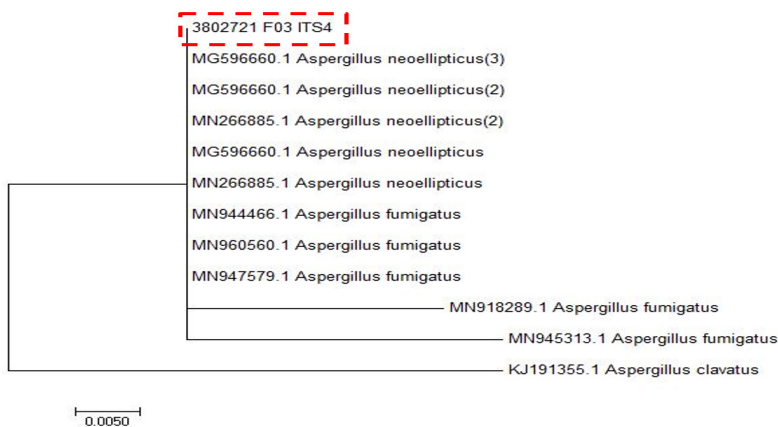
F14



F39



F03



F65

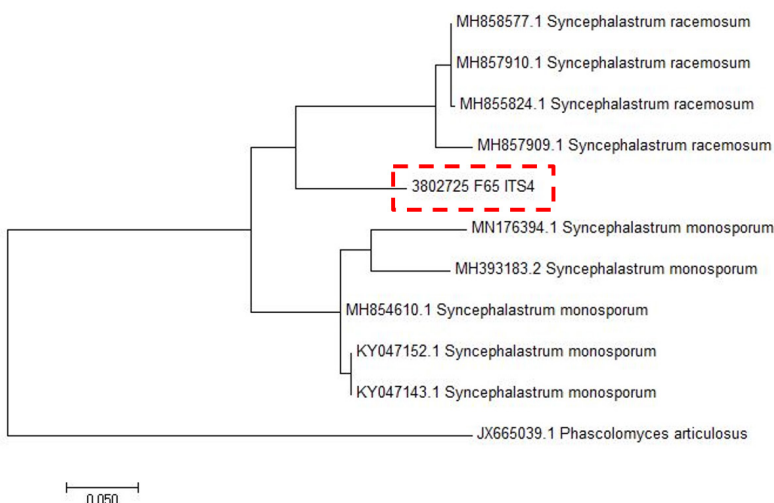


Table S3

The microscopic structure of S. commune (a) morphology on PDA agar media, (b) The microscopic structure of S. commune, (c) The morphology reference of S. commune (Sigler et al., 1999)

F14

(a)

(b)

(c)

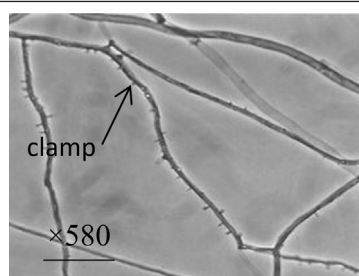
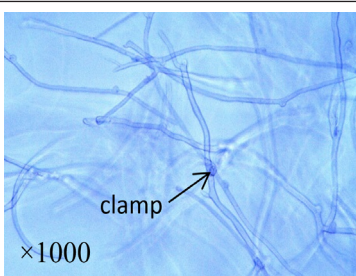
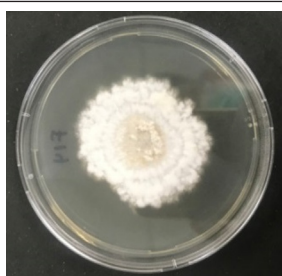


Table S4

The microscopic structure of *A. ellipticus* (a) morphology on PDA agar media, (b) The microscopic structure of *A. ellipticus*, (c) SEM image of *A. ellipticus* (Zafar et al., 2017)

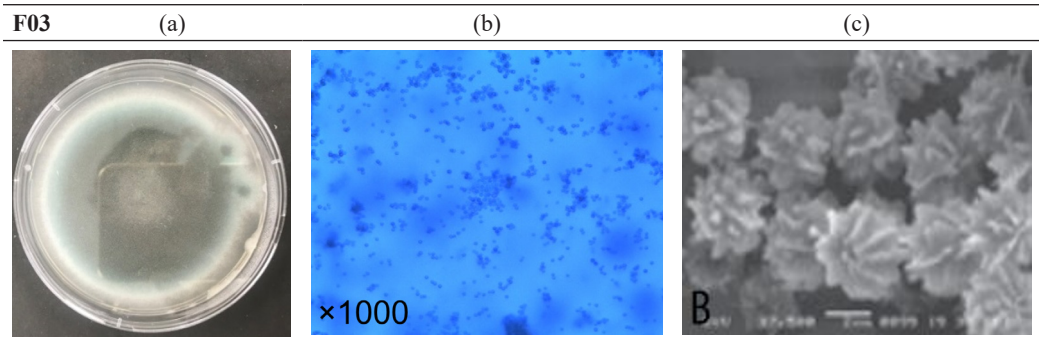


Table S5

The microscopic structure of *T. asperellum* (a) morphology on PDA agar media, (b) The microscopic structure of *T. asperellum*, (c) The morphology reference of *T. asperellum* (Podder & Ghosh, 2019)

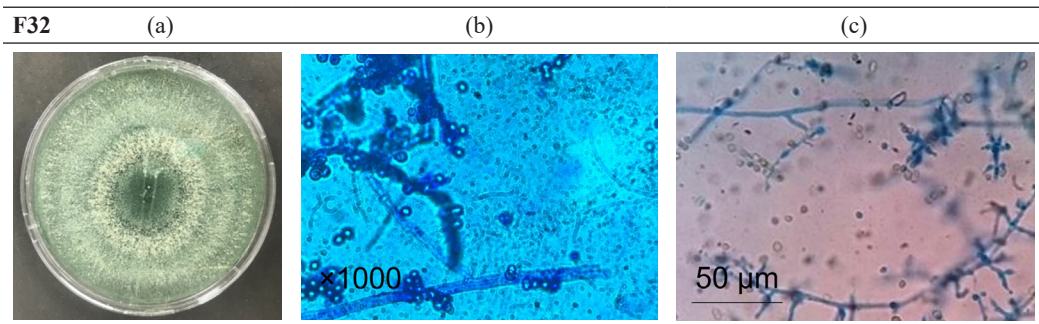


Table S6

The microscopic structure of *P. mellea* (a) morphology on PDA agar media, (b) The microscopic structure of *P. mellea* (c) The morphology reference of *P. mellea* (Miettinen et al., 2016)

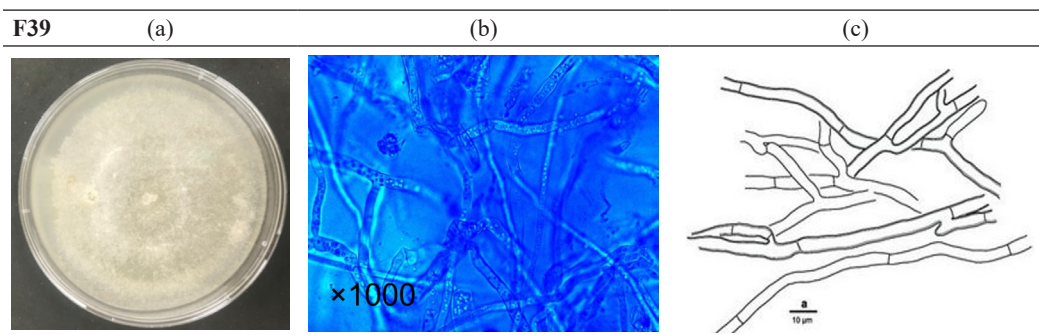


Table S7

The microscopic structure of *M. palmivorus* (a) morphology on PDA agar media, (b) The microscopic structure of *M. palmivorus*, (c) The morphology reference of *M. palmivorus* (Tamur et al., 2019)

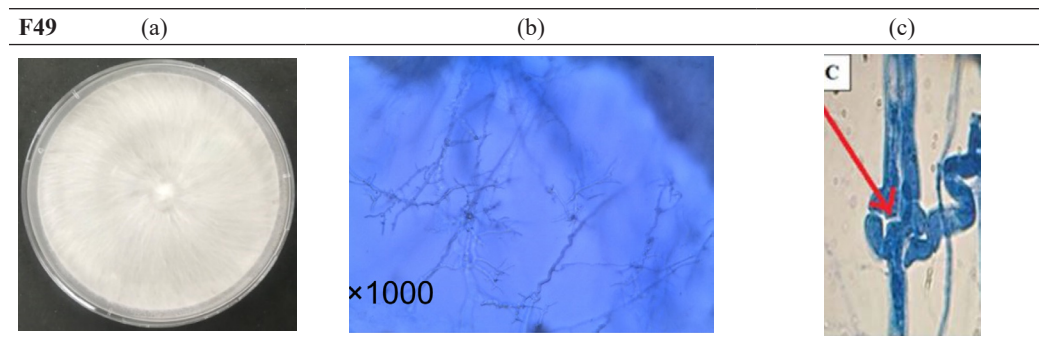


Table S8

The microscopic structure of *S. racemosum* (a) morphology on PDA agar media, (b) The microscopic structure of *S. racemosum*, (c) The morphology reference of *S. racemosum* (Raju et al., 2020)

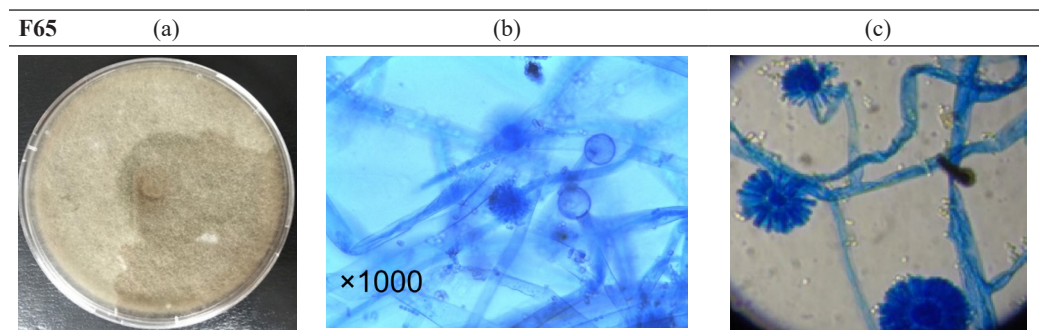


Table S9

The microscopic structure of *P. citrinum* (a) morphology on PDA agar media, (b) The microscopic structure of *P. citrinum*, (c) The morphology reference of *P. citrinum* (Saif et al., 2020)

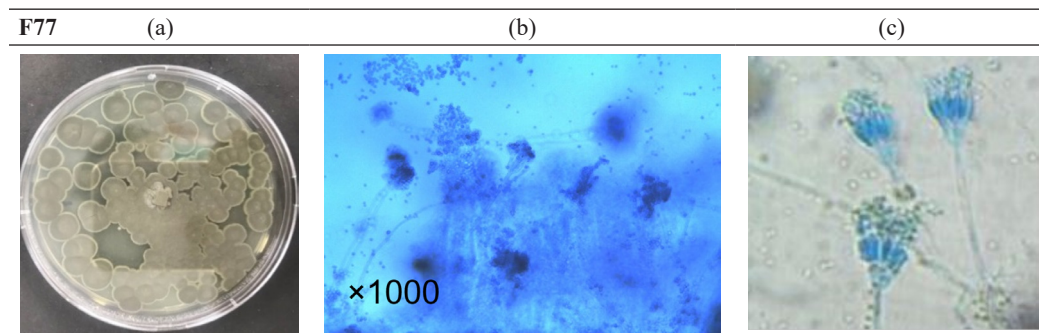
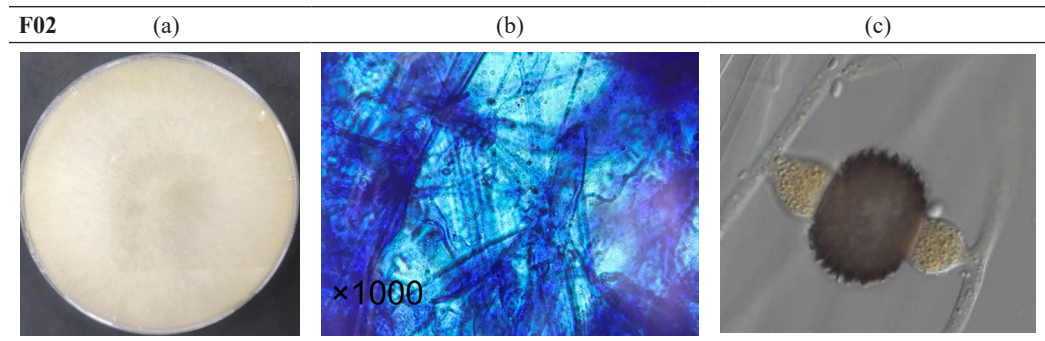


Table S10

The microscopic structure of M. fusiformis (a) morphology on PDA agar media, (b) The microscopic structure of M. Fusiformis, (c) The morphology reference of M. fusiformis (Walther et al., 2013)



Chemical Composition of Acid Soluble Collagen (ASC) Isolated from Indonesia Local “Kacang” Goat Skin (*Capra aegagrus hocus*)

Dita Prameswari Trenggono Putri¹, Rina Wahyuningsih^{2*}, Rusman¹, Nurliyani¹ and Yuny Erwanto^{1,3}

¹Department of Animal Products Technology, Faculty of Animal Science, Universitas Gadjah Mada, Bulaksumur, Yogyakarta, Indonesia

²Research Center for Food Technology and Processing - National Research and Innovation Agency (BRIN), Yogyakarta, Indonesia

³Institute of Halal Industry & System, Universitas Gadjah Mada, Yogyakarta, Indonesia

ABSTRACT

Collagen from the local “Kacang” goat skin is a natural raw material in the halal food industry in Indonesia. This study aims to isolate acid-soluble collagen (ASC) from “Kacang” goat skin and characterize its chemical properties. The collagen was derived from one-year-old goat skin and cured in acid condition for 48 hours at 4°C to eliminate meats, fat, and hair. The cleaned skins were treated at 1:10 (w/v) of 0.1 M NaOH for 0, 24, and 48 h at 4°C. It was then neutralized in distilled water and extracted with 0.5 M acetic acid at a 1:10 (w/v) ratio for 24, 48, and 72 h at 4°C. The yield of ASC was 21%, characterized by chemical composition, soluble protein, differential scanning calorimeter (DSC), and protein molecular weight. The chemical composition of ASC was 11.15% (moisture), 9.04% (protein), 0.98% (fat), and 0.052% (ash). ASC has the highest collagen

solubility in NaCl 5% at pH 2. ASC also has thermal stability with a low profile pattern of molecular weight. In conclusion, “Kacang” goat skin from Indonesia might be used to make a value-added product because it has a high moisture content and low fat level.

ARTICLE INFO

Article history:

Received: 06 December 2023

Accepted: 09 May 2024

Published: 25 October 2024

DOI: <https://doi.org/10.47836/pjst.32.6.07>

E-mail addresses:

dita.p@mail.ugm.ac.id (Dita Prameswari Trenggono Putri)

aisukuiimuniwa@gmail.com (Rina Wahyuningsih)

rusman@ugm.ac.id (Rusman)

lilin@yahoo.co.id (Nurliyani)

yunyer@ugm.ac.id (Yuny Erwanto)

*Corresponding author

Keywords: Acid soluble collagen (ASC), chemical composition, DSC, Indonesia local “kacang” goat skin, molecular weight, soluble protein

INTRODUCTION

The need for collagen as raw material in food and non-food industries, such as medicine and cosmetics, is increasing yearly (Veeruraj et al., 2015). Due to the huge demand for collagen, humans explored and isolated collagen from the extracellular matrix of multicellular animals, from vertebrates to echinoderms. According to Chen et al. (2018), collagen makes up about 30% of the total protein in a vertebrate animal's body. Fibril collagen is organized into a network that creates a stable body frame (Holmes et al., 2018). There are currently 29 types of collagen molecules known from types I-XXIX from various animal tissues, with each type having a unique molecular structure, amino acid sequence, functional characteristics, and biophysical properties (Luo et al., 2018; Zhao et al., 2018). The collagen from cow and pig skins is used for functional foods, tissue engineering, and cosmetics because it has unique properties, physically and functionally (Luo et al., 2018; Subhan et al., 2015; Venkatesan et al., 2017).

The arrangement of peptides, structures, and functions varies among all these collagen molecules (Yousefi et al., 2017). Even though Indonesia has a huge potential for raw materials, the country currently depends on imported goods for its collagen supply. Wang et al. (2014) reported that the use of raw materials from pigs' skin and bones as a source of collagen is an issue for Muslims, even though the use of local materials other than pork is an alternative source for collagen production. Some industries make halal collagen due to Muslim consumers' growing awareness of halal food. Furthermore, collagen, the primary component of capsule shells used in the pharmaceutical business, is an imported good (Hidaka & Liu, 2003), mostly from the United States and Europe. These countries often use pig skin (46%), cow bones (23.1%), and other sources (1.5%) to isolate collagen. It has occurred because of the low cost of raw materials (Karim & Bhat, 2009). Additionally, some countries have high cases of foot and mouth disease (FMD) (Huang et al., 2011).

The "Kacang" goat skin holds great promise as a source of collagen in Indonesia. There are various local livestock species spread over Indonesia. Goat skin is typically a by-product used to make jackets and gloves. For best usage and to maximize its worth and reduce disposal costs, this by-product should be converted into a source of collagen. A chemical substance and a skin protein react during the collagen isolation process. Pepsin and materials derived from acids are still used as pre-extraction agents in collagen isolation. Animal collagen can be isolated through salting out, alkaline, acid, and enzymes (Yang & Shu, 2014). The acid and enzyme procedures are the ones that scientists like to use. Collagen can be extracted using the acid method using organic acids like citric, lactic, or chloroacetic acid (Skierka & Sadowska, 2007).

The results of isolating collagen from a material are then physically and chemically characterized to determine the properties of the collagen obtained. Protein concentration, moisture, ash, soluble protein, and fat content are examples of chemical properties. Physical characterizations include viscoelasticity, thermal stability, functional group, and solubility

(Matmaroh et al., 2011; Singh et al., 2011; Wang et al., 2014). As a result, this study's objectives are to isolate acid-soluble collagen (ASC) from "Kacang" goat skin and define its chemical composition.

MATERIALS AND METHODS

Materials

Collagen was prepared from goatskin at the age of one year. It was carefully removed by hand, cleaned with distilled water, and removed manually. We purchased acetic acid, sodium hydroxide, sodium chloride, HCl, methanol, BSA, and commasie blue from Merck in Darmstadt, Germany. In this study, only analytical-grade reagents were employed.

Method

Chemical Composition of Raw "Kacang" Goat Skin

The chemical compositions of "Kacang" goat skin, such as moisture, protein, fat, ash content and isolated collagen, were analyzed and determined according to AOAC (2000).

Condition for the Optimum Process of Isolation of Collagen

In the extraction process, 0.1 M NaOH was used to isolate and optimize collagen and acetic acid for 24, 48, and 72 h. Each treatment in the study was carried out five times. The experimental design extracted collagen using a slightly modified technique (Wahyuningsih et al., 2018). The local slaughterhouse provided "Kacang" goat skin. Figure 1 shows a flow diagram of the collagen extraction procedure. The cleaned skins were trimmed to a length of around 10 cm. The treated skins were washed and placed in 0.1 M NaOH at a ratio of 1:10 (w/v) for 0, 24, and 48 h at 4°C. After the alkaline treatment, the skin was cleansed and neutralized with distilled water to a pH of 7. For 24, 48, and 72 h at 4°C, the skin was extracted with 0.5 M acetic acid at 1:10 (w/v). The extract was filtrated with filter paper, and then it was precipitated with 2.6 M NaCl. At 4°C and 10,000 g, the sample solution was centrifuged for 30 min. Total precipitates were collected, dialyzed with 0.1 M acetic acid, and then mixed with 0.5 M acetic acid a ratio of 1:5 w/v). The highest yields of the freeze-dried collagen that had been isolated were employed in the tests. Figure 2 displays the collagen from "Kacang" goat skin.

Characterization of "Kacang" Goat Skin Extracted Collagen

Protein Concentration

Lowry's method is used to calculate the protein concentration of ASC (Ledward, 2000). As a protein standard, 10 ml of distilled water was mixed with about 100 mg of bovine

serum albumin (BSA). The biuret reagent was added and allowed at room temperature for 30 min, and with a spectrophotometer (Shimadzu, United States), absorbance at 570 nm was determined. The absorbance at 570 nm was graphed against the volume of the protein standard solution. The collagen powder was then diluted 1:5 with distilled water. As a result, the final protein concentrations in the calibration curve's range were established.

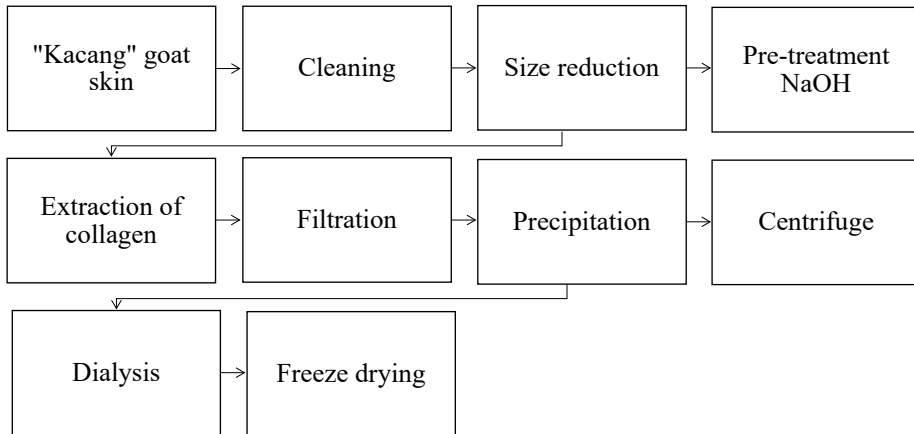


Figure 1. The process flow diagram for collagen extraction



Figure 2. The collagen freeze-dried from “Kacang” goat skin

Solubility determination

With a few minor modifications, Jongjareonrak et al. (2005a) and Corre-Bordes et al. (2018) used varied pH levels to test the solubility of isolated collagens. The lyophilized collagen was dissolved in 0.5 M acetic acid with moderate stirring for 24 h to achieve a final 3 mg/ml concentration. The sample was transferred to a centrifuge tube with a volume of around 8 ml with 6 N NaOH or 6 N HCl; the pH values were changed from 1 to 10 across the pH scale. Distilled water was used to increase the volume to 10 ml. The solutions were agitated for 30 min at 4°C, followed by a 30 min centrifugation at 4°C. Lowry's method determined protein concentrations in the supernatant (Lowry et al., 1951). Calculations of protein solubility were made using data from the pH level with the highest protein content. Equation 1 was used to determine the relative solubility of collagen.

$$\text{Relative solubility (\%)} = \frac{\text{Protein concentration of supernatant}}{\text{The highest protein concentration}} \times 100 \quad [1]$$

Differential Scanning Calorimeter (DSC)

Liang et al. (2014) and Jeevithan et al. (2014) employed the differential scanning calorimeter with minor adjustments. The samples were sealed after being weighed on an aluminum pan. Temperature calibrations were done using an indium standard. Denaturation and melting temperatures are determined using DSC heating patterns. The first endothermic peak (Td), or thermal denaturation of collagen and the second peak (Tm), or melting temperature, were measured.

Protein Molecular Weight by SDS-Page Electrophoresis

SDS-PAGE electrophoresis was used to determine the proteins' molecular weight. Following the Laemmli (1970) method, SDS-PAGE was carried out using 5% stacking gels and 7.5% separating gels. The gels were separated and connected to the power source at 10 mA to track the dye introduced into the bromophenol blue. Gel staining was done using Coomassie blue and a 2:1 methanol to the acetic acid solution. The separated protein bands were recognized using a typical Sigma molecular mixture marker (protein marker).

Statistical Analysis

The condition optimization of collagen was analyzed using SPSS 16.0 with the General Linear Model (GLM) factorial pattern with each of the three replicates. The chemical and solubility collagen of the ASC “Kacang” goat collagen was analyzed using SPSS 16.0 with a one-way analysis of variance (ANOVA) design for each of the three replicates. Each analysis result was presented as a mean (SD). ANOVA and mean were compared statistically using SPSS to determine whether any differences were statistically significant ($p < 0.05$).

RESULTS AND DISCUSSION

Chemical Composition

The analysis objectives in this study are to determine the chemical composition of raw material and compare it with raw material extracted into ASC. Table 1 presents the chemical compositions of raw skin and ASC. The result showed raw skin has moisture ($29.81 \pm 2.31\%$), protein ($31.05 \pm 0.21\%$), and ash ($0.36\% \pm 0.03$), whereas the chemical composition of ASC is moisture ($11.15 \pm 0.08\%$), protein ($9.04 \pm 0.32\%$), and ash ($0.052 \pm 0.09\%$), the raw material has it higher than ASC. Collagen isolated by acid treatment contained higher fat (0.98%) than raw material (0.52%). The separate collagen's high-fat content demonstrated an effective defatting process. Silver catfish collagen only included $0.81 \pm 0.32\%$ ASC and $0.92 \pm 0.08\%$ fat, according to research by Sarbon et al. (2013). Ash content indicating low value also provides well on the collagen produced. The protein content of ASC was 9.04% lower than the raw skin material (31.05%). The extraction process may have failed, so the extracted protein was not optimal, and there was still much left in the raw material. Therefore, further study is needed to obtain optimal results so that the extracted protein can be optimal.

The moisture content of the raw skin of the “Kacang” goat and extracted collagen differs significantly ($p < 0.05$). Li et al. (2020) reported that collagen from the carapace tissue of a Chinese soft-shelled turtle (*Pelodiscus sinensis*) contains moisture (14.21%), protein (32.02%), fat (0.40%), and ash (48.6%). The extracted collagen of ASC showed low moisture, protein, and ash but high fat. High-fat content in the raw material can interfere with collagen extraction, so the yield cannot be optimal. It was removed before collagen extraction with NaOH, and this also indicates that the NaOH curing process before extraction in this study was not optimal, or the pre-treatment of NaOH was not long enough because there was still much fat involved during extraction.

Table 1
Chemical composition and soluble protein concentration of ASC

Samples	Chemical composition (%)			
	Moisture	Protein	Fat	Ash
Raw skin	29.81 ± 2.31^a	31.05 ± 0.21^c	0.52 ± 0.07^a	0.36 ± 0.03^d
ASC	11.15 ± 0.08^b	9.04 ± 0.23^b	0.98 ± 0.32^b	0.052 ± 0.09^a

*Different superscripts (^{a-d}) in the same column of collagen are the significant differences ($p < 0.05$)

Condition for Optimum Process of Isolating Collagen

Optimization of collagen isolation was analyzed using the General Linear Model (GLM) factorial pattern (Table 2). Pre-treatment with NaOH is followed by collagen extraction in

two phases (Pal & Suresh, 2016). The optimization of collagen isolation is based on the highest yields. Yield is the final result obtained from collagen extraction in the method is the more effective or not used (Alhana et al., 2015). Yield shows the effectiveness of raw materials in converting into products (Wulandari & Suptijah, 2015). Wet yield data of acid extraction was used to analyze the optimum method for isolating collagen from Indonesia's local goat skin. The optimum process of isolating collagen in this study was at 0 h pre-treatment of NaOH and extraction 48 h at 4°C with yields of 21%. Treatment extraction collagen without NaOH has the highest yield and was significant to the pre-treatment of NaOH in 24 and 48 h. Long pre-treatment NaOH and acid extraction time is known to impact the yield of acid-soluble collagen. Decreasing collagen yield can impact the pre-treatment time of NaOH and the extraction process. Based on the data analysis results in this study, pre-treatment time with NaOH and acid extraction can impact the yield produced.

Table 2
Yields of acid soluble collagen from “Kacang” goat skin

Pre-treatment of NaOH (h)	Yield (%)		
	Time to extraction (h)		
	24	48	72
0	11.40 ± 4.39 ^a	21.00 ± 8.34 ^a	17.8 ± 2.78 ^a
24	18.20 ± 4.15 ^b	8.89 ± 2.34 ^b	6.45 ± 3.29 ^b
48	3.60 ± 1.14 ^c	3.20 ± 1.64 ^c	4.80 ± 1.64 ^c

^{a,b,c} Different Superscript differences in some letters indicated significant differences ($p < 0.05$)

The optimum conditions in this study were different from previous studies by Woo et al. (2008), who explained that the optimum condition for collagen extraction from yellow tuna skin was 24 h NaOH pre-treatment time and collagen extraction time was 23.5 h with a yield of 27.1% using NaOH concentrations of 0.2 and 0.5 M, but if NaOH is used with a concentration of 0.05 and 0.1 M is only a small amount of protein dissolves. So, in this study, a concentration of 0.1 M NaOH only caused slight swelling of the goat skin, but the longer the soaking, the greater the yield produced. Yoshimura et al. (2000) stated that soaking using NaOH in collagen extraction can affect swelling on the skin of *C. striata* fish. The telopeptide region of the collagen molecule can be damaged by alkaline treatment with NaOH during the pre-treatment method, which results in the soluble OH group that binds to the protein (Jaswir et al., 2011). The process can be caused by the migration of non-protein collagen and other components in the collagen matrix so that it is easily detached (Cho et al., 2005). Time, temperature, concentration of NaOH, and the type of raw material utilized impacted how effective the NaOH pre-treatment time was (Liu et al., 2015)—the period of hydrolysis impacted the extraction method because the mass transfer

rate was regulated by the duration of the diffusion process, which in turn impacted the total yield. The type of solvent, solvent concentration, temperature, and the raw material utilized can all impact the variations in ideal circumstances in the extraction process. The most often used organic solvent for collagen extraction was acetic acid. pH is linked to changes in protein density, which can affect electrostatic interactions and protein structure. At the same time, the solubility of collagen in acetic acid can impact the pH value during the extraction process (Verheul et al., 1998). When the pH is lower or higher than the isoelectric point (pI) of protein, the solubility of protein will increase due to the repulsive force between charges (Chi et al., 2014). The pI value of collagen is usually between pH 6-9 (Li et al., 2013; Wu et al., 2015). In addition, collagen solubility was affected by the number and sequence of amino acids, molecular weight and conformation. Environmental factors also play an important role, such as pH, type of solvent, ionic strength, temperature and extraction process (Li et al., 2018; Zayas, 1997).

Characterization of Extracted “Kacang” Goat Skin Collagen

Soluble Protein Concentration

NaCl Effect on the Solubility of Collagen. The precipitation process greatly influences the total amount of soluble collagen. Collagen can be precipitated using NaCl. Adding salt in high concentrations causes protein aggregation through salting out, where the salt binds to water and precipitation occurs. The precipitation can happen because the ionic strength of the salt is higher than that of protein, so water is easily bound. The decrease in total protein bonding in water can cause the protein to precipitate easily (Winarno, 2008). Figure 3 shows ASC solubility with various concentrations of NaCl (1%, 2%, 3%, 4%, 5%, 6%). This study showed collagen solubility of ASC at 1% NaCl was significantly lower to 5% and 6% NaCl concentration treatment but similar with NaCl 2%, 3%, and 4% concentrations. The collagen solubility of ASC at 5% NaCl was significantly higher at 1% and 2% NaCl concentration treatment but showed similar results to NaCl 3%, 4%, and 6%. ASC solubility decreased and gradually declined from 1 to 5% NaCl concentration. ASC was more soluble in treatment NaCl 5% ($580 \pm 0,11$ ppm).

The higher solubility of ASC with treatment NaCl 5% is $580 \pm 0,11$ ppm, which was significant with 1% NaCl. The collagen solubility of ASC in this study generally decreases at a 6% increase in concentration of NaCl. According to the research by Li et al. (2020), the collagen of the skin of the Nile tilapia by chemical and fermentation has a solubility of collagen at 1% and 2%. Other studies have also been reported by Li et al. (2013) on collagen solubility of ASC from bone and skin of Spanish mackerel (*Scomberomorus phonics*) constant of NaCl up to 2% (w/v) and decreasing of NaCl concentration is 3% (w/v). According to research by Woo et al. (2008), collagen solubility of ASC from yellowfin tuna dorsal skin collagen decreases when the concentration of NaCl increases at 2% (w/v).

In Song et al. (2021), FASC and CASC from Nile tilapia skin have high solubility at 3% and decrease at 4% (w/v) NaCl. It is probably caused by the structure of ASC from the Indonesian local Kacang” goatskin, which is different from the structure of collagen from fish. The protein solubility of ASC in this study was relatively stable, increasing at over a concentration of NaOH 2% and slowly decreasing at a concentration of 6% NaCl. The collagen structure of ASC in this study was relatively stronger and resistant to NaCl at above 2%. The salting-out phenomenon was affected by collagen solubility when NaCl concentration was increased. The collagen solubility decreases because of increasing ionic strength, so salt ions compete with water and protein precipitates (Vojdani, 1996). Collagen solubility declines when an increase in NaCl concentration causes the protein to precipitate by combinations of chains and the competition with salts ionic water and enhancing hydrophobic-hydrophobic interactions (Bae et al., 2008; Jongjareonrak et al., 2005b). NaCl with high concentrations causes the hydration layer on the collagen surface to be destroyed and hydrophobic sites to be exposed, thereby causing increased interactions and hydrophobicity collagen precipitation and aggregation (Woo et al., 2008; Yu et al., 2014).

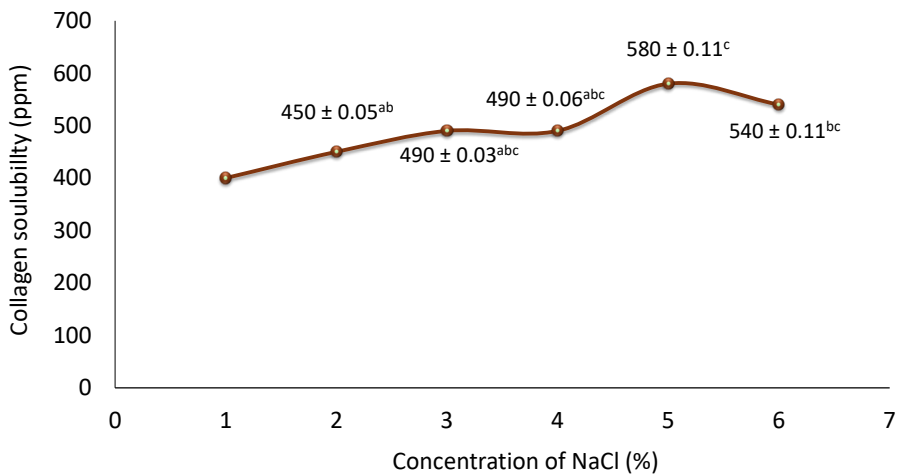


Figure 3. ASC solubility with variation concentration of NaCl

pH Effect on the Solubility of Collagen. pH conditions highly influence the collagen solubility of the solution. ASC samples were observed at pH 1–10. Figure 4 illustrates how pH affects ASC collagen solubility. In this study, collagen solubility was pH neutral, and the level of solubility of collagen in each sample experienced a decrease. However, the solubility of collagen increased once again when the pH was increased to an alkaline. Dissolved collagen levels in this study showed that the solubility of collagen in the treatment

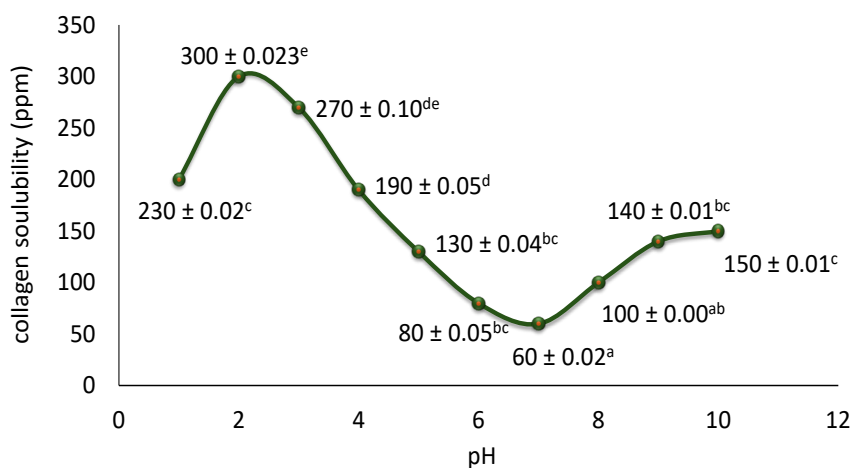


Figure 4. ASC solubility with variation pH

at pH 2 with a value of 300 ppm was significant to the treatment at pH 1, 4, 5, 6, 7, 8, 9, and 10 but not significant with treatment at pH 3 (Figure 4). The higher collagen solubility of ASC in this study was at pH 2 (300 ± 0.03 ppm). Collagen is easily dissolved in acid conditions. Protein can be positively or negatively charged if the pH value is above and below the isoelectric point, which causes protein solubility to increase due to repulsive forces between protein chains (Vojdani, 1996).

Based on research, the higher collagen ASC solubility in acidic conditions at pH 3 is 300 ± 0.03 ppm and decreases at pH 3 to 7. In a different study from Li et al. (2013), the collagen solubility of ASC from the skin of Spanish mackerel reduced at pH 7 and increased at a pH range between 1–4. Woo et al. (2008) reported that higher ASC solubility in the dorsal skin of yellowfin tuna at pH 4 slowly decreases at pH 5 to pH 6, then increases at pH 7 and becomes relatively stable to pH 9. In Kittiphattanabawon et al. (2005), collagen from Bigeye snapper fish (*P. Tayenus*) skin is pH 7–8 and has low solubility and higher collagen solubility in pH 2 and 5. In Song et al. (2021), FASC and CASC from Nile tilapia skin are highly soluble at pH 1–4 and increase at pH 7–11. Increased protein solubility can be caused by an increase in the negative charge of collagen molecules and repulsive forces between chains (Jongjareonrak et al., 2005b). ASC's higher average collagen solubility in acidic conditions decreases in alkaline conditions. The point of isoelectric (*pI*) value is affected by protein solubility. When *pI* is lower or higher than pH in a protein solution, it will cause protein solubility to increase due to an increase in the attraction between protein molecules net positive or negative charge residues. In contrast, *pI* induces aggregation, and precipitation causes the protein's overall charge to be almost zero because it increases as interactions between hydrophobic sites occur (Wong et al., 1989). Collagen has the *pI* range of pH 6–9 (Foegeding et al., 1996).

Differential Scanning Calorimeter (DSC)

Based on changes in physical and chemical properties, thermal analysis can characterize materials and determine their thermodynamic properties (Klančnik et al., 2010). The glass transition (T_g), melting point (T_m), and temperature in the polymer (T_d) are three thermal properties that can be measured using DSC of the thermal analysis. The DSC thermograms of ASC from Indonesian local goatskin are shown in Figure 5. A sample of ASC from “Kacang” goatskin was used and rehydrated before DSC analysis using 0.05 M acetic acid. ASC has one endothermic peak (T_{max}) at 99.92°C, which means thermal denaturation of collagen and heat resistance at 99.92°C. ASC's temperature starts at 30.34°C, and the final melting temperature is 153.71°C. Thermal denaturation is related to the first endothermic peak, with maximum peak denaturation temperature (T_d) of 30.3°C and 99.9°C. T_d is indicated as an amino acid composition from the compact structure of collagen (Zhang et al., 2016). The number of amino acids has intramolecular and intermolecular cross-linking, correlated with the T_d of collagen (Veeruraj et al., 2013; Zhang et al., 2016). The second peak is a melting temperature (T_m), which destroys material due to structural damage to the peptide crystal by high temperature (Liang et al., 2014). Kozłowska et al. (2015) reported in ASC that the fish skin of the Northern pike has an exothermic peak; T_1 is 79.3°C, and T_2 is 198.4°C. The first peak is related to the temperature at collagen denaturation, and water is bonding with protein molecules. The second exothermic peak describes the change in the structure of complex collagen parts into protein, which is destroyed. Based on this literature, ASC in this study at a temperature of 99.92°C and changes in collagen structure were denatured.

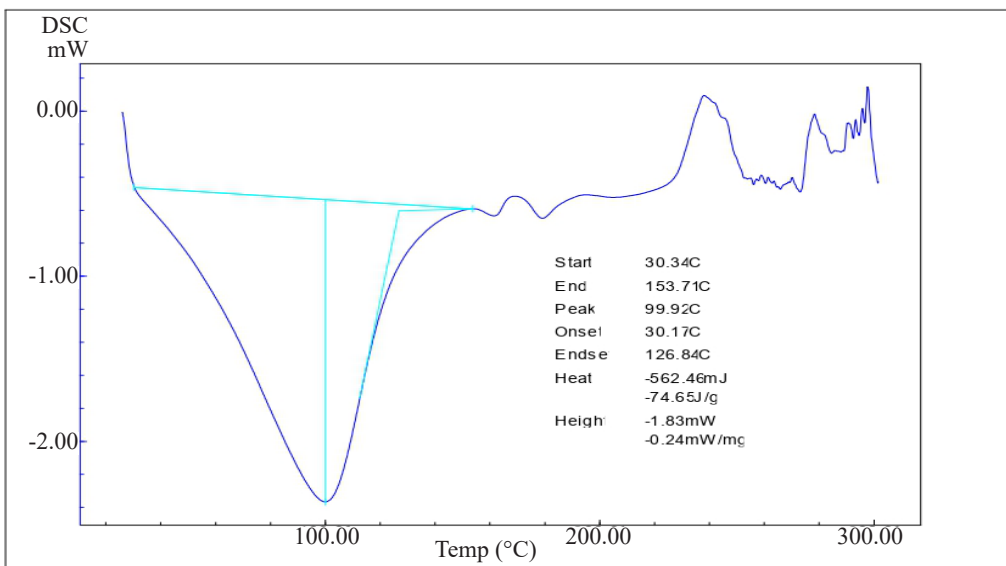


Figure 5. The DSC thermograms of ASC from Indonesian local goatskin

ASC from Indonesian local racing goatskin has thermal stability (T_d and T_m) was lower than ASC from turtle carapace (40°C and 125°C) (Li et al., 2020), Chinese soft-shell turtle calipash collagen (between 35°C and 105.14°C) (Zhang et al., 2016), and CASC and FASC from Nile tilapia skin has T_d values was 36.8 and 36.5 (Song et al., 2021). Different tissues in collagen feed and the animal's environment suggest the difference in thermal stability. Bae et al. (2008) said collagen with a high amino acid (proline and hydroxyproline) would be more heat-resistant. Besides that, the amino acid composition of collagen varies between species because it depends on the habitat, especially the temperature of the initial habitat. The collagen derived from a habitat with high temperatures will have a higher amino acid compared to the collagen derived from species in a habitat with low temperatures, so it has a higher melting temperature and thermal stability. T_d of collagen is related to amino acid composition and non-helical regions with more regular regions and compact collagen structure (Ali et al., 2017; Zhang et al., 2016). In addition, collagen T_d also directly correlates with the number of amino acids related to intra-molecular and intermolecular cross-link, and collagen stability is greatly influenced by the number of amino acids (Song et al., 2021; Veeruraj et al., 2013; Zhang et al., 2016). Besides that, collagen molecular weight also influences the thermal stability of collagen (Pal et al., 2015).

Protein Molecular Weight

SDS-PAGE profiles ASC's protein patterns and assesses collagen's type and composition (Figure 6). In this study, the protein pattern in ASC for each step of the collagen extraction process (Step 1), the initial screening after each sample extraction did not look clean, and other bands were still visible. It may be due to the initial step of extraction being contaminated with other materials besides collagen. However, after the precipitation step, until freeze-drying, the bands formed were clear, and no other material was contaminated. ASC has α_1 -chain, α_2 -chain, and β -chain. The molecular weight of ASC was between 57.82 and 162.06 kDa, with the α_1 -chain being 57.8 kDa and 71.83 kDa for α_2 -chain.

There are cross-linked collagen molecules because of the collagen structure's high molecular weight component. The high amount of cross-linked collagen is indicated by the thickness of structural protein band intensity in β structure (Singh et al., 2011). In general, the structure of ASC from Indonesian Local "Kacang" Goat Skin is indicated as Type 1 collagen. Damodaran (2017) stated that Type 1 collagen has a triple helix structure with a molecular weight of around 100 kDa on the α_1 and α_2 chains. Giraud-Guille et al. (2000) said the collagen derived from bovine and fish skin consists of 2 α -chains (α_1 and α_2 chains). Woo et al. (2008) added collagen derived from yellowfin tuna dorsal skin also consists of 2 α -chains (α_1 and α_2 chain). Saito et al. (2002) reported that Type 1 collagen consists of heterologous α_1 and α_2 chains forming a triple helix (α_1) $2\alpha_2$, where the dimers and trimers of the chain are high molecular weight components.

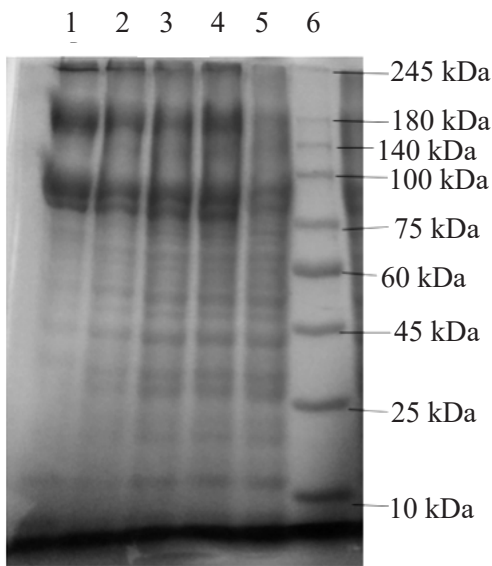


Figure 6. SDS-Page patterns of ASC from Indonesia's local "Kacang" goatskin. (1) step of freeze-drying, (2) step of dialysis, (3) step of centrifugation, (4) step of precipitation, (5) step of filtration, (6) marker of protein.

and cornea has a molecular composition $[\alpha 1(I) 2\alpha 2(I)]$. ASC-SK and ASC-SP from spines and skulls of skipjack tuna (*Katsuwonus pelamis*) are Type 1 collagen because it has heterotrimers containing two identical $\alpha 1$ chains and one $\alpha 2$ chain in the form of $[\alpha 1(I)]_2\alpha 2(I)$ molecules (Sato et al., 1989). In general, the Type I collagen consists of two $\alpha 1$ chains and one $\alpha 2$ chain as the main component ($[\alpha 1]_2\alpha 2$). Hwang et al. (2007) stated that the intensity of the $\alpha 2$ chain band is lower due to the presence of components dimerized into β components and forming $\beta 12$ dimer. Kimura et al. (1991) reported that the Type I collagen from lathyrus carp bones had two molecular forms: the first molecule $[\alpha 1]_2\alpha 2$ is the main component. The second molecule $\alpha 1\alpha 2\alpha 3$ is minor, and Ogawa et al. (2004) reported that the Type I collagen heterotrimer ($\alpha 1\alpha 2\alpha 3$) was found as the main component of ASC from sheep head bone and black drum. The $\alpha 3$ chain has the same molecular weight as the $\alpha 1$ chain using electrophoresis (Di et al., 2014).

The study of Han et al. (2011) showed that collagen derived from bluefin tuna skin has a molecular weight of $\alpha 1$ chain in 120 kDa, $\alpha 2$ chain in 112 kDa, and β -chain in 205 kDa, whereas Type 1 collagen carp scales have $\alpha 1$ chain in 117.3 kDa and $\alpha 2$ chain in 107.4 kDa. In this study, ASC was known to have a higher molecular weight found in the structures and high cross-linking, as in Type 1 collagen. The research from Singh et al. (2011) showed that the structure in β and γ chains is a cross-linked collagen molecule

The ASC from Northern fish pike skin has a molecular weight of 118 kDa for the $\alpha 1$ and 108 kDa for the $\alpha 2$ chain (Kozłowska et al., 2015). In a study by Li et al. (2020), collagen ASC from the carapace tissue of a Chinese soft-shelled turtle (*Pelodiscus sinensis*) has a molecular weight between 100 kDa and 135 kDa and suggests Type 1 collagen. A comparable study from Martínez-Ortiz et al. (2015) used collagen derived from rabbit skin. The collagen has a molecular weight of 118 kDa for $\alpha 1$ and 102 kDa for the $\alpha 2$ chain, so ASC in this study was lower than the molecular weight from fish, turtle, and rabbit skin. The difference in molecular weight can occur due to several factors, such as the type of species, habitat, feed, and age of species. Collagen has two bands, $\alpha 1$ and $\alpha 2$ chains. Type 1 collagen found in bones, dermis, tendons, ligaments,

forming dimers and trimers. The higher the number of collagen molecules, the thicker the intensity in the protein structure band. Thermal stability also has a relationship with molecular weight. The result of the previous characterization stated that ASC had high thermal stability. According to Duan et al. (2009), high molecular-weight collagen has more stable heat resistance than low molecular-weight collagen. ASC in this study was higher in solubility at acidic pH conditions. When the pH is higher or lower than pI , it causes protein molecules to be greater, and the solubility of collagen increases as the repulsive force between the chains increases. Collagen stability decreases, possibly due to increased NaCl concentration, which is affected by protein precipitation and salting-out. The changes in collagen solubility in several types of fish can be caused by changes in structure, molecular weight, and number of amino acids (Li et al., 2020).

CONCLUSION

ASC from Indonesia's Local “Kacang” goat skin has a high moisture content but a low fat level. Additionally, collagen has an optimum process at 0 h pre-treatment of NaOH and extraction time of 48 h at 4°C with yields of 21%. Collagen has higher solubilization in NaCl 5% and at the acid pH ranges; besides, it has a temperature thermal stability with low molecular weight. Therefore, this study suggested that “Kacang” goat skin might be used to manufacture a product that has added value. Therefore, it is necessary to carry out further studies on the functional properties of this collagen.

ACKNOWLEDGMENT

This study was supported by the DIKTI Ministry of Research, Technology and Higher Education Indonesia under contract No: 4586/UN1-III/LT/DIT-LIT/2016 and by the Master to Doctoral for an Excellent Bachelor Program (PMDSU) under contract No: 2207/UN1/DITLIT/DitLit/PT.01.03/2023.

REFERENCES

- Alhana, A., Suptijah, P., & Tarman, K. (2015). Extraction and characterization of collagen from sea cucumber flesh. *Jurnal Pengolahan Hasil Perikanan Indonesia*, 18(2), 150-161.
- AOAC. (2000). *Official Methods of Analysis* (17th ed.). Association of Official Analytical Chemists.
- Bae, I., Osatomi, K., Yoshida, A., Osako, K., Yamaguchi, A., & Hara, K. (2008). Biochemical properties of acid-soluble collagens extracted from the skins of underutilised fishes. *Food Chemistry*, 108(1), 49–54. <https://doi.org/10.1016/j.foodchem.2007.10.039>
- Chen, J., Li, L., Yi, R., Gao, R., & He, J. (2018). Release kinetics of Tilapia scale collagen I peptides during tryptic hydrolysis. *Food Hydrocolloids*, 77, 931–936. <https://doi.org/10.1016/j.foodhyd.2017.11.040>

- Chi, C. F., Wang, B., Li, Z. R., Luo, H. Y., Ding, G. F., & Wu, C. W. (2014). Characterization of acid-soluble collagen from the skin of hammerhead shark (*Sphyrna lewini*). *Journal of Food Biochemistry*, *38*(2), 236–247. <https://doi.org/10.1111/jfbc.12042>
- Cho, S., Lowe, L., Hamilton, T. A., Fisher, G. J., Voorhees, J. J., & Kang, S. (2005). Long-term treatment of photoaged human skin with topical retinoic acid improves epidermal cell atypia and thickens the collagen band in papillary dermis. *Journal of the American Academy of Dermatology*, *53*(5), 769–774. <https://doi.org/10.1016/j.jaad.2005.06.052>
- Corre-Bordes, D. L., Hofman, K., & Hall, B. (2018). Guide to electrospinning denatured whole chain collagen from hoki fish using benign solvents. *International Journal of Biological Macromolecules*, *112*, 1289–1299. <https://doi.org/10.1016/j.ijbiomac.2018.02.088>
- Damodaran, S. (2017). *Food Proteins and their Applications*. CRC Press.
- Di, Y., Chang-Feng, C., Bin, W., Guo-Fang, D., & Li, Z. R. (2014). Characterization of acid-and pepsin-soluble collagens from spines and skulls of skipjack tuna (*Katsuwonus pelamis*). *Chinese Journal of Natural Medicines*, *12*(9), 712-720. [https://doi.org/10.1016/S1875-5364\(14\)60110-2](https://doi.org/10.1016/S1875-5364(14)60110-2)
- Duan, R., Zhang, J., Du, X., Yao, X., & Konno, K. (2009). Properties of collagen from skin, scale and bone of carp (*Cyprinus carpio*). *Food Chemistry*, *112*(3), 702–706. <https://doi.org/10.1016/j.foodchem.2008.06.020>
- Foegeding, E. A., Lanier, T. C., & Hultin, H. O. (1996). Characteristics of edible muscle tissues. In O. R. Fennema (Ed.), *Food Chemistry* (pp. 902-906). Marcel Dekker Inc.
- Giraud-Guille, M. M., Besseau, L., Chopin, C., Durand, P., & Herbage, D. (2000). Structural aspects of fish skin collagen which forms ordered arrays via liquid crystalline states. *Biomaterials*, *21*(9), 899–906. [https://doi.org/10.1016/S0142-9612\(99\)00244-6](https://doi.org/10.1016/S0142-9612(99)00244-6)
- Han, S. H., Uzawa, Y., Moriyama, T., & Kawamura, Y. (2011). Effect of collagen and collagen peptides from bluefin tuna abdominal skin on cancer cells. *Health*, *3*(3), 129-134. <https://doi.org/10.4236/health.2011.33024>
- Hidaka, S., & Liu, S. Y. (2003). Effects of gelatins on calcium phosphate precipitation: A possible application for distinguishing bovine bone gelatin from porcine skin gelatin. *Journal of Food Composition and Analysis*, *16*(4), 477–483. [https://doi.org/10.1016/S0889-1575\(02\)00174-6](https://doi.org/10.1016/S0889-1575(02)00174-6)
- Holmes, D. F., Lu, Y., Starborg, T., & Kadler, K. E. (2018). Collagen fibril assembly and function. *Current Topics in Developmental Biology*, *130*, 107–142. <https://doi.org/10.1016/bs.ctdb.2018.02.004>
- Huang, L., Chai, X., Cheng, S., & Chen, G. (2011). Evaluation of carbon-based materials in tubular biocathode microbial fuel cells in terms of hexavalent chromium reduction and electricity generation. *Chemical Engineering Journal*, *166*(2), 652–661. <https://doi.org/10.1016/j.cej.2010.11.042>
- Hwang, J. H., Mizuta, S., Yokoyama, Y., & Yoshinaka, R. (2007). Purification and characterization of molecular species of collagen in the skin of skate (*Raja kenoi*). *Food Chemistry*, *100*(3), 921–925. <https://doi.org/10.1016/j.foodchem.2005.10.046>
- Jaswir, I., Monsur, H. A., & Salleh, H. M. (2011). Nano-structural analysis of fish collagen extracts for new process development. *African Journal of Biotechnology*, *10*(81), 18847–18854. <https://doi.org/10.5897/AJB11.2764>

- Jeevithan, E., Wu, W., Nanping, W., Lan, H., & Bao, B. (2014). Isolation, purification and characterization of pepsin soluble collagen isolated from silvertip shark (*Carcharhinus albimarginatus*) skeletal and head bone. *Process Biochemistry*, 49(10), 1767–1777. <https://doi.org/10.1016/j.procbio.2014.06.011>
- Jongjareonrak, A., Benjakul, S., Visessanguan, W., Nagai, T., & Tanaka, M. (2005a). Isolation and characterisation of acid and pepsin-solubilised collagens from the skin of Brownstripe red snapper (*Lutjanus vitta*). *Food Chemistry*, 93(3), 475–484. <https://doi.org/10.1016/j.foodchem.2004.10.026>
- Jongjareonrak, A., Benjakul, S., Visessanguan, W., & Tanaka, M. (2005b). Isolation and characterization of collagen from bigeye snapper (*Priacanthus macracanthus*) skin. *Journal of the Science of Food and Agriculture*, 85(7), 1203–1210. <https://doi.org/10.1002/jsfa.2072>
- Karim, A. A., & Bhat, R. (2009). Fish gelatin: properties, challenges, and prospects as an alternative to mammalian gelatins. *Food Hydrocolloids*, 23(3), 563–576. <https://doi.org/10.1016/j.foodhyd.2008.07.002>
- Kimura, S., Miyauchi, Y., & Uchida, N. (1991). Scale and bone type I collagens of carp (*Cyprinus carpio*). *Comparative Biochemistry and Physiology. B, Comparative Biochemistry*, 99(2), 473–476. [https://doi.org/10.1016/0305-0491\(91\)90073-m](https://doi.org/10.1016/0305-0491(91)90073-m)
- Kittiphattanabawon, P., Benjakul, S., Visessanguan, W., Nagai, T., & Tanaka, M. (2005). Characterisation of acid-soluble collagen from skin and bone of bigeye snapper (*Priacanthus tayenus*). *Food Chemistry*, 89(3), 363–372. <https://doi.org/10.1016/j.foodchem.2004.02.042>
- Klančnik, G., Medved, J., & Mrvar, P. (2010). Differential thermal analysis (DTA) and differential scanning calorimetry (DSC) as a method of material investigation *RMZ–Materials and Geoenvironment*, 57(1), 127–142.
- Kozłowska, J., Sionkowska, A., Skopinska-Wisniewska, J., & Piechowicz, K. (2015). Northern pike (*Esox lucius*) collagen: Extraction, characterization and potential application. *International Journal of Biological Macromolecules*, 81, 220–227. <https://doi.org/10.1016/j.ijbiomac.2015.08.002>
- Laemmli, U. (1970). Most commonly used discontinuous buffer system for SDS electrophoresis. *Nature*, 227, 680–686.
- Ledward, D. A. (2000). Gelatin. In G. O. Philips & P. A. Williams (Eds.), *Handbook of Hydrocolloids* (pp. 67–86). CRC Press.
- Li, C., Song, W., Wu, J., Lu, M., Zhao, Q., Fang, C., Wang, W., Park, Y. D., & Qian, G. Y. (2020). Thermal stable characteristics of acid-and pepsin-soluble collagens from the carapace tissue of Chinese soft-shelled turtle (*Pelodiscus sinensis*). *Tissue and Cell*, 67, Article 101424. <https://doi.org/10.1016/j.tice.2020.101424>
- Li, L. Y., Zhao, Y. Q., He, Y., Chi, C. F., & Wang, B. (2018). Physicochemical and antioxidant properties of acid- And pepsin-soluble collagens from the scales of Miiuy croaker (*Miichthys miiuy*). *Marine Drugs*, 16(10), Article 394. <https://doi.org/10.3390/md16100394>
- Li, Z. R., Wang, B., Chi, C., Zhang, Q. H., Gong, Y., Tang, J. J., Luo, H., & Ding, G. (2013). Isolation and characterization of acid soluble collagens and pepsin soluble collagens from the skin and bone of Spanish mackerel (*Scomberomorus niphonius*). *Food Hydrocolloids*, 31(1), 103–113. <https://doi.org/10.1016/j.foodhyd.2012.10.001>

- Liang, Q., Wang, L., Sun, W., Wang, Z., Xu, J., & Ma, H. (2014). Isolation and characterization of collagen from the cartilage of Amur sturgeon (*Acipenser schrenckii*). *Process Biochemistry*, 49(2), 318–323. <https://doi.org/10.1016/j.procbio.2013.12.003>
- Liu, D., Wei, G., Li, T., Hu, J., Lu, N., Regenstein, J. M., & Zhou, P. (2015). Effects of alkaline pretreatments and acid extraction conditions on the acid-soluble collagen from grass carp (*Ctenopharyngodon idella*) skin. *Food Chemistry*, 172, 836–843. <https://doi.org/10.1016/j.foodchem.2014.09.147>
- Luo, Q. Bin, Chi, C. F., Yang, F., Zhao, Y. Q., & Wang, B. (2018). Physicochemical properties of acid- and pepsin-soluble collagens from the cartilage of Siberian sturgeon. *Environmental Science and Pollution Research*, 25(31), 31427–31438. <https://doi.org/10.1007/s11356-018-3147-z>
- Lowry, O. H., Rosebrough, N. J., Farr, A. L., & Randall, R. J. (1951). Protein measurement with the Folin phenol reagent. *Journal of Biological Chemistry*, 193(1), 265–275.
- Martínez-Ortiz, M. A., Hernández-Fuentes, A. D., Pimentel-González, D. J., Campos-Montiel, R. G., Vargas-Torres, A., & Aguirre-Álvarez, G. (2015). Extraction and characterization of collagen from rabbit skin: partial characterization. *CyTA-Journal of Food*, 13(2), 253–258. <https://doi.org/10.1080/19476337.2014.946451>
- Matmaroh, K., Benjakul, S., Prodpran, T., Encarnacion, A. B., & Kishimura, H. (2011). Characteristics of acid soluble collagen and pepsin soluble collagen from scale of spotted golden goatfish (*Parupeneus heptacanthus*). *Food Chemistry*, 129(3), 1179–1186. <https://doi.org/10.1016/j.foodchem.2011.05.099>
- Ogawa, M., Portier, R. J., Moody, M. W., Bell, J., Schexnayder, M. A., & Losso, J. N. (2004). Biochemical properties of bone and scale collagens isolated from the subtropical fish black drum (*Pogonia cromis*) and sheepshead seabream (*Archosargus probatocephalus*). *Food Chemistry*, 88(4), 495–501. <https://doi.org/10.1016/j.foodchem.2004.02.006>
- Pal, G. K., Nidheesh, T., & Suresh, P. V. (2015). Comparative study on characteristics and in vitro fibril formation ability of acid and pepsin soluble collagen from the skin of catla (*Catla catla*) and rohu (*Labeo rohita*). *Food Research International*, 76(3), 804–812. <https://doi.org/10.1016/j.foodres.2015.07.018>
- Pal, G. K., & Suresh, P. v. (2016). Sustainable valorisation of seafood by-products: Recovery of collagen and development of collagen-based novel functional food ingredients. *Innovative Food Science & Emerging Technologies*, 37(Part B), 201–215. <https://doi.org/10.1016/j.ifset.2016.03.015>
- Saito, R., Suzuki, H., & Hayashizaki, Y. (2002). Interaction generality, a measurement to assess the reliability of a protein–protein interaction. *Nucleic Acids Research*, 30(5), 1163–1168. <https://doi.org/10.1093/nar/30.5.1163>
- Sarbon, N. M., Badii, F., & Howell, N. K. (2013). Preparation and characterisation of chicken skin gelatin as an alternative to mammalian gelatin. *Food Hydrocolloids*, 30(1), 143–151. <https://doi.org/10.1016/j.foodhyd.2012.05.009>
- Sato, K., Yoshinaka, R., Itoh, Y., & Sato, M. (1989). Molecular species of collagen in the intramuscular connective tissue of fish. *Comparative Biochemistry and Physiology Part B: Comparative Biochemistry*, 92(1), 87–91. [https://doi.org/10.1016/0305-0491\(89\)90317-9](https://doi.org/10.1016/0305-0491(89)90317-9)
- Singh, P., Benjakul, S., Maqsood, S., & Kishimura, H. (2011). Isolation and characterisation of collagen extracted from the skin of striped catfish (*Pangasianodon hypophthalmus*). *Food Chemistry*, 124(1), 97–105. <https://doi.org/10.1016/j.foodchem.2010.05.111>

- Skierka, E., & Sadowska, M. (2007). The influence of different acids and pepsin on the extractability of collagen from the skin of Baltic cod (*Gadus morhua*). *Food Chemistry*, 105(3), 1302–1306. <https://doi.org/10.1016/j.foodchem.2007.04.030>
- Song, Z., Liu, H., Chen, L., Chen, L., Zhou, C., Hong, P., & Deng, C. (2021). Characterization and comparison of collagen extracted from the skin of the Nile tilapia by fermentation and chemical pretreatment. *Food Chemistry*, 340, Article 128139. <https://doi.org/10.1016/j.foodchem.2020.128139>
- Subhan, F., Ikram, M., Shehzad, A., & Ghafoor, A. (2015). Marine collagen: An emerging player in biomedical applications. *Journal of Food Science and Technology*, 52, 4703–4707. <https://doi.org/10.1007/s13197-014-1652-8>
- Veeruraj, A., Arumugam, M., Ajithkumar, T., & Balasubramanian, T. (2015). Isolation and characterization of collagen from the outer skin of squid (*Doryteuthis singhalensis*). *Food Hydrocolloids*, 43, 708–716. <https://doi.org/10.1016/j.foodhyd.2014.07.025>
- Veeruraj, A., Arumugam, M., & Balasubramanian, T. (2013). Isolation and characterization of thermostable collagen from the marine eel-fish (*Evenchelys macrura*). *Process Biochemistry*, 48(10), 1592–1602. <https://doi.org/10.1016/j.procbio.2013.07.011>
- Venkatesan, J., Anil, S., Kim, S.-K., & Shim, M. S. (2017). Marine fish proteins and peptides for cosmeceuticals: A review. *Marine Drugs*, 15(5), Article 143. <https://doi.org/10.3390/md15050143>
- Verheul, M., Roefs, S. P. F. M., & de Kruif, K. G. (1998). Kinetics of heat-induced aggregation of β -lactoglobulin. *Journal of Agricultural and Food Chemistry*, 46(3), 896–903.
- Vojdani, F. (1996). 2 Solubility. In G. M. Hall (Ed.), *Methods of Testing Protein Functionality* (pp. 11-37). Springer
- Wahyuningsih, R., Nurliyani, R., Pertiwinigrum, A., Rohman, A., Fitriyanto, N. A., & Erwanto, Y. (2018). Optimization of acid soluble collagen extraction from Indonesian local “Kacang” goat skin and physico-chemical properties characterization. *Chemical Engineering Transactions*, 63, 703-708. <https://doi.org/10.3303/CET1863118>
- Wang, L., Liang, Q., Chen, T., Wang, Z., Xu, J., & Ma, H. (2014). Characterization of collagen from the skin of Amur sturgeon (*Acipenser schrenckii*). *Food Hydrocolloids*, 38, 104–109. <https://doi.org/10.1016/j.foodhyd.2013.12.002>
- Winarno, F. G. (2008). *Kimia Pangan dan Gizi: Edisi Terbaru* [Food Chemistry and Nutrition: Latest Edition]. Gramedia Pustaka.
- Wong, M. W., Nobes, R. H., Bouma, W. J., & Radom, L. (1989). Isoelectronic analogs of molecular nitrogen: Tightly bound multiply charged species. *The Journal of Chemical Physics*, 91(5), 2971–2979. <https://doi.org/10.1063/1.456967>
- Woo, J. W., Yu, S. J., Cho, S. M., Lee, Y. B., & Kim, S. B. (2008). Extraction optimization and properties of collagen from yellowfin tuna (*Thunnus albacares*) dorsal skin. *Food Hydrocolloids*, 22(5), 879–887. <https://doi.org/10.1016/j.foodhyd.2007.04.015>
- Wu, Q. Q., Li, T., Wang, B., & Ding, G. F. (2015). Preparation and characterization of acid and pepsin-soluble collagens from scales of croceine and redlip croakers. *Food Science and Biotechnology*, 24(6), 2003–2010. <https://doi.org/10.1007/s10068-015-0264-z>

- Wulandari, W., & Suptijah, P. (2015). Effectiveness of alkaline pretreatment and acetic acid hydrolysis on the characteristics of collagen from fish skin of snakehead. *Jurnal Pengolahan Hasil Perikanan Indonesia*, 18(3), 287-302. <https://doi.org/10.17844/jphpi.v18i3.11309>
- Yang, H., & Shu, Z. (2014). The extraction of collagen protein from pigskin. *Journal of Chemical and Pharmaceutical Research*, 6(2), 683–687.
- Yoshimura, K., Terashima, M., Hozan, D., & Shirai, K. (2000). Preparation and dynamic viscoelasticity characterization of alkali-solubilized collagen from shark skin. *Journal of Agricultural and Food Chemistry*, 48(3), 685–690. <https://doi.org/10.1021/jf990389d>
- Yousefi, M., Ariffin, F., & Huda, N. (2017). An alternative source of type I collagen based on by-product with higher thermal stability. *Food Hydrocolloids*, 63, 372–382. <https://doi.org/10.1016/j.foodhyd.2016.09.029>
- Yu, Z., An, B., Ramshaw, J. A. M., & Brodsky, B. (2014). Bacterial collagen-like proteins that form triple-helical structures. *Journal of Structural Biology*, 186(3), 451–461. <https://doi.org/10.1016/j.jsb.2014.01.003>
- Zayas, J. F. (1997). Solubility of proteins. In *Functionality of Proteins in Food* (pp.6–75). Springer.
- Zhang, Y., Herling, M., & Chenoweth, D. M. (2016). General solution for stabilizing triple helical collagen. *Journal of the American Chemical Society*, 138(31), 9751–9754. <https://doi.org/10.1021/jacs.6b03823>
- Zhao, W. H., Chi, C. F., Zhao, Y. Q., & Wang, B. (2018). Preparation, physicochemical and antioxidant properties of acid-and pepsin-soluble collagens from the swim bladders of miiuy croaker (*Miichthys miiuy*). *Marine Drugs*, 16(5), Article 161. <https://doi.org/10.3390/md16050161>

Low-temperature Deposited Highly Sensitive Integrated All-Solid Electrodes for Electrochemical pH Detection

Norhidayatul Hikmee Mahzan^{1,2}, Shaiful Bakhtiar Hashim^{1,2}, Rosalena Irma Alip^{2*}, Zuhani Ismail Khan³ and Sukreen Hana Herman^{2,3}

¹Nano-Electronic Center (NET), School of Electrical Engineering, College of Engineering, Universiti Teknologi MARA, 40450 Shah Alam, Selangor, Malaysia

²Integrated Sensors Research Group, School of Electrical Engineering, College of Engineering, Universiti Teknologi MARA, 40450 Shah Alam, Selangor, Malaysia

³Microwave Research Institute, Universiti Teknologi MARA, 40450 Shah Alam, Selangor, Malaysia

ABSTRACT

This article describes the process of fabricating an integrated all-solid electrode (IASE) by integrating thin films of titanium dioxide (TiO₂) and silver/silver chloride (Ag/AgCl) onto an indium tin oxide (ITO) substrate. The fabrication of a pH sensing electrode (SE) involved utilizing a spin-coated thin film composed of TiO₂. Thermally produced thin films of Ag/AgCl were used to develop solid reference electrodes (RE). The present work examined the impact of the drying process on the pH sensitivity and linearity of the low-temperature deposited IASE. The drying procedure was carried out within a temperature range from room temperature to 100°C. The investigation involved the examination of crystallinity, surface morphology, and thin film composition through the utilization of field effect scanning electron microscopy (FESEM), X-ray diffraction (XRD), and energy-dispersive X-ray (EDX) methods. In addition, a comparison was made between the pH sensing performance of the IASE and a commercially available Ag/AgCl RE. The

findings of this research demonstrate that the IASE sample, which underwent a drying process at a temperature of 100°C, exhibited remarkable sensitivity and linearity values of 66.7 mV/pH and 0.9827, separately, when compared to the commercially available RE.

ARTICLE INFO

Article history:

Received: 11 December 2023

Accepted: 10 June 2024

Published: 25 October 2024

DOI: <https://doi.org/10.47836/pjst.32.6.08>

E-mail addresses:

hikmee@uitm.edu.my (Norhidayatul Hikmee Mahzan)
shaifulbakhtiar@uitm.edu.my (Shaiful Bakhtiar Hashim)
rosalena@uitm.edu.my (Rosalena Irma Alip)
zuhai629@uitm.edu.my (Zuhani Ismail Khan)
hana1617@uitm.edu.my (Sukreen Hana Herman)
*Corresponding author

Keywords: Integrated-all solid electrodes, pH sensor; reference electrodes, sensing electrodes, titanium dioxide

INTRODUCTION

pH is an essential parameter in various fields, including agriculture (Gao et al., 2022; He et al., 2022), medical applications (Chalitangkoon & Monvisade, 2021), and food processing (Fathi et al., 2022; Zou et al., 2023). The ability to determine the level of acidity or alkalinity in a solution is significantly influenced by the pH value. The conventional method of pH measurement involves using glass electrodes, which have gained widespread popularity. However, the fragility of glass-based electrodes limits their utility and hinders their miniaturization for certain applications, particularly in the medical field (Manjakkal et al., 2020). Additionally, the maintenance of such pH sensors is labor-intensive due to the requirement of an internal solution, typically saturated potassium chloride (KCl). Consequently, there is a need for alternative pH sensing approaches that offer improved durability and reduced maintenance.

In 1972, P. Bergveld introduced a novel solid-state pH sensor, the ion-sensitive field effect transistor (ISFET), in response to the challenges associated with glass electrode fragility and maintenance requirements (Bergveld, 1972). The utilization of ISFETs enabled the quantification of ionic reactions occurring in electrochemical and biological surroundings. Nevertheless, certain drawbacks were discovered upon its implementation, particularly in relation to temperature sensitivity, susceptibility to light interference, and ionic penetration issues. To address these challenges, Spiegel proposed an alternative solution in 1983: the extended gate field effect transistor (EGFET) detection method (Spiegel et al., 1983). The EGFET pH sensor offered several notable advantages over the ISFET, including enhanced stability in varying light and temperature conditions, heightened sensitivity, reduced impedance, cost-effectiveness, and simplified packaging (Mokhtarifar et al., 2018; Pullano et al., 2018).

Various metal oxides, including tantalum oxide (Ta_2O_5), zinc oxide (ZnO), copper oxide (CuO), tin oxide (SnO_2) and titanium dioxide (TiO_2) have found widespread applications in diverse fields (Beale et al., 2022; Khizir & Abbas, 2022; Palit et al., 2020; Ramakrishnappa et al., 2020; Sharma & Kumar, 2022). Among these metal oxides, TiO_2 has emerged as a highly promising material, demonstrating significant potential in various applications such as memristors, dye-sensitized solar cells, photocatalysts, capacitors, gas sensors, pH-sensing electrodes (SE) and tailoring the charge storage properties (Krishnan et al., 2016; Özdemir et al., 2022; Pal et al., 2018; Sadig et al., 2019; Tayeb et al., 2022; Zamiri et al., 2022; Zulkefle et al., 2021). When employed as a SE, TiO_2 offers exceptional attributes, including excellent chemical stability, flexibility, robustness, and a high dielectric constant. Several fabrication techniques for TiO_2 SE have been documented, including sputtering, spin coating, physical and chemical vapor deposition, immersion techniques, spray pyrolysis, electron beam deposition, and pulsed laser deposition (Dave & Chauhan, 2022; Radha et al., 2022; Song et al., 2023; Yang et al., 2023). The sol-gel spin coat process is the simplest

and least expensive of these options. It makes it easier for chemicals to react evenly with the thin films and the substrate, especially when the temperatures are high.

The primary aim of this investigation is to examine the performance of sensitivity for integrated all-solid electrodes (IASE) through the application of a TiO₂ SE and an Ag/AgCl reference electrode (RE) onto a singular indium tin oxide (ITO) substrate. It is hypothesized that utilizing TiO₂ as the SE and Ag/AgCl as the RE will result in enhanced durability, potential for downsizing, and reduced maintenance demands compared to conventional glass-based pH sensors. In this study, we analyzed the operational efficiency of the developed IASE system and compared it to a TiO₂ SE paired with a commercially available RE. The present studies are anticipated to provide an important and useful addition to the advancement of pH sensing devices that are both efficient and dependable, hence enhancing their applicability across several domains.

MATERIALS AND METHODS

Sample Preparations

The IASE was fabricated by constructing an SE and a RE on a single ITO-coated glass substrate. Figure 1 shows the top view configuration of the IASE, with the Ag/AgCl RE and TiO₂ SE occupying an area of 0.35 cm² and being separated by 0.6 cm² of the insulation region. The insulation region was created by removing the conductive ITO coating using zinc powder and hydrochloric acid (HCl). This removal was crucial to prevent electrical linkage between the SE and the RE.

Prior to fabricating the IASE, the ITO substrate underwent ultrasonic cleaning using Hwashin Technology Powersonic 405. The substrate was cleaned by submerging it for ten minutes at a time in a solution of ethanol and deionized water and then drying it with inert nitrogen gas.

To produce TiO₂, a solution containing mixtures A and B was combined. Mixture A comprised absolute ethanol as a solvent, glacial acetic acid as a stabilizer, and titanium (IV) isopropoxide as the precursor. In contrast, mixture B consists of deionized water, Triton X-100 utilized as a surfactant and absolute ethanol. Both mixtures were organized separately, each undergoing a one-hour stirring process. Subsequently, the mixtures were combined and subjected to an additional hour of stirring at room temperature.

The sol-gel spin coater (Laurell Model WS-650MZ-8NPP/LITE) was used to deposit a thin film of TiO₂ from the TiO₂ solution that had been prepared. This spin-coating method has been recognized to yield uniform thin films. The deposition process was initiated by carefully positioning the cleaned ITO substrate onto the spin coater's chuck and dispensing 10 drops of TiO₂ solution onto the substrate. Initially, the substrate was rotated at 500 rpm for 10 seconds, after which the rotational speed was increased to 3000 rpm for one minute. High-speed spinning evenly dispersed the solution across the substrate surface, creating

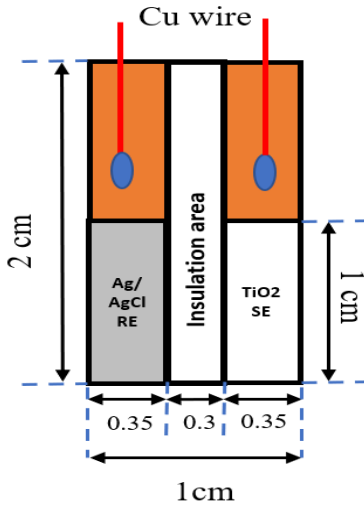


Figure 1. IASE top view configuration

the substrate, forming a thin film. The process was carefully handled to ensure that the thickness of the Ag layer was roughly 300 nm.

After the deposition process, a 5-second chlorination step was carried out using FeCl_3 to form the Ag/AgCl RE. This process involved the reaction between Ag and FeCl_3 , forming AgCl on the surface of the Ag layer. The Ag/AgCl RE provides a stable potential for pH-sensing measurements. After forming Ag/AgCl, the area of Ag/AgCl was covered using Kapton tape, as shown in Figure 2(b), for deposited TiO_2 .

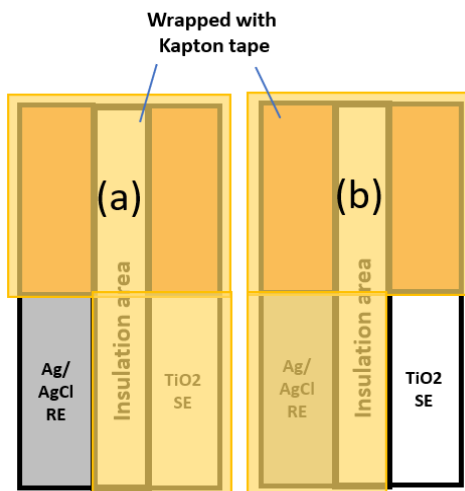


Figure 2. Schematic diagram during (a) Ag layer and (b) TiO_2 deposition process

a thin coating with consistent thickness. After that, the film was dried at 100°C for 10 minutes to remove any remaining solvents, including ethanol and water, thus leaving behind a pure TiO_2 thin film. A single layer of TiO_2 thin film with an approximate thickness of 23 nm was produced on the substrate by annealing the sample for 15 minutes at 400°C after drying it.

A thermal evaporator (TE) was employed to deposit the Ag layer, a commonly utilized thin metal film deposition method. Figure 2(a) shows the opening area for the deposited Ag. In this process, the Ag material was heated to a high temperature, causing it to evaporate and subsequently condense onto

Measurement Setup

Figure 3 illustrates the experimental arrangement employed for conducting EGFET measurements, comprising the integration of an IASE and TiO_2 SE with a commercialized RE connected with a semiconductor device analyzer (SDA). Furthermore, the commercialized RE was linked to SMU 3, while the TiO_2 SE was connected to the pin gate of a commercially available CD4007UBE

MOSFET, serving as the extended gate SE. This transistor was used as a readout to extract a potential change on the gate site

by converting it to drain current. This commercialized transistor can be assembled on a printed circuit board (Kwon et al., 2019).

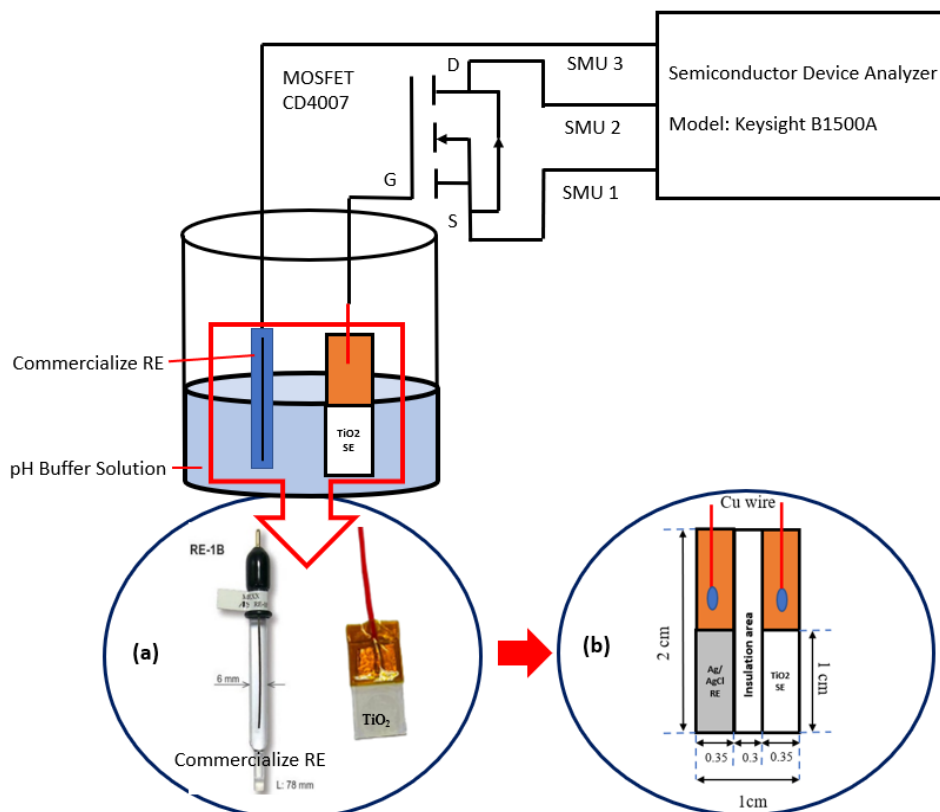


Figure 3. EGFET measurement setup (a) TiO₂ SE and commercialize RE (b) IASE

Various pH buffer solutions were employed to explore the sensor's response capabilities. The IASE was immersed in different pH buffer solutions, including those with 2, 4, 7, 10, and 12 pH values. The transfer characteristic (drain current, I_D versus reference voltage, V_{REF}) and the output characteristic (drain current, I_D versus drain-source voltage, V_{DS}) were obtained from these measurements. During transfer characteristic measurement, the V_D was set at 100 mV, and V_{REF} sweeps from 0 to 3 V. To assess the pH sensitivity performance of the fabricated IASE, a graph depicting the relationship between the drain current and the reference voltage was evaluated. The output voltage was extracted from the I_D versus V_{REF} curve as the obtained I_D of 100 μ A corresponding to an applied reference voltage.

RESULTS AND DISCUSSION

Figures 4 to 8 show the transfer characteristics (left) and output voltage graphs (right) for fabricated IASE at room temperature, 30°C, 50°C, 70°C, and 100°C, respectively.

All transfer characteristic graphs exhibit similar patterns from the result obtained with the threshold voltage shifted from a rightward direction. As can be seen on the graph, by increasing the pH value from pH 2 to pH 12, the threshold voltage shifted from the left to the right direction due to a decrease in hydrogen ion concentration, which reduced the surface potential (Das et al., 2014). The sensitivity and linearity were recorded at 66.1 mV/pH and 0.9561 at room temperature deposition. As the deposition temperature increased to 30°C, the sensitivity and linearity were around 64.2 mV/pH and 0.9423, respectively. Further, the temperature was increased to 50°C, and the sensitivity increased to 67.3 mV/pH, but the linearity slightly decreased to 0.9211. The sensitivity and linearity were around 66 and 66.7 mV/pH and 0.9343 and 0.9287, respectively, for temperature deposition at 70°C and 100°C. This result investigates site binding theories to explain how the oxide surface of a gate electrode detects the pH. The surface of the metal oxide goes through a process that causes it to create hydroxyl groups when immersed in a solution. These hydroxyl groups In general, the oxide surface is composed of a hydroxyl group, OH-

Thus, when the metal oxide surface comes into contact with a solution, the surface reaction could be protonated by acidic or deprotonated ions in an alkaline solution, thus leaving positively or negatively charged ions on the surface of the sensing electrodes can either donate or accept a proton as shown in Figure 9. The surface of the sensing membrane denoted Ti can be in three different forms: neutral (TiOH), negative (TiO⁻), and positive (TiOH₂⁺). The changes in the surface potential depend on the value of the pH buffer solution. At a lower pH (acidic), hydrogen ions concentration is high, where more positive charges accumulate near the extended gate (SE) and attract more electrons to the interface between the gate and the substrate, allowing current to flow from the source to drain. However, a higher pH (alkaline) indicates low hydrogen ions concentration; the decrease in positive charge near the gate causes the threshold voltage to shift positively. In other words, the voltage required to turn on the MOSFET is increased (Sabah et al., 2017). The dependency of threshold voltage on the pH value can be illustrated using Equation 1.

$$[H^+]_s = [H^+]_b \exp(-q\phi_o/kT) \quad [1]$$

Where the $[H^+]_s$ and $[H^+]_b$ are the bulk and the surface activity of the H^+ ions, q is the electron charge, ϕ_o is the potential on the gate of the transistor, k is the Boltzmann constant, and T is the absolute temperature. It was discovered that a lower value of ϕ_o leads to a lower output voltage based on Equation 1.

Table 1 presents a comparative analysis of the sensitivity and linearity values of the IASE and TiO₂ SE compared to a commercially available RE. The impact of increasing drying temperature on these parameters was examined. The findings indicate no significant alterations as the drying temperature was raised. The average sensitivity of the IASE

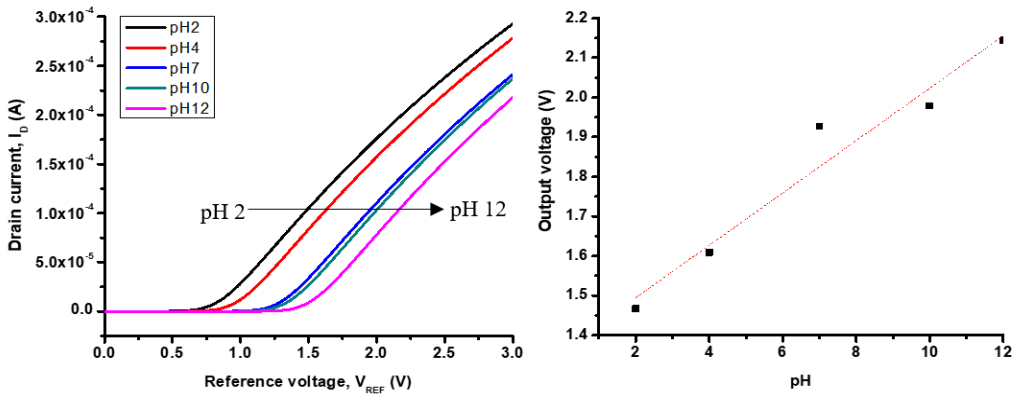


Figure 4. Transfer characteristic I_D versus V_{REF} and the graph of output voltage for IASE at room temperature

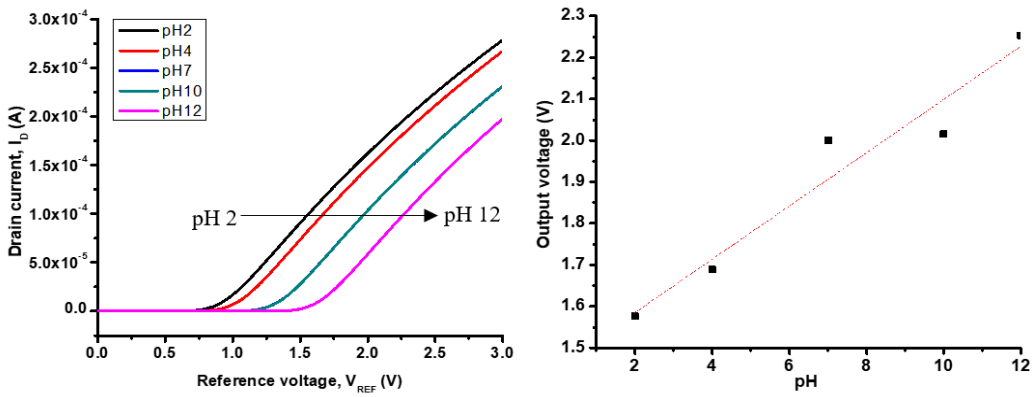


Figure 5. Transfer characteristic I_D versus V_{REF} and the graph of output voltage for IASE at 30°C

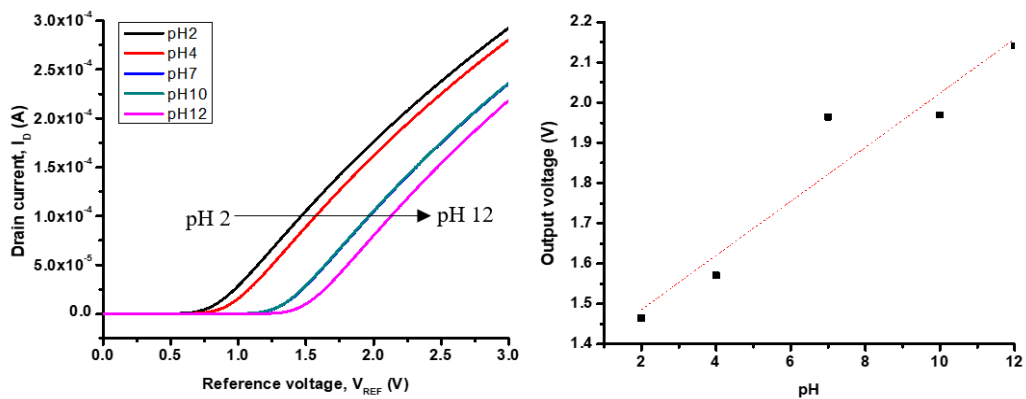


Figure 6. Transfer characteristic I_D versus V_{REF} and the graph of output voltage for IASE at 50°C

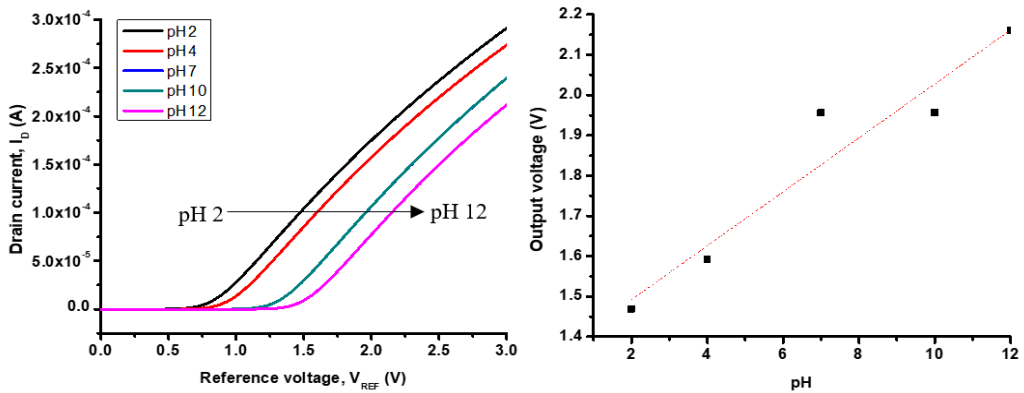


Figure 7. Transfer characteristic I_D versus V_{REF} and the graph of output voltage for IASE at 70°C

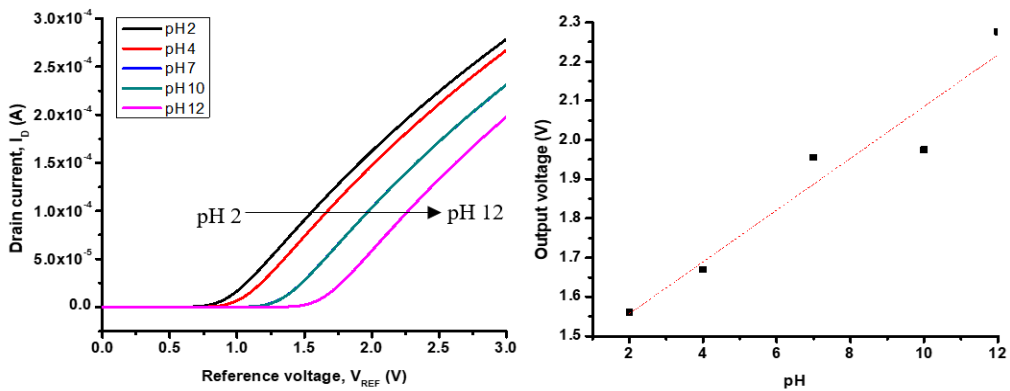


Figure 8. Transfer characteristic I_D versus V_{REF} and the graph of output voltage for IASE at 100°C

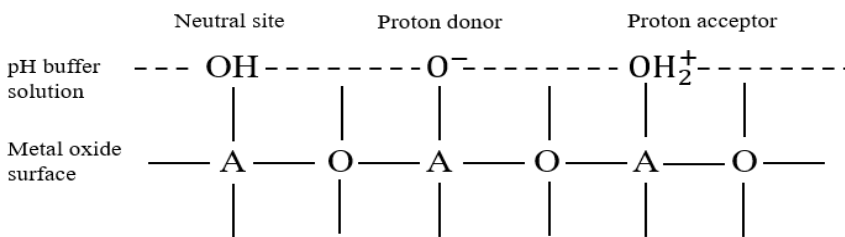


Figure 9. Schematic diagram of energy site binding

electrode was approximately 66.12 mV/pH, with the highest sensitivity of 67.3 mV/pH recorded at a drying temperature of 50°C. In the case of the TiO₂ SE and commercialized RE, the sensitivity increased from 46.3 mV/pH to 56.3 mV/pH as the drying temperature rose from room temperature to 70°C. Subsequently, it decreased to 52.7 mV/pH when

the drying temperature reached 100°C. Table 1 demonstrates that the TiO₂ SE and the commercialized RE exhibited superior linearity compared to the deposited IASE, albeit the disparity was still within an acceptable range.

Table 1
Comparison sensitivity and linearity value of IASE and TiO₂SE

Temperature (°C)	IASE		SE+Commercialize RE	
	Sensitivity	Linearity	Sensitivity	Linearity
Room Temperature	66.1	0.9561	46.3	0.9565
30	64.2	0.9423	48.8	0.9935
50	67.3	0.9211	55.7	0.9999
70	66	0.9343	56.3	0.9994
100	66.7	0.9827	52.7	0.9947

The X-ray diffraction (XRD) pattern of TiO₂ thin films at various temperatures is shown in Figure 10. Based on the XRD analysis, it shows clearly notable peaks at 2θ values of approximately 26.24°, 35.41°, and 50.81° corresponding to the (101), (110), and (202) orientations, respectively. These peaks show similarity with several reported works (Abdullah et al., 2019; Bakri et al., 2017; Yao et al., 2014). The XRD peaks demonstrate that increasing temperature results in higher intensity of diffraction peaks. The intensity of XRD peaks reflects the amount and orientation of crystalline material in the thin film. The intensity of the TiO₂ redox peak increased with increased temperature, indicating a higher degree of crystallinity.

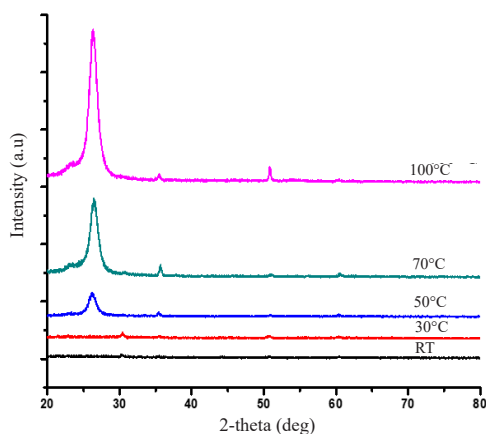


Figure 10. XRD pattern of TiO₂ thin films at different temperatures

Figure 11 shows the field effect scanning electron microscope (FESEM) images of TiO₂ thin film on an ITO-coated glass substrate at different deposition temperatures from RT to 100°C. As can be observed, the images at lower temperatures indicate a substrate covered in an uneven shape that contains a few gaps or cracks between TiO₂ particles. It shows that the TiO₂ particles are not sufficiently mobile to migrate and form a more compact structure during the first stages of heating. When the temperature is increased, a noticeable change can be seen in the FESEM images, in which fewer cracks were observed, and TiO₂ covered a larger surface area as the temperature increased

from 50 to 100°C. From Figure 11, the temperature also influences the grain size of TiO₂. As the temperature increases, the grain size becomes larger. Kamrosni et al. (2022) have discussed the effect of the annealing temperature of TiO₂ on the SEM images. This observation agrees with the hypothesis that higher temperatures promote denser coverage on the ITO-coated glass substrate by increasing the diffusion and aggregation of the TiO₂ particles.

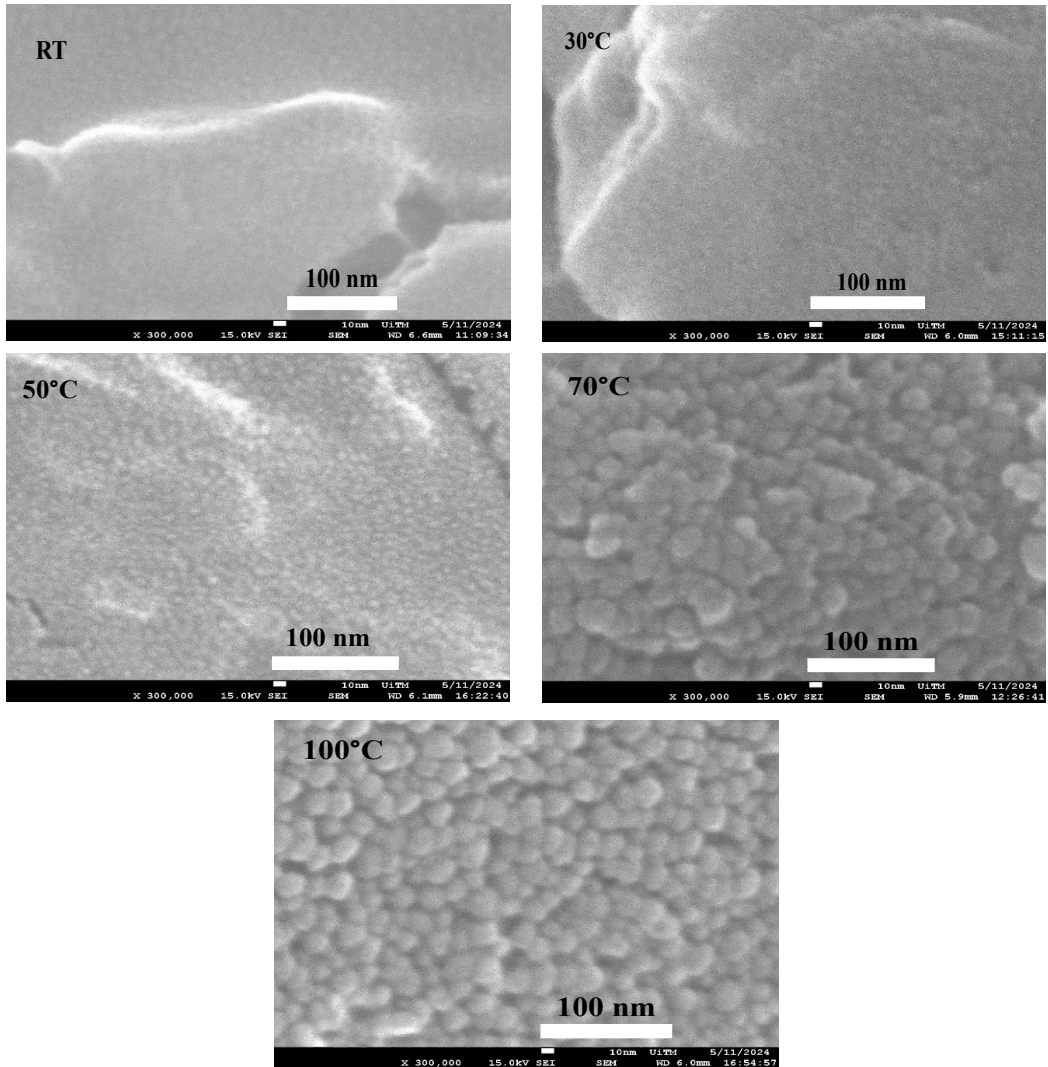


Figure 11. FESEM images of TiO₂ thin film on ITO-coated glass substrate at different temperatures (room temperature–100°C)

The connection between the FESEM observations and the XRD results depicted in Figure 10 is particularly intriguing. It is believable to suggest that the increased coverage

and combination of TiO_2 particles at higher temperatures, as seen in the SEM images, may be responsible for the structural changes reflected in the XRD data. Specifically, the XRD patterns may reveal shifts or alterations in the crystalline phases of the TiO_2 thin film as a consequence of the temperature-dependent structural evolution witnessed in the SEM images.

The energy dispersive x-ray (EDX) spectra of the TiO_2 thin film are depicted in Figure 12. Figure 10 displays the peaks representing the elements found in the sample. It was determined that titanium (Ti) and oxygen (O) were present in the sample. This peak's energy is associated with the Ti electron shells, which were found to be between 4.5 and 5.0 keV, and O, which was seen to be at roughly 0.5 keV. The table in the inset illustrates the percentages of each element's atomic weight as well as its relative weight. Ti has the highest weight percentage at 54.6%, followed by element O with 31.4%, and both come from the ITO substrate and TiO_2 , respectively.

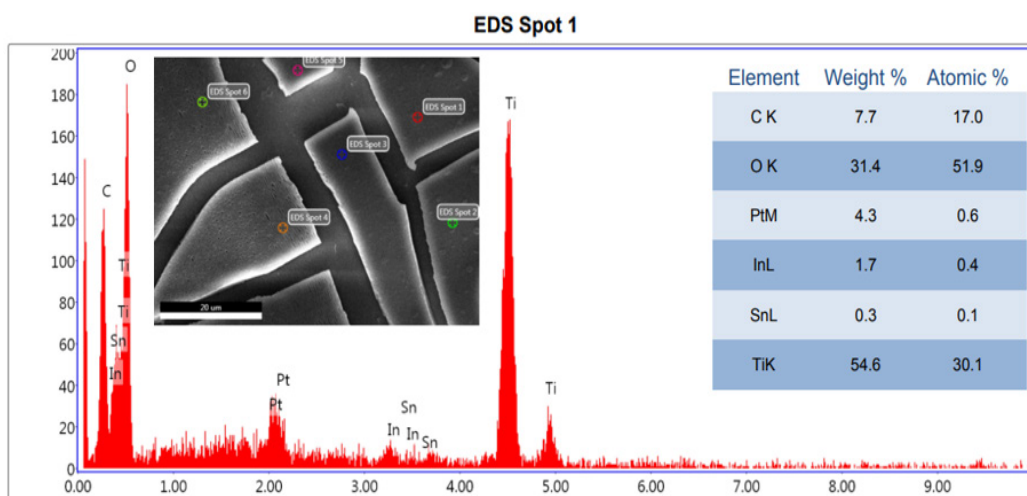


Figure 12. EDX spectra of TiO_2 thin film

CONCLUSION

In conclusion, the IASE-based TiO_2 SE and Ag/AgCl RE have been successfully fabricated on an ITO-coated glass substrate and are being compared TiO_2 SE with commercialized RE. The deposited IASE was more sensitive to pH measurement than TiO_2 SE with commercialized RE. However, the drying temperature does not show significant changes in IASE performance as the drying temperature increases. In addition, the TiO_2 SE and the commercialized RE's linearity were better than that of the deposited IASE. Although, the linearity of the IASE was still considered acceptable.

ACKNOWLEDGMENTS

The present study acknowledges the financial support the Ministry of Higher Education Malaysia provided through the Fundamental Research Grant Scheme [Project Code: FRGS/1/2021/TK0/UITM/02/50]. The authors would also like to thank the NANO Electronic Centre (NET) UiTM for their support.

REFERENCES

- Abdullah, S. A., Sahdan, M. Z., Nafarizal, N., Saim, H., Cik Rohaida, C. H., & Adriyanto, F. (2019, July 24-25). *XRD and Raman spectroscopy study on the effects of post-annealing temperature of TiO₂ thin films*. [Paper presentation]. IEEE International Conference on Sensors and Nanotechnology, Penang, Malaysia. <https://doi.org/10.1109/SENSORSNANO44414.2019.8940092>
- Bakri, A. S., Sahdan, M. Z., Adriyanto, F., Raship, N. A., Said, N. D. M., Abdullah, S. A., & Rahim, M. S. (2017). Effect of annealing temperature of titanium dioxide thin films on structural and electrical properties. *AIP Conference Proceedings*, 1788, Article 030030. <https://doi.org/10.1063/1.4968283>
- Beale, C., Altana, A., Hamacher, S., Yakushenko, A., Mayer, D., Wolfrum, B., & Offenhäusser, A. (2022). Inkjet-printed Ta₂O₅ on a flexible substrate for capacitive pH sensing at high ionic strength. *Sensors and Actuators B: Chemical*, 369, Article 132250. <https://doi.org/10.1016/j.snb.2022.132250>
- Bergveld, P. (1972). Development, operation, and application of the ion-sensitive field-effect transistor as a tool for electrophysiology. *IEEE Transactions on Biomedical Engineering*, BME-19(5), 342–351. <https://doi.org/10.1109/TBME.1972.324137>
- Chalitangkoon, J., & Monvisade, P. (2021). Synthesis of chitosan-based polymeric dyes as colorimetric pH-sensing materials: Potential for food and biomedical applications. *Carbohydrate Polymers*, 260, Article 117836. <https://doi.org/10.1016/j.carbpol.2021.117836>
- Das, A., Ko, D. H., Chen, C. H., Chang, L. B., Lai, C. S., Chu, F. C., Chow, L., & Lin, R. M. (2014). Highly sensitive palladium oxide thin film extended gate FETs as pH sensor. *Sensors and Actuators, B: Chemical*, 205, 199–205. <https://doi.org/10.1016/j.snb.2014.08.057>
- Dave, D. P., & Chauhan, K. V. (2022). Synthesis of visible spectrum-active TiO₂ thin film induced by RF magnetron sputtering. *Materials Today: Proceedings*, 62, 4254–4259. <https://doi.org/10.1016/j.matpr.2022.04.755>
- Fathi, M., Babaei, A., & Rostami, H. (2022). Development and characterization of locust bean gum-Viola anthocyanin-graphene oxide ternary nanocomposite as an efficient pH indicator for food packaging application. *Food Packaging and Shelf Life*, 34, Article 100934. <https://doi.org/10.1016/j.fpsl.2022.100934>
- Gao, L., Liu, P., Liu, L., Li, S., Zhao, Y., Xie, J., & Xu, H. (2022). κ-carrageenan-based pH-sensing films incorporated with anthocyanins or/and betacyanins extracted from purple sweet potatoes and peels of dragon fruits. *Process Biochemistry*, 121, 463–480. <https://doi.org/10.1016/j.procbio.2022.07.019>
- He, Y., Lu, L., Lin, Y., Li, R., Yuan, Y., Lu, X., Zou, Y., Zhou, W., Wang, Z., & Li, J. (2022). Intelligent pH-sensing film based on polyvinyl alcohol/cellulose nanocrystal with purple cabbage anthocyanins for visually monitoring shrimp freshness. *International Journal of Biological Macromolecules*, 218, 900–908. <https://doi.org/10.1016/j.ijbiomac.2022.07.194>

- Kamrosni, A. R., Suryani, C. H. D., Azliza, A., Mohd. Mustafa, A. B. A., Mohd. Arif Anuar, M. S., Norsuria, M., Chobpattana, V., Kaczmarek, L., Jez, B., & Nabialek, M. (2022). Microstructural studies of Ag/TiO₂ thin film; Effect of annealing temperature. *Archives of Metallurgy and Materials*, 67(1), 241–245. <https://doi.org/10.24425/amm.2022.137496>
- Khizir, H. A., & Abbas, T. A. H. (2022). Hydrothermal synthesis of TiO₂ nanorods as sensing membrane for extended-gate field-effect transistor (EGFET) pH sensing applications. *Sensors and Actuators A: Physical*, 333, Article 113231. <https://doi.org/10.1016/j.sna.2021.113231>
- Krishnan, S. G., Archana, P. S., Vidyadharan, B., Misnon, I. I., Vijayan, B. L., Nair, V. M., Gupta, A., & Jose, R. (2016). Modification of capacitive charge storage of TiO₂ with nickel doping. *Journal of Alloys and Compounds*, 684, 328–334. <https://doi.org/10.1016/j.jallcom.2016.05.183>
- Kwon, J., Yoo, Y. K., Lee, J. H., & Ahn, J. H. (2019). pH sensing characteristics of extended-gate field-effect transistor with Al₂O₃ layer. *Journal of Nanoscience and Nanotechnology*, 19(10), 6682–6686. <https://doi.org/10.1166/jnn.2019.17093>
- Manjakkal, L., Szwagierczak, D., & Dahiya, R. (2020). Metal oxides based electrochemical pH sensors: Current progress and future perspectives. *Progress in Materials Science*, 109, Article 100635. <https://doi.org/10.1016/j.pmatsci.2019.100635>
- Mokhtarifar, N., Goldschmidtboeing, F., & Woias, P. (2018, May 14-17). Low-cost EGFET-based pH-sensor using encapsulated ITO / PET-electrodes. *IEEE International Instrumentation and Measurement Technology Conference (I2MTC)*, Texas, USA. <https://doi.org/10.1109/I2MTC.2018.8409571>
- Özdemir, A. O., Caglar, B., Çubuk, O., Coldur, F., Kuzucu, M., Guner, E. K., Doğan, B., Caglar, S., & Özdokur, K. V. (2022). Facile synthesis of TiO₂-coated cotton fabric and its versatile applications in photocatalysis, pH sensor and antibacterial activities. *Materials Chemistry and Physics*, 287, Article 126342. <https://doi.org/10.1016/j.matchemphys.2022.126342>
- Pal, B., Bakr, Z. H., Krishnan, S. G., Yusoff, M. M., & Jose, R. (2018). Large scale synthesis of 3D nanoflowers of SnO₂/TiO₂ composite via electrospinning with synergistic properties. *Materials Letters*, 225, 117–121. <https://doi.org/10.1016/j.matlet.2018.04.120>
- Palit, S., Singh, K., Lou, B. S., Her, J. L., Pang, S. T., & Pan, T. M. (2020). Ultrasensitive dopamine detection of indium-zinc oxide on PET flexible based extended-gate field-effect transistor. *Sensors and Actuators, B: Chemical*, 310, Article 127850. <https://doi.org/10.1016/j.snb.2020.127850>
- Pullano, S. A., Critello, C. D., Mahbub, I., Tasneem, N. T., Shamsir, S., Islam, S. K., Greco, M., & Fiorillo, A. S. (2018). EGFET-based sensors for bioanalytical applications: A review. *Sensors*, 18(11), Article 4042. <https://doi.org/10.3390/s18114042>
- Radha, E., Komaraiah, D., Sayanna, R., & Sivakumar, J. (2022). Influence of dysprosium ions on structural, optical, luminescence properties and photocatalytic ability of spin coated dysprosium ions doped TiO₂ thin films. *Thin Solid Films*, 761, Article 139519. <https://doi.org/10.1016/j.tsf.2022.139519>
- Ramakrishnappa, T., Sureshkumar, K., & Pandurangappa, M. (2020). Copper oxide impregnated glassy carbon spheres based electrochemical interface for nitrite/nitrate sensing. *Materials Chemistry and Physics*, 245, Article 122744. <https://doi.org/10.1016/j.matchemphys.2020.122744>

- Sabah, F. A., Ahmed, N. M., Hassan, Z., & Almessiere, M. A. (2017). Influences of substrate type on the pH sensitivity of CuS thin films EGFET prepared by spray pyrolysis deposition. *Materials Science in Semiconductor Processing*, 63, Article 269–278. <https://doi.org/10.1016/j.mssp.2017.02.032>
- Sadig, H. R., Cheng, L., & Xiang, T. F. (2019). Synthesis of tetra-metal oxide system based pH sensor via branched cathodic electrodeposition on different substrates. *Arabian Journal of Chemistry*, 12(5), 610–620. <https://doi.org/10.1016/j.arabjc.2018.10.010>
- Sharma, N., & Kumar, R. (2022). Effect of spin speed on the properties of TiO₂ thin films. *Materials Today: Proceedings*, 62, 6615–6618. <https://doi.org/10.1016/j.matpr.2022.04.614>
- Song, J., Lee, D., Oh, S., Kim, H. K., & Choi, S. (2023). Restacking-free crumpled anatase TiO₂ nanosheets synthesized by spray pyrolysis for high-performance Na-ion battery anodes. *Journal of Alloys and Compounds*, 941, Article 169028. <https://doi.org/10.1016/j.jallcom.2023.169028>
- Spiegel, J. V. D., Lauks, I., Chan, P., & Babic, D. (1983). The extended gate chemically sensitive field effect transistor as multi-species microprobe. *Sensors and Actuators*, 4, 291–298. [https://doi.org/10.1016/0250-6874\(83\)85035-5](https://doi.org/10.1016/0250-6874(83)85035-5)
- Tayeb, A. M., Solyman, A. A. A., Hassan, M., & el-Ella, T. M. A. (2022). Modeling and simulation of dye-sensitized solar cell: Model verification for different semiconductors and dyes. *Alexandria Engineering Journal*, 61(12), 9249–9260. <https://doi.org/10.1016/j.aej.2022.02.057>
- Yang, K., Zhong, S., Zhou, X., Tang, S., Qiao, K., Ma, K., Song, L., Yue, H., & Liang, B. (2023). Controllable Al₂O₃ coating makes TiO₂ photocatalysts active under visible light by pulsed chemical vapor deposition. *Chemical Engineering Science*, 277(24), Article 118792. <https://doi.org/10.1016/j.ces.2023.118792>
- Yao, P. C., Lee, M. C., & Chiang, J. L. (2014, June 10-12). *Annealing effect of sol-gel TiO₂ thin film on pH-EGFET sensor*. [Paper presentation]. International Symposium on Computer, Consumer and Control, Taichung, Taiwan. <https://doi.org/10.1109/IS3C.2014.157>
- Zamiri, G., Haseeb, A. S. M. A., Jagadish, P., Khalid, M., Kong, I., & Krishnan, S. G. (2022). Three-dimensional graphene-TiO₂-SnO₂ ternary nanocomposites for high-performance asymmetric supercapacitors. *ACS Omega*, 7(48), 43981–43991. <https://doi.org/10.1021/acsomega.2c05343>
- Zulkefle, M. A., Herman, S. H., Rahman, R. A., Yusof, K. A., Rosli, A. B., Abdullah, W. F. H., & Zulkifli, Z. (2021). Evaluation on the egfet ph sensing performance of sol-gel spin coated titanium dioxide thin film. *Jurnal Teknologi*, 83(4), 119–125. <https://doi.org/10.11113/jurnalteknologi.v83.16313>
- Zou, Y., Sun, Y., Shi, W., Wan, B., & Zhang, H. (2023). Dual-functional shikonin-loaded quaternized chitosan/polycaprolactone nanofibrous film with pH-sensing for active and intelligent food packaging. *Food Chemistry*, 399, Article 133962. <https://doi.org/10.1016/j.foodchem.2022.133962>

Design an Agricultural Soil and Environment Monitoring System Based on IoT

Bayu Rima Aditya^{*}, Elis Hernawati, Tedi Gunawan and Pramuko Aji

School of Applied Science, Telkom University, Bandung 40257, Indonesia

ABSTRACT

One of the problems farmers face is the inability to make complete, real-time, and accurate observations of their farmland. The system proposed in this paper helps farmers to know the condition of farmland from anywhere and anytime by using a web-based application. The main objective of this prototype is to reduce the failure of the growth process of farming commodities by knowing the conditions inside and outside the soil with a total of 14 parameters. Internet of Things (IoT) technology is used to implement the prototype, which consists of Sensor Panels, Controllers, Message Broker, and Backend Service. All obtained data, created and tested in real-time, are displayed on the application. In addition to real-time data display, the system also includes monitoring history, alerts, and site location management.

Keywords: Agricultural, environment, Internet of Things, monitoring system, soil

INTRODUCTION

Soil and environmental monitoring in agriculture is essential to improve the effectiveness of agriculture itself (Huang & Hartemink, 2020; Tahat et al., 2020). By understanding

soil conditions such as fertility levels, soil texture, and water availability, farmers can plan for more efficient planting and fertilisation. Monitoring also helps farmers identify problems such as eroded or terraced soils to take timely corrective actions to improve crop productivity (Hilali et al., 2023; Segarra et al., 2020). In addition, environmental monitoring helps anticipate the negative impacts of weather and climate changes so farmers can better adapt their

ARTICLE INFO

Article history:

Received: 13 December 2023

Accepted: 09 May 2024

Published: 25 October 2024

DOI: <https://doi.org/10.47836/pjst.32.6.09>

E-mail addresses:

bayu@tass.telkomuniversity.ac.id (Bayu Rima Aditya)

elishernawati@tass.telkomuniversity.ac.id (Elis Hernawati)

tedi@tass.telkomuniversity.ac.id (Tedi Gunawan)

pramukoaji@tass.telkomuniversity.ac.id (Pramuko Aji)

^{*}Corresponding author

farming practices, reduce the risk of crop failure, and increase the effectiveness of agricultural production (Ahmad & Pothuganti, 2020; Huang & Hartemink, 2020; Popescu et al., 2020).

In traditional agriculture, farmers often face obstacles in monitoring the condition of their farmland. Farmers only conduct limited visual monitoring of their land (Sahbeni et al., 2023). Limited visual observations can hinder early identification of changes that may occur in the farm environment. The inability to obtain accurate and up-to-date information on parameters such as temperature, soil moisture, nutrient availability, and other environmental factors often makes it difficult for farmers to manage their land effectively (Sudharson et al., 2023).

If these conditions continue, it can lead to failure in the growth process of farming commodities and even result in crop failure. In addition, agricultural yields will not be maximised. Therefore, there is an urgent need to develop solutions that allow farmers to monitor and manage their farms more effectively and efficiently. Internet of Things (IoT) technology is emerging as a promising solution to help address this challenge (Ahlawat & Rana, 2021; Boddu et al., 2023; Rehman et al., 2022). By utilising sensors embedded in the fields, data can be collected continuously. Sensors can accurately record agricultural parameters (Billa et al., 2023). The data will then be processed and displayed on a digital platform for easy understanding. Farmers can access the sensors' data remotely through the digital platform. Thus, problems in monitoring agricultural land will be resolved.

The main contribution of this research is to present the design and development of a monitoring system that uses a soil data and environmental data approach. The developed approach can collect and display data in real-time. The hardware component includes a control box that connects and acquires soil data such as NPK levels, acidity, temperature, moisture, conductivity, salinity, and TDS, and environmental data such as wind speed, rainfall, temperature, humidity, and brightness. It allows farmers to respond quickly to changes in soil and environmental conditions and take necessary measures. The system also stores historical data. It allows farmers to track changes in conditions over time, identify patterns, and make decisions based on long-term trends.

RELATED WORKS

IoT in agriculture uses sensors for field monitoring and control to learn about the agricultural sector (Rifat et al., 2022). According to Dhal et al. (2023), the application of various IoT platforms, wireless sensor networks, and other related technologies, including remote sensing, cloud computing, and big data analytics in digital agriculture. Shafira et al. (2023) have designed a simple monitoring tool and made automatic irrigation systems that measure soil moisture, temperature, and water distance in reservoirs in urban agriculture. It used an Internet of Things (IoT)-based design developed using the Solar Cell as an energy

source and could be monitored with a smartphone/PC. According to Shafique et al. (2020), IoT technology is from a top-down perspective, outlining its statistical and architectural trends, application cases, difficulties, and hopes for the future. The report also provides a comprehensive and in-depth assessment of the new 5G-IoT situation. Cellular networks of the fifth generation (5G) offer essential enabling technologies for the widespread adoption of IoT technology. However, findings and analysis revealed that the Basic IoT system is reasonably priced for agricultural farms; however, the cost is greatly increased by incorporating specific features in the smart sensors. Additionally, the internet connectivity in farms and communities is subpar, hindering information exchange between farmers and agricultural professionals (Kumhar et al., 2022). As stated in the research of Yang et al. (2021), one implementation of the IoT system is NB-IoT, which is utilised in creating a monitoring system for the greenhouse environment (Narrowband Internet of Things). The system can wirelessly communicate data to the OneNET cloud platform and monitor the greenhouse's air temperature, relative humidity, light intensity, and carbon dioxide concentration. Additionally, the device can measure the greenhouse's air temperature. Growers may access the website and obtain information on the conditions in the greenhouse using a mobile phone or any portable device of their choosing.

The soil's moisture has a direct bearing on the growth and yield of the crop, which is an essential component of plant life. The soil's moisture is an important aspect of the plant that directly impacts how it develops and how much harvest it produces (Sankar et al., 2023). In addition to monitoring the environmental parameters such as Temperature, Humidity, Soil Moisture, Rain level and Light Intensity to monitor the conditions of agricultural farmland (Babu et al., 2023). Hossain et al. (2023) proposed an effective Internet of Things (IoT)-based soil nutrient monitoring and machine learning-based crop recommendation system. This system is intended to assist farmers by providing crop-related details and recommendations for crops based on various soil and weather attributes. The machine learning approach will recommend what kinds of crops have the greatest production potential for this land by monitoring N, P, K, temperature, pH, humidity, and rainfall values and analysing the permanent and temporary behaviour of the soil N, P, K, temperature, pH, humidity, and rainfall values. They studied how the Internet of Things (IoT), machine learning, and other sensor-based improvements have made environmental monitoring smart (Pal et al., 2023). Nalendra et al. (2022) developed IoT-Agri to assist farmers in monitoring soil, water, and environment data. IoT-Agri comprises several components, including sensors, applications, network elements, and other electronic devices. IoT-based soil nutrient monitoring and analysis systems employ Arduino and ESP8266 (Gomathi et al., 2022).

MATERIALS AND METHODS

Hardware Design

The hardware used in the research includes soil sensors and sensor stations. The main function of these sensors is to monitor the progress of the crops grown in the area, as well as to capture relevant data. The sensor system installed on the farm is designed to ensure efficient monitoring and surveillance of the crops. The devices installed in the farm area include various components, as shown in Figure 1. This system of sensors is capable of optimising agriculture and can accurately monitor and regulate the environmental conditions of the farm.

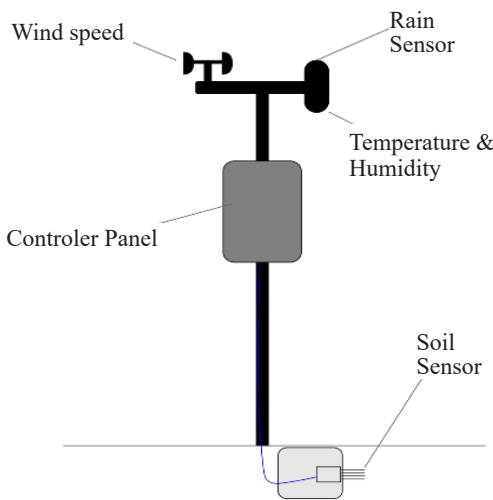


Figure 1. Controller and sensor panel

Table 1 shows the parameters and units related to data collection based on the sensor installation results.

Software Design

The software design of the proposed IoT-based farmland information system can be seen in Figure 2. First, each sensor collects data from the physical environment or monitored device, such as temperature, humidity, pressure, and other devices. This data is transmitted via the RS485 Modbus connection. Second, the controller acts as an interface between the sensor and the message broker. It collects data from various sensors connected using the RS485 Modbus

Table 1

Farmland data collection parameters

No	Parameters	Unit	Symbol
1	Environmental humidity	Per cent	%
2	Environmental temperature	Degree Celsius	°C
3	Rainfall	Millimetres	mm
4	Brightness	Lux	lx
5	Wind speed	Meter/Second	m/s
6	Soil Moisture	Prosen	%
7	Soil Temperature	Degree Celsius	°C
8	Conductivity	Micro siemens per centimetre	us/cm
9	Soil acidity	Part per million	ppm
10	N content	Part per million	ppm

Table 1 (Continue)

No	Parameters	Unit	Symbol
11	P content	Part per million	ppm
12	Potassium Content	Part per million	ppm
13	Salinity	Milligrams per Liter	mg/L
14	TDS (soluble solids)	Part per million	ppm

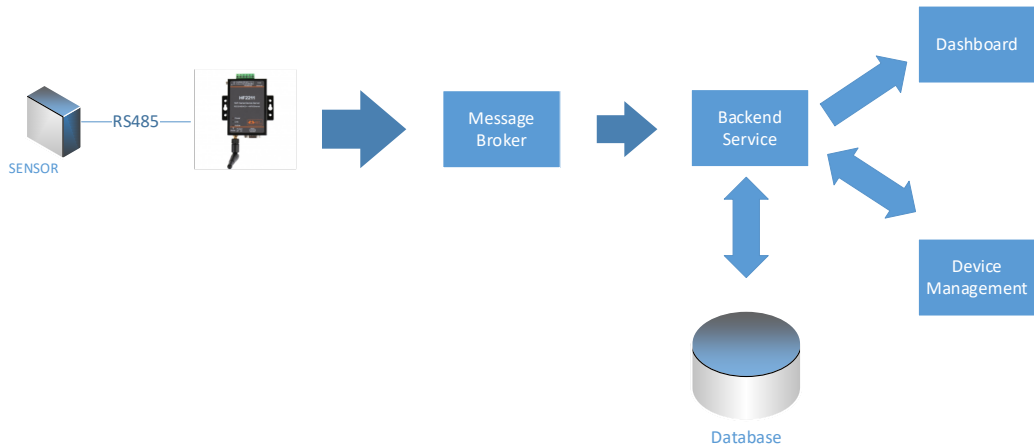


Figure 2. Data flow architecture

protocol and sends it to the message broker. This controller can also organise sensors and apply simple logic before sending data. Third, the message broker is responsible for receiving and distributing the data sent by the controller. The message broker is an intermediary between the controller and the backend service. When data is received from the controller, the message broker will send it to the backend service. Finally, the backend service is the core of the IoT application. Here, data from the message broker is received and processed. The backend service contains the business logic and algorithms required to process sensor data and generate useful information. Some of the main tasks of the backend service include:

a. Database Management

The backend service will store the accumulated data in the database. The stored data includes raw data from sensors as well as processed data.

b. Device Management

The backend service is also responsible for organising and managing IoT devices with device management.

c. Dashboard

The backend service will apply the appropriate algorithms and logic to process the data received from the sensors or database. The results of this processing will be displayed on the dashboard. Users can view the data in visualisations such as graphs and tables.

RESULTS AND DISCUSSION

Results in Proposed System

The prototype of the proposed IoT-based farmland information system can be seen in Figure 3. It is a web-based application designed for farmers who want real-time information about farmland conditions. The application will display information about soil conditions and its environment, such as soil temperature, temperature, moisture, humidity, rainfall, light, wind speed, soil acidity, conductivity, N content, P content, K content, TDS, and salinity. The proposed system includes a sensor panel, controller, message broker, and backend service.

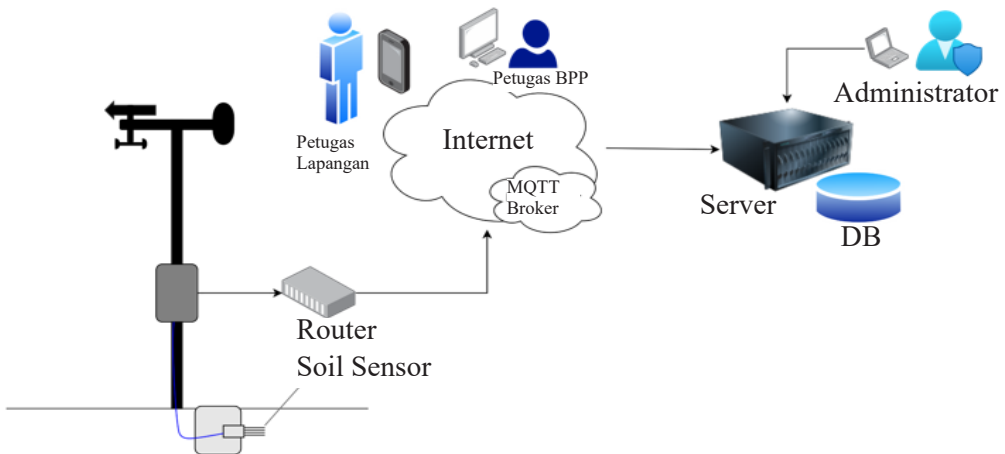


Figure 3. Prototype of farmland information system architecture

The installed sensors consist of two parts (Figure 3). The lower part contains soil sensors embedded in the ground to monitor conditions in the soil. In contrast, the upper part contains rain sensors, wind speed, and temperature and humidity sensors to measure environmental conditions above ground. All these sensors will be connected to the router via the Internet. Internet from the sensors will be collected and directed to one controller, and then from the controller, the data will be sent via the Internet to the router stage. After that, the data will go through the Internet and be received by the server, which is then stored in the database and displayed on websites or mobile phones. The MQTT Broker mechanism is used in this study to transmit the data on the Internet of Things (IoT). MQTT is a lightweight protocol, so it is suitable for IoT, which uses limited power.

In addition, the data from the database is accessed using SSH (secure shell). The SSH allows backend services to connect securely to the database. The backend is required to enter the appropriate SSH server IP address and password to connect. Furthermore, enter the appropriate information to connect to the database.

d. Soil Sensor

Soil sensors embedded in the farming area measure the soil conditions around the plants. The sensor can retrieve seven important parameters about the soil, such as moisture level, pH, and nutrient level. The system can use the data to regulate crop fertilisation appropriately and prevent soil quality problems.

e. Sensor Station

Sensor stations are important in capturing information about wind speed, rainfall, and air temperature and humidity around the plantation area. Data from various sensors, including soil sensors and controllers, will be sent through the internet router network.

f. Router

Data from sensor stations and controllers are collected and routed to one controller. The controller sends the data over the Internet to the stage. Next, the data passes through the Internet to the server, which is stored in the database.

g. Internet

The Internet is a medium for transmitting data from each stage installed on the sensor. It ensures the creation of accurate data, which will be stored in the DB Server.

h. MQTT Broker

The MQTT Broker mechanism is used to transmit data on the Internet of Things (IoT), but other messaging mechanisms can also be used.

i. DB Server

The DB Server is responsible for storing all farm-related data. The administrator can access this server database to monitor soil and crop conditions efficiently.

j. Admin

Administrators can monitor soil conditions on farmland through the database server. With the right information, farm officers can optimise crop growth and accurately manage farm environmental conditions for better results.

Implementation of the Proposed System

The implementation of the proposed system in this research is shown in Figure 4. The prototype is installed in one farming area, and the Internet is provided to monitor the soil and environmental conditions of the farming area using the Internet of Things. As an observation location, this research was conducted in 110 square meters of rainfed land in Garut district, West Java, Indonesia. The agricultural commodity observed is the Balinese Shallots. The duration of observations was carried out during two planting cycles. The first planting cycle was carried out from May to July 2023, while the second was carried out from August to October 2023.



Figure 4. Implementation of the prototype on limited land

Soil sensors and sensor stations are installed to collect and record data from when the seeds are planted until harvest time. This information is sent via the Internet to the server and the application. Figures 5 to 8 show the results displayed in the end-user application for the IoT-based farmland information system.

Real-time Monitoring

Real-time monitoring directly monitors the condition of the agricultural environment and related elements. The sensors that have been installed will generate data or information about soil temperature, ambient temperature, soil moisture, ambient humidity, rainfall, light, and wind speed, and then the data is retrieved and displayed instantly. So that farmers and agricultural administrators can access the latest information and make decisions based on accurate data. Overall, real-time monitoring provides accurate data to improve agricultural production and management while helping to reduce risks and increase efficiency.

Soil and Environment Monitoring System

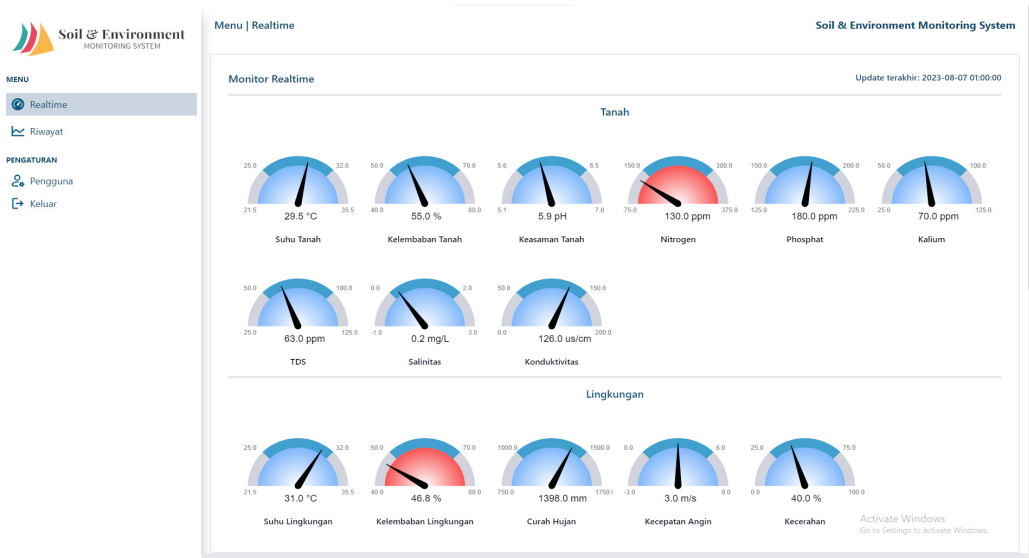


Figure 5. Application for real-time monitoring

Monitoring History

History monitoring has the function of storing historical data and information collected from monitoring processes in agricultural areas. It involves recording and storing data relating to environmental conditions, crop development, and other factors that affect the farm over time. This monitoring history describes the data obtained from the sensors that have been installed. The user is then given the option to activate specific sensors to compare parameters, which provides flexibility in making comparisons. The information displayed includes the date, hour, minute, and second when the data was collected. Users also can set the time and change the day and time as needed.



Figure 6. Application for monitoring history

Notifications

The notification function here is to provide information to the administrator regarding sensor values that do not meet the standards or exceed normal limits. This notification is important in ensuring a quick and responsive response to situations affecting the farm environment. In addition, notifications can also monitor weather temperature, soil moisture, and the condition of the farm environment area. Overall, notifications in agricultural monitoring provide the ability to adapt to changing environmental conditions in real-time, ultimately enabling a faster and more efficient response to situations that impact agricultural yields.

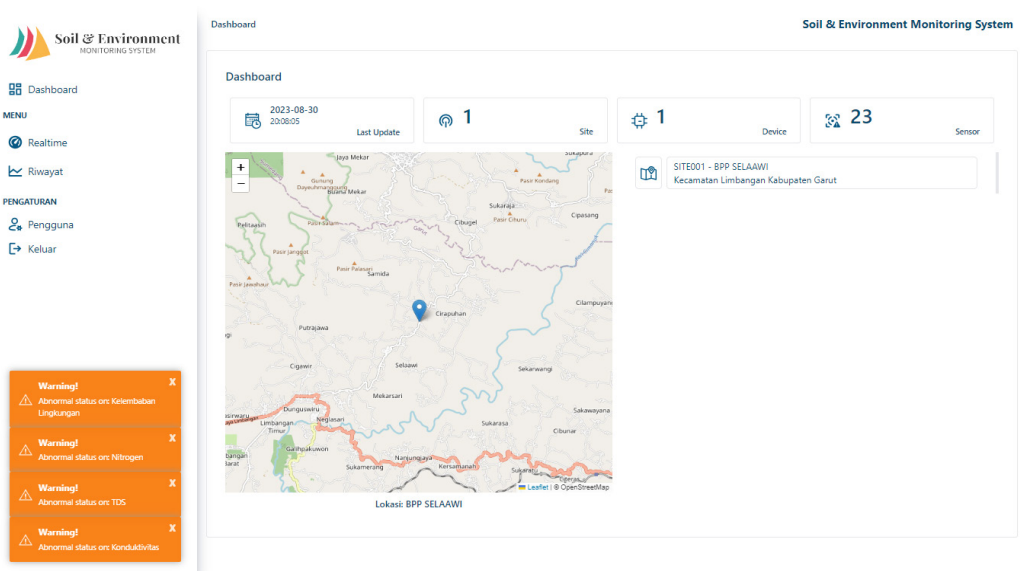


Figure 7. Application for notification

This dashboard shows the last update on the date, month, year, and time to second. It also shows the number of locations, devices, and sensors. In the bottom left corner are notifications indicating any sensor values that are out of standard or over normal limits.

Site Location

Site location plays an important role in displaying sensor positions and server locations. Furthermore, it enables the selection of the most optimal place to set up a facility or carry out agricultural activities. This process involves in-depth study and analysis of various factors that affect agricultural productivity and sustainability.

The location details page provides complete information about the location ID, location name, and address and contains a highly accurate location map.

In sum, the IoT-based land monitoring system that we have proposed has several advantages compared to other IoT-based agricultural monitoring options, including three

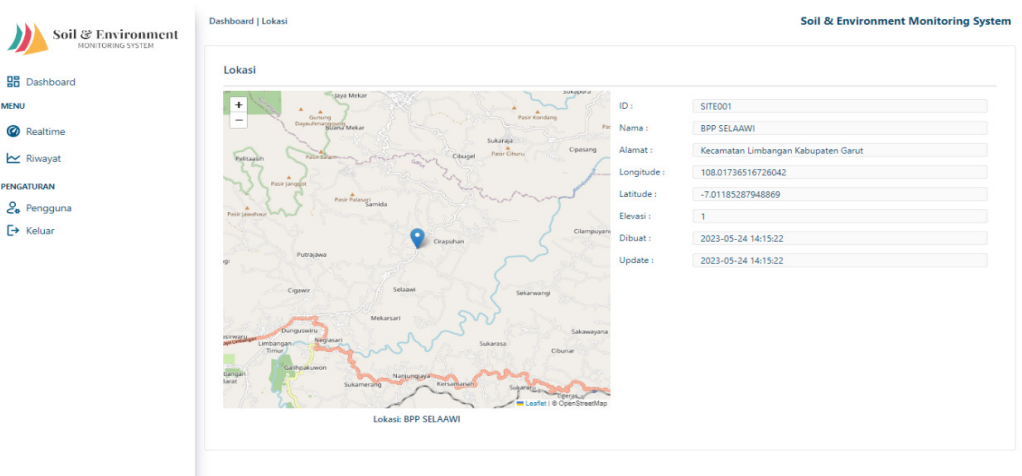


Figure 8. Application for site location

main features: (1) real-time monitoring of various parameters, (2) historical monitoring that stores data from the monitoring process, and (3) warnings about sensor values that do not meet standards or exceed normal limits. Scalability is also a key focus, possibly adding additional sensors or integrating new technology in agricultural recommendation systems. The significance of attributes like adaptable sensor integration, expandable system capabilities, and effortless setup was underscored when selecting a monitoring solution that aligns with the agricultural sector's demands. We compare the results of this study to assess the benefits of the suggested system within the larger framework of the advancement of Internet of Things-based agricultural monitoring technologies.

User Perception and Feedback

The prototype was demonstrated and tested by the relevant Agricultural Extension officers. This prototype has received very positive reviews during testing. The staff were enthusiastic during the test and were actively involved in the question-and-answer session. One thing we learned during the trial was that the staff said that this system would help monitor agricultural land conditions effectively and help make better decisions to ensure crop productivity was as planned. Also, the intuitive system design allows decision-makers to quickly understand how to use the system without experiencing difficulties in the form of colour on the real-time monitoring feature, which states that red indicates that sensor parameters do not meet standards or exceed normal limits.

CONCLUSION

This research proposes a prototype farmland information system designed and implemented using IoT technology. The system features real-time monitoring. Through sensors connected to the IoT network, data on soil and environmental conditions can be collected and displayed in real-time. It allows farmers to respond quickly to environmental changes and take necessary measures. Furthermore, the system has a Historical data Monitoring feature. The system also stores historical data on land and environmental conditions. This feature allows farmers to track changes in conditions over time, identify patterns, and make decisions based on long-term trends. In addition, the system has a Dashboard page. The Dashboard page displays a summary of data from the system, a map of sensor locations, and a list of monitored locations. It provides a visual understanding of where each sensor is located and the area covered by each device, allowing farmers to understand the geographical distribution of data. The Dashboard page can also display notifications to anticipate unusual or abnormal situations. When the data collected from the sensors shows values outside the normal limits, the system will notify the farmer. It allows for quick action to address any issues that may arise.

In conclusion, this system will help them reduce crop failures by providing farmers with the necessary information about their crops' growth. The system is practical and accurate for transmitting data using Wi-Fi. Further studies can focus on analysing the data collected using Machine Learning, such as farmland classification and recommendations. In addition, other parameters, such as special crop treatments, could be included for further study.

Data incompatibility is one of the problems or constraints that can occur during system setup or field use. To address this issue, ensure that there is an accessible tool for data transformation so that data from different sources can be converted into a format that the system can understand. If possible, standardise the form of data. Security vulnerabilities and system performance bottlenecks are additional challenges that need to be addressed. To find hardware or system code bottlenecks, use profiling tools. If necessary, fix the hardware or optimise the code. If possible, consider scalable cloud-based solutions. Conduct regular security audits to find and fix vulnerabilities. Implement strict access control and security measures. Keep up to date with the latest security risks.

ACKNOWLEDGEMENTS

This research activity is supported through RIIM Kompetisi funding from the Indonesia Endowment Fund for Education Agency, the Ministry of Finance of the Republic of Indonesia, and the National Research and Innovation Agency of Indonesia (BRIN) according to contract numbers 128/IV/KS/11/2022 and 374/SAM4/PPM/2022. We also thank Telkom University, Indonesia and UPT Pertanian Wilayah 5 Kabupaten Garut, Indonesia for supporting this research activity.

REFERENCES

- Ahlawat, P., & Rana, C. (2021). An era of recommendation technologies in IoT: Categorisation by techniques, challenges and future scope. *Pertanika Journal of Science and Technology*, 29(4), 2355-2381. <https://doi.org/10.47836/pjst.29.4.07>
- Ahmad, I., & Pothuganti, K. (2020, September 10-12). *Smart field monitoring using ToxTrac: A cyber-physical system approach in agriculture*. [Paper presentation]. International Conference on Smart Electronics and Communication (ICOSEC), Trichy, India. <https://doi.org/10.1109/ICOSEC49089.2020.9215282>
- Babu, T. A., Sadiya, S., Teja, M. S., Geetha, G. S., & Reshma, C. (2023). Monitoring agricultural environment using IoT. *Interantional Journal of Scientific Research in Engineering and Management*, 07(3), 1-7. <https://doi.org/10.55041/IJSREM17981>
- Billa, P., Venkatesh, K., Venkata Sai, J., Lohith, K., & Kumar, A. S. (2023). Effective monitoring and protecting system for agriculture farming using IoT and raspberry pi. *Materials Today: Proceedings*, 80(Part 3), 2917–2920. <https://doi.org/10.1016/j.matpr.2021.07.065>
- Boddu, R. D., Ragam, P., Pendhota, S. P., Goni, M., Indrala, S., & Badavath, U. R. (2023). Iot-based smart agricultural monitoring system. In *Proceedings of Fourth International Conference on Computer and Communication Technologies: IC3T 2022* (pp. 377-385). Springer. https://doi.org/10.1007/978-981-19-8563-8_36.
- Dhal, S., Wyatt, B. M., Mahanta, S., Bhattarai, N., Sharma, S., Rout, T., Saud, P., & Acharya, B. S. (2023). Internet of things (IoT) in digital agriculture: An overview. *Agronomy Journal*, 116(3), 1144-1163. <https://doi.org/10.1002/agj2.21385>
- Gomathi, S., Raj, K. V., & Aakash, R. V. (2022, November 9-10). *Design and Implementation of an IoT-based system for monitoring nutrients and irrigation in agricultural soil*. [Paper presentation]. 1st International Conference on Computational Science and Technology (ICCST), Chennai, India. <https://doi.org/10.1109/ICCST55948.2022.10040340>
- Hilali, A., El Baghdadi, M., & Halim, Y. (2023). Environmental monitoring of heavy metals distribution in the agricultural soil profile and soil column irrigated with sewage from the Day River, Beni-Mellal City (Morocco). *Modeling Earth Systems and Environment*, 9(2), 1859–1872. <https://doi.org/10.1007/s40808-022-01592-3>
- Hossain, M. D., Kashem, M. A., & Mustary, S. (2023, February 23-25). *IoT based smart soil fertilizer monitoring and ML based crop recommendation system*. [Paper presentation]. International Conference on Electrical, Computer and Communication Engineering (ECCE), Chittagong, Bangladesh. <https://doi.org/10.1109/ECCE57851.2023.10100744>
- Huang, J., & Hartemink, A. E. (2020). Soil and environmental issues in sandy soils. *Earth-Science Reviews*, 208, Article 103295. <https://doi.org/10.1016/j.earscirev.2020.103295>
- Kumhar, S. H., Rafi, S. M., Gupta, A. D., Prakash, V., Kirmani, M. M., & Shukla, S. K. (2022, April 28-29). *A comprehensive study of using internet of things (IOT) in monitoring system for smart agriculture*. [Paper presentation]. 2nd International Conference on Advance Computing and Innovative Technologies in Engineering (ICACITE), Noida, India. <https://doi.org/10.1109/ICACITE53722.2022.9823934>

- Nalendra, A. K., Wahvudi, D., Mujiono, M., Fuad, M. N., & Kholila, N. (2022, December 8-9). *IoT-agri: IoT-Based environment control and monitoring system for agriculture*. Seventh International Conference on Informatics and Computing (ICIC), Bali, Indonesia. <https://doi.org/10.1109/ICIC56845.2022.10006964>
- Pal, Y., Nagendram, S., Saleh Al Ansari, M., Singh, K., Gracious, L. A. A., & Patil, P. (2023, February 23-25). *IoT based weather, soil, earthquake, and air pollution monitoring system*. [Paper presentation]. 7th International Conference on Computing Methodologies and Communication (ICCMC), Erode, India. <https://doi.org/10.1109/ICCMC56507.2023.10083932>
- Popescu, D., Stoican, F., Stamatescu, G., Ichim, L., & Dragana, C. (2020). Advanced UAV-WSN system for intelligent monitoring in precision agriculture. *Sensors*, 20(3), Article 817. <https://doi.org/10.3390/s20030817>.
- Rehman, A., Ma, H., Khan, M. K., Khan, S. U., Murshed, M., Ahmad, F., & Mahmood, H. (2022). The asymmetric effects of crops productivity, agricultural land utilization, and fertilizer consumption on carbon emissions: Revisiting the carbonization-agricultural activity nexus in Nepal. *Environmental Science and Pollution Research*, 29(26), 39827-39837. <https://doi.org/10.1007/s11356-022-18994-6>
- Rifat, A., Patel, P., & Babu, B. S. (2022). The Internet of Things (IOT) in smart agriculture monitoring. *European Journal of Information Technologies and Computer Science*, 2(1), 14-18. <https://doi.org/10.24018/compute.2022.2.1.49>
- Sahbeni, G., Ngabire, M., Musyimi, P. K., & Székely, B. (2023). Challenges and opportunities in remote sensing for soil salinization mapping and monitoring: A review. *Remote Sensing*, 15(10), Article 2540. <https://doi.org/10.3390/rs15102540>
- Sankar, K. M., Booba, B., Rangaswamy, C., Pramila, P. V., Kar, S. R., Kumar, A., & Sudhakar, M. (2023, February 22-24). *IoT based weather, soil, earthquake, air pollution monitoring system*. [Paper presentation]. 3rd International Conference on Innovative Practices in Technology and Management (ICIPTM), Uttar Pradesh, India. <https://doi.org/10.1109/ICIPTM57143.2023.10118160>
- Shafique, K., Khawaja, B. A., Sabir, F., Qazi, S., & Mustaqim, M. (2020). Internet of Things (IoT) for next-generation smart systems: A review of current challenges, future trends and prospects for emerging 5G-IoT scenarios. *IEEE Access*, 8, 23022-23040. <https://doi.org/10.1109/ACCESS.2020.2970118>
- Shafira, A., Nugraha, S., & Suhendra, T. (2023, October 11-13). *Design of Internet of Things (IoT) based soil moisture monitoring system using solar power in urban agriculture (Horticulture)*. [Paper presentation]. Proceedings of the 1st International Conference on Sustainable Engineering Development and Technological Innovation (ICSEDTI), Tanjungpinang, Indonesia. <https://doi.org/10.4108/cai.11-10-2022.2326280>
- Segarra, J., Buchailot, M. L., Araus, J. L., & Kefauver, S. C. (2020). Remote sensing for precision agriculture: Sentinel-2 improved features and applications. *Agronomy*, 10(5), Article 641. <https://doi.org/10.3390/agronomy10050641>.
- Sudharson, K., Alekhya, B., Abinaya, G., Rohini, C., Arthi, S., & Dhinakaran, D. (2023, February 18-19). *Efficient soil condition monitoring with IoT enabled intelligent farming solution*. [Paper presentation]. IEEE International Students' Conference on Electrical, Electronics and Computer Science (SCEECS), Bhopal, India. <https://doi.org/10.1109/SCEECS57921.2023.10063050>

- Tahat, M. M., Alananbeh, K. M., Othman, Y. A., & Leskovar, D. I. (2020). Soil health and sustainable agriculture. *Sustainability*, 12(12), Article 4859. <https://doi.org/10.3390/su12124859>
- Yang, J., Xu, Z., & Sun, Q. (2021, May 22-24). *Research and design of greenhouse environment monitoring system based on NB-IoT*. [Paper presentation]. 33rd Chinese Control and Decision Conference (CCDC), Kunming, China. <https://doi.org/10.1109/CCDC52312.2021.9601377>

Analysis of Soil Viability Monitoring System for In-House Plantation Growth Using an Internet of Things Approach

Spoorthi Singh¹, Utkarsh Ojha¹, Prashant M Prabhu², Poothi Rohan Reddi² and Shivashankar Hiremath^{1,3*}

¹Department of Mechatronics, Manipal Institute of Technology, Manipal Academy Higher Education (MAHE), Manipal, Karnataka, 576104, India

²Department of Electronics and Communication Engineering, Manipal Institute of Technology, Manipal Academy Higher Education (MAHE), Manipal, Karnataka, 576104, India

³Survivability Signal Intelligence Research Center, Hanyang University, Seongdong-gu, Seoul 04763, South Korea

ABSTRACT

Houseplant cultivation has become increasingly popular, allowing individuals to bring nature into their homes. However, successful indoor gardening requires careful monitoring of soil parameters to ensure optimal plant growth. To address this need, sensor technology and Internet of Things (IoT) devices are utilized to monitor soil temperature and moisture levels, which play crucial roles in plant growth. Various soil factors are sensed and collected using an IoT-based microcontroller, with data transmission facilitated by a Message Queue Telemetry Transport (MQTT) broker. Visualization of the data is achieved through the Node-RED programming tool, simplifying dashboard creation for easy monitoring. Furthermore, the collected data is stored in a MySQL server, enabling further analysis through SQL queries. The day is divided into four quarters with six-hour intervals, allowing for soil data collection using temperature and moisture sensors. The resulting

information on the dashboard facilitates informed decision-making to enhance soil conditions for optimal indoor plant growth. Experimentation has revealed a reduction in soil temperature of 3°C during daytime due to air conditioning operation, while soil moisture content remains consistently between 60 to 65% during early mornings and late evenings. Additionally, emphasis is placed on remote management using IoT systems, enabling monitoring of plant

ARTICLE INFO

Article history:

Received: 02 February 2024

Accepted: 10 June 2024

Published: 25 October 2024

DOI: <https://doi.org/10.47836/pjst.32.6.10>

E-mail addresses:

spoorthi.shekar@manipal.edu (Spoorthi Singh)

utkarsh.ojha@learner.manipal.edu (Utkarsh Ojha)

prashant.prabhu@manipal.edu (Prashant M Prabhu)

poothi.reddi@learner.manipal.edu (Poothi Rohan Reddi)

ss.hiremath@manipal.edu; sssnitk@gmail.com (Shivashankar Hiremath)

*Corresponding author

growth even when access is limited. Overall, monitoring soil factors using IoT technology offers a promising approach to optimizing indoor gardening practices and minimizing environmental resource consumption.

Keywords: In-house plantation, internet of things, MQTT, sensor, soil factors

INTRODUCTION

Farm industries continuously seek ways to improve operational efficiency, fast production, cut costs, and maintain good quality products in today's competitive world. One prominent method is the concept of "in-house forming." This method entails bringing agricultural products or in-house forming rather than growing forma products outside the land, which takes longer, is more expensive, takes more time to reach consumers, and many more. The advantages of in-house forming are numerous. Organizations have more control over every aspect of production by creating and managing forming activities within their facilities. They may tune processes to fulfill precise design specifications, assure product quality, and adapt quickly to changing market demands. In-house forming also provides cost savings by eliminating the requirement for price hikes associated with outsourcing. Further, there is a potential that the amount of water utilized or the time it takes for the water to arrive might be excessive during a conventional method of agriculture, causing the crops to dry up. Real-time temperature and humidity monitoring are critical in many agricultural applications (Prathibha et al., 2017; Kassim, 2020; Bittner et al., 2019).

Recently, researchers have explored agriculture using IoT technology, which has addressed various challenges and proposed different approaches to the faster development of agricultural products (Abbasi et al., 2022; Xu et al., 2022). The key challenges in implementing IoT systems in agriculture include high investment costs, connectivity issues, and needing trained personnel. Also, the main focus is scalability, affordability, and robust models in designing IoT-based agriculture (Dhanaraju et al., 2022). The system requires different assembling units like sensors, controllers, actuators, and software to develop code for appropriate tasks. A few research studies have shown that the IoT-enabled plant watering system uses a different controller and sensors for soil moisture observation (Sheth & Rupani, 2019; Al-Omary et al., 2018). The soil is an important constituent for any growth of agricultural production. Thus, soil-related parameters such as moisture, pH, and temperature were appropriately monitored to boost soil potency (Nguemezi et al., 2020). Also, improving soil productivity is critical for long-term agricultural sustainability and healthy ecosystems. Different sensor technology is used to monitor soil parameters sensibly and accurately. The same concept was adopted in-house forming, which can regularly monitor soil factors and improve the richness of the plant. In-house agriculture can provide a more stable and sustainable source of fresh produce, as well as financial

savings, educational possibilities, and environmental advantages. It frequently corresponds to bigger concepts such as urban farming, local food production, and sustainability (Specht et al., 2014).

Pechlivani et al. (2023) have used 3D printing technology to develop an agro toolbox to access the soil parameters using IOT technology. The toolbox is used to integrate the different soil monitoring sensors that are deployed across the farmland. A continuously monitored soil key parameters such as temperature, humidity, intensity of visible light, and other parameters were gathered through IOT technology. Researchers have replaced the manual field inspection with mobile applications (Ngoc et al., 2023). They have developed embedded technology for monitoring soil nutrients, moisture, organics, Matara, and clay parameters. Different techniques are used to link the sensor located in the diverse places of the farmland. The sensor data were continuously recorded utilizing Wireless Fidelity (Wi-Fi), Low-Power Wide-Area Network (LPWAN), Long Range (LoRa), and Bluetooth before broadcasting to the base station (Nedham & Al-Qurabat, 2023). This method helps lower the agricultural costs related to labor and other expenses.

Jain et al. (2023) studied soil monitoring systems using IoT technology, showing that automatic irrigation is used in agriculture. They have built a system architecture for soil monitoring and controlling irrigation using IoT technique, where the different sensors and actuators like humidity, soil moisture, temperature, and pump are connected with a node microcontroller unit and message queuing telemetry transport (MQTT) protocol for enhancing communication capabilities. The sensor data is displayed on a PC or mobile phone through wireless communication and an IoT cloud platform. Luo and Pu (2024) have used the Underground Internet of Things (UIoT) for soil monitoring using ultra-high-frequency (UHF) radio energy. The UIoT nodes utilize harvested energy to measure soil parameters and transmit data to the Unmanned aerial vehicle (UAV) via the ZigBee protocol. Once the data is collected from the UIoTs, the UAV uploads it to a cloud server for real-time soil quality analysis. Sumarsono et al. (2024) have used an IOT webserver android and machine learning approach to monitor the soil PH factor.

Multiple sensors were used to monitor soil parameters like pH-moisture, Temperature-Humidity, and Sunlight. Arduino Uno microcontroller for serial communication with the ESP 8266 microcontroller for the Wi-Fi module was used for sensor data collection. The collected data was monitored using the web application containing a MySQL database and a local web page. Some of the research has shown that in-house crop monitoring has involved different technologies such as sensor modules, communication, web servers, and controllers, which provide the moisture content and temperature of the soil in hand (Obaideen et al., 2022; Rao & Sridhar, 2018). Based on this monitoring system, an automated watering system and ingredients can be provided to the soil to improve crop growth.

In recent years, Internet of Things (IoT) technologies have developed a system for plants for life, where the automated care of potted plants improves the air quality and makes the indoor environment healthier (Guerrero-Ulloa et al., 2023). Most in-house systems rely on manual temperature and humidity monitoring, which can be inconvenient for personnel who are required to visit the greenhouse daily and manually control it. Riskiawan et al. (2024) have automated the process using the Internet of Things (IoT) and artificial intelligence systems to independently predict and control IoT devices. Also, the intelligent platform based on IoT and low-cost wireless sensors based on radio frequency communication for collecting and sending greenhouse data like temperature, humidity, and soil moisture is used for smart and optimum management of in-house irrigation (Benyezza et al., 2023). Wireless Sensor Network (WSN)--based Internet of Things (IoT) networks are used for clustering methods to optimize energy efficiency while collecting the sensor node data (Mohammed et al., 2022; Nedham & Al-Qurabat, 2022). Furthermore, the author has discussed the agricultural challenges while collecting field data, such as soil conditions and meteorological data locally to accelerate the adoption of appropriate decisions that help the growth of the product (Al-Qurabat et al., 2021; Al-Qurabat et al., 2022). Also, the position of the sensor and the efficient way of collecting the data is another challenging task. Thus, recent studies have shown that it is possible to collect data in an efficient way to improve agriculture environmental conditions using IoT and WSN (Al-Qurabat, 2022).

Nowadays, most plant monitoring systems consider internet-enabled microcontrollers with sensor units leading to soil parameters and crop yield; in one of the recent developments, Message Queue Telemetry Transport (MQTT) protocol was used to transfer the sensor data to a remote server instead of using Hyper Text Transfer Protocol (HTTP). MQTT has been designed to be lightweight and efficient, which makes it ideal for bandwidth-limited real-time applications. Also, it uses the publish-subscribe model, which reduces the data transfer size and makes it ideal for IoT-based applications (Morchid et al., 2024; Min & Park, 2018; Kodali & Sarjerao, 2017).

Further, compared to conventional farming, smart and precision farming produces higher productivity at a lower cost. It requires the proper communication methods and online interfaces for efficient improvement in smart framing systems. Hence, the MQTT is used to communicate with the Node.js server worker. The system directly processes data from numeric image feeds and images. The server would store all received data, including numeric data and live feeds, for future use (Turnip et al., 2023). Also, the author has used monitoring soil properties, like soil pH, electrical conductivity, soil humidity, and temperature, through cloud MQTT (Aarthi & Sivakumar, 2023), which has shown an effective way of communicating with field data.

In addition, IoT systems may have limitations in terms of scalability, making it difficult to deploy them across large agricultural fields or indoor environments with numerous

plants. In environments with poor network coverage or interference, such as indoor spaces with thick walls, connectivity issues may arise, leading to data transmission failures or delays. The accuracy and reliability of IoT sensors can vary, leading to discrepancies in the collected data. Factors such as sensor calibration, environmental conditions, and sensor degradation over time can affect data accuracy and reliability. Implementing an IoT-based soil monitoring system requires an initial investment in hardware, software, and infrastructure setup, which may be prohibitive for some users, especially small-scale in-house farming. The in-house plantation data monitoring lacks real-time, comprehensive monitoring systems that can continuously track key soil parameters where the plants are grown in the closed area. Current methods often rely on manual data collection, which can be time-consuming, need continuous observation, and are prone to human error. Additionally, existing monitoring systems may not provide sufficient data granularity or frequency, limiting the ability to detect subtle changes in soil conditions. As a result, there is a need for more advanced, automated monitoring solutions that leverage IoT technology to provide continuous, high-resolution data collection and analysis for optimal plant growth and resource management.

The study investigates soil suitability for indoor plant growth by employing IoT technology as a novel method used to assess real-time soil data. Real-time sensors, including those for temperature and soil moisture, were utilized to monitor soil conditions. Data collected from these sensors was transmitted to an MQTT broker and stored in a MySQL database. Node-RED was employed to develop a monitoring system with low-code capabilities, enabling analysis of soil parameters for optimal plant growth in an indoor environment. This approach offers a cost-effective solution that can be implemented in farms or homes to enhance crop irrigation efficiency, minimize water usage, and optimize plant growth.

METHODOLOGY

The study was designed to investigate plants' indoor growth using IoT technology. It involved designing an experimental setup where internet-connected devices and technologies could monitor and manage the growth of plants in an indoor environment. The design focused on creating a controlled and automated system that could provide optimal conditions for plant growth, including soil type, pot size, and environmental factors. The study was carried out by setting up an experimental environment where plants could be grown indoors under controlled conditions (i.e., indoor air conditioner room). Various soil types with different grain sizes were used to determine their impact on plant growth. Different pots or containers were also selected to assess their effect on soil moisture retention and plant growth. IoT devices were installed to monitor and collect data on environmental parameters such as temperature, humidity, and soil moisture levels.

The data collected from the IoT devices were analyzed to assess the growth of plants under different soil conditions. Based on these variables, the collected data analyzed the effect of soil and indoor room conditions on plant growth. Additionally, correlations between environmental parameters and plant growth were examined to understand the factors influencing indoor plant growth. Overall, the data analysis aimed to provide insights into the optimal indoor conditions for indoor growing plants using IoT technology.

Layout of Soil

Adopting a systematic and careful approach is necessary to create an environment for controlled plant growth in pots. Based on the plant's requirement and its intention to grow in a controlled environment, they are arranged in such a way as to influence soil factors. It will ensure consistency and fairness in the experiment, which can provide uniform growing conditions for all plants. The pots used in the current process are transparent polyethylene terephthalate (PET) bottles, which can help monitor and easily arrange the sensor per the requirements. Each pot was equipped with equal drainage holes made using identical drill bits. Proper drainage is crucial for preventing waterlogging and root rot. The soil used in the pots was divided into four layers, emphasizing maintaining consistent granule size and volume for each layer in every pot. This standardization helps ensure that each plant has access to the same amount and type of soil. The use of a layering technique in the present work demonstrates a thoughtful approach to replicating natural growing conditions for the proposed plants. With objectives of effective drainage and aeration by prioritizing the primary goal to create a soil structure that would facilitate optimal drainage and aeration for the plants. These factors are crucial for preventing issues like root rot and ensuring that the roots receive sufficient oxygen by dividing the soil into distinct layers based on granule size. This approach allows us to control the characteristics of each layer to meet plants' specific needs by employing a manual multi-level sieving process to separate soil based on its size. This process involved using various sieve sizes one at a time to isolate materials with specific granule sizes.

The paces followed for arranging the pot with sieved soil have four sieved soils. There were 2.36 mm sieves used to filter soil into two layers, and after the sieve, it was left with more prominent granules in the sieve, and the large size granules for the bottom were settled. Mid-size granules were sieved soil and were used for a second from the bottom layer. The soil was sieved again with a sieve size of 1.18 mm, and the soil left in the sieve was used for the third layer from the bottom, and the top layer had fine soil added into the transparent bottle. Four sets with dimensions of 8cm height and 5.6 cm diameter, as well as an overall volume of 217.5 cm size bottles, were used for the experiment. One of the bottles with soil of different granular sizes is displayed in Figure 1.

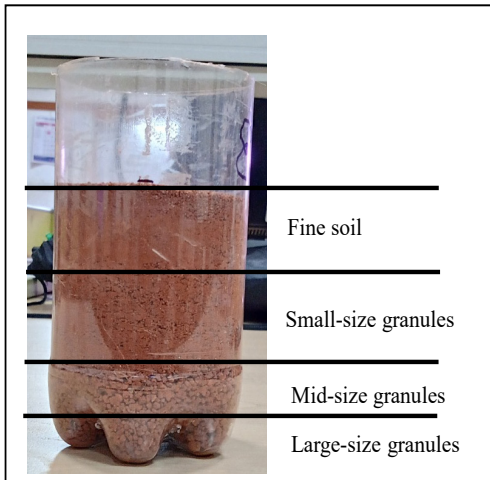


Figure 1. Soil profile after layering

Sensor and IoT Monitoring System

The virtual and real circuit connection for monitoring the soil parameters is shown in Figure 2. Four sets of temperature and moisture sensors connected to an Arduino UNO board could access continuous soil data. The setup consists of four sets of Dallas Semiconductor DS1820b sensors and a Digital Temperature and Humidity Sensor DHT11, which measures the temperature and soil moisture. A resistor is required between the power and data line of the DS1820b sensor for proper functioning, which is why four resistors were used. The

four analog capacitive moisture sensors were connected to four pins, with Analogue to Digital Converter (ADC) inputs enabled on the ESP32. In the case of the Arduino UNO board, the analog sensors would be connected to the analog pins, and the DS1820b sensors would be connected to digital pins, respectively.

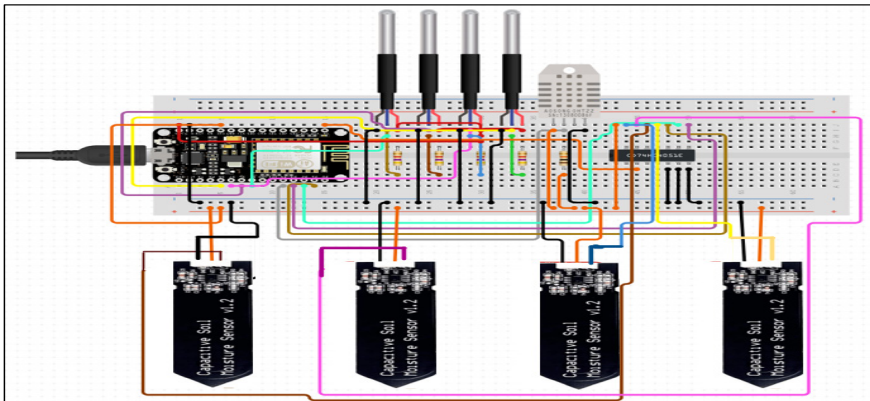
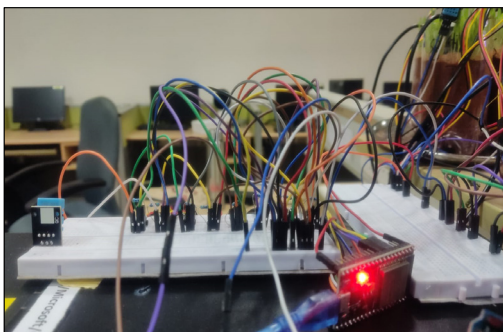


Figure 2. The virtual and real circuit connections are used to monitor the soil parameters.



The overall flowchart of the soil monitoring system is depicted in Figure 3 shows. The data collecting system is assembled with sensors and a controller, integrating the nodes with the database and dashboard. The sensor sends the soil

temperature and moisture to the ESP32 controller and then publishes those data through the MQTT protocol. Once sensor data is in the MQTT protocol, which can help push it to any other platform, node-RED is subscribed to access the sensor data. The IP address of the MQTT broker must be provided to the “MQTT-in” node to subscribe to node RED. The values received from these sensors are then connected to “graph” and “gauge” nodes, which allows visualization of these values using the dashboard.

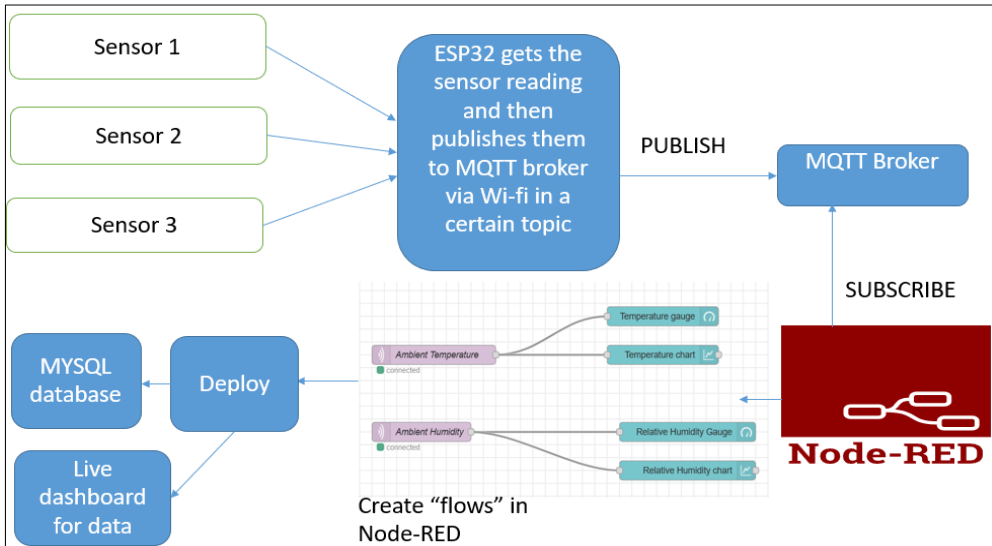


Figure 3. Flowchart used in the soil monitoring system

The nodes used in the Node-RED subscriber are displayed in Figure 4. Additionally, the data from these sensors are combined into a single string separated by a chosen delimiter, a comma mark. The data is joined to send the collected data to a MySQL database, which runs as a service on the computing device. SQL queries must be made in such a way that the entire table must get updated at the same instance to avoid null values in the table.

The data collected at varying times with short delay due to functional programming in Arduino Integrated Development Environment (IDE) is joined into a single string separated by a comma mark using the join node previously configured. This string is then fed into a JavaScript function node, where JavaScript code is written to split the joined data into an array of strings. These strings in the array then become the values to be updated into the columns of the table. The SQL query is then written in the function node and fed into the “MySQL” node in node-RED to update the table. Thus, it ensures that the data collected from the sensors is stored in the table. The debug nodes are used to debug and check queries. The email node is configured along with a JavaScript function node to send an email notifying the soil moisture percentage going below a threshold that can be adjusted

by the user in the JavaScript function node. Finally, the accuracy of the sensors should be checked regularly, and any necessary calibrations or replacements should be executed. Ascertain that the IoT system is functioning properly.

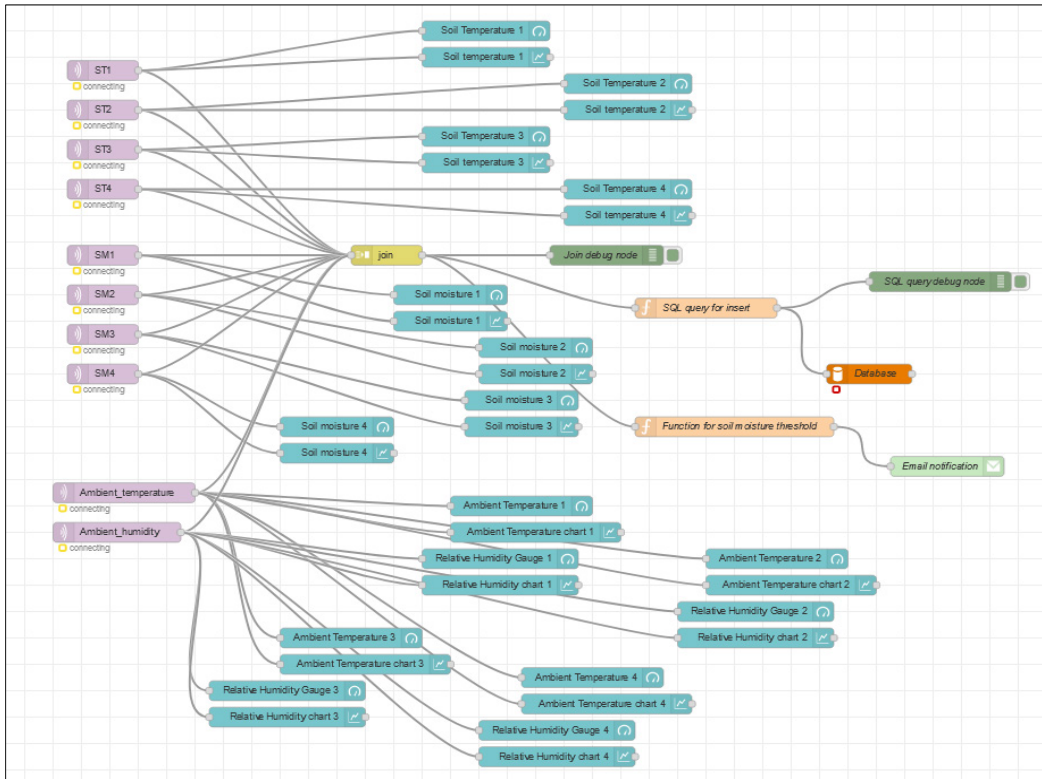


Figure 4. The node-RED flow is used to connect the sensors to the database

RESULTS AND DISCUSSION

The subsequent discussion provides an in-depth exploration of soil health and its profound impact on plant growth. The IoT system adeptly monitored soil moisture levels and temperature throughout four quarters of the day. The output of this monitoring system was meticulously crafted using Node-RED, and it was seamlessly connected to the Mosquitto MQTT broker as a subscriber. Sensors interfaced with the ESP32 microcontroller diligently published the readings acquired from the soil sensors to MQTT topics, meticulously configured within the Arduino code programmed into the microcontroller. These MQTT topics were then subscribed to by Node-RED using specialized "MQTT-in" nodes, configured with precise details, including the MQTT broker's IP address, the port used for connection, and other crucial parameters such as Quality of Service and Transport Layer Security (TLS). Upon reception, the data from these sensors were intelligently amalgamated

into a cohesive string, precisely separated by a selected delimiter, typically a comma, leveraging the functionality of the "join" node within Node-RED. The configuration of the join node ensured that the string output was synchronized with the reception of all individual messages, a process facilitated by setting the join node to a "manual" mode within its configuration settings. The chosen delimiter and formatting specifications, such as a string separated by commas, were carefully configured within the "join" node.

Figure 5 vividly demonstrates the culmination of this accurate data processing effort, showcasing the dashboard output of the soil parameters monitoring system. Here, a comprehensive array of data is presented, including soil temperature, moisture levels, ambient temperature, and relative humidity, captured by four distinct sets of sensors housed within different containers. Each container hosts four sensors, transmitting continuous data streams to the dashboard interface for real-time monitoring and analysis.

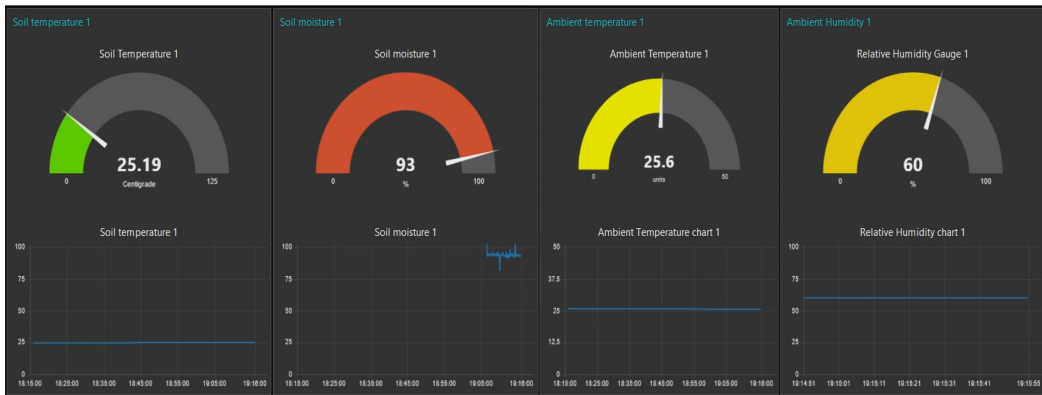


Figure 5. The dashboard for monitoring the soil parameters

The sensor data is carefully collected column-wise and elegantly displayed through the MySQL node, as showcased in Table 1. The abbreviations "ST" and "SM" in the table aptly denote soil temperature and soil moisture, respectively. Notably, the column designated as the serial number is crucial for the primary key in the MySQL table. Primary keys serve as unique identifiers for individual rows within the table, necessitating that they remain non-null and distinct. Consequently, the serial number column is thoughtfully configured to automatically increment upon data insertion into the table, ensuring the dataset's uniqueness and integrity. With the sensor data seamlessly integrated into the MySQL database, real-time updates are effortlessly captured and reflected as time progresses. A noteworthy observation emerges from the dataset: all four temperature sensors exhibit nearly identical readings for soil temperature, closely mirroring ambient temperature fluctuations. Conversely, the soil humidity readings consistently register marginally higher values compared to ambient humidity levels. This accurate synchronization of sensor data underscores the accuracy

and reliability of the recorded information, further reaffirming the seamless functionality of IoT devices in capturing and presenting essential environmental parameters.

The sensor data is collected column-wise and displayed through the MySQL node displayed in Table 1. ST and SM abbreviations stand for soil temperature and soil moisture, respectively. The serial number column was chosen as the primary key in the MySQL table. Primary keys are used to identify the rows in the table; hence, they cannot be null while also being unique. Hence, the serial number column was chosen to be auto-increased upon data insertion into the table. The sensor data is received and automatically updated in the MySQL database as time passes. It is noticed that all four temperature sensors update soil temperature nearly the same as ambient temperature. At the same time, the humidity of the soil is slightly higher than that of the ambient humidity. It proves that data recorded by sensors and displayed on the dashboard through IoT devices are synchronized properly.

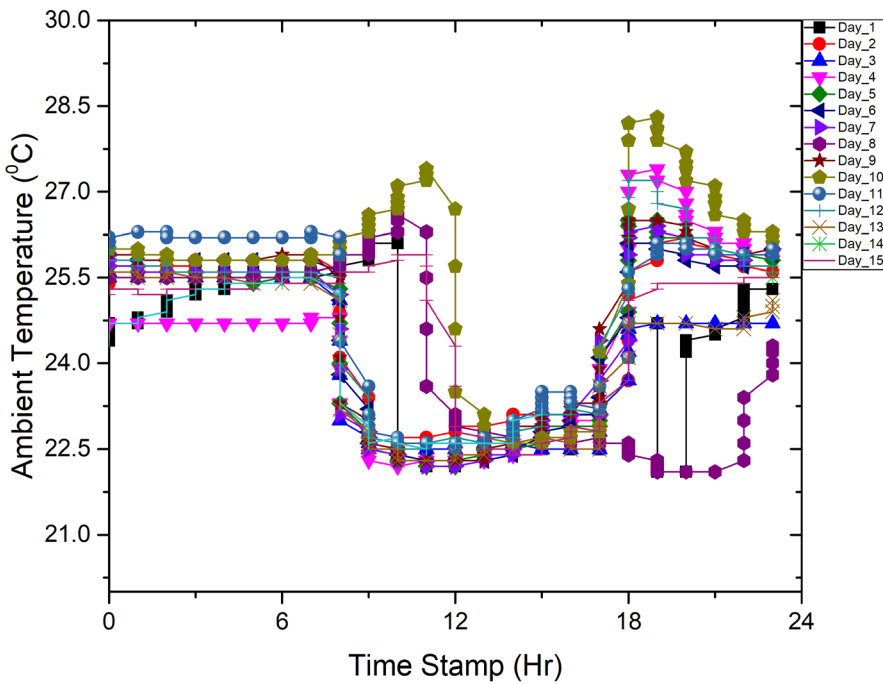
Table 1
MySQL node data collected from sensors

<i>ST1</i>	<i>ST2</i>	<i>ST3</i>	<i>ST4</i>	<i>SM1</i>	<i>SM2</i>	<i>SM3</i>	<i>SM4</i>	<i>AH</i>	<i>AT</i>
22.56	22.69	22.13	20.56	87	69	70	96	65	22.3
22.56	22.69	22.19	20.56	86	69	70	96	65	22.3
22.56	22.69	22.13	20.62	86	69	71	89	65	22.3
22.50	22.69	22.13	20.62	86	70	71	97	65	22.4
22.56	22.69	22.13	20.56	86	70	70	96	65	22.4
22.56	22.69	22.13	20.56	87	69	71	97	65	22.4
22.56	22.69	22.06	20.56	86	69	71	98	65	22.4
22.56	22.69	22.06	20.62	86	69	71	97	65	22.3
22.50	22.69	22.13	20.56	86	69	70	95	65	22.3
22.50	22.69	22.13	20.62	86	69	71	97	65	22.4
22.56	22.69	22.13	20.56	87	69	71	96	65	22.3
22.56	22.69	22.13	20.56	87	69	70	97	65	22.4
22.50	22.69	22.13	20.62	87	68	70	97	65	22.3
22.56	22.69	22.13	20.56	86	69	73	97	65	22.3
22.50	22.69	22.13	20.62	87	69	71	97	64	22.3
22.50	22.69	22.13	20.56	86	68	71	96	65	22.3
22.50	22.69	22.06	20.62	87	69	70	97	64	22.3
22.50	22.69	22.06	20.62	86	69	70	97	64	22.3

The ambient temperature and moisture fluctuations over four quarters across all days are particularly delineated into six-hour intervals, as illustrated in Figures 6(a) and (b). In the first quarter, ambient temperature remains relatively stable, attributed to the cessation of air conditioning within the indoor environment. Subsequently, during the second quarter, a noticeable decline in ambient temperature is observed, coinciding with the activation

of the air conditioning system. Quarter 3 unveils an intriguing trend discernible from the graph. On select days, the efficacy of the air conditioning appears diminished, resulting in comparatively elevated temperatures. Notably, a temperature surge is evident around 5 pm, coinciding with the deactivation of the air conditioning system, as depicted in the ambient temperature graph. Moreover, the moisture levels in the environment closely mirror the ambient temperature trend. While the pot remains in the air-conditioned room, the moisture content during early mornings and late evenings hovers between 60% and 65% on varying days. A noteworthy observation emerges from the impact of air conditioning on humidity levels. During the second and third quarters of the day, when the air conditioning is operational, the dry air circulated within the room effectively diminishes heat and humidity. This process entails the refrigerant absorbing heat and moisture from the indoor air, thereby leading to a discernible reduction in room humidity during daytime, as evident in Figure 6(b).

The four pots are equipped with individual soil temperature and moisture sensors, continuously transmitting data throughout a 15-day experimental period. The study reveals that all sensors exhibit closely aligned variations in soil temperature. Soil temperature remains consistent when air conditioning is inactive in the first and fourth quarters. Conversely, a decline in soil temperature is observed during the activation of



(a)

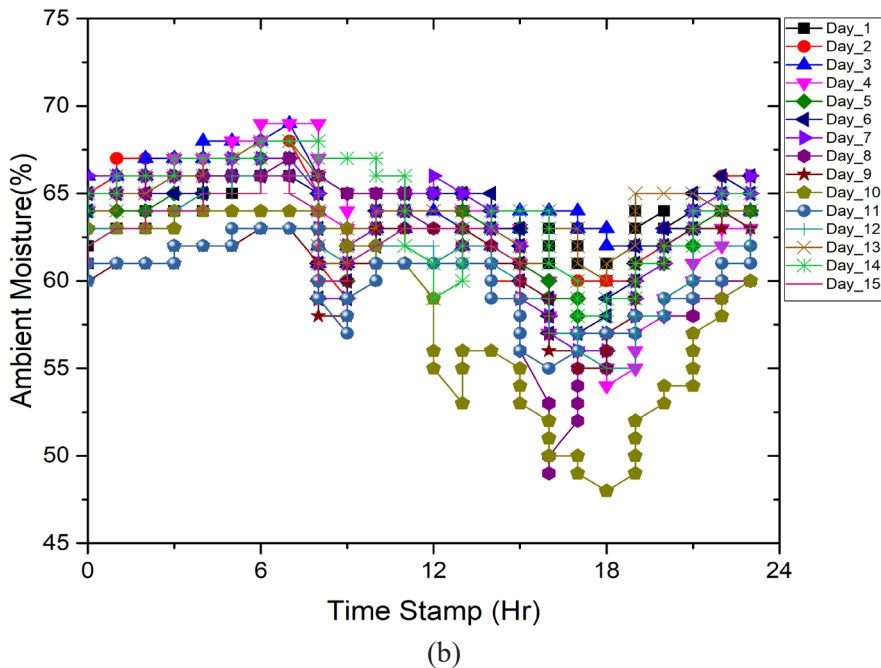


Figure 6. The variation of (a) Ambient temperature and (b) Ambient Moisture

air conditioning, typically occurring between 9 am and 6 pm. Figure 7 illustrates the comprehensive pattern of soil temperature fluctuations over a full day. Notably, a distinct decrease in soil temperature is evident during quarters two and three, attributed to the cooling effect induced within the soil. Subsequently, as air conditioning ceases in the room, soil temperature stabilizes from the third quarter onwards. This stabilization is followed by a temperature rise in the fourth quarter, aligning with ambient temperature.

The subplot depicted in Figure 7 highlights a three-degree Celsius reduction in soil temperature during quarters two and three over the 15 days. Such temperature variations hold promise for enhancing in-house plant growth.

Additionally, soil moisture plays a crucial role in herb growth. Throughout the day, soil moisture levels exhibit an average increase ranging from 60 to 90% compared to ambient moisture levels. Figure 8(a) provides an overview of the average soil moisture data recorded by all sensors. The consistent maintenance of soil moisture within this range throughout the day is a positive indication that the necessary nutrients for plant growth are evenly distributed. Hourly variations in soil moisture content are depicted in Figures 8(b) and 8(c) subplots. These variations, ranging from 2 to 4%, highlight the need for proactive measures to prevent soil moisture depletion and subsequent plant dryness. Quarters two and three consistently exhibit lower moisture levels compared to other periods of the day.

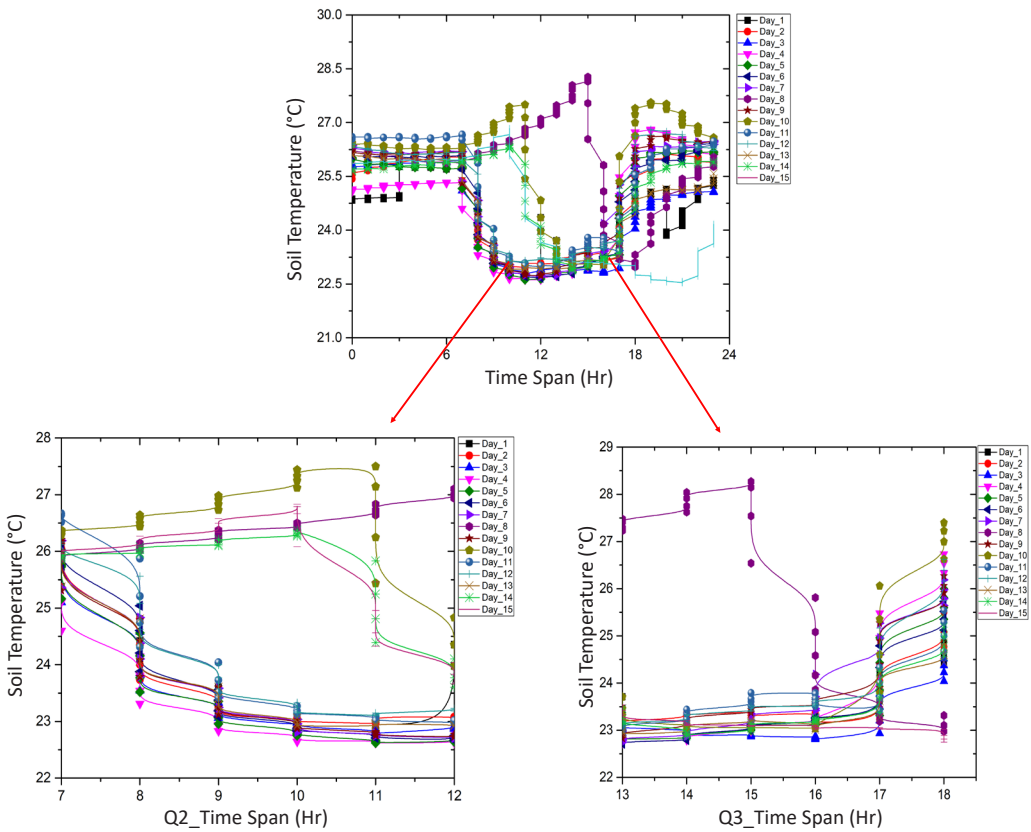
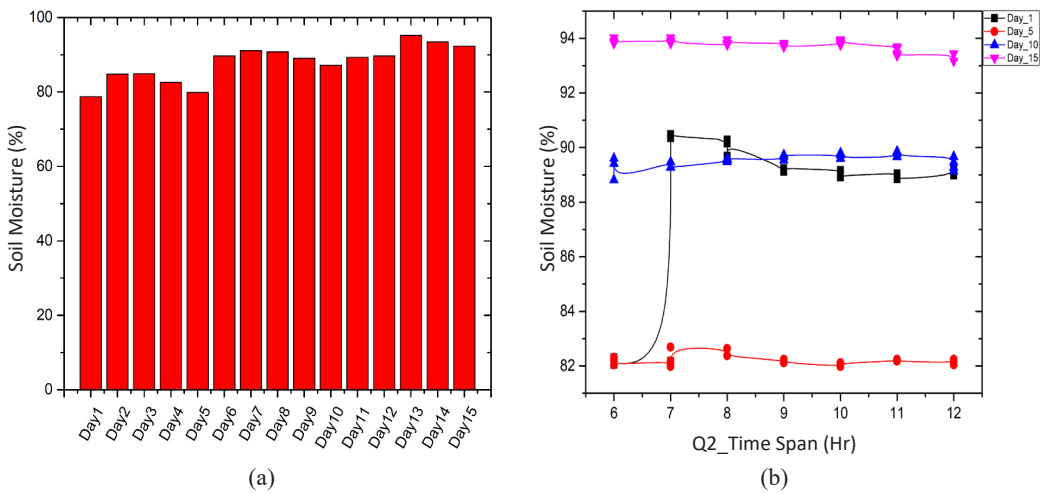


Figure 7. The soil temperature is monitored via a sensor and IoT gateway



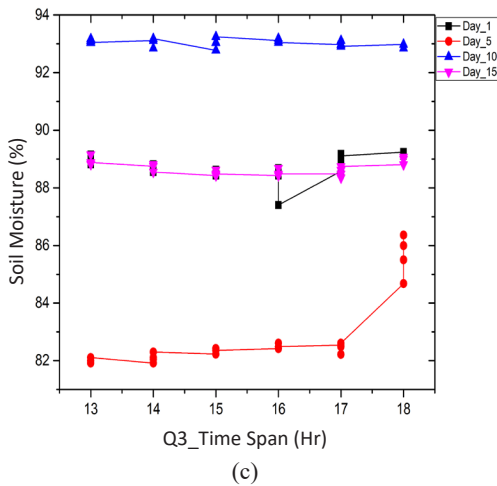


Figure 8. Illustrates the recoded soil moisture data for all the days

enables growers and cultivators to make informed decisions that improve soil health, resulting in more successful and long-term in-house plant growth. Assembling recent technology such as ESP32, node-RED, and MQTT protocol to record soil factors leads to estimating in-house plantation. The different grain sizes of soil were considered for monitoring soil temperature and moisture for crop growth. The four sensor data sets were stored in a MySQL table using the “MySQL” through node-RED subscriber. The “email” node was used to send email notifications regarding the soil moisture to a user-specified email address. The temperature and moisture were recorded throughout the day, lasting six hours of four quarters for fifteen days. Also, the study divides the day into quarters, collecting soil data from various layers using temperature and moisture sensors. An in-house experiment showed that the temperature of 30C was reduced during the day due to air conditioning operation. The soil's moisture has changed to a 50% increment as the day proceeds. Further, soil conditions were displayed continuously through a dashboard, which helped to emphasize remote management via IoT in situations when physical access to plants is limited, promoting efficient resource usage in indoor gardening.

ACKNOWLEDGMENTS

The authors extend their gratitude to the Department of Mechatronics at Manipal Institute of Technology, Manipal, India for their invaluable support and provision of facilities, which were instrumental in successfully implementing this work.

The sensors' consistent detection of soil moisture variations underscores their reliability. Moisture levels within the potting bags remain between approximately 75% and 95%, reflecting the soil's water-holding capacity. Continuously monitoring soil moisture and temperature throughout the day and over extended periods can significantly enhance plant growth potential by optimizing soil conditions.

CONCLUSION

Monitoring soil parameters with IoT technology effectively improves soil health and promotes healthy plant growth. It

REFERENCES

- Aarathi, R., & Sivakumar, D. (2023). Internet of things based on field soil property prediction system: For optimally monitoring the soil fertility status. In *Internet of Things* (pp. 143-154). Chapman and Hall/CRC.
- Abbasi, R., Martinez, P., & Ahmad, R. (2022). The digitization of agricultural industry – A systematic literature review on agriculture 4.0. *Smart Agricultural Technology*, 2, Article 100042. <https://doi.org/10.1016/J.ATECH.2022.100042>
- Al-Omary, A., Alsabbagh, H. M., & Al-Rizzo, H. (2018). Cloud based IoT for smart garden watering system using Arduino uno. *Smart Cities Symposium*, 1–6. <https://doi.org/10.1049/cp.2018.1401>
- Al-Qurabat, A. K. M. (2022). A lightweight huffman-based differential encoding lossless compression technique in IoT for smart agriculture. *International Journal of Computing and Digital Systems*, 11(1), 117–127. <https://doi.org/10.12785/IJCDS/110109>
- Al-Qurabat, A. K. M., Mohammed, Z. A., & Hussein, Z. J. (2021). Data traffic management based on compression and MDL techniques for smart agriculture in IoT. *Wireless Personal Communications*, 120(3), 2227–2258. <https://doi.org/10.1007/S11277-021-08563-4>
- Al-Qurabat, A. K. M., Salman, H. M., & Finjan, A. A. R. (2022). Important extrema points extraction-based data aggregation approach for elongating the WSN lifetime. *International Journal of Computer Applications in Technology*, 68(4), 357–368. <https://doi.org/10.1504/IJCAT.2022.125182>
- Benyezza, H., Bouhedda, M., Kara, R., & Rebouh, S. (2023). Smart platform based on IoT and WSN for monitoring and control of a greenhouse in the context of precision agriculture. *Internet of Things*, 23, Article 100830. <https://doi.org/10.1016/J.IOT.2023.100830>
- Bittner, B., Aslan, I., Dang, C. T., & André, E. (2019). Of smarthomes, IoT plants, and implicit interaction design. In *TEI 2019 - Proceedings of the 13th International Conference on Tangible, Embedded, and Embodied Interaction* (pp. 145–154). ACM Publishing. <https://doi.org/10.1145/3294109.3295618>
- Dhanaraju, M., Chenniappan, P., Ramalingam, K., Pazhanivelan, S., & Kaliaperumal, R. (2022). Smart farming: Internet of Things (IoT)-based sustainable agriculture. *Agriculture*, 12(10), Article 1745. <https://doi.org/10.3390/AGRICULTURE12101745>
- Guerrero-Ulloa, G., Méndez-García, A., Torres-Lindao, V., Zamora-Mecías, V., Rodríguez-Domínguez, C., & Hornos, M. J. (2023). Internet of Things (IoT)-based indoor plant care system. *Journal of Ambient Intelligence and Smart Environments*, 15(1), 47–62. <https://doi.org/10.3233/AIS-220483>
- Jain, R. K., Mukherjee, A., Karmakar, P., Banerjee, A., Akbarov, H., & Hasanov, S. (2023). Experimental performance of soil monitoring system using IoT technique for automatic drip irrigation. *International Journal of Communication Systems*, 36(18), Article e5617. <https://doi.org/10.1002/DAC.5617>
- Kassim, M. R. M. (2020). IoT applications in smart agriculture: Issues and challenges. In *2020 IEEE conference on open systems (ICOS)* (pp. 19-24). IEEE. <https://doi.org/10.1109/ICOS50156.2020.9293672>
- Kodali, R. K., & Sarjerao, B. S. (2017, July). A low cost smart irrigation system using MQTT protocol. In *2017 IEEE Region 10 Symposium (TENSYMP)* (pp. 1-5). IEEE Publishing. <https://doi.org/10.1109/TENCONSpring.2017.8070095>

- Luo, Y., & Pu, L. (2024). UAV Remotely-powered underground IoT for soil monitoring. *IEEE Transactions on Industrial Informatics*, 20(1), 972–983. <https://doi.org/10.1109/TII.2023.3272016>
- Min, B., & Park, S. J. (2018). A smart indoor gardening system using IoT technology. *Lecture Notes in Electrical Engineering*, 474, 683–687. https://doi.org/10.1007/978-981-10-7605-3_110
- Mohammed, A., Abdulzahra, K., Kadhum, A., Al-Qurabat, M., Abdulzahra, A. M., Kadhim, A. Q., & Abdulzahra, A. M. K. (2022). A clustering approach based on fuzzy C-means in wireless sensor networks for IoT applications. *Karbala International Journal of Modern Science*, 8(4), 579–595. <https://doi.org/10.33640/2405-609X.3259>
- Morchid, A., El Alami, R., Raetzah, A. A., & Sabbar, Y. (2024). Applications of internet of things (IoT) and sensors technology to increase food security and agricultural Sustainability: Benefits and challenges. *Ain Shams Engineering Journal*, 15(3), Article 102509. <https://doi.org/10.1016/J.ASEJ.2023.102509>
- Nedham, W. B., & Al-Qurabat, A. K. M. (2023). A review of current prediction techniques for extending the lifetime of wireless sensor networks. In *International Journal of Computer Applications in Technology* (Vol. 71, Issue 4, pp. 352–362). Inderscience Publishers. <https://doi.org/10.1504/IJCAT.2023.132401>
- Nedham, W. B., & Al-Qurabat, A. K. M. (2022). An improved energy efficient clustering protocol for wireless sensor networks. In *2022 International Conference for Natural and Applied Sciences (ICNAS)* (pp. 23–28). IEEE. <https://doi.org/10.1109/ICNAS55512.2022.9944716>
- Ngoc, T. T. H., Khanh, P. T., & Pramanik, S. (2023). Smart agriculture using a soil monitoring system. In *Handbook of Research on AI-Equipped IoT Applications in High-Tech Agriculture* (p. 21). IGI Global. <https://doi.org/10.4018/978-1-6684-9231-4.CH011>
- Nguemezi, C., Tematio, P., Yemefack, M., Tsozue, D., & Silatsa, T. B. F. (2020). Soil quality and soil fertility status in major soil groups at the Tombel area, South-West Cameroon. *Heliyon*, 6(2), Article e03432. <https://doi.org/10.1016/j.heliyon.2020.e03432>
- Obaideen, K., Yousef, B. A. A., Almallahi, M. N., Chai Tan, Y., Mahmoud, M., Jaber, H., & Ramadan, M. (2022). An overview of smart irrigation systems using IoT. *Energy Nexus*, 7, Article 100124. <https://doi.org/10.1016/j.nexus.2022.100124>
- Pechlivani, E. M., Papadimitriou, A., Pemas, S., Ntinis, G., & Tzovaras, D. (2023). IoT-based agro-toolbox for soil analysis and environmental monitoring. *Micromachines*, 14(9), Article 1698. <https://doi.org/10.3390/M14091698>
- Prathibha, S. R., Hongal, A., & Jyothi, M. P. (2017). IOT based monitoring system in smart agriculture. In *2017 International Conference on Recent Advances in Electronics and Communication Technology (ICRAECT)* (pp. 81-84). IEEE Publishing. <https://doi.org/10.1109/ICRAECT.2017.52>
- Rao, R. N., & Sridhar, B. (2018, January). IoT based smart crop-field monitoring and automation irrigation system. In *2018 2nd International Conference on Inventive Systems and Control (ICISC)* (pp. 478-483). IEEE Publishing. <https://doi.org/10.1109/ICISC.2018.8399118>
- Riskiawan, H. Y., Gupta, N., Setyohadi, D. P. S., Anwar, S., Kurniasari, A. A., Hariono, B., Firmansyah, M. H., Yogiswara, Y., Mansur, A. B. F., & Basori, A. H. (2024). Artificial intelligence enabled smart monitoring and controlling of IoT-green house. *Arabian Journal for Science and Engineering*, 49(3), 3043–3061. <https://doi.org/10.1007/S13369-023-07887-6>

- Sheth, M., & Rupani, P. (2019). Smart gardening automation using IoT with BLYNK App. In *2019 3rd International Conference on Trends in Electronics and Informatics (ICOEI)* (pp. 266-270). IEEE Publishing. <https://doi.org/10.1109/ICOEI.2019.8862591>
- Specht, K., Siebert, R., Hartmann, I., Freisinger, U. B., Sawicka, M., Werner, A., Thomaier, S., Henckel, D., Walk, H., & Dierich, A. (2014). Urban agriculture of the future: An overview of sustainability aspects of food production in and on buildings. *Agriculture and Human Values*, *31*, 33–51. <https://doi.org/10.1007/s10460-013-9448-4>
- Sumarsono, Afiatna, F. A. N. F., & Muffihah, N. (2024). The monitoring system of soil pH factor using IoT-webserver-android and machine learning: A case study. *International Journal on Advanced Science, Engineering, and Information Technology*, *14*(1), 118–130. <https://doi.org/10.18517/IJASEIT.14.1.18745>
- Turnip, A., Pebriansyah, F. R., Simarmata, T., Sihombing, P., & Joelianto, E. (2023). Design of smart farming communication and web interface using MQTT and Node.js. *Open Agriculture*, *8*(1), Article 20220159. <https://doi.org/10.1515/OPAG-2022-0159>
- Xu, J., Gu, B., & Tian, G. (2022). Review of agricultural IoT technology. *Artificial Intelligence in Agriculture*, *6*, 10–22. <https://doi.org/10.1016/J.AIIA.2022.01.001>

Evaluating Convolutional Neural Network Architecture for Historical Topographic Hardcopy Maps Analysis: A Study on Training and Validation Accuracy Variation

Saiful Anuar Jaafar¹, Abdul Rauf Abdul Rasam^{1,2} and Norizan Mat Diah^{3*}

¹Centre of Studies Surveying Science and Geomatics, College of Built Environment, Universiti Teknologi MARA, Shah Alam, Selangor, Malaysia

²Malaysia Institute of Transport (MITRANS), Universiti Teknologi MARA, Shah Alam, Selangor, Malaysia

³School of Computing Sciences, College of Computing, Informatics and Mathematics, Universiti Teknologi MARA, Shah Alam, Selangor, Malaysia

ABSTRACT

Convolutional Neural Networks (CNN) are widely used for image analysis tasks, including object detection, segmentation, and recognition. Given the advanced capability, this study evaluates the effectiveness and performance of CNN architecture for analysing Historical Topographic Hardcopy Maps (HTHM) by assessing variations in training and validation accuracy. The lack of research specifically dedicated to CNN's application in analysing topographic hardcopy maps presents an opportunity to explore and address the unique challenges associated with this domain. While existing studies have predominantly focused on satellite imagery, this study aims to uncover valuable insights, patterns, and characteristics inherent to HTHM through customised CNN approaches. This study utilises a standard CNN architecture and tests the model's performance with different epoch settings (20, 40, and 60) using varying dataset sizes (288, 636, 1144, and 1716 images). The results indicate that the optimal operation point for training and validation accuracy is achieved at epoch 40. Beyond epoch 40, the widening gap between training and validation accuracy suggests overfitting. Hence, adding more epochs does not significantly

improve accuracy beyond the optimum phase. The experiment also shows that the CNN model obtains a training accuracy of 98%, validation accuracy of 67%, and F1-score overall performance of 77%. The analysis demonstrates that the CNN model performs reasonably well in classifying instances from the HTHM dataset. These

ARTICLE INFO

Article history:

Received: 12 December 2023

Accepted: 10 July 2024

Published: 25 October 2024

DOI: <https://doi.org/10.47836/pjst.32.6.11>

E-mail addresses:

saifulanuar@uitm.edu.my (Saiful Anuar Jaafar)

rauf@uitm.edu.my (Abdul Rauf Abdul Rasam)

norizan289@uitm.edu.my (Norizan Mat Diah)

* Corresponding author

findings contribute to a better understanding of the strengths and limitations of the model, providing valuable insights for future research and refinement of classification approaches in the context of topographic hardcopy map analysis.

Keywords: Convolutional Neural Network (CNN), deep learning, feature map recognition, Historic Topographic Hardcopy Map (HTHM)

INTRODUCTION

The digitisation of archive collections by heritage and library institutions has led to the accessibility of vast amounts of historical data, including the topographic hardcopy maps. Existing methodologies in historical map analysis have traditionally relied on manual and semi-automatic procedures of feature extraction techniques for vectorisation. This process is often labour-intensive, time-consuming, and prone to subjectivity (Anuar et al., 2021). In contrast, CNNs offer the potential to automate and streamline the analysis process, especially in object detection. According to research in the field of CNNs, increasing the epoch number and the training dataset size can potentially enhance the accuracy of both training and validation (Althnian et al., 2021; Barry-Straume et al., 2018).

However, the influence of these factors on accuracy may be contingent upon various aspects, such as the specific dataset characteristics and the complexity of the problem at hand (Ali et al., 2021). The number of epochs plays a crucial role in the learning process of a CNN. By increasing the number of epochs, the model can iterate over the training dataset multiple times, enabling it to capture more intricate patterns and improve accuracy (Garbin et al., 2020; Kumar et al., 2024). Nonetheless, it is essential to strike a balance, as excessively high epoch numbers may lead to overfitting (Chauhan et al., 2018; Poojary et al., 2020). Overfitting occurs when the model becomes overly specialised in the training data and fails to generalise well to unseen data. Monitoring the validation accuracy during training is recommended to determine an optimal number of epochs. Once the validation accuracy plateaus or begins to decrease, further training may not yield substantial improvements (Dawson et al., 2023; Johny & Madhusoodanan, 2021).

The training dataset size also influences the CNN performance. Increasing the dataset size gives the model a more diverse set of examples, enhancing its ability to generalise and perform well on unseen data. However, ensuring that the dataset remains representative of the problem domain and encompasses an adequate range of variations and scenarios is essential. Acquiring or generating a more extensive dataset may entail additional costs and efforts, necessitating careful consideration of the available resources. Increasing the number of epochs and training dataset size generally positively impacts CNN accuracy (Kandel & Castelli, 2020). However, finding the optimal values requires empirical investigation and diligent monitoring of validation performance to prevent overfitting. Achieving the

best possible accuracy necessitates carefully balancing model complexity, computational resources, and data availability.

Thus, the evaluation results were presented, highlighting the CNN architecture performance on the HTHM dataset. The relationship between epoch variation, dataset size, and training and validation accuracy was analysed and discussed. The findings provide insights into the effectiveness of the CNN architecture for analysing HTHM and offer guidance for determining the optimal epoch value and dataset size for achieving satisfactory performance. This study aims to test the CNN architecture on the Historical Topographic Hardcopy Map (HTHM) dataset; thus, the objectives of this study are:

1. To review the CNN model structure on trained Historical Topographic Hardcopy Map dataset.
2. To evaluate the training and validation accuracy by varying the epoch on different dataset amounts.

By explicitly comparing the CNN approach to existing methodologies, the study contributes to the growing body of literature on computational methods for historical map analysis, offering insights into the strengths and limitations of CNNs and providing guidance for future research in this area.

BACKGROUND STUDY

While numerous studies have focused on using satellite imagery as the dataset for CNN-based research, this study stands out by utilising topographic hardcopy maps as the dataset's domain. This novel approach introduces a unique perspective in applying CNN, exploring the potential of extracting valuable information and insights from traditional cartographic representations. By shifting the focus from satellite imagery to topographic hardcopy maps, this research opens new avenues for leveraging CNN in geospatial analysis. It contributes to a broader understanding of the digital transformation in cartography and spatial data analysis.

Based on the available literature, a significant body of research has utilised CNN for analysing satellite imagery as their primary dataset in various domains, including remote sensing and geospatial analysis (Bhosle & Musande, 2022; Li et al., 2021). These studies have demonstrated the effectiveness of CNN in extracting meaningful information and patterns from satellite images, leading to advancements in fields such as land cover classification, object detection, and change detection. Audebert et al. (2019) introduced a deep-learning approach for hyperspectral data classification using CNNs. The proposed framework surpasses the limitations of traditional methods by leveraging the power of CNNs to capture both spatial and spectral information. The results highlight the effectiveness of CNNs in enhancing hyperspectral data analysis through improved classification accuracy and better utilisation of the rich information in hyperspectral images. Chen et al. (2016) and Sharifi et al. (2022) proposed a CNN-based method for accurate hyperspectral image

classification by leveraging its hierarchical representation learning capabilities. The study demonstrated the effectiveness of CNN in extracting discriminative features from complex hyperspectral data. This finding underscores the potential of CNN as a valuable tool for improving the analysis and classification of hyperspectral imagery. Ji et al. (2018) presented a 3D CNN-based method for deep feature extraction and classification of hyperspectral images. By harnessing CNN's hierarchical representation learning capabilities, the aim is to enhance the accuracy of hyperspectral image classification. Hamouda et al. (2020) demonstrated that smart feature extraction and classification of hyperspectral images using CNN improves classification accuracy while reducing computing time. Findings from Liu et al. (2020) demonstrate the effectiveness of CNN in extracting discriminative features from complex and high-dimensional hyperspectral data and focus on multi-label land cover classification using CNN for remote sensing images. The aim is to tackle the challenge of simultaneous classification of multiple land cover types from satellite imagery. The study achieved promising results by employing CNN to identify various land cover categories accurately. These findings highlight the potential of CNN in facilitating comprehensive land cover analysis in remote sensing applications.

For instance, Liu et al. (2020) and Dwivedi and Patil (2022) employed CNN for land cover classification using satellite imagery, achieving high accuracy in identifying different land cover classes. Guo et al. (2018) utilised CNN for object detection in satellite images, enabling the automated identification of specific objects, such as buildings, roads, and vegetation. Similarly, Li et al. (2020) employed CNN for change detection in satellite imagery, facilitating the identification of temporal changes in land cover over different periods. Based on this evidence, CNNs have gained popularity in Remote Sensing due to their effectiveness in handling various image analysis tasks.

However, concerning Geospatial and Digital Cartography (Geospatial Cartography), CNNs are also utilised for performing vectorisation through hardcopy maps, object classification, and image analysis. It highlights the versatile capabilities of CNNs in both Remote Sensing and Geographic Information Systems (GIS) domains, enabling the extraction of valuable information from various types of data sources and facilitating comprehensive spatial analysis. It is important to note that there appears to be limited research explicitly focusing on applying CNN in analysing topographic hardcopy maps as the dataset domain. While topographic maps are crucial in various fields, such as urban planning, environmental assessment, and infrastructure development, most existing studies have primarily focused on satellite imagery. Therefore, the study on CNN using topographic hardcopy maps as the dataset introduces a novel perspective to the field. By exploring the application of CNN in analysing topographic maps, the study will have the opportunity to address unique challenges and extract valuable insights specific to this domain. It includes identifying features, patterns, and characteristics inherent to topographic maps, which may require customised approaches for effective analysis and interpretation.

This study expands the scope of CNN applications in geospatial analysis and provides a valuable contribution to the field, focusing on topographic hardcopy maps. It fills a gap in the existing literature and opens avenues for further exploration, ultimately advancing the understanding and utilisation of topographic maps in various domains. The study also explores and identifies its limitations and areas for improvement. Analysing misclassifications reveals patterns or challenges the model struggles with, informing refinements in pre-processing, training data augmentation, and model architecture. Addressing these insights can enhance the model's accuracy and reliability for HTHM analysis.

METHODOLOGY

The HTHM dataset was utilised to train the CNN architecture. The selected CNN model underwent rigorous evaluation and analysis on the HTHM dataset to determine its effectiveness in extracting meaningful information from the maps. Various metrics, including training and validation accuracy, were assessed to quantify the CNN architecture performance. The impact of varying the epoch during training and utilising different dataset sizes was investigated. This analysis involved training the CNN model with different epoch values on subsets of the HTHM dataset and observing the corresponding training and validation accuracy changes. Epochs in this study refer to the number of times the entire training dataset is presented to the model during training. Setting epochs at intervals of 20 allowed the study to assess the model's performance early in training (20 epochs), at a mid-point (40 epochs), and after further training (60 epochs). This approach enabled the study to analyse how accuracy varied as the model underwent different stages of learning and whether additional training beyond a certain point yielded significant improvements or led to overfitting. By exploring different epoch durations and dataset sizes, valuable insights regarding optimal training conditions can be obtained.

The study expected that training and validation accuracy would improve by increasing the number of epochs and datasets. Thus, the outcomes of this paper were used to further improve the selection of the best architecture for implementing automatic vectorisation for HTHM. The following are the detailed steps of this research methodology: Data Collection, Data Pre-processing, CNN Training Model, Evaluation of Performance, and lastly, Result and Conclusion.

Data Collection

The scanned HTHM were collected from Perpustakaan Tun Abdul Razak at UiTM Shah Alam, specifically in the Mapping section. The study classified four objects: buildings, water bodies, land use, and roads. All the images were cropped on ten hardcopy map samples, which moderated conditions. The map was scanned using an A0 flatbed scanner with 500

dpi. All the datasets were cropped in dimensions of 224 pixels by 224 pixels (Figure 1) to ensure the dataset is of standard size. Figure 1 shows a sample of each object class in HTHM. The examples of every dataset class are shown in Table 1.

Table 1 and Figure 1 outline the composition of the dataset. The dataset focuses on map features, including contour building, land use, road and water bodies. Each dataset presents unique challenges for model generalisation. Variations in map feature complexity and quality may introduce bias and affect the model’s ability to generalise across diverse conditions. The dataset may not fully represent the diversity of historical topographic hardcopy maps (HTHM) in terms of geographical regions, periods, or map styles. This limitation could result in the model being biased towards the characteristics of the included maps.

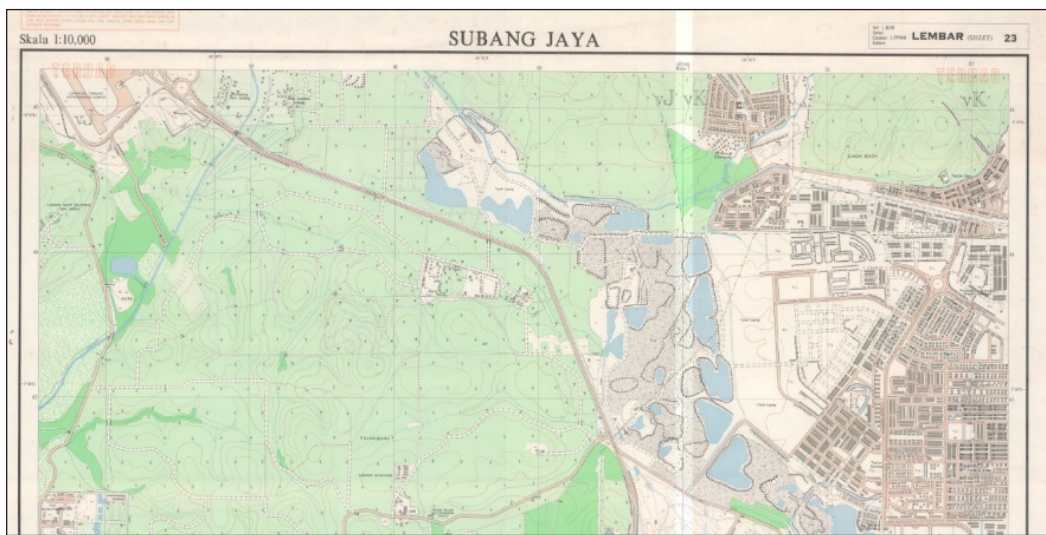


Figure 1. Sample of historical topographic hardcopy map

Table 1
Object in historical topographic hardcopy map

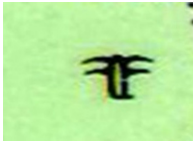
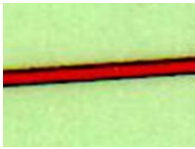
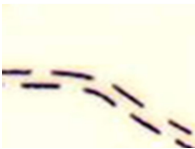
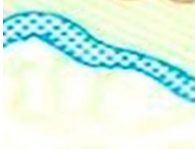
Dataset	Sample 1	Sample 2	Sample 3
Building	 Building 1	 Building 2	 Building 3
Land Use	 Rubber Tree Plantation	 Palm Oil Plantation	 Forest

Table 1 (continue)

Dataset	Sample 1	Sample 2	Sample 3
Road	 Main Road	 Small Road	 Small Road
Water Bodies	 River 1	 River 2	 River 3

Data Pre-processing

Four datasets in this study represent objects on hardcopy maps. Dataset 1 represents buildings, Dataset 2 represents land use, Dataset 3 represents roads, and Dataset 4 represents water bodies. While preparing the datasets, each image was augmented with the following techniques: rotations of 90°, 180°, 270°, flip vertical, and flip horizontal. Data augmentation can assist in lessening overfitting, a significant issue in Deep Learning, and enhancing model performance (Khalifa et al., 2022). All classes of objects were subjected to image augmentation. The specifics of the augmentation are shown in Figure 2.

The dataset was divided into a 70:20:10 ratio, with 70% of samples for training, 20% for validation, and 10% for model testing. The study performed five training sets, each with several datasets and epochs. The distribution of training sets is shown in Table 2.

Based on Table 2, experiments 1 to 4 undergo training using the CNN model at epochs 20, 40, and 60. Each training was tested for its capability of achieving training and validation accuracy. Experiment 1 used 288 images; experiment 2 used 636 images; experiment 3 used 1144 images; and experiment 4 used 1716 images.

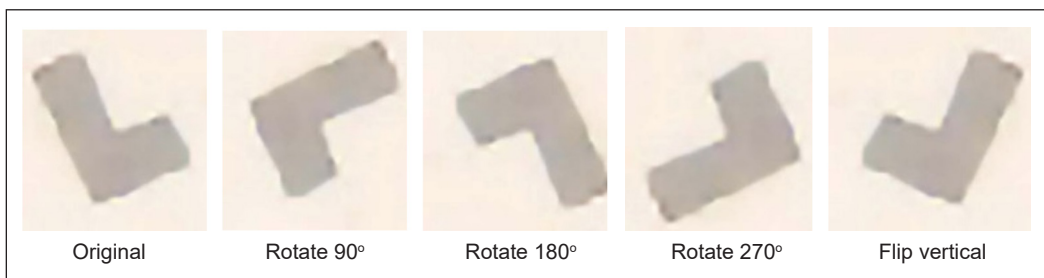


Figure 2. Example of augmentation image on building dataset

Table 2
Training set details

No. experiment	1	2	3	4
Epochs	20/40/60	20/40/60	20/40/60	20/40/60
Training data	200	444	800	1200
Validate data	60	128	228	344
Testing data	28	64	116	172
Total data set	288	636	1144	1716

The Proposed CNN Training Model

In this study, a CNN model was developed to detect the objects on HTTM that had already been scanned. Figure 3 shows the structure of the CNN model, and Table 3 displays the layers and details for each layer.

The model used an adopted technique from Roslan et al. (2023). The first layer in this model is a convolutional layer, calculating 16 features for each 3×3 kernel. The second

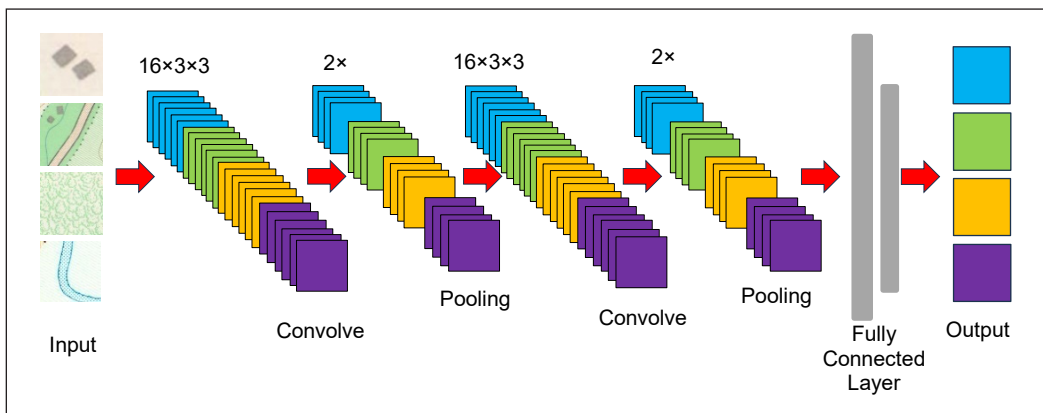


Figure 3. The proposed structure of the CNN model

Table 3
CNN layers in the proposed model

No	Layer (Type)	Layer type and filter shape
1	Conv2D	Convolution-ReLU, Kernel $\langle 16 \times 3 \times 3 \rangle$
2	Pooling2D	Max pooling, 2×2
3	Batch_normalization	-
4	Conv2D_1	Convolution-ReLU, Kernel $\langle 32 \times 3 \times 3 \rangle$
5	Pooling2D_1	Max pooling, 2×2
6	Batch_normalization_1	-
7	Flatten	Flatten
8	Dense	ReLU activation
9	Activation_5 (Softmax)	Classifier

layer is a max-pooling layer with a 2×2 kernel. In the next step, another convolutional layer calculates 32 features for each 3×3 kernel. It is followed by another max pooling with a 2×2 filter. Note that the batch normalisation was applied after each max-pooling layer, and the rectified linear unit (ReLU) served as an activation function. After four layers, a fully connected layer can be found. In the last phase, a SoftMax layer creates a vector with four entries from the proceeding layers' results vector. These four entries indicate the four types of objects in HTHM.

In this study, dropout was applied to hidden layers of the CNN architecture with varying dropout rates. By randomly masking a fraction of neurons during each training iteration, dropout helped prevent overfitting by ensuring that no single neuron or feature became overly reliant on specific input patterns. The impact of dropout regularisation was observed through improvements in validation accuracy and reduced overfitting tendencies, particularly as the model underwent additional training epochs. In the study methodology, optimising hyperparameters such as learning rate and batch size was essential to ensure the CNN model's optimal performance. The learning rate and batch sizes determine the step size taken during the optimisation process by analysing the learning curve on the graph to update the model's weights.

Evaluation of Performance

Each of the training sets underwent an accuracy evaluation. The observation was based on four elements, which are the results of this study.

Training and Validation Accuracy of the Model's Accuracy Graph Interpretation Analysis

Visualising the model's accuracy over epochs is valuable for understanding its performance and learning progress during training. It provides insights into how well the model fits the training data and its ability to generalise to unseen data. The benefits of visualising accuracy over epochs are as follows: First, it allows monitoring of the training progress by observing the accuracy trends over time. Steady increases or high plateaus indicate effective learning. Second, comparing training and validation accuracy helps detect overfitting or underfitting. A large gap suggests overfitting, while low values for both indicate underfitting. Third, it aids in determining convergence by identifying stable performance, where training and validation accuracy reach a plateau or show diminishing improvements. Finally, it facilitates model comparison by visualising the accuracy trends of multiple models, enabling the selection of the best-performing one based on convergence, generalisation, and overall accuracy (Alzubaidi et al., 2021).

Model Loss Graph Pattern

The loss function quantifies the disparity between the model's predicted and expected output to minimise this difference during training. Plotting the loss over epochs provides valuable information about the model's learning progress and convergence. The significance of the loss graph and its interpretation are as follows: First, it allows monitoring of the model's learning progress, with decreasing or plateauing loss indicating effective learning. Second, overfitting or underfitting can be identified by comparing the training loss with the validation loss. A significant decrease in training loss with high validation loss suggests overfitting, while high values for both indicate underfitting. Third, the loss plot helps determine if the model has converted to stable performance, as evidenced by a plateau or diminishing improvements in training and validation losses. By analysing the loss over epochs, valuable insights can be gained regarding the model's learning behaviour, issues like overfitting or underfitting, and an overall assessment of its convergence and performance.

Confusion Matrix

Confusion Matrix is an important measure to evaluate the accuracy of credit scoring models (Zeng, 2020). The confusion matrix is a comprehensive summary of a model's predictions and the actual labels of the data points, particularly in classification problems (Tharwat, 2020). It consists of a table where rows represent true labels and columns represent predicted labels. The matrix provides counts or proportions of true positives (correctly predicted positives), true negatives (correctly predicted negatives), false positives (incorrectly predicted positives), and false negatives (incorrectly predicted negatives). True positives and true negatives indicate correct predictions, while false positives and false negatives represent prediction errors. Analysing the confusion matrix helps identify the model's accuracy and the specific types of errors it makes, enabling targeted improvements.

Classification Report

Evaluation metrics, such as accuracy, precision, recall, and F1-score, are commonly used to measure a model's performance in predicting correct class labels. Accuracy represents the overall correctness of the predictions, precision measures the ability to identify positive instances correctly, recall measures the ability to identify positive instances out of all actual positives correctly, and the F1-score provides a balanced measure between precision and recall. Comparing predictions against a labelled dataset with known ground truth is crucial to assess model accuracy. These metrics help evaluate performance, identify areas for improvement, and inform decisions on model selection, hyperparameter tuning, and feature engineering. The accuracy, precision, recall, and F1 score will be calculated after implementing the model. It will use the confusion matrix, including true positive (TP),

true negative (TN), false positive (FP), and false negative (FN), to measure accuracy, precision, recall, and F1-score. The formulas for accuracy, precision, recall, and F1-score are represented in Equations 1 to 4.

$$Accuracy = \frac{TP+TN}{TP+TN+FP+FN} \tag{1}$$

$$Precision = \frac{TP}{TP+FP} \tag{2}$$

$$Recall = \frac{TP}{TP+FN} \tag{3}$$

$$F1\text{-score} = 2 \times \frac{Precision \times Recall}{Precision + Recall} \tag{4}$$

EXPERIMENT RESULTS AND ANALYSIS

The experiment was conducted by performing data training based on several train datasets. The datasets were based on four classes: buildings, roads, water bodies, and land use. The images from these four classes totalled 288, 636, 1144, and 1716. These were tested on 20, 40, and 60 epoch variations to find the best training performance for the HTHM dataset. Each dataset was evaluated based on its model accuracy, model loss, confusion matrix, and classification report as the model’s performance indicator. The results are shown below:

Experiment 1: 288 Data Set

In Table 4, the CNN model’s results show an improvement in accuracy as the number of epochs increases. At epoch 20, the model achieved a training accuracy of 69% and a validation accuracy of 45%. By epoch 40, the training accuracy had significantly improved to 97.5%, with a validation accuracy of 48.33%. Concerning epoch 60, the training accuracy drops to 87.5%, while the validation accuracy drops to 41.67%.

Table 5 shows the validation accuracy of the model’s accuracy graph for experiment 1. The confusion matrix and Classification report for HTHM data are tabulated in Table 6. The total image of a confusion matrix for testing data is 28, 10% for data testing from 288

Table 4
Result of performance loss, accuracy, validation loss, and validation accuracy achieved for Experiment 1

288 data set				
Epoch	Loss	Accuracy	Val_loss	Val_accuracy
20	0.9605	0.6900	1.2575	0.4500
40	0.1490	0.9750	1.9651	0.4833
60	0.3450	0.8750	2.4341	0.4167

images. Table 7 shows that epoch 40 achieved high accuracy by testing average precision, recall F1 score and accuracy.

Table 5
Validation accuracy of the model's accuracy graph for Experiment 1

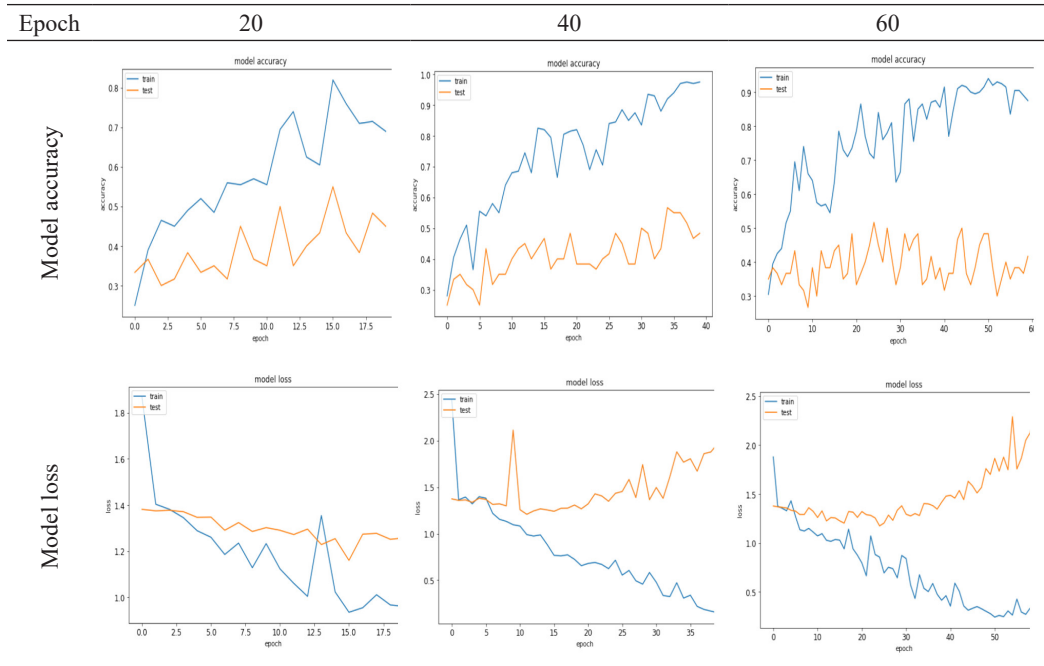


Table 6
Result of the performance confusion matrix and classification report for the testing model Experiment 1

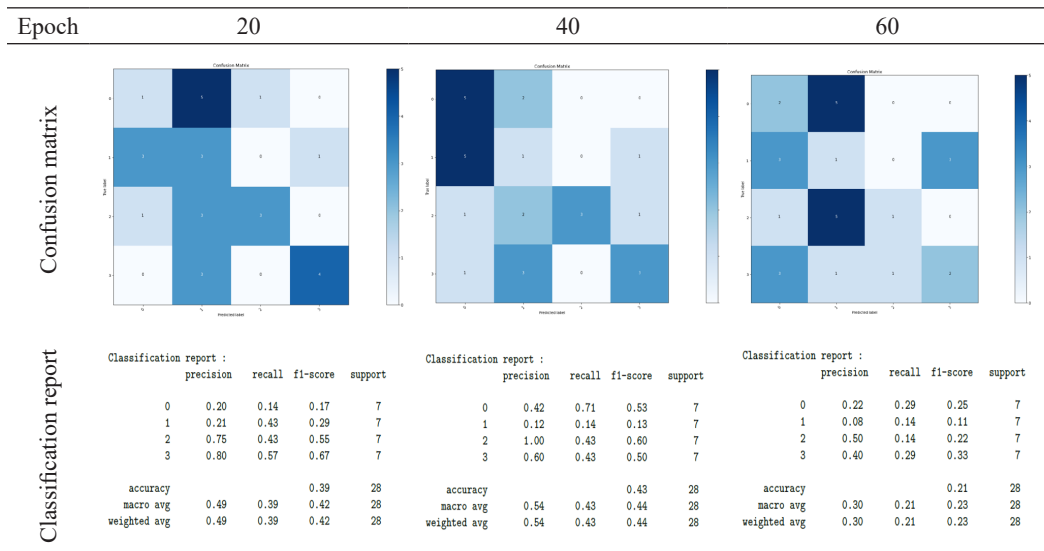


Table 7

Average precision, average recall, average F1-score, and accuracy for the testing model in Experiment 1

288 data set				
Epoch	average precision	average recall	average F1-score	Accuracy
20	0.49	0.39	0.42	0.39
40	0.54	0.43	0.44	0.43
60	0.30	0.21	0.23	0.21

Experiment 2: 636 Data Set

The trained datasets were set to 636 images, and the implemented CNN architecture results are shown in Table 8.

In Table 8, the results of the CNN model show an improvement in accuracy as the number of epochs increases. At epoch 20, the model achieved a training accuracy of 81% and a validation accuracy of 46%. By epoch 40, the training accuracy had significantly improved to 98%, with a validation accuracy of 51.56%. Concerning epoch 60, the training accuracy peaks at 100%, while the validation accuracy drops at 50.78%. The model accuracy graph was shown in Tables 9 and 10 for the confusion matrix with its classification report.

The confusion matrix and classification report for HTHM data are tabulated in Table 11. The total image of a confusion matrix for testing data is 64, 10% for data testing from 636 images.

Table 8

Result of performance loss, accuracy, validation loss, and validation accuracy achieved for Experiment 2

636 data set				
Epoch	Loss	Accuracy	Val_loss	Val_accuracy
20	0.4528	0.8176	1.7168	0.4609
40	0.1169	0.9797	3.5790	0.5156
60	0.0054	1.0000	3.4112	0.5078

Table 9

Validation accuracy of the model's accuracy graph for Experiment 2

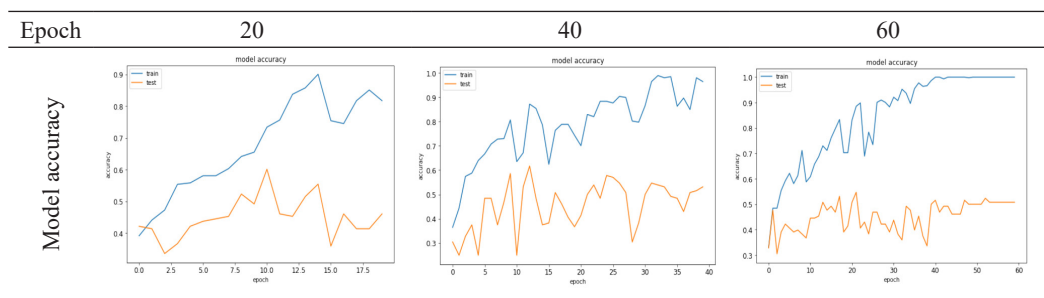


Table 9 (continue)

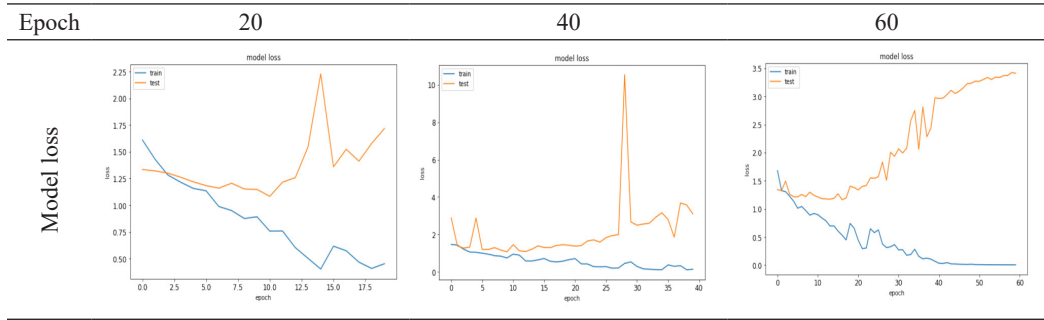


Table 10

Result of the performance confusion matrix and classification report for the testing model Experiment 2

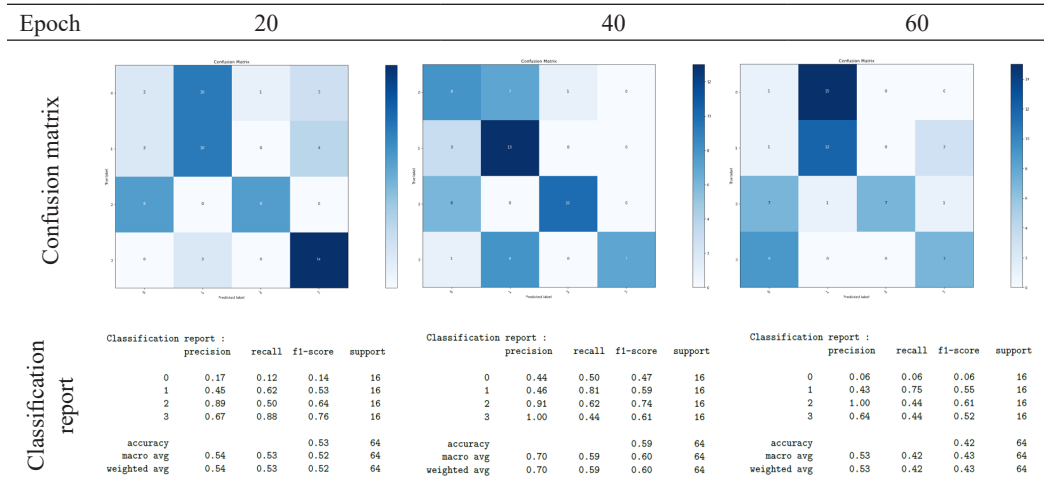


Table 11

Average precision, average recall, average F1-score, and accuracy for the testing model in Experiment 2

636 data set				
Epoch	average precision	average recall	average F1-score	Accuracy
20	0.54	0.53	0.52	0.53
40	0.70	0.59	0.60	0.59
60	0.53	0.42	0.43	0.42

Experiment 3: 1144 Data Set

The trained datasets were set to 1144 images, and the implemented CNN architecture results are shown in Table 12.

In Table 12, the results of the CNN model show an improvement in accuracy as the number of epochs increases. At epoch 20, the model achieved a training accuracy of 22.12%

and a validation accuracy of 25%. By epoch 40, the training accuracy had significantly improved to 86.62%, with a validation accuracy of 57%. Concerning epoch 60, the training accuracy dropped to 76.62%, followed by its validation accuracy at 52.19%. The model accuracy graph was shown in Tables 13 and 14 for the confusion matrix with its classification report.

Based on the result in Table 15, epoch 40 achieved high accuracy by testing average precision, recall F1 score and accuracy compared to epochs 20 and 60. It shows that epoch 40 was the optimum epoch for the dataset training.

Table 12

The results of performance loss, accuracy, validation loss, and validation accuracy were achieved for Experiment 3

1144 data set				
Epoch	Loss	Accuracy	Val_loss	Val_accuracy
20	1.3872	0.2212	1.3863	0.2500
40	0.3649	0.8662	1.9437	0.5702
60	0.5658	0.7662	1.6103	0.5219

Table 13

Validation accuracy of the model's accuracy graph for Experiment 3

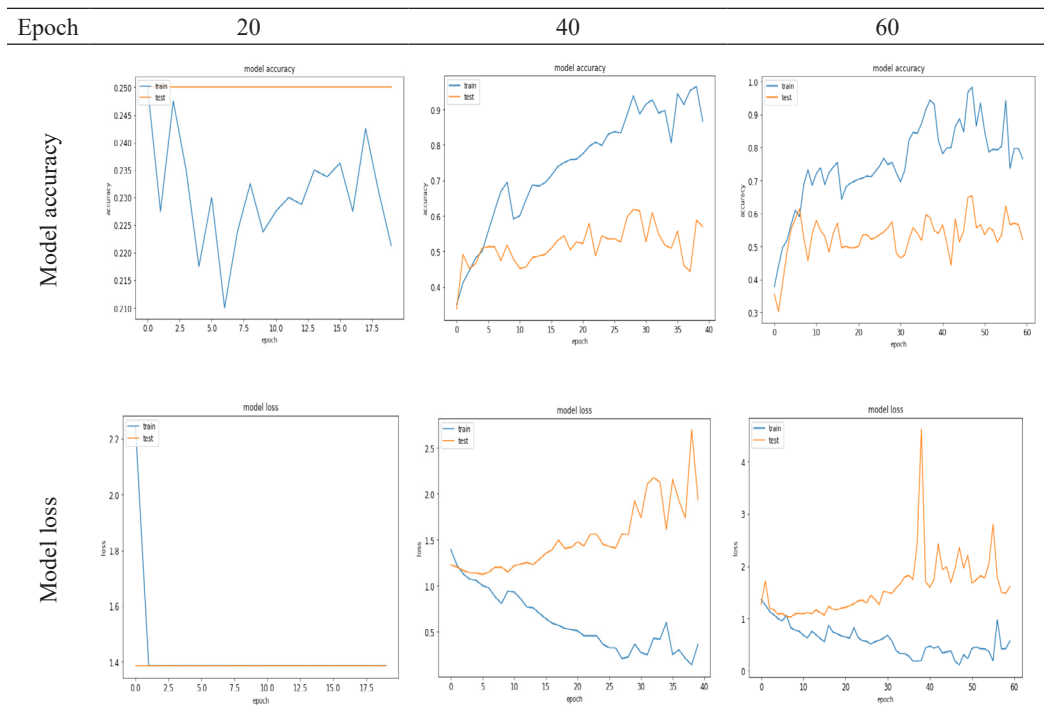


Table 14
Result of the performance confusion matrix and classification report for the testing model Experiment 3

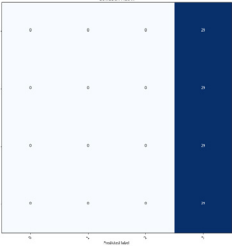
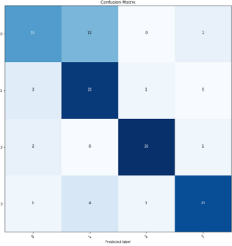
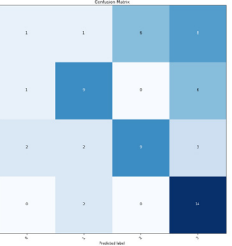
Epoch	20	40	60																																																																																																																							
Confusion matrix																																																																																																																										
	<p>Classification report :</p> <table border="1"> <thead> <tr> <th></th> <th>precision</th> <th>recall</th> <th>f1-score</th> <th>support</th> </tr> </thead> <tbody> <tr> <td>0</td> <td>0.00</td> <td>0.00</td> <td>0.00</td> <td>29</td> </tr> <tr> <td>1</td> <td>0.00</td> <td>0.00</td> <td>0.00</td> <td>29</td> </tr> <tr> <td>2</td> <td>0.00</td> <td>0.00</td> <td>0.00</td> <td>29</td> </tr> <tr> <td>3</td> <td>0.25</td> <td>1.00</td> <td>0.40</td> <td>29</td> </tr> <tr> <td>accuracy</td> <td></td> <td>0.25</td> <td></td> <td>116</td> </tr> <tr> <td>macro avg</td> <td>0.06</td> <td>0.25</td> <td>0.10</td> <td>116</td> </tr> <tr> <td>weighted avg</td> <td>0.06</td> <td>0.25</td> <td>0.10</td> <td>116</td> </tr> </tbody> </table>		precision	recall	f1-score	support	0	0.00	0.00	0.00	29	1	0.00	0.00	0.00	29	2	0.00	0.00	0.00	29	3	0.25	1.00	0.40	29	accuracy		0.25		116	macro avg	0.06	0.25	0.10	116	weighted avg	0.06	0.25	0.10	116	<p>Classification report :</p> <table border="1"> <thead> <tr> <th></th> <th>precision</th> <th>recall</th> <th>f1-score</th> <th>support</th> </tr> </thead> <tbody> <tr> <td>0</td> <td>0.71</td> <td>0.52</td> <td>0.60</td> <td>29</td> </tr> <tr> <td>1</td> <td>0.61</td> <td>0.86</td> <td>0.71</td> <td>29</td> </tr> <tr> <td>2</td> <td>0.93</td> <td>0.90</td> <td>0.91</td> <td>29</td> </tr> <tr> <td>3</td> <td>0.88</td> <td>0.79</td> <td>0.84</td> <td>29</td> </tr> <tr> <td>accuracy</td> <td></td> <td>0.77</td> <td></td> <td>116</td> </tr> <tr> <td>macro avg</td> <td>0.78</td> <td>0.77</td> <td>0.77</td> <td>116</td> </tr> <tr> <td>weighted avg</td> <td>0.78</td> <td>0.77</td> <td>0.77</td> <td>116</td> </tr> </tbody> </table>		precision	recall	f1-score	support	0	0.71	0.52	0.60	29	1	0.61	0.86	0.71	29	2	0.93	0.90	0.91	29	3	0.88	0.79	0.84	29	accuracy		0.77		116	macro avg	0.78	0.77	0.77	116	weighted avg	0.78	0.77	0.77	116	<p>Classification report :</p> <table border="1"> <thead> <tr> <th></th> <th>precision</th> <th>recall</th> <th>f1-score</th> <th>support</th> </tr> </thead> <tbody> <tr> <td>0</td> <td>0.25</td> <td>0.06</td> <td>0.10</td> <td>16</td> </tr> <tr> <td>1</td> <td>0.64</td> <td>0.56</td> <td>0.60</td> <td>16</td> </tr> <tr> <td>2</td> <td>0.60</td> <td>0.56</td> <td>0.58</td> <td>16</td> </tr> <tr> <td>3</td> <td>0.45</td> <td>0.88</td> <td>0.60</td> <td>16</td> </tr> <tr> <td>accuracy</td> <td></td> <td>0.52</td> <td></td> <td>64</td> </tr> <tr> <td>macro avg</td> <td>0.49</td> <td>0.52</td> <td>0.47</td> <td>64</td> </tr> <tr> <td>weighted avg</td> <td>0.49</td> <td>0.52</td> <td>0.47</td> <td>64</td> </tr> </tbody> </table>		precision	recall	f1-score	support	0	0.25	0.06	0.10	16	1	0.64	0.56	0.60	16	2	0.60	0.56	0.58	16	3	0.45	0.88	0.60	16	accuracy		0.52		64	macro avg	0.49	0.52	0.47	64	weighted avg	0.49	0.52	0.47
	precision	recall	f1-score	support																																																																																																																						
0	0.00	0.00	0.00	29																																																																																																																						
1	0.00	0.00	0.00	29																																																																																																																						
2	0.00	0.00	0.00	29																																																																																																																						
3	0.25	1.00	0.40	29																																																																																																																						
accuracy		0.25		116																																																																																																																						
macro avg	0.06	0.25	0.10	116																																																																																																																						
weighted avg	0.06	0.25	0.10	116																																																																																																																						
	precision	recall	f1-score	support																																																																																																																						
0	0.71	0.52	0.60	29																																																																																																																						
1	0.61	0.86	0.71	29																																																																																																																						
2	0.93	0.90	0.91	29																																																																																																																						
3	0.88	0.79	0.84	29																																																																																																																						
accuracy		0.77		116																																																																																																																						
macro avg	0.78	0.77	0.77	116																																																																																																																						
weighted avg	0.78	0.77	0.77	116																																																																																																																						
	precision	recall	f1-score	support																																																																																																																						
0	0.25	0.06	0.10	16																																																																																																																						
1	0.64	0.56	0.60	16																																																																																																																						
2	0.60	0.56	0.58	16																																																																																																																						
3	0.45	0.88	0.60	16																																																																																																																						
accuracy		0.52		64																																																																																																																						
macro avg	0.49	0.52	0.47	64																																																																																																																						
weighted avg	0.49	0.52	0.47	64																																																																																																																						

Table 15
Average precision, average recall, average F1-score, and accuracy for the testing model in Experiment 3

636 data set					
Epoch	average precision	average recall	average F1-score	Accuracy	
20	0.06	0.25	0.10	0.25	
40	0.78	0.77	0.77	0.77	
60	0.49	0.52	0.47	0.52	

Experiment 4: 1716 Data Set

The trained datasets were set to 1716 images, and the implemented CNN architecture results are shown in Table 16.

In Table 16, the results of the CNN model show an improvement in accuracy as the number of epochs increases. At epoch 20, the model achieved a training accuracy of 79.50% and a validation accuracy of 57.27%. By epoch 40, the training accuracy significantly improved to 94.75%, with a validation accuracy of 67.44%. Concerning epoch 60, the training accuracy dropped to 89.17%, followed by its validation accuracy at 61.34%. The model accuracy graph was shown in Tables 17 and 18 for the confusion matrix with its classification report.

Based on the results in Table 19, epochs 40 and 60 achieve high accuracy by testing average precision, recall F1 score and accuracy compared to epoch 20. It shows that the optimum epoch for the dataset training was at epochs 40 and 60. Through experiments 1, 2, 3 and 4, the variation in quality and diversity of topographic map datasets also pose significant challenges to CNN-based analysis. Variations in image quality and features also impact

Table 16

Result of performance loss, accuracy, validation loss, and validation accuracy achieved for Experiment 4

1716 data set				
Epoch	Loss	Accuracy	Val_loss	Val_accuracy
20	0.4311	0.7950	1.2615	0.5727
40	0.1296	0.9475	5.3041	0.6744
60	0.2567	0.8917	2.1453	0.6134

Table 17

Validation accuracy of the model's accuracy graph for Experiment 4

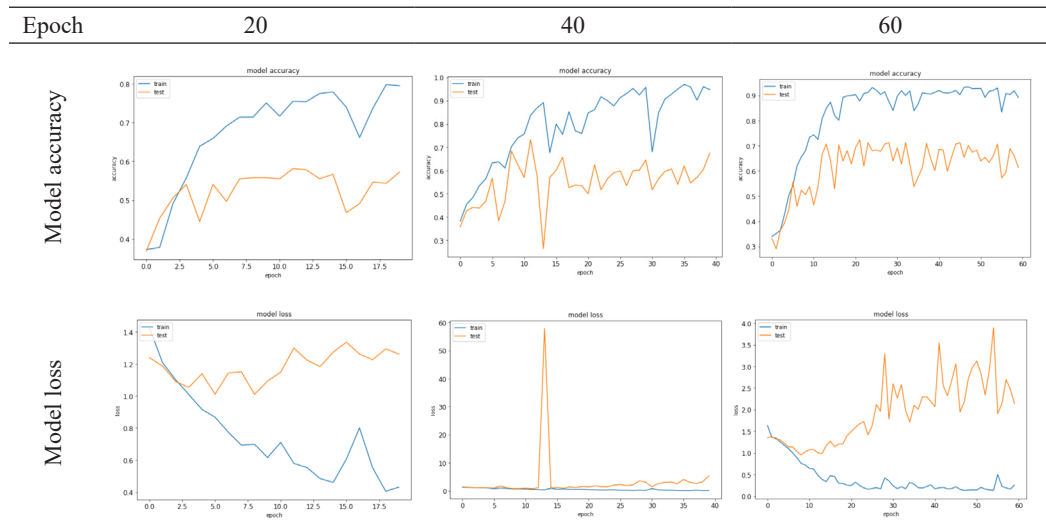


Table 18

Result of the performance confusion matrix and classification report for the testing model Experiment 4

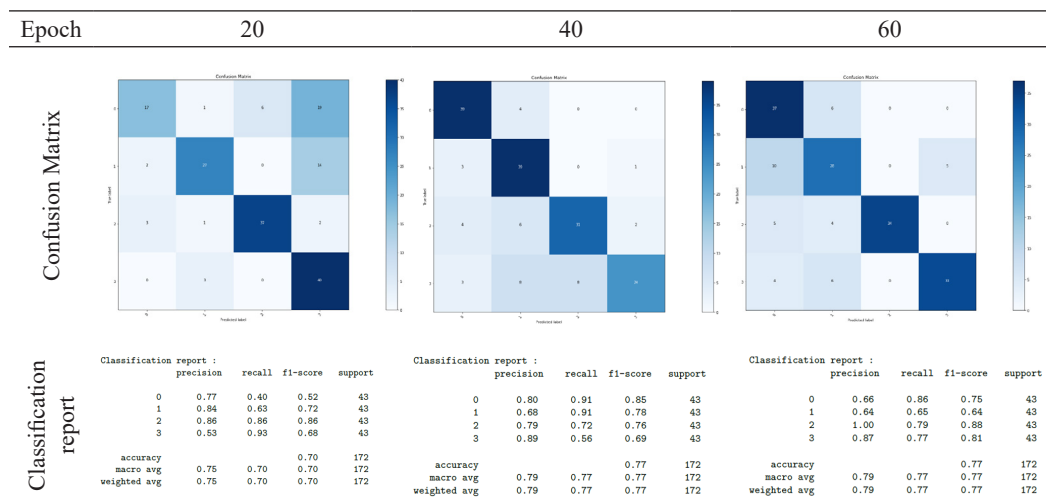


Table 19

Average precision, average recall, average F1-score, and accuracy for the testing model in Experiment 4

1716 data set				
Epoch	average precision	average recall	average F1-score	Accuracy
20	0.75	0.70	0.70	0.70
40	0.79	0.77	0.77	0.77
60	0.79	0.77	0.77	0.77

the model's accuracy and generalizability. Future research should address these challenges by evaluating computational efficiency and resource requirements and exploring methods to enhance the model's adaptability to diverse map characteristics. Integrating CNN models with GIS enhances the usability of topographic map data, supporting automated feature extraction and spatial analysis for informed decision-making in various domains. Additionally, visualisation tools are crucial for ensuring user understanding, with detection boxes overlaid on maps facilitating the interpretation of model outputs. Developing system tools for object detection can further streamline the application of CNN models to topographic map analysis. Throughout the experiment, findings also reveal that all testing achieved their optimum accuracy at epoch 40. It indicates that the greater number of epochs does not affect the higher accuracy achieved for this dataset. Thus, the epoch number needs to be compatible with the dataset types to achieve an optimal detection model.

Examples of practical challenges encountered during map analysis include complex cartographic details and variability in map quality. The complex detail varies in size, shape, and clarity, posing challenges for accurate feature extraction and classification. The challenges introduce the capability of the CNN model, which is able to handle diverse datasets of HTHMs. The model is designed to learn hierarchical representations of these complex cartographic features. The model can capture local spatial patterns and semantic information by leveraging convolutional layers, accurately classifying and interpreting various map elements and quality.

CONCLUSION

In summary, the classification report analysis demonstrates that the model performs reasonably well classifying instances from the dataset. However, further improvements can be made to enhance the model to achieve a more balanced performance for each class. Findings from this study also contribute to understanding the model's strengths and limitations, providing valuable insights for future research and refinement of the classification approach. Overall, evaluating CNN architecture for analysing HTHM has provided valuable insights into its effectiveness and potential applications. The study demonstrated that CNNs can accurately classify instances from the HTHM dataset, showcasing their suitability for analysing complex cartographic details, such as contour

lines, symbols, and textual annotations. The model exhibited satisfactory performance in most classes, with room for improvement in specific categories. This study also provides a foundation for advancing map analysis and interpretation within GIS. It underscores the potential of CNNs in automating the vectorisation process and facilitating the broader access and preservation of valuable historical records embedded in topographic maps. For potential future research directions, a hybrid CNN model with other machine learning algorithms for its higher accuracy in classification tasks could enhance the study's accuracy, and additional datasets covering maps from various years would provide a broader range of topographical map data for analysis.

ACKNOWLEDGMENTS

The authors sincerely thank Universiti Teknologi MARA Selangor, Malaysia, for providing Geran Intensif Penyelidikan (GIP) Research Fund 600-RMC/GIP 5/3 (074/2022) and to all those directly or indirectly involved in this research.

REFERENCES

- Ali, L., Alnajjar, F., Jassmi, H. A., Gocho, M., Khan, W., & Serhani, M. A. (2021). Performance evaluation of deep CNN-based crack detection and localization techniques for concrete structures. *Sensors*, *21*(5), Article 1688. <https://doi.org/10.3390/s21051688>
- Alzubaidi, L., Zhang, J., Humaidi, A. J., Al-Dujaili, A., Duan, Y., Al-Shamma, O., Santamaria, J., Fadhel, M. A., Al-Amidie, M., & Farhan, L. (2021). Review of deep learning: Concepts, CNN architectures, challenges, applications, future directions. *Journal of Big Data*, *8*, Article 53. <https://doi.org/10.1186/s40537-021-00444-8>
- Althnian, A., AlSaeed, D., Al-Baity, H., Samha, A., Dris, A., Alzakari, N., Elwafa, A. A., & Kurdi, H. (2021). Impact of dataset size on classification performance: An empirical evaluation in the medical domain. *Applied Sciences*, *11*(2), Article 796. <https://doi.org/10.3390/app11020796>
- Anuar, S., Ibrahim, J., Rauf, A., & Rasam, A. (2021). Towards automated digitization of cartographic hardcopy maps: Reviews of issues, challenges and potentials in Malaysia Library archives. *Malaysian Journal of Remote Sensing & GIS*, *10*(1), 43-51.
- Audebert, N., Le Saux, B., & Lefevre, S. (2019). Deep learning for classification of hyperspectral data: A comparative review. *IEEE Geoscience and Remote Sensing Magazine*, *7*(2), 159–173. <https://doi.org/10.1109/MGRS.2019.2912563>
- Bhosle, K., & Musande, V. (2022). Evaluation of CNN model by comparing with convolutional autoencoder and deep neural network for crop classification on hyperspectral imagery. *Geocarto International*, *37*(3), 813–827. <https://doi.org/10.1080/10106049.2020.1740950>
- Barry-Straume, J., Tschannen, A., Engels, D. W., & Fine, E. (2018). An evaluation of training size impact on validation accuracy for optimized convolutional neural networks. *SMU Data Science Review*, *1*(4), Article 12.

- Chen, Y., Jiang, H., Li, C., Jia, X., & Ghamisi, P. (2016). Deep feature extraction and classification of hyperspectral images based on convolutional neural networks. *IEEE transactions on geoscience and remote sensing*, 54(10), 6232-6251. <https://doi.org/10.1109/TGRS.2016.2584107>
- Chauhan, R., Ghanshala, K. K., & Joshi, R. C. (2018, December 15-17). *Convolutional Neural Network (CNN) for image detection and recognition*. [Paper presentation]. First International Conference on Secure Cyber Computing and Communication (ICSCCC), Jalandhar, India. <https://doi.org/10.1109/ICSCCC.2018.8703316>.
- Dawson, H. L., Dubrule, O., & John, C. M. (2023). Impact of dataset size and convolutional neural network architecture on transfer learning for carbonate rock classification. *Computers and Geosciences*, 171, Article 105284. <https://doi.org/10.1016/j.cageo.2022.105284>
- Dwivedi, D., & Patil, G. (2022). Lightweight convolutional neural network for land use image classification. *Journal of Advanced Geospatial Science & Technology*, 2(1), 31-48. <https://doi.org/10.11113/jagst.v2n1.31>
- Garbin, C., Zhu, X., & Marques, O. (2020). Dropout vs. batch normalization: An empirical study of their impact to deep learning. *Multimedia Tools and Applications* 79(19), 12777-12815. <https://doi.org/10.1007/s11042-019-08453-9>
- Guo, W., Yang, W., Zhang, H., & Hua, G. (2018). Geospatial object detection in high resolution satellite images based on multi-scale convolutional neural network. *Remote Sensing*, 10(1), Article 131. <https://doi.org/10.3390/rs10010131>
- Hamouda, M., Etabaa, K. S., & Bouhleb, M. S. (2020). Smart feature extraction and classification of hyperspectral images based on convolutional neural networks. *IET Image Processing*, 14(10), 1999-2005. <https://doi.org/10.1049/iet-ipr.2019.1282>
- Ji, S., Zhang, C., Xu, A., Shi, Y., & Duan, Y. (2018). 3D convolutional neural networks for crop classification with multi-temporal remote sensing images. *Remote Sensing*, 10(1), Article 75. <https://doi.org/10.3390/rs10010075>
- Johny, A., & Madhusoodanan, K. N. (2021). Dynamic learning rate in deep CNN model for metastasis detection and classification of histopathology images. *Computational and Mathematical Methods in Medicine*, 2021(1), Article 5557168. <https://doi.org/10.1155/2021/5557168>
- Kandel, I., & Castelli, M. (2020). The effect of batch size on the generalizability of the convolutional neural networks on a histopathology dataset. *ICT Express*, 6(4), 312-315. <https://doi.org/10.1016/j.ict.2020.04.010>
- Khalifa, N. E., Loey, M., & Mirjalili, S. (2022). A comprehensive survey of recent trends in deep learning for digital images augmentation. *Artificial Intelligence Review*, 55(3), 2351-2377. <https://doi.org/10.1007/s10462-021-10066-4>
- Kumar, A., Gaur, N., Chakravarty, S., Alsharif, M. H., Uthansakul, P., & Uthansakul, M. (2024). Analysis of spectrum sensing using deep learning algorithms: CNNs and RNNs. *Ain Shams Engineering Journal*, 15(3), Article 102505. <https://doi.org/10.1016/j.asej.2023.102505>
- Li, Z., Xin, Q., Sun, Y., & Cao, M. (2021). A deep learning-based framework for automated extraction of building footprint polygons from very high-resolution aerial imagery. *Remote Sensing*, 13(18), Article 3630 <https://doi.org/10.3390/rs13183630>

- Liu, B., Du, S., & Zhang, X. (2020). Land cover classification using convolutional neural network with remote sensing data and digital surface model. *ISPRS Annals of the Photogrammetry, Remote Sensing and Spatial Information Sciences*, 5(3), 39–43. <https://doi.org/10.5194/isprs-annals-V-3-2020-39-2020>
- Poojary, R., Raina, R., & Mondal, A. K. (2021). Effect of data-augmentation on fine-tuned CNN model performance. *IAES International Journal of Artificial Intelligence*, 10(1), 84-92, <https://doi.org/10.11591/ijai.v10.i1.pp84-92>
- Roslan, N. A. M., Diah, N. M., Ibrahim, Z., Munarko, Y., & Minarno, A. E. (2023). Automatic plant recognition using convolutional neural network on Malaysian medicinal herbs: The value of data augmentation. *International Journal of Advances in Intelligent Informatics*, 9(1), 136-147. <https://doi.org/10.26555/ijain.v9i1.1076>
- Sharifi, O., Mokhtarzadeh, M., & Beirami, B. A. (2022). A new deep learning approach for classification of hyperspectral images: Feature and decision level fusion of spectral and spatial features in multiscale CNN. *Geocarto International*, 37(14), 4208-4233. <https://doi.org/10.1080/10106049.2021.1882006>
- Tharwat, A. (2020). Classification assessment methods. *Applied Computing and Informatics*, 17(1), 168-192. <https://doi.org/10.1016/j.aci.2018.08.003>
- Zeng, P. (2020) On the confusion matrix in credit scoring and its analytical properties. *Communications in Statistics-Theory and Methods*, 49(9), 2080-2093. <https://doi.org/10.1080/03610926.2019.1568485>

A Comprehensive Analysis of a Framework for Rebalancing Imbalanced Medical Data Using an Ensemble-based Classifier

Jafhate Edward¹, Marshima Mohd Rosli^{1,2*} and Ali Seman¹

¹College of Computing, Informatics and Mathematics, Universiti Teknologi MARA, Shah Alam 40450, Selangor, Malaysia

²Institute for Pathology, Laboratory and Forensic Medicine (I-PPerForM), Universiti Teknologi MARA, 47000 UiTM, Sungai Buloh, Selangor, Malaysia

ABSTRACT

In medical data, addressing imbalanced datasets is paramount for accurate predictive modeling. This paper delves into exploring a well-established rebalancing framework proposed in previous research. While acknowledged for its effectiveness, the adaptability of this framework across diverse medical datasets remains unexplored. We conduct a comprehensive investigation to bridge this gap by integrating an ensemble-based classifier into the existing framework. By leveraging seven imbalanced medical binary datasets, our study comprises three distinct experiments: utilizing standard baseline classifiers from the framework (original), incorporating the baseline with an ensemble-based classifier, and introducing our novel ensemble-based classifier with the self-paced ensemble (SPE) algorithm. Our novel ensemble, composed of decision tree (DT), radial support vector machine (R.SVM), and extreme gradient boosting (XGB) classifiers, serves as the foundation for the SPE. Our primary objective is to demonstrate the potential improvement of the existing framework's overall performance through the integration of an ensemble. Experimental results reveal significant enhancements, with our proposed ensemble classifier outperforming the original by 4.96%, 5.89%, 5.68%, 7.85%, and 6.84% in terms of accuracy, precision, recall, F-score, and G-mean, respectively. This study contributes valuable insights into the adaptability

and performance augmentation achievable through ensemble methods in addressing class imbalances within the medical domain.

Keywords: Ensemble classifier, ensemble learning, imbalance classification, machine learning algorithms, medical data, predictive modeling, rebalancing framework

ARTICLE INFO

Article history:

Received: 14 December 2023

Accepted: 10 Jun 2024

Published: 25 October 2024

DOI: <https://doi.org/10.47836/pjst.32.6.12>

E-mail addresses:

jafhate@gmail.com (Jafhate Edward)

marshima@uitm.edu.my (Marshima Mohd Rosli)

alisesman@uitm.edu.my (Ali Seman)

* Corresponding author

INTRODUCTION

Class imbalance poses a common challenge across various data domains, particularly in medical datasets where its presence is unavoidable (Bai et al., 2015; Rahman & Davis, 2013). Imbalance occurs when the majority class overwhelms instances of the minority class (Abraham & Elrahman, 2013). Predictive models trained on imbalanced data often exhibit bias, resulting in a higher misclassification rate when predicting the target outcome. Conventional sampling methods, such as random oversampling, undersampling, and the synthetic minority oversampling technique (SMOTE), are commonly applied to address this issue. These methods involve modifying imbalanced datasets to create a more balanced distribution, significantly improving the overall performance of classifiers (Fernández et al., 2018).

In the medical domain, the consequences of such misclassifications can be considerably more significant, as they may lead to the misdiagnosis of cancerous patients as noncancerous or vice versa (Belarouci & Chikh, 2017; Rahman & Davis, 2013). Consequently, various cutting-edge techniques for dealing with this issue have emerged (Rahman & Davis, 2013; Pes, 2019). One such approach employs the rebalancing framework proposed by Zhao et al. (2018), which implements several standard classifiers and relies on four rebalancing strategies to address data imbalance. A satisfactory increase in overall classification performance has been reported by Zhao et al. (2018), especially in terms of accuracy, recall, precision, and F-score.

Despite promising results, the framework's effectiveness with medical datasets of varying imbalance levels remains unexplored. This uncharted nature motivates the current research study. However, the validity and effectiveness of the rebalancing framework may vary between datasets based on the imbalance ratio (IR), necessitating classifiers capable of enhancing performance across different IR (Mohammed et al., 2020; Krishnan & Sangar, 2021; Tantithamthavorn et al., 2020; Jiang et al., 2020).

Therefore, our research investigates the effectiveness of ensemble-based classifiers within the Zhao et al. (2018) rebalancing framework while exploring additional datasets, aligning with the author's attention to experimentally test the framework with more imbalanced medical datasets.

An ensemble-based classifier is a combination of more than one classifier (Valentini & Dietterich, 2004) that performs better than individual ones. Researchers across various domains have widely implemented ensembles for enhanced classification (Mohandes et al., 2018). The advantages of employing an ensemble approach are: (1) it combines stronger classifiers to address class imbalance, ensuring efficient imbalance learning (Khalilia et al., 2011; Cahyana et al., 2019); (2) our previous work (Edward & Rosli, 2021), a systematic mapping study (SMS) on ensemble-based classifiers, highlighted the favorability of the ensemble approach among researchers in the medical domain, particularly for its

effectiveness in diagnostic classification. The SMS also uncovered a prevailing trend where many researchers prefer the hard-level majority voting technique as their primary choice for ensemble combination methods, especially in medical research. Thus, we selected the hard-level majority voting technique as our preferred combination method. These reasons alone were enough to spark our interest in exploring this method via Zhao et al. (2018) rebalancing framework.

To further leverage the capabilities of the assembling approach, we adapted our proposed ensemble-based classifier as the baseline estimator within the Self-paced Ensemble (SPE), an imbalance learning method introduced by Liu et al. (2020). SPE introduces the classification ‘hardness’ concept to demonstrate a trained classifier’s difficulty in identifying a particular sample. Based on this hardness, SPE iteratively selects the most informative majority data samples in accordance with their distribution rather than simply balancing the positive and negative data or applying instance weights. Implementing SPE for highly imbalanced data is expected to yield significant results (Liu et al., 2020).

This study conducts three experiments to determine whether ensemble-based classifiers improve the existing framework. Initially, we assessed the performance of each imbalanced dataset used in this study. We compared the results obtained using the original baseline classifier recommended by Zhao et al. (2018) framework with those achieved with ensemble-based baseline classifiers. Subsequently, we conducted another experiment with our proposed ensemble-based classifier to evaluate the effectiveness of the ensemble approach. The results were then comprehensively compared to determine which method demonstrated a more substantial performance improvement.

The overall results of our experiments revealed that our proposed ensemble-based classifiers with SPE outperformed both the original baseline and the baseline with the ensemble approach in terms of overall performance measures (accuracy, precision, recall, F-score, and G-mean). This outcome highlights the effectiveness of the ensemble method in addressing class imbalances in medical data, demonstrating its potential for enhanced performance in imbalance learning. In summary, the key contributions of this article are as follows:

1. To investigate and provide a comprehensive analysis of the effectiveness of ensemble-based classifiers in the rebalancing framework proposed by Zhao et al. (2018).
2. To explore and experimentally test the framework of Zhao et al. (2018) with more imbalanced medical datasets.
3. To introduce and evaluate SPE(EM), a novel ensemble approach. SPE(EM), combining decision tree (DT), radial support vector machine (R.SVM), and extreme gradient boosting (XGB) classifiers, outperformed the baseline with significant improvements (4.96%, 5.89%, 5.68%, 7.85%, and 6.84%) in accuracy,

precision, recall, F-score, and G-mean. This contribution extends the understanding of ensemble methods in addressing class imbalances in medical datasets.

THE FRAMEWORK

As previously mentioned, the framework we adopted and tested in this research study is the rebalancing framework developed by Zhao et al. (2018). In their research, the authors experimented with medical incidents due to look-alike (LASA) mix-ups dataset, which exhibited class imbalance. This dataset comprises 227 records with structured text, including eight features and binary class target variables (LASA and non-LASA). The authors' framework demonstrated a notable ability to classify LASA incident reports with high predictive accuracy. Although their primary focus was on incident report classification, the authors suggested that their rebalancing framework holds broad applicability, extending beyond the classification of medical incident reports to address other medical datasets with similar imbalanced properties.

Zhao et al.'s (2018) framework incorporates algorithmic and data-level approaches to rebalance the unequal class distribution to address the class imbalance issue. A detailed investigation was conducted to assess the impact and performance of various classifiers, utilizing a sequence of three key stages within the framework. Specifically, these stages are based on classifier selection, incorporating four rebalancing strategies, and leave-one-out cross-validation (LOOCV). In the initial stage, the performance of each candidate classifier is evaluated based on standard metrics (accuracy, precision, recall, and F-score) to determine the best-performing classifier. Zhao et al. (2018) suggest that candidate classifiers can be linear or non-linear for binary classification. However, for their experimental studies, they opted for logistic regression (LR), support vector machine with linear kernels (L.SVM), support vector machine with radial kernels (R.SVM), and decision tree (DT) as their baseline classifiers.

The second stage involves rebalancing imbalanced medical data using four strategies: the SMOTE (Chawla et al., 2002), cost-sensitive learning (Elkan, 2013), and random oversampling and undersampling techniques (Japkowicz, 2000). Similarly, when training with the base classifiers selected from the previous stage, the framework suggests determining which of the four strategies yields the most substantial performance improvements across various parameter configurations for each rebalancing strategy. The available hyperparameter tuning range must be developed using criteria for each rebalancing strategy's parameter/threshold.

As Zhao et al. (2018) suggested, datasets with imbalanced distributions need to be rebalanced (using each strategy) and validated using the LOOCV in stage three. A conventional cross-validation technique in which one sample is excluded (leave-out) for validation and training is performed on the other samples supplied to the model; this

procedure is repeated on all samples. LOOCV is widely favored by many researchers for extensive validation processes, where the number of cross-validations is determined by the number of instances in a dataset (Cheng et al., 2017). In the medical domain, it has been implemented in many model validations, such as the biomedical phenotype predictive model (deAndrés-Galiana et al., 2016), Alzheimer's classification model (Cuingnet et al., 2011), breast cancer model (Liang et al., 2018), and kidney stone predictive model (Shabaniyan et al., 2019).

Table 1 summarizes the adapted framework process by Zhao et al. (2018) in stages. The framework provides detailed insight into the framework we adapted for our experiments.

Table 1
Stages of the adapted (Zhao et al., 2018) rebalancing framework process

Stage	Process	Description	Selections
1 Classifier • R.SVM baseline	Selecting base linear or non-linear	Candidate classifiers can be either Select the classifier that performs best as	• LR • L.SVM • DT
2 Rebalancing strategies • Strategy parameter/ threshold • Sensitive learning	Incorporating strategies according to results of each parameter tune	Select best-performed rebalancing Oversampling Tune according to each rebalancing	• SMOTE • Random • Random undersampling cost
3 Validate model		Estimate finalized model performance	• LOOCV

MATERIALS AND METHODS

Ensemble-based Classifier

A unified classifier overcomes the limitations of each counterpart in terms of accuracy and performance (Utami et al., 2014). As mentioned earlier, we employed the hard-level technique using majority voting for classifier combinations in this study. This approach combines the highest predicted class output from each classifier. For instance, if six out of eleven classifiers vote for the same class output, the class with the highest number of votes is considered the final result. The formulation for our hard-level majority voting, Em , is calculated using Equation 1:

$$Em = \sum_{i=1}^M d_{i,k} = \max_{j=1}^h \sum_{i=1}^M d_{i,j} \quad [1]$$

where M is the total number of classifiers and h is the total number of classes. However, the class that received the same maximal vote (tie) can be resolved using the weighted

majority voting (Kuncheva, 2014) to choose the class with higher weighted votes. The weighted majority voting is calculated using Equation 2:

$$\sum_{i=1}^M b_i d_{i,k} = \max_{j=1}^h \sum_{i=1}^M b_i d_{i,j} \tag{2}$$

where b_i is the weighting coefficient for classifier D_i .

Self-paced Ensemble

Classifiers tend to prioritize a class with more samples when learning from highly skewed data, leading to biased predictions. Consequently, the ability of classifiers to distinguish between minority and majority classes is highly dependent on the data distribution they learn. Conventional rebalancing techniques (e.g., random oversampling, undersampling, SMOTE) offer common approaches for imbalanced learning. Going further, Liu et al. (2020) introduce a novel imbalance learning method, the Self-paced Ensemble (SPE). SPE incorporates the concept of ‘hardness’ in classification, describing the difficulty of categorizing a sample for a given classifier. Derived from this difficulty, SPE systematically chooses the most informative data samples that align with their distribution. Equation 3 calculates the hardness:

$$H(x, y, F) = \frac{1}{n} \sum_{i=1}^n |f_i(x_i) - y_i| \tag{3}$$

where H is the hardness function, F can be any chosen classifier and dataset as (x,y) . $F(x_i)$ indicates the classifier’s probability. Liu et al. (2020) state that SPE can be adapted to any classifier. As mentioned previously, to align with the use case of this study, we adapted our proposed ensemble-based classifier, Em , as the SPE base estimator to enhance its effectiveness. The new adapted hardness function with Em is defined in Equation 4:

$$SPE(Em) = H(x, y, Em) = \frac{1}{n} \sum_{i=1}^n |f_i(x_i) - y_i| \tag{4}$$

SPE enhances the significance of boundary samples by incorporating an undersampling technique to reduce the presence of noisy and insignificant data samples. It is achieved by dividing most samples into k bins based on their hardness rating, where k is the hyperparameter. Each bin is then undersampled to create a balanced dataset, ensuring that every bin has similar hardness. The formulation of SPE with our adapted Em , $SPE(Em)$, is shown in Equation 5:

$$B_l = \left\{ (x, y) \mid \frac{(l-1)}{k} SPE(Em) \leq \frac{l}{k} \right\} w. l. o. g. H \in [0,1] \tag{5}$$

where B_l is used to denote the l -th bin.

Performance Evaluation Metrics

The most commonly used metrics for classifier model performance are accuracy, precision, and recall. Accuracy represents the overall proportion of correctly predicted instances across all classes, calculated using Equation 6:

$$Accuracy = (TP + TN)/(TP + FP + TN) \quad [6]$$

where TP is the true positive, TN is the true negative, and FP is the false negative.

Meanwhile, precision focuses on the true positive rate within the positive predictions, while recall measures the ability of classifiers to correctly identify the actual positive class (Grandini et al., 2020). Equation 7 calculates the precision, while Equation 8 calculates the recall:

$$Precision = (TP)/(TP + FP) \quad [7]$$

$$Recall = (TP)/(TP + FN) \quad [8]$$

where FN is the false negative.

However, accuracy alone may not offer a comprehensive view of a classifier's performance in class imbalance due to the bias inherent in the class distribution between the minority and majority classes. High precision may come at the cost of low recall and vice versa when it comes to precision and recall. Maintaining an appropriate balance between these metrics becomes crucial for effectively handling imbalanced data. Therefore, depending solely on these metrics in an imbalanced class scenario can be misleading (Akosa, 2017).

In this study, we have incorporated F-score and G-mean as additional metrics to obtain a more accurate and comprehensive assessment in such scenarios. The F-score, in particular, offers a balanced evaluation that takes into account both precision and recall, as it offers a well-rounded assessment of a classifier's performance. It considers FPs and FNs to determine the harmonic mean of precision and recall (Phoungphol et al., 2012). Equation 9 calculates the F-score:

$$F - score = \frac{(Recall \times Precision)}{(Recall + Precision)} \quad [9]$$

The G-mean metric offers valuable insights into a classifier's capability to classify minority class instances, a crucial metric for class imbalance. Additionally, it considers both TPs and TNs, ensuring a comprehensive evaluation of a classifier's performance with equal weight given to both classes. Consequently, it prevents excessive bias toward the majority class, fostering a more balanced approach. (Błaszczuk & Jedrzejowicz, 2021). Equation 10 calculates the G-mean:

$$G - mean = \sqrt{Recall \times Precision} \quad [10]$$

Rebalancing Strategies

As per the recommendation by the adapted framework, this study incorporates four rebalancing strategies: random oversampling, random undersampling, SMOTE, and CSL. Random oversampling involves duplicating instances from the minority class to balance class distribution (Barua et al., 2014). This strategy is effective when the dataset has a small number of minority class instances, but it may lead to overfitting if not applied cautiously. Conversely, random undersampling randomly reduces the number of majority class instances to match the minority class, making it suitable for datasets with a large majority class and when computational efficiency is a concern. However, it may lead to the loss of valuable information from the majority class (Barua et al., 2014).

SMOTE generates synthetic instances in the minority class by interpolating between existing instances, thereby enhancing the representation of the minority class and achieving a balanced class distribution while removing bias. It is commonly employed in various imbalance learning scenarios and proves particularly useful when limited data is available for the minority class (Kotsiantis et al., 2006). CSL, on the other hand, assigns different misclassification costs to different classes, emphasizing the importance of the minority class. This approach is beneficial in cases of severe class imbalance, where misclassifying the minority class carries higher consequences (Krawczyk, 2016). CSL aims to reduce the misclassification of the minority class by making it more costly for the classifier.

The rationale for choosing which rebalancing strategy to use depends on the specific characteristics of the dataset, such as the class distribution, dataset size, and the consequences of misclassification. While one strategy may yield enhanced performance for a certain dataset, it might not prove as effective for another. The choice of strategy can also be influenced by the type of classifier used, as different classifiers may interact differently with rebalancing techniques (Cipriano et al., 2021), leading to varied performance outcomes. Therefore, this study independently implemented each strategy to identify the most effective strategy for the specific dataset.

Experimental Setup

In our first experiment, we assessed the overall performance of the rebalancing framework outlined by Zhao et al. (2018) on each dataset. It entailed using the initial baseline classifiers recommended within the framework: LR, L.SVM, R.SVM, and DT. We directly applied these classifiers, compared their results, and identified the top-performing classifier as our baseline. This experimental approach is denoted as ‘Experiment 1’.

In our second experiment, rather than comparing individual candidate classifiers, we amalgamated them into a unified classifier using hard-level majority voting. Following this, we applied the framework utilizing the ensemble baseline classifier to assess its performance. This experimental approach is designated as ‘Experiment 2’.

Finally, in the third experiment, we employed our proposed SPE with an ensemble-based classifier as the base estimator, denoted as SPE(*Em*). *Em* represents a combination of DT C4.5, R.SVM, and XGB. This experimental approach is designated as ‘Experiment 3’.

The DT c4.5 algorithm is a conventional yet powerful classification method frequently used to solve medical diagnosis problems (Breiman, 2001). Radial is a well-known kernel function that is utilized in a variety of kernelized learning techniques. It is part of a kernel function embedded in the standard support vector machine (SVM). Hence, the name R.SVM. Kernels is the application-specific measure of similarity between data instances used by SVM. R.SVM proved to show significant classification performance in the medical domain for predicting diseases (Harimoorthy & Thangavelu, 2021). Meanwhile, XGB is a more regularized, expanded version of a gradient boosting method that provides a robust boosted tree model with high accuracy and is known for its ability to classify imbalanced datasets (Cahyana et al., 2019; Ma et al., 2022).

Finally, we compared the performance results obtained from each experiment to ascertain which experiment yielded robust overall performance across all datasets. Five evaluation performance metrics were used to measure the performance in each experiment: accuracy, precision, recall, F-score, and G-mean to measure the performance in each experiment. Additionally, we incorporated the receiver operating characteristic curve (ROC) and root mean square error (RMSE) as part of our evaluation metrics. These metrics are commonly used to evaluate the performance of a model in a binary classification. The overall workflow is shown in Figure 1. Our experiment setup codes are available on GitHub (<https://tinyurl.com/vxphztf>).

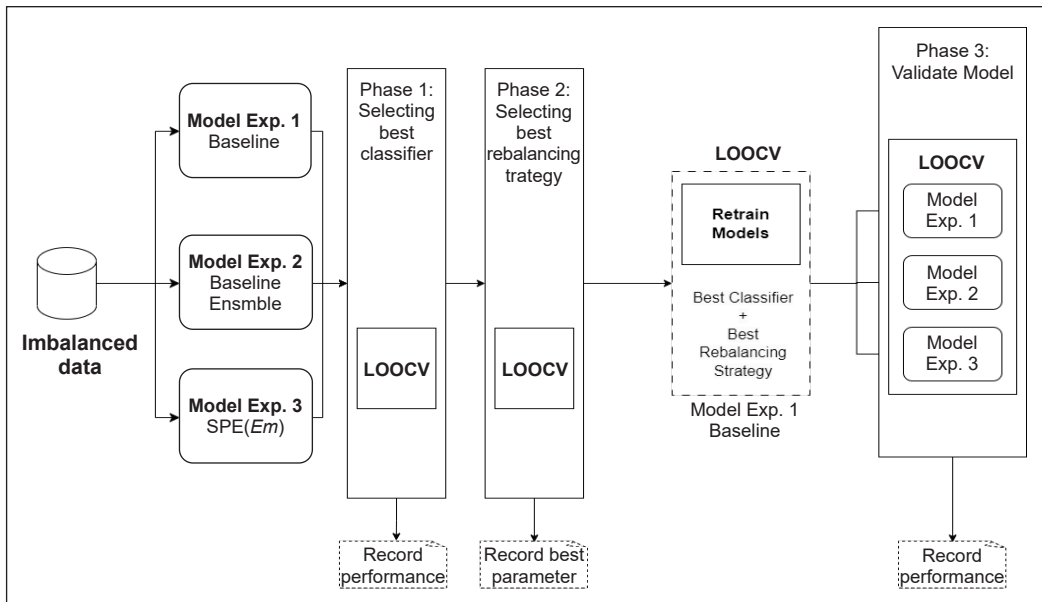


Figure 1. Workflow of experimental approaches

Statistical Test

In this study, we employed the paired t-test as the preferred statistical analysis method to assess the significance of the results. The paired t-test is a well-known statistical test that allows us to compare the means of two related groups while taking into account the dependency between them (Newcombe, 1992). Additionally, it assesses whether there is a significant difference in the means of paired observations while taking into account that the observations are dependent. It does so by calculating a t-statistic that measures the standardized difference between the means of the paired observations.

In the case of the paired t-test, it is calculated based on the differences between paired observations. Meanwhile, the p-value associated with the t-statistic indicates the likelihood of observing such a difference by chance. A lower p-value indicates a higher degree of statistical significance. If the p-value is below a predetermined significance level (<0.05), we can infer a statistically significant difference in the performance outcomes between the experiments. By employing the paired t-test, we aimed to rigorously assess the statistical significance of the improvements observed in Experiment 3, thus providing robust evidence of the effectiveness of our proposed ensemble-based classifier.

Datasets

Our experiments utilized seven imbalanced medical datasets from the UC Irvine machine learning repository (UCI), Kaggle, and Knowledge Extraction based on Evolutionary Learning (KEEL). These datasets are identified as Heart disease (Cleveland0vs4), eColi4, Yeast3, SPECT, SPECTF, Parkinson, and Cirrhosis. Each dataset exhibits a distinct level of imbalanced class distribution. The datasets are structured in a tabular and binary format. We calculated the class ratios for each dataset, representing the level of imbalance as the IR. A higher IR indicates a more imbalanced distribution (Zhu, Guo, & Xue, 2020). Equation 11 is used to calculate the IR for a binary class problem:

$$IR = \frac{N_{max}}{N_{min}} \quad [11]$$

where N_{maj} is the number of majority instances, and N_{min} is the number of minority instances.

Note that in this study, our focus is solely on binary classification. We selected datasets initially formatted for binary classification to maintain the binary setting. Table 2 summarizes the structure of these datasets. It shows that the Cirrhosis dataset has the highest level of imbalance, with $IR = 18.90$. It is followed by the eColi4 and Cleveland0vs4 datasets, with $IR = 15.80$ and 12.62 , respectively. The others have IR below 8.10, and Parkinson has a minimum $IR=3.06$.

Table 2
Summary of imbalanced medical datasets

Dataset	No. of Records	No. of Features	Class Distribution			Imbalance Ratio (N_{maj}/N_{min})	Source
			Class	Samples	Percentage (%)		
Cleveland0vs4	177	13	0	164	92.65%	12.62	KEEL ¹
			1	13	7.35%		
eColi4	336	7	0	316	92.65%	15.80	KEEL ¹
			1	20	5.95%		
Yeast3	1484	8	0	1321	89.02%	8.10	Kaggle ²
			1	163	10.98%		
SPECT	267	22	0	55	20.60%	3.85	UCI ³
			1	212	79.40%		
SPECTF	267	44	0	55	20.59%	3.85	UCI ³
			1	212	79.41%		
Parkinson	195	22	0	48	24.61%	3.06	UCI ³
			1	147	75.39%		
Cirrhosis	418	13	0	21	5.02%	18.90	Kaggle ²
			1	397	94.98%		

¹<http://www.keel.es>; ²<https://www.kaggle.com/>; ³<http://archive.ics.uci.edu/ml>

RESULTS

To facilitate readers' understanding of the experimental part, we run each experiment according to the process explained in the previous discussion. We then discuss and compare the results with and without the rebalancing strategy applied.

Experimental Results

We executed the original framework from Zhao et al. (2018) across all the imbalanced datasets. The main focus was to assess the performance of each candidate classifier recommended by the framework and identify the classifier that demonstrated the highest performance on each dataset. In our experiments, we performed LOOCV for stages 1,2 and 3. We then record the performance of each stage. The results for stages 1 and 3 are shown in Table 3, which shows the average LOOCV results of all experimental approaches with and without the rebalancing strategy applied. Meanwhile, the results for stage 2 are shown in Table 4.

The analysis based on the experimental results is as follows:

1. According to Table 3, the datasets highlighted in bold demonstrated the best overall performance on each dataset in terms of accuracy, precision, recall, F-score, and G-mean. The left side of the table (no rebalancing) shows that all models have relatively acceptable accuracy but low values for the other metrics. The imbalanced nature of data distribution contributes to this degradation, especially in Cirrhosis,

Table 3
Comparison of average LOOCV classification performance with/without rebalancing strategy

Dataset	Exp.	Classifier	No Rebalancing					With Rebalancing						
			Acc	Prec	Rec	F-score	G-mean	TPFN/FP/TN	Acc	Prec	Rec	F-score	G-mean	TPFN/FP/TN
Cleveland0vs4	Exp 1	L.SVM	93.22%	53.85%	53.85%	53.85%	72.03%	7/6/6/158	85.31%	32.43%	92.31%	48%	88.45%	12/1/25/139
	Exp 2	Base Em.	93.79%	62.5%	38.46%	47.62%	61.45%	5/8/3/161	95.48%	72.73%	61.54%	66.67%	77.73%	8/5/3/161
	Exp 3	SPE(Em)	94.35%	57.89%	84.62%	68.75%	89.71%	11/2/8/156	93.79%	54.55%	92.31%	68.77%	93.10%	12/1/10/154
eColi4	Exp 1	DT	96.13%	65.22%	75%	67.77%	85.50%	15/5/8/308	97.62%	87.50%	70%	77.78%	83.40%	14/6/2/314
	Exp 2	Base Em.	98.81%	110%	80%	88.89%	89.44%	16/4/0/316	98.51%	100%	75%	85.71%	86.60%	15/5/0/316
	Exp 3	SPE(Em)	98.21%	85%	85%	85%	91.76%	17/3/3/313	98.21%	81.82%	90%	85.71%	94.27%	18/2/4/312
Yeast3	Exp 1	L.SVM	94.61%	78.23%	70.55%	74.19%	82.97%	115/48/32/1289	93.87%	69.15%	79.75%	74.07%	87.32%	130/33/58/1263
	Exp 2	Base Em.	94.61%	82.17%	65.03%	72.60%	79.94%	106/57/23/1298	94.95%	74.72%	81.60%	78.01%	88.78%	133/30/45/1276
	Exp 3	SPE(Em)	95.15%	75.71%	82.21%	78.82%	89.18%	134/29/43/1278	94.61%	72.93%	80.98%	76.74%	88.31%	132/31/49/1272
SPECT	Exp 1	L.SVM	82.77%	88.43%	90.09%	89.25%	70.10%	191/21/25/30	76.40%	91.16%	77.83%	83.97%	74.29%	165/47/16/39
	Exp 2	Base Em.	81.27%	88.21%	88.21%	88.21%	69.36%	187/25/25/30	74.53%	92.35%	74.06%	82.20%	75.20%	157/55/13/42
	Exp 3	SPE(Em)	76.78%	94.12%	75.47%	83.77%	78.58%	160/52/10/45	79.40%	91.53%	81.60%	86.28%	76.07%	173/39/16/39
SPECTF	Exp 1	L.SVM	79.78%	86.57%	88.21%	87.38%	64.57%	187/25/29/26	73.78%	88.17%	77.36%	82.41%	68.13%	164/48/22/33
	Exp 2	Base Em.	80.90%	87.44%	88.68%	88.06%	67.19%	188/24/27/28	69.29%	92.76%	66.51%	77.47%	72.94%	141/71/11/44
	Exp 3	SPE(Em)	73.03%	94.87%	69.81%	80.43%	77.24%	148/64/8/47	77.15%	90.37%	79.72%	84.71%	73.23%	169/43/18/37
Parkinson	Exp 1	L.SVM	87.69%	87.73%	97.28%	92.26%	75.33%	143/4/20/28	80.51%	90.37%	82.99%	86.52%	77.79%	122/25/13/35
	Exp 2	Base Em.	87.69%	88.20%	96.60%	92.21%	76.39%	142/5/19/29	78.46%	93.39%	76.87%	84.33%	80.04%	113/34/8/40
	Exp 3	SPE(Em)	92.31%	95.21%	94.56%	94.88%	89.87%	139/8/7/41	93.85%	94.70%	97.28%	95.97%	90.04%	143/4/8/40
Cirrhosis0vs4	Exp 1	L.SVM	94.98%	94.98%	100%	97.42%	0%	397/0/21/0	76.56%	96.00%	78.59%	86.43%	54.72%	312/85/13/8
	Exp 2	Base Em.	94.74%	94.96%	99.75%	97.30%	0%	396/1/21/0	78.95%	97.54%	79.85%	87.81%	70.31%	917/80/8/13
	Exp 3	SPE(Em)	62.44%	98%	61.71%	75.73%	68.57%	245/152/5/16	84.21%	97.42%	85.64%	91.15%	69.96%	340/57/9/12

Acc=Accuracy, Prec = Precision, Rec = Recall

eColi4, and Cleveland0vs4. The ensemble baseline in Experiment 2 performed poorly due to the individual weak learners underachieving the final output. However, SPE(*Em*) in Experiment 3 achieved considerably adequate balance results in all the performance measures across most of the dataset. For instance, it has a higher G-mean in Cirrhosis with 68.57%, 89.71% for Cleveland0vs4, and 91.76% for eColi4.

2. Table 3, on the right side of the table (with the best rebalancing strategy), shows that all experimental models substantially improved overall performance across all the metrics. Rebalancing data contributes to better classifier performance.
3. Comparing the experimental results in Table 3, SPE(*Em*) outperforms the other experiment models with significant improvements, followed by Experiment 2 and Experiment 1. For instance, SPE(*Em*) achieved an increase of F-score from 75.73% to 91.15% in the Cirrhosis dataset after rebalancing with the best strategy. Experiment 2 slightly outperforms Experiment 1 in terms of f-score and G-mean, especially in Cleveland0vs4, eColi4, Yeast3, and Cirrhosis. Notice that the results for Experiment 3 have adequate performance even without rebalancing and achieved slightly better performance after rebalancing.

Table 4 compares the best-selected base classifier and rebalancing strategy with the best performance. For SMOTE, the number of oversampled minority instances, α , and undersampled majority instances, γ , are controlled by these two parameters, respectively. SMOTE handles imbalanced datasets by oversampling the minority class. Even if the examples provide no new information to the model, SMOTE will duplicate the instances from the minority class and construct new instances by synthesizing the existing examples (Chawla et al., 2002). We applied SMOTE during the LOOCV to resample each training fold and validate on the test fold; the same approach also applies to the random sampling (under and oversampling) method.

Note that for each rebalancing strategy, we only applied the parameter settings that showed the highest improvement in overall results. Table 4 shows that Cost-sensitive

Table 4
A comparison of the selected base classifier and rebalancing strategy gives the best performance with LOOCV

Experiment	Dataset	Best Base Classifier	Best Rebalancing Strategy	
			Best Strategy	Best Parameter Setting
Exp 1	Cleveland0vs4	L.SVM	SMOTE	$\alpha = 0.68, \gamma = 0.85$
	eColi4	DT	Oversampling	ratio = 0.85
	Yeast3	L.SVM	Oversampling	ratio = 0.35
	SPECT	L.SVM	SMOTE	$\alpha = 0.5, \gamma = 0.5$
	SPECTF	L.SVM	Oversampling	ratio = 0.68
	Parkinson	L.SVM	SMOTE	$\alpha = 0.75, \gamma = 0.35$
	Cirrhosis0vs4	L.SVM	Undersampling	Ratio = 0.5

Table 4 (continue)

Experiment	Dataset	Best Base Classifier	Best Rebalancing Strategy	
			Best Strategy	Best Parameter Setting
Exp 2	Cleveland0vs4	Baseline	Oversampling	ratio = 0.85
	eColi4	Ensemble	CSL	Threshold = 0.015
	Yeast3	(LR+L.SVM+	Oversampling	ratio = 0.5
	SPECT	R.SVM+DT)	CSL	Threshold = 0.25
	SPECTF		SMOTE	$\alpha = 0.65, \gamma = 0.65$
	Parkinson		SMOTE	$\alpha = 0.5, \gamma = 0.5$
	Cirrhosis0vs4		CSL	Threshold = 15
Exp 3	Cleveland0vs4		Undersampling	ratio = 0.15
	eColi4		CSL	Threshold = 0.5
	Yeast3	SPE(<i>Em</i>)	CSL	Threshold = 0.015
	SPECT		Undersampling	ratio = 0.28
	SPECTF		SMOTE	$\alpha = 0.65, \gamma = 0.65$
	Parkinson		Oversampling	ratio = 0.75
	Cirrhosis0vs4		Oversampling	Ratio = 0.1

learning (CSL), oversampling and SMOTE performed best with most of the datasets in all experiments. Most datasets in Experiment 1 were best rebalanced with oversampling, while Experiments 2 and 3 favored the other sampling methods.

Overall Results

Per the framework's recommendation, we performed the LOOCV with varying repetitions according to the number of instances on each dataset (Zhao et al., 2018). We obtained the results and recorded them as the average validation performance across all datasets by an experimental approach. Table 5 presents a comparative analysis of overall performance metrics, as average LOOCV across all datasets for each experimental approach.

According to Table 5, Experiment 1 with baseline classifier (LR, L.SVM, R.SVM and DT) performs at 84.10%, 79.34%, 80.71%, 77.53%, and 76.70% in terms of accuracy, precision, recall, F-score, and G-mean, respectively. In Experiment 2, there was a noticeable increase in F-score and G-mean by 81.36% and 79.70%; however, recall declined to 75.32%. Meanwhile, the average performance obtained in Experiment 3 was 89.06%, 85.23%, 86.39%, 85.38%, and 83.54% in terms of accuracy, precision, recall, F-score, and G-mean, respectively. Overall, the proposed method used in Experiment 3 has improved the overall performance compared with the baseline conditions (Experiment 1) by 4.96%, 5.89%, 5.68%, 7.85%, and 6.84% in terms of accuracy, precision, recall, F-score, and G-mean respectively. The results also show that the combined baseline classifier in Experiment 2 has increased performance and is slightly better than Experiment 1, especially in the F-score of 81.36%.

Table 5
Average LOOCV performance comparison on all datasets for each experimental approach

xp.	Classifier	Performance Achieved				
		Acc	Prec	Rec	F-score	G-mean
Exp 1	Baseline: LR, L.SVM,R.SVM,DT	84.10%	79.34%	80.71%	77.53%	76.70%
Exp 2	Baseline En	85.04%	89.14%	75.32%	81.36%	79.70%
Exp 3	SPE(Em)	89.06%	85.23%	86.39%	85.38%	83.54%
	SPE(Em) Increase from Exp 1	+4.96%	+5.89%	+5.68%	+7.85%	+6.84%

Acc= Accuracy, Prec = Precision, Rec = Recall

The ROC, which plots the true positive rate (TPR) against the false positive rate (FPR) for each experiment, is depicted in Figure 2. These are used to assess the robustness of the three experimental approaches. Applied by many researchers, ROC curves are a useful way to evaluate imbalanced data (Turlapati & Prusty, 2020; Phoungphol et al., 2012; Yao & Chen, 2019). We performed the ROC analysis with the LOOCV. The area under ROC (AUROC) curves for each approach are shown in blue, green, and red for Experiments 1, 2 and 3, respectively, in Figure 2. The performance of a ‘random guessing classifier’ for the class of observations is depicted by the grey dashed line in each figure (no-discrimination line). A successful classification technique should provide points close to or in the top part of the graph (0,1) (Saito & Rehmsmeier, 2015; Mandrekar, 2010).

All plots of TPR versus FPR lie above the grey line, indicating that all three approaches are able to handle the binary class classification problem. However, the ROC for SPE(Em) in Experiment 3 is closer to coordinate (0,1) on Cleveland0vs4, eColi4, SPECT, SPECTF, Parkinson, and Cirrhosis with AUC 0.97, 0.99, 0.83, 0.84, 0.96, and 0.73, respectively. However, all experiments achieved a similar AUC of 0.97 on the Yeast3 dataset, with Experiment 3 having a slightly closer curve, followed by the second-best model in Experiments 2 and 1. Decisively, Experiment 3 demonstrates higher ROC results than the other two experiments across most of the datasets, indicating the model could significantly distinguish between the positive and negative classes for better classification.

We also record the RMSE on each fold of LOOCV with respect to each dataset to evaluate the error rate. The square root of MSE is referred to as RMSE. The error rate is a percentage measure of the difference between the actual and estimated values. The lower the RMSE (>=0), the lower the error rate. The RMSE is reported in Table 6.

Table 6
RMSE of all experimental models on each dataset

Dataset	Exp 1	Exp 2	Exp 3
	RMSE	RMSE	RMSE
Cleveland0vs4	0.36	0.21	0.24
eColi4	0.17	0.15	0.14
Yeast3	0.22	0.2	0.21
SPECT	0.57	0.4	0.4
SPECTF	0.4	0.42	0.43
Parkinson	0.35	0.32	0.25
Cirrhosis	0.23	0.21	0.19
Average	0.3286	0.2729	0.2657

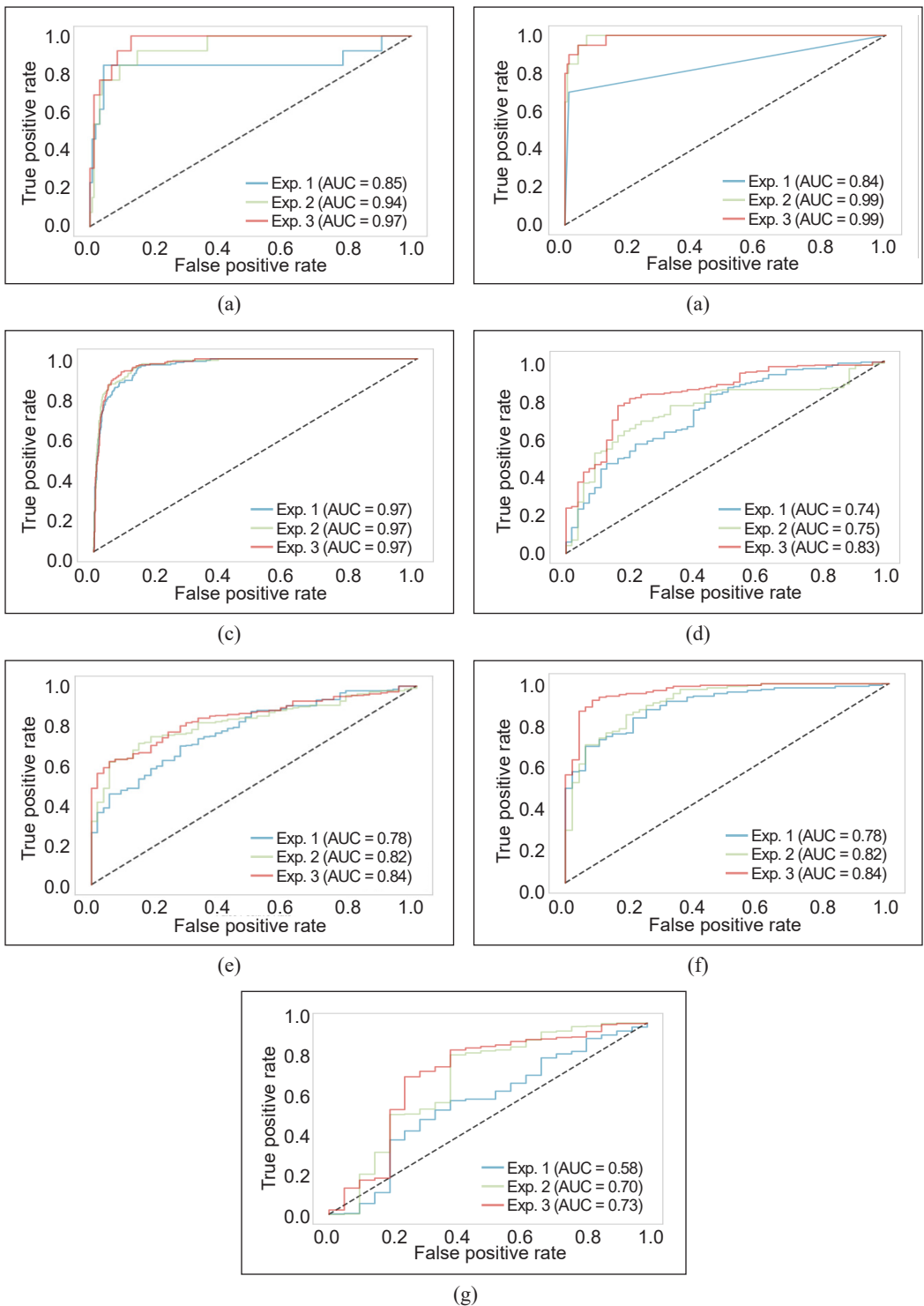


Figure 2. ROC curves for each dataset with different experimental approaches: (a) Cleveland0vs4; (b) eColi4; (c) Yeast3; (d) SPECT; (e) SPECT; (f) Parkinson; and (g) Cirrhosis

As shown in Table 6, the $SPE(Em)$ in Experiment 3 performed best with RMSE values of 0.14, 0.25, and 0.19 for eColi4, Parkinson's, and Cirrhosis, respectively. Averaged at 0.2657 overall RMSE. While Experiment 2 has an RMSE average of 0.2729, it is slightly closer to Experiment 3. Experiment 1 was performed at an RMSE value of 0.3286, distinctly higher than the other experiments. Comparing the experimental models, $SPE(Em)$ seems to have a slight edge over the Experiment 2 model.

Table 7

Paired t-test statistical results of Experiment 3 with the other two experimental approaches

	Paired Differences					t	df	p-value
	Mean	Std. Deviation	Std. Error mean	95% Confidence Interval of the Difference				
				Lower	Upper			
Exp 3 – Exp 1	6.24	1.0026	0.4484	4.990	7.4890	12.4550	4	.000239
Exp 3 – Exp 2	3.81	4.7412	2.1203	-2.079	9.6950	1.6063	4	.1835

Table 7 shows the statistical test results using the paired t-test between Experiment 3 and the other two experimental approaches. The comparison between Experiment 3 and Experiment 1 revealed a significant difference in performance. Experiment 3 displayed a substantial improvement with a mean difference of 6.24, a low standard error (0.4484), and a narrow confidence interval (4.990 to 7.4890). Additionally, the high t-statistic (12.4550) and the extremely low p-value (0.000239) emphasized the statistical significance of Experiment 3's superior performance over Experiment 1. Meanwhile, the comparison between Experiment 3 and Experiment 2 was not statistically significant due to its p-value of 0.1835, which is more than the significant level of 0.05. However, it is important to note that both Experiment 3 and Experiment 2 utilized the same ensemble method. It highlights the effectiveness of the ensemble approach, as both Experiment 3 and Experiment 2 consistently outperformed Experiment 1, the baseline method. Although statistical significance may not be established in every case, the shared use of the ensemble method highlights its effectiveness in enhancing overall performance.

DISCUSSION

This study presents our investigation into the performance of ensemble-based classifiers within the Zhao et al. (2018) framework, employing seven imbalanced datasets. Our experimental results clearly indicate that rebalancing methods enhance the overall predictive learning of classifiers (Table 3). To evaluate the performance of each experimental model, we LOOCV for Stages 1 to 3 and recorded the results. Significantly, the performance of each model improved, with $SPE(Em)$ in Experiment 3 demonstrating the best overall performance, followed by Experiment 2 and 1. Our primary metrics for imbalance learning

are AUROC, F-score, and G-mean. Specifically, the F-score is apt for discriminating between the minority and majority classes. AUROC summarizes a model's capacity to discriminate between classes, and G-mean measures the minority class performance. In terms of overall performance (Table 5 and Figure 2), our proposed SPE(*Em*) yielded significant results for all three metrics, followed by the baseline ensemble in Experiments 2 and 1.

SPE(*Em*) also improved the overall performance compared to the baseline by 4.96%, 5.89%, 5.68%, 7.85% and 6.84% in accuracy, precision, recall, F-score, and G-mean, respectively. The improved performance observed in Experiments 2 and 3 is attributed to utilizing an ensemble of classifiers, particularly stronger classifiers capable of mitigating class imbalances. It aligns with findings from prior studies (Jiang et al., 2020; Valentini & Dietterich, 2004) that demonstrate how incorporating ensemble methods leads to a unified improvement in overall performance. In Experiment 3, boosting the performance of the ensemble classifier (R.SVM, DT, and XGB) with SPE showed increased results. It is also relevant to point out that the ensemble-based classifiers can achieve consistent and stable performance with increased results compared to the baseline (Experiment 1). Therefore, classifying imbalanced data proves to have a significant impact on the objective of this study.

Experiment 1 served as the essential baseline for comparison with the other two experiments; hence, we refer to it as the benchmark experiment. By comparing the results of this benchmark experiment, we have demonstrated that the proposed ensemble-based classifier in Experiment 3 achieved superior outcomes. The findings from both Experiments 2 and 3 offer compelling evidence of the effectiveness of ensemble-based classifiers in enhancing the existing framework (Zhao et al., 2018). Consequently, the results from Experiment 3 will serve as the cornerstone for our future endeavors in developing a rebalancing framework integrated with ensemble-based classifiers soon.

The results of these experiments are in line with Zhao et al. (2018), which further supports its applicability on various applications not just limited to medical incident reports but also various medical data with similar class imbalanced properties. Additionally, it is also worth mentioning that these results are consistent with previous studies implementing ensemble-based classifiers to address class imbalances in medical data (Zhu et al., 2015; Sandhan & Choi, 2014). Notably, prior similar works (Krishnan & Sangar, 2021; Song et al., 2022; Bi & Ma, 2021; Tang et al., 2021) incorporating ensemble methods in their rebalancing frameworks have shown significant results, further supporting the effectiveness of ensembles in handling class imbalances. That said, this study is not a replacement for the original framework by Zhao et al. (2018); instead, it provides ample insight and opportunities for researchers to explore more ensemble disciplines in addressing class imbalanced problems in different domains. Future studies may still implement Zhao et al.'s

(2018) for class imbalance; however, with the results of this experiment, our future works will involve a new multi-class rebalancing framework incorporating an ensemble method.

LOOCV was used to evaluate the finalized model, as recommended by Zhao et al.'s (2018) framework. The downside of using LOOCV is that it requires a high time complexity, depending on the number of replications applied. Nonetheless, due to the small dataset used by the authors (Zhao et al., 2018), this issue was inconsequential to their research and was neglected. However, this is not the case in our experiment since our datasets have varying sizes (especially Yeast3). Despite the time complexity concern, we opted to use LOOCV to ensure a comparative analysis of Zhao et al.'s (2018) framework with minimal bias. In future works, we may explore using k-fold cross-validation as a more convenient method for estimating model performances.

Furthermore, it is worth noting that this study is limited to imbalanced binary classification problems, as was true in the previous authors' results (adapted framework). It ensures a fair comparison while maintaining fidelity to the framework and avoiding potential bias.

In this study, we investigated the imbalanced nature of the medical dataset with a state-of-the-art rebalancing framework combined with our proposed ensemble approach (Zhao et al., 2018). However, we also observed that class imbalance is not the sole issue in the medical domain. Another complicating factor is the limited availability of data. Due to strict privacy regulations and data-sharing constraints, medical data has become scarce. Consequently, many machine learning researchers resort to publicly available medical datasets. For this reason, we could not obtain more medical datasets with high dimensionality; hence, the small sample size dataset (Cleveland0vs4, Parkinson, SPECT, and SPECTF) was used in our experiment. Since our focus is on imbalanced learning, these seven publicly available datasets proved sufficient for this study. However, we plan to explore state-of-the-art synthetic data generation methods in future works, such as Generative Adversarial Networks (GAN) and Variational Autoencoders (VAE). These techniques offer the advantage of creating synthetic data that closely resembles real-world data (Abedi et al., 2022; Elbattah et al., 2021).

CONCLUSION

This paper comprehensively analyses an ensemble-based classifier within a rebalancing framework for imbalanced medical data. Our experimental results demonstrate significant performance improvements, particularly incorporating $SPE(Em)$ in Experiment 3. The effectiveness of ensemble-based classifiers in addressing class imbalances is highlighted, with consistent performance enhancements observed across experimental approaches. Additionally, imbalanced data are prevalent in the medical domain, encompassing binary and multi-class classification scenarios. Although this study is limited to binary

classification, it becomes evident that the issue also exists in the context of multi-class classification. Therefore, we intend to develop a multi-class rebalancing framework incorporating an ensemble-based classifier to address the challenges of multi-class imbalanced datasets in the medical domain.

ACKNOWLEDGEMENT

The authors thank the Ministry of Higher Education Malaysia and Universiti Teknologi MARA, Malaysia, for financially supporting this project under the Fundamental Research Grant Scheme (FRGS) Grant No. FRGS/1/2023/ICT01/UITM/02/4. The authors would also like to thank the College of Computing, Informatics and Mathematics and Faculty of Medicine, Universiti Teknologi MARA, Selangor, Malaysia, for all the support.

REFERENCES

- Abedi, M., Hempel, L., Sadeghi, S., & Kirsten, T. (2022). GAN-based approaches for generating structured data in the medical domain. *Applied Sciences*, *12*(14), Article 7075. <https://doi.org/10.3390/app12147075>
- Abraham, A., & Elrahman, S. M. A. (2013). A review of class imbalance problem. *Journal of Network and Innovative Computing*, *1*, 332–340.
- Belarouci, S., & Chikh, M. A. (2017). Medical imbalanced data classification. *Advances in Science, Technology and Engineering Systems*, *2*(3), 116–124. <https://doi.org/10.25046/aj020316>
- Bi, W., & Ma, R. (2021). Unbalanced data set processing method for colorectal cancer prediction in TCM diagnosis. In *2020 IEEE International Conference on E-health Networking, Application & Services (HEALTHCOM)* (pp. 1-6). IEEE Publishing. <https://doi.org/10.1109/HEALTHCOM49281.2021.9615914>
- Breiman, L. (2001). Random forests. *Machine Learning*, *45*(1), 5–32. <https://doi.org/10.1023/A:1010933404324>
- Cahyana, N., Khomsah, S., & Aribowo, A. S. (2019). Improving imbalanced dataset classification using oversampling and gradient boosting. In *2019 5th International Conference on Science in Information Technology (ICSITech)* (pp. 217-222). IEEE Publishing. <https://doi.org/10.1109/ICSITech46713.2019.8987499>
- Chawla, N. V., Bowyer, K. W., Hall, L. O., & Kegelmeyer, W. P. (2002). SMOTE: Synthetic minority over-sampling technique. *Journal of Artificial Intelligence Research*, *16*(2), 321–357. <https://doi.org/10.1613/jair.953>
- Cheng, H., Garrick, D. J., & Fernando, R. L. (2017). Efficient strategies for leave-one-out cross validation for genomic best linear unbiased prediction. *Journal of Animal Science and Biotechnology*, *8*(1), 1–5. <https://doi.org/10.1186/s40104-017-0164-6>
- Cuingnet, R., Gerardin, E., Tessieras, J., Auzias, G., Lehéricy, S., Habert, M. O., Chupin, M., Benali, H., & Colliot, O. (2011). Automatic classification of patients with Alzheimer’s disease from structural MRI: A comparison of ten methods using the ADNI database. *NeuroImage*, *56*(2), 766–781. <https://doi.org/10.1016/j.neuroimage.2010.06.013>

- deAndrés-Galiana, E. J., Fernández-Martínez, J. L., & Sonis, S. T. (2016). Design of biomedical robots for phenotype prediction problems. *Journal of Computational Biology*, 23(8), 678–692. <https://doi.org/10.1089/cmb.2016.0008>
- Edward, J., & Rosli, M. M. (2021). A systematic mapping study on ensemble-based classifier. In *2021 IEEE International Conference on Computing (ICOCO)* (pp. 43–48). IEEE Publishing. <https://doi.org/10.1109/ICOCO53166.2021.9673563>
- Elbattah, M., Loughnane, C., Guérin, J.-L., Carette, R., Cilia, F., & Dequen, G. (2021). Variational autoencoder for image-based augmentation of eye-tracking data. *Journal of Imaging*, 7(5), Article 83. <https://doi.org/10.3390/jimaging7050083>
- Elkan, C. (2013). The foundations of cost-sensitive learning. In *International Joint Conference on Artificial Intelligence* (Vol. 17, No. 1, pp. 973–978). Lawrence Erlbaum Associates Ltd.
- Harimoorthy, K., & Thangavelu, M. (2021). Multi-disease prediction model using improved SVM-radial bias technique in healthcare monitoring system. *Journal of Ambient Intelligence and Humanized Computing*, 12(3), 3715–3723. <https://doi.org/10.1007/s12652-019-01652-0>
- Japkowicz, N. (2000, June 28 – July 1). The class imbalance problem: Significance and strategies. In *Proceedings of the 2000 International Conference on Artificial Intelligence* (pp. 111–117). Las Vegas, NV, USA.
- Jiang, Z., Ji, R., & Chang, K.-C. (2020). A machine learning integrated portfolio rebalance framework with risk-aversion adjustment. *Journal of Risk and Financial Management*, 13(7), Article 155. <https://doi.org/10.3390/jrfm13070155>
- Khalilia, M., Chakraborty, S., & Popescu, M. (2011). Predicting disease risks from highly imbalanced data using random forest. *BMC Medical Informatics and Decision Making*, 11(1), 1–13. <https://doi.org/10.1186/1472-6947-11-51>
- Krishnan, U., & Sangar, P. (2021). A rebalancing framework for classification of imbalanced medical appointment no-show data. *Journal of Data and Information Science*, 6(1), 178–192. <https://doi.org/doi:10.2478/jdis-2021-0011>
- Kuncheva, L. I. (2014). *Combining pattern classifiers*. John Wiley & Sons, Inc. <https://doi.org/10.1002/9781118914564>
- Liang, C., Bian, Z., Lyu, W., Zeng, D., & Ma, J. (2018). A deep features-based radiomics model for breast lesion classification on FFDM. In *2018 IEEE Nuclear Science Symposium and Medical Imaging Conference Proceedings (NSSMIC)* (pp. 1–4). IEEE Publishing. <https://doi.org/10.1109/NSSMIC.2018.8824722>
- Liu, Z., Cao, W., Gao, Z., Bian, J., Chen, H., Chang, Y., & Liu, T. Y. (2020). Self-paced ensemble for highly imbalanced massive data classification In *2020 IEEE 36th International Conference on Data Engineering (ICDE)* (pp. 841–852). IEEE Publishing. <https://doi.org/10.1109/ICDE48307.2020.00078>
- Ma, T., Wu, L., Zhu, S., & Zhu, H. (2022). Multiclassification prediction of clay sensitivity using extreme gradient boosting based on imbalanced dataset. *Applied Sciences*, 12(3), Article 1143. <https://doi.org/10.3390/app12031143>

- Mandrekar, J. N. (2010). Receiver operating characteristic curve in diagnostic test assessment. *Journal of Thoracic Oncology*, 5(9), 1315–1316. <https://doi.org/10.1097/JTO.0b013e3181ec173d>
- Mohammed, R. A., Wong, K. W., Shiratuddin, M. F., & Wang, X. (2020). Pwldb: A framework for learning to classify imbalanced data streams with incremental data re-balancing technique. *Procedia Computer Science*, 176, 818–827. <https://doi.org/10.1016/j.procs.2020.09.077>
- Mohandes, M., Deriche, M., & Aliyu, S. O. (2018). Classifiers combination techniques: A comprehensive review. *IEEE Access*, 6, 19626–19639. <https://doi.org/10.1109/ACCESS.2018.2813079>
- Pes, B. (2019). Handling class imbalance in high-dimensional biomedical datasets. In *2019 IEEE 28th International Conference on Enabling Technologies: Infrastructure for Collaborative Enterprises (WETICE)* (pp. 150-155). IEEE Publishing. <https://doi.org/10.1109/WETICE.2019.00040>
- Phoungphol, P., Zhang, Y., & Zhao, Y. (2012). Robust multiclass classification for learning from imbalanced biomedical data. *Tsinghua Science and Technology*, 17(6), 619–628. <https://doi.org/10.1109/TST.2012.6374363>
- Rahman, M. M., & Davis, D. N. (2013). Addressing the class imbalance problem in medical datasets. *International Journal of Machine Learning and Computing*, 3(2), Article 224. <https://doi.org/10.7763/ijmlc.2013.v3.307>
- Saito, T., & Rehmsmeier, M. (2015). The precision-recall plot is more informative than the ROC plot when evaluating binary classifiers on imbalanced datasets. *PLoS ONE*, 10(3), 1–21. <https://doi.org/10.1371/journal.pone.0118432>
- Sandhan, T., & Choi, J. Y. (2014). Handling imbalanced datasets by partially guided hybrid sampling for pattern recognition. In *2014 22nd International Conference on Pattern Recognition* (pp. 1449-1453). IEEE Publishing. <https://doi.org/10.1109/ICPR.2014.258>
- Shabaniyan, T., Parsaei, H., Aminsharifi, A., Movahedi, M. M., Jahromi, A. T., Pouyesh, S., & Parvin, H. (2019). An artificial intelligence-based clinical decision support system for large kidney stone treatment. *Australasian Physical and Engineering Sciences in Medicine*, 42(3), 771–779. <https://doi.org/10.1007/s13246-019-00780-3>
- Song, L., Lin, J., Wang, Z. J., & Wang, H. (2020). An end-to-end multi-task deep learning framework for skin lesion analysis. *IEEE Journal of Biomedical and Health Informatics*, 24(10), 2912–2921. <https://doi.org/10.1109/JBHI.2020.2973614>
- Tang, X., Cai, L., Meng, Y., Gu, C., Yang, J., & Yang, J. (2021). A novel hybrid feature selection and ensemble learning framework for unbalanced cancer data diagnosis with transcriptome and functional proteomic. *IEEE Access*, 9, 51659–51668. <https://doi.org/10.1109/ACCESS.2021.3070428>
- Tantithamthavorn, C., Hassan, A. E., & Matsumoto, K. (2020). The impact of class rebalancing techniques on the performance and interpretation of defect prediction models. *IEEE Transactions on Software Engineering*, 46(11), 1200–1219. <https://doi.org/10.1109/TSE.2018.2876537>
- Turlapati, V. P. K., & Prusty, M. R. (2020). Outlier-SMOTE: A refined oversampling technique for improved detection of COVID-19. *Intelligence-Based Medicine*, 3–4, Article 100023. <https://doi.org/10.1016/j.ibmed.2020.100023>

- Utami, I. T., Sartono, B., & Sadik, K. (2014). Comparison of single and ensemble classifiers of support vector machine and classification tree. *Journal of Mathematical Sciences and Applications*, 2(2), 17–20. <https://doi.org/10.12691/jmsa-2-2-1>
- Valentini, G., & Dietterich, T. G. (2004). Bias-variance analysis of support vector machines for the development of SVM-based ensemble methods. *Journal of Machine Learning Research*, 5, 725–775.
- Yao, J. R., & Chen, J. R. (2019). A new hybrid support vector machine ensemble classification model for credit scoring. *Journal of Information Technology Research*, 12(1), 77–88. <https://doi.org/10.4018/JITR.2019010106>
- Zhao, Y., Wong, Z. S. Y., & Tsui, K. L. (2018). A framework of rebalancing imbalanced healthcare data for rare events' classification: A case of look-alike sound-alike mix-up incident detection. *Journal of Healthcare Engineering*, 2018(2010), Article 6275435. <https://doi.org/10.1155/2018/6275435>
- Zhu, R., Guo, Y., & Xue, J.-H. (2020). Adjusting the imbalance ratio by the dimensionality of imbalanced data. *Pattern Recognition Letters*, 133, 217–223. <https://doi.org/10.1016/j.patrec.2020.03.004>
- Zhu, W., Oh, B. S., Huang, W., Lin, Z., Pan, Y., & Zhou, J. (2015). Hybrid classifiers ensemble with an undersampling scheme for liver tumor segmentation. In *2015 10th International Conference on Information, Communications and Signal Processing (ICICIS)* (pp. 1-4). IEEE Publishing. <https://doi.org/10.1109/ICICIS.2015.7459850>

Improved Early Detection of Tube Leaks Faults in Pulverised Coal-fired Boiler Using Deep Feed Forward Neural Network

Abdul Munir Abdul Karim^{1*}, Yasir Mohd Mustafah¹ and Zainol Arifin Zainal Abidin²

¹Kulliyah of Engineering, International Islamic University Malaysia, Jalan Gombak, 53100 Kuala Lumpur, Malaysia

²Faculty of Computing, Engineering & Technology, Asia Pacific University of Technology & Innovation, Jalan Teknologi 5, Taman Teknologi Malaysia, 57000 Kuala Lumpur, Malaysia

ABSTRACT

Boiler tube leaks significantly reduce the operational availability of power units, yet their early detection and prediction have not been fully realised in the industry. This paper introduces a novel approach employing deep feedforward neural networks for early detection of boiler tube leaks in pulverised coal-fired boilers. Early detection enhances repair planning, minimising downtime and production losses. It also improves monitoring and control of boiler tube failures, thereby optimising power plant operations and revenue. Diverse deep neural network models were developed and rigorously tested by leveraging 9 years of operational data (2012–2020). Exhaustive hyper-parameter optimisation, involving seven parameters, substantially improved predictive accuracy. By achieving training and testing accuracies of 82.8% to 99.3%, the study assessed their ability to detect boiler tube leaks over the same 9-year span, providing insights into leak detection capabilities. The models notably predicted all 12 identified tube leak events, averaging a 14-day lead time before boiler shutdown. In addition to leak prediction, a leak detection matrix was devised to analyse residual behaviour and reduce the likelihood of false alarms. However, the models' predictive performance was observed to be limited to the following year, with satisfactory results for 2021 only. Incorporating the 2021 data into retraining significantly improved the predictions for 2022. The study concludes that while the models demonstrate robust short-term prediction capabilities,

they require continuous retraining to maintain accuracy and relevance. This ongoing refinement is essential for keeping the models up-to-date and reliable in predicting future boiler tube leaks.

ARTICLE INFO

Article history:

Received: 15 December 2023

Accepted: 12 April 2024

Published: 25 October 2024

DOI: <https://doi.org/10.47836/pjst.32.6.13>

E-mail addresses:

abdul.munir@gmail.com (Abdul Munir Abdul Karim)

yasir@iiu.edu.my (Yasir Mohd Mustafah)

zainol@gmail.com (Zainol Arifin Zainal Abidin)

* Corresponding author

Keywords: Boiler, detection, hyper-parameter, neural network, prediction, tube leak, tuning

INTRODUCTION

Coal-fired units grapple with persistent forced outages primarily attributed to boiler tube failures. The cyclic duty of the boiler results in fatigue, affecting both the boiler and associated heat exchanger tubes. In a benchmarking survey by the Electric Utility Cost Group (EUCG), covering 167 units of various sizes (from 8 MW to 1264 MW) across seventeen utilities, it was highlighted that despite the units maintaining high capacities relative to their size and age, boiler tube failures remained the predominant cause of downtime for these steam power plants (Pfeuffer, 2009). A more recent study by Kokkinos (2019) in the U.S. revealed that between 2013 and 2017, tube leaks persisted in water walls, followed by the second superheater, primary reheater, and primary superheater. Boiler leaks accounted for 54% of total outages, with the remainder caused by balance of plant (BOP), steam turbine, and generator issues. Coal-fired units struggle with forced outages due to cyclic-induced fatigue, with boiler tube failures being the primary culprit. Surveys and recent studies emphasise the persistence of these issues across various-sized units, leading to substantial downtime and high repair costs.

In the power generation industry, outage costs due to production loss, whether planned or forced, are substantial (Tam et al., 2007). One of the main reasons for the increased rate of failures of boiler pressure parts is the requirement of power units to work at greater load variability, resulting in frequent changes in operating pressure and temperature of the working fluid, i.e., feedwater and/or steam. Consequently, those units are subjected to increased sediment precipitation from the working fluid. While being transported by the working fluid, these sediments may easily be deposited on rough regions of the inner surfaces of boiler tubes. It causes further flow disorder and can result in overheating of tubes. Thus, there is interest in developing early detection methods to predict these types of faults earlier. It has been reported in a few case studies that boiler tube failures escalate slowly, sometimes up to ten days or so, before they may be detected by the staff of the power plant through conventional means (Alouani & Chang, 2003; Barszcz & Czop, 2011; Lang et al., 2004; Sun et al., 2002).

These tube leaks constitute a potential for severe physical harm to boiler pressure parts owing to pipe whip and/or steam cutting of the impacted and adjacent pipes. The ultimate harm caused by severe tube failures can range from \$2 to \$10 million per leak for a commercial steam generator. These high costs result from forced boiler shutdowns for repairs, which could last up to a week if the leak is not detected for an extended period (Lang et al., 2004). Tube failures can be repaired before disastrous damage if detected early, with such repairs only lasting several days and costing a fraction of the price of late detection.

The power industry does not put considerable effort into early boiler tube leak detection amid the high-cost implications of late detection. The AI approach to boiler tube leak detection is also not well established. Several studies have been conducted using AI-based

methods on pulverised coal-fired boiler tube leak detection. Nistah et al. (2018) proposed a boiler fault prediction model using artificial neural networks (ANN) with multi-layered perceptrons (MLP), which achieved a 92% prediction rate of accuracy. Singh et al. (2017) developed an Intelligent Warning System (IWS) that combines ANN and Genetic Algorithms (GA) in their prediction model. The prediction model was trained and tested based on three real cases of boiler tube leak trips at a power plant with six operational units totalling a generation capacity of 2420 MW in Malaysia. Ismail et al. (2016) also employed ANN in their prediction model for one boiler unit of a power plant with a total generation capacity of 2400 MW in Malaysia. The sample data was based on a boiler tube leak incident in 2013. Rostek et al. (2015) focused their research on a boiler tube leak prediction model for a fluidised-bed coal-fired boiler in Poland. They employed a 2-stage structure of ANN in their study. The model could predict boiler tube leaks at least 2 days before the boiler shutdown.

Despite extensive prior research on the early prediction of boiler tube leaks in coal-fired power plants, several issues remain to be addressed to enhance prediction accuracy. Rostek et al. (2015) utilised a basic multilayer perceptron neural network with 19 input variables, a single hidden layer containing 16 neurons, and an output layer with one neuron. However, the training accuracy was suboptimal, with the highest-quality model needing an 80% correlation coefficient (R^2) between actual and predicted data. While some models successfully identified boiler tube leaks 2 to 9 days in advance, certain leak incidents were not detected by the selected signal sensitive to tube leaks. Furthermore, this prediction method was only validated in fluidised-bed coal-fired boilers and has not yet proven effective for pulverised coal-fired boilers.

In Malaysia, attempts to accurately predict boiler tube leaks in pulverised coal-fired boilers faced challenges due to limited available data. Ismail et al. (2016) utilised only one week of data collected at one-minute intervals, comprising approximately 11,000 data sets, selected based on a single boiler tube leak incident. The neural network algorithm was trained using 26 sensors, employing a simple feedforward neural network structure with a maximum of two hidden layers and no more than ten neurons per layer. However, this model could only detect boiler tube leaks with a 10-minute advance notice, which is inconsequential for power plant operators. Similarly, Singh et al. (2017) examined only 12 days of data collected at one-minute intervals from three boiler tube leak incidents to train their network. Their neural network, employing feedforward and backpropagation with two hidden layers, utilised only 17 sensors as input. However, the model achieved only a 20-minute advance prediction, which was also deemed insignificant.

In essence, two primary concerns need to be addressed. Firstly, previous studies have suffered from the simplicity of their neural network structures, leading to a notable difference between the actual and predicted data during training. Additionally, this simplicity

has led to the failure to detect several tube leak incidents throughout the studies. Secondly, there is a limitation of available operational data from the boilers, with a relatively small number of sensors being considered during the training of the neural network algorithm. Consequently, this has resulted in insignificant early detection (within 10 to 20 minutes) before the plant operator identifies the leak.

MATERIALS AND METHODS

Deep Feed Forward Neural Network as Learning Architecture for Time-series Prediction

The power plant's data structure necessitates applying multivariate time series analysis to predict boiler tube leak occurrences. A time series is a sequence of values arranged chronologically and observed over time. While time is measured as a continuous variable, the values in a time series are sampled at constant intervals (fixed sampling frequency) (Torres et al., 2021).

The Deep Feedforward Neural Networks (DFFNN) algorithm was carefully considered for this study over alternative architectures such as Convolutional Neural Networks (CNN) and Recurrent Neural Networks (RNN) based on several key factors. Firstly, the sensor data collected from the power plant environment comprises multivariate time series data, where each data point is influenced by multiple input variables recorded over time. In this context, DFFNN is well-suited for handling the complex interdependencies and nonlinear relationships in such data, as it can effectively model the interactions between input variables without relying on sequential processing. Furthermore, DFFNN offers scalability and computational efficiency advantages, which are crucial considerations for large-scale time series prediction tasks involving millions of data points, as in the researchers' study.

While CNN excels in capturing spatial dependencies within data, particularly in image processing tasks, and RNNs are effective for sequential data modelling due to their ability to retain information over time, DFFNN was opted for due to the unique characteristics of their dataset and the specific requirements of their prediction task. Additionally, while RNNs are capable of capturing temporal dependencies within sequential data, they may encounter challenges with long-range dependencies and vanishing/exploding gradient problems, particularly in deep architectures. In contrast, DFFNN does not suffer from these limitations and can effectively model long-range dependencies by incorporating multiple hidden layers.

The DFFNN was developed in response to the limitations of single-layer neural networks in learning certain functions. The structure of a DFFNN comprises an input layer, an output layer, and multiple hidden layers, each housing a specific number of neurons. The connections between neurons in two adjacent layers are modelled using

weights determined during the network's training phase. These weights are computed by minimising a cost function through gradient descent optimisation methods, with the backpropagation algorithm used to calculate the gradient of the cost function. Once the weights are determined, the values of the output neurons are obtained using a feedforward process.

In time series forecasting, the rectified linear unit function is commonly employed as the activation function for all layers except the output layer, which uses the hyperbolic tangent function to derive predicted values. Various hyperparameters, such as the number of layers, neurons, learning rate, momentum, and mini-batch size, need to be pre-selected. The choice of these hyperparameters significantly influences the network's predictive outcomes.

Research Objective

The study was conducted on a single unit of a pulverised coal-fired boiler at a power plant in Malaysia. This study utilised data collected from the plant's process control system from 2012 to 2020.

Figure 1 illustrates the breakdown of faults that contributed to the decreased available capacity for power generation at the plant. This figure provides an overview of the key plant systems responsible for these faults across two power units during the 2012 to 2020 period. Notably, the boiler system was identified as the primary source of faults, accounting for 73.6% of all recorded incidents. Following the boiler system, the auxiliary, electrical, coal pulverising, and turbine systems contributed to these faults, with the coal supply and handling system being the least affected. Within the 73.6% of faults attributed to the boiler system, 50.3% were due to boiler tube leaks. In comparison, the remaining 23.3% were related to other issues within the boiler system, such as the air and flue gas system and operational management of the boiler.

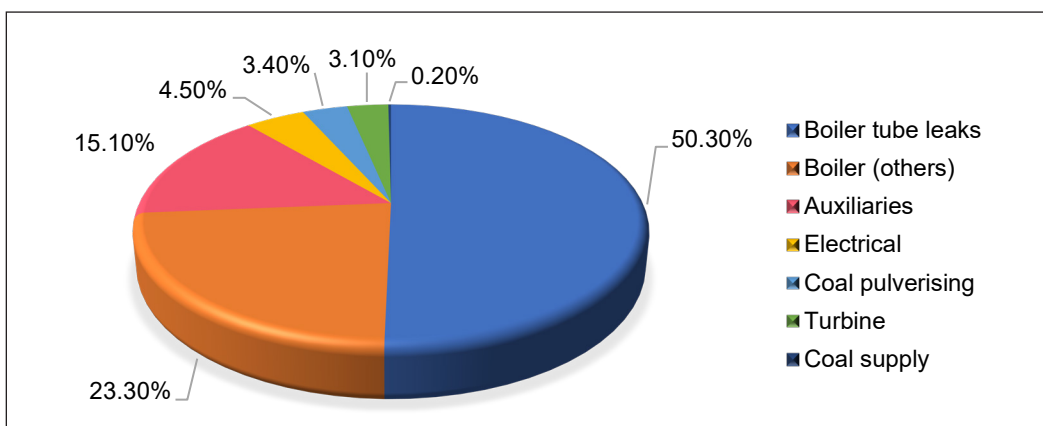


Figure 1. Main plant system contributor to power unit fault (2012 to 2020)

Data Collection

The selected algorithm for early detection of tube leaks in this study was the DFFNN. This network's structure includes an input layer, several hidden layers, and a single output layer. For DFFNN training, the input variables are boiler operation parameters not influenced by tube leaks, while the output variables are those impacted by such leaks (Karim & Mustafah, 2022). The power plant employs 120 sensors to measure the input variables, which are integrated into the input layer for training and testing the DFFNN configurations. Selected sensors for input variables include main feedwater pressure and temperature, as well as pressures and temperatures for hot and cold reheat steam and superheaters inlet and outlet steam.

Conversely, 10 sensors are dedicated to measuring output variables, creating 10 distinct DFFNN models. Each model is named according to the sensitive output variable it tracks, as listed in Table 1.

Table 1 presents the output variables sensitive to tube leaks and their corresponding model names, such as "COND WTR FLOW" for condensate water flow rate and "DEA WTR FLOW" for deaerator and feedwater tank water flow rate.

Table 1
Output variables sensitive (affected) to tube leak occurrence and the corresponding model name

No.	Output variables	Model name
1	Condensate water flow rate	COND WTR FLOW
2	Deaerator and feedwater tank water flow rate	DEA WTR FLOW
3	Main feedwater flow rate	MAIN FW FLOW
4	Economiser outlet flue gas O ₂ concentration (sensor A)	ECO A OTL O ₂
5	Economiser outlet flue gas O ₂ concentration (sensor B)	ECO B OTL O ₂
6	Primary air flow rate	TOTAL PA FLOW
7	Secondary air flow rate (sensor A)	HOT SA A FLOW
8	Secondary air flow rate (sensor B)	HOT SA B FLOW
9	Induced draught fan suction pressure (sensor A)	IDF A FG PRESS
10	Induced draught fan suction pressure (sensor B)	IDF B FG PRESS

This study stands out by utilising a more extensive array of sensors over a longer period compared to previous studies. Sensor data spanning 9 years, from 2012 to 2020, were collected at 10-minute intervals for neural network model training and testing and at 5-minute intervals for leak prediction. The study used 120 sensors for network inputs and 10 for outputs per data set, a significant increase from previous research, which typically used fewer than 30 sensors for inputs and a maximum of 4 for outputs. Approximately 473,000 data sets containing around 130 sensor data points were utilised, resulting in over 61 million data points collected and employed for model learning. Table 2 compares the data structures employed in earlier research for the early prediction of boiler tube leaks.

Table 2
Comparison of data structures with previous research

	This research	Rostek et al. (2015)	Ismail et al. (2016)	Singh et al. (2017)
No. of boiler units studied	1	1	1	1
No. of boiler tube leak incident	12	12	1	3
Data period	9 years (2012–2020)	8 years (2005–2012)	7 days	36 days
Sampling interval				
- Network training and testing	10 minutes	20 minutes	1 minute	1 minute
- Leak prediction	5 minutes	1 minute	1 minute	1 minute
No. of sensors for input variables	120	19	26	17
No. of sensors for output variables	10	4	1	1

DFNN Training and Testing

The model's training data excluded periods when the boiler experienced tube leaks, starting 30 days before the leak event and ending on the event day. It ensured that all training data came from when the plant operated normally, with stable parameters. The data was divided, with 80% used for training and the remaining 20% for validation during testing.

Input variables for training were those not influenced by tube leaks, while output variables were leak-sensitive. The input data passes through the network's layers, producing output data. In this forward pass, the network's weights were initially set. The outputs were then compared to the desired values. In the backward pass, the difference (error) between the desired and calculated outputs was used to adjust the network's weights to reduce error. The supervised learning process continued iteratively until the error reached an acceptable level. Each complete cycle of processing the data set, forward and backwards, was termed an epoch. The network training aimed to reduce the error with each epoch.

Various well-known loss functions, such as Mean Squared Error (MSE), Root Mean Squared Error (RMSE), Mean Absolute Error (MAE), Mean Square Logarithmic Error (MSLE), and Mean Absolute Percentage Error (MAPE), were used to minimise the difference between the desired and calculated outputs.

The effectiveness of network training and testing was assessed using the square of the correlation coefficient (R^2), per Behera et al. (2014). R^2 values close to 1 indicate a strong relationship. After training the network to satisfactory performance, it was validated or tested with the remaining 20% of the data. Through hyper-parameter tuning, various network configurations were explored to identify the best model for representing leak-sensitive variables. Figure 2 depicts finding the most efficient DFFNN structures for fault detection.

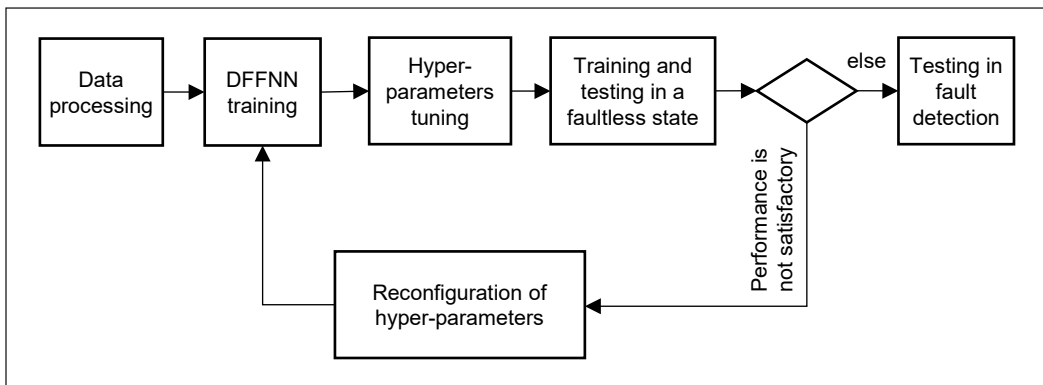


Figure 2. The algorithm for finding the best structures of DFFNN for fault detection

The models were developed, trained, and tested using Keras, an advanced programming interface for neural networks that emphasises rapid experimentation. Keras is Python-based and operates on the TensorFlow backend.

Hyper-parameter Tuning

Most hyperparameters used in this research’s DFFNN were tuned to achieve optimum accuracy and minimum loss. A DFFNN network structure from Mishra et al. (2020) was selected as the base model to start the hyperparameter tuning. The model was used to analyse deep learning performance for multivariate prediction of time series wind power generation and temperature. The initial network configuration for this study can be summarised in Table 3.

ADAM was selected as an optimiser, with a default learning rate of 0.001. The 120 input data were fed to the network in mini-batches size 512 throughout 10 epochs. Once the performance of the network was obtained, the hyper-parameters were tuned in the following order:

- (i) Layer activation function
- (ii) Number of hidden layers
- (iii) Number of neurons in each hidden layer
- (iv) Optimisers
- (v) Losses
- (vi) Mini-batch size
- (vii) Learning rate and number of epochs

Each hyper-parameter tuning step was considered one set of experiments. Therefore, seven experiments were conducted to determine the best network structure for the

Table 3
Initial DFFNN network structure

	Hidden Layer		Output Layer
	1	2	
No of neurons	512	128	2
Activation	ReLU	ReLU	NA
Dropout	0.5	0.5	NA

10 parameters affected by tube leak prediction models. The best hyper-parameter setting for the 10 models in each experiment was carried over to the next experiment, where a different hyper-parameter was tuned in the order above.

Once the models' network structure was finalised, it was revalidated by changing to different layer activation functions to confirm the initial assumption that the activation function was the most hyperparameter affecting model performance.

Detection of Leaks Using Method of Residue

In a similar approach to Rostek et al. (2015), this study also implemented a residue method for leak detection. After the models were thoroughly trained and tested under normal, fault-free conditions, they were then applied to data from periods of tube leak faults. This fault data, encompassing 30 days leading up to the boiler shutdown, was sampled at 5-minute intervals. It was then input into the models to predict the leak-sensitive variables under normal conditions. Figure 3 illustrates this data division process.

The model's predicted output was compared against the actual process signals measured. When a leak occurred, the measured signal deviated from the predicted output, creating a residual value indicative of a boiler tube leak fault. This residual value was then evaluated against a predetermined threshold, established from the network's training and testing results, to confirm the presence of a leak.

Determining the leak detection threshold involved analysing histograms from averaged time series in the fault-free state and comparing them to a normal distribution. In the residue method, the acceptable probability for false alarms was less than 0.5%. Figure 4 shows an example of leak detection using the residue method for the ECO A OTL O2 model. This model compares the residual value r against the leak detection threshold. If r exceeds this threshold, it signals a potential boiler tube leak.

Evaluation of Model Ability for Early Tube Leak Detection

The last phase of the research was to evaluate the trained models with the next 2 years of plant data in 2021 and 2022. The sensor data from 120 variables not affected by tube

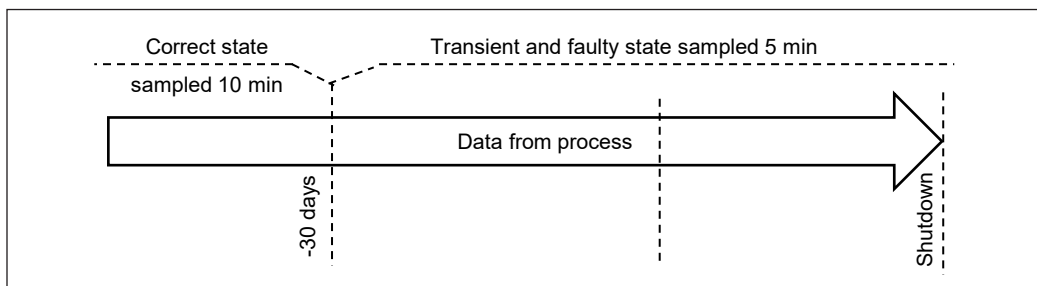


Figure 3. Data division before boiler emergency shutdown

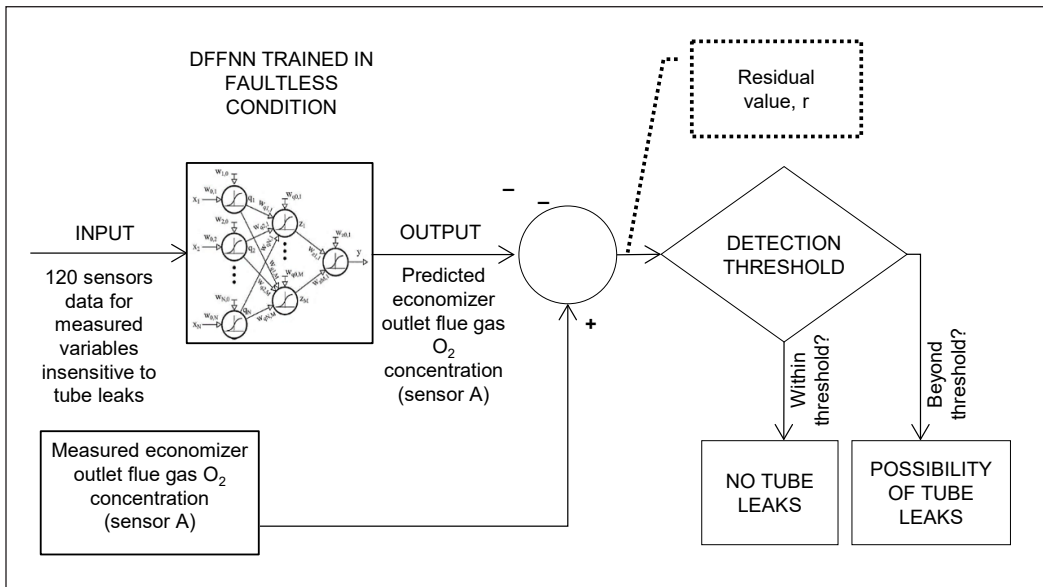


Figure 4. Example of economiser outlet flue gas O₂ concentration model for fault detection by residue method

leaks for 2021 and 2022 were input to the 10 trained models, and the predicted output by each model was recorded. The data structure was the same as in training the model, with the sensor data sampled every 10 minutes and undergoing data cleansing, treatment, and normalisation before inputting the models.

The predicted sensor data from the models' output for the 2 years was then compared with the actual data, and the residuals were subjected to a threshold for boiler tube leak detection. The performance of each model prediction was evaluated by the ability to detect tube leak events during those 2 years.

RESULTS AND DISCUSSION

Model Training and Testing with Hyper-parameters Tuning

The overall model training and testing with hyper-parameters tuning results showed that all the models' performance increased throughout the series of hyper-parameters tuning experiments. Changing the layer activation function significantly impacted the model training and testing accuracy from the initial model. The following tuning experiments on the number of hidden layers, number of neurons in the hidden layer, optimiser, and loss function did improve the accuracy slightly. Finally, increasing the number of training epochs to 50 increased the accuracy significantly, especially for the ECO A OTL O₂ and ECO B OTL O₂ models, which showed increments of 12.51% and 13.54%, respectively, in training accuracy. Examples of the progress on two model training and testing accuracy and losses after each hyper-parameter tuning experiment are shown in Table 4.

Table 4

Example of results of hyper-parameters tuning for COND WTR FLOW and ECO B OTL O2 model

Exp.	Hyper-parameter	COND WTR FLOW				ECO B OTL O2			
		Accuracy (R ²)		Losses		Accuracy (R ²)		Losses	
		Train	Test	Train	Test	Train	Test	Train	Test
1	Initial model	0.988	-8E+04	0.0001	5E+02	0.773	-1E+06	0.0002	3E+02
2	Layer activation function	0.970	0.759	0.0003	0.0013	0.677	-0.157	0.0003	0.0002
3	No. of hidden layer	0.989	0.938	0.0001	0.0003	0.773	-0.263	0.0002	0.0002
4	No. of neurons in the hidden layer	0.990	0.938	0.0001	0.0003	0.773	-0.263	0.0002	0.0002
5	Optimizer	0.991	0.952	0.0001	0.0003	0.788	0.544	0.0002	0.0004
6	Losses function	0.991	0.952	0.0001	0.0003	0.796	0.612	0.0002	0.0004
7	Learning rate and no. of epochs	0.996	0.964	0.0000	0.0002	0.932	0.828	0.0002	0.0003

The finalised models' training and testing accuracy and losses after completion of hyper-parameters tuning are shown together with their corresponding network structures in Table 5. All models can be considered high quality since they achieved considerably high training accuracy of more than 93%, the lowest being ECO B OTL O2 with 93.16% and the highest, IDF A FG PRESS, at 99.63%. ECO A OTL O2 had the lowest testing accuracy at 75.65%, while the highest was DEA WTR FLOW at 98.88%. The summary of this research's optimised DFFNN network structure has the characteristics in Table 6.

Table 5

Overall results of hyper-parameters tuning

	COND WTR FLOW	DEA WTR FLOW	ECO A OTL O2	ECO B OTL O2	HOT SAA FLOW
Layer Activation Function	Tanh	Tanh	Tanh	Tanh	Tanh
No Hidden Layer	9	7	9	9	8
No neurons in the hidden layer	512-256-128-64-32-16-8-4-2	512-256-128-64-32-16-8	512-256-128-64-32-16-8-4-2	512-256-128-64-32-16-8-4-2	512-256-128-64-32-16-8-4
Optimizer	Adam	Adam	Adam	Nadam	Adam
Learning Rate	0.001	0.001	0.001	0.001	0.001
Losses function	msle	mse	mse	mae	mae
No of Epoch	50	50	50	50	50
Mini Batch size	512	512	512	512	512
Accuracy (R ²)					
Train	0.9922	0.9925	0.9472	0.9316	0.9752
Test	0.9838	0.9888	0.7565	0.8275	0.8789
Losses					
Train	0.0000	0.0001	0.0000	0.0031	0.0108
Test	0.0002	0.0024	0.0006	0.0048	0.0214

Table 5 (continue)

	HOT SA B FLOW	IDF A FG PRESS	IDF B FG PRESS	MAIN FW FLOW	TOTAL PA FLOW
Layer Activation Function	Tanh	Tanh	Tanh	Tanh	Tanh
No of Hidden Layer	9	6	9	8	7
No of neurons in the hidden layer	256-128-64-32-16-8-4-2-2	128-64-32-16-8-4	512-256-128-64-32-16-8-4-2	512-256-128-64-32-16-8-4	512-256-128-64-32-16-8
Optimizer	Adam	Adamax	Adam	AMSGrad	Adam
Learning Rate	0.001	0.001	0.001	0.001	0.001
Losses function	mse	mse	rmse	mse	mse
No of Epoch	50	50	50	50	50
Mini Batch size	512	512	512	512	512
Accuracy (R ²)					
Train	0.9724	0.9963	0.9948	0.9889	0.9921
Test	0.8562	0.9639	0.8946	0.9658	0.8473
Losses					
Train	0.0002	0.0000	0.0070	0.0001	0.0002
Test	0.0254	0.0002	0.0215	0.0004	0.0206

Table 6

Summary of the optimised network structure

Hyper-parameter	Properties	Applicable model
Layer activation function	tanh	All models
No of hidden layer	9	5 out of 10 models
No of neurons in the first hidden layer	512	8 out of 10 models
Optimizer	Adam	7 out of 10 models
Losses function	mse	5 out of 10 models
Learning rate & no of epochs	0.001 & 50	All models
Mini batch size	512	All models

Assessment of Fault Detection by Models of the Variables Sensitive to Leaks

The validated models were subsequently applied to data from periods when tube leaks occurred. This fault data, encompassing 30 days leading up to the boiler shutdown, was sampled at 5-minute intervals and used as input to forecast variables influenced by tube leaks under normal conditions. Table 7 displays the fault detection outcomes for the top 10 models across 12 boiler tube leak events, considering leaks in the boiler pressure parts system (including the furnace water wall, radiant superheater, and reheater and heat recovery area). The final row sums up the number of faults each model detected, as shown in Table 7.

The residuals generated by the DFFNN models enabled the detection of all 12 faults, with a minimum of 3 residual variables per fault. At least 5 variables identified

Table 7
Detection of tube leak faults by means of the residue of ten variables (sensors) affected by tube leaks

No	Year	Tube Leaks Location	COND WTR FLOW	DEA WTR FLOW	ECO A OTL O2	ECO B OTL O2	HOT SA A FLOW	HOT SA B FLOW	IDF A FG PRESS	IDF B FG PRESS	MAIN FW FLOW	TOTAL PA FLOW
1	2012	Heat Recovery Area	17 days		13 days			13 days	3 days			17 days
2	2013	Heat Recovery Area	11 days				28 days	7 days	26 days	18 days		
3	2014	Heat Recovery Area	18 days	22 days	18 days			30 days	21 days	28 days		
4	2014	Heat Recovery Area	6 days	6 days				8 days			3 days	14 days
5	2016	Furnace Waterwall					29 days	22 days				21 days
6	2017	Radiant Superheater					6 days		1 day	2 days	26 days	4 days
7	2017	Radiant Superheater	7 days				18 days	18 days		3 days	3 days	
8	2018	Heat Recovery Area				15 days	9 days				6 days	
9	2019	Economiser		28 days	4 days	14 days	23 days				5 days	
10	2019	Economiser		4 days		11 days	12 days		18 days	14 days	4 days	
11	2020	Heat Recovery Area		11 days	5 days	17 days	3 days			28 days		18 days
12	2020	Radiant Superheater	9 days	9 days				21 days			9 days	6 days
Detected tube leaks			6 of 12	5 of 12	6 of 12	4 of 12	8 of 12	7 of 12	5 of 12	6 of 12	7 of 12	6 of 12

the most faults. Exceptions were Fault #5 and Fault #8, where only 3 variables' residues detected the fault. The average lead time between fault detection and boiler shutdown was approximately 14 days. The most effective variable for fault detection was HOT SA A FLOW, followed by HOT SA B FLOW and MAIN FW FLOW. These variable models could detect over half of the fault cases at least 3 days in advance. On the other hand, the ECO B OTL O2 model was the least efficient, detecting only 4 out of 12 faults at least 11 days in advance.

Example - Fault Detection by HOT SAA FLOW Model

The forced draught fan supplies hot secondary airflow in the boiler for coal combustion in the furnace. If boiler tube leaks, the main steam pressure will decrease due to the loss of steam. More steam needs to be produced; thus, more fuel needs to be burned to supply the additional heat to compensate for this loss. Additional fuel burning would require additional air to support combustion, increasing the hot secondary air. Therefore, during a tube leak event, the actual sensor reading will be more than the prediction, and the residual will increase as the tube leaks are prolonged.

The threshold for leak detection was found by analysing histograms of the difference between actual and predicted sensor readings, which were used for training the model. Compared with a normal distribution, the threshold was set at 99.5% of the distribution, yielding 1.165%, as shown in Figure 5. Tube leaks are indicated whenever the residual plot goes above the threshold.

In Figure 6, the model output for hot secondary air A flow is plotted against the measured value 30 days before boiler shutdown due to Fault #10 in 2019. The difference between the model output and the measured value is increasing around 12 days prior to the boiler shutdown, which is a symptom of a fault. Figure 7 illustrates the residual value and its 24-hour moving average from Figure 6. The moving average is considered

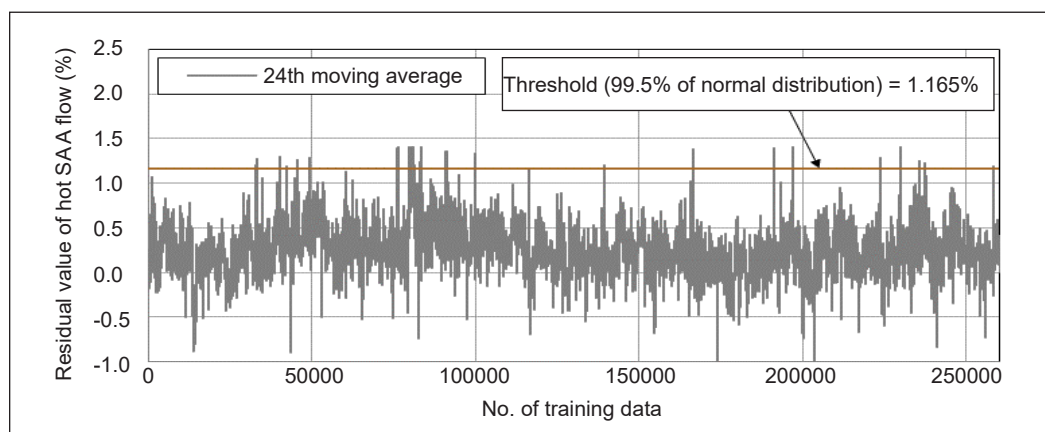


Figure 5. Determination of threshold of the detection limit for the residual value of hot secondary air A flow

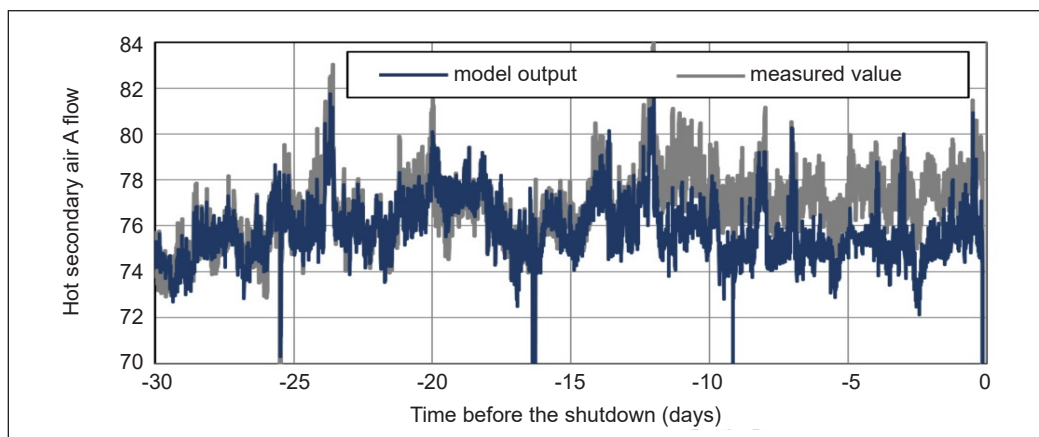


Figure 6. Exemplary courses of hot secondary air A flow, measured value and output from DFFNN model prior to shutdown of a boiler for tube leak Fault #10

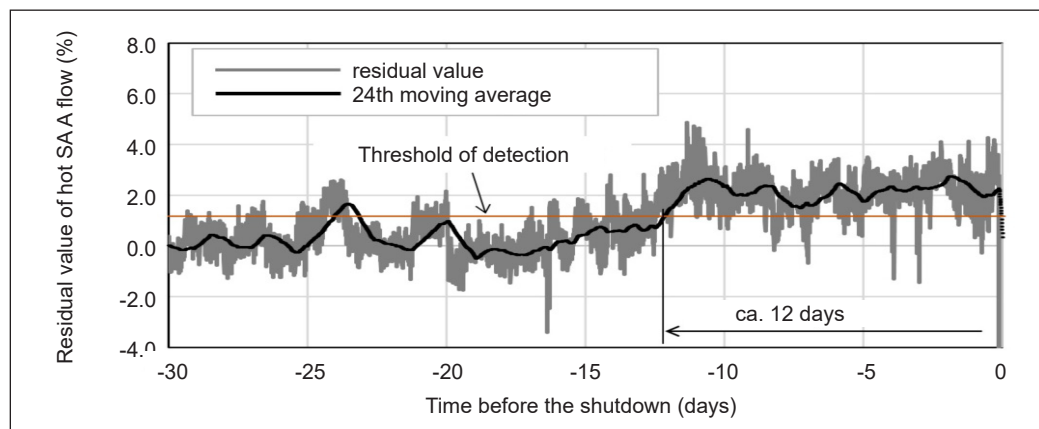


Figure 7. The residual value of hot secondary air A flow and its 24-hour moving average for tube leak Fault #10

in the detection process to smooth out transient fluctuations of process data and reduce the possibility of false alarms in leak detection. The predetermined threshold allows fault detection approximately 12 days before the boiler shutdown.

Leak Detection Matrix

Based on the leak detection analysis of all 10 models, it can be concluded that a particular boiler tube leak occurrence is confirmed if it is detected concurrently by at least three models' residuals. Referring to the leak detection time by the respective model for each Fault #1 to Fault #12 from Table 7, the following observation on the number of days that the boiler tube leaks were confirmed prior to the boiler shutdown was made and shown in Table 8.

The maximum number of days that the boiler tube leak was confirmed was for Fault #3 (circa 22 days), while the least was for Fault #6 (circa 4 days). On average, the boiler tube leak detection could be confirmed 12 days prior to boiler shutdown. As an example, referring to Fault #10 in Figure 8, the first boiler tube leak detection was by the IDF A FG PRESS model 18 days before boiler shutdown, followed by the second detection by the IDF B FG PRESS model on the 14th day. The tube leak was confirmed by the third detection from HOT SA A FLOW on the 18th day prior to boiler shutdown. Another 3 models detected the tube leaks after that, with ECO B OTL O2 on the 11th day and DEA WTR FLOW and MAIN FW FLOW on the fourth day.

Table 8
Fault detection time by at least 3 models' residuals

Fault no.	No of days that boiler tube leak was confirmed prior to boiler shutdown (detected by at least 3 model's residual)
1	13
2	18
3	22
4	6
5	21
6	4
7	9
8	6
9	14
10	12
11	17
12	9

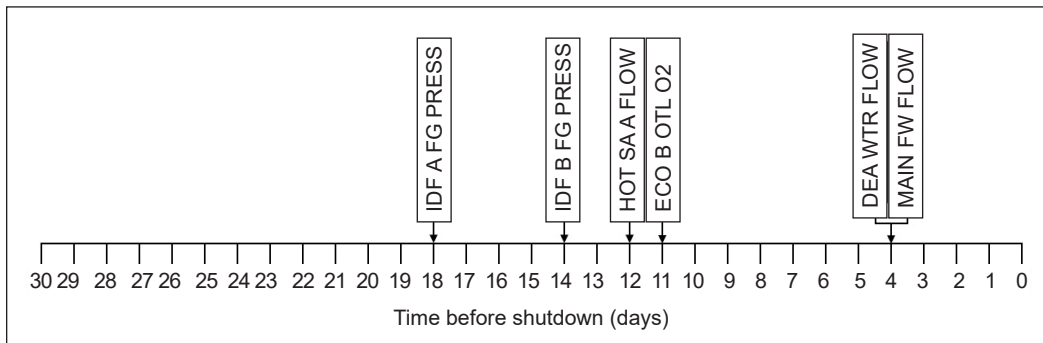


Figure 8. Sequence of boiler tube leak detection time by the corresponding models' residuals for Fault #10

Evaluation of Fault Detection Models

The 10 models, which were trained using boiler process data from 2012 to 2020, were then inputted with data from January 2021 to November 2022 to evaluate their ability to detect two tube leak faults, named Fault #13 and Fault #14, in May 2021 and September 2022, respectively.

Fault Detection in Year 2021

The results for predictions in 2021 were decent, as 5 models produced residuals beyond the threshold limit in May. It confirmed the authenticity of the detection since Fault #13 happened in the same month. There were several false alarms during other months: 2

models gave false alarms in February, and 1 model gave false alarms in April, September, and December, respectively. Detailed analysis of Fault #13 detection is shown in Figure 9. The first detection was made 28 days before boiler shutdown by the TOTAL PA FLOW model, followed by the ECO B OTL O2 model on day 17 prior to boiler shutdown. The boiler tube leak, Fault #13, was confirmed with the third detection by the HOT SA B FLOW model 14 days prior to boiler shutdown. The next detection was made by another 2 models, IDF A FG PRESS and ECO A OTL O2, on day 7 prior to boiler shutdown.

As an example, in the case of detection by the HOT SA B FLOW model, the predicted outputs of the HOT SA B FLOW model were plotted against the actual sensor readings for the 23-month period (January 2021–November 2022), as shown in Figure 10. The corresponding residuals were plotted in Figure 11. It was observed that the residual plot went above the threshold in May, at the same time when boiler tube leak Fault #13 happened. A more detailed residual trend with a 30-day period prior to boiler shutdown was plotted, as shown in Figure 12. It showed an early detection approximately 14 days

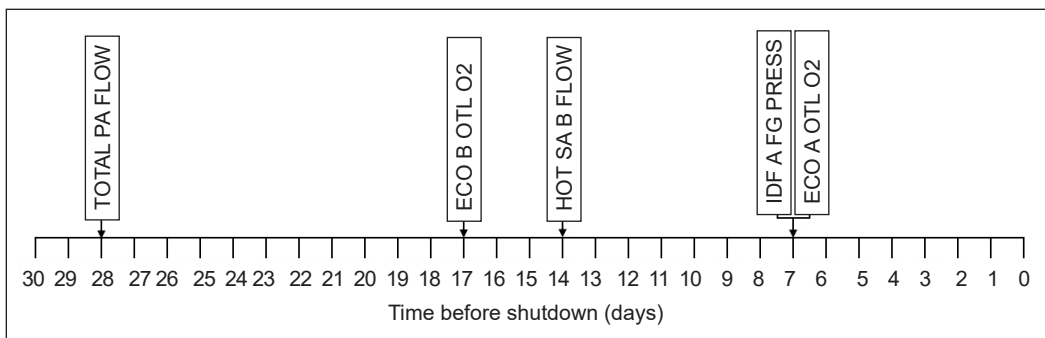


Figure 9. Sequence of boiler tube leak detection time by the corresponding models' residuals for Fault #13

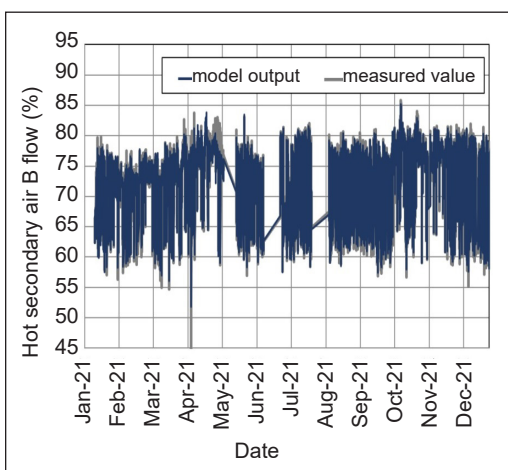


Figure 10. Measured value and output from the HOT SA B FLOW model for the year 2021

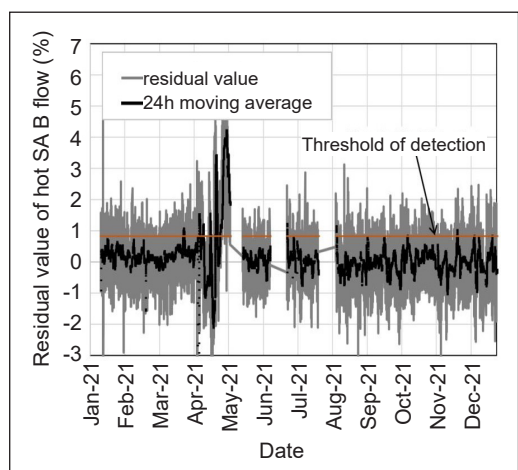


Figure 11. The residual value of hot secondary air B flow and its 24-hour moving average for the year 2021

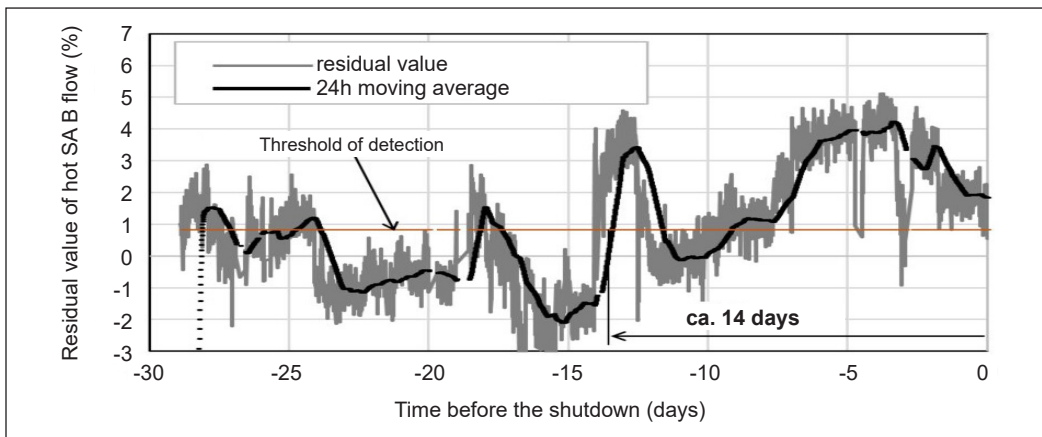


Figure 12. The residual value of hot secondary air B flow and its 24-hour moving average for tube leak Fault #13

earlier before the tube leak was detected by power plant personnel, which was followed by boiler shutdown.

Fault Detection in Year 2022

The prediction for the year 2022 was observed to be inaccurate for all 10 models. All residual plots showed values significantly beyond the threshold for most of the months in 2022, which was unusual. For example, the predicted output against actual sensor readings for total primary airflow and its residuals were plotted in Figures 13(a) and 14(a), respectively. The residual plot shows it went above the threshold many times throughout the year, from March to June and August to November. It was concluded that the trained models could not predict future sensor data accurately beyond one year from the data used in training the model.

In an attempt to improve the prediction for the year 2022, all 10 models were retrained by adding boiler operational data from the year 2021 to the process. As a result, the predictions improved significantly, with 5 models having residuals going beyond the threshold limit in September. The authenticity of this detection was confirmed with the record that Fault #14 happened in September. There were also false alarms detected, with 2 models giving false alarms in February, June, and August, respectively. On the other hand, 1 model gave false alarms in March, April, May, and October, respectively.

Illustrations of these improvements were indicated in a similar plot of predicted against actual sensor data for total primary airflow and its residuals for 2022, as shown in Figures 13(b) and 14(b), respectively. The residual plot was observed to go above the threshold in September when boiler tube leaks Fault #14 happened. A more detailed residual trend with 60 days prior to boiler shutdown was plotted in Figure 15. It showed an early detection of circa 37 days before the tube leak was detected by power plant personnel, which was

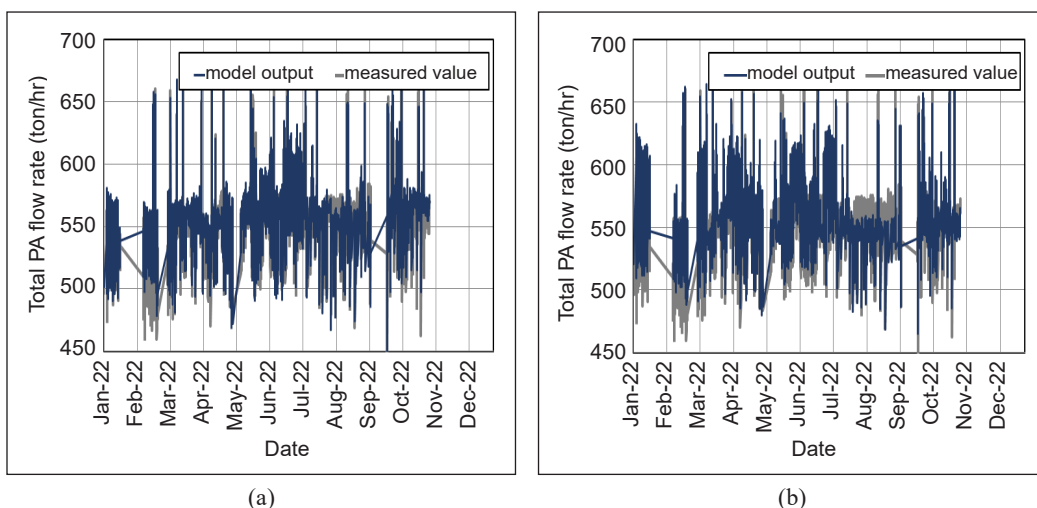


Figure 13. Measured value and output from TOTAL PA FLOW model in the year 2022 for: (a) model trained with 2012 to 2020 data; and (b) model retrained with 2012 to 2021 data

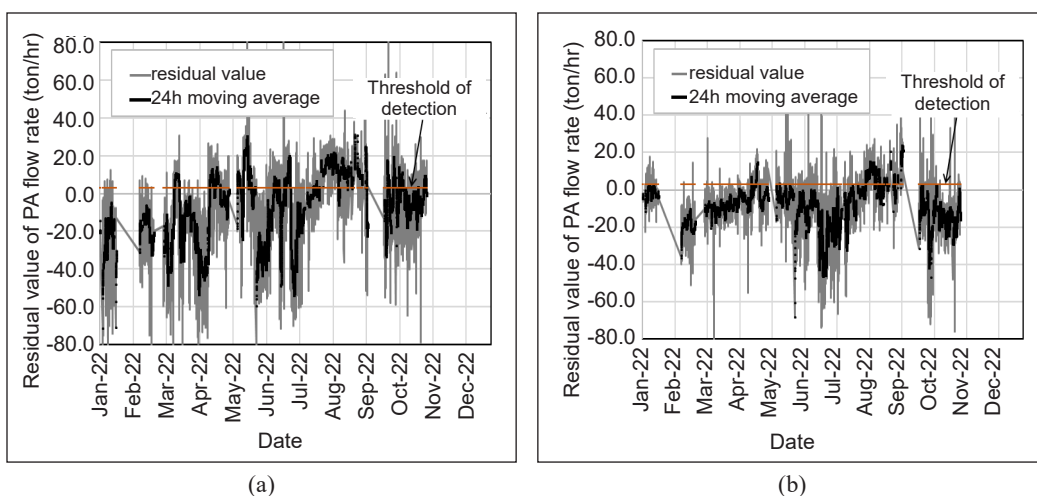


Figure 14. The residual value of total primary airflow and its 24-hour moving average in the year 2021 for: (a) model trained with 2012 to 2020 data; (b) model retrained with 2012 to 2021 data

followed by boiler shutdown. There was also a short period in April 2022 when the residual plot went above the threshold. However, other models did not detect this and considered it a false alarm.

Detailed analysis of Fault #14 detection is shown in Figure 16. The first detection occurred 37 days before boiler shutdown by the TOTAL PA FLOW model, followed by the HOT SAB FLOW model 37 days prior to boiler shutdown. The boiler tube leak, Fault #14, was confirmed with the third detection by the COND WTR FLOW model 24 days prior to boiler shutdown. Subsequent detections were made by two other models, DEA WTR

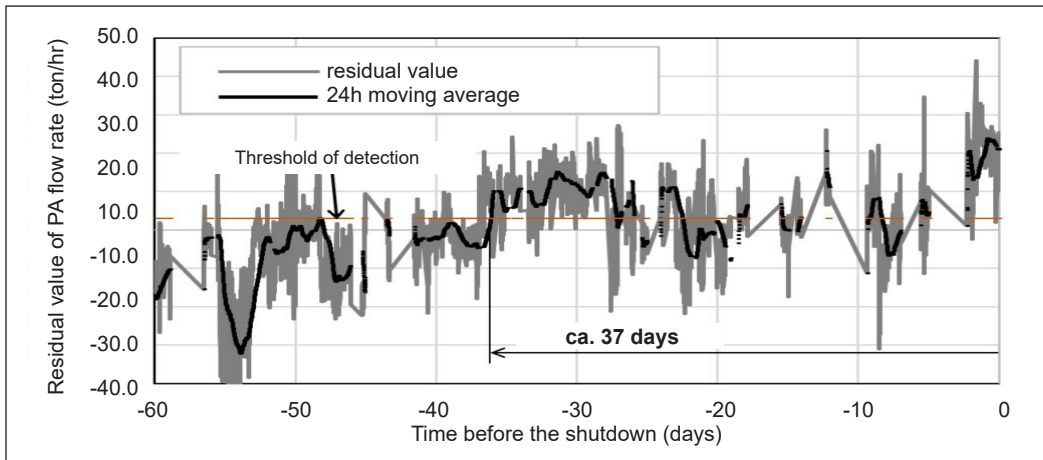


Figure 15. The residual value of total primary airflow and its 24-hour moving average for tube leak Fault #14

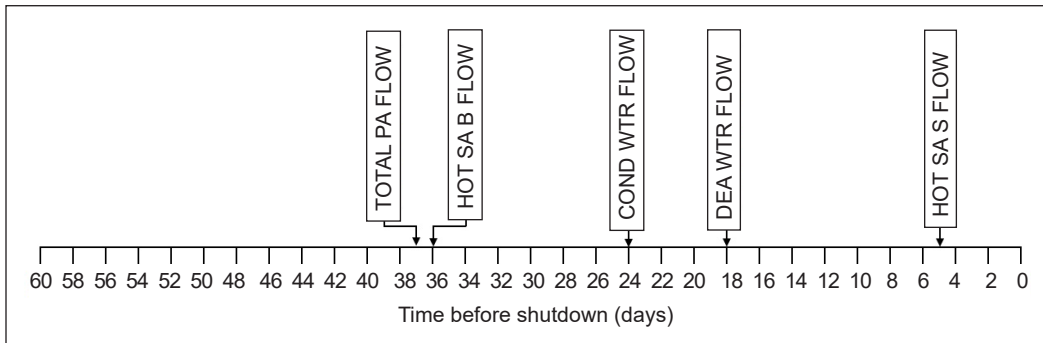


Figure 16. Sequence of boiler tube leak detection time by the corresponding models' residuals for Fault #14

FLOW and HOT SAA FLOW, on days 18 and 5 prior to boiler shutdown, respectively.

Comparison of Results with Other Studies

In benchmarking results from this study, comparisons were made with several other studies, notably Rostek et al. (2015), Kim, Lee and Park (2019), Kim, Lee, Kim et al. (2019), Khalid et al. (2020), Ramezani et al. (2020), and Ismail et al. (2020).

Rostek et al. (2015) initiated research into fault detection in fluidised bed coal-fired boilers, utilising eight years of data from 19 input and 4 output sensors. Their study, employing a simple multilayer perceptron, achieved a training R^2 exceeding 80% and demonstrated a notable improvement in leak detection time, ranging from 2 to 9 days earlier than traditional methods. However, details on model quality and validation were not provided, limiting comprehensive assessment.

Kim, Lee, and Park (2019) extended their research to thermal power plants, employing an auto-associative neural network based on 18 days of data from 13 sensors. Despite lacking

detailed network structure information, their study reported a significant advancement in leak detection time, 30 minutes earlier than traditional methods. However, the absence of comprehensive performance metrics and validation results impedes thorough evaluation.

Similarly, Kim, Lee, Kim, et al. (2019) investigated fault detection in fluidised bed coal-fired boilers using a multilayer neural network. Although their study showcased a 35-minute improvement in leak detection time compared to traditional methods, the lack of detailed model quality assessment and validation data limits comprehensive comparison with other studies.

Khalid et al. (2020) explored fault detection in fluidised bed coal-fired boilers using various classifiers, including SVM, k-NN, NB, and LDA. While their study demonstrated promising accuracy results, the absence of information on leak detection time and validation with data outside the learning period limits comprehensive comparison with other studies.

Ramezani et al. (2020) focused on fault detection in pulverised coal-fired boilers, employing a deep bidirectional LSTM network. Although they demonstrate the potential of recurrent neural networks for fault detection, the lack of detailed information on network structure and performance metrics hinders thorough evaluation.

Ismail et al. (2020) addressed boiler shutdown scenarios using a backpropagation neural network. Their study reported a leak detection time of 5 minutes earlier than traditional methods. However, the absence of detailed accuracy metrics and validation results limits the comprehensive assessment of their methodology.

In contrast, the current study significantly advances fault detection methodologies for pulverised coal-fired boilers. Leveraging nine years of data from 120 input and 10 output sensors, it employed a deep feedforward neural network with optimisation of seven hyper-parameters. The network architecture included up to nine hidden layers with varying numbers of neurons and optimisation algorithms such as Adam, Adamax, Nadam, Nesterov, and AMSGrad. Notably, the study achieved impressive training and testing accuracies, with R^2 ranging from 82.8% to 99.3%. Furthermore, the leak detection time ranged from 3 to 30 days earlier than traditional methods, showcasing significant improvement in predictive maintenance capabilities. Importantly, validation with external data sets demonstrated reliable predictions for up to one-year post-learning. These findings underscore the robustness and efficacy of the methodology in enhancing fault detection capabilities in boiler and thermal power plant operations.

In summary, while previous studies have significantly contributed to fault detection in boiler and thermal power plants, the current study represents a notable advancement in data comprehensiveness, algorithm sophistication, performance metrics, and validation results. By benchmarking against this study and considering the insights from other research works, it is evident that there is immense potential for further advancements in machine learning-based fault detection methodologies in the energy sector.

CONCLUSION

The studies highlighted here achieved notable success in early leak detection and prediction through deep-feedforward neural network models. The fine-tuning of hyper-parameters notably enhanced the accuracy of predictions for parameters impacted by boiler tube leaks. The most effective model demonstrated a 99.63% correlation in training and 96.39% in testing with actual process data. During the network's learning phase, it successfully detected all 12 tube leak faults, identifying them 3 to 30 days before the necessary boiler shutdown. A leak was confirmed when at least three models consistently predicted its occurrence. However, assessments of the model using data from two years post-learning period indicated that its predictions were reliable only for the first year. To maintain accuracy, continual updating and learning of the model are essential. The recommendation is to deploy these models in real-time operations at the studied plant, which would allow for evaluating their effectiveness in identifying real-time boiler tube leak faults.

For future research, it is recommended that researchers prioritise the real-time implementation and deployment of predictive models. Integrating these models into operational workflows will enable proactive maintenance strategies and minimise downtime due to tube leaks. Collaboration with industry partners to streamline deployment protocols and optimise computational efficiency is essential for ensuring seamless integration into operational workflows.

After deploying predictive models, conducting extensive field validation and case studies emerges as a critical next step. Real-world validation across diverse operational conditions and geographical locations provides empirical evidence of the model's effectiveness and reliability. Leveraging insights gained from field validation studies, researchers can refine and optimise predictive models to address specific challenges encountered in operational environments.

ACKNOWLEDGEMENT

The authors thank the Kulliyyah of Engineering, International Islamic University Malaysia, for supporting this research work.

REFERENCES

- Alouani, A. T., & Chang, P. S. (2003). *Artificial neural network and fuzzy logic based boiler tube leak detection systems*. U.S. Patent No. 6,192,352. Washington, DC: U.S. Patent and Trademark Office.
- Barszcz, T., & Czop, P. (2011). A feedwater heater model intended for model-based diagnostics of power plant installations. *Applied Thermal Engineering*, 31(8-9), 1357-1367. <https://doi.org/10.1016/j.applthermaleng.2010.12.012>

- Behera, S. K., Rene, E. R., Kim, M. C., & Park, H. S. (2014). Performance prediction of a RPF-fired boiler using artificial neural networks. *International Journal of Energy Research*, 38(8), 995-1007. <https://doi.org/10.1002/er.3108>
- Ismail, F. B., Singh, D., & Nasif, M. S. (2020). Adoption of intelligent computational techniques for steam boilers tube leak trip. *Malaysian Journal of Computer Science*, 33(2), 133-151. <https://doi.org/10.22452/mjcs.vol33no2.4>
- Ismail, F. B., Singh, D., Maisurah, N., & Musa, A. B. B. (2016). Early tube leak detection system for steam boiler at KEV power plant. In *MATEC Web of Conferences* (Vol. 74, p. 00006). EDP Sciences. <https://doi.org/10.1051/mateconf/20167400006>
- Karim, A. M. A., & Mustafah, Y. M. (2022). *Early detection of tube leaks faults in pulverised coal-fired boiler using deep neural network*. In *8th International Conference on Mechatronics Engineering (ICOM 2022)* (Vol. 2022, pp. 125-132). IET Publishing. <https://doi.org/10.1049/icp.2022.2277>
- Khalid, S., Lim, W., Kim, H. S., Oh, Y. T., Youn, B. D., Kim, H. S., & Bae, Y. C. (2020). Intelligent steam power plant boiler waterwall tube leakage detection via machine learning-based optimal sensor selection. *Sensors*, 20(21), Article 6356. <https://doi.org/10.3390/s20216356>
- Kim, K. H., Lee, H. S., & Park, J. H. (2019). Detection of boiler tube leakage fault in a thermal power plant using k-means algorithm based on auto-associative neural network. In *2019 20th International Conference on Intelligent System Application to Power Systems (ISAP)* (pp. 1-5). IEEE Publishing. <https://doi.org/10.1109/ISAP48318.2019.9065940>
- Kim, K. H., Lee, H. S., Kim, J. H., & Park, J. H. (2019). Detection of boiler tube leakage fault in a thermal power plant using machine learning based data mining technique. In *2019 IEEE International Conference on Industrial Technology (ICIT)* (pp. 1006-1010). IEEE Publishing. <https://doi.org/10.1109/ICIT.2019.8755058>
- Kokkinos, A. (2019). Coal R&D Beyond 2020. In *DOE-NETL-EPRI Technical Exchange Meeting*. Pittsburgh, PA, USA: EPRI.
- Lang, F. D., Rodgers, D. A., & Mayer, L. E. (2004). Detection of tube leaks and their location using input/loss methods. In *ASME Power Conference* (Vol. 41626, pp. 143-150). <https://doi.org/10.1115/power2004-52027>
- Mishra, S., Bordin, C., Taharaguchi, K., & Palu, I. (2020). Comparison of deep learning models for multivariate prediction of time series wind power generation and temperature. *Energy Reports*, 6, 273-286. <https://doi.org/10.1016/j.egy.2019.11.009>
- Nistah, N. N. M., Lim, K. H., Gopal, L., & Alnaimi, F. B. I. (2018). Coal-fired boiler fault prediction using artificial neural networks. *International Journal of Electrical and Computer Engineering*, 8(4), Article 2486. <https://doi.org/10.11591/ijece.v8i4.pp2486-2493>
- Pfeuffer, S. (2009). Update: Benchmarking boiler tube failures. *Power*, 153(10), 68-71.
- Ramezani, M. G., Hasanian, M., Golchinfar, B., & Saboonchi, H. (2020). Automatic boiler tube leak detection with deep bidirectional LSTM neural networks of acoustic emission signals. In *Sensors and Smart Structures Technologies for Civil, Mechanical, and Aerospace Systems 2020* (Vol. 11379, pp. 205-213). SPIE Publishing. <https://doi.org/10.1117/12.2558885>

- Rostek, K., Morytko, Ł., & Jankowska, A. (2015). Early detection and prediction of leaks in fluidized-bed boilers using artificial neural networks. *Energy*, *89*, 914-923. <https://doi.org/10.1016/j.energy.2015.06.042>
- Singh, D., Ismail, F. B., & Nasif, M. S. (2017). Hybrid intelligent warning system for boiler tube leak trips. In *MATEC Web of Conferences* (Vol. 131, p. 03003). EDP Sciences. <https://doi.org/10.1051/mateconf/201713103003>
- Sun, X., Chen, T., & Marquez, H. J. (2002). Efficient model-based leak detection in boiler steam-water systems. *Computers & Chemical Engineering*, *26*(11), 1643-1647. [https://doi.org/10.1016/S0098-1354\(02\)00147-3](https://doi.org/10.1016/S0098-1354(02)00147-3)
- Tam, A. S., Price, J. W., & Beveridge, A. (2007). A maintenance optimisation framework in application to optimise power station boiler pressure parts maintenance. *Journal of Quality in Maintenance Engineering*, *13*(4), 364-384. <https://doi.org/10.1108/13552510710829461>
- Torres, J. F., Hadjout, D., Sebaa, A., Martínez-Álvarez, F., & Troncoso, A. (2021). Deep learning for time series forecasting: A survey. *Big Data*, *9*(1), 3-21. <https://doi.org/10.1089/big.2020.0159>

A Framework for Prioritising the Performance Criteria of Natural Fibre Composite Materials: Incorporation of CRITIC-TOPSIS Method

Mohd Hidayat Ab Rahman^{1,2}, Siti Mariam Abdul Rahman¹, Ridhwan Jumaidin² and Jamaluddin Mahmud^{1*}

¹*School of Mechanical Engineering, College of Engineering, Universiti Teknologi MARA, 40450 Shah Alam, Selangor, Malaysia*

²*Fakulti Teknologi dan Kejuruteraan Industri dan Pembuatan, Universiti Teknikal Malaysia Melaka, Hang Tuah Jaya, 76100 Durian Tunggal, Melaka, Malaysia*

ABSTRACT

Selecting an appropriate Multi-Criteria Decision-Making (MCDM) method to provide a solution to assist design engineers in prioritising the right criteria in the early design process is essential. Part of the aim of this study is to establish an integration CRITIC-TOPSIS for selecting the most efficient framework to choose performance criteria, namely density, tensile strength, Young's modulus, cellulose, and elongation at break for natural fibre material intended for cap toe shoes like abaca, bamboo, coir, jute, kenaf, sisal. Hence, a new framework was proposed and tested based on integrating Criteria Importance Through Inter Criteria Correlation (CRITIC)-Technique Order Preference by Similarity to Ideal Solution (TOPSIS). Therefore, this proposed framework consists of two phases: the first involves determining the weights of attributes using the CRITIC method, and the second consists of making material criteria decisions using the TOPSIS method. Meanwhile, to achieve this

objective, numerical validation was obtained using data from selected past case studies, which were then replicated to validate the output of the proposed framework. According to the validation conducted using CRITIC-TOPSIS, the results show a significant level of similarity, with the rankings being consistent. Therefore, the proposed methodology may provide imprecise and ambiguous information for prioritising the performance criteria of

ARTICLE INFO

Article history:

Received: 18 December 2023

Accepted: 10 July 2024

Published: 25 October 2024

DOI: <https://doi.org/10.47836/pjst.32.6.14>

E-mail addresses:

2022640652@student.uitm.edu.my (Mohd Hidayat Ab Rahman)

mariam4528@uitm.edu.my (Siti Mariam Abdul Rahman)

ridhwan@utem.edu.my (Ridhwan Jumaidin)

jm@uitm.edu.my (Jamaluddin Mahmud)

* Corresponding author

natural fibre composite materials. Moreover, design engineers can utilise this framework in the composite industry to create the best possible evaluation model for composite material criteria selection for various applications.

Keywords: CRITIC method, framework, MCDM, natural fibre, TOPSIS method

INTRODUCTION

Decision Making (DM) is selecting an option by recognising a decision, collecting data, and evaluating several alternatives. One of the first in-depth studies on the concept of DM was published by the Psychological Bulletin, where the paper elaborates on the risk and psychology behind DM (Edwards, 1954). In order to make the best possible choice when dealing with numerous options, conflicts, or decision criteria, the Multi Criteria Decision Making (MCDM) methods are typically utilised (Jigeesh et al., 2018; Mastura et al., 2015; Mufazzal & Muzakkir, 2018). They are typically used to evaluate issues relating to the environment, society, technology, and material choice.

Past studies have reported on developing MCDM tools for various applications to determine the best alternative by considering more than one criterion in the selection process. An innovative study was undertaken to select a logistics service provider (Jharkharia & Shankar, 2007), where the selection procedure employed the Analytic Network Process (ANP). On the other hand, Han et al. (2020) examined road selection based on the Analytical Hierarchy Process (AHP) that involves a point of interest, model of roads, constituent density partitions and global connectivity of the selected network. Stević et al. (2019) studied sustainability in a supply chain where the need was to select a sustainable supplier using Simple Additive Weighting (SAW). Recently, Chan and Ch'ng (2023) analysed the risk factors of suicidal ideation among university students in Malaysia using the Technique Order Preference by Similarity to Ideal Solution (TOPSIS). Therefore, the MCDM method is well known for helping people solve complex real-life issues. It can compare choices based on different decision-making criteria and find the best acceptable criteria (Emovon & Oghenenyero, 2020; Zavadskas et al., 2016). MCDM has gained popularity since it can assist decision-makers in evaluating all significant factors and making decisions based on priority (Kabir et al., 2014; Mufazzal & Muzakkir, 2018; Sattar & Ghazwan, 2023). When numerous aspects are concluded as a good design, an expert decision-maker may occasionally search for either technical or economic elements that can be compromised to prioritise decision-making. A DM can utilise MCDM to assign relative value to criteria to measure them.

Numerous studies have been done on selecting natural fibre for composite preparation. For example, an innovative study using the AHP method was undertaken to select biopolymer composites as a potential material for food packaging (Salwa et al., 2019).

However, the assumption of criteria independence (no correlation) is a limitation of AHP (Ishizaka & Labib, 2009). On the other hand, Maidin et al. (2022) examined a material selection of natural fibre using Grey Relational Analysis (GRA).

One of the tools used in MCDM approaches is the ability to determine ranking and define preferences. Hwang and Yoon (1981) introduced the TOPSIS method to assist decision-makers in making reliable and consistent judgments. Nevertheless, a significant weakness of the TOPSIS method is its lack of provisions for weight elicitation and consistency testing for judgment, as Shih et al. (2007) pointed out. Diakoulaki et al. (1995) developed the CRITIC method to establish an objective weight. Therefore, both methods can be utilised to prioritise performance requirements for natural fibre composite materials and integrating both methods may improve the decision-making outcome. Apart from these methods, Table 1 highlights the utilisation of both CRITIC and TOPSIS methods, which have been explored in information technology, financial and banking, sustainable energy, environmental and heavy industries. The CRITIC method is utilised to score and determine the importance of the relative weights for the decision criteria set. In contrast, the TOPSIS method determines the final ranking of all alternatives.

Although studies have been conducted on utilising both CRITIC and TOPSIS methods in material selection, there is still a lack of reported studies on natural fibre material selection using the integration of the CRITIC-TOPSIS method. Therefore, by fulfilling this research gap, designers and material engineers would greatly benefit from a clear

Table 1
Application sectors and domains covered by CRITIC and TOPSIS

Application sectors	References
Information technology	Berdie et al., 2017
- Computing software	Ertemel et al., 2023
- Smartphone addiction	
Environmental	Chen et al., 2022
- Monte Carlo simulation	
Supply chain management	Abdel-Basset & Mohamed, 2020
Sustainable Energy	Lakshmi et al., 2022
- Green energy	Babatunde & Ighravwe, 2019; Ighravwe & Babatunde, 2018
- Renewable energy	
- Value Added Intellectual Capital (VAIC)	Polcyn, 2022; Hassan et al., 2023
- Solar PV	
Financial and banking	Kazan & Ozdemir, 2014
- Financial	
Heavy industries	Mohamadghasemi et al., 2020
- Crane Industries	Wu et al., 2020
- Bridge construction	
Material	Slebi-Acevedo et al., 2019
- Polymer-modified binder (PMB)	

and methodical methodology selection procedure. Hence, this study is interested in using an innovative approach known as Criteria Importance Through Inter-criteria Correlation (CRITIC) and Technique for Order Preference by Similarity to Ideal Solution (TOPSIS) to eliminate the need to compare characteristics and determine their weights. The following will ultimately reduce the decision maker’s dependence on choosing the most suitable natural fibre material. Hence, incorporating these two MCDM methods is appropriate for evaluating the natural fibre composite materials. It will assist the business’s design engineer and manufacturing team choose the most suitable materials for product design and development.

METHODOLOGY FOR FRAMEWORK DEVELOPMENT

The overall methodology of this study is presented in four phases for better clarity. Phase 1 involves criteria selection and prioritisation. Weightage determination using the CRITIC method and material ranking using the TOPSIS method were gathered in Phase 2. The conceptual framework review was gathered in Phase 3 through validation of the framework, and the study was concluded with a ranking of the material performance in Phase 4.

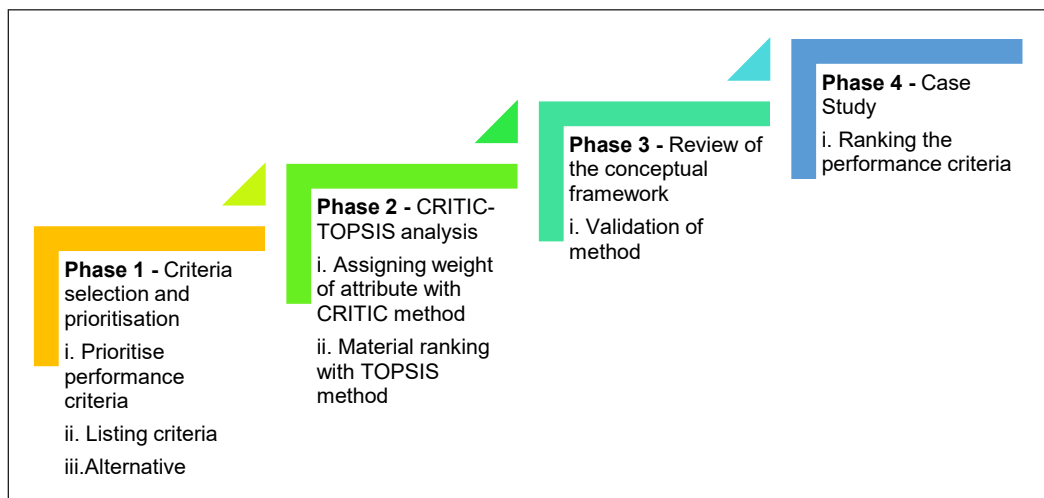


Figure 1. Methodology for framework development

Phase 1: Criteria Selection and Prioritization

The main objective of the DM process was established in the structural hierarchy at Level 1 (goal); that is, the performance criteria were ranked according to priority. In Level 2 (criteria), the performance specifications were listed as length (mm), diameter (m), tensile strength (MPa), Young’s modulus (GPa), elongation at break (%), and cellulose (%). Lastly, in Level 3 (alternative), the performance standards list must be prioritised to meet the target in Level 1. A perspective structural hierarchy is shown in Figure 2 at Phase 1.

Phase 2: CRITIC-TOPSIS Analysis

The performance requirements of natural fibre composite materials are prioritised in this work using the CRITIC and TOPSIS methods. Figure 2 shows the proposed framework model structure for prioritising performance criteria. The framework is divided into 2 phases: (1) Phase 1 starts with collecting data and building a structural hierarchy, and (2) Phase 2 assigns weight by the CRITIC method, and the TOPSIS method is used to rank the criteria.

Weightage Determination Using CRITIC Method

The Criteria Importance Through Intercriteria Correlation (CRITIC) method is mostly employed to calculate attribute weights. The qualities in the current technique do not conflict

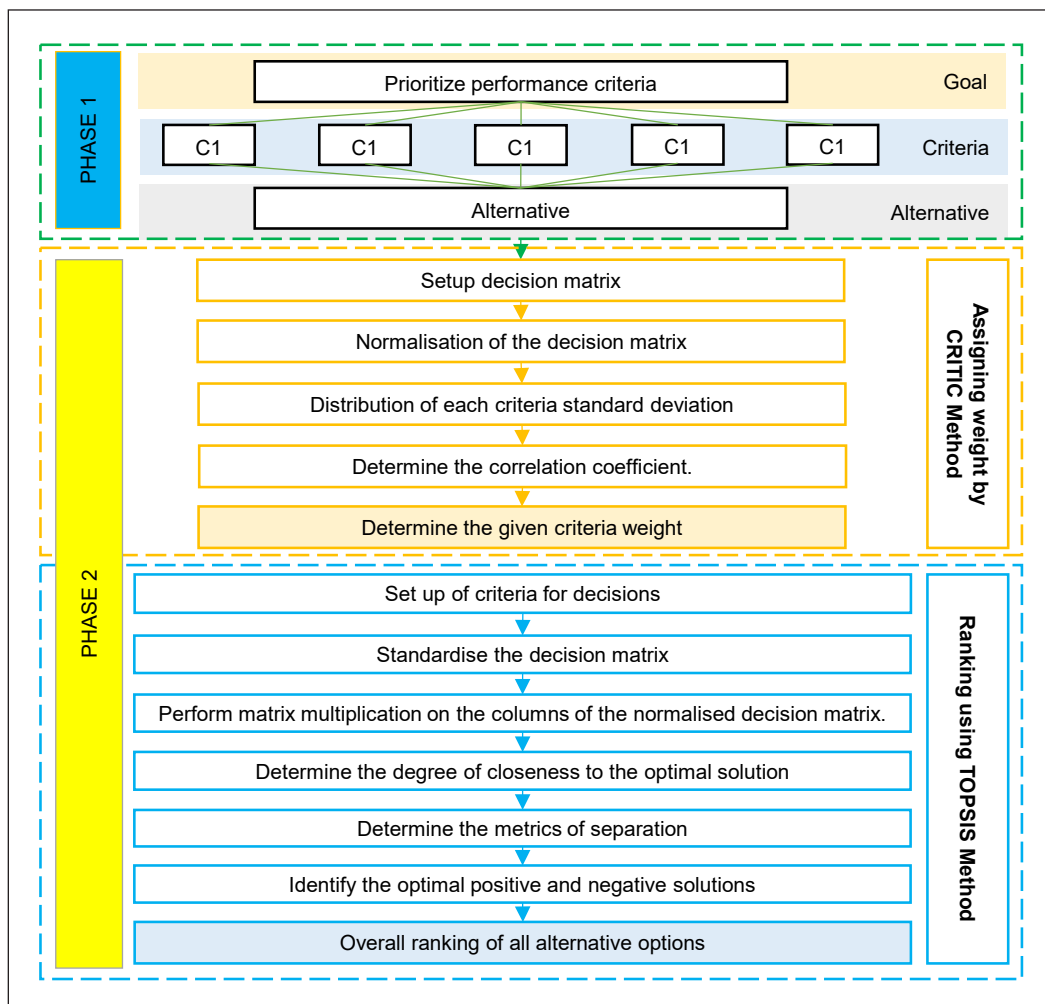


Figure 2. The proposed framework model structure

with one another, and the decision matrix is used to find the weights of the attributes. The CRITIC method is a correlation method that utilises correlation coefficients of all paired columns and the standard deviation of alternatives' ranking criteria values to determine criteria contrasts (Pamucar et al., 2022; Žižovic et al., 2020). Steps 1 to 5 detail the process's weightage (Alinezhad & Khalili, 2019; Anand et al., 2022; Diakoulaki et al., 1995).

Step 1: Starting from an initial decision matrix

The initial decision matrix is obtained using Equation 1 (Anand et al., 2022).

$$A = \begin{bmatrix} x_{11} & \cdots & x_{1j} & \cdots & x_{1n} \\ \vdots & \ddots & \vdots & \ddots & \vdots \\ x_{i1} & \cdots & x_{ij} & \cdots & x_{in} \\ \vdots & \ddots & \vdots & \ddots & \vdots \\ x_{m1} & \cdots & x_{mj} & \cdots & x_{mn} \end{bmatrix}_{m \times n} ; i = 1, \dots, m, j = 1, \dots, n \quad [1]$$

Step 2: Normalisation of the decision matrix

The scores of the various criteria cannot be compared since they are expressed using various measuring scales or units. As part of the normalisation procedure, the scores are transformed into standard scales with a 0 to 1 range. The choice matrix's scores are initially determined using the suggested method by utilising Equation 2.

$$\overline{X}_{ij} = \frac{x_{ij} - x_j^{worst}}{x_j^{best} - x_j^{worst}} \quad [2]$$

Where \overline{X}_{ij} is the normalised score of alternative i with respect to criterion j , x_{ij} is the actual score of alternative i with respect to criterion j , x_j^{best} is the best score of criterion j , and x_j^{worst} is the worst score of criterion j .

Step 3: Distribution of each criteria standard deviation

In the third step, the standard deviation of each criterion, s_j , is calculated using Equation 3. Note that \overline{X}_j in Equation 2 is the mean score of criterion j and that m is the total number of alternatives.

$$s_j = \sqrt{\left(\frac{\sum_{i=1}^m x_{ij} - \overline{X}_j}{m-1}\right)^2} \quad [3]$$

Where \overline{X}_j is the mean score of the criterion j and m is the total number of alternatives.

Step 4: Determine the correlation coefficient

The correlation coefficient among attributes is determined by Equation 4.

$$\rho_{jk} = \frac{\sum_{i=1}^m (x_{ij} - \overline{x}_j)(x_{ik} - \overline{x}_k)}{\sqrt{\sum_{i=1}^m (x_{ij} - \overline{x}_j)^2 \sum_{i=1}^m (x_{ik} - \overline{x}_k)^2}} \quad [4]$$

Step 5: Determine the given criteria weight

The weights of attributes are determined by Equation 5

$$w_j = \frac{C_j}{\sum_{j=1}^n C_j}; j = 1, \dots, n \quad [5]$$

Material Ranking Using TOPSIS Method

The Technique Order Preference by Similarity to the Ideal Solution (TOPSIS) method is based on the idea that the chosen option should be most distant from the worst possible solution and the closest to the best possible solution (Hwang & Yoon, 1981). Steps 1 until 7 detailed the processes of the material ranking (Chodha et al., 2021; Pavić & Novoselac, 2013; Rahim et al., 2018).

Step 1: Set up of criteria for decisions (A)

The criteria for decisions are set up using Equation 6 (Chodha et al., 2021).

$$A = (x_{ij})_{m \times n} = \begin{bmatrix} x_{11} & x_{12} & \dots & x_{1n} \\ x_{21} & x_{22} & \dots & x_{2n} \\ \vdots & \vdots & \ddots & \vdots \\ x_{m1} & x_{m2} & \dots & x_{mn} \end{bmatrix} \quad [6]$$

Step 2: Standardise the decision matrix

The standardised value r_{ij} is calculated using Equation 7.

$$r_{ij} = \frac{f_{ij}}{\sqrt{\sum_{j=1}^n f_{ij}^2}}; j=1,2,\dots,j; i=1,2,\dots,n \quad [7]$$

Step 3: Perform matrix multiplication on the columns of the normalised decision

The weighted normalised value v_{ij} is calculated using Equation 8.

$$v_{ij} = w_j \times r_{ij}, j = 1, 2, \dots, J; i = 1, 2, \dots, n, \quad [8]$$

Where w_j is the weight of the i^{th} criterion and $\sum_{i=1}^n w_j = 1$.

Step 4: Determine the degree of closeness to the optimal solution, the positive ideal (A) and the negative ideal (A-) solutions*

The positive ideal (A*) and negative ideal (A-) solutions are expressed using Equation 9 (Rahim et al., 2018).

$$A^* = \left\{ \left(\max_i v_{ij} \mid j \in C_b \right), \left(\min_i v_{ij} \mid j \in C_c \right) \right\} = \{v_j^* \mid j = 1, 2, \dots, m\}$$

$$A^- = \left\{ \left(\min_i v_{ij} \mid j \in C_b \right), \left(\max_i v_{ij} \mid j \in C_c \right) \right\} = \{v_j^- \mid j = 1, 2, \dots, m\} \quad [9]$$

Step 5: Determine the metrics of separation

The measures of separation between each alternative and the positive and negative ideal solutions, respectively, are as in Equation 10:

$$S_i^* = \sqrt{\sum_{j=1}^m (v_{ij} - v_j^*)^2}, \quad j = 1, 2, \dots, m \tag{10}$$

Similarly, the distance from the negative ideal solution is stated in Equation 11.

$$S_i^- = \sqrt{\sum_{j=1}^m (v_{ij} - v_j^-)^2}, \quad j = 1, 2, \dots, m \tag{11}$$

Step 6: Identify the optimal positive and negative solutions

The proximity of the alternate P_i with respect to P^* is defined as stated in Equation 12.

$$Pi_i^* = \frac{S_i^-}{S_i^* + S_i^-}, \quad i = 1, 2, \dots, m \tag{12}$$

Step 7: Overall ranking of all alternative options

Phase 3: Review of the Conceptual Framework: Data Validation of the Framework

Before being used in a case study, the suggested method conducted validation by applying it to previous research. Validation data was gathered from studies from past researchers (Saputra et al., 2018). Sample S1 (Muhammad Musa), S2 (Alvin Syahrin), S3 (Noviyanti), S4 (Sofia), S5 (Syyaiful Aswad). The researcher studies a comparison between AHP and SAW, which was selected and replicated. Saputra et al. (2018) studied a decision support system that helps solve the problem of selecting a department chief.

Table 2 displays the findings collected from the CRITIC-TOPSIS (current), AHP (Saputra et al., 2018) and SAW (Saputra et al., 2018) with extent analysis methods that provide equivalent rankings. For instance, according to the CRITIC-TOPSIS method, the ranking of the alternative based on the numerical validation were $S1 > S2 > S3 > S4 > S5$, AHP and SAW method produced the same ranking as CRITIC-TOPSIS. Therefore, the

Table 2
Result Ranking for validation

Alternative	MCDM Method					
	CRITIC-TOPSIS (current)		AHP (Saputra et al., 2018)		SAW (Saputra et al., 2018)	
	Value	Rank	Value	Rank	Value	Rank
S1	0.997	1	0.274	1	0.993	1
S2	0.629	2	0.241	2	0.883	2
S3	0.435	3	0.193	3	0.707	3
S4	0.237	4	0.158	4	0.578	4
S5	0.015	5	0.135	5	0.490	5

proposed framework utilising the CRITIC-TOPSIS method for ranking calculation is considered suitable, as it provides equivalent preference rankings to those obtained via AHP and SAW.

Phase 4: Case Study

In this phase, the ranking of the performance criteria for cap-toe shoes is taken as an investigation of a case. A case study is carried out to determine the suitability of the suggested framework. The following part will explain the upcoming tasks.

CASE STUDY ON THE PERFORMANCE CRITERIA FOR CAP TOE SHOES

Phase 1: Criteria Selection and Prioritization

Table 3 shows the performance criteria for cap-toe shoes. The six established alternatives are composed of six criteria.

Table 3

Selection of performance criteria adapted from (Biagiotti et al., 2004 Luhar et al., 2020 Peças et al., 2018)

	Diameter (μm)	Length (mm)	Tensile Strength (MPa)	Young's Modulus (GPa)	Elongation at Break (%)	Cellulose (%)
Abaca	20	4.9	621.5	41	2.9	59.5
Bamboo	58	2.75	566	53	4.65	34.5
Coir	18.2	1.65	175	6	20	45.6
Jute	15	3.4	547.5	46.25	2.3	65.25
Kenaf	24	6.2	612.5	41	4.8	53.5
Sisal	27	4.4	681	15.5	2.45	68.5

Phase 2: CRITIC-TOPSIS Analysis

CRITIC Method

The application of the CRITIC method in choosing the performance criterion for the design process is shown below.

Step 1: Starting from an initial decision matrix

The decision matrix shown in Table 3, all criteria are beneficial.

Step 2: Normalisation of the decision matrix

After calculating x_j^{best} and x_j^{worst} , the normalisation of the decision matrix can be determined from Equation 2. Where x_j^{best} is the maximum value of the dataset, and x_j^{worst} is the minimum value of the dataset. For the example $\bar{x}_{ij} = (20-15)/(58-15) = 0.1163$. The entire results of the normalisation of the decision matrix are shown in Table 4.

Step 3: Determine the standard deviation of each criterion

The distribution of each criterion’s standard deviation can be determined from Equation 3. For the example $\bar{x} = (0.1163+1+0.0814+0+0.2093+0.2791)/6 = 0.2810$, and $s_j = \sqrt{((0.1163 - 0.2810)^2 + (1 - 0.2810)^2 + (0.0814 - 0.2810)^2 + (0 - 0.2810)^2 + (0.2093 - 0.2810)^2 + (0.2791 - 0.2810)^2)/(6 - 1)} = 0.3655$. The entire results of the standard deviation of each criterion are shown in Table 5.

Step 4: Determine the correlation coefficient

Table 6 shows the pairwise criteria correlation coefficient values. Equation 4 was used to measure the correlation.

Step 5: Determine the given criteria weight W_j

After calculating $c_j = \sum_{j=1}^n c_j$, the Weight of the selected criteria can be determined from Equation 5. For the example $c_j = \sum_{j=1}^n c_j = ((1-1) + (1-(-1.1914)) + (1-0.2122) + (1-0.4168) + (1-(-0.1694)) + (1-(-0.7022))) \times 0.3655 = 1.9863$, $\sum c_j = 1.9863 + 7.5357 + 1.4437 + 3.0608 + 2.0520 = 11.8920$, and $w_j = 1.9863/11.8920 = 0.1670$. The weight of all the results of the selected criteria is shown in Table 7.

Figure 3 illustrates the relative importance of evaluation indicators. The findings show that the ranking order for criteria = Elongation at Break > Cellulose > Diameter > Young’s

Table 4
Normalisation of the decision matrix

	Diameter (µm)	Length (mm)	Tensile Strength (MPa)	Young’s Modulus (GPa)	Elongation at Break (%)	Cellulose (%)
Abaca	0.1163	0.7143	0.8824	0.7447	0.0339	0.7353
Bamboo	1.0000	0.2418	0.7727	1.0000	0.1328	0.0000
Coir	0.0814	0.0000	0.0000	0.0000	1.0000	0.3265
Jute	0.0000	0.3846	0.7362	0.8564	0.0000	0.9044
Kenaf	0.2093	1.0000	0.8646	0.7447	0.1412	0.5588
Sisal	0.2791	0.6044	1.0000	0.2021	0.0085	1.0000

Table 5
Distribution of each criteria standard deviation

	Diameter (µm)	Length (mm)	Tensile Strength (MPa)	Young’s Modulus (GPa)	Elongation at Break (%)	Cellulose (%)
Abaca	0.1163	0.7143	0.8824	0.7447	0.0339	0.7353
Bamboo	1.0000	0.2418	0.7727	1.0000	0.1328	0.0000
Coir	0.0814	0.0000	0.0000	0.0000	1.0000	0.3265
Jute	0.0000	0.3846	0.7362	0.8564	0.0000	0.9044
Kenaf	0.2093	1.0000	0.8646	0.7447	0.1412	0.5588
Sisal	0.2791	0.6044	1.0000	0.2021	0.0085	1.0000
STDEV	0.3655	0.3567	0.3596	0.3963	0.3873	0.3759

Table 6
Pairwise criteria correlation coefficient values

	Diameter (µm)	Length (mm)	Tensile Strength (MPa)	Young's Modulus (GPa)	Elongation at Break (%)	Cellulose (%)
Diameter (µm)	1.0000	-0.1914	0.2122	0.4168	-0.1694	-0.7022
Length (mm)	-0.1914	1.0000	0.7488	0.3231	-0.6419	0.4565
Tensile Strength (MPa)	0.2122	0.7488	1.0000	0.5469	-0.9631	0.4401
Young's Modulus (GPa)	0.4168	0.3231	0.5469	1.0000	-0.6690	-0.1933
Elongation at Break (%)	-0.1694	-0.6419	-0.9631	-0.6690	1.0000	-0.4596
Cellulose(%)	-0.7022	0.4565	0.4401	-0.1933	-0.4596	1.0000

Table 7
Determine the weight of the selected criteria

Major Criteria	C_j	W_j
Diameter (µm)	5.4341	0.1670
Length (mm)	4.3049	0.1291
Tensile Strength (MPa)	4.0151	0.1214
Young's Modulus (GPa)	4.5756	0.1525
Elongation at Break (%)	7.9031	0.2574
Cellulose (%)	5.4586	0.1725
TOTAL	11.8920	1.0000

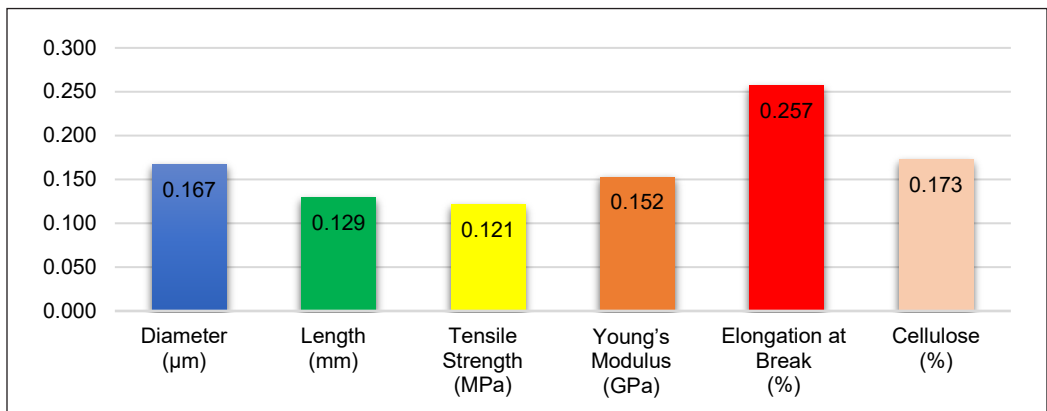


Figure 3. Weight for each performance criterion

Modulus > Length > Tensile Strength. The most preferred criterion is Elongation at Break, and the least preferred criterion is Tensile Strength. The Elongation at Break (%) and the Cellulose (%) correspond to the two highest weights in the results, indicating that these two performance criteria were given preferences. At the same time, Tensile Strength (MPa) has the lowest value corresponding to the least preferred criterion.

TOPSIS Method

The TOPSIS method has been used to solve evaluation and selection problems. Here is the implementation of the TOPSIS approach for selecting the criteria for design process performance.

Step 1: Set up of criteria for decisions (A)

Table 8 shows the decision matrix. Equation 6 is used to obtain the construction decision matrix.

Step 2: Standardise the decision matrix

After calculating $\sum f_{ij}^2$ all, the standardised decision matrix can be determined from Equation 7. For the example $\sum f_{ij}^2 = (20^2) + (58^2) + (18.5^2) + (15^2) + (24^2) + (27^2) = 5636.25$, $r_{ij} = 20/\sqrt{5636.25} = 0.2664$. The entire results of the standardised decision-making matrix are shown in Table 9.

Step 3: Perform matrix multiplication on the columns of the normalised decision by the associated weights to generate the weighted normalised decision matrix, which is the weighted normalised value

Equation 8 can determine the weighted normalisation value—for example, $v_{ij} = 0.266 \times 0.1670 = 0.445$. The entire results of the weighted normalisation value are shown in Table 10.

Step 4: Determine the degree of closeness to the optimal, positive ideal (A) and negative ideal (A-) solutions*

The degree of closeness to the optimal solution can be determined using Equation 9. For example, the positive ideal (A*) is the maximum value of the dataset, maximum = 0.1290, and the negative ideal (A-) is the minimum value of the dataset, minimum = 0.0334. The entire results of the degree of closeness to the optimal solution are shown in Table 11.

Step 5: Determine the separation measures: The separation measures of each alternative from the positive ideal solution and the negative ideal solution, respectively, are as follows:

All separation measures can be determined from Equations 10 and 11. For the example,

$$S_i^+ = \sqrt{\frac{(0.445 - 0.1290)^2 + (0.0622 - 0.0786)^2 + (0.0551 - 0.0604)^2 + (0.0675 - 0.0872)^2 + (0.0346 - 0.2389)^2 + (0.0752 - 0.0866)^2}{}} = 0.2229$$

$$S_i^- = \sqrt{\frac{(0.445 - 0.0334)^2 + (0.0622 - 0.0209)^2 + (0.0551 - 0.0155)^2 + (0.0675 - 0.0099)^2 + (0.0346 - 0.0275)^2 + (0.0752 - 0.0436)^2}{}} = 0.0881$$

The entire results of the separation measure for each performance criterion are shown in Table 12.

Step 6: Identify the optimal positive and negative solutions. The relative closeness of the alternative P_i with respect to P^ is defined as follows:*

Relative closeness to the ideal solution can be determined using Equation 12. For the example, $P_i = 0.0881/(0.2229+0.0881)=0.2832$. The results of relative closeness to the ideal solution are shown in Table 13.

Equation 12 is used to calculate the relative closeness to the ideal solution.

Table 13 presents six natural fibre alternatives, ordered according to their priority P_i scores. Based on the findings, coir has the highest P_i score of 0.6006. Bamboo has the second-highest score of 0.4047, followed by kenaf, abaca, jute, and sisal, which gathered P_i values of 0.3351, 0.2832, 0.2688, and 0.2523, respectively. The result showed that coir has exceptional mechanical and thermal stability. It corresponds to research by Hasan et al. (2021).

Step 7: Establish a ranking of preference

The ranking of each alternative according to the performance score is displayed in Table 14.

As a result, the ranking results of the CRITIC-TOPSIS method are shown in Table 14. The results from synthesising data on the critical criteria were used to generate a list

Table 8
Original data matrix

	Diameter (μm)	Length (mm)	Tensile Strength (MPa)	Young's Modulus (GPa)	Elongation at Break (%)	Cellulose (%)
WEIGHT	0.1670	0.1291	0.1214	0.1525	0.2574	0.1725
Abaca	20	4.9	621.50	41	2.90	59.50
Bamboo	58	2.75	566	53	4.65	34.50
Coir	18.5	1.65	175	6	20	45.60
Jute	15	3.40	547.50	46.25	2.30	65.25
Kenaf	24	6.20	612.50	41	4.80	53.50
Sisal	27	4.40	681	15.5	2.45	68.50

Table 9
Normal decision-making matrix

	Diameter (μm)	Length (mm)	Tensile Strength (MPa)	Young's Modulus (GPa)	Elongation at Break (%)	Cellulose (%)
WEIGHT	0.1670	0.1291	0.1214	0.1525	0.2574	0.1725
Abaca	0.2664	0.4813	0.4538	0.4425	0.1346	0.4360
Bamboo	0.7726	0.2701	0.4132	0.5720	0.2158	0.2528
Coir	0.2464	0.1621	0.1278	0.0648	0.9281	0.3342
Jute	0.1998	0.3340	0.3997	0.4991	0.1067	0.4782
Kenaf	0.3197	0.6090	0.4472	0.4425	0.2227	0.3921
Sisal	0.3596	0.4322	0.4972	0.1673	0.1137	0.5020

Table 10
Decision matrix with weights and normalisation

	Diameter (µm)	Length (mm)	Tensile Strength (MPa)	Young's Modulus (GPa)	Elongation at Break (%)	Cellulose (%)
WEIGHT	0.1670	0.1291	0.1214	0.1525	0.2574	0.1725
Abaca	0.0445	0.0622	0.0551	0.0675	0.0346	0.0752
Bamboo	0.1290	0.0349	0.0502	0.0872	0.0555	0.0436
Coir	0.0412	0.0209	0.0155	0.0099	0.2389	0.0577
Jute	0.0334	0.0431	0.0485	0.0761	0.0275	0.0825
Kenaf	0.0534	0.0786	0.0543	0.0675	0.0573	0.0676
Sisal	0.0601	0.0558	0.0604	0.0255	0.0293	0.0866

Table 11
Compared to negative ideal solutions, positive ideal solutions

	Diameter (µm)	Length (mm)	Tensile Strength (MPa)	Young's Modulus (GPa)	Elongation at Break (%)	Cellulose (%)
A*	0.1290	0.0786	0.0604	0.0872	0.2389	0.0866
A-	0.0334	0.0209	0.0155	0.0099	0.0275	0.0436

Table 12
Separation Measure for each performance criterion

	Abaca	Bamboo	Coir	Jute	Kenaf	Sisal
S_i⁺	0.2229	0.1936	0.1410	0.2353	0.1987	0.2303
S_i⁻	0.0881	0.1316	0.2120	0.0865	0.1001	0.0777

Table 13
Relative closeness to the ideal solution for each performance criterion

	Abaca	Bamboo	Coir	Jute	Kenaf	Sisal
Pi	0.2832	0.4047	0.6006	0.2688	0.3351	0.2523

of six (6) natural fibres. These fibres were ordered based on their positive ideal solution (Pi) scores, which were calculated using the Microsoft Excel 2016 software and a specific method. According to Guerrero (2010), excel has become as common as calculators in data analysis and decision-making. Table 14 displays the results. Coir achieved the highest score of 0.6006,

Table 14
Overall ranking of all alternative options

Alternatives	Pi	Ranking
Abaca	0.2832	4
Bamboo	0.4047	2
Coir	0.6006	1
Jute	0.2688	5
Kenaf	0.3351	3
Sisal	0.2523	6

positioning it in the highest position in the rating. Bamboo received the grade that is ranked just behind the highest score determined by a score of 0.4047, followed by kenaf, abaca, jute, and sisal with values of 0.3351, 0.2832, 0.2688, and 0.2523, respectively.

This study demonstrates that coir has a potential material for cap-toe shoes, as indicated by its top rating among the alternatives, as shown in Table 14. Despite the decisive confirmation of the results, incorporating extra details from other criteria could have made the natural fibre selection procedure more comprehensive. When developing requirement criteria, it is essential to consider multiple variables to make informed selections. Hence, while choosing natural fibres, decision-makers should meticulously establish precise selection criteria based on specific requirements, as this will significantly impact the outcome of the selection process.

Coir fibre is a good alternative to traditional materials due to its cost-effectiveness, renewability, recyclability, biodegradability, and environmental friendliness compared to synthetic fibres. Several industries, including mat production, yarn making, rope manufacturing, floor articles, insulating panels, stockings, and textile goods, can utilise Coir due to its versatility. The automotive and construction sectors extensively utilise Coir to enhance the strength of polymer composites (Goyat et al., 2022). Onukwuli et al. (2022) demonstrate that coir fibre has the benefits of being lightweight, having a high strength-to-weight ratio, being inexpensive, and being widely available.

DISCUSSION

Analysing natural fibre's chemical composition and shape of natural fibre to comprehend their distinct features is crucial. Although the framework has been thoroughly tested, the authors argue that the natural fibre selection approach could have been more comprehensive if it had incorporated additional features from other criteria. When making a decision, multiple considerations must be examined in order to ensure the appropriate selection of natural fibres that fulfil a certain requirement; it is imperative for individuals responsible for the selection process to establish highly detailed criteria about that need.

The framework of integrating the CRITIC-TOPSIS method can be applied as a substitute to combine different performance indicators or criteria into a single score that can be used to compare and rank different options. Data validation was carried out to verify the suggested framework and ascertain whether the rankings provided by the suggested combined CRITIC-TOPSIS and the rankings produced by other MCDM approaches were comparable. The results indicate that the proposed framework can provide a ranking compatible with other DM methods.

The TOPSIS method has been well recognised by researchers for its ability to effectively determine the optimal decision by considering selection criteria and their connections when combined with competing criteria and alternative solutions. The main

benefit of using the CRITIC-TOPSIS methodology over other MCDM methods is that it allows for the simultaneous consideration of negative and positive criteria in decision-making. Furthermore, it is simpler and more effective than other methods like AHP. TOPSIS algorithm chooses the alternative most similar to the positive ideal solution and most dissimilar to the negative ideal alternative. Therefore, this approach offers a more accurate representation of models than non-compensatory alternatives.

CONCLUSION

This study has successfully developed a framework for prioritising performance criteria in selecting natural fibre materials. Hence, it provides helpful knowledge for selecting constituent materials based on the integrated CRITIC-TOPSIS framework. The enhancement of knowledge and findings of this study can benefit material designers and engineers in selecting the most suitable fibre by prioritising performance criteria.

The validation of the proposed framework is illustrated based on the data and results from a reputable past study, where the present results are shown to have good conformance. For comparison, an effective ranking method has been developed to address this issue, where the decision-making (DM) method is suggested to involve the integration of the CRITIC and TOPSIS methods. Generally, the CRITIC method is used to acquire the weight of criteria. However, the TOPSIS method is employed to prioritise the criterion. As far as the authors know, there has been limited research on applying the CRITIC-TOPSIS method towards material selection for natural fibre composite materials. Hence, this study is novel as it has successfully incorporated the CRITIC and TOPSIS methods to prioritise performance criteria of natural fibre materials for cap toe shoes, using performance criteria. The results have been verified using a reliable publication. The CRITIC-TOPSIS method is an effective tool for objectively evaluating and ranking the performance criteria of natural fibre composite materials. This framework can help design engineers identify the most suitable natural fibre composite materials.

In summary, this study presents a structure for determining the order of importance of performance requirements for natural fibre composite materials. The current study shows the effectiveness of using the integrated CRITIC-TOPSIS method as a classification tool for selecting natural fibre composite materials. It is especially relevant when selecting a decision-making method, as it frequently involves evaluating numerous criteria and can be described as an MCDM problem.

As the present study only involves performance criteria of the material, the outcome may not represent the overall condition of all the natural fibre composite materials, which constitutes the present study's main limitation. Furthermore, the number of fibres studied is limited (only six), as the complete information for many other natural fibres is currently unavailable for comparison. Nevertheless, the result of the present study is promising,

showing that Coir has the optimum performance criteria for natural fibre composite material. Further research is necessary to support the statistical judgment of selecting the optimum natural fibre. The interconnections of input data can also be investigated in depth to understand the selection process.

ACKNOWLEDGEMENTS

The authors express deep gratitude to the Ministry of Higher Education (MOHE) Malaysia for awarding the scholarship to the principal author to conduct this research. The acknowledgements also extend to the College of Engineering, Universiti Teknologi MARA, Shah Alam, and Universiti Teknikal Malaysia Melaka (UTeM) for providing facilities and assistance. The College of Engineering, Universiti Teknologi MARA, Shah Alam, also provides financial support for publication.

REFERENCES

- Abdel-Basset, M., & Mohamed, R. (2020). A novel plithogenic TOPSIS- CRITIC model for sustainable supply chain risk management. *Journal of Cleaner Production*, 247, Article 119586. <https://doi.org/10.1016/j.jclepro.2019.119586>
- Alinezhad, A., & Khalili, J. (2019). CRITIC Method. In A. Alinezhad & J. Khalili (Eds.), *New Methods and Applications in Multiple Attribute Decision Making (MADM)* (pp. 199–203). Springer International Publishing. https://doi.org/10.1007/978-3-030-15009-9_26
- Anand, A., Agarwal, M., & Aggrawal, D. (2022). Chapter 4 CRITIC method for weight determination. In *Applications for Managerial Discretion* (pp. 25–30). De Gruyter. <https://doi.org/doi:10.1515/9783110743630-004>
- Babatunde, M. O., & Ighravwe, D. E. (2019). A CRITIC-TOPSIS framework for hybrid renewable energy systems evaluation under techno-economic requirements. *Journal of Project Management*, 4, 109–126. <https://doi.org/10.5267/j.jpm.2018.12.001>
- Berdie, A. D., Osaci, M., Muscalagiu, I., & Barz, C. (2017). A combined approach of AHP and TOPSIS methods applied in the field of integrated software systems. In *IOP Conference Series: Materials Science and Engineering* (Vol. 200, No. 1, p. 012041). IOP Publishing. <https://doi.org/10.1088/1757-899X/200/1/012041>
- Biagiotti, J., Puglia, D., & Kenny, J. M. (2004). A review on natural fibre-based composites-Part I. *Journal of Natural Fibers*, 1(2), 37–68. http://www.tandfonline.com/doi/abs/10.1300/J395v01n02_04
- Chan, S. Y., & Ch'ng, C. K. (2023). TOPSIS for analyzing the risk factors of suicidal ideation among university students in Malaysia. *Pertanika Journal of Science and Technology*, 31(2), 977–994. <https://doi.org/10.47836/pjst.31.2.17>
- Chen, Y. L., Shen, S. L., & Zhou, A. (2022). Assessment of red tide risk by integrating CRITIC weight method, TOPSIS-ASSETS method, and Monte Carlo simulation. *Environmental Pollution*, 314, Article 120254. <https://doi.org/10.1016/j.envpol.2022.120254>

- Chodha, V., Dubey, R., Kumar, R., Singh, S., & Kaur, S. (2021). Selection of industrial arc welding robot with TOPSIS and Entropy MCDM techniques. *Materials Today: Proceedings*, 50, 709–715. <https://doi.org/10.1016/j.matpr.2021.04.487>
- Diakoulaki, D., Mavrotas, G., & Papayannakis, L. (1995). Determining objective weights in multiple criteria problems: The critic method. *Computers and Operations Research*, 22(7), 763–770. [https://doi.org/10.1016/0305-0548\(94\)00059-H](https://doi.org/10.1016/0305-0548(94)00059-H)
- Edwards, W. (1954). The theory of decision making. *Psychological Bulletin*, 51(4), 380–417. <https://doi.org/10.1037/h0053870>
- Emovon, I., & Oghenyerovwho, O. S. (2020). Application of MCDM method in material selection for optimal design: A review. *Results in Materials*, 7, Article 100115. <https://doi.org/10.1016/j.rinma.2020.100115>
- Ertemel, A. V., Menekse, A., & Camgoz Akdag, H. (2023). Smartphone addiction assessment using Pythagorean Fuzzy CRITIC-TOPSIS. *Sustainability*, 15(5), Article 3955. <https://doi.org/10.3390/su15053955>
- Goyat, V., Ghangas, G., Sirohi, S., Kumar, A., & Nain, J. (2022). A review on mechanical properties of coir based composites. *Materials Today: Proceedings*, 62, 1738–1745. <https://doi.org/10.1016/j.matpr.2021.12.252>
- Guerrero, H. (2010). *Excel data analysis: Modeling and simulation*. Springer. <https://doi.org/10.1007/978-3-642-10835-8>
- Han, Y., Wang, Z., Lu, X., & Hu, B. (2020). Application of AHP to road selection. *International Journal of Geo-Information*, 9(2), Article 86. <https://doi.org/10.3390/ijgi9020086>
- Hasan, K. M. F., Horváth, P. G., Bak, M., & Alpár, T. (2021). A state-of-the-art review on coir fiber-reinforced biocomposites. *RSC Advances*, 11(18), 10548–10571. <https://doi.org/10.1039/d1ra00231g>
- Hassan, I., Alhamrouni, I., & Azhan, N. H. (2023). A CRITIC–TOPSIS multi-criteria decision-making approach for optimum site selection for solar PV farm. *Energies*, 16(10), Article 4245. <https://doi.org/10.3390/en16104245>
- Hwang, C. L., & Yoon, K. (1981). Basic concepts and foundations. In *Multiple Attribute Decision Making* (pp. 16–57). Springer. https://doi.org/10.1007/978-3-642-48318-9_2
- Ighravwe, D. E., & Babatunde, M. O. (2018). Selection of a mini-grid business model for developing countries using CRITIC-TOPSIS with interval type-2 fuzzy sets. *Decision Science Letters*, 7(4), 427–442. <https://doi.org/10.5267/j.dsl.2018.1.004>
- Ishizaka, A., & Labib, A. (2009). Analytic hierarchy process and expert choice: Benefits and limitations. *OR Insight*, 22(4), 201–220. <https://doi.org/10.1057/ori.2009.10>
- Jharkharia, S., & Shankar, R. (2007). Selection of logistics service provider: An analytic network process (ANP) approach. *The International Journal of Management Science*, 35, 274–289. <https://doi.org/10.1016/j.omega.2005.06.005>
- Jigeesh, N., Joseph, D., & Yadav, S. K. (2018). A review on industrial applications of TOPSIS approach. *International Journal of Services and Operations Management*, 30(1), Article 23. <https://doi.org/10.1504/ijssom.2018.10012402>

- Kabir, G., Sadiq, R., & Tesfamariam, S. (2014). A review of multi-criteria decision-making methods for infrastructure management. *Structure and Infrastructure Engineering*, 10(9), 1176–1210. <https://doi.org/10.1080/15732479.2013.795978>
- Kazan, H., & Ozdemir, O. (2014). Financial performance assessment of large scale conglomerates via TOPSIS and critic methods. *International Journal of Management and Sustainability*, 3(4), 203–224. <https://doi.org/10.18488/journal.11/2014.3.4/11.4.203.224>
- Lakshmi, B. M., Mathew, M., Kinol, A. M. J., Vedagiri, B., Perumal, S. B., Madhu, P., & Dhanalakshmi, C. S. (2022). An integrated CRITIC-TOPSIS- and Entropy-TOPSIS-based informative weighting and ranking approach for evaluating green energy sources and its experimental analysis on pyrolysis. *Environmental Science and Pollution Research*, 29(40), 61370–61382. <https://doi.org/10.1007/s11356-022-20219-9>
- Luhar, S., Suntharalingam, T., Navaratnam, S., Luhar, I., Thamboo, J., Poologanathan, K., & Gatheeshgar, P. (2020). Sustainable and renewable bio-based natural fibres and its application for 3d printed concrete: A review. *Sustainability*, 12(24), 1–25. <https://doi.org/10.3390/su122410485>
- Maidin, N. A., Sapuan, S. M., Taha, M. M., Yusoff, M. Z. M. (2022). Material selection of natural fibre using a grey relational analysis (GRA) approach. *BioResources*, 17(1), Article 109. <https://doi.org/10.15376/biores.17.1.109-131>
- Mastura, M. T., Sapuan, S. M., & Mansor, M. R. (2015). A framework for prioritizing customer requirements in product design: Incorporation of FAHP with AHP. *Journal of Mechanical Engineering and Sciences*, 9, 1655–1670. <https://doi.org/10.15282/jmes.9.2015.12.0160>
- Mohamadghasemi, A., Hadi-Vencheh, A., & Hosseinzadeh Lotfi, F. (2020). The multiobjective stochastic CRITIC–TOPSIS approach for solving the shipboard crane selection problem. *International Journal of Intelligent Systems*, 35(10), 1570–1598. <https://doi.org/10.1002/int.22265>
- Mufazzal, S., & Muzakkir, S. M. (2018). A new multi-criterion decision making (MCDM) method based on proximity indexed value for minimizing rank reversals. *Computers and Industrial Engineering*, 119, 427–438. <https://doi.org/10.1016/j.cie.2018.03.045>
- Onukwuli, S., Okpala, C., & Nnaemeka, F. (2022). Review of benefits and limitations of coir fiber filler material in composites. *International Journal of Latest Technology, Management & Applied Science*, 11(5), 13–20. <https://hal.science/hal-04104230> <https://hal.science/hal-04104230/document>
- Pamucar, D., Žižović, M., & Đuričić, D. (2022). Modification of the critic method using fuzzy rough numbers. *Decision Making: Applications in Management and Engineering*, 5(2), 362–371. <https://doi.org/10.31181/dmame0316102022p>
- Pavić, Z., & Novoselac, V. (2013). Notes on TOPSIS Method. *International Journal of Research in Engineering and Science*, 1(2), 5–12.
- Peças, P., Carvalho, H., Salman, H., & Leite, M. (2018). Natural fibre composites and their applications: A review. *Journal of Composites Science*, 2(4), 1–20. <https://doi.org/10.3390/jcs2040066>
- Polcyn, J. (2022). Determining value added intellectual capital (VAIC) using the TOPSIS-CRITIC method in small and medium-sized farms in selected European countries. *Sustainability*, 14(6), Article 3672. <https://doi.org/10.3390/su14063672>

- Rahim, R., Supiyandi, S., Siahaan, A. P. U., Listyorini, T., Utomo, A. P., Triyanto, W. A., Irawan, Y., Aisyah, S., Khairani, M., Sundari, S., & Khairunnisa, K. (2018). TOPSIS method application for decision support system in internal control for selecting best employees. *Journal of Physics: Conference Series*, 1028(1), Article 012052. <https://doi.org/10.1088/1742-6596/1028/1/012052>
- Salwa, H. N., Sapuan, S. M., Mastura, M. T., & Zuhri, M. Y. M. (2019). Analytic hierarchy process (AHP)-based materials selection system for natural fiber as reinforcement in biopolymer composites for food packaging. *BioResources*, 14(4), 10014–10036. <https://doi.org/10.15376/biores.14.4.10014-10036>
- Saputra, M., Sitompul, O. S., & Sihombing, P. (2018). Comparison AHP and SAW to promotion of head major department SMK Muhammadiyah 04 Medan. *Journal of Physics: Conference Series*, 1007(1), Article 012034. <https://doi.org/10.1088/1742-6596/1007/1/012034>
- Sattar, M. A., & Ghazwan, A. (2023). Multi criteria decision making for optimal below knee prosthetic design. *Periodicals of Engineering and Natural Sciences*, 11(3), 29–38. <https://doi.org/10.21533/pen.v11i3.3551.g1286>
- Shih, H. S., Shyur, H. J., & Lee, E. S. (2007). An extension of TOPSIS for group decision making. *Mathematical and Computer Modelling*, 45(7–8), 801–813. <https://doi.org/10.1016/j.mcm.2006.03.023>
- Slebi-Acevedo, C. J., Pascual-Muñoz, P., Lastra-González, P., & Castro-Fresno, D. (2019). Multi-response optimization of porous asphalt mixtures reinforced with aramid and polyolefin fibers employing the CRITIC-TOPSIS based on Taguchi methodology. *Materials*, 12(22), Article 3789. <https://doi.org/10.3390/ma12223789>
- Stević, Ž., Durmić, E., Gajić, M., Pamučar, D., & Puška, A. (2019). A novel multi-criteria decision-making model: Interval Rough SAW method for sustainable supplier selection. *Information*, 10(10), Article 0292. <https://doi.org/10.3390/info10100292>
- Wu, H., Liu, S., Wang, J., & Yang, T. (2020). Construction safety risk assessment of bridges in the marine environment based on CRITIC and TOPSIS models. *Journal of Coastal Research*, 108(sp1), 206–210. <https://doi.org/10.2112/JCR-SI108-040.1>
- Zavadskas, E. K., Mardani, A., Turskis, Z., Jusoh, A., & Nor, K. M. (2016). Development of TOPSIS method to solve complicated decision-making problems - An overview on developments from 2000 to 2015. *International Journal of Information Technology & Decision Making*, 15(03), 645-682. <https://doi.org/10.1142/S0219622016300019>
- Žižovic, M., Miljkovic, B., & Marinkovic, D. (2020). Objective methods for determining criteria weight coefficients: a modification of the critic method. *Decision Making: Applications in Management and Engineering*, 3(2), 149–161. <https://doi.org/10.31181/dmame2003149z>

Machine Learning and Remote Sensing Applications for Assessing Land Use and Land Cover Changes for Under-monitored Basin

Muhammad Amiruddin Zulkifli¹, Jacqueline Isabella Anak Gisen^{1*}, Syarifuddin Misbari¹, Shairul Rohaziawati Samat¹ and Qian Yu^{2,3}

¹Faculty of Civil Engineering Technology, Universiti Malaysia Pahang Al-Sultan Abdullah, Lebuhraya Persiaran Tun Khalil Yaakob, 26300 Kuantan, Pahang, Malaysia

²China Institute of Water Resources and Hydropower Research, State Key Laboratory of Simulation and Regulation of Water Cycle in River Basin, 100038 Beijing, China

³Ministry of Water Resources of the People's Republic of China, Research Center on Flood and Drought Disaster Reduction, 100038 Beijing, China

ABSTRACT

Urban sprawling caused by industrial and economic growth has significantly affected land use and land cover (LULC). Using satellite imagery for real-time examination in Kuantan has become exceedingly expensive due to the scarcity and obsolescence of real-time LULC data. With the advent of remote sensing and geographical information systems, LULC change assessment is feasible. A quantitative assessment of image classification schemes (supervised classification using maximum likelihood and deep learning classification using random forest) was examined using 2022 Sentinel-2 satellite imagery to measure its performance. Kappa coefficient and overall accuracy were used to determine the classification accuracy. Then, 32 years of LULC changes in Kuantan were investigated using Landsat 5 TM, Landsat 8 OLI, and Sentinel-2 based on the best classifier. Random forest classification outperformed maximum likelihood classification with an overall

accuracy of 85% compared to 92.8%. The findings also revealed that urbanisation is the main factor contributing to land changes in Kuantan, with a 32% increase in the build-up region and 32% in forest degradation. Despite the subtle and extremely dynamic connection between ecosystems, resources, and settlement, these LULC changes can be depicted using satellite imagery. With the precision of using a suitable classification

ARTICLE INFO

Article history:

Received: 20 December 2023

Accepted: 29 April 2024

Published: 25 October 2024

DOI: <https://doi.org/10.47836/pjst.32.6.15>

E-mail addresses:

amiruddinzulkifli7@gmail.com (Muhammad Amiruddin Zulkifli)

isabella@umpsa.edu.my (Jacqueline Isabella Anak Gisen)

syarifuddinm@umpsa.edu.my (Syarifuddin Misbari)

shairul@umpsa.edu.my (Shairul Rohaziawati Samat)

yuqian@iwhr.com (Qian Yu)

* Corresponding author

scheme based on comprehensive, accurate and precise LULC maps can be generated, capturing the essence of spatial dynamics, especially in under-monitored basins. This study provides an overview of the current situation of LULC changes in Kuantan, along with the driving factors that can help the authorities promote sustainable development goals.

Keywords: Geographical information system (GIS), image classification, LULC changes, maximum likelihood, random forest

INTRODUCTION

Rapid spawning of population growth significantly affected the LULC rates, especially with the economic and industrial revolution over the past few years (Talukdar et al., 2020). LULC can act as an efficient method to measure land transformation for land use management. With temporal information used in land use maps, a better understanding of dynamic LULC changes to serve different purposes such as urban and town planning, ecosystem and environmental assessment, hazard monitoring and management, natural resources exploration and management, and soil erosion and desertification detection is significant, especially for water resource management. Considering global dynamics and the response to environmental and socioeconomic factors, land use and land cover change is an essential subject.

Conventionally, Land Use and Land Cover (LULC) changes are determined through field surveys with a manual classification that requires more time and energy. It consequently causes data redundancy due to constant changes in land use in a short period. Besides, LULC is important in flood risk assessment, as well as hydrology, meteorology, and geomorphology. Different LULC profiles provide varying surface water retention values, affecting surface runoff. The scarcity of updated LULC data has contributed to increased flooding incidents (Zaidi et al., 2014). High costs, substantial time investment, and considerable human resources often characterise traditional methods of studying LULC. It underscores the growing demand for more convenient, user-friendly, and innovative approaches for identifying and analysing LULC, particularly in regions such as Kuantan. While some governmental agencies and local authorities provide LULC data, accessing this information can often prove to be a significant challenge. It tends to be expensive and difficult to obtain, frequently requiring extensive paperwork and time to access. Another major issue is the lack of updated information. The data these entities provide is often outdated, failing to reflect the current state of land use and land cover in the region. This situation further amplifies the need to develop and implement more efficient and accessible LULC study methods.

In situations where updated and accurate LULC data is lacking, access to remote sensing technology becomes crucial as it can provide this data. Advancement of data acquisition through online databases and advanced equipment based on remote sensing

technology such as hyperspectral satellites, airborne, light detection and ranging (LIDAR), and unmanned aerial vehicle (UAV) has helped in providing a relatively good and accurate data (Gaur & Singh, 2023). These high-accuracy and low-error data tend to be expensive and difficult to obtain. In contrast, lower-quality data is freely accessible and requires less computation time. The advent of open-source satellite imagery, like Sentinel-2 and Landsat, has expanded its technology to meet the needs of various fields. The capacity of satellites to identify surface features and create classifications using different algorithmic approaches makes them ideal for LULC studies. Furthermore, the geographic information systems (GIS) technology has improved time and energy efficiency in surveying LULC analysis. Data acquisition is a critical component as it acts as a foundation for successful analysis and decision-making. These upgrades in remote sensing and GIS technology integration also enormously contribute when handling inaccessible and unavailable information in poorly gauged areas, such as disaster assessment, environmental monitoring, and urban management (Maryantika & Lin, 2017). LULC has also significantly helped provide mitigation solutions, policy-making decisions, and sustainable development (Isola et al., 2023; Yulianto et al., 2020; Shahbudin et al., 2009).

Land cover classification through remote sensing imagery analysis is associated with modification and spectral distinction based on each pixel to define the category. The techniques include supervised and unsupervised classifications with different computational algorithms (classifiers). However, the classification of satellite imagery for LULC changes studies can contain several obstacles. Despite the diverse acquisition periods, obtaining similar multi-temporal and spatial satellite image data sets involves extensive work. Other disturbances, such as atmospheric and radiometric interference, may necessitate extra care in image processing (Vicenteserrano et al., 2008). In this regard, advancement in the quality and quantity of algorithms and mathematical equations for image analysis and manipulation has enhanced the capability of extracting information for many applications (Abdullah et al., 2019). Artificial intelligence (AI) and machine learning have been used to integrate remote sensing and geospatial analysis and interpretation of Earth data in recent years (Lary et al., 2016). Among the best algorithms used include random forest (RF) (Abdullah et al., 2019; Balha et al., 2021), support vector machine (SVM) (Balha et al., 2021), k-Nearest Neighbour Network (KNN) (Gondwe et al., 2021; Ngondo et al., 2021), Artificial Neural Network (ANN) (Saini & Rawat, 2023) and Dynamic Time Warping (DTW) (Viana et al., 2019). Given that all the approaches pose different outcomes and accuracy levels, the result highly depends on the training input and regression output. High training input and high regression value generate better classification. Additionally, quantitative measures of LULC mapping based on satellite observations through a machine learning algorithm have been proven efficient (Talkudar et al., 2020). It is important to note that each of these algorithms has unique strengths and application areas. Choosing the right algorithm is crucial to the success of any analytical project.

LULC generation can vary significantly based on software, data availability, study area, and project prerequisites. A pixel-based classification model can improve the classification of satellite imagery based on the training samples. As for ANN, the classification requires an enormous amount of quality data set and poses several problems, including potential overfitting without proper regularisation, computationally intensive and resource-consuming, and high sensitivity to input data quality and pre-processing. However, supervised classification through maximum likelihood (ML) is also considered an excellent parameter for obtaining good results (Nath et al., 2018; Geidam et al., 2020). The probability distribution based on the statistical model of normal distribution has made an ML classifier among the established classification functions (Shahbudin et al., 2009; Seyam et al., 2023). This likelihood is calculated using the highest probability of a certain occurrence within the data. It is worth noting that this approach is grounded in the assumption of a normal distribution within each class. ML can also provide a consistent result that will eventually converge to the true value of the parameter (Gaur & Singh, 2023). Meanwhile, the classifier based on RF imputation compromises the decision tree from backscatter training variables to compute the land cover class of interest. It entails creating several decision trees from a provided training dataset and then producing output classes for each tree. Due to its robustness and efficiency, it has been deemed one of the best and most commonly used methods for classifying satellite imagery. This spatial analysis can provide significantly good results, especially in tropical and subtropical sites (Aja et al., 2022; Abdullah et al., 2019). RF technique serves a relatively good accuracy value with acceptable results, outperforming other machine learning SVM, ANN, and KNN (Saini & Rawat, 2023). The RF algorithm is also considered a stable and consistent overall accuracy compared to ANN and SVM classifiers.

Mapping LULC regularly with remote sensing data can provide insight into the environmental impact of human activities, especially regarding forest disturbances. Forests are among the primary land use categories that play an enormous role, especially in providing various resources for humankind. It helps to maintain the hydrological cycle and atmospheric temperature, reduce natural disaster impacts, and prevent global warming (Ngondo et al., 2021). Terrestrial forests near urbanised areas play significant roles in maintaining carbon flux. Over time, the depletion of total forest cover deteriorates the ecosystem as it causes loss of biodiversity and clean water, the emergence of zoonotic diseases and health issues, and environmental degradation such as floods, soil erosion, and heat island effects. Most of the forest in low-lying regions, like Kuantan, contains a collection of trees and shrubs that can withstand extreme conditions like high salinity, high temperature, and less humidity. In Malaysia, a total of 612580.11 ha of land use and land cover (LULC) area is defined as mangrove forest, with about 17% covering Peninsular Malaysia (Lokman, 2004). Due to rapid population and economic growth, climate change, and global warming, there have been significant shifts in forest distribution. This

necessitates improved analysis of LULC changes, especially in cities near high biodiversity and environmental ecosystems.

There is a need for convenient and user-friendly methods to identify LULC changes in Kuantan that enable the efficient identification of forest distribution while minimising time, human resources, and cost. These LULC changes can be identified through satellite image classification, which describes the land uses. This study analysed LULC changes in Kuantan over 32 years (1994 to 2022) using Landsat 5 TM, Landsat 8 OLI, and Sentinel-2 satellite imagery. These varied satellite imageries were used following the need for more unavailability of data in a satellite. Variation in spatial resolution based on satellite imagery is less significant to affect the quality of analysis on primary output (Fisher et al., 2017). Most LULC classifications based on satellite imagery for change detection studies used more than two image satellites with more than 25 years of timeframe. Higher spectral imagery has many elements to be considered because of limitations in terms of cost, processing resources, and data accessibility. Moreover, a high spectral resolution image tends to sacrifice temporal resolution, which implies the frequency of available data in a single pass. The viability of a lower spectral with suitable pixel resolution imagery of Landsat and Sentinel imagery that are openly accessible and cost-efficient has contributed massive amounts of interest to the LULC study. Landsat 5 TM and Landsat 8 OLI have occupied the whole territory of the study area, so it is possible to conduct the study in the study area. However, for Sentinel-2 imagery, the study area of Kuantan required two different distinctive images despite the higher spatial resolution.

The objectives of this study are (1) to perform LULC classification based on the ML classifier and RF classifier and (2) to analyse the LULC changes in the city of Kuantan between 1994 and 2022 using the best classifier between ML and RF algorithm. A reliable and accurate classification based on remote sensing is expected to improve the LULC databases in Kuantan. The need for LULC as a baseline study for managing urban sprawling conservatively and comprehensively without damaging the natural ecosystem and habitat is highly significant, especially in cities in low-lying regions near the river mouth. These regions are exposed to various threats, from sea level rise, climate changes, global warming, and flooding, because of their highly sensitive ecology, which leads to societal vulnerability. Therefore, the study of LULC changes can effectively help in planning, managing, and monitoring the development of cities to ensure sustainable urban development is achieved.

METHODOLOGY

Study Area

This study focused on the LULC patterns in Kuantan (Figure 1), located on the latitude of 3° 48' 27.72" N and longitude of 103° 19' 33.60" E, east coast of Peninsular Malaysia. Kuantan is the capital city of Pahang and was originally dominated by natural forests along

the Kuantan River. Over time, the increasing demand for various industries has significantly changed the LULC. Following its location at the lower part of the Kuantan River, Kuantan is characterised by a high surface temperature with a low range for minimum and maximum temperature. It is also considered one of the largest cities on the East Coast of Peninsular Malaysia. Kuantan's rapid urban development is mainly prompted by the government's support through economic corridors, which has significantly influenced the LULC by expanding transportation facilities and physical infrastructure. As a result, highly rapid development has influenced the distribution of the environmental ecosystem.

Kuantan also has a unique community rich with values, culture, history, and economic power that contributes to a prosperous quality of life for its population. The local population was recorded at 548,014 people and is expected to increase significantly with 2.1% annual growth. Two of the major economic activities in Kuantan are tourism and industries. The emergence of the petrochemical, timber, and fishing industries has had a significant influence on the city's population growth. Furthermore, the Special Economic Zone was introduced to catalyse the fast-tracking economic development on the East Coast, subsequently leading to a significant increase in employment opportunities. Consequently, there is a possibility of LULC due to the need to explore forests for civilisation.

The local weather in Kuantan has been almost uniform over the years. The area is exposed to the Northeast monsoon that annually happens from early November to March and eventually affects the wind flow patterns. During this period, the region is

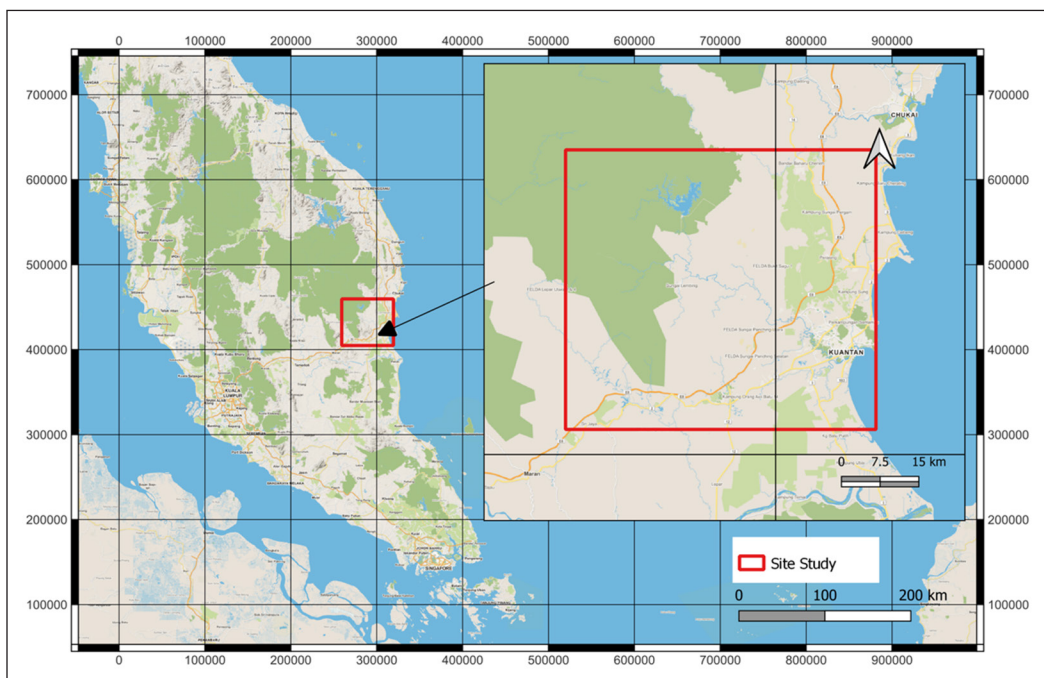


Figure 1. The study area of LULC Classification in Kuantan

susceptible to flooding because the rainfall usually reaches the maximum from November to January, while the driest is usually between June and July. According to the Malaysian Meteorological Department, the average monthly rainfall in Kuantan is between 3000 mm and 3500 mm, which indicates high humidity. As the Kuantan is relatively located near the equator, the region receives an average of 6 hours of sunshine daily. Moreover, the study area also has a uniform temperature throughout the year with relatively small changes in annual variation.

Geographically, Kuantan is among the low-lying cities in Malaysia that are exposed to flooding threats. Rapid development because of increased population growth and extensive industrial development has contributed to increased flooding incidence in Kuantan in recent years. Significant changes in land cover over the past few years have promoted the demand for flood hazard assessment. Furthermore, Kuantan is exposed to the threat of flooding due to its proximity to the estuary and low-lying coastal region, especially during heavy rainfall in the monsoon season. Historically, flooding has happened annually but hardly hit in 1926, 1967, 1999, 2001, 2007, 2011, and 2013, where it caused most areas in Kuantan City to be submerged, resulting in significant damage and loss of life (Zaidi et al., 2014).

Data Acquisition and Preparation

Figure 2 illustrates the processes involved in the implementation of this study. Five satellite imagery data were obtained from the United States Geological Survey (USGS) website (Table 1). Between 1994 and 2002, Landsat 5 TM was the preferred imaging satellite; however, it was replaced by Landsat 8 OLI satellite imagery with a resolution of 30 metres in 2013 and 2017, followed by 10-metre resolution Sentinel-2 satellite imagery in 2022. This selection of satellite images was based on the quality of the images, the availability of satellite images with less cloud coverage, and the absence of line stripping or shot noise. All three satellites provide identical optical images with non-false colour composites. However, Sentinel and Landsat images have slightly different spectral band indications.

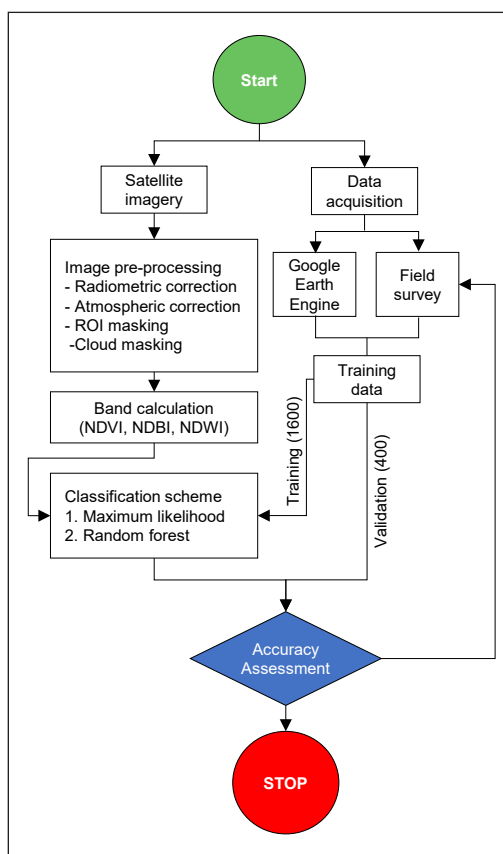


Figure 2. Flow chart of the study for LULC classification in Kuantan

Table 1
Satellite imagery used in the study for LULC classification

Data Type and Date	Description	Source
Landsat 5 TM (1994, 2002)	The data was atmospherically corrected, and four visible and near-infrared bands were obtained: two short-wave infrared bands and a thermal infrared band. The spatial resolution of 30-m, single scene data, Sun-synchronous	Google Earth Engine database—USGS
Landsat 8 OLI (2013, 2017)	The data was atmospherically corrected, and five visible and near-infrared bands, two short-wave infrared bands, and two thermal infrared bands. The spatial resolution of 30-m, single scene data, Sun-synchronous	Google Earth Engine database—USGS
Sentinel-2 (2022)	The data was atmospherically and geographically corrected, and three visible bands, five near-infrared bands, four short-wave infrared bands, and an ultra-blue band were obtained. The spatial resolution of 10-m, double scene data, Sun-synchronous	Google Earth Engine database—USGS

A relatively high sensor of Sentinel-2 provides a good spectral indication for detailed vegetation analysis compared to Landsat 8.

Once the satellite images were obtained, radiometric correction techniques were applied. For Landsat 5 TM imagery, the sensors convert the data quantisation scale at an 8-bit digital number (DN), equal to 256 greyness level. Then, the DN values were converted to radiance values using bias and gain values. Then, the radiance values were converted to a Top-of-Atmosphere (ToA) reflectance unit. Meanwhile, for Landsat 8 OLI, the data was rescaled to 16-bit DN values, equal to 65536 greyness level, which also required conversion from the DN value to the radiance value. Based on the radiance values, the data were converted to a ToA reflectance unit. As for Sentinel-2 imagery, the DN values were converted directly to the ToA reflectance unit. After radiometric correction, atmospheric correction through Dark Object Subtraction 1 (DOS1) was applied using the Sentinel Application Platform (SNAP) engine. Noise from atmospheric and spectral interference on satellite images was minimised through this process. Then, the satellite images underwent cloud removal through the threshold value of the reflectance range on the Near-Infrared band (NIR). Then, the masking process focuses on the region of interest (ROI) area after the image stacking from different bands is performed.

While Landsat imagery required a single satellite image, Sentinel-2 required two-scene images to cover the study area. Therefore, image mosaicking was required for the preprocessing analysis. The characteristics of each pixel for image classification were identified based on the colour, shape, size, pattern, location, and DN associated with each object. The classification was performed with the help of spectral indexing on the satellite imagery to allow each class to be prominent compared to other classes. Subsequently, it will reduce the redundancy of pixel classification. The index-based technique was also utilised by manipulating the spectral properties of satellite imagery through the derivative

equations of Normalised Difference Built-up Index (NDBI) (Equation 1), Normalised Difference Vegetation Index (NDVI) (Equation 2), and Normalised Difference Water Index (NDWI) (Equation 3) for better visualisation.

$$\text{NDBI} = \frac{\text{SWIR} - \text{NIR}}{\text{SWIR} + \text{NIR}} \quad [1]$$

$$\text{NDVI} = \frac{\text{NIR} - \text{RED}}{\text{NIR} + \text{RED}} \quad [2]$$

$$\text{NDWI} = \frac{\text{GREEN} - \text{RED}}{\text{GREEN} + \text{RED}} \quad [3]$$

Training Data Based on Field Data Survey

The satellite image was selected to complement the site investigation, where a set of training areas with a training-to-accuracy sample ratio of 4:1 was generated for each class. It adhered to the recommendation by Aja et al. (2022) to avoid any systematic error caused by redundant pixels for training and validation. A total of 2000 randomly selected training sample points were used, with 1600 points for training and 400 points for validation. These training data, consisting of positional coordinates and LULC information, were collected through a mixture of field measurements and Google Earth Engine. It is to ensure that the training data are correctly assigned as they reflect the characteristics of each classified object. Upon completing the image classification, 400 points were used for accuracy analysis. Some classes of LULC tend to have similar spectral properties and less heterogeneity, making LULC classification difficult to process. Therefore, several LULC classes were combined to represent a major class, as presented in Table 2.

Table 2
Description of LULC types for the study

ID Class	LULC Types	Description
1	Urbanisation/Build-up area	Consists of all build-up regions, residential, industrial, commercial regions, villages, transportation, infrastructure, and buildings.
2	Vegetation	Consists of mixed forest, dense forest, shrub and mangrove forest, and agriculture plants.
3	Water Body	Consists of water bodies, including rivers, oceans, lakes, reservoirs, ponds, and others.
4	Barren Land	Consists of less to no plantation with only soil exposed at the Earth's surface.

Satellite Image Classifier Test

LULC Classification

For classifier testing, the satellite data of the year 2022 from Sentinel-2 was acquired from the USGS website and utilised for LULC mapping by employing consistent and

stable classification algorithms, which are RF and ML techniques. Equation 4 presents the mathematical representation of the RF algorithm, showcasing its function in reducing errors and improving efficiency. Meanwhile, the ML model is mathematically represented as $L(\theta|x)$, a function of the parameters (θ) and the observed data (x), as shown in Equations 5 to 7. Here, θ denotes the model parameters that influence the final result. The observed data, labelled x , refers to the collected and analysed real data. For optimal classification, the parameters of θ are characterised by the mean (μ) and standard deviation (σ). The mean is the central value of a data set, providing an average point, while the standard deviation measures the data's dispersion or variation.

$$RF = 1 - \sum_{i=1}^n (P_i)^2 \tag{4}$$

$$L(\mu, \sigma|x) = \frac{1}{\sqrt{2\pi\sigma^2}} e^{-\left[\frac{(x-\mu)^2}{2\sigma^2}\right]} \tag{5}$$

$$\mu_{ML} = \frac{1}{n} \sum_i^n x_i \tag{6}$$

$$\sigma_{ML} = \sqrt{\frac{1}{n} \sum_i^n (x_i - \mu)^2} \tag{7}$$

Additionally, the QGIS applications and SNAP engine were applied. The RF algorithm was run using 100 trees based on 4 input features (Table 2) from 1600 points training dataset. As for ML, a classification based on normal estimation with 1600 points of training dataset was applied.

Accuracy Analysis

The overall accuracy and Kappa coefficient were calculated using Equations 8 and 9. The training dataset (400 points) was undertaken in a specific area based on a random location. The Kappa coefficient (K) (Equation 7) and overall accuracy (OA) (Equation 8) analyses based on the confusion matrix were applied to conduct an accuracy analysis in determining the classification's validity and reliability, where P_0 indicates the relative probability of observed agreement while P_e indicates the hypothetical probability of chance of agreement.

$$K = \frac{P_0 - P_e}{1 - P_e} \tag{8}$$

$$OA = \frac{\text{Number of correct prediction}}{\text{Number of total prediction}} \times 100 \tag{9}$$

Time Series Comparison

Once the classification testing was done for the LULC map in 2022, LULC maps for 1994, 2002, 2013, and 2017 were produced using the best image classifier. The highest

overall accuracy and kappa coefficient were the definitive indicators for selecting the best classifier to determine the LULC changes. A total of 5 LULC maps were constructed using computational analysis, Google Earth Engine, and field surveys in 1994, 2002, 2013, 2017, and 2022. The distribution area of each LULC class for 1994, 2002, 2013, 2017, and 2022 was also calculated. This inconsistent interval of satellite images from 1994 to 2022 is due to the unavailability of good-quality satellites caused by high cloud cover and spectral noise in the study area. Sentinel and Landsat satellites provide the same optical sensor for non-false colour composite imagery, allowing for comparative analysis. A comparative analysis examined the effects of differing spatial and spectral resolutions. Sentinel-2 appeared to offer superior technical satellite properties compared to the Landsat satellite. However, due to the higher quality of Landsat 9's 16-bit radiometric resolution, compared to Sentinel-2's 12-bit radiometric resolution, the accuracy of classification results was nearly identical. Hence, the same technique (normalised treatment) was used to compensate for these different resolutions. This distinction is necessary to identify the differential impacts on the results from the same approach. Moreover, resampling of the training for different approaches is not required in this context, as the technique acts equivalently to the same training sample.

RESULTS AND DISCUSSION

Training Classifier

LULC Classification

The supervised classification of the ML method was used to classify the LULC map (Figure 3). By using threshold probabilities to look at the binary profiles of individual pixels, it was possible to classify the data using the spectral band's normal distribution and determine the statistics and odds for each class. Five classes were developed: water, urban area, vegetation, bare land, and an unnamed class. Due to the unknown parameters in the defective proportion, the normal distribution adopted in maximum likelihood, this unidentified class was established as a defective item. The LULC map based on the RF technique (Figure 4) was divided into four primary categories: water, urban area, vegetation, and barren terrain. This classification was done using a decision tree that included multiple regression and classification trees from a random subset of samples. Subsequently, the data from the ML tends to avoid misinterpretation compared to RF classification.

Accuracy Assessment

A confusion matrix based on pixels was used to provide a statistically accurate assessment of both classifications. The accuracy achieved a 0.05 confidence interval for the statistically significant correlation of the two LULC classifications using ML

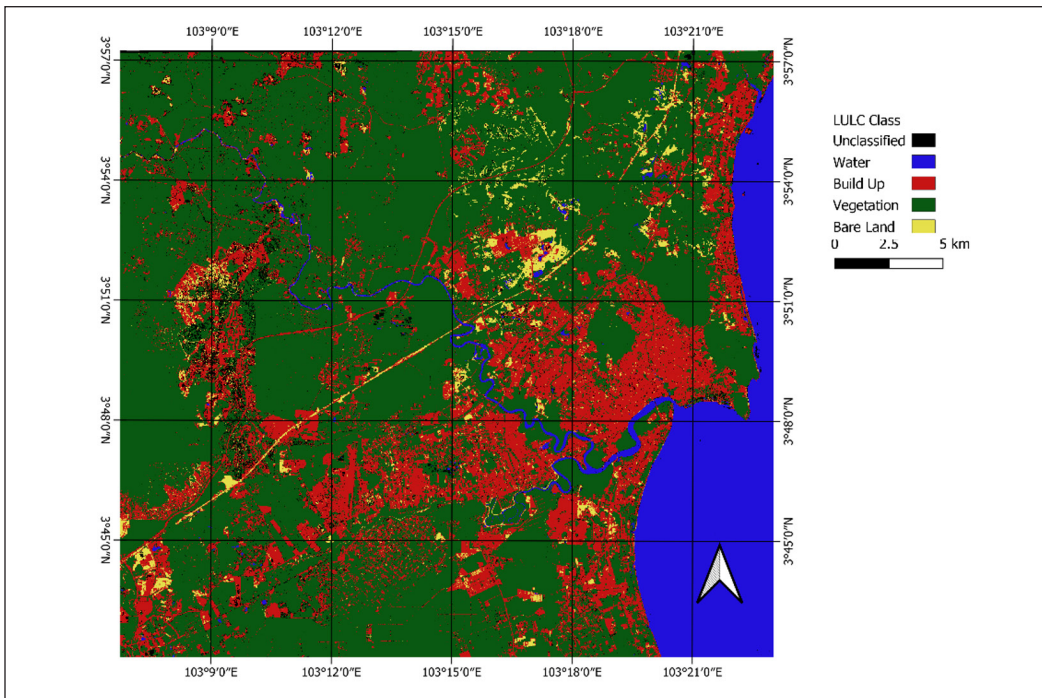


Figure 3. LULC map using ML algorithm in 2022

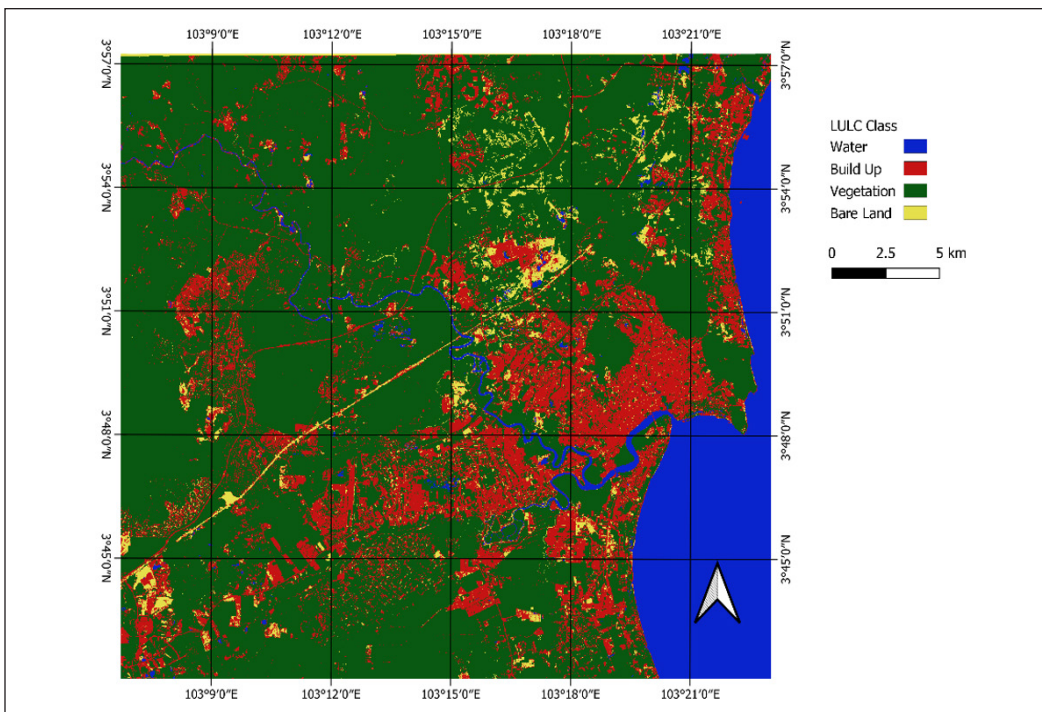


Figure 4. LULC map using RF algorithm in 2022

and RF, which were significantly good at 92.8% and 85%, respectively (Tables 3 & 4). The large number of estimates in the training dataset caused the large differences in the classifier results between RF and ML classifications. RF classifiers can handle large-scale heterogeneous distributions and complex data with less data bias. A study by Talukdar et al. (2020) proved that LULC classification poses a significant result using an RF classifier. Lary et al. (2016) also found that RF classifiers can reduce classification bias compared to other classifiers. However, RF classification has certain problems with the initial variable biases and overfitting of the regression model. Misclassification and overlaps significantly influenced the accuracy of the classification (Saini & Rawat, 2023). The bias of the majority RF classification emerges from uneven classes in the training dataset. It can also be deduced that the RF classifier produced less overall accuracy compared to the ML classifier because of the quality of the training dataset. The training dataset for the classification was monitored in a highly dense area with various classifications summarised into four main classes. These available datasets might be insufficient for training the RF algorithm, limiting the variety of predictions.

The effectiveness of the RF classifier in handling highly heterogeneous features can be proven with a well-trained sample. Abdullah et al. (2019) showed that training dataset preparation is highly important in generating a good image classification. The authors also emphasised that the training dataset for the RF model is relatively sensitive to changes that can cause a biased result. Talukdar et al. (2020) further emphasised that the RF classifier can pose a good result when dealing with heterogeneous data containing various types of features. As for ML, the classification of the imaging satellite was relatively good since the data was derived from the normal distribution of the dataset, making the classifier suitable for a relatively immense dataset. Lower variance estimation affected the classifier's ability to withstand a broad sample size, as a high sample size can produce less biased outcomes. Therefore, the data was consistent and almost identical to its actual value.

Table 3
Area-based error matrix between LULC-based ML by 400 points

		Training Data Set					Total
Classes		Unclassified	Water	Urban Area	Vegetation	Barren Land	
Maximum likelihood	Water	0	28	0	0	0	28
	Urban Area	5	1	161	4	0	171
	Vegetation	3	0	6	163	0	172
	Barren Land	4	0	4	2	19	29
Total		12	29	171	169	19	1
Overall Accuracy (Confident interval of 95%)							92.8
Kappa Hat Classification							0.85

Table 4
Area-based error matrix between LULC-based RF by 400 points

Classes		Training Data Set				Total
		Water	Urban Area	Vegetation	Barren Land	
Random Forest	Water	25	2	1	0	28
	Urban Area	1	145	24	1	171
	Vegetation	0	13	150	9	172
	Barren Land	0	6	3	20	29
Total		26	166	178	30	400
Overall Accuracy (Confident interval of 95%)						85
Kappa Hat Classification						0.75

LULC Changes

LULC Changes Analysis

The classifier testing results indicate that classification using ML yields higher overall accuracy compared to RF. Therefore, the LULC changes for the years 1994, 2001, 2013, and 2017 were performed using the ML classifier. The results of the LULC classification for 1994, 2001, 2013, 2017, and 2022 are presented in Figures 6 to 10, respectively. The total coverage of LULC in all studied years is presented in Table 5. In general, LULC observation in Kuantan based on image classification from 1994 to 2022 was dominated by urbanisation and vegetation. There was a significant inverse relationship between the build-up and vegetation classes. Figure 5 shows a constant increase of build-up coverage by approximately 32% of the total coverage area changes found from 1994 to 2022. As for vegetation, the coverage dropped from 1440 ha of the total area to approximately 1171 ha before it bounced back with a slight increment of 30 ha in 2017. Meanwhile, 2022 recorded

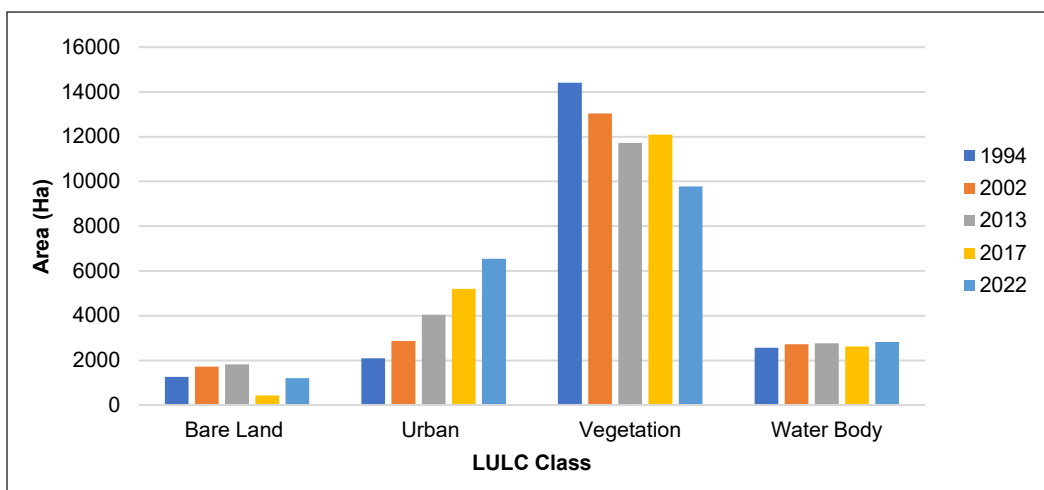


Figure 5. LULC changes using the ML classifier in Kuantan by area coverage from 1994 to 2022

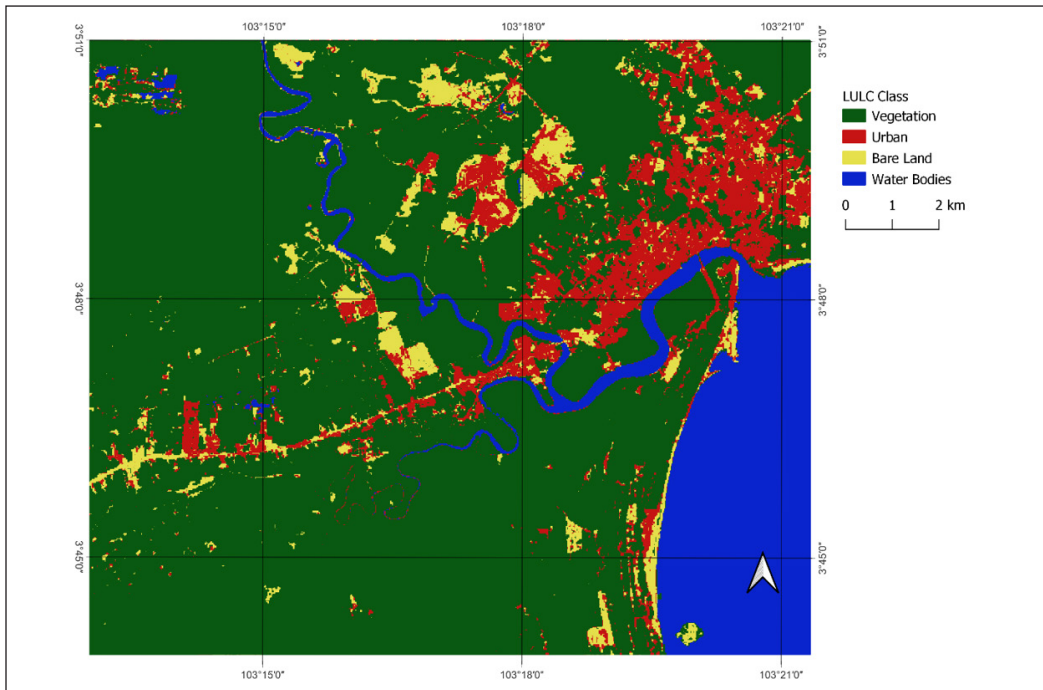


Figure 6. LULC coverage map for 1994 in Kuantan using ML classifier

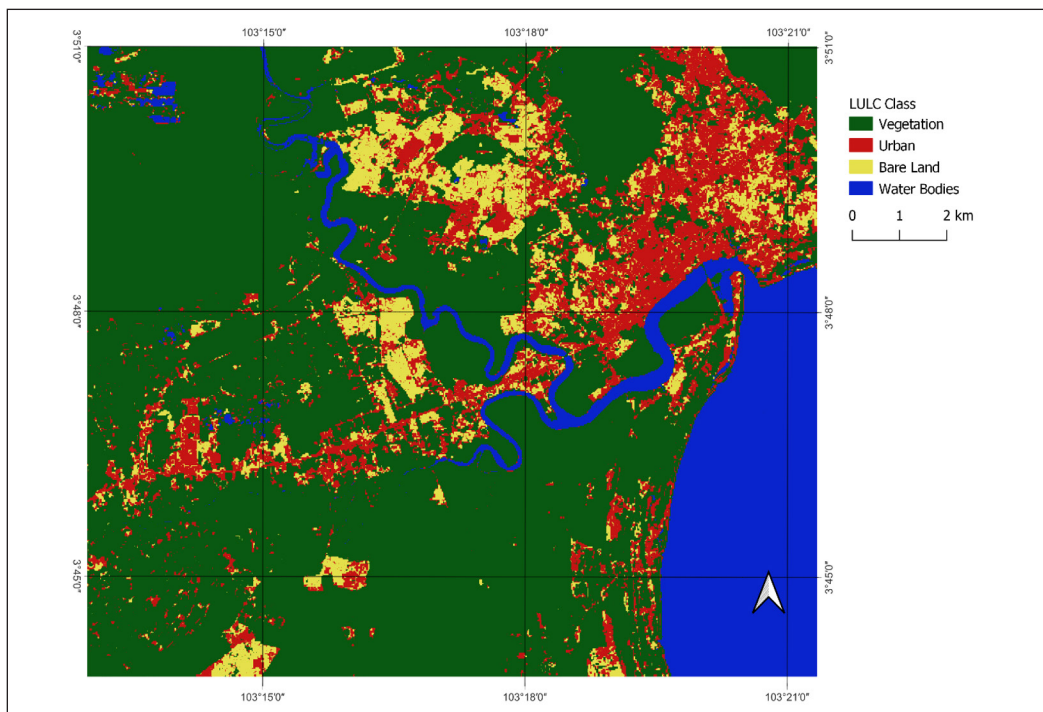


Figure 7. LULC coverage map for 2001 in Kuantan using ML classifier

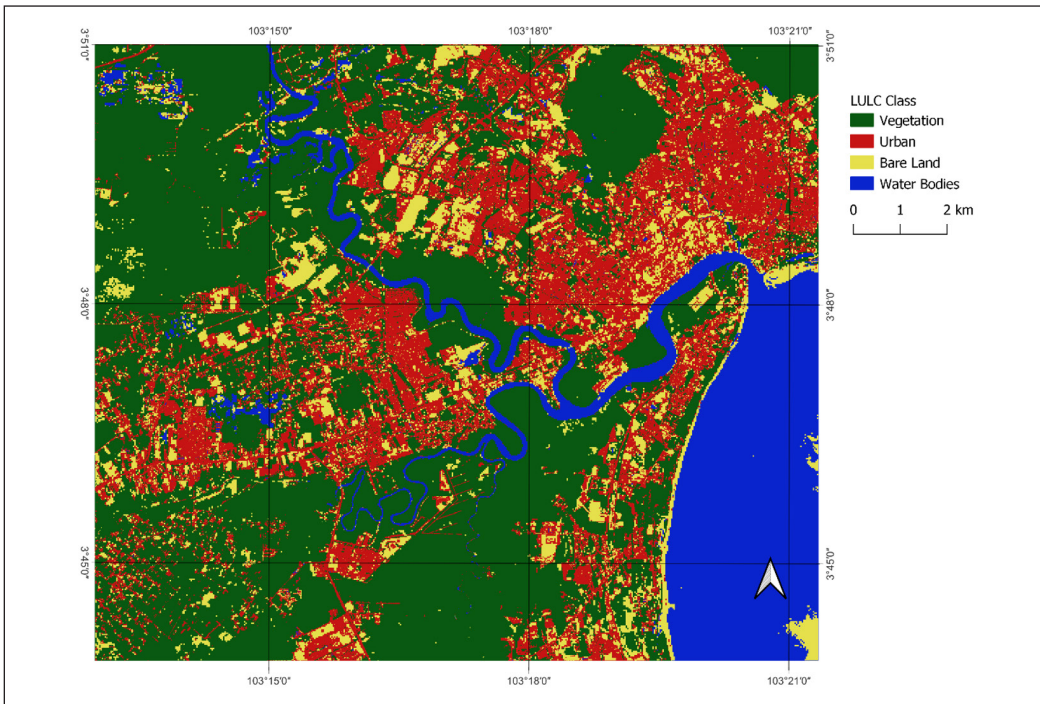


Figure 8. LULC coverage map for 2013 in Kuantan using ML classifier

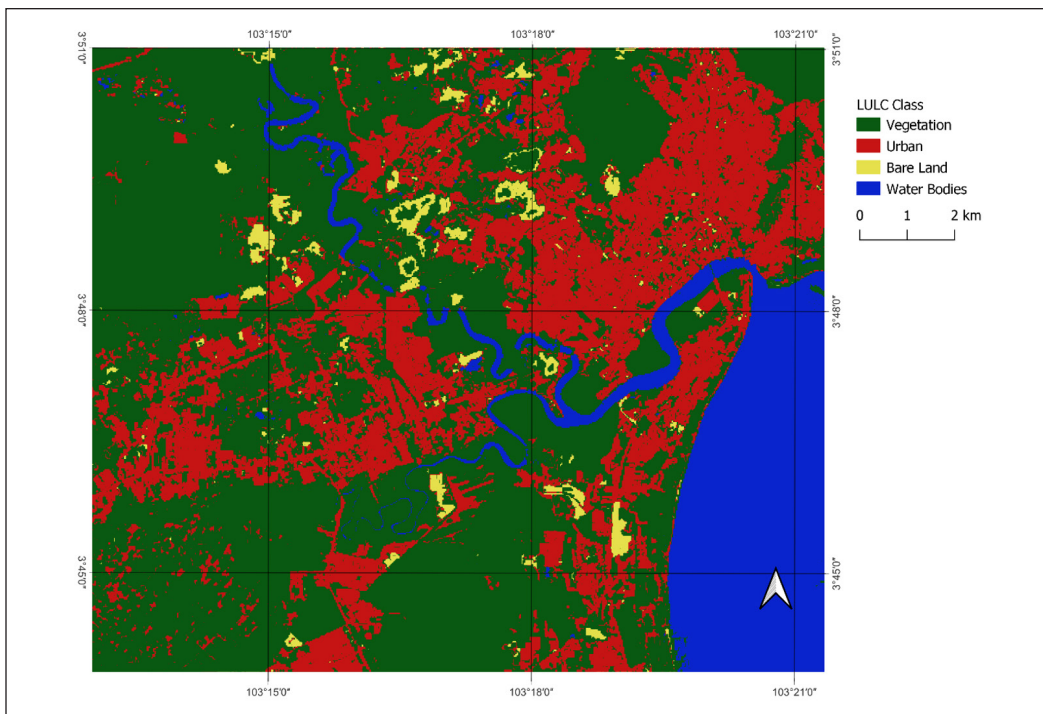


Figure 9. LULC coverage map for 2017 in Kuantan using ML classifier

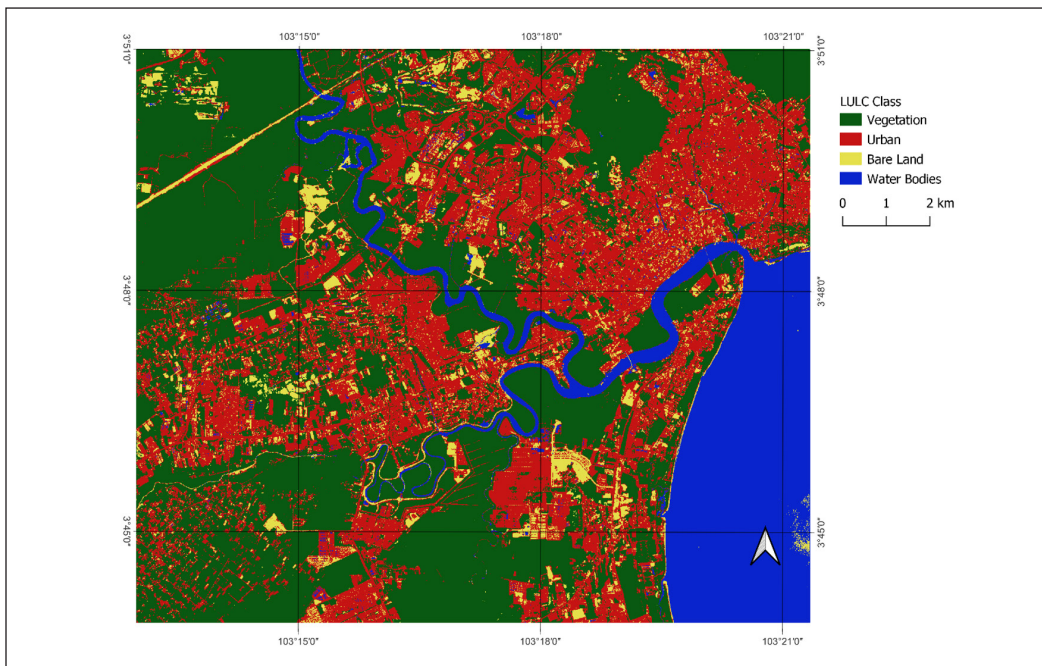


Figure 10. LULC coverage map for 2022 in Kuantan using ML classifier

the lowest coverage with less than 1000 ha. Overall, the vegetation coverage depicted 32% of the total coverage in the study area. Bare land faced a slight fluctuation over the past 28 years. There were also less significant changes in water outlet and storage in Kuantan. Furthermore, LULC in Kuantan has been experiencing major urban development due to the increasing demand for various needs. The increment of build-up coverage from 1994 to 2022 has been affecting the vegetation distribution as well as the bare land. The increase in socioeconomic growth and development has also attracted more migration into the city. Therefore, the build-up coverage expanded at a higher rate starting from 2013 compared to the early mid-90s.

According to the Kuantan Municipal Council, the city of Kuantan has been experiencing an annual population growth of 2.68%, causing changes in land use and extending the urban limit. Such a change has significantly increased the flooding frequency following the fluctuation of the runoff-discharge relationship. It is important to note that in 2013, the land area of Kuantan experienced the highest coverage during the past three decades when a massive flooding event occurred at the year's end. Zaidi et al. (2014) propounded that prolonged rainfalls and land use changes in 2013 had exposed low-lying regions, including Kuantan, to the risk of massive flooding. A constant change in build-up coverage and slight increments of bare land may bring about significant effects on river capacity, especially in Kuantan, as both the area coverage of bare land and built-up increased from 1995 to 2013. It has been supported by a study by Konrad (2014) that validated the effect of

Table 5
LULC changes for the years 1994, 2001, 2013, 2017, and 2022

LULC Classification	Yearly LULC Coverage (Ha)				
	1994	2001	2013	2017	2022
Bare Land	1267.0165	1715.6422	1815.7364	434.6605	1205.9481
Build-up	2098.2353	2859.1095	4071.0507	5193.9036	6546.9908
Vegetation	14409.1381	13044.0127	11719.9452	12088.9712	9779.5833
Water Body	2564.4092	2720.0977	2762.1378	2621.3023	2824.0054

urbanisation and massive land openings for development activities in flood-prone regions, increasing the flooding risk. Besides, changes from dense vegetation cover to agricultural and residential areas affect the hydrological ecosystem, including soil degradation imbalance and streamflow (Tewabe & Fentahun, 2020). It has been proven that, in late 2013, massive flooding hit the city of Kuantan, affecting local communities and the environment. Besides that, this flooding event significantly deteriorated buildings, properties, utility structures, the transportation system, agricultural crops, and vegetation (Rahman, 2014; Romali et al., 2019).

Climate change and global warming also contribute significantly to the hydrological system of the watershed through extreme evapotranspiration and imbalanced water components, thus increasing the rate of overflow events (Neidhardt & Shao, 2023; Johnson et al., 2022). According to Amini et al. (2022), the fluctuation of vegetation in the past few decades was caused by extreme drought. However, a study by Husain et al. (2023) suggested that massive population per area and vegetation cover can influence the surface temperature, which can cause global warming and heat islands. Furthermore, there is a substantial correlation between water abundance obtained from the LULC map and surface temperature, which affects glacier reduction and sea level rise (Samra, 2021). This indicates that LULC changes play an enormous part in contributing to climate change.

The special Economic Zone proposed by the Malaysian government in Kuantan City has a significant effect on the LULC, where high rates of anthropogenic activities contribute to the LULC changes. Extensive bare land exploration and reduction of forest cover for urbanisation and industrial expansion can modify the surface runoff and infiltration rates, percolation, and lateral flow, exposing the city to the threat of flash floods. As the data from 2022 indicates, the built-up area in Kuantan has seen substantial growth, expanding to three times its size compared to 1994. This considerable expansion underscores the rapid urbanisation and development this area has experienced over the span of nearly three decades. Extensive industrial and economic growth movement in the main city has highly contributed to the formation of LULC (Amini et al., 2022). A study by Saddique et al. (2020) suggested that LULC changes can massively influence the water balance components in a river basin, such as surface runoff, base flow, water yield, and evapotranspiration. The influence of agriculture and the main forest may also contribute to the increase in LULC

change rates. The phenomenon also happened in Tanzania, where agriculture is the main source of income for the communities living there (Ngondo et al., 2021). The coastal forest has indicated a significant decline as urbanisation rates increased (Maryantika & Lin, 2017). These changes have a substantial effect on urban growth, especially in Kuantan.

LULC Accuracy Analysis

The Kappa coefficient and confusion matrix were generated based on the classification of LULC for the years 1994, 2002, 2013, 2017, and 2022 (Figure 11). The accuracy assessment seemed reliable and acceptable for all classifications across the years. Nevertheless, the image classification 1994 recorded a notably low accuracy, which may have resulted from the misclassification and high noise in the image satellite. The overall accuracy of image classification in 2013 and 2022 was slightly less significant compared to those in 2017 due to the differences in spatial resolution and image quality. Despite the high resolution of Sentinel-2, the classification could not provide distinctive features for recognising real classes because of the insufficient training sample. Since all images used the same training dataset, the high-resolution imagery would be affected the most as the image size ratio did not influence the classification algorithm. It suggests that although Sentinel-2 data provides images with higher spatial resolution, the Landsat data may be a better source to investigate LULC changes following its capability to monitor Earth for more than five decades.

Based on the results, it is evident that image classification classifiers can distinguish more relevant features and provide an accurate prediction. Different spatial quality and quantity may cause poor overall accuracy. The image with a larger pixel size can serve a huge number of features due to the increased level of detail. It may lead to better discriminative power and improved accuracy of the classification. Fisher et al. (2017)

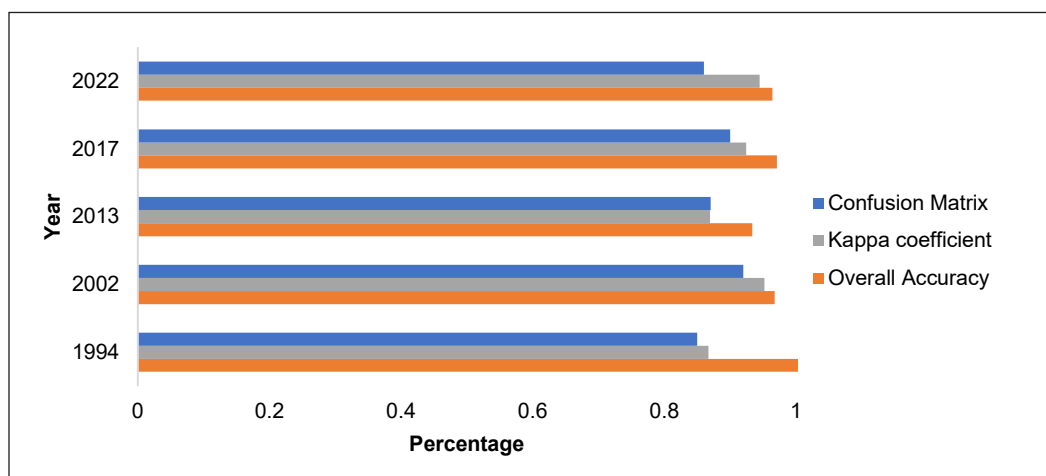


Figure 11. Graph of accuracy analysis for LULC classification in 1994, 2002, 2013, 2017 and 2022 based on ML

indicated that spatial resolution has a significant impact on the outcome of the classification, with higher resolution providing higher overall accuracy. However, this result has caused a significant increase in processing time and cost. Aja et al. (2022) highlighted that image classification using Sentinel satellite imagery produced less significant results compared to Landsat satellite imagery. It is consistent with the results of this study, where sentinel imagery, which provided higher spatial resolution imagery, required a detailed assessment compared to less spatial resolution. Moreover, handling a high-quality image requires significantly higher computational resources and processing time than a low-quality image. The amount of training data and inference speed of image classification also varied with the image pixel size. Therefore, it is recommended to consider the trade-off between computational complexity and accuracy, depending on the application requirement.

LIMITATION AND IMPLICATION

Comprehensive and cost-effective monitoring technology for LULC studies associated with forest distribution holds imperative importance. Introducing remote sensing satellite technology and GIS offers significant advantages for a highly dense city such as Kuantan, which has high land use heterogeneity. The capability of the Sentinel-2 satellites to identify surface features and generate classifications based on different algorithmic approaches stands as an acceptable method for LULC studies. While machine learning techniques have shown promising results in identifying LULC changes, some limitations include insufficient training pixels. Obtaining the training datasets in highly concentrated areas, especially in residential areas, is relatively difficult as the coarse satellite image with a low level of detail covers a huge area of a single training dataset. Eventually, misclassification of certain pixels tends to occur, especially during the execution of RF algorithms that are highly sensitive to input data.

Integrating a diverse data source from different satellite imageries for LULC changes makes it possible for recent data with the new remote sensing technology but not for historical data, especially satellite images from the 1990s to 2000s in Kuantan. The outdated and incomplete LULC maps are constrained to the LULC analysis, especially for the image availability before the 2000s. Recent remote sensing and GIS technology to obtain LULC data has benefited the stakeholders in terms of time, cost, and effort to study the LULC changes. Complimentary field surveys, online database monitoring or real-time supporting data can increase the study's reliability and accuracy. As the study progresses, LULC will be crucial in flood risk management as it helps identify susceptible flooding areas, especially in under-monitor regions like Kuantan. Furthermore, extensive changes in LULC coverage, especially in natural vegetation and wetlands, can alter the environmental ecosystem. Considering the LULC function, comprehensive green development practices can be implemented in developing policies and designing management strategies.

CONCLUSION AND RECOMMENDATION

LULC maps have a wide application, including natural resource management, baseline mapping for GIS input, and legal boundaries for tax and property evaluation. Generating LULC maps is impossible without the help of other geospatial datasets. This study applied remote sensing and GIS technology to analyse the significant LULC changes underlined by the continuous development in Kuantan. RF and ML classifiers generated an acceptable LULC classification based on the satellite imagery. ML posed a higher overall accuracy of 92% compared to RF, with 85% overall accuracy. RF tends to be overfitted and requires a huge training dataset to compute the image classification. However, it is most suitable for the high heterogeneity of LULC with detailed features compared to the ML classifier. It is recommended that both RF and ML classifiers be integrated with other classifiers to increase their validity and reliability. Given that both classifiers have significantly good results, an integrated, comprehensive classification scheme that compromises supervised classification and machine learning can be achieved in the near future.

As for LULC changes, high-intensity development in Kuantan affected the LULC pattern from 1994 to 2022. Primarily, build-up coverage significantly increased while vegetation coverage degraded. Sustainable landscape and town planning management is necessary because population growth and economic demand are the main factors influencing LULC changes. These elements are important for smart urban city planning and are aligned with the Sustainable Development Goal (SDG)-11. Therefore, LULC identification based on the surface spectrum of satellite images utilising remote sensing data is a proper technique to investigate land use status as part of the effort to provide ecosystem balance. Yet, there have been recommendations for LULC to use satellite imaging to improve coverage and spatial data observation by satellite imagery, particularly in Kuantan. It includes practising deep learning and artificial intelligence (AI) interfaces with advanced imputation for image analysis. In conclusion, accessible and transparent information on LULC changes can be introduced as a tool to support the establishment of an advanced technological revolution towards the construction of smart cities.

ACKNOWLEDGEMENTS

This work received funding from the Ministry of Higher Education Malaysia under the Fundamental Research Grant Scheme (FRGS) No. FRGS/1/2021/WAB02/UMP/02/2 (RDU210120) and Universiti Malaysia Pahang Al-Sultan Abdullah under the International Grant (Grant Number: UIC221507). The research was also supported by the National Natural Science Foundation of China (Grant Number: 51909273) and the Program for the Introduction of High-End Foreign Experts (Grant Number: G2021058002L).

REFERENCES

- Abdullah, A. Y., Masrur, A., Adnan, M. S., Baky, M. A., Hassan, Q. K., & Dewan, A. (2019). Spatio-temporal patterns of land use/land cover change in the heterogeneous coastal region of Bangladesh between 1990 and 2017. *Remote Sensing*, *11*(7), Article 790. <https://doi.org/10.3390/rs11070790>
- Aja, D., Miyittah, M. K., & Angnuureng, D. B. (2022). Quantifying mangrove extent using a combination of optical and radar images in a wetland complex, Western Region, Ghana. *Sustainability*, *14*(24), Article 16687. <https://doi.org/10.3390/su142416687>
- Amini, S., Saber, M., Rabiei-Dastjerdi, H., & Homayouni, S. (2022). Urban land use and land cover change analysis using random forest classification of landsat time series. *Remote Sensing*, *14*(11), Article 2654. <https://doi.org/10.3390/rs14112654>
- Balha, A., Mallick, J., Pandey, S., Gupta, S., & Singh, C. K. (2021). A comparative analysis of different pixel and object-based classification algorithms using multi-source high spatial resolution satellite data for LULC Mapping. *Earth Science Informatics*, *14*(4), 2231–2247. <https://doi.org/10.1007/s12145-021-00685-4>
- Fisher, J. R., Acosta, E. A., Dennedy-Frank, P. J., Kroeger, T., & Boucher, T. M. (2017). Impact of satellite imagery spatial resolution on land use classification accuracy and modeled water quality. *Remote Sensing in Ecology and Conservation*, *4*(2), 137–149. <https://doi.org/10.1002/rse2.61>
- Gaur, S., & Singh, R. (2023). A comprehensive review on land use/land cover (LULC) change modeling for urban development: Current status and future prospects. *Sustainability*, *15*(2), Article 903. <https://doi.org/10.3390/su15020903>
- Geidam, K. K., Adnan, N. A., & Alhaji Umar, B. (2020). Analysis of land use land cover changes using remote sensing data and Geographical Information Systems (GIS) at an urban set up of Damaturu, Nigeria. *Journal of Science and Technology*, *12*(2), 24-37. <https://doi.org/10.30880/jst.2020.12.02.003>
- Gondwe, J. F., Lin, S., & Munthali, R. M. (2021). Analysis of land use and land cover changes in urban areas using remote sensing: Case of Blantyre City. *Discrete Dynamics in Nature and Society*, *2021*, 1–17. <https://doi.org/10.1155/2021/8011565>
- Husain, M. A., Kumar, P., & Gonencgil, B. (2023). Assessment of spatio-temporal land use/cover change and its effect on land surface temperature in lahaul and Spiti, India. *Land*, *12*(7), Article 1294. <https://doi.org/10.3390/land12071294>
- Isola, F., Lai, S., Leone, F., & Zoppi, C. (2023). Land take and landslide hazard: Spatial assessment and policy implications from a study concerning Sardinia. *Land*, *12*(2), Article 359. <https://doi.org/10.3390/land12020359>
- Johnson, T., Butcher, J., Santell, S., Schwartz, S., Julius, S., & LeDuc, S. (2022). A review of climate change effects on practices for mitigating water quality impacts. *Journal of Water and Climate Change*, *13*(4), 1684–1705. <https://doi.org/10.2166/wcc.2022.363>
- Konrad, C. P. (2014). *Effects of Urban Development on Floods [Fact Sheet]*. U. S. Geological Survey. <https://doi.org/10.3133/fs07603>
- Lary, D. J., Alavi, A. H., Gandomi, A. H., & Walker, A. L. (2016). Machine learning in geosciences and remote sensing. *Geoscience Frontiers*, *7*(1), 3–10. <https://doi.org/10.1016/j.gsf.2015.07.003>

- Lokman, M. (2004). *Exploring the interface: The enigmatic mangroves*. Kolej Universiti Sains dan Teknologi Malaysia.
- Maryantika, N., & Lin, C. (2017). Exploring changes of land use and mangrove distribution in the economic area of Sidoarjo District, East Java using multi-temporal landsat images. *Information Processing in Agriculture*, 4(4), 321–332. <https://doi.org/10.1016/j.inpa.2017.06.003>
- Nath, B., Niu, Z., & Singh, R. (2018). Land use and land cover changes, and environment and risk evaluation of Dujiangyan City (SW China) using remote sensing and GIS techniques. *Sustainability*, 10(12), Article 4631. <https://doi.org/10.3390/su10124631>
- Neidhardt, H., & Shao, W. (2023). Impact of climate change-induced warming on groundwater temperatures and quality. *Applied Water Science*, 13(12), Article 235. <https://doi.org/10.1007/s13201-023-02039-5>
- Ngondo, J., Mango, J., Liu, R., Nobert, J., Dubi, A., & Cheng, H. (2021). Land-use and land-cover (LULC) change detection and the implications for coastal water resource management in the Wami–Ruvu Basin, Tanzania. *Sustainability*, 13(8), Article 4092. <https://doi.org/10.3390/su13084092>
- Rahman, H. A. (2014). An overview of environmental disaster in Malaysia and preparedness strategies. *Iranian Journal of Public Health*, 43(3), 17–24.
- Romali, N. S., Yusop, Z., Zaki, N. I. M., Sulaiman, M. K., Ghani, N. A. A. A., & Sulaiman, S. (2019). Flood damage function model for residential area in Kuantan: A preliminary study. *International Journal of Integrated Engineering*, 11(2). <https://doi.org/10.30880/ijie.2019.11.02.022>
- Saddique, N., Mahmood, T., & Bernhofer, C. (2020). Quantifying the impacts of land use/land cover change on the water balance in the afforested river basin, Pakistan. *Environmental Earth Sciences*, 79(19), Article 448. <https://doi.org/10.1007/s12665-020-09206-w>
- Saini, R., & Rawat, S. (2023). Land use land cover classification in remote sensing using Machine Learning Techniques. In *2023 1st International Conference on Innovations in High Speed Communication and Signal Processing (IHCSPP)* (pp. 99-104). IEEE Publishing. <https://doi.org/10.1109/ihcsp56702.2023.10127126>
- Samra, R. M. A. (2021). Dynamics of human-induced lakes and their impact on land surface temperature in Toshka Depression, Western Desert, Egypt. *Environmental Science and Pollution Research*, 29(14), 20892–20905. <https://doi.org/10.1007/s11356-021-17347-z>
- Seyam, M. M., Haque, M. R., & Rahman, M. M. (2023). Identifying the land use land cover (LULC) changes using remote sensing and GIS approach: A case study at Bhaluka in Mymensingh, Bangladesh. *Case Studies in Chemical and Environmental Engineering*, 7, Article 100293. <https://doi.org/10.1016/j.cscee.2022.100293>
- Shahbudin, S., Zuhairi, A., Kamaruzzaman, Y., & Jalal, K. C. A. (2009, October 20-22). Impact of coastal development on mangrove distribution in Kuantan, Pahang. In *International Workshop on Integrated Coastal Zone Management* (pp. 1-11). Izmir, Turkey.
- Talukdar, S., Singha, P., Mahato, S., Shahfahad, Pal, S., Liou, Y. A., & Rahman, A. (2020). Land-use land-cover classification by machine Learning classifiers for satellite observations - A review. *Remote Sensing*, 12(7), Article 1135. <https://doi.org/10.3390/rs12071135>

- Tewabe, D., & Fentahun, T. (2020). Assessing land use and land cover change detection using remote sensing in the lake tana basin, Northwest Ethiopia. *Cogent Environmental Science*, 6(1), Article 1778998. <https://doi.org/10.1080/23311843.2020.1778998>
- Viana, C. M., Girão, I., & Rocha, J. (2019). Long-term satellite image time-series for land use/land cover change detection using refined open source data in a rural region. *Remote Sensing*, 11(9), Article 1104. <https://doi.org/10.3390/rs11091104>
- Vicenteserrano, S., Perezcabello, F., & Lasanta, T. (2008). Assessment of radiometric correction techniques in analyzing vegetation variability and change using time series of landsat images. *Remote Sensing of Environment*, 112(10), 3916–3934. <https://doi.org/10.1016/j.rse.2008.06.011>
- Yulianto, F., Suwarsono, Nugroho, U. C., Nugroho, N. P., Sunarmodo, W., & Khomarudin, M. R. (2020). Spatial-temporal dynamics land use/land cover change and flood hazard mapping in the upstream citarum watershed, West Java, Indonesia. *Quaestiones Geographicae*, 39(1), 125–146. <https://doi.org/10.2478/quageo-2020-0010>
- Zaidi, S., M., Akbari, A., & Ishak, W., M., (2014) A critical review of flood history in Kuantan River basin: Challenges and potential solutions. *International Journal of Civil Engineering and Geo-Environment*, 5, 1-5.

Variation and Forecasting of Land Surface Temperature in Malaysia

Munawar Munawar^{1*}, Rhysa McNeil^{2,3}, Rohana Jani⁴, Edwar M Nur⁵ and Don McNeil²

¹Faculty of Mathematics and Natural Sciences, Universitas Syiah Kuala, Banda Aceh, Aceh 23111, Indonesia

²Faculty of Science and Technology, Prince of Songkla University, Pattani Campus, Pattani, 94000, Thailand

³Centre of Excellence in Mathematics, Commission on Higher Education (CHE), Ministry of Education, Ratchathewi, 10400 Bangkok, Thailand

⁴Department of Decision Science, Faculty of Business and Economics, Universiti Malaya, 50603 UM, Kuala Lumpur, Malaysia

⁵Faculty of Economics, Universitas Abulyatama, Aceh Besar 23372, Aceh, Indonesia

ABSTRACT

Long-term variations in temperature and weather patterns provide evidence that the planet is experiencing global warming. The detrimental consequences of global warming on the ecosystem have affected people, plants, and animals. The rising Land Surface Temperature (LST) in a region has become a crucial indicator for determining specific climate change policies. Malaysia is divided into Peninsular Malaysia and Sabah Sarawak, located on Borneo Island, comprising four super-regions and 36 sub-regions. The distance between sub-regions, measured in latitudes and longitudes, is 150 pixels (equivalent to 95 kilometres), covering the entire country. This study uses data from NASA's Terra satellites' Moderate Resolution Imaging Spectroradiometers (MODIS) covering 2000–2022. Eight, four, and three knots were deployed on the cubic spline equation to analyse cyclical data, variation, and the LST forecast from 2022 to 2030. The global mean rise in LST variation per decade is 0.445°C , with a significance level of 5%, from a confidence interval of $[0.377, 0.507]^{\circ}\text{C}$. The average predicted fluctuation in LST indicates a significant rise of 0.383°C per decade. Malaysia has not shown a significant decrease in LST acceleration

at the 0.05 significance level, and a p -value of 0.06 suggests that LST variation is still increasing. Compared to the Sabah Sarawak group, which experiences LST deceleration, most Peninsular Malaysia group experiences LST acceleration.

Keywords: Cubic spline, forecasting, LST increase, Malaysia, NASA MODIS

ARTICLE INFO

Article history:

Received: 24 December 2023

Accepted: 10 June 2024

Published: 25 October 2024

DOI: <https://doi.org/10.47836/pjst.32.6.16>

E-mail addresses:

munawar@usk.ac.id (Munawar Munawar)

rhysa.m@psu.ac.th (Rhysa McNeil)

Rohanaj@um.edu.my (Rohana Jani)

edwar_ekm@abulyatama.ac.id (Edwar M Nur)

don.mcneil@mq.edu.au (Don McNeil)

* Corresponding author

INTRODUCTION

The world is undergoing climate change due to human activities, including industrial operations that utilise gas, coal, and oil for transportation and other purposes. It is evidenced by long-term temperature and weather patterns shifts, impacting the greenhouse effect by trapping solar heat and increasing temperature and precipitation variability (Mikhaylov et al., 2020). The mean global surface temperature rose by 0.3 to 0.6°C during the 20th century; this increase is unlikely to have occurred naturally (Bruce et al., 1996; Metz et al., 2001). People, plants, and animals have all been impacted by the negative environmental effects of global warming (Mall et al., 2021). The rate of economic growth worldwide may be affected by climate change, and certain species may become more susceptible to extinction.

These events will have quite different relative effects in the developed and developing worlds. Climate events serve as the foundation for strategic decisions made by government agencies regarding regional and national economies (Chinowsky et al., 2011; Tol, 2018). In poor nations, agriculture is the industry most recognised to be negatively impacted economically by climate change due to its size and sensitivity (Mendelsohn, 2009). A region's increasing Land Surface Temperature (LST) becomes a significant signal for choosing particular climate change policies as a climate science variable (Fox et al., 2019).

Malaysia is one of the Southeast Asian nations dealing with LST problems because of its expansionist aspirations. Malaysia's average LST increased between 1990 and 2015, ranging from 25.39°C to 32.74°C, as a result of deforestation's impact on LST (Himayah et al., 2019; Jaafar et al., 2020). Malaysia's LST is assumed to have increased variation between 2000–2022, which aligns with the acceleration of LST and LST forecasting from 2023–2030. The Malaysian peninsula and the island of Borneo together comprise the country of Malaysia, which is part of Southeast Asia (SEA). Like other Southeast Asian nations, Malaysia's economy primarily depends on agriculture, fisheries, and industry. According to Murad et al. (2010), the rate of agricultural extension and the climate change score do not exhibit a positive correlation. Malaysia's temperature may impact neighbouring South China Sea nations, including Indonesia, the Philippines, Singapore, and Thailand.

This study used NASA MODIS Web data from 2000 to 2022, along with Eight, four, and three knots deployed on the cubic spline equation, respectively, to analyse the cyclical pattern, variation, and forecast of LST from 2022 to 2030. Unlike previous studies from Munawar et al. (2022, 2023), they examined the cyclical pattern and variance of LST on the main island using the cubic spline function with eight and seven knots. After eliminating the annual seasonality and deploying the cubic spline equation, any long-term trends in LST are identified by analysing the residual data. The LST variation depends on the annual season in an area; a typical tropical area only has two main seasons: dry and wet. The dry season will increase the LST and vice versa. Mapping the LST condition in a region requires not only LST fluctuation but also LST acceleration and forecasting.

MATERIALS AND METHODS

Study Area

Malaysia is situated between 5.5°N, 20.5°N Latitudes and 97.5°, 105.5° Longitudes, as shown in Figure 1. The Malaysian peninsula shares boundaries with Singapore to the south, Thailand to the north, and Sumatra Island in Indonesia to the west. East Malaysia is a country on the island of Borneo. The South China Sea borders it to the north, the Philippines to the west, and Indonesia to the east.

Figure 1 depicts all the super-regions and sub-regions of Malaysia. In Peninsular Malaysia, super-regions A and B represent the west and central-west super-regions, respectively (AB group). Super-region C denotes the central-east super-region, and D represents the east super-region on Sabah Sarawak of Borneo Island (CD group). This results in four super-regions and 36 sub-regions that encompass the entire island.

Sub-regions were created with centres placed at latitudes and longitudes 150 pixels apart, equivalent to 95 kilometres. The 36 sub-regions systematically resulted from the 150-pixel distance between sub-regions from northern Malaysia to eastern Malaysia, covering the whole country. 150-pixel distance minimises the spatial correlation between sub-regions, and the distance results in the representative data rather than using the bigger pixel. Subsequently, super-regions A and B were combined into the Peninsular Malaysia (AB group), and super-regions C and D were grouped into the Sabah Sarawak (CD group).

Data

This investigation utilised the online NASA MODIS Terra Satellite database, which provides LST data during daytime and nighttime, covering the entire globe. The information includes mean temperatures recorded every eight days for an area of 0.859 km², assuming

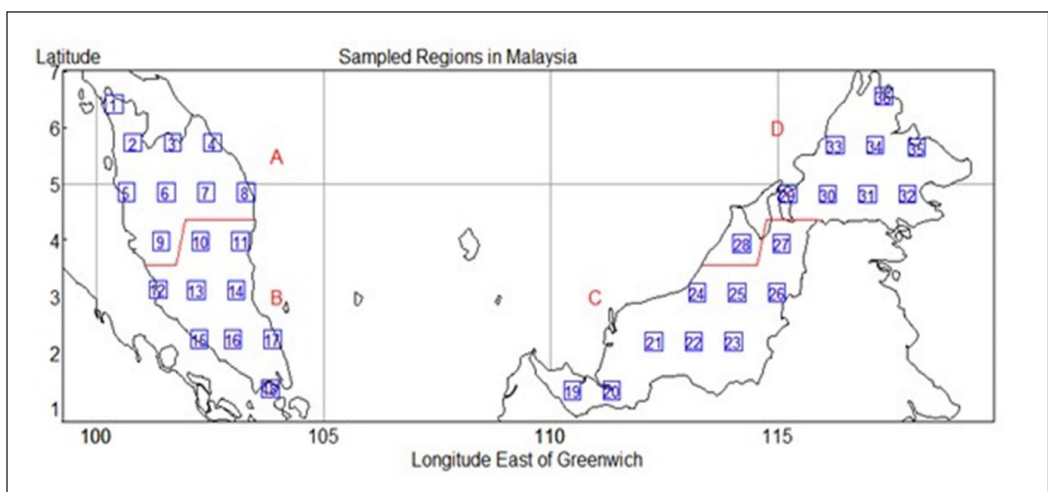


Figure 1. Malaysia area of study

clear skies (Phan et al., 2018; ORNL DAAC, 2018; Wan, 2008). A sinusoidal computation was carried out using tiles with dimensions of 10×10 latitude degrees divided into $1,200 \times 1,200$ pixels each to ensure uniformity across all pixels in the dataset. The downloaded LST data was processed at the island’s sub-regional centre to minimise data loss, and any missing values were excluded from the analysis. If the sky was not clear, the satellite could not provide LST data for the target sub-region pixel; thus, such pixels were considered missing values. Natural disasters that could lead to unforeseen changes in data behaviour were not accounted for. All outliers were retained in the dataset to preserve the integrity of the LST data. Before analysis, temperature data originally stored in Kelvin were converted to Celsius.

Methods

The standard cubic spline and linear model was employed and was defined as Equation 1 (Alberg et al., 1967):

$$y = a + bx + \sum_{k=1}^{p-3} c_k S_k(x) \tag{1}$$

where $a, b, c_1, c_2, \dots, c_{p-3}$ are the constants for the linear function. A cubic spline is a segmented cubic function used to interpolate data points while ensuring smooth transitions between these points. The cubic spline model can also manage the seasonal pattern from time series data.

The cubic spline model can be expanded as in Equation 2 (Wongsai et al., 2017):

$$S_k(x) = (x - x_k)_+^3 - \frac{(x_p - x_k)(x_{p-1} - x_k)}{d_3 d_2} (x - x_{p-2})_+^3 + \frac{(x_p - x_k)(x_{p-2} - x_k)}{d_1 d_2} (x - x_{p-1})_+^3 - \frac{(x_{p-2} - x_k)(x_{p-1} - x_k)}{d_3 d_1} (x - x_p)_+^3 \tag{2}$$

Three limits’ circumstances apply for $d_1 = x_p - x_{p-1}$, $d_2 = x_{p-1} - x_{p-2}$ with $x_+ = \max(x,0)$, and also $d_3 = x_p - x_{p-2}$.

The seasonally modified LST model was fitted with a second-order AR(2) model. The model’s basis is as stated in Equation 3 (Venables & Ripley, 2002):

$$Y_{at} = \alpha_1 Y_{at-1} + \alpha_2 Y_{at-2} + \varepsilon_t \tag{3}$$

It is necessary to approximate the unknown parameters α_1 and α_2 , and the random error with zero average and defined variance is represented by ε_t , where $t = 1, \dots, 365$ days. At $t-1$, Y_{at-1} is the time of LST, and at t time, Y_{at} is the time of LST that has been seasonally corrected. R was used for all analyses and visual displays (Team, 2018).

RESULTS AND DISCUSSION

Figure 2 manifests the seasonal trend of LST, which corresponds to super-region A from Peninsular Malaysia (AB group) in Malaysia. Similar graphs were used to investigate the seasonal tendencies of the other super-regions.

The average temperature for each of the 22 years corresponds to the same day, as indicated by Figure 2, displaying 46 stacks of data (966 points if none are missing). Solid red curves and blue crosses depict the eight knots fitted natural spline functions. Eight knots were distributed, four at the beginning and four at the end of the year, to anticipate the increase of LST at the start and the decrease of LST at the end of the year. With one summer peak in March and a low LST seasonal pattern in October, the super-region A curves show a modest seasonal trend. The first day (in January) of the year, during the wet cycle, had the lowest LST between 2000 and 2022, and the ninth month (day 267) had the greatest LST. The extreme area sub-region 4 has the highest average day LST, measuring in at 31.176°C.

The cyclically adjusted time series in Figure 3 were analysed for the Malaysian super-region A from the Peninsular Malaysia (AB group). The cyclical trends of the other super-regions were examined, and a figure related to this one was deployed.

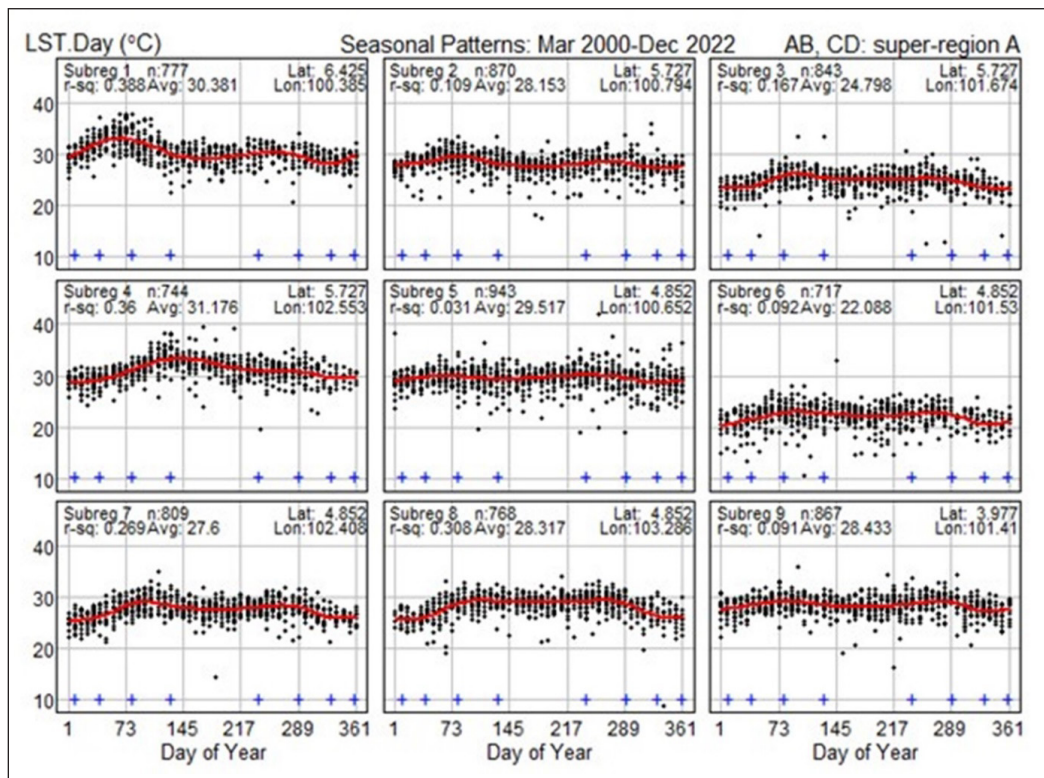


Figure 2. Super-region A LST seasonal pattern

The mean-corrected data was subtracted from the fitted seasonal trends to acquire the seasonally modified temperatures in Figure 3's panels. The daily LST time series were independent, as indicated by the moderately high estimated coefficients of the AR(1) first-order auto-regressive model. The second-order auto-regressive model, stationary at AR(2), had a lower coefficient than AR(1).

The left panels of Figure 3 use black curves to show the LST development over 22 years in all sub-regions, whereas the right panels use dotted lines with different scales. The linear models or zero knots with two parameters have *p*-values that indicate most sub-regions showed a statistically significant rise in LST, except sub-region 4.

The cubic spline's four knots, which correspond to sub-regions 7, 8, and 9, have *p*-values for each knot that indicates statistical significance for the LST rising acceleration. The three knots of the cubic spline revealed sub-regions 1, 2, 4, 5, 7, 8, and 9, and the *p*-values for these three knots show that sub-regions had statistically significant LST forecasting. In the right panel of Figure 3, the fitted cubic splines with four knots for 2000–2022. The tropical area's four knots are sufficient to forecast the variation of LST because the tropical area has two seasons: dry and wet. The knots were distributed two at the beginning and two at the end of the period 2000–2022; with four knots, the model became a polynomial model with three orders.

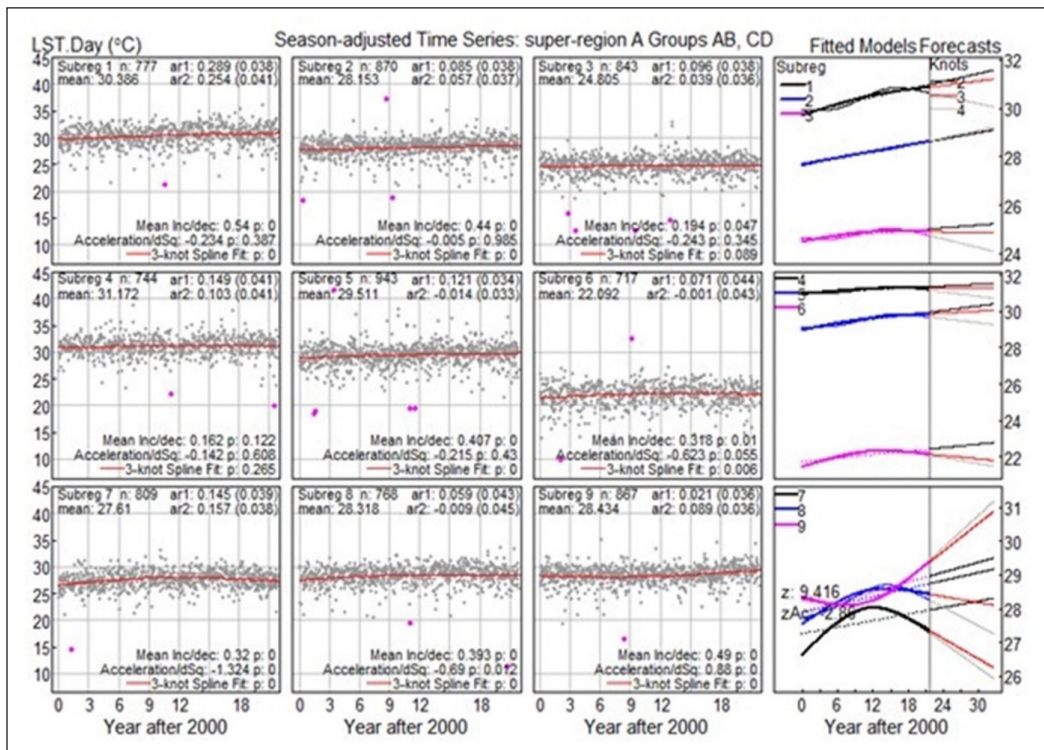


Figure 3. Super-region A seasonal adjusted and forecasting of LST

Three knots for the years 2023–2030 are displayed as solid curves for every sub-region with significant p -values. The model becomes a quadratic model to examine the acceleration of LST variation for the 2023–2030 period. The knots are placed at the period’s beginning, middle, and end. Figure 3 in the bottom-right panel displays statistically significant z -values of 9.416 for the average daily LST rise and 2.860 for the acceleration. A z -value is considered statistically significant if it is an absolute value of 1.96 or above at a 95% confidence level.

Based on sub-region latitude, Figure 4 depicts the expected variations in LST for all sub-regions in Malaysia. There are only two sub-regions where LST declines occur; LST rises differ per sub-region. The red line represents the overall average increase in LST predicted for the next ten years, expected to be 0.381°C for the Peninsular Malaysia (AB group) and 0.387°C for the Sabah Sarawak (CD group). The blue line shows the average annual rise in LST for both the AB and CD groups, which is 0.464°C and 0.285°C, respectively, over ten years.

The LST change at a 5% confidence level and the LST change forecasts for the Peninsular Malaysia (AB) and Sabah Sarawak (CD) groups are shown in Figure 5. The overall mean of the LST predicted change rise is 0.383°C every ten years, with a 95% confidence interval of [0.377, 0.507]°C and a z -value of 15.278. However, the overall mean of the LST difference increase is 0.445°C every ten years. These values are accurate, with an LST prediction variance increase of 0.480°C per decade for the AB group, an LST variation increase of 0.302°C, a z -value of 14.262, a 95% confidence interval of [0.222, 0.381]°C. With a z -value of 8.555 and a 95% confidence interval of [0.180, 0.328]°C, the LST variance increase for the CD group is 0.254°C when compared to the AB group with an increase of LST.

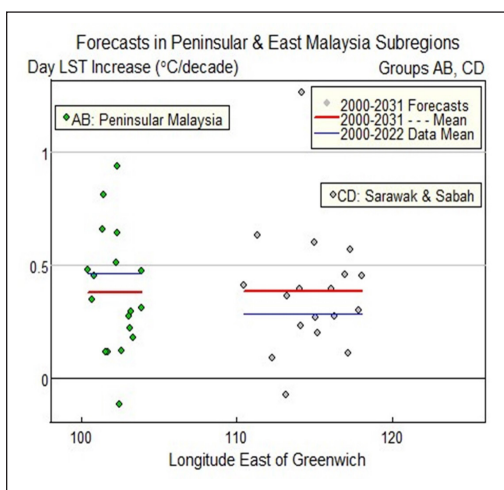


Figure 4. LST forecast increase (°C/decade) and location

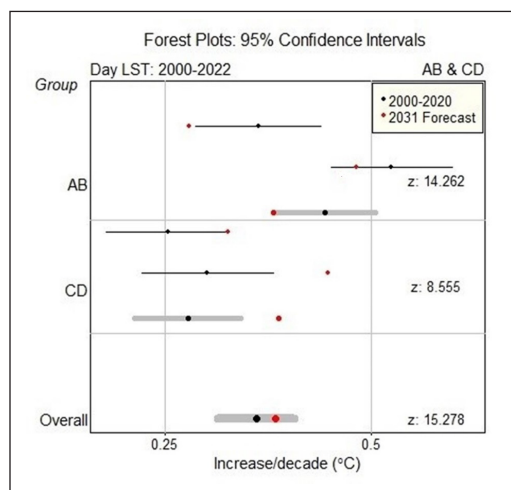


Figure 5. 95% confidence interval of LST variation

Figure 6 presents a 95% confidence interval LST acceleration/decade²(°C). The overall average acceleration of LST is 0.027°C per decade, and the 95% confidence interval is [-0.193,0.199] with a z-value of 0.429. The Peninsular Malaysia (AB) group has a deceleration of LST -0.238°C per decade, and the 95% confidence interval is [-0.336, -0.108] with a z-value -2.931. The Sabah Sarawak (CD) group has a z-value of 3.440 and an acceleration of LST 0.291°C per ten years with a 95% confidence interval of [0.125, 0.458].

Figure 7 shows the acceleration of Malaysia’s LST from 2000 to 2022 in the Peninsular Malaysia (AB) and Sabah Sarawak (CD) groups. Malaysia experiences no significant decrease in the acceleration of LST at a 0.05 significance level, with a p-value of 0.06. In contrast, the CD group exhibits LST deceleration, whereas most AB groups demonstrate LST acceleration.

Super-region A’s seasonal pattern of LST data shows a modest seasonal pattern with low LST values all year round and a single summer peak in March. Seasonal trends and changes in LST for the Peninsular Malaysia (AB) and Sabah Sarawak (CD) super-regions were investigated using a cubic spline approach. The results of the investigation showed that daily LST increased significantly in both super-regions, AB and CD. Furthermore, the estimate shows that LST will increase dramatically between 2021 and 2031. Several investigations conducted in Malaysia have documented an increase in temperature in December (Ismail et al., 2019). A comparable study of regions with four distinct seasons indicates that summertime LST peaks from June to September in a year, as reported by Khorchani et al. (2018) and Singh et al. (2014).

Our findings presented that Malaysia’s mean LST increased by 0.445°C every decade, equivalent to 4°C over ten years. Tangang et al. (2012) estimated an increase of 3-5°C per century, which is higher than this trend. The average annual rise in LST variation is

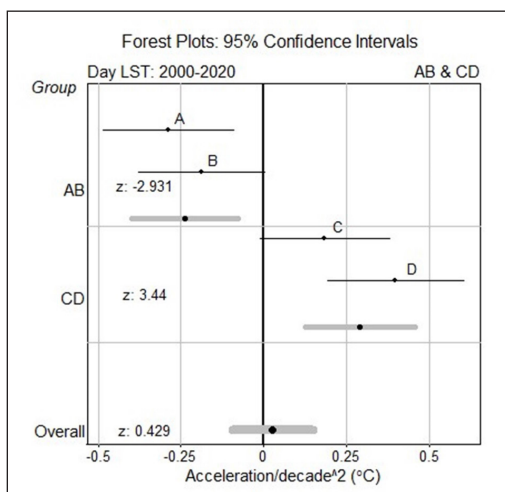


Figure 6. 95% confidence interval LST acceleration/decade²(°C)

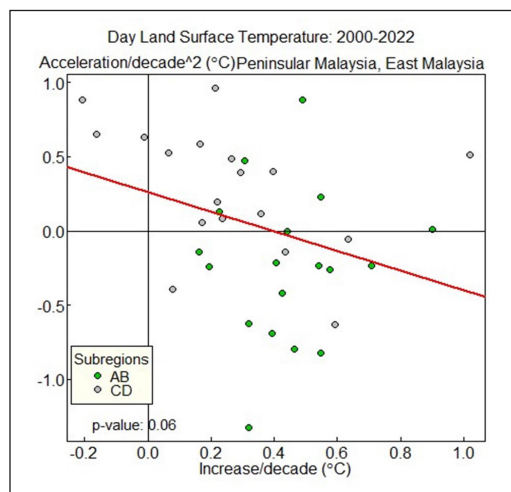


Figure 7. LST acceleration 2000–2022

0.383°C. We discovered that Malaysia exhibits a sizable variation in LST. Wolff et al. (2018) suggest that the increase in LST variance could be attributed to land use changes and deforestation. Eight knots for the cubic spline can model the seasonal pattern, and four can forecast the LST variation over a decade. Although the overall average acceleration of LST is 0.027°C per decade with no significant LST acceleration, the LST variation in Malaysia continues to increase in the next decade.

Variations in land surface temperatures can be determined by the type of land cover, especially vegetation (Buyadi et al., 2014). Dense vegetation in an area can act as a filter or absorbent material to prevent the surface temperature from rising. According to Babalola and Akinsanola (2016), green vegetation has the capacity to absorb solar radiation and use it for photosynthesis. Research has found that changes in the island's vegetation were a reliable predictor of temperature increases in Malaysia (Evans, 2018). Deforestation in the area was considered the cause of the rising temperatures. Additional research (Ferreira & Duarte, 2019) has demonstrated a significant inverse relationship between the Normalised Difference Vegetation Index (NDVI) and Land Surface Temperature (LST). Malaysia's vegetation index shows that LST temperatures have risen (Suherman et al., 2014).

According to Prevedello et al. (2019), differences in land cover—such as those conducted by reforestation or deforestation—ultimately influence the temperature in each place. Previous studies have connected land cover change and land use to LST (Majumder et al., 2020; Odindi et al., 2015; Rasul et al., 2017). According to Parmesan and Hanley (2015), the temperature will rise if a region's land cover decreases. A study carried out in Malaysia found a correlation between rising temperatures and a notable decline in freshwater fish species and functional richness (Wilkinson et al., 2018). A study from Malaysia also demonstrates that built-up regions have the warmest climates, while locations with the coldest climates are those near forests and mangroves (Sheikhi & Kanniah, 2018).

CONCLUSION

The LST in Malaysia exhibited variation and was predicted between 2023 and 2030 using the cubic spline model. The proper quantity and arrangement of knots were established to provide a smoother equation. The cyclical pattern in the cubic spline equation was demonstrated to be adequately captured by eight knots; four knots were utilised to evaluate the variation acceleration in LST (2020–2022), and three knots were employed to predict the variation in LST over a 2023–2030 period. The study discovered that the mean daily LST had increased statistically significantly in Malaysia's Peninsular (AB) and Sabah Sarawak (CD) super-regions. It is anticipated that between 2023 and 2030, the LST variation in these areas will rise, with no discernible slowdown in its acceleration.

While forests persist on the Malaysian peninsula, the rise in LST is predominantly driven by urban expansion spurred by development. According to Kamal et al. (2019), the

increase in LST across Peninsular Malaysia is primarily influenced by the heat exposure index, particularly evident in northern and urban locales. In contrast, the Sabah Sarawak region, boasting extensive tropical areas and the elevated Kinabalu Mountain, experiences a surge in LST attributed to El Niño Southern Oscillations, as discovered in Kuching Sarawak by Anak (2022).

One evidence of regional warming has occurred in Malaysia, which is characterised by increased LST. However, additional research is needed to more comprehensively validate the conclusions of this study. Other strategies, such as including larger islands farther from the equator, like China and America, are required to enhance estimation accuracy. Most large islands have mountains (LE), NDVI, a variety of land use/land cover, economic development/urbanisation, industrial activities, natural disasters and climate changes/meteorological factors (e.g., air temperature) as additional factors that could be considered in future LST research. In addition to the variables influencing LST, it is crucial in future research to compare the variation in LST data obtained from MODIS Terra and Aqua satellites.

The constraints inherent in projecting future LST trends must be considered, considering the implications of hindcast results from LST data spanning 2000 to 2022 for forthcoming research. Enhancing hindcast simulations entails fulfilling various prerequisites, including ample data availability, rigorous process refinement, and precise depiction of key climate change indicators, as de Hauteclocque et al. (2023) emphasised.

ACKNOWLEDGEMENTS

The authors express their highest appreciation to the following: Department of Statistics, Faculty of Mathematics and Natural Sciences, Universitas Syiah Kuala, Banda Aceh, Aceh, Indonesia; Department of Mathematics and Computer Science, Faculty of Science and Technology, Prince of Songkla University, Pattani, Thailand; Department of Decision Science, Faculty of Business and Economics, Universiti Malaya, Kuala Lumpur, Malaysia; and Faculty of Economics, Universitas Abulyatama, Aceh Besar, Aceh, Indonesia, for all the invaluable assistance received by the authors so far.

REFERENCES

- Alberg, J. H., Nilson, E. N., & Walsh, J. L. (1967). *The theory of splines and their applications*. Academic.
- Anak, R. (2022). Statistical modeling of impacts El Niño Southern Oscillations (ENSO) on land surface temperature in small medium size city: Case study Kuching Sarawak. *Journal of Sustainable Natural Resources*, 3(1), 14-22.
- Babalola, O. S., & Akinsanola, A. A. (2016). Change detection in land surface temperature and land use land cover over Lagos Metropolis, Nigeria. *Journal of Remote Sensing & GIS*, 5(3), 1-7.

- Bruce, J. P., Lee, H., & Haites, E. F. (1996). *Climate change 1995*. Contribution of Working Group III to the Second Assessment Report of the Intergovernmental Panel on Climate Change (No. 574.5222 C639co 1995). Cambridge University Press.
- Buyadi, S. N. A., Mohd, W. M. N. W., & Misni, A. (2014). Impact of vegetation growth on urban surface temperature distribution. In *IOP Conference Series: Earth and Environmental Science* (Vol. 18, No. 1, p. 012104). IOP Publishing. <https://doi.org/10.1088/1755-1315/18/1/012104>
- Chinowsky, P., Hayles, C., Schweikert, A., Strzepek, N., Strzepek, K., & Schlosser, C. A. (2011). Climate change: comparative impact on developing and developed countries. *The Engineering Project Organization Journal*, 1(1), 67-80. <https://doi.org/10.1080/21573727.2010.549608>
- de Hauteclouque, G., Maretic, N. V., & Derbanne, Q. (2023). Hindcast based global wave statistics. *Applied Ocean Research*, 130, Article 103438.
- Evans, M. (2018, April 25). Forest loss leads to local climate change effect in Borneo. *ThinkLandscape*. <https://thinklandscape.globallandscapesforum.org/27161/forest-loss-leads-to-local-climate-change-effect-in-borneo/>
- Ferreira, L. S., & Duarte, D. H. S. (2019). Exploring the relationship between urban form, land surface temperature and vegetation indices in a subtropical megacity. *Urban Climate*, 27, 105-123. <https://doi.org/10.1016/j.uclim.2018.11.002>
- Fox, M., Zuidema, C., Bauman, B., Burke, T., & Sheehan, M. (2019). Integrating public health into climate change policy and planning: state of practice update. *International journal of environmental research and public health*, 16(18), Article 3232. <https://doi.org/10.3390/ijerph16183232>
- Himayah, S., Ismail, A., Ridwana, R., Arrasyid, R., Affriani, A. R., & Ihsan, M. (2019). Correlation between land surface temperature and vegetation greenness using multi-temporal images. In *IOP Conference Series: Earth and Environmental Science* (Vol. 286, No. 1, p. 012043). IOP Publishing. <https://doi.org/10.1088/1755-1315/286/1/012043>
- Ismail, N. A., Zin, W. Z. W., Ibrahim, W., & Yeun, L. C. (2019). Eight-day daytime land surface temperature pattern over Peninsular Malaysia. *International Journal of Recent Technology and Engineering*, 8(4), 11949-11955. <https://doi.org/10.35940/ijrte.D9911.118419>
- Jaafar, W. S. W. M., Maulud, K. N. A., Kamarulzaman, A. M. M., Raihan, A., Sah, S. M., Ahmad, A., Saad, S. N. M., Azmi, A. T. M., Syukri, N. K. A. J., & Khan, W. R. (2020). The influence of deforestation on land surface temperature - A case study of Perak and Kedah, Malaysia. *Forests*, 11(6), Article 670. <https://doi.org/10.3390/f11060670>
- Kamal, N. I. A., Ash'aari, Z. H., & Abdullah, A. M. (2019). Spatio-temporal variability of heat exposure in Peninsular Malaysia using land surface temperature. *Disaster Advances*, 12(12), 1-9.
- Khorchani, M., Martin-Hernandez, N., Vicente-Serrano, S. M., Azorin-Molina, C., Garcia, M., Domínguez-Duran, M. A., Reig, F., Peña-Gallardo, M., & Domínguez-Castro, F. (2018). Average annual and seasonal land surface temperature, Spanish Peninsular. *Journal of Maps*, 14(2), 465-475. <https://doi.org/10.1080/17445647.2018.1500316>
- Majumder, A., Kingra, P. K., Setia, R., Singh, S. P., & Pateriya, B. (2020). Influence of land use/land cover changes on surface temperature and its effect on crop yield in different agro-climatic regions of Indian Punjab. *Geocarto International*, 35(6), 663-686. <https://doi.org/10.1080/10106049.2018.1520927>

- Mall, R. K., Chaturvedi, M., Singh, N., Bhatla, R., Singh, R. S., Gupta, A., & Niyogi, D. (2021). Evidence of asymmetric change in diurnal temperature range in recent decades over different agro-climatic zones of India. *International Journal of Climatology*, 41(4), 2597-2610. <https://doi.org/10.1002/joc.6978>
- Mendelsohn, R. (2009). The impact of climate change on agriculture in developing countries. *Journal of Natural Resources Policy Research*, 1(1), 5-19. <https://doi.org/10.1080/19390450802495882>
- Metz, B., Davidson, O., Swart, R., & Pan, J. (Eds.). (2001). *Climate change 2001: Mitigation: Contribution of Working Group III to the Third Assessment Report of the Intergovernmental Panel on Climate Change*. Cambridge University Press.
- Mikhaylov, A., Moiseev, N., Aleshin, K., & Burkhardt, T. (2020). Global climate change and greenhouse effect. *Entrepreneurship and Sustainability Issues*, 7(4), Article 2897. [http://doi.org/10.9770/jesi.2020.7.4\(21\)](http://doi.org/10.9770/jesi.2020.7.4(21))
- Munawar, M., Prasetya, T. A. E., McNeil, R., & Jani, R. (2022). Statistical modeling for land surface temperature in Borneo island from 2000 to 2019. *Theoretical and Applied Climatology*, 147, 1627–1634. <https://doi.org/10.1007/s00704-021-03891-8>
- Munawar, M., Prasetya, T. A. E., McNeil, R., Jani, R., & Buya, S. (2023). Spatio and temporal analysis of indonesia land surface temperature variation during 2001–2020. *Journal of the Indian Society of Remote Sensing*, 51, 1393–1407. <https://doi.org/10.1007/s12524-023-01713-0>
- Murad, W., Molla, R. I., Mokhtar, M., & Raquib, A. (2010). Climate change and agricultural growth: an examination of the link in Malaysia. *International Journal of Climate Change Strategies and Management*, 2(4), 403-417. <https://doi.org/10.1108/17568691011089927>
- Odindi, J. O., Bangamwabo, V., & Mutanga, O. (2015). Assessing the value of urban green spaces in mitigating multi-seasonal urban heat using MODIS land surface temperature (LST) and landsat 8 data. *International Journal of Environmental Research*, 9(1), 9-18. <https://doi.org/10.22059/ijer.2015.868>
- ORNL DAAC. (2018). *MODIS and VIIRS Land Products Global Subsetting and Visualization Tool*. Oak Ridge National Laboratory Distributed Active Archive Center. <https://doi.org/10.3334/ornl daac/1379>
- Parmesan, C., & Hanley, M. E. (2015). Plants and climate change: Complexities and surprises. *Annals of Botany*, 116(6), 849-864. <https://doi.org/10.1093/aob/mcv169>
- Phan, T. N., Kappas, M., & Tran, T. P. (2018). Land surface temperature variation due to changes in elevation in northwest Vietnam. *Climate*, 6(2), Article 28. <https://doi.org/10.3390/cli6020028>
- Prevedello, J. A., Winck, G. R., Weber, M. M., Nichols, E., & Sinervo, B. (2019). Impacts of forestation and deforestation on local temperature across the globe. *PloS one*, 14(3), Article e0213368. <https://doi.org/10.1371/journal.pone.0213368>
- Rasul, A., Balzter, H., Smith, C., Remedios, J., Adamu, B., Sobrino, J. A., Srivani, M., & Weng, Q. (2017). A review on remote sensing of urban heat and cool islands. *Land*, 6(2), Article 38. <https://doi.org/10.3390/land6020038>
- Sheikhi, A., & Kanniah, K. D. (2018). Impact of land cover change on urban surface temperature in Iskandar Malaysia. *Chemical Engineering Transactions*, 63, 25-30. <https://doi.org/10.3303/CET1863005>

- Singh, R. B., Grover, A., & Zhan, J. (2014). Inter-seasonal variations of surface temperature in the urbanized environment of Delhi using landsat thermal data. *Energies*, 7(3), 1811–1828. <https://doi.org/10.3390/en7031811>
- Suherman, A., Rahman, M. Z. A., & Busu, I. (2014). Albedo and land surface temperature shift in hydrocarbon seepage potential area, case study in Miri Sarawak Malaysia. In *IOP Conference Series: Earth and Environmental Science* (Vol. 18, No. 1, p. 012148). IOP Publishing. <https://doi.org/10.1088/1755-1315/18/1/012148>
- Tangang, F. T., Juneng, L., Salimun, E., Sei, K. M., Le, L. J., & Muhamad, H. (2012). Climate change and variability over Malaysia: Gaps in science and research information. *Sains Malaysiana*, 41(11), 1355–1366.
- Team, R. C. (2018). *A language and environment for statistical computing*. R Foundation for Statistical Computing, Vienna, Austria. <https://www.r-project.org/>
- Tol, R. S. (2018). The economic impacts of climate change. *Review of Environmental Economics and Policy*, 2(1), 4-25.
- Venables, W. N., & Ripley, B. D. (2002). *Modern applied statistics with S*. Springer.
- Wan, Z. (2008). New refinements and validation of the MODIS land-surface temperature/emissivity products. *Remote sensing of Environment*, 112(1), 59-74. <https://doi.org/10.1016/j.rse.2006.06.026>
- Wilkinson, C. L., Yeo, D. C., Tan, H. H., Fikri, A. H., & Ewers, R. M. (2018). Land-use change is associated with a significant loss of freshwater fish species and functional richness in Sabah, Malaysia. *Biological Conservation*, 222, 164-171. <https://doi.org/10.1016/j.biocon.2018.04.004>
- Wolff, N. H., Masuda, Y. J., Meijaard, E., Wells, J. A., & Game, E. T. (2018). Impacts of tropical deforestation on local temperature and human well-being perceptions. *Global Environmental Change*, 52, 181–189. <https://doi.org/10.1016/j.gloenvcha.2018.07.004>
- Wongsai, N., Wongsai, S., & Huete, A. R. (2017). Annual seasonality extraction using the cubic spline function and decadal trend in temporal daytime MODIS LST data. *Remote Sensing*, 9(12), Article 1254. <https://doi.org/10.3390/rs9121254>

The Application of Smart Drip Irrigation System for Precision Farming

Suhardi¹, Bambang Marhaenanto¹ and Bayu Taruna Widjaja Putra^{1,2*}

¹*Agricultural Engineering, Faculty of Agricultural Technology, University of Jember, Jember 68121, Indonesia*

²*Center of Excellence in Artificial Intelligence for Industrial Agriculture, University of Jember, Jember 681213, Indonesia*

³*Laboratory of Precision Agriculture and Geoinformatics, University of Jember, Jember 68121, Indonesia*

ABSTRACT

Managing water resources in urban areas is relatively expensive due to the costs of electricity and water distribution from wells and water companies. Therefore, water resource management for urban agricultural purposes needs to be made efficient, such as through smart irrigation technologies, one of which is the drip irrigation system that engages soil moisture sensors and the Internet of Things (IoT) to control the amount of distributed water. This study aims to apply and evaluate the performance of a drip irrigation system based on soil moisture sensors and IoT in urban agriculture. The results showed that the distribution uniformity in the system was identified at fair levels, with a Coefficient of Uniformity (CU) of 90.15% and 86.58%, respectively. Furthermore, our study also found that the IoT-assisted drip irrigation system that engaged a Deep Neural Networks (DNN) model to meet the water requirement led to better peanut yield than the irrigation system based on soil moisture as a control.

Keywords: Coefficient of uniformity, drip irrigation, IoT, soil moisture

ARTICLE INFO

Article history:

Received: 27 December 2023

Accepted: 09 May 2024

Published: 25 October 2024

DOI: <https://doi.org/10.47836/pjst.32.6.17>

E-mail addresses:

hardi.ftp@unej.ac.id (Suhardi)

bmarhaen@unej.ac.id (Bambang Marhaenanto)

bayu@unej.ac.id (Bayu Taruna Widjaja Putra)

* Corresponding author

INTRODUCTION

Overpopulation in urban areas has increased the need for housing, employment opportunities, water, and food resources. Water and food resources are strongly related to basic needs in that food from the agricultural sector largely relies on the availability of water resources. This becomes even more critical for urban

agriculture since it depends on wells and water companies. Inefficient management of water resources will increase the costs of living due to the higher usage of electricity to extract and distribute water.

Smart irrigation is one solution for regulating and monitoring agricultural irrigation to maintain the efficient use of water resources and subsequently improve farmer's economy (Jaafar & Kharroubi, 2021). Therefore, smart irrigation technology has become a decent complement to urban agriculture, as indicated by improved efficiency in water management (Gimpel et al., 2021; Kullu et al., 2020; Mason et al., 2019; Quimbita et al., 2022). Previous work has confirmed that the technology has been widely applied to drip irrigation in distributing water and has, in turn, saved water by 48% compared to traditional irrigation systems (Jaafar & Kharroubi, 2021). Other research results also show that the drip irrigation system increased the efficiency of water usage by 36% compared to the border irrigation system (Y. Wang et al., 2021). Simply put, drip irrigation can be a decent choice for the most efficient irrigation despite limited water resources (Zahid et al., 2020).

In general, using smart irrigation can increase the efficiency of water distribution to plants. However, its use in urban agriculture needs to be studied further to determine the efficiency level in using water resources, especially in drip irrigation systems. The selection of the appropriate microcontroller and sensors is decisive in the efficiency of irrigation water distribution. Smart irrigation systems based on soil moisture controllers and those based on the Internet of Things (IoT) adapted to plant evapotranspiration (ETc) are alternative smart irrigation systems in urban agriculture. These two smart irrigation systems need to be studied to determine the efficiency level of water distribution and its effect on plant growth. This IoT-based smart irrigation system utilizes temperature (T) and air humidity (RH) data on agricultural land to predict evapotranspiration so that the distribution of irrigation water is adjusted to the amount of evotranspired water.

Smart irrigation utilizes microcontrollers and sensors as control systems, including NodeMCU ESP8266, ESP32, and Arduino. Soil moisture sensors are often used to monitor soil water and increase water management efficiency (Ferrarezi et al., 2020). Meanwhile, NodeMCU helps to monitor and control irrigation with the aid of IoT by engaging Blynk, telegram, and other applications from a distance. NodeMCU has been widely used for IoT-assisted irrigation research (Rani et al., 2022). Likewise, Arduino is often used in automatic irrigation control based on soil water content detected by soil moisture sensors. When the water content reaches a predetermined minimum or maximum limit, the microcontroller triggers the relay to activate the drip irrigation system even without data on plant water requirements. On the other hand, an IoT-assisted irrigation system needs data on crop water requirements as a reference for deciding the volume and duration of water distribution. The data are produced by calculating water requirements using trained and tested DNN

models to reach exemplary reliability and accuracy. The present study was projected to evaluate and apply a drip irrigation system based on soil moisture sensors and IoT in an urban agricultural setting.

MATERIALS AND METHODS

Study Site

The research examined peanut growth as sample plants at the University of Jember, East Java, Indonesia, from October 2022 to January 2023. The university is located at -8.16346° and 113.71305° and is characterized by a tropical climate with two seasons: dry and rainy. The dry season occurs from June to October, while the rainy season occurs from November to May.

Dataset

This study examines the use of intelligent irrigation systems in conditions of limited water resources, especially in the dry season. High temperatures and low air humidity during the dry season greatly influence the level of plant evapotranspiration, thus affecting the water requirements of plants. Therefore, IoT-based temperature (T) and air humidity (RH) data collection was carried out to monitor the temperature and RH conditions at the research site in real time. Next, TMean and RHMean data for 4 hours for 7 days were used as input data for the DNN-based evapotranspiration prediction model. Previous research shows that DNN-based evapotranspiration predictions are accurate with TMean and RHMean input data of 4 hours duration (Suhardi et al., 2023). Thus, the IoT-based smart irrigation system was carried out every 7 days based on the DNN model output. On the other hand, a smart irrigation system based on soil moisture sensors was also used to control the distribution of irrigation water to plants. The volume of water distributed to plants, plant height and plant canopy diameter were recorded periodically.

This study was carried out on two demonstration plots measuring 1m x 1m in a greenhouse. The distance between peanuts in each plot was 25 cm x 25 cm with the following drip irrigation systems. The first system was a drip irrigation system controlled by an Arduino Uno microcontroller based on a soil moisture sensor with a pump control that started when water content reached 17%, and the pump stopped at >30% water content. The other was a drip irrigation system using NodeMCU ESP8266 with Blynk to control the pump to meet water requirements. The irrigation was performed every 7 days with the amount of water emitted following the DNN-based ETo and Kc prediction model. Pipes were installed on the plot to channel water through each emitter around the peanut roots (Figure 1).

The reservoir's water level was monitored to determine the volume of water distributed through the system. Furthermore, the height and diameter of the peanut canopy were also

observed at the initial crop development and mid-season stages. The cost of this IoT-assisted irrigation was fairly affordable at US\$289.00 (Table 1).

As seen in Figure 1, the soil moisture sensor is placed 10 cm from the plant stem and is responsible for delivering data to the microcontroller. At $\geq 30\%$ soil moisture content, the relay turns off the system, and it will be active when the water content is $\leq 17\%$. The IoT-assisted system uses the Blynk by pressing the switch button. When Blynk is activated via Smartphone, the NodeMCU ESP8266 microcontroller will control the relay to connect and disconnect the power line from a 220V AC source to the pump. Blynk determines this

Table 1
The list of development costs for the IoT-assisted system

Instruments	Functions	Cost (USD)
Bamboo, insect net, transparent wave fiber, plastic	Supporting plant cultivation to protect plants from pests	\$ 195.00
IoT-assisted tools to measure temperature, RH, and soil water content	Monitoring temperature, RH, and soil water content in demonstration plots	\$ 16.00
Drip irrigation system	Maintaining the drip system for the plants	\$ 78.00
Total		\$ 289.00

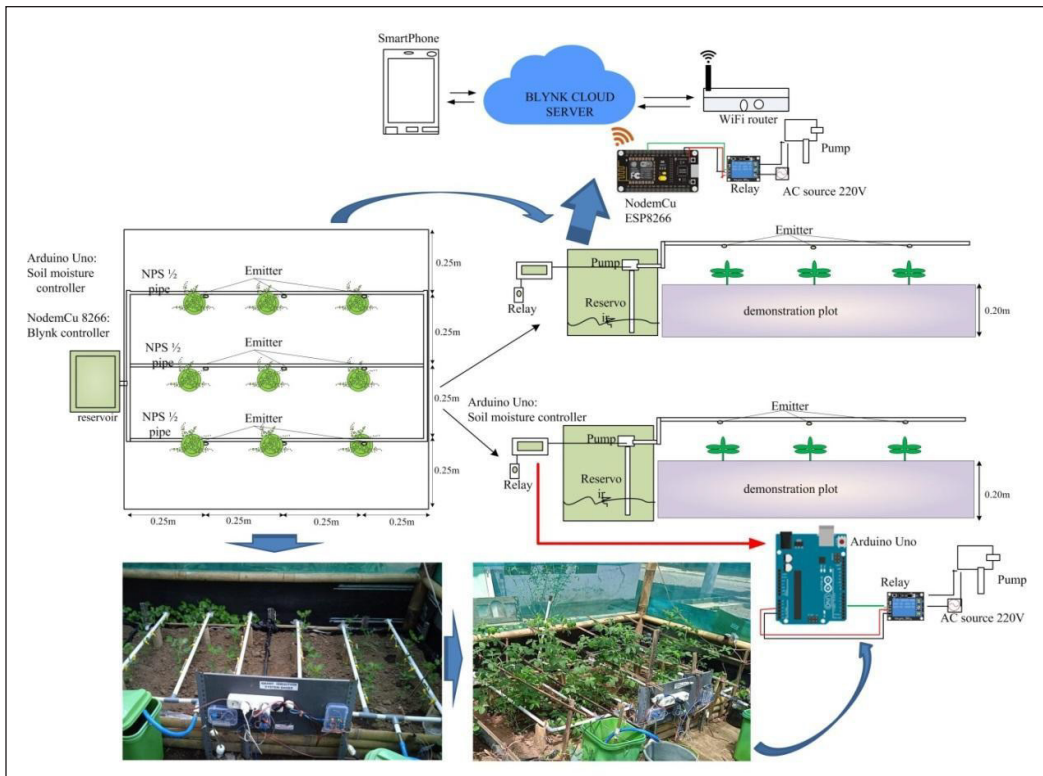


Figure 1. The plan and design of the drip irrigation system

mechanism when calculating crop water requirements. The instrument specification of the IoT-assisted system can be seen in Table 2.

Figure 2 shows two drip irrigation systems: a drip irrigation system based on a soil moisture sensor assisted by an Arduino Uno microcontroller and an IoT-assisted drip irrigation system with a NodeMCU microcontroller. The employment of these different microcontrollers was aimed at the ease of compiling the codes. Automatic drip irrigation systems based on soil moisture sensors with Arduino Uno have been widely used to ease programming code. However, this system is less effective because it requires a wireless transceiver module as a microcontroller and signal receiver. Likewise, adding a soil moisture sensor will make programming code more complex and affect the success rate and completion of the irrigation system. Coupled with Blynk, the NodeMCU Esp8266 microcontroller is equipped with an onboard antenna, making accessing and programming the code more practical.

Table 2
Specification of soil moisture sensor, water pump, Arduino Uno, and nodeMCU ESP8266

Instruments	Specification
Soil moisture sensor	Working Voltage: 3.3–5.5VDC; Output Voltage: 0–3.0VDC; Port: PH2.54–3P; Material: Plastic; Item size: 9.8 * 2.3 * 0.7cm (L * W * H); Item weight: Approx. 9g/0.32oz; price: US\$1.62.
Aquarium pump Powerhead SP 1200	AC Power: 220–240 V; Frequency: 50/60 Hz; Max Rate: 1.000 L/H; Head Max: 1.0 m; Power: 7 Watt; Price: US \$1.62.
Arduino Uno R3	Microcontroller: ATmega328; Operating Voltage: 5V; Input Voltage (recommended): 7–12V; Input Voltage (limits): 6–20V; Digital I/O Pins: 14 (of which 6 provide PWM output); Analog Input Pins: 6; DC Current per I/O Pin: 40 mA; DC Current for 3.3V Pin: 50 mA Flash; Memory: 32 KB; SRAM: 2 KB; EEPROM: 1 KB; Clock Speed: 16 MHz; Length: 68.6 mm Width: 53.4 mm; Price: US \$ 6.48.
NodeMCU ESP8266	Chip: ESP8266 (ESP-12E); Pin I/O digital: 11; Pin I/O analog: 1; Operating Voltage: 3.3 V; Clock speed: 80Mhz/160Mhz; Flash: 4M USB; price: US \$ 4.53

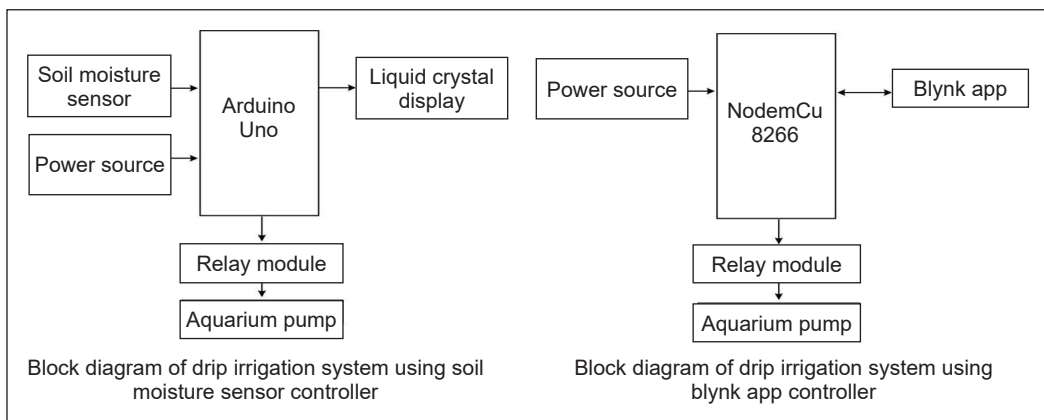


Figure 2. Block diagram of drip irrigation system

Coefficient of Uniformity (CU) Analysis

Drip irrigation is a well-known technology that reduces water consumption in the event of limited water resources while enabling proper plant growth (Kumar et al., 2022). Water distribution using drip irrigation technology utilizes hoses or pipes attached to a water tank with specific management to allow a constant water flow. It is necessary to perform a distribution uniformity test to maintain an even output, as this helps to determine the feasibility of system installation (Chaer et al., 2016; Mohamed et al., 2019). The distribution uniformity is considered very good when CU is over 90% (Henrique & França, 2022). CU ranging from 80%–90% corresponds to a good rate, while any lower rates between 70%–80% are classified under fair CU, and poor CU ranges between 60%–70% (Darimani et al., 2021). Researchers have widely used CU as a parameter to estimate the uniformity of drip irrigation (Al-Mefleh et al., 2021; Henrique & França, 2022; C. Liu et al., 2022). CU can be calculated using Equation 1.

$$CU = 100 \left(1 - \frac{\sum_{i=1}^N |x_i - \bar{x}|}{\sum_{i=1}^N x_i} \right) \quad [1]$$

Where: C_u : coefficient of uniformity in drip irrigation (%); x_i : average volume of water of the i^{th} container (ml); and \bar{x} : average volume of water (ml)

Crop Evapotranspiration (ETc) Analysis

The crop evapotranspiration (ETc) is obtained by multiplying evapotranspiration (ETo) and plant coefficient (Kc) using Equation 2. However, the Kc value is calculated using Equation 3 in conditions of limited water resources. Meanwhile, the Ke value is calculated using Equation 4, which is converted from the fraction of vegetation cover (Fc) value (Zhang et al., 2019; T. Wang et al., 2021). Fc value based on FAO is between 0–0.1 at the initial stage, 0.1–0.8 at the crop development stage, 0.8–1 at the mid-season stage, and 0.8–0.2 at the late season stage. The present study measured the Kcb rate for the peanut samples by using the DNN model, as shown in Figure 3.

$$ETc = Kc + ETo \quad [2]$$

$$Kc = Kcb + Ke \quad [3]$$

$$Ke = 0.9 * (1 - Fc) \quad [4]$$

The site's ETo rate was examined using the DNN model based on Tmean and RHmean resulting from 4 hours of observation (Figure 4). Meanwhile, the daily Tmean and RHmean are the conversion result of the 4-hour Tmean and RHmean observations (Figure 5). The ETo value was calculated every 7 days as a reference for managing the irrigation on day 8. Next, the aggregate ETo rate for 7 days was multiplied by Kc. The

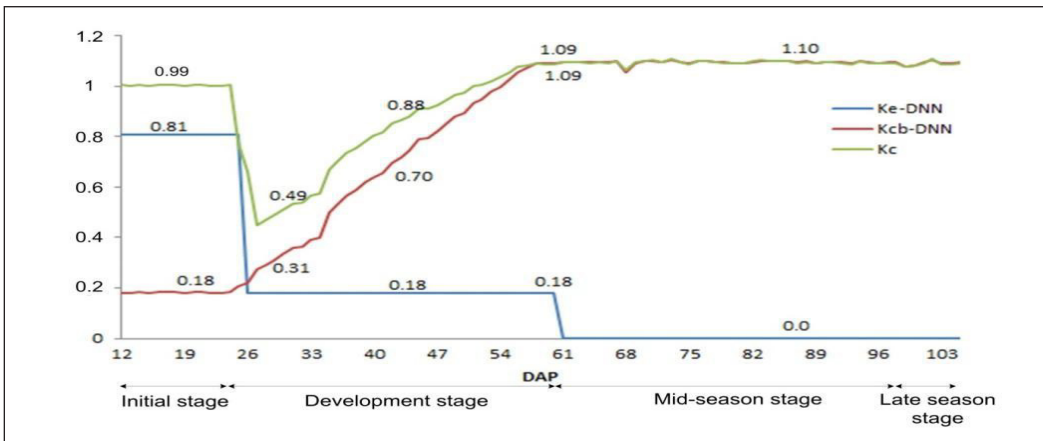


Figure 3. Value of Ke, Kcb, and Kc of peanuts

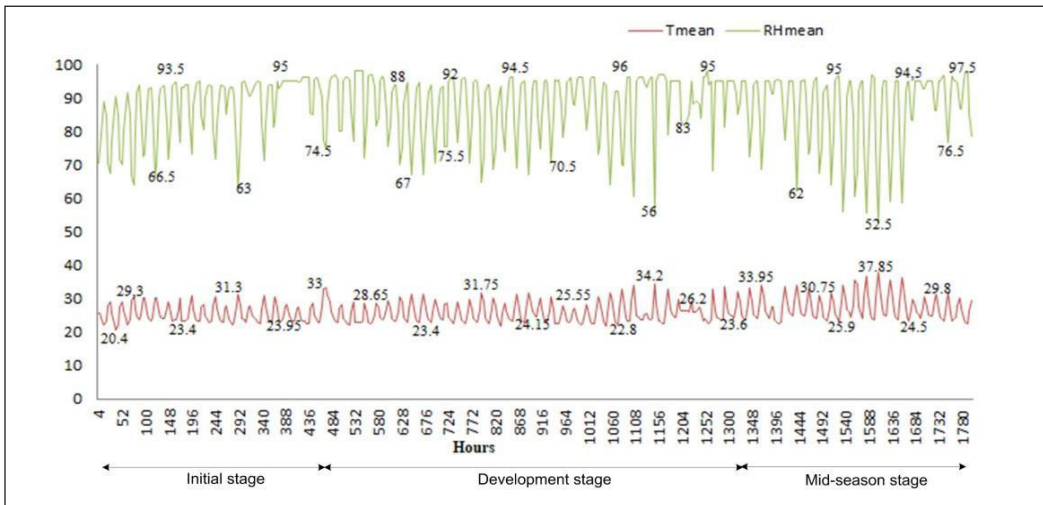


Figure 4. TMean and RHMean across stages

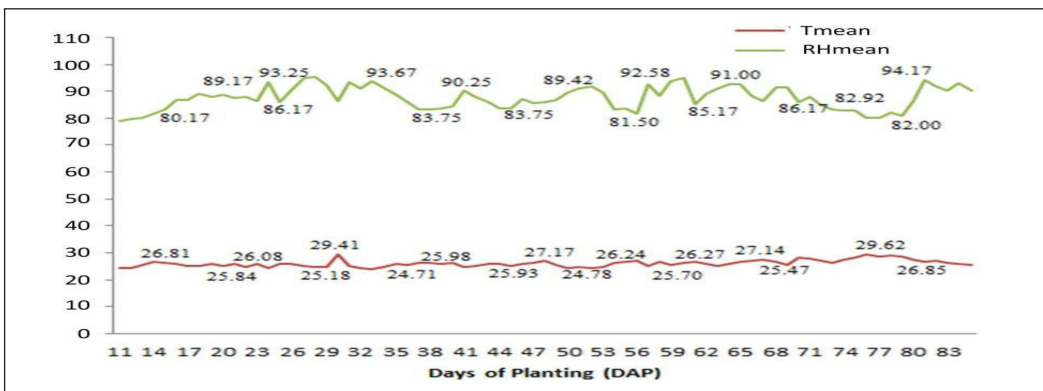


Figure 5. Daily RHmean and Tmean across DAPs

findings show that the area of the demonstration plot positively relates to the amount of water given to the plants.

DNN and Artificial Neural Networks (ANN) employ similar learning principles: supervised, semi-supervised, and unsupervised. However, DNN has more than 3 hidden layers, where multiplying and adding weights, inputs, and biases occurs in each neuron in the hidden layer using Equation 5. This difference gives DNN better performance than ANN (Ali et al., 2022; Han et al., 2018; Irfan et al., 2021). Meanwhile, the results of the multiplication and addition in the previous hidden layers are used as the input for the next hidden layer (Figure 6). The DNN architecture in this research is shown in Figure 7.

$$Y = \phi\left(\sum_{i=1}^n W_i * X_i + b\right) \tag{5}$$

Where: Y = Output; ϕ = activation function; W = weights; Xi = input; and b=bias

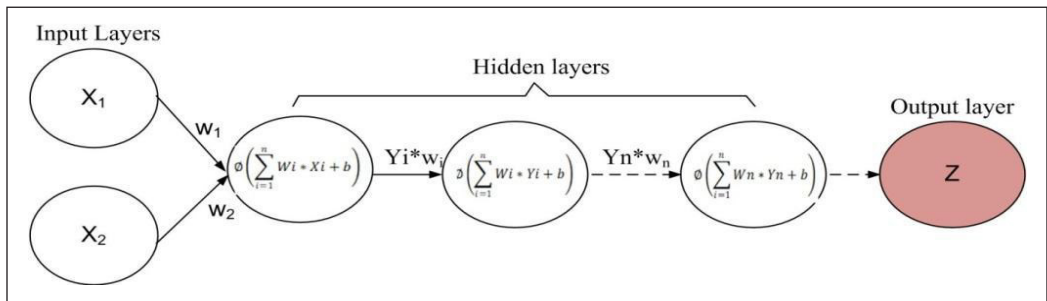


Figure 6. Calculation in DNN

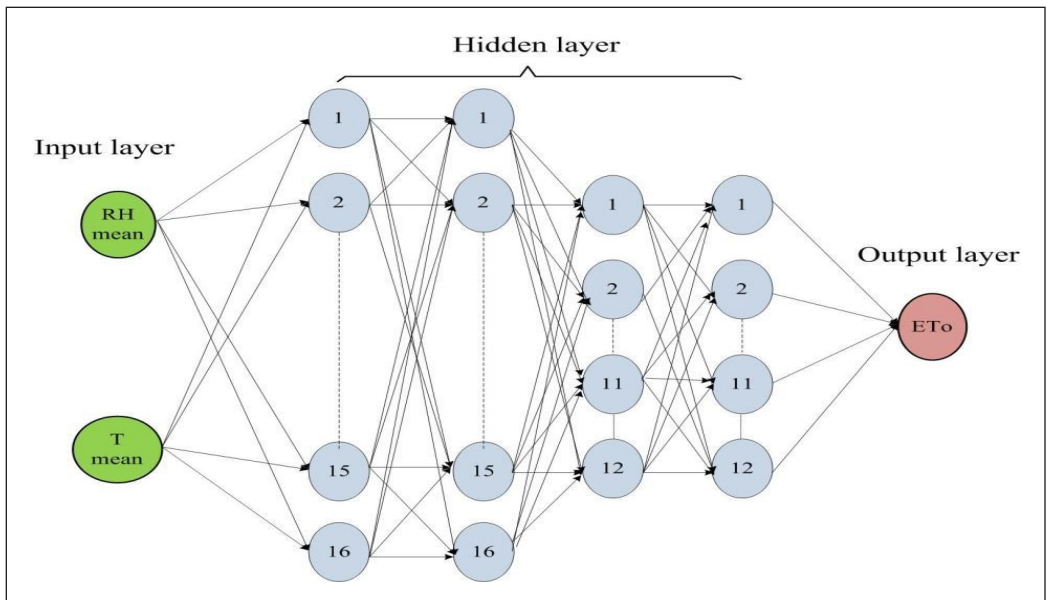


Figure 7. DNN architecture

RESULTS AND DISCUSSION

The Calibration of Reservoir and Soil Moisture

The drip irrigation system's water tank as a reservoir was calibrated to monitor the water volume. The calibration was performed using a measuring cup to find a linear relationship between the water level and volume in the tank and to predict the water distribution in the system using a linear equation. The soil moisture sensor was used to detect soil moisture or soil water content indicated by an analog value after the soil moisture sensor had been connected to an Arduino microcontroller or ESP8266 NodeMCU. Therefore, the soil moisture sensor had to be calibrated to the soil water content using the gravimetric method to predict the linear equation, as shown in Figure 8.

Figure 8 shows two essential calibration results. The first result corresponds to a strong positive correlation in the water tank with the equation $Y = 0.688x - 55.795$ and $R^2 = 0.997$. Afterward, this equation was used to calculate the volume of water distributed through the irrigation system. Another result confirmed a robust negative linear correlation between the soil moisture sensor's analog output and the gravimetric method's water content with the equation $Y = -0.1631x + 102.43$ and $R^2 = 0.932$. This linear equation was formulated in programming the code and uploaded to the Arduino Uno microcontroller to generate the data on soil water content. A drip irrigation system based on a soil moisture controller is expected to detect soil water content accurately. It is crucial to manipulate the duration of water distribution to meet predetermined water requirements.

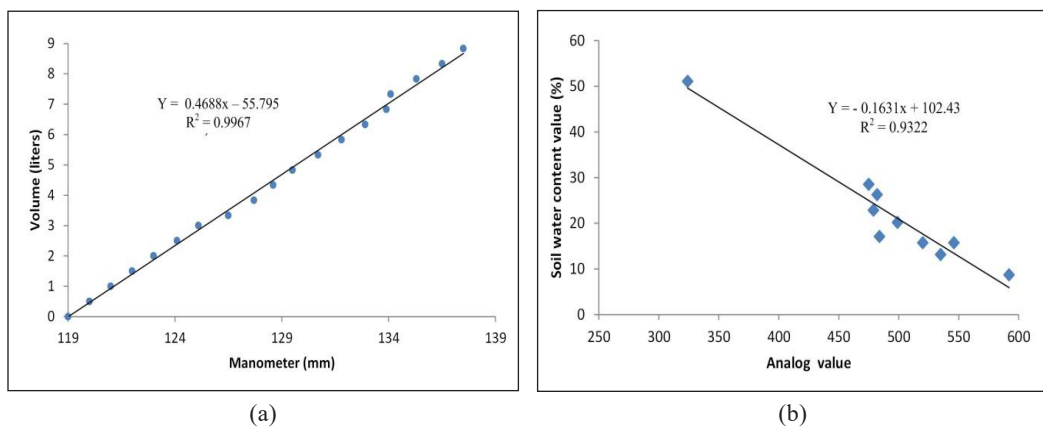


Figure 8. Calibration of: (a) water tank (a); and (b) soil moisture sensor

Coefficient of Uniformity (CU)

CU was measured on 2 different drip irrigation systems, namely drip irrigation systems with soil moisture controller and Blynk controller. The measurements were carried out at 9 emitter points with 2 repetitions (Table 3). Previous work demonstrated a decent CU

of water discharge (Q) flowing through each emitter, as indicated by CU over 90% and between 80%–90% (Martinez et al., 2022). The present study also reported similar results where the drip irrigation system with soil moisture and Blynk controller generated CUs of 90.15% and 86.58%, respectively. This difference was presumed to occur due to the challenge of maintaining uniform water flow at each emitter.

Table 3
The CU of drip irrigation system

Emitter	Controller System			
	Soil moisture		Blynk	
No.	Q1 (ml/min)	Q2 (ml/min)	Q1 (ml/min)	Q2 (ml/min)
1	77.14	62.96	50.00	51.85a
2	77.14	77.78	36.36	51.85
3	60.00	74.07	50.00	44.44
4	68.57	81.48	31.82	44.44
5	60.00	70.37	59.09	44.44
6	77.14	81.48	59.09	62.96
7	68.57	59.26	50.00	62.96
8	68.57	66.67	50.00	44.44
9	51.43	66.67	63.64	59.26
CU (%)	90.15		86.58	
Drip Irrigation Discharge (ml/min)	624.66		458.33	

Crop Evapotranspiration (ET_c)

Evapotranspiration (ET_o) was examined using a DNN model with 4 hidden layers and 2 input parameters, temperature (T) and air humidity (RH), logged for 7 days with a 4-hour observation each day. Next, the ET_o rate predicted by DNN (ET_o-DNN) was multiplied by the K_c for peanuts to determine ET_c and water requirements for each demonstration plot.

Figure 9 shows that the ET_o rates in the initial and development phases are higher than the ET_c rates. However, at the end of the development phase, the K_c rate reaches 1.09, which implies a higher ET_c rate than ET_o. Meanwhile, the ET_o rate varies across phases, apparently because it was generated by the DNN model on different rates of temperature (T) and air humidity (RH) across days after planting (DAPs). It is congruent with previous studies stating that increasing temperature leads to higher ET_o rates, while a negative correlation applies to RH (Dong et al., 2020; Zhu et al., 2022).

Crop Growth

Providing irrigation to plants will escalate plant growth and yields. It can only be achieved when water resources are used efficiently to maximize growth. In this regard, excessive or

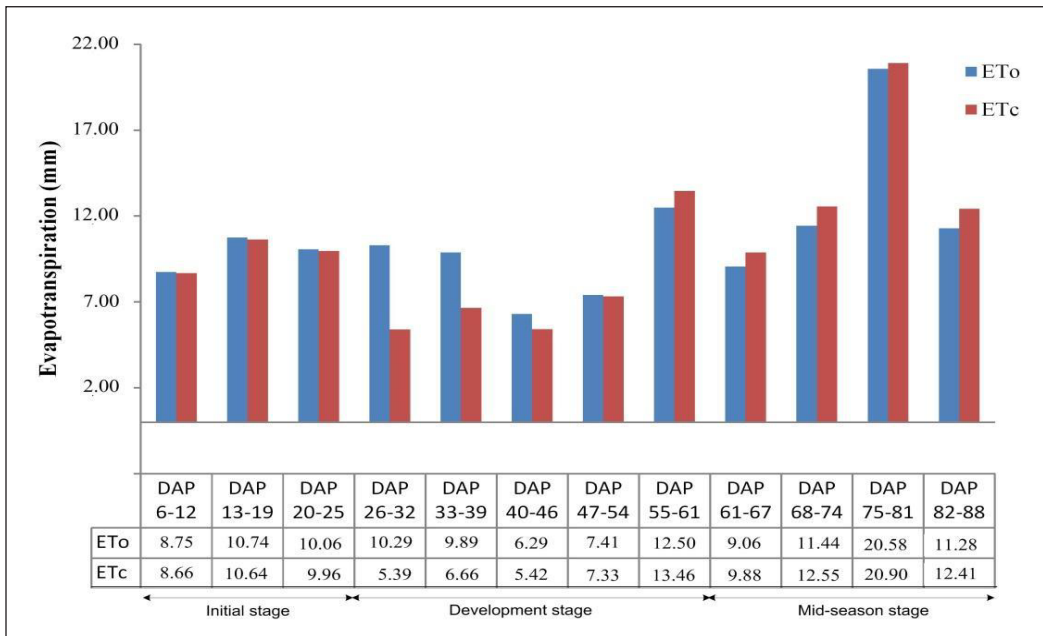


Figure 9. ETo and ETc rates for the peanut samples

insufficient water supply will adversely affect plant growth, so irrigation must be adjusted to the water required (Sezen et al., 2022).

The growth of peanuts was significantly influenced by the water availability in the soil, as shown by the growth of plant height and canopy area. The irrigation system also influenced plant growth due to differences in the volume of water emitted on plant surfaces. It can be seen in Figure 10, which shows that the irrigation system driven by a soil moisture sensor controller (SC) leads to a better height in the initial phase than the irrigation system with the Blynk controller (BC). However, in the development and mid-season phases, a higher water supply with BC results in better height than SC.

The canopy diameter increases in line with the increment of DAP, which affects the increasing evapotranspiration (Figure 10). It is also evidenced by the increasing water supply in each irrigation system from the initial phase to the mid-season phase. The figure also documents that the BC-based irrigation system generates an exemplary effect on plant height and canopy diameter due to the optimal water supply.

Yield

The use of AI-based analysis to generate ETc-DNN models helps to accurately determine the volume of water flow relative to crop water requirement, thus ensuring optimal photosynthesis, metabolism, and transportation of food materials from the roots to all parts of the plant. The results of the previous study also confirm a positive linear

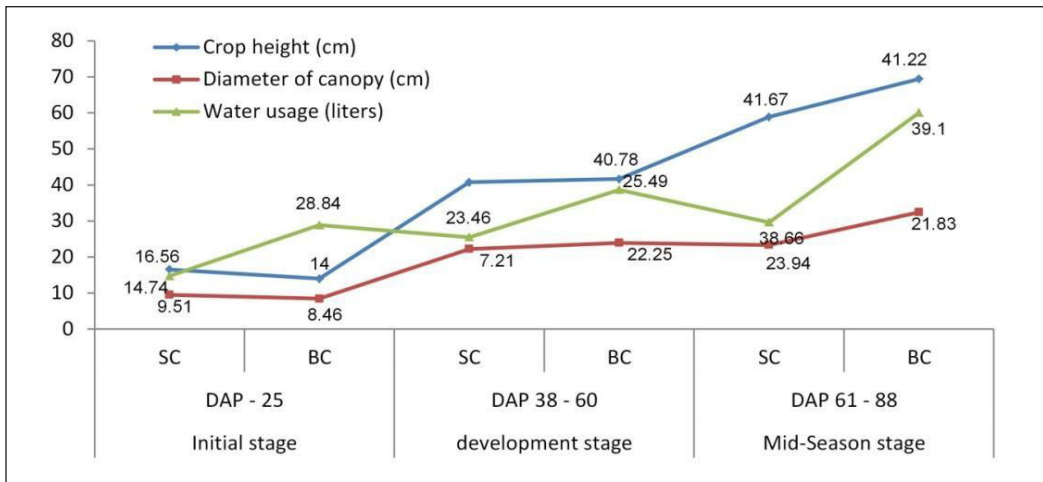


Figure 10. The height and diameter of the peanut canopy

relationship between crop yields and crop water requirement, where appropriate water supply stimulates better harvest (Bennett & Harms, 2011; J. Liu et al., 2022). Figure 11 shows higher peanut yield in a drip irrigation system that engages the AI-based analysis (ETc-DNN) to determine water requirement compared to another system assisted by a soil moisture sensor controller (SC), which determines soil water content around plant roots (ETc-SC).

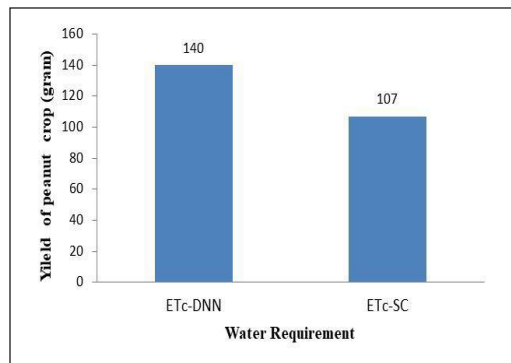


Figure 11. Peanut yield in irrigation systems based on soil moisture, blynk, and timer controllers

CONCLUSION

This study has corroborated that the IoT-assisted drip irrigation system with AI-based analysis (ETc-DNN) has helped meet crop water requirements better than ETc-SC. The system has also been influential in attaining higher peanut yields than a drip irrigation system with a soil moisture sensor controller (SC). Another advantage of using an IoT-assisted irrigation system with AI-based analysis is better efficiency in water distribution based on the plant’s water needs. Thus, the plants’ height and canopy area were improved, and their growth and yields improved.

ACKNOWLEDGEMENT

The authors extend their utmost gratitude to their mentors and all who have contributed to this research.

REFERENCES

- Ali, A., Rehman, A. U., Almogren, A., Eldin, E. T., & Kaleem, M. (2022). Application of deep learning gated recurrent unit in hybrid shunt active power filter for power quality enhancement. *Energies*, *15*(20), Article 7553. <https://doi.org/10.3390/en15207553>
- Al-Mefleh, N. K., Talazi, S., & Naser, K. A. (2021). Assessment of treated wastewater reuse in drip irrigation under different pressure conditions. *Water*, *13*(8), 1–15. <https://doi.org/10.3390/w13081033>
- Bennett, D. R., & Harms, T. E. (2011). Crop yield and water requirement relationships for major irrigated crops in Southern Alberta. *Canadian Water Resources Journal*, *36*(2), 159–170. <https://doi.org/10.4296/cwrj3602853>
- Chaer, M. S. I., Abdullah, S. H., & Priyati, A. (2016). Application of arduino microcontroller on drip irrigation system for mustard plant (*Brassica juncea*). *Jurnal Ilmiah Rekayasa Pertanian Dan Biosistem*, *4*(2), 228–238.
- Darimani, H. S., Kpoda, N., Suleman, S. M., & Luut, A. (2021). Field performance evaluation of a small-scale drip irrigation system installed in the Upper West Region of Ghana. *Computational Water, Energy, and Environmental Engineering*, *10*, 82–94. <https://doi.org/10.4236/cweee.2021.102006>
- Dong, W., Li, C., Hu, Q., Pan, F., Bhandari, J., & Sun, Z. (2020). Potential evapotranspiration reduction and its influence on crop yield in the North China Plain in 1961–2014. *Advances in Meteorology*, *2020*(1), Article 3691421. <https://doi.org/10.1155/2020/3691421>
- Ferrarezi, R. S., Nogueira, T. A. R., & Zepeda, S. G. C. (2020). Performance of soil moisture sensors in Florida sandy soils. *Water*, *12*(2), Article 358. <https://doi.org/doi:10.3390/w12020358>
- Gimpel, H., Graf-Drasch, V., Hawlitschek, F., & Neumeier, K. (2021). Designing smart and sustainable irrigation: A case study. *Journal of Cleaner Production*, *315*, Article 128048. <https://doi.org/10.1016/j.jclepro.2021.128048>
- Han, R., Yang, Y., Li, X., & Ouyang, D. (2018). Predicting oral disintegrating tablet formulations by neural network techniques. *Asian Journal of Pharmaceutical Sciences*, *13*(4), 336–342. <https://doi.org/10.1016/j.ajps.2018.01.003>
- Henrique, G., & França, F. (2022). Advance time to determine injection and flushing times in drip fertigation. *Horticulturae Article*, *8*(1103), 1–11.
- Irfan, M., Ramlie, F., Widiyanto, Lestandy, M., & Faruq, A. (2021). Prediction of residential building energy efficiency performance using deep neural network. *IAENG International Journal of Computer Science*, *48*(3), 1–7.
- Jaafar, H., & Kharroubi, S. A. (2021). Views, practices and knowledge of farmers regarding smart irrigation apps: A national cross-sectional study in Lebanon. *Agricultural Water Management*, *248*, Article 106759. <https://doi.org/10.1016/j.agwat.2021.106759>
- Kullu, P., Majeedullah, S., Pranay, P. V. S., & Yakub, B. (2020). Smart urban farming (entrepreneurship through Epics). *Procedia Computer Science*, *172*(2019), 452–459. <https://doi.org/10.1016/j.procs.2020.05.098>
- Kumar, C. N., Selvam, S. P., Ramanathan, S. P., Kalarani, S., Nagarajan, G., & Duraisamy, S. (2022). Effect of drip irrigation and inter cropping systems on growth characters of maize. *International Journal of Plant & Soil Science*, *34*(2), 36–42. <https://doi.org/10.9734/ijpss/2022/v34i230834>

- Liu, C., Wang, R., Wang, W., Hu, X., Wu, W., & Liu, F. (2022). Different irrigation pressure and filter on emitter clogging in drip phosphate fertigation systems. *Water*, *14*(6), 1–18. <https://doi.org/10.3390/w14060853>
- Liu, J., Sun, B., Shen, H., Ding, P., Ning, D., Zhang, J., & Qiu, X. (2022). Crop water requirement and utilization efficiency-based planting structure optimization in the Southern Huang-Huai-Hai Plain. *Agronomy*, *12*(9), 1–21. <https://doi.org/10.3390/agronomy12092219>
- Martinez, C. G., Wu, C. L. R., Fajardo, A. L., & Ella, V. B. (2022, June). Hydraulic performance evaluation of Low-cost gravity-fed drip irrigation systems under constant head conditions. In *IOP Conference Series: Earth and Environmental Science* (Vol. 1038, No. 1, p. 012005). IOP Publishing. <https://doi.org/10.1088/1755-1315/1038/1/012005>
- Mason, B., Rufi-Salis, M., Parada, F., Gabarrell, X., & Gruden, C. (2019). Intelligent urban irrigation systems: Saving water and maintaining crop yields. *Agricultural Water Management*, *226*, Article 105812. <https://doi.org/10.1016/j.agwat.2019.105812>
- Mohamed, A. Z., Peters, R. T., Zhu, X., & Sarwar, A. (2019). Adjusting irrigation uniformity coefficients for unimportant variability on a small scale. *Agricultural Water Management*, *213*, 1078–1083. <https://doi.org/10.1016/j.agwat.2018.07.017>
- Quimbata, W., Toapaxi, E., & Llanos, J. (2022). Smart irrigation system considering optimal energy management based on model predictive control (MPC). *Applied Sciences*, *12*(9), 1–18. <https://doi.org/10.3390/app12094235>
- Rani, S. B., Venu, N., Ananthula, M. K., & Engli, A. (2022). IoT based smart irrigation system using node MCU. *International Journal for Innovative Engineering and Management Research*, *11*(06), 100–106.
- Sezen, S. M., Ahmad, I., Habib-ur-Rahman, M., Amiri, E., Tekin, S., Oz, K. C., & Maambo, C. M. (2022). Growth and productivity assessments of peanut under different irrigation water management practices using CSM-CROPGRO-Peanut model in Eastern Mediterranean of Turkey. *Environmental Science and Pollution Research*, *29*(18), 26936–26949. <https://doi.org/10.1007/s11356-021-17722-w>
- Suhardi, Marhaenanto, B., Taruna, B., Putra, W., & Winarso, S. (2023). IoT-based evapotranspiration estimation of peanut plant using deep neural network. *INMATEH - Agricultural Engineering*, *70*(2), 487–496. <https://doi.org/https://doi.org/10.35633/inmateh-70-47>
- Wang, T., Melton, F. S., Pôças, I., Johnson, L. F., Thao, T., Post, K., & Cassel-Sharma, F. (2021). Evaluation of crop coefficient and evapotranspiration data for sugar beets from landsat surface reflectances using micrometeorological measurements and weighing lysimetry. *Agricultural Water Management*, *244*, Article 13. <https://doi.org/10.1016/j.agwat.2020.106533>
- Wang, Y., Li, S., Cui, Y., Qin, S., Guo, H., Yang, D., & Wang, C. (2021). Effect of drip irrigation on soil water balance and water use efficiency of maize in northwest China. *Water*, *13*(2), Article 217. <https://doi.org/10.3390/w13020217>
- Zahid, B., Ansari, R., Cheema, M. J. M., & Anjum, L. (2020). Evaluation of deficit irrigation regime, row spacing and dual plantation of drip irrigated tomato under high tunnel. *Journal of Central European Agriculture*, *21*(4), 851–860. <https://doi.org/10.5513/JCEA01/21.4.2990>

- Zhang, Y., Han, W., Niu, X., & Li, G. (2019). Maize crop coefficient estimated from UAV-measured multispectral vegetation indices. *Sensors*, *19*(23), 1–17. <https://doi.org/10.3390/s19235250>
- Zhu, B., Zhang, Q., Yang, J. H., & Li, C. H. (2022). Response of potential evapotranspiration to warming and wetting in Northwest China. *Atmosphere*, *13*(2), Article 21. <https://doi.org/10.3390/atmos13020353>

Assessment of Nitrate Reduction by Microbes in Artificial Groundwater Medium

Preeti Thakur and Pammi Gauba*

Department of Biotechnology, Jaypee Institute of Information & Technology, Noida, Uttar Pradesh 201307, India

ABSTRACT

There are significant reasons for nitrate contamination in groundwater (Delhi, India): sewage, runoff from landfill sites, nitrogenous chemical fertilisers, and pesticides from agricultural lands. The highest recorded concentration of nitrate in Delhi's groundwater is reported to be 1500 mg/l. Consumption of high nitrate through water may pose serious health problems in humans, especially children (below five years). The study's primary objective was to isolate and identify nitrate-remediating microbes from the nitrate-contaminated site Okhla Barrage, located on the Yamuna River in Delhi, India. A total of 11 different strains were isolated from this site. Among these four strains exhibited 40%–50% remediation efficiency at a nitrate concentration of 1000 mg/l. Molecular characterisation revealed that these four strains, *Enterobacter aerogenes*, *E. coli* K12, *Klebsiella oxytoca* and *Lelliottia amnigena*, belong to the Enterobacteriaceae family. This study assessed the nitrate remediation potential of isolated microbes in groundwater with 1000 and 1500 mg/l nitrate concentrations. By using a 2% inoculum, the microbes were incubated anaerobically at room temperature for ten days. Nitrate concentrations were monitored every 48 hours. *Lelliottia*, *E. coli*, and *Enterobacter* reduced nitrate (1500 mg/l) by approximately 42%, 24%, and 29%, respectively, while *K. oxytoca* showed minimal reduction. *L. amnigena* exhibited superior nitrate removal efficiency compared to other strains. According to the reported data, these strains are known to reduce nitrate concentrations of 620 mg/l. However, our findings demonstrate a remarkable nitrate remediation capacity of 1500 mg/l, showcasing

a novel contribution to this study. Further detailed analysis for condition optimisation and association of microbe-microbe could be more helpful.

Keywords: Enterobacteriaceae, groundwater, microbe-microbe association, nitrate, remediation

ARTICLE INFO

Article history:

Received: 21 January 2024

Accepted: 10 June 2024

Published: 25 October 2024

DOI: <https://doi.org/10.47836/pjst.32.6.18>

E-mail addresses:

preetithakur603@gmail.com (Preeti Thakur)

pammi.gauba@jiit.ac.in (Pammi Gauba)

* Corresponding author

INTRODUCTION

Many pollutants, such as heavy metals and organic and inorganic pollutants, cause water pollution. Among them, a significant contribution is from inorganic pollutants. Nitrate is one of those inorganic pollutants with a substantial presence in groundwater and has become one of the leading problems worldwide (Zhang et al., 2018; Zhao et al., 2022). In India, its high concentration in drinking water is regulated by an Indian agency, BIS, which sets the permissible limit (ideal for use) at 45 mg/l (Tyagi et al., 2020; Raja & Neelakantan, 2021). Excess nitrate concentration in groundwater causes significant effects on human health and the environment (Addiscott & Benjamin, 2004; Karunanidhi et al., 2021). These include respiratory problems (Fewtrell, 2004), hypertension (Malberg et al., 1978), goiter (Morris et al., 2011), thyroid cancer (Tariqi & Naughton, 2021), genetic mutations, gastrointestinal cancer (Hameed et al., 2021), congenital disabilities, and Blue Baby syndrome (Majumdar, 2003). The main reason for the rising nitrate concentration is the excessive use of nitrogenous chemical fertilisers for agricultural activity (Singh & Craswell, 2021). Additionally, inadequate treatment of domestic and industrial wastewaters, leachate from landfill sites and livestock manure contribute to nitrate pollution.

Delhi, the capital of India, is heavily affected by nitrate contamination of groundwater (Tirkey et al., 2017). Some parts of Delhi, like Chattarpur, Inderlok, and Inderapuri, are affected by a high nitrate concentration of 1500mg/l according to 'groundwater yearbook 2011-12' by CGWB (Central Ground Water Board). Consequently, BIS (Bureau of Indian standard) is allowed to set the maximum limit (this concentration can be treated, but above this level, water can be shut down until corrected) for nitrate at 100 mg/l for drinking water (Reddy, 2023). Furthermore, several other states, including Bihar, Haryana, Uttar Pradesh, Punjab, Rajasthan, Karnataka, and Kerala, also contend with elevated nitrate concentrations, surpassing the safety benchmark of 45 mg/l (Sikdar, 2018).

A high nitrate concentration in drinking water creates many health issues in humans. Approximately 85% of people depend on groundwater. Nitrate in water makes it unsafe for human consumption (Ward et al., 2018). It is, therefore, necessary to treat the polluted groundwater. Several technologies have been developed to remove nitrate from drinking water. It includes ion exchange (Jaeshin & Benjamin, 2004), reverse osmosis (Schoeman & Steyn, 2003; Kim et al., 2007), electro dialysis (Elmidaoui et al., 2003; Sahli et al., 2006), chemical denitrification (Lin & Wu, 1996), ion exchange (Matos et al., 2006) and catalytic reduction (Reddy & Lin, 2000; Maia et al., 2007). These techniques are effective in nitrate removal, but the commercial application of these techniques is pretty expensive.

On the other side, many researchers and scientists focus on bioremediation. Bioremediation of nitrate became practically possible when using exogenous carbon sources (Li et al., 2021). A large number of organic carbon sources are required in the denitrification process, where microbial strains use organic carbon as electron donors (Qin

et al., 2017). Several strains with known nitrate remediation potential are listed in Table 1. Their remediation capacity typically extends only to concentrations up to 620 mg/l. As per the literature, it is known that these isolates (*E. coli*, *Enterobacter aerogenes*, *Lelliottia amnigena*) have nitrate remediation potential. However, our study showed that these strains now remediate high nitrate concentration.

Table 1
Nitrate remediation potential of reported microbial strains

Microbial strain/ consortium	Initial nitrate concentration (mg/l)	Percentage of nitrate remediation/reduced up to (%)	References
1. <i>Escherichia coli</i>	620	90	Bing & Hollocher, 1988
2. <i>Enterobacter aerogenes</i>	620	90	Bing & Hollocher, 1988
3. <i>Enterobacter amnigenus</i>	138	50	Fazzolari et al., 1990
4. <i>Pseudomonas</i> sp. KW1 and <i>Bacillus</i> sp. YW4	100	99.4	Rajakumar et al., 2008
5. <i>Pseudomonas putida</i> AD-2	254.6	95.9	Kim et al., 2008
6. <i>Bacillus subtilis</i> JD-014	100	98.99	Yang et al., 2021
7. <i>Enterobacter cloacae</i> DK-6	101.70	86.98	Liao et al., 2022
8. <i>Pseudomonas aeruginosa</i>	100	93	Rajta et al., 2020

All isolated strains had the potential to remediate nitrate (Thakur & Gauba, 2021). Additionally, these microbes also showed nitrate remediation in groundwater except *K. oxytoca*. An *in-silico* study was also done of two microbes where *L. amnigena* has assimilatory and respiratory nitrate reductase genes while *E. coli* K12 has only the respiratory nitrate reductase gene (Thakur & Gauba, 2023). As per the literature, *Enterobacter aerogenes* had only the respiratory nitrate reductase gene, a membrane-bound enzyme (Riet & Planta, 1975).

The assimilation of the nitrate reductase gene found in the cytoplasm is involved in the nitrate assimilation process. It converts the nitrate into amino acids, which are finally uptake by microbes to increase their number. Conversely, the respiratory nitrate gene is a membrane-bound enzyme involved in denitrification, which converts the nitrate into nitrogen. Therefore, the presence of both processes in *L. amnigena* makes this bacterium more potent in nitrate remediation in comparison with the other two (*E. coli* K12 and *Enterobacter aerogenes*) (Thakur & Gauba, 2024). Besides this, all microbes showed nitrate remediation under strict anaerobic conditions, whereas *Enterobacter aerogenes* remediated nitrate under aerobic and anaerobic conditions (Madmanang & Sriwiryarat, 2019).

In the previous study, four microbes were isolated belonging to the Enterobacteriaceae family, which were subsequently molecularly characterised and identified as *Lelliottia amnigena*, *E. coli* K12, *K. oxytoca* and *Enterobacter aerogenes* (Thakur & Gauba, 2021).

This paper assessed the potential of these isolated microbes in a groundwater medium containing nitrate concentrations of 1000 mg/l and 1500 mg/l. The microbes exhibited 25%–42% nitrate remediation except *K. oxytoca* at the 1500 mg/l concentration. *L. amnigena* demonstrated the highest remediation potential compared to the other two strains.

MATERIALS AND METHODS

Study Area

Water samples were collected from the polluted Yamuna River site (Okhla Barrage) as per the reported data (CPCB, 2015; Srivastava et al., 2015), as presented in Figure 1.

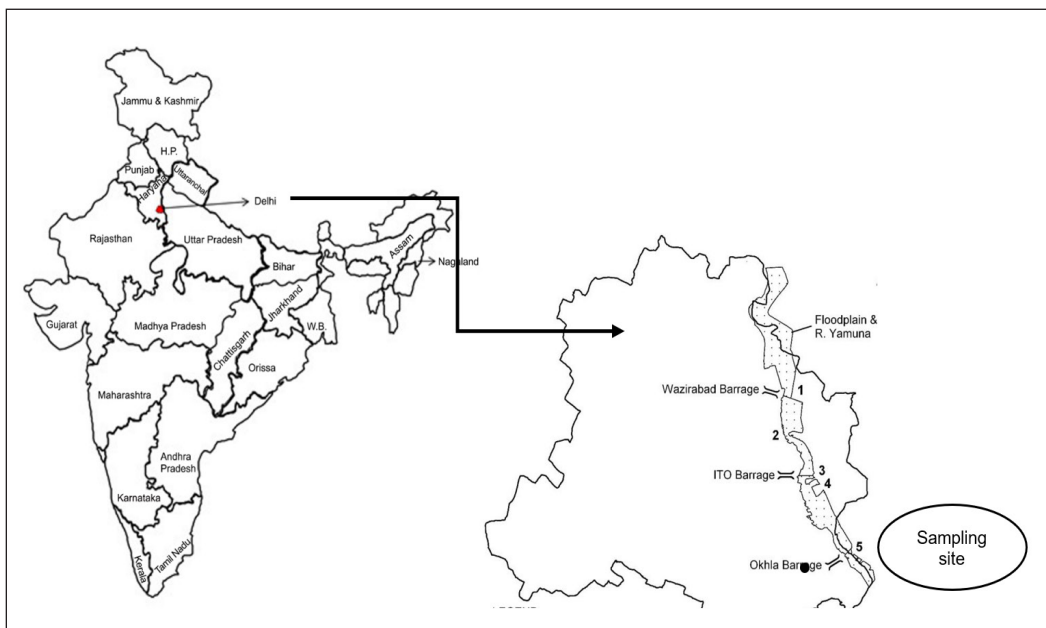


Figure 1. Sampling site of Yamuna River (Okhla Barrage) Delhi

Isolation of Microbes from Polluted Yamuna River Site

The stock solution was prepared where 1 ml water sample was taken in 10 ml demineralised water; further, the samples underwent serial dilution ranging from 10^{-1} to 10^{-9} , and 100 μ l aliquots were transferred from dilutions 10^{-7} to 10^{-9} onto nutrient agar petriplates containing 500 mg/l nitrate concentration. These plates were then incubated at 37°C for 48 hours. Following incubation, each colony was carefully picked up using a sterile inoculating loop and transferred to fresh petri plates containing nitrate. Quadrant streaking was performed until pure colonies were obtained. Concurrently, Gram staining was conducted repeatedly until consistent morphology was observed on two consecutive occasions. The remediation

rate of isolated microbes was calculated at 500–1000 mg/l nitrate concentration, and they were further Molecular characterised (Thakur & Gauba, 2021).

Assessment of Nitrate Remediation Rate of Isolated Microbes in Groundwater Medium

Preparation of Groundwater Medium

Groundwater media was designed with composition KH_2PO_4 - 0.235 g/l, K_2HPO_4 - 0.09 g/l, NH_4Cl - 0.1 g/l, MgCl_2 - 0.0248 g/l, CaCl_2 - 0.141 g/l (Pan et al., 2014) and 5 ml/l Vitamin and minerals mixture (Lovley et al., 1988), amended with acetate (10 mM concentration) and nitrate (1000 and 1500 mg/l) dissolved in demineralised water where acetate prepared from sodium acetate and nitrate from potassium nitrate.

Preparation of Nitrate Standard Solution

The process involved drying 3.6 g of KNO_3 at 105°C for 24 hours, then dissolved in 1000 ml of deionised water, resulting in a solution labelled 1000 mg/L nitrate-nitrogen. Subsequent calculations converting between nitrate and nitrate-nitrogen were conducted using the Equations 1 and 2:

$$\text{Nitrate} = \text{Nitrate-nitrogen} \times 4.43 \quad [1]$$

$$\text{Nitrate-nitrogen} = \text{Nitrate} \times 0.226 \quad [2]$$

Inoculation of Enterobacteriaceae Strains in Groundwater Medium

Eleven microbes were isolated from a polluted site (DebRoy et al., 2012). Among these, four bacterial strains exhibited promising capabilities in nitrate remediation, effectively reducing it to a concentration of 1000 mg/l. All four strains belong to the Enterobacteriaceae family. These isolates were then inoculated in a groundwater medium containing 1000 mg/l and 1500 mg/l of nitrate concentration. Each strain was inoculated (2% inoculum) in a groundwater medium and incubated at room temperature (27°C), in an anaerobic state, and kept under dark conditions for 10 days (192–240 hours). Following the incubation period, samples were extracted to assess the residual nitrate concentration in the media at 420 nm (LABMAN UV-VIS), concurrently with the measurement of bacterial growth at 600 nm. Both the optical density of the microbes and the nitrate concentration in the media were monitored at regular intervals. The optical density was primarily measured by bacteria, followed by centrifugation to separate the cells from the supernatant. The supernatant was then collected to determine the nitrate concentration. In both conditions, media is used as blank and set as zero. Then, a sample reading was taken. LABMAN UV-VISIBLE spectro was used to measure the optical density.

Method to Calculate Nitrate Remediation Rate (Sodium Salicylate Method)

Cultures were centrifuged for 10 mins at 8609RCF (Relative Centrifugal Force). The supernatant (40 µl) and 5% salicylic acid in sulphuric acid (200 µl) were added. The mixture was vortexed and incubated in the dark for 10 minutes (DebRoy et al., 2012). The reaction was stopped after adding 2 ml NaOH (4N NaOH). The absorbance was taken at 420 nm after 20 mins of incubation. The nitrate remediation rate was calculated using Equation 3.

$$\text{Degree of remediation} = \frac{(X_0 - X_1) \times 100}{X_0} \quad [3]$$

Where X_0 is the initial amount of nitrate, and X_1 is the amount after remediation. The final results are calculated using control samples (media without microorganisms) (Chouhan et al., 2012).

A control sample (media with nitrate concentration but devoid of microbes) was included for each experimental set, and its initial optical density was recorded at 420 nm. Following incubation, the optical density of samples containing both nitrate concentration and microbes was measured. The percentage change in nitrate concentration was calculated using Equation 4.

$$\frac{(\text{Initial concentration of nitrate} - \text{Final concentration of nitrate})}{\text{Initial concentration of nitrate}} \times 100 \quad [4]$$

Initial Concentration of Nitrate

This method uses 5% salicylic acid in sulphuric acid and sodium hydroxide chemical. This method is based on an electrophilic aromatic substitution reaction in which Sulfosalicylic acid (5% salicylic acid in sulphuric acid) reacts with nitrate and forms nitrobenzoic compounds. After adding sodium hydroxide (alkaline condition), this nitrobenzoic compound converts into a quinoid compound, which gives it a yellow colour. The darkness of the yellow colour shows the presence of high nitrate in media and vice versa. It is a colourimetric method. This yellow complex gives maximum absorption at 420 nm wavelength, and the absorbance is directly proportional to the nitrate content.

Molecular Characterisation of Microbes by 16S rRNA Gene

Genomic DNA Extraction from Microbes

Each isolated colony was transferred into 5 ml of Nitrate Broth and incubated at 37°C with agitation at 200 rpm in a shaker incubator. After growth, 1.5 ml of bacterial culture was centrifuged at 4°C for 10 minutes at 4000 rpm. Following centrifugation,

the supernatant was carefully removed, and the pellet was resuspended in 180 µl of lysozyme solution (pH 8.0) before incubating at 37°C for 30 minutes until lysis occurred. The lysed cells were then briefly kept at -80°C for 10 minutes. Subsequently, 30µl of lysis solution (pH 8.0) was added, and the mixture was incubated on ice for 10 minutes. A volume of Phenol-Chloroform (1:1) was added to the tube to facilitate DNA separation from proteins (1). After centrifugation at 8000 rpm for 5 minutes at 4°C, the upper layer containing DNA was carefully transferred to a new tube. Chloroform (500 µl) was added to this upper layer, followed by another round of centrifugation. After centrifugation, the upper layer was collected, and 1/10th part of 1M NaCl and 2–2.5 volumes of absolute ethanol were added. The tube was then placed at -80°C for 30 minutes and subsequently centrifuged at 10,000 rpm for 30 minutes at 4°C. After centrifugation, the supernatant was completely decanted, and the DNA pellet was washed with 70% chilled ethanol. The washed pellet was centrifuged at 8000 rpm for 5 minutes at 4°C, dried, and dissolved in 20 µl of TE buffer.

Amplification of 16S rRNA Gene

Microbes were identified using the polymerase chain reaction (PCR) method, with bacterial genomic DNA isolated following the Sambrook protocol. Universal primers 27F (5-AGAGTTTGATCCTGGCTCAG-3) and 1492r (5-CGGTACCTTGTTACGACTT-3) were amplified. The reaction mix was prepared in a total volume of 20 µl, comprising 10µl of PCR master mix (Genex), 0.4 µl of Primer F, 0.4 µl of Primer R, 2 µl of DNA template (50 ng/µl), and 7.2µl of nuclease-free water (Hyclone). The amplification was carried out with a thermal profile consisting of an initial denaturation step at 95°C for 5 minutes, followed by 30 cycles of denaturation at 95°C for 1 minute, annealing at 58°C for 1 minute, and extension at 72°C for 2 minutes. A final extension step at 72°C for 10 minutes was performed. The PCR products were then analysed using 1% agarose gel electrophoresis. After electrophoresis, the gel was stained with ethidium bromide and visualised under UV light to detect the amplified DNA bands.

RESULTS

Four different microbes were isolated and identified from water samples of the polluted site of Yamuna River (Okhla Barrage). After molecular characterisation, the sequence of the 16S rRNA gene of each strain was submitted to GenBank. They belong to the Enterobacteriaceae family and are identified as *Enterobacter aerogenes* (MN252552), *E. coli* K12 (MN754025), *K. oxytoca* (MT457847) and *Lelliottia amnigena* (MN647560). Further, the remediation rate of microbes was checked in a Groundwater medium containing various nitrates.

Remediation Rate of Strains in Groundwater Medium

Following an initial incubation period of 2 days, a sample was extracted after 48 hours to assess the remaining nitrate concentration. This process was repeated at 48-hour intervals. Figures 2 to 7 illustrate the remediation rates of microbes at different nitrate concentrations of 1000 mg/l and 1500 mg/l. Analysis of the readings suggests that *Lelliottia amnigena*, *E. coli* K12, and *Enterobacter aerogenes* exhibit significant potential for remediating nitrate in groundwater medium. The comparative remediation rates of the isolated microbes are presented in Table 2.

Figure 2 represents the optical density and remediation rate with time. Per our experimental observation, at least 48 hours are required for microbial growth at those provided conditions (room temperature, anaerobic and dark conditions) Table 3. In Figure 2 (*L. amnigena*), the optical density increases steadily over time, yet after 200 hours (8 days), a slight downturn is observed, although the remediation rate continues to rise consistently.

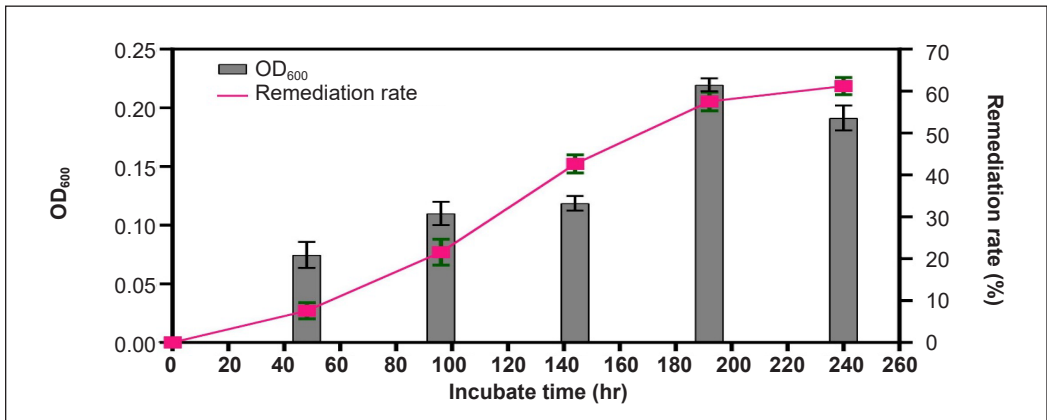


Figure 2. Absorbance and nitrate reduction by *Lelliottia amnigena* at 1000 mg/l nitrate concentration in groundwater medium

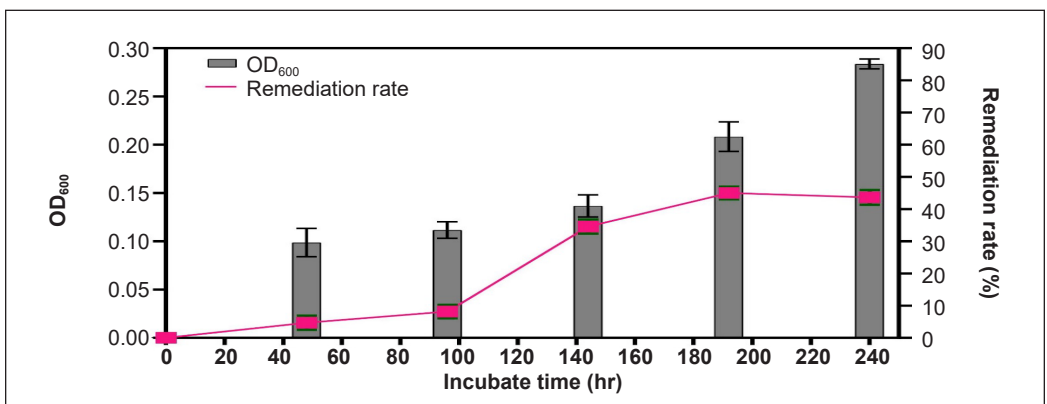


Figure 3. Absorbance and nitrate reduction by *Escherichia coli* K12 at 1000 mg/l nitrate concentration in groundwater medium

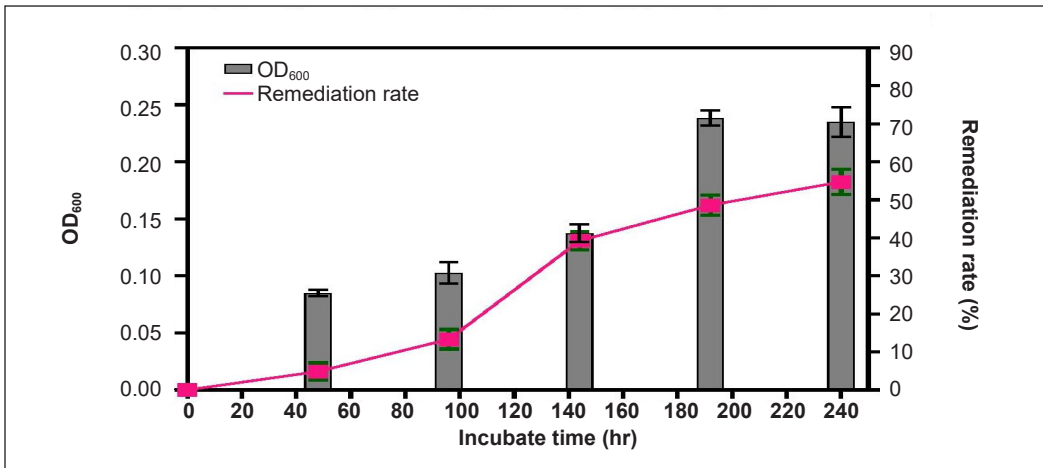


Figure 4. Absorbance and nitrate reduction by *Enterobacter aerogenes* at 1000 mg/l nitrate concentration in groundwater medium

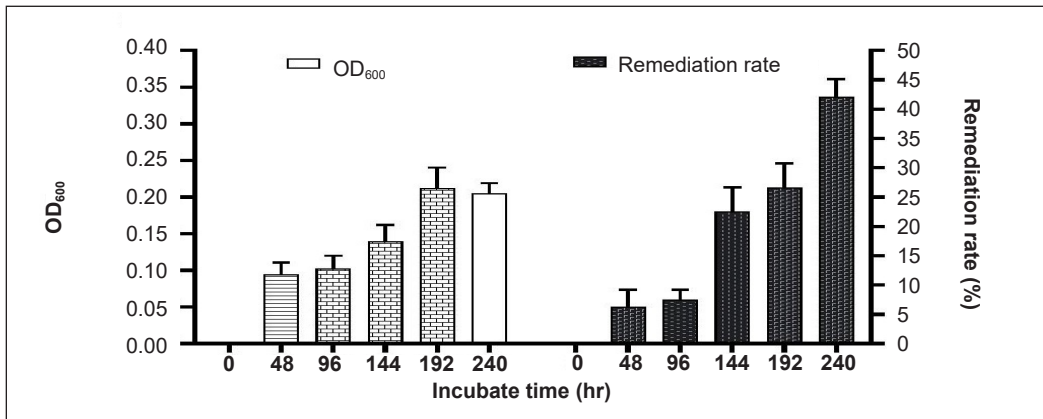


Figure 5. Absorbance and nitrate reduction by *Lelliottia amnigena* at 1500 mg/l nitrate concentration in groundwater medium

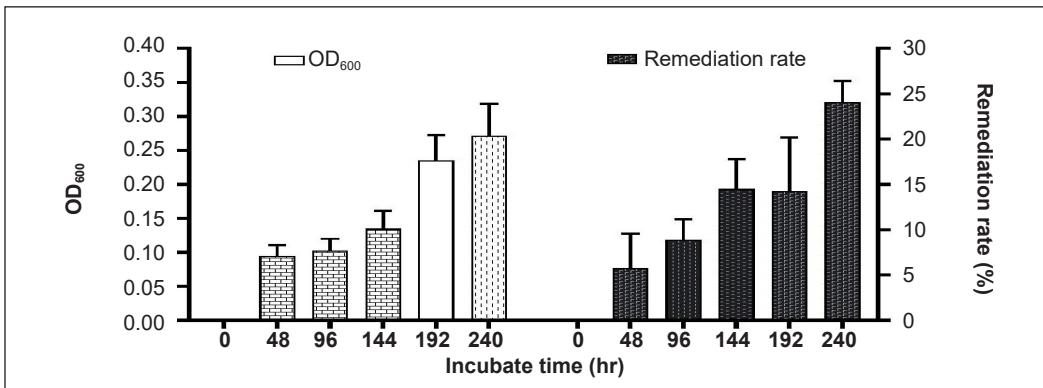


Figure 6. Absorbance and nitrate reduction by *Escherichia coli* K12 at 1500 mg/l nitrate concentration in groundwater medium

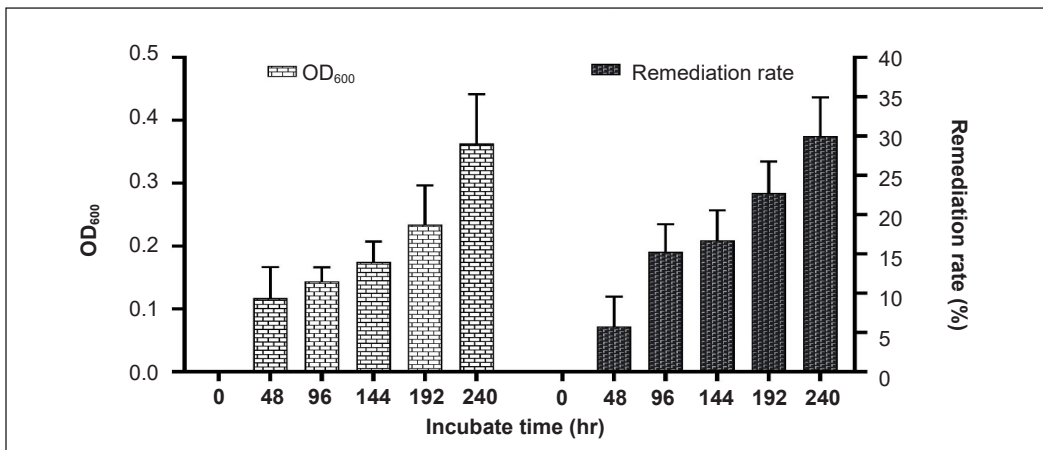


Figure 7. Absorbance and nitrate reduction by *Enterobacter aerogenes* at 1500 mg/l nitrate concentration in groundwater medium

Table 2

Comparison of nitrate remediation rate among microbes in groundwater medium

Enterobacteriaceae strains	Remediation rate at 1000 mg ^l ⁻¹ nitrate (Total 10 days incubation)	Remediation rate at 1500 mg ^l ⁻¹ nitrate (Total 10 days incubation)
<i>Lelliottia amnigena</i>	~61%	~42%
<i>Escherichia coli</i> K12	~43%	~24%
<i>Enterobacter aerogenes</i>	~54%	~29%

Table 3

Observed optical density of nitrate remediation of isolated strains at 420 nm

Optical Density	<i>Lelliottia amnigena</i>	<i>E. coli</i> K12	<i>Enterobacter aerogenes</i>	Optical density of control
Mean optical density at 1000 mg/l nitrate concentration	0.343	0.534	0.428	0.938
Mean optical density at 1500 mg/l nitrate concentration	0.576	0.752	0.706	0.996

Figure 3 (*E. coli* K12) exhibits growth for up to 10 days, with remediation activity persisting until day 9 before experiencing a minor decline. Conversely, in Figure 4 (*Enterobacter aerogenes*), optical density and remediation rates demonstrate continuous increases for up to 10 days. Figure 5 (*L. amnigena*) depicts a continuous rise in optical density until 192 hours, followed by a slight decline, while the remediation rate maintains an upward trend throughout. Figure 6 (*E. coli* K12) illustrates a continuous increase in optical density and remediation rate, with a notable overlap in nitrate remediation rates observed at 144 and 192 hours. Finally, in Figure 7 (*Enterobacter aerogenes*), optical density and remediation rate exhibit uninterrupted growth over time.

Genotypic Characterization of Microbes

These microbes were molecularly characterised to identify particular microbes' genus and species. Further, the similarity percentage with strains was checked using BLAST. Genomic DNA and PCR bands of isolates (initially designated as PP3, PP5, PP7 and PP10) are shown in Figures 8 and 9. The partial 16S rRNA gene sequences of strain PP10 (1399 base pairs) exhibited 99% similarity with *Enterobacter aerogenes* (KP764198). For strain PP3, the 1476 base pair sequence displayed 99% similarity with *Lelliotia amnigena*, while the 1409 base pair sequence of PP5 showed similarity with *E. coli* K12. For strain PP7, the 1436bp displayed 99% similarity with *Klebsiella oxytoca*. The nucleotide sequence of PP3, PP5, PP7 and PP10 isolates were deposited in the GenBank nucleotide sequence database under accession numbers MN647560, MN754025, MT457845 and MN252552, respectively.

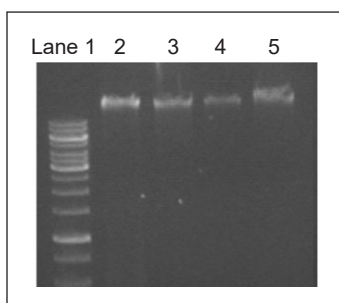


Figure 8. Extraction of Genomic DNA from all isolates (Lane 1 = DNA ladder; Lane 2 = PP3; Lane 3 = PP5; Lane 4 = PP7; and Lane 5 = PP10 strain)

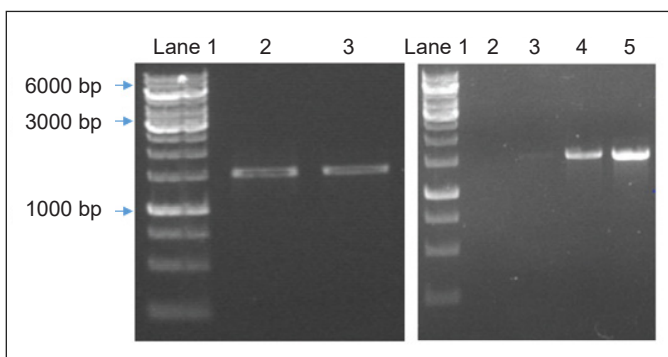


Figure 9. PCR bands of isolates PP3 and PP5 in lane 2, lane 3, PCR bands of strain PP7 and PP10 in lane 4 and lane 5, 1 kb plus DNA ladder in lane 1

Statistical Analysis

One-way ANOVA is used to compare different groups. Each experiment was repeated three times in replicates. Microsoft Excel calculated the average and standard deviation in Tables 4 and 5, and the

Table 4
Results of statistical analysis

Groups	Count	Sum	Average	Variance
Data 1	3	8	2.666667	0.33333
Data 2	3	12	4	1
Data 3	3	12	4	1

Table 5
Represent the degree of freedom, F value and P-value

Source of variation	SS	df	MS	F	p-value	F crit
Between Groups	3.55556	2	1.77778	2.285714	0.182832	5.143253
Within Groups	4.666667	6	0.77778			
Total	8.222222	8				

associated probability (P) <0.05 was statistically insignificant. The nitrate removal by isolates was within 24%–42%, the average being removal 31.86%.

DISCUSSION

According to the literature, *Lelliottia amnigena* is reported to remediate 50% of 138 mg/l nitrate-nitrogen (equivalent to 611.34 mg/l nitrate) (Fazzolari et al., 1990), while *E. coli* and *Enterobacter aerogenes* are known to remediate 90% of 10 mM nitrate (equivalent to 620 mg/l nitrate) (Bing et al., 1988). Our experimental study corroborates these findings, demonstrating the nitrate remediation potential of these isolated microbes. Our study assessed their efficacy at the maximum reported nitrate concentration in a groundwater medium supplemented with nitrate and acetate (as a carbon source). *Lelliottia*, *E. coli* K12, and *Enterobacter* exhibited remediation rates of approximately 42%, 24%, and 29%, respectively, at a nitrate concentration of 1500 mg/l. Notably, *Lelliottia* displayed the highest remediation rate among the three microbes, followed by *Enterobacter* and *E. coli*.

The *in-silico* study further validates the superior remediation potential of *L. amnigena* over *E. coli* K12, attributing it to the presence of both assimilatory and denitrification pathways (Thakur & Gauba, 2023; Thakur & Gauba, 2024). Moreover, the low nitrate reduction rate of these microbes may be influenced by various factors such as temperature, pH variations, and nutrient availability, as each microbe requires specific conditions for optimal growth, thereby enhancing nitrate reduction. Potential factors contributing to the nitrate remediation by these microbes include their slow growth, the impact of nitrate by-products, and the presence of specific metabolic pathways. Additionally, certain chemicals in the groundwater medium did not impede the nitrate reduction, as confirmed by detecting nitrite and ammonium using Griess reagent, indicating successful nitrate reduction.

CONCLUSION

This study successfully demonstrates the nitrate remediation capacity of isolates in groundwater, achieving approximately 25%–40% reduction at a concentration of 1500 mg/l. While numerous studies on nitrate bioremediation exist, they often remain confined to laboratory scales. Exploring large-scale remediation methods and determining optimal microbial conditions are critical next steps. Future research aims to refine conditions and investigate microbe-microbe interactions, which holds promise for improving the efficiency and affordability of bioremediation techniques and effectively addressing this urgent environmental concern.

ACKNOWLEDGEMENTS

Both authors contributed to the research and acknowledged the Jaypee Institute of Information & Technology, India, for financial support.

REFERENCES

- Addiscott, T. M., & Benjamin, N. (2004). Nitrate and human health. *Soil Use and Management*, 20(2), 98–104. <https://doi.org/10.1079/sum2004256>
- Bing, X., & Hollocher, T. (1988). Reduction of nitrite to nitric oxide by Enteric bacteria. *Biochemical and Biophysical Research Communications*, 157(1), 106–108. <https://doi.org/10.1016/j.bbrc.2019.05.052>
- Chouhan, S., Tuteja, U., & Flora, S. J. (2012). Isolation, identification and characterization of fluoride resistant bacteria: Possible role in bioremediation. *Applied Biochemistry and Microbiology*, 48(1), 51–58. <https://doi.org/10.1134/S0003683812010036>
- DebRoy, S., Das, S., Ghosh, S., Banerjee, S., Chatterjee, D., Bhattacharjee, A., Mukherjee, I., & RayChaudhuri, S. (2012). Isolation of nitrate and phosphate removing bacteria from various environmental sites. *Online Journal of Biological Sciences*, 12(2), 62–71. <https://doi.org/10.3844/ojbsci.2012.62.71>
- Elmidaoui, A., Sahli, M. A. M., Tahaikt, M., Chay, L., Taky, M., Elmghari, M., & Hafsi, M. (2003). Selective nitrate removal by coupling electro dialysis and a bioreactor. *Desalination*, 153(1–3), 389–397. [https://doi.org/10.1016/S0011-9164\(02\)01133-5](https://doi.org/10.1016/S0011-9164(02)01133-5)
- Fazzolari, E., Mariotti, A., & Germon, J. C. (1990). Nitrate reduction to ammonia: A dissimilatory process in *Enterobacter amnigenus*. *Canadian Journal of Microbiology*, 36(11), 779–785. <https://doi.org/10.1139/m90-134>
- Fewtrell, L. (2004). Drinking-water nitrate, methemoglobinemia, and global burden of disease: A discussion. *Environmental Health Perspectives*, 112(14), 1371–1374. <https://doi.org/10.1289/ehp.7216>
- Hameed, A., Nazir, S., Rehman, J. U., Ahmad, N., Hussain, A., Alam, I., Nazir, A., & Tahir, M. B. (2021). Assessment of health hazards related to contaminations of fluorides, nitrates, and nitrites in drinking water of Vehari, Punjab, Pakistan. *Human and Ecological Risk Assessment*, 27(6), 1509–1522. <https://doi.org/10.1080/10807039.2020.1858021>
- Jaeshin, K., & Benjamin, M. (2004). Modeling a novel ion exchange process for arsenic and nitrate removal. *Water Research*, 38(8), 2053–2062. <https://doi.org/10.1016/j.watres.2004.01.012>
- Karunanidhi, D., Subramani, T., Roy, P. D., & Li, H. (2021). Impact of groundwater contamination on human health. *Environmental Geochemistry and Health*, 43(2), 643–647. <https://doi.org/10.1007/s10653-021-00824-2>
- Kim, M., Jeong, S. Y., Yoon, S. J., Cho, S. J., Kim, Y. H., Kim, M. J., Ryu, E. Y., & Lee, S. J. (2008). Aerobic denitrification of *Pseudomonas putida* AD-21 at different C/N ratios. *Journal of Bioscience and Bioengineering*, 106(5), 498–502. <https://doi.org/10.1263/jbb.106.498>
- Kim, Y. H., Hwang, E. D., Shin, W. S., Choi, J. H., Ha, T. W., & Choi, S. J. (2007). Treatments of stainless steel wastewater containing a high concentration of nitrate using reverse osmosis and nanomembranes. *Desalination*, 202(1–3), 286–292. <https://doi.org/10.1016/j.desal.2005.12.066>
- Li, E., Deng, T., Yan, L., Zhou, J., He, Z., Deng, Y., & Xu, M. (2021). Elevated nitrate simplifies microbial community compositions and interactions in sulfide-rich river sediments. *Science of the Total Environment*, 750, Article 141513. <https://doi.org/10.1016/j.scitotenv.2020.141513>

- Liao, M., Luo, Y., Xu, N., Xie, X., Gan, X., & Cao, D. (2022). Nitrogen removal and metabolic pathway of *Enterobacter cloacae* DK-6. *Environmental Technology and Innovation*, 28, Article 102630. <https://doi.org/10.1016/j.eti.2022.102630>
- Lin, S. H., & Wu, C. L. (1996). Electrochemical removal of nitrite and ammonia for aquaculture. *Water Research*, 30(3), 715–721. [https://doi.org/10.1016/0043-1354\(95\)00208-1](https://doi.org/10.1016/0043-1354(95)00208-1)
- Lovley, D. R., & Phillips, E. J. P. (1988). Novel mode of microbial energy metabolism: Organic carbon oxidation coupled to dissimilatory reduction of iron or manganese. *Applied & Environmental Microbiology*, 54(6), 1472–1480. <https://doi.org/10.1128/aem.54.6>
- Madmanang, R., & Sriwiriyarat, T. (2019). Capacity enhancement of *Enterobacter aerogenes* for heterotrophic nitrification in integrated fixed film activated sludge (IFAS) wastewater treatment process. *Engineering Journal*, 23(1), 1–12. <https://doi.org/10.4186/ej.2019.23.1.1>
- Maia, M. P., Rodrigues, M. A., & Passos, F. B. (2007). Nitrate catalytic reduction in water using niobia supported palladium-copper catalysts. *Catalysis Today*, 123(1–4), 171–176. <https://doi.org/10.1016/j.cattod.2007.01.051>
- Majumdar, D. (2003). The blue baby syndrome: Nitrate poisoning in humans. *Resonance*, 8(10), 20-30. <https://doi.org/10.1007/BF02840703>
- Malberg, J. W., Savage, E. P., & Osteryoung, J. (1978). Nitrates in drinking water and the early onset of hypertension. *Environmental Pollution*, 15(2), 155–160. [https://doi.org/10.1016/0013-9327\(78\)90103-9](https://doi.org/10.1016/0013-9327(78)90103-9)
- Matos, C. T., Fortunato, R., Velizarov, S., Reis, M. A. M., & Crespo, J. G. (2006). Optimisation of the removal of toxic mono-valent anions from water supplies in the ion exchange membrane bioreactor. *Desalination*, 199(1–3), 322–324. <https://doi.org/10.1016/j.desal.2006.03.076>
- Morris, A. L., Hamlin, H. J., Francis-Floyd, R., Sheppard, B. J., & Guillette, L. J. (2011). Nitrate-induced goiter in captive whitespotted bamboo sharks *Chiloscyllium plagiosum*. *Journal of Aquatic Animal Health*, 23(2), 92–99. <https://doi.org/10.1080/08997659.2011.574079>
- Pan, D., Watson, R., Wang, D., Tan, Z. H., Snow, D. D., & Weber, K. A. (2014). Correlation between viral production and carbon mineralization under nitrate-reducing conditions in aquifer sediment. *ISME Journal*, 8(8), 1691–1703. <https://doi.org/10.1038/ismej.2014.38>
- Qin, S., Zhang, Z., Yu, L., Yuan, H., Clough, T. J., Wrage-Mönnig, N., Luo, J., & Zhou, S. (2017). Enhancement of subsoil denitrification using an electrode as an electron donor. *Soil Biology and Biochemistry*, 115, 511–515. <https://doi.org/10.1016/j.soilbio.2017.09.020>
- Raja, V., & Neelakantan, M. A. (2021). Evaluation of groundwater quality with health risk assessment of fluoride and nitrate in Virudhunagar district, Tamil Nadu, India. *Arabian Journal of Geosciences*, 14, Article 52. <https://doi.org/10.1007/s12517-020-06385-5>
- Rajakumar, S., Ayyasamy, P. M., Shanthi, K., Thavamani, P., Velmurugan, P., Song, Y. C., & Lakshmanaperumalsamy, P. (2008). Nitrate removal efficiency of bacterial consortium (*Pseudomonas* sp. KW1 and *Bacillus* sp. YW4) in synthetic nitrate-rich water. *Journal of Hazardous Materials*, 157(2–3), 553–563. <https://doi.org/10.1016/j.jhazmat.2008.01.020>

- Rajta, A., Bhatia, R., Setia, H., & Pathania, P. (2020). Role of heterotrophic aerobic denitrifying bacteria in nitrate removal from wastewater. *Journal of Applied Microbiology*, 128(5), 1261–1278. <https://doi.org/10.1111/jam.14476>
- Reddy, A. G. S. (2023). A review on violation of drinking water specifications in water supply and research publications. *Environment, Development and Sustainability*, 25(2), 1084–1100. <https://doi.org/10.1007/s10668-021-02038-z>
- Reddy, K. J., & Lin, J. (2000). Nitrate removal from groundwater using catalytic reduction. *Water Research*, 34(3), 995–1001. [https://doi.org/10.1016/S0043-1354\(99\)00227-4](https://doi.org/10.1016/S0043-1354(99)00227-4)
- Riet, J. V. T., & Planta, R. J. (1975). Purification, structure and properties of the respiratory nitrate reductase of *Klebsiella aerogenes*. *Biochimica et Biophysica Acta (BBA)-Protein Structure*, 379(1), 81–94. [https://doi.org/10.1016/0005-2795\(75\)90010-0](https://doi.org/10.1016/0005-2795(75)90010-0)
- Sahli, M. A. M., Tahaikt, M., Achary, I., Taky, M., Elhanouni, F., Hafsi, M., Elmghari, M., & Elmidaoui, A. (2006). Technical optimization of nitrate removal for groundwater by ED using a pilot plant. *Desalination*, 189(1-3 SPEC. ISS.), 200–208. <https://doi.org/10.1016/j.desal.2005.06.025>
- Schoeman, J. J., & Steyn, A. (2003). Nitrate removal with reverse osmosis in a rural area in South Africa. *Desalination*, 155(1), 15–26. [https://doi.org/10.1016/S0011-9164\(03\)00235-2](https://doi.org/10.1016/S0011-9164(03)00235-2)
- Sikdar, P. K. (2018). *Groundwater development and management: Issues and challenges in South Asia*. Springer. <https://doi.org/10.1007/978-3-319-75115-3>
- Singh, B., & Craswell, E. (2021). Fertilizers and nitrate pollution of surface and ground water: An increasingly pervasive global problem. *SN Applied Sciences*, 3(4), 1–24. <https://doi.org/10.1007/s42452-021-04521-8>
- Srivastava, D. A., Yadav, D., & Gaur, B. (2015). Groundwater quality assessment around Gazipur Landfill site, Delhi. *Science & Technology*, 1(4), 149–156.
- Tariqi, A. Q., & Naughton, C. C. (2021). Water, health, and environmental justice in California: Geospatial analysis of nitrate contamination and thyroid cancer. *Environmental Engineering Science*, 38(5), 377–388. <https://doi.org/10.1089/ees.2020.0315>
- Thakur, P., & Gauba, P. (2021). Tolerance and remediation potential of water microbes against nitrate. *International Journal of Current Research and Review*, 13(19), 58–64. <https://doi.org/10.31782/ijcr.2021.131908>
- Thakur, P., & Gauba, P. (2023). Identification and examination of nitrogen metabolic genes in *Lelliottia amnigena* PTJIIT1005 for their ability to perform nitrate remediation. *BMC Genomics*, 24(1), 1–11. <https://doi.org/10.1186/s12864-023-09207-6>
- Thakur, P., & Gauba, P. (2024). Expression analysis of nitrogen metabolism genes in *Lelliottia amnigena* PTJIIT1005, comparison with *Escherichia coli* K12 and validation of nitrogen metabolism genes. In *Biochemical Genetics* (pp. 1-31). Springer. <https://doi.org/10.1007/s10528-024-10677-w>
- Tirkey, P., Bhattacharya, T., Chakraborty, S., & Baraik, S. (2017). Assessment of groundwater quality and associated health risks: A case study of Ranchi city, Jharkhand, India. *Groundwater for Sustainable Development*, 5, 85–100. <https://doi.org/10.1016/j.gsd.2017.05.002>

- Tyagi, S., Sharma, B., Singh, P., & Dobhal, R. (2020). Water quality assessment in terms of water quality index. *American Journal of Water Resources, 1*(3), 34–38. <https://doi.org/10.12691/ajwr-1-3-3>
- Ward, M. H., Jones, R. R., Brender, J. D., de Kok, T. M., Weyer, P. J., Nolan, B. T., Villanueva, C. M., & van Breda, S. G. (2018). Drinking water nitrate and human health: An updated review. *International Journal of Environmental Research and Public Health, 15*(7), 1–31. <https://doi.org/10.3390/ijerph15071557>
- Yang, T., Yang, Q., Shi, Y., Xin, Y., Zhang, L., Gu, Z., & Shi, G. (2021). Insight into the denitrification mechanism of *Bacillus subtilis* JD-014 and its application potential in bioremediation of nitrogen wastewater. *Process Biochemistry, 103*, 78–86. <https://doi.org/10.1016/j.procbio.2021.02.007>
- Zhang, W., Ruan, X., Bai, Y., & Yin, L. (2018). The characteristics and performance of sustainable-releasing compound carbon source material applied on groundwater nitrate in-situ remediation. *Chemosphere, 205*, 635–642. <https://doi.org/10.1016/j.chemosphere.2018.04.133>
- Zhao, B., Sun, Z., & Liu, Y. (2022). An overview of in-situ remediation for nitrate in groundwater. *Science of the Total Environment, 804*, 1–14. <https://doi.org/10.1016/j.scitotenv.2021.149981>

Review Article

A Comprehensive Review of State-of-the-art Optical Methods for Methane Gas Detection

Sayma Khandaker, Nurulain Shaipuzaman, Md Mahmudul Hasan, Mohd Amir Shahlan Mohd Aspar and Hadi Manap*

Faculty of Electrical and Electronics Engineering Technology, Universiti Malaysia Pahang Al-Sultan Abdullah, 26600 Pekan, Pahang, Malaysia

ABSTRACT

Methane (CH₄), a potent greenhouse gas, significantly contributes to climate change and global warming. Its impact over 100 years surpasses carbon dioxide (CO₂) by 28 times. Addressing methane emissions, particularly from oil and gas production activities such as transmission pipelines, is imperative. One promising avenue is the development of reliable sensors to detect and mitigate methane leaks and prevent hazardous issues. Optical-based methods present notable advantages, including versatility and remote operation, making them pivotal in this endeavor. This review article provides a concise overview of optical-based methane identification technologies, encompassing sensing materials, absorption spectra, operational mechanisms, and recent advancements. Potential perspectives are explored, and inferences from this assessment are also derived. Emphasizing the significance of optical fiber-based methane detection methods, the authors advocate for further research to support ongoing efforts and foster innovation in this critical area.

Keywords: Methane absorption spectra, methane detection, methane sensing materials, optical fiber sensor, optical methods

ARTICLE INFO

Article history:

Received: 31 January 2024

Accepted: 19 August 2024

Published: 25 October 2024

DOI: <https://doi.org/10.47836/pjst.32.6.19>

E-mail addresses:

saymakhandaker27@gmail.com (Sayma Khandaker)

ainnadhirah93@gmail.com (Nurulain Shaipuzaman)

mhasan.just@gmail.com (Md Mahmudul Hasan)

amirs@umpsa.edu.my (Mohd Amir Shahlan Mohd Aspar)

hadi@umpsa.edu.my (Hadi Manap)

* Corresponding author

INTRODUCTION

The main component of natural gas is methane (CH₄). It is an odorless, colorless gas with melting and boiling points of -183°C and -164°C, respectively. Its high heating value and excellent igniting properties make it a popular fuel for heating and power generation worldwide. Compared to coal,

CH₄ has a higher calorific value and produces fewer toxic and harmful compounds when burned, making it an essential resource for economies aiming to reduce carbon emissions. Due to its lower production costs and reduced combustion-related CO₂ emissions, it is increasingly replacing coal, particularly in the US power sector (Jaramillo et al., 2008).

However, the utilization of CH₄ and its release into the atmosphere have serious implications. After CO₂, CH₄ is the second most common greenhouse gas. Its potential to contribute to global warming is roughly thirty times higher per molecule than that of CO₂. Since the onset of industrialization, there has been a significant increase in the quantity of methane in the atmosphere, reaching as high as 1800 parts per billion (ppb) in 2016 (Turner et al., 2019), compared to less than 800 parts per billion at the beginning of the nineteenth century.

Waste disposal facilities, livestock waste disposal systems, coal extraction, petrochemical exploration, electricity transformers, and gas and oil transportation and manufacturing facilities are the primary human causes of emissions responsible for this rise. Additionally, if the concentration of methane gas in an enclosed area exceeds 5% to 15%, it may ignite and cause an explosion (Stocker et al., 2014).

Given its abundant supply and relatively safe combustion process, natural gas is expected to be utilized extensively despite its negative environmental implications (Tran & Fowler, 2020). The World Health Organization (WHO) claims that CH₄ may remain in the atmosphere for a maximum of 12 years before being gradually depleted by molecules such as OH radicals, which pose a significant environmental risk when discharged into the atmosphere (Lawrence, 2006).

Over the past two centuries, the atmospheric concentration of methane has more than doubled. This significant increase is primarily due to the exponential rise in human activity, which elevates atmospheric methane concentration through various emission pathways. Methane is a crucial component of natural gas in the atmosphere and is also found in adjacent regions of the world's layers. It is generated by the decomposition of animals, plants, or microorganisms inhabiting oceans, lakes, and other bodies of water.

Approximately 36% of the total methane volume originates from naturally occurring wetland emissions produced by termites and the ocean. About 64% of all methane emissions come from human activities, including landfills, paddy fields, agriculture, and livestock digestion, as depicted in Figure 1 (Vasiliev et al., 2014). Nevertheless, depending on the source, methane emission numbers can differ considerably.

The Conference Board of Canada found that 8.5% of Canada's greenhouse gas emissions are attributed to methane leakage from wells and equipment (Bachu, 2017). According to Olmer et al. (2019), methane emissions from transporting liquefied natural gas account for over five percent of the 932 million tons of CO₂ equivalent emissions worldwide. Ingraffea et al. (2020) discovered that Pennsylvania's oil and gas wells emit

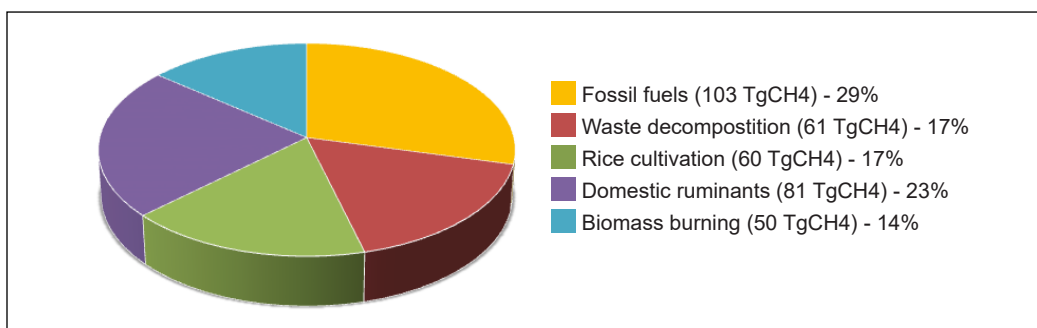


Figure 1. Individual sources of the world's total emissions of methane

an average of 55,600 tons of methane annually. The shale gas basins in northern British Columbia are estimated to leak 75,000 metric tons of methane annually (Wisén et al., 2020). Formisano et al. (2004) revealed methane in the Martian atmosphere. The planet's concentration ranges from 0 to 30 parts per billion by volume (ppbv), with an average of 10 ± 5 ppbv. The measurements were taken with the Mars Express spacecraft's planetary FTIR spectrometer. This gas is expected to increase the likelihood of uncovering evidence of life on Mars. Methane in the Martian atmosphere decomposes rapidly through various processes. Therefore, large clouds of this gas in Mars' northern hemisphere suggest continuous methane emissions. Methane is also used in small quantities for medical diagnosis. When the stomach microbiota is imbalanced, methane can be detected in the air, indicating irritable bowel syndrome. Consequently, methane is released into the bloodstream and travels to the lungs.

However, numerous methods are available for detecting CH₄ nowadays, each with benefits and drawbacks. Optical fiber-based methane detection methods stand out for their remote operation, deployment versatility, high sensitivity to low concentrations, real-time monitoring capabilities, minimal interference, and cost-effectiveness, making them ideal for continuous and reliable methane surveillance. Unfortunately, detecting methane at leak-relevant quantities with these methods using widely deployable, reasonably priced equipment over long distances and/or wide geographic areas remains challenging. Due to their low polarizability, this difficulty stems from the inherently low reactivity of CH₄ molecules compared to other frequently researched gas molecules, such as H₂, CO₂, and CO.

This article provides an in-depth review of a wide range of commonly used optical fiber-based methane detection sensors, including information on their performance characteristics and current developments to enhance sensitivity, selectivity, response and recovery times, and long-term stability. It also meticulously analyzes the challenges and limitations associated with these sensors. Future research directions, including materials and optical sensor advancements, are explored to guide the development of more reliable and efficient methane detection systems.

METHANE SENSING MATERIALS

Depending on the surrounding gas environment, gas-sensing materials can modify their electrical, optical, or auditory properties. This article will compile the most recent research on CH₄ sensing materials in this domain, focusing on five categories: metal oxides, supramolecular materials, carbon-based substances, conductive polymers, and metal-organic frameworks. The sensing mechanism and effectiveness of each category will be explained. Additionally, the suitability and feasibility of utilizing diverse sensing materials on the platforms above and mechanisms will be compiled in Table 1. Table 2 also offers an overview of the CH₄ sensing capabilities of various materials. The ranges for response time, temperature requirements, and detection limits have been compiled based on the highest and lowest values from published studies. Materials for highly specific and reversible CH₄ sensing are continuously under investigation, unlike other gas sensors, including NH₃, H₂, and others. Therefore, the assessment of selective and reversible changes in these sensors is typically minimal or moderate, as listed in Table 2. The deposition of the sensing materials typically occurs in the formation of a polycrystalline layer or film onto a substrate that incorporates heating as well as embedded electrodes (Figure 2).

Table 1

Summary of the materials used for CH₄ sensing across various platforms and techniques (Hong et al., 2020)

Platform	Techniques		
	Electrical	Optical	Mass
Optical Fiber	-	1,3,4,5	-
Chemi-resistive	1,2,3	-	-
SAW/QCM	1	-	3,4,5

Note. 1: Metal-oxide; 2: Carbon; 3: Conducting polymer; 4: Supramolecular and 5: Metal-organic framework

Table 2

An overview of the various materials' characteristics for detecting CH₄ (Hong et al., 2020)

Material	Temperature of Operation	Time of Response (s)	Sensing Reversible Nature	Selection Level	Detection Threshold (ppm)
Metal-Oxide	25°C–900°C (normally > 150°C)	10 ⁰ –10 ²	Minimum-Medium	Minimum-Medium	10 ⁰ –10 ³
Carbon	Room Temperature - 450°C	10 ¹ –10 ²	Minimum-Medium	Minimum-Medium	10 ¹ –10 ⁴
Conducting Polymer	Room Temperature	10 ¹ –10 ²	Minimum-Medium	Minimum-Medium	10 ² –10 ³
Supramolecular	Room Temperature	10 ¹ –10 ²	Minimum-Medium	Minimum-Medium	10 ¹ –10 ⁴
Metal-organic Structure	Room Temperature	10 ¹ –10 ²	Medium-Maximum	Medium	10 ⁴ –10 ⁵

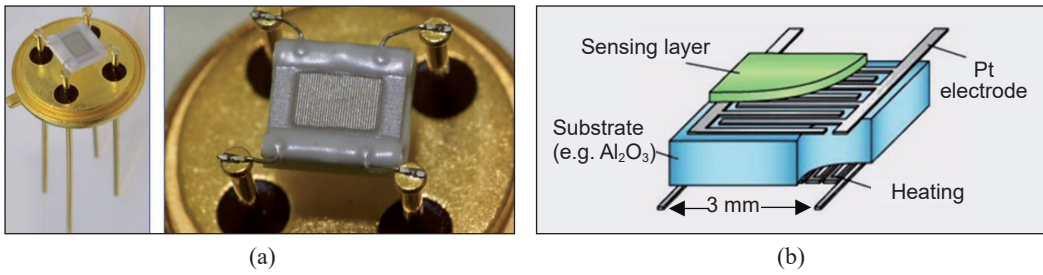


Figure 2. (a) A graphical representation; and (b) snapshots of an illustrative sensing material, taken from (Tiemann, 2007)

METHANE ABSORPTION SPECTRA

The Lambert-Beer rule is the basis of optical gas detection using absorption spectrum analysis in Equations 1 and 2.

$$I(\lambda) = I_0(\lambda) \exp[-a(\lambda, C) \cdot L] \quad a[cm^2] \quad [1]$$

$$I(\lambda) = I_0(\lambda) \exp[-\alpha(\lambda, C) \cdot L] \quad \alpha[ppm \cdot cm^2] \quad [2]$$

Where I is the amount of light transmission through the gas-filled medium; I_0 is the brightness of the incident light on the medium; C is the concentration; a , α is the coefficient of absorptions; and L is the optical path length.

The Pacific Northwest National Laboratory, part of the US Department of Energy (DOE), provides quantitative gas spectra, which can be determined using the HITRAN database (Rothman et al., 2009). Optical approaches for detecting methane rely on its infrared absorption properties. The absorption spectrum of methane, displayed in Figure 3,

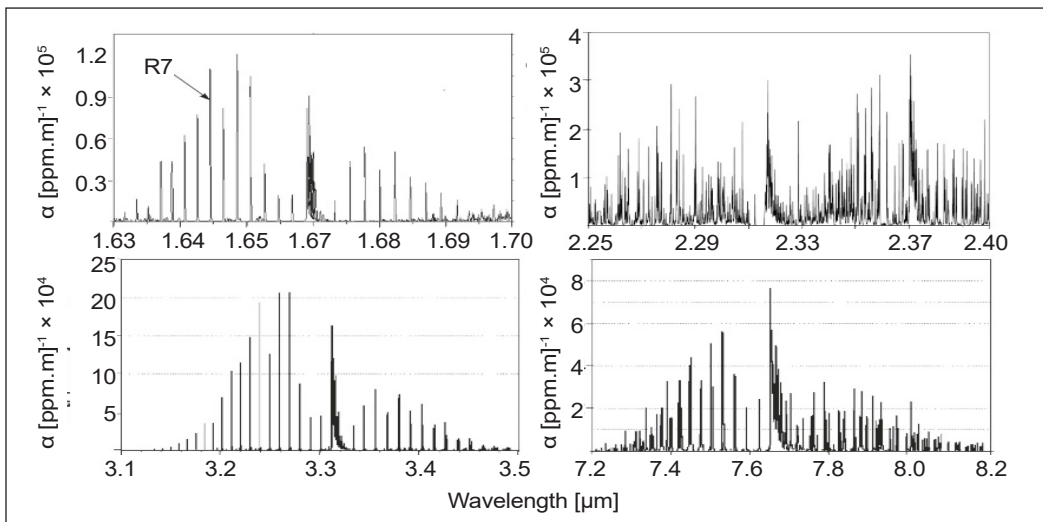


Figure 3. Methane absorption spectra (Adapted from Kwaśny & Bombalska, 2023)

shows that the strongest bands occur within the zone of deformation vibrations, followed by valence vibrations; these are weaker in the overtone spectrum.

There are numerous absorption lines for methane in the 1.63–1.69 μm range, with a composite absorption cross-section of $5.13 \times 10^{-20} \text{ cm}^2$, making them highly influential. However, there are bands of carbon dioxide with an overall absorption of $4.95 \times 10^{-23} \text{ cm}^2$ and water with an overall absorption of $4.34 \times 10^{-23} \text{ cm}^2$ (Kwaśny & Bombalska, 2023). It is important to carefully select methane absorption lines to avoid interference from these absorbers. Figure 4 illustrates the selection of relevant bands for investigation, as well as the proximity of CH_4 and H_2O absorption lines to each other. It effectively operates immersion cells at lower pressures of 50–100 hPa to enhance spectral resolution and line separation and reduce half-width. Cooled detectors are unnecessary for instruments operating in the NIR region (0.8–2.5 μm) due to their expense.

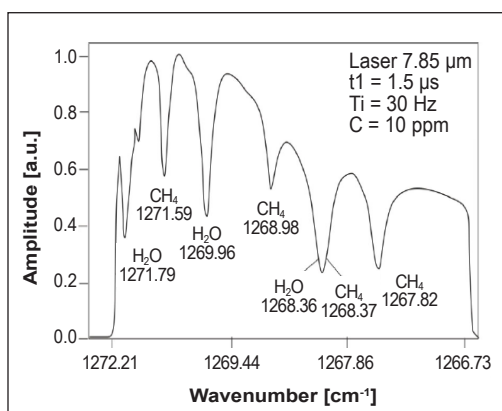


Figure 4. Atmospheric transmission spectrum with methane (Kwaśny & Bombalska, 2023)

METHANE GAS DETECTION BASED ON OPTICAL METHODS

Gas-detecting applications can represent a wide range of gas concentrations, generally indicated as a volumetric ratio in the air or another matrix. Since most gases behave as ideal gases to a large extent at normal temperatures and pressures, the molar concentration in the matrix is also identical or nearly equal (Hodgkinson & Tatam, 2013). An example of methane, which has multiple applications requiring measurement over a range of concentrations, can be used to illustrate gas concentrations. Table 3 provides a summary of several examples. Concentrations can be expressed as % volume, ppt, ppm, or ppb.

Different approaches now exist for identifying methane in the air, depending on whether the measurement is conducted in a laboratory, where samples are analyzed under stationary conditions, or outdoors, where continuous observation is performed. Various sensors can detect methane, including optical, pyroelectric, semiconducting metal oxide, electrochemical, and calorimetric sensors.

Thermal Conductivity Detector is one of the earliest sensors used to assess the composition of gas mixtures. This method involves detecting changes in the thermal conductivity of a carrier gas resulting from alterations in its chemical structure. The sensor is an imbalanced Wheatstone bridge consisting of two or four thermistors heated by current passing through them. High sensitivity, a linear response over a broad measurement range,

Table 3

Methane detection application that demonstrates the requirement for gas measurement across a range of concentrations (Hodgkinson & Tatam, 2013)

Execution	Major concerns	Desired concentration spectrum	Reference
Process monitoring: gas quality, i.e., the composition of natural gas measured for regulatory purposes, metering and the alteration of custody	Accuracy to 'fiscal standards' (0.1%)	70–100% volume	Wild, 2000
Process monitoring: tracking the combustion process	Accuracy throughout a broad range of temperatures and pressures	0.1%–100% volume	Pyun et al., 2011
Process/environment: measurement of methane residue in a flare for the exchange of carbon	Consistency: 100 parts per billion. Methane background concentration: 1.8 ppm; higher near sources	100 ppb - 1000 ppm (plus a background level of 1 Accuracy e.g., to ± 5.8 ppm)	Kannath et al., 2011
Environment-based modeling: The 1.8 ppm methane background assessment	Compared with previous data. Accuracy of 0.1%– 5% of reading required	30 ppb - 3 ppm (plus a background level of 1.8 ppm)	Gardiner et al., 2010
Environment-based modeling: measuring methane flux using eddy covariance technology	Interaction at data rates higher than 10 Hz with local atmospheric eddy currents	5 ppb - 25 ppm (plus a background level of 1.8 ppm)	McDermitt et al., 2011
Safety: Cleaning gas pipelines to prevent explosions and make sure the pilot lights stay sparked	Accuracy, e.g., to $\pm 5\%$ volume at 50% volume	1%–100% volume	Agius et al., 2000
Safety: measurement of gas leakage in relation to the 4.9% volume lower explosive limit	Accurate at action points, e.g., 20% lower explosive limit (1% volume) for evacuation of buildings	0.1%–5% volume	Gao et al., 2013; Hodgkinson & Pride, 2010
Safety: where gas spills are located, usually outside	Dependable detection threshold of about 1 ppm	1–10000 ppm	Hodgkinson & Pride, 2010; Hodgkinson et al., 2006

and a straightforward design characterize this sensor. However, key disadvantages include a lack of discrimination and the need to maintain constant sensor temperature, gas flow rate, and reference conditions.

In catalytic combustion sensors, a catalytic combustion reaction occurs on the active element, while changes in humidity, pressure, and temperature are measured using a passive component as a reference. The sensor utilizes a Wheatstone bridge. Catalytic combustion sensors are currently used in pellistors and hot fibers. A flammable gas and air stream is directly exposed to a hot platinum fiber in pellistors. In addition to serving as a heating element and resistance thermometer, the platinum wire also acts as a catalyst

for combustion. When an electric current passes through the circuit, the platinum wire reaches a temperature range of 400 to 500°C, allowing the gas mixture to undergo catalytic oxidation (Kwaśny & Bombalska, 2023).

Optical sensor technologies have become increasingly popular in recent decades due to their inherent advantages over other sensing platforms. These benefits include sensing remotely, immunity to electromagnetic interference, eliminating electrical lines and contacts in combustible gaseous settings, and non-invasive measurement techniques (Shemshad et al., 2012). Several research investigations and review studies have focused on optical technique-based gas sensors (Shemshad et al., 2012; Wang & Wolfbeis, 2016). Optical gas sensors detect variations in electromagnetic waves or visible light when the analyte comes into contact with the receptor section. Absorption and scattering are the basic mechanisms optical gas sensors use to detect emissions. A visual representation of a functional optical gas sensor for methane is depicted in Figure 5. It consists of an optical spectrum detector, a tube that holds the tested gas sample, and a light source that produces mid-IR light.

Optical technologies offer numerous benefits, including the ability to test methane remotely and at very low concentrations, such as ppm, ppb, and ppt. However, a primary drawback is the overlap of water bands during absorption and the presence of other hydrocarbons.

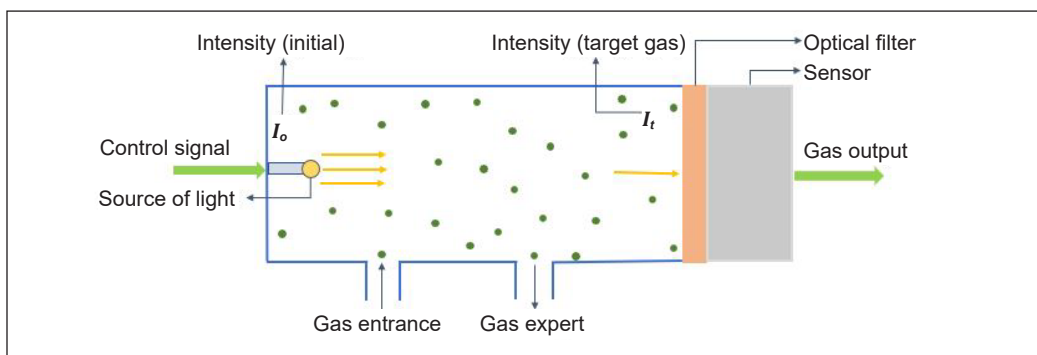


Figure 5. The working mechanism of an optical sensor for detecting methane

Tunable Diode Laser Absorption Spectroscopy

Tunable diode laser absorption spectroscopy (TDLAS) has been employed to detect temperature readings and gas concentrations in applications requiring high resolution, sensitivity, and precision. By adjusting the output wavelength of a diode laser, a single narrow linewidth laser can scan across distinct absorption paths to acquire measurements. Additionally, since absorption lines widen as pressure increases, high selectivity can be achieved at low pressures. Numerous researchers have developed methods for tracking trace gases. The TDLAS approach is a robust identification method that applies to all species absorbing infrared light and can produce a variety of laser wavelengths without requiring

additional equipment. Using a multiplexing method that pairs multiple laser outputs and utilizes a multipass cell, multiple gases can be monitored simultaneously. This approach responds quickly, typically in the range of 1 to 1000 μs , and is highly sensitive (Beckwith et al., 1987). However, limitations include the difficulty sustaining and employing this technology as a stand-alone system without routine technical repair and the restricted availability of laser initiation.

Various techniques utilize tunable diode laser spectroscopy to measure gas concentration and absorption, including wavelength, frequency modulation, and direct absorption spectroscopy. TDLAS achieves high resolution through a solitary channel of gas absorption across the emission wavelength of a narrow linewidth laser diode. The measurement can be self-referenced successfully by comparing the central peak absorption to the zero level on both sides of the spectrum. There are two main approaches for TDLAS: direct spectroscopy and wavelength modulation spectroscopy (WMS). Commercially available tools developed using these approaches include the SS2100 hydrogen sulfide analyzer (<http://www.spectrasensors.com/asp/Site/Products/ByProduct/index.asp>). Typically, a lock-in amplifier at the receiver is employed to recover the second harmonic of AC excitation to detect methane gas, as illustrated in Figure 6. Figure 7 displays the probable configurations of various demodulating waveforms for a single gas line.

The quality of the laser mode can significantly affect TDLAS. Achieving a high laser mode quality involves determining the pedestal temperature and driving current settings at which the laser produces strong, steady emission in a single mode at the targeted absorption

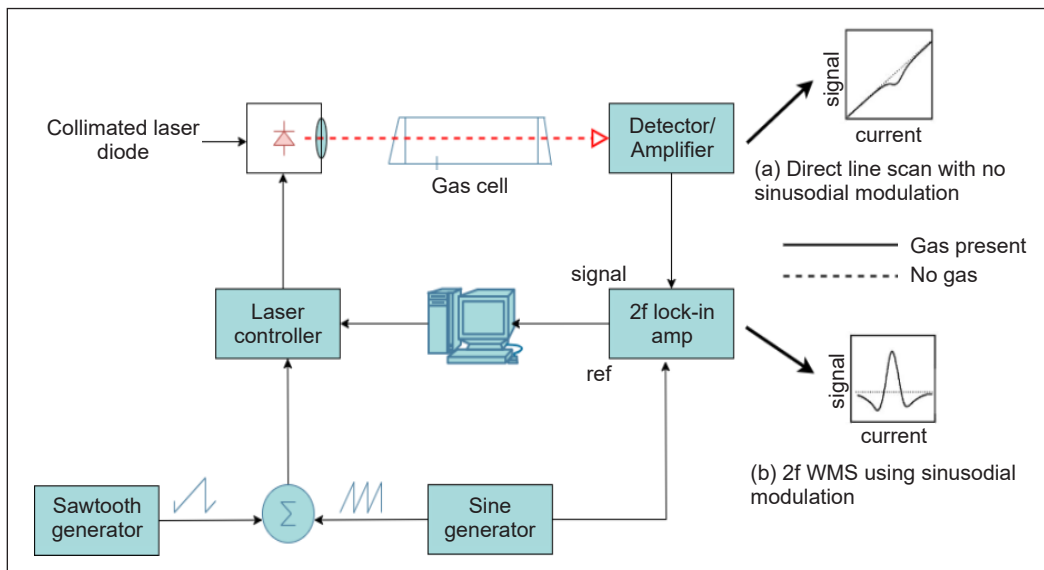


Figure 6. A laser diode is used in the conventional configuration of TDLAS to display observed signals as two objectives using a measure of laser drive current: (a) direct gas line scanning; or (b) second harmonic wavelength modulating spectroscopy (2f WMS)

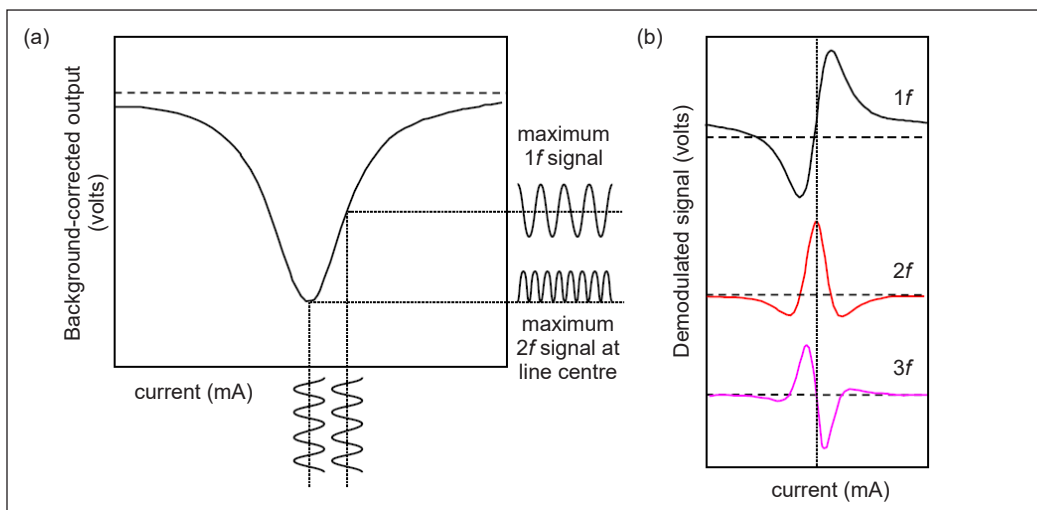


Figure 7. Various harmonic signals are generated in the WMS: (a) Background-corrected DC scan of a single gas line, with the RAM removed for clarity; and (b) The 1f, 2f, and 3f harmonics' form shifted for clarity, as a function of the current scan location. On the 1f signal, the RAM produces a slight but detectable dc offset extracted from (Hodgkinson & Tatam, 2013)

wavelength. However, this can be challenging as thermal cycling may cause changes in mode structure that alter the properties of the laser over time. Nevertheless, single-mode operation is preferred to minimize mode partition noise and remove interference from absorption signals of other modes with the primary absorption signal of the target species.

We have comprehensively reviewed recent publications on methane identification using TDLAS and compiled a summary of these findings in Table 4.

Table 4
Comparison measurements of performance for optical-based methane detection

Wavelength (µm)	Path	Response Time (s)	Minimum Detectable Concentration	Minimum Detectable Absorbance	Minimum Detectable Absorption Coefficient	Reference
2.3	72 m	137	0.487 ppm	Not stated	Not stated	Shao et al., 2019
1.65	80 mm	0.3	52 ppb	$2.1 \times 10^{-8} \text{ cm}^{-1} \text{ W/Hz}^{1/2}$	$1.455 \times 10^{-21} \text{ cm}^{-1}$	Wei et al., 2021
1.684	20 cm	2	4.3 ppm	Not stated	Not stated	Hennig et al., 2003
1.6482	74 m	1.5–10	0.1 ppm	$4 - 8 \times 10^{-5}$	Not stated	Gurlit et al., 2005
1.654	252 m	2	20 ppb	Not stated	Not stated	Richard et al., 2002
8.03	76 m	1	1 ppb	$4.6 \times 10^{-5} \text{ Hz}^{-1/2}$	$6.1 \times 10^{-9} \text{ cm}^{-1} \text{ Hz}^{-1/2}$	McManus et al., 2008

Non-dispersive Infrared

To compensate for the laser wavelength shift caused by heat in laser absorption spectroscopy, one of the most straightforward methods is the construction of broadband non-dispersive infrared (NDIR) sensors, which hold significant importance from a business standpoint. These sensors feature robust housing that serves as a gas flow measurement chamber, accommodating both a broadband light source and a combination detector. Figure 8 presents a visual representation of a basic NDIR sensor. Typically, two filters spanning a non-absorbed area are employed in the target channel and the reference channel, allowing the passage of emissions from a broadband source. Broadbands are employed for non-dispersive measurements. The two primary advantages of using micro bulbs in conventional NDIR sensors are their low cost and relatively high spectral emission.

Cuvettes with various optical path lengths are designed based on the volume of the concentrations and the absorption characteristics of the contaminants under investigation. Figure 9 shows an opto-pair (optoelectronic pair), an optical sensor. The method for distinguishing methane absorption in the opto-pair sensor is depicted in Figure 10. While the reference channel's optical filter transmits data within the 3.0–2.9 μm range, the working channel transmits in the range of 3.23 μm (Kwaśny & Bombalska, 2023).

A diffusion-type measurement cuvette filters light emitted by the radiation-emitting light source. Detectors operating in the absorption and reference bands separate it into two beams for analysis (Kwaśny & Bombalska, 2023). A spatial control network with up to 128 meters can be built using the RS-485 digital output. Its low drift and good measurement stability distinguish it from similar devices. The microprocessor inside the device generates pulses for the photosensitive sensor. Digital analysis is then used to measure the amplitudes of the signal pulses originating from amplifiers 4

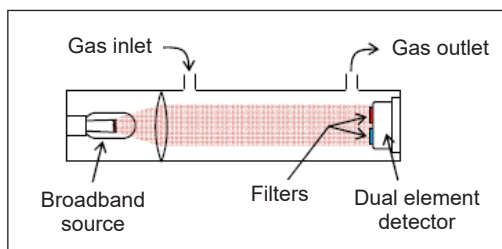
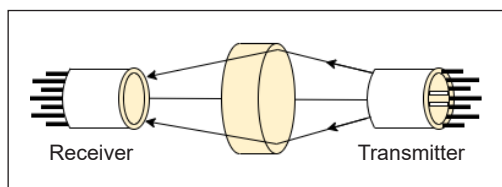
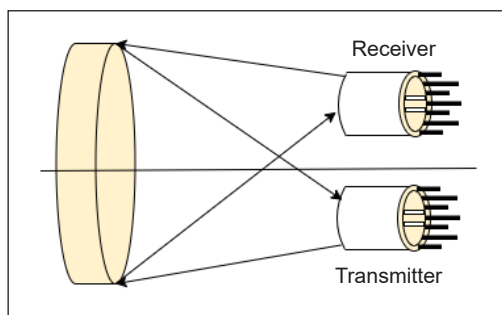


Figure 8. Conceptual illustration of a distinctive non-dispersive infrared gas sensor with optical path length, taken from (Hodgkinson & Tatam, 2013)



(a)



(b)

Figure 9. The notion of an opto pair (a) single radiation pass, (b) two radiation passes

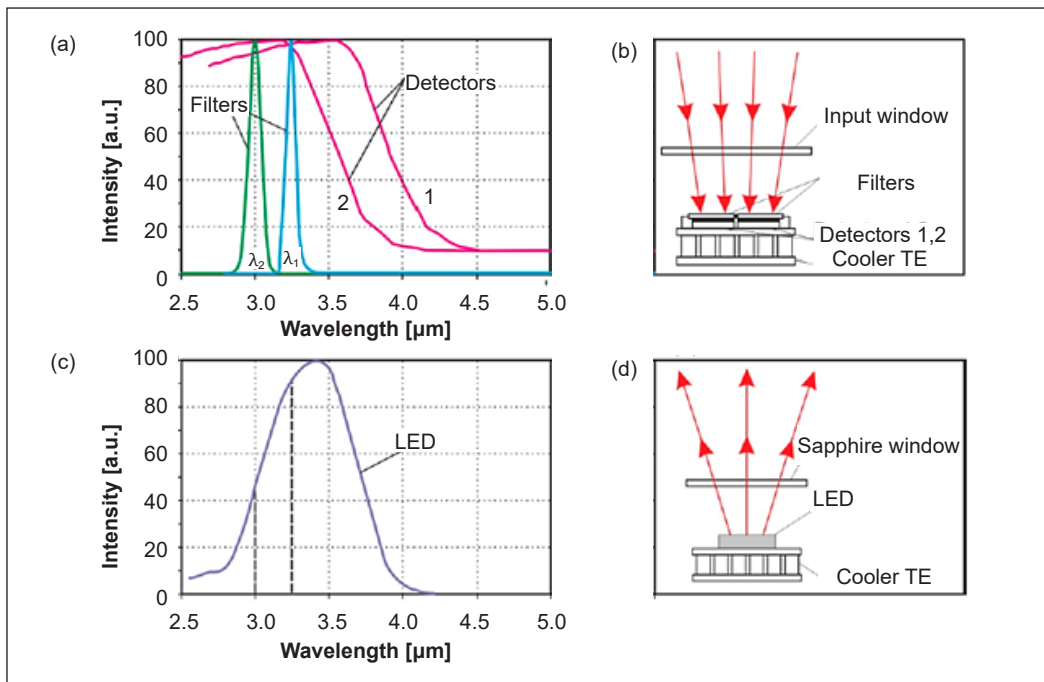


Figure 10. The opto-pair principle of methane measurement consists of: (a) filter transmittance and detector sensitivity; (b) detector block; (c) source emission spectrum; and (d) light source block. Adapted from Kwaśny & Bombalska, 2023

and 5 for the reference and working channels, respectively. The microprocessor controls the amplitude of the current, and the photodiode driver keeps it protected and stabilized at a predetermined level. The radiation emitted by the infrared photodiode covers the absorption bands of the examined gases, which are detected by detectors 1 and 2 in the absorption band and outside the band, respectively. Finally, the microprocessor computes the working and reference pulse amplitudes. Equation 3 is used to calculate their mathematical processing as well as the gas concentration.

$$C = -\ln(I_p - I_0) / L[\alpha(\lambda_p) - \alpha(\lambda_0)] \quad [3]$$

Where, L is the optical path length; I_p and I_0 are the operating channel's and reference's amplitude; and α is the coefficient of absorption at a specific wavelength.

Operating in temperatures ranging from -20 to 50°C, the sensor utilizes LEDs with an operating wavelength of around 1660 nm. The system employs two optically filtered detectors and stabilizes the temperatures of the source and detectors. Vargas-Rodríguez and Rutt (2009) further exemplify opto-pair sensors operating in the 3.5 μm wavelength region, using InAsSb(P)- and InGaAs(Sb)-based LEDs as radiation sources. These novel analyzers offer small, responsive, and energy-efficient advantages. Previous non-dispersive optical techniques for methane detection relied on narrowband interference filters to

absorb infrared light in the 3.2–3.4 or 1.65–1.67 μm bands (Kwaśny & Bombalska, 2023). Instruments relying on photoacoustic conditions or opto-pairs can detect the presence of additional hydrocarbons. Moreover, an optical correlator mimicking the features of gas absorption lines can provide substantially higher selectivity for methane determination.

Raman Spectroscopy

Raman spectroscopy, a non-destructive method, can characterize methane, even when dissolved in salty water samples, as demonstrated by Caumon et al. (2014). They utilize novel high-pressure optic cells with capillaries made of fused silicon, depicted in Figure 11. The system works by modifying the external pressure in capillaries in order to capture methane internally. Raman spectroscopy, a vibrational spectroscopic technique, offers insight into the chemical composition of gases, molecular interactions, and structure (Kamieniak et al., 2015). Similar to infrared spectroscopy, Raman spectroscopy focuses an electromagnetic radiation beam on a sample, which interacts with specific molecular vibrational modes. Unlike infrared spectroscopy, Raman spectroscopy allows for a wider range of laser wavelengths, resulting in the observable Raman Effect, characteristic of inelastic light scattering processes such as the Stokes or anti-Stokes shift. In the anti-Stokes shift, the laser stimulates a molecular structure from a vibrating state, and after light scattering, it returns to its ground state. In the Stokes shift, a molecular structure is stimulated from its ground state after light scattering and returns to a vibrating state. Since the 1930s, Raman spectroscopy has been utilized to describe compounds inorganic and organic. According to Hansuld and Briens (2014), the primary advantage of this approach is its extremely high spatial resolution and minimal sample preparation requirements. Despite each molecule having a distinct set of molecular bonds, the Raman spectrum can be used to identify the molecular signature of each molecule.

Vibrational coherent anti-Stokes Raman spectroscopy is commonly employed for methane detection (Kamieniak et al., 2015). This technique involves irradiating the sample with two powerful laser beams at different frequencies, causing medium-frequency waves to mix and polarize, resulting in a signal laser beam. This method can measure the temperature and relative concentration ratio of CH_4 to N_2 in fuel-rich CH_4 air. Coherent anti-Stokes Raman spectroscopy focuses on vibrations within molecules by using numerous photons, producing an appropriate signal superior to that of standard Raman spectroscopy. Compared to spontaneous Raman, the resulting CARS spectrum offers substantially larger peak magnitudes (Bito et al., 2013). The primary benefits of this approach include high time, spectral, and spatial resolutions. However, a drawback of CARS is that it requires the initiation of the process, as the anti-Stokes situation results in a less energetically favorable final vibrational state, causing the released photons to have a higher frequency and be in an excited state (Hansuld & Briens, 2014; Schlücker, 2014).

Methane dissolved in water exhibits two significantly weaker bands at 3017 cm^{-1} and 3066 cm^{-1} , along with a stretched vibrational peak at approximately 2915 cm^{-1} (Hester et al., 2007). The key limitation of this method is the dimensions and cost of equipment. Due to its large size and permanent connections, the equipment is typically used in laboratories and cannot be transported to the field. Therefore, this method is not suitable for online measurements in the industry. Further research into handheld Raman devices for gaseous samples is needed if this technology is to be used in the field.

Raman spectroscopy, a non-destructive method, can characterize methane, even when dissolved in salty water samples, as demonstrated by Caumon et al. (2014). They utilize novel high-pressure optical cells with capillaries made of fused silicon, depicted in Figure 11. The system works by modifying the external pressure in capillaries to capture methane internally.

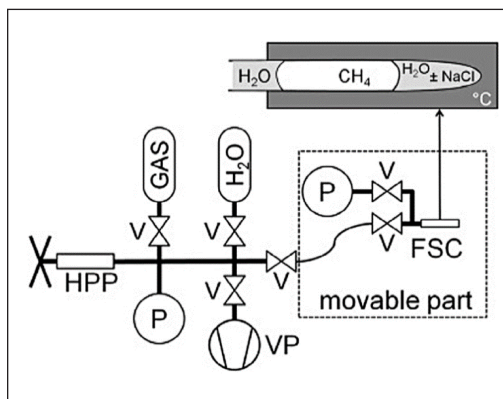


Figure 11. Optical cells under high pressure are utilized (Caumon et al., 2014). Here, FSC stands for fused-silica capillary, HPP for high-pressure pump, V for valve, P for pressure transducer, and VP for vacuum pump

Surface Plasmon Resonance

A sensor based on surface plasmon generation is known as a plasmonic sensor. Surface plasmons are a sort of light that occurs at a metal-dielectric interaction when incident radiation excites electrons, generating an electric field that propagates along the metal surface (Allsop & Neal, 2021). The parameters influencing spectrum behavior, optical properties, and surface plasmon sensing capabilities include the refracting index of metal, thickness, surface roughness, topology, extinction coefficient, and the surrounding refracting index, which forms an interface (Homola & Piliarik, 2006). These different scenarios lead to various types of surface plasmon processes.

By focusing on an optical instance, surface plasmon resonance (SPR) is triggered at the metal-dielectric connection by a diagonal magnetically polarized light source, known as surface plasmon waves (SPWs). A noteworthy decrease in the intensity of light reflection occurs due to the significance in absorption caused by the excitation of SPWs when the energy of the incident light coincides with that of SPW (Figure 12).

The study of sensitive NIR absorbance sensing tools with improved selectivity over traditional IR absorbance sensors involves a method recognized as surface-enhanced infrared resonant absorption spectroscopy. This method entails fine-tuning the SPR peak to align with the vibrating band of CH_4 molecules at the NIR wavelength (Abb et

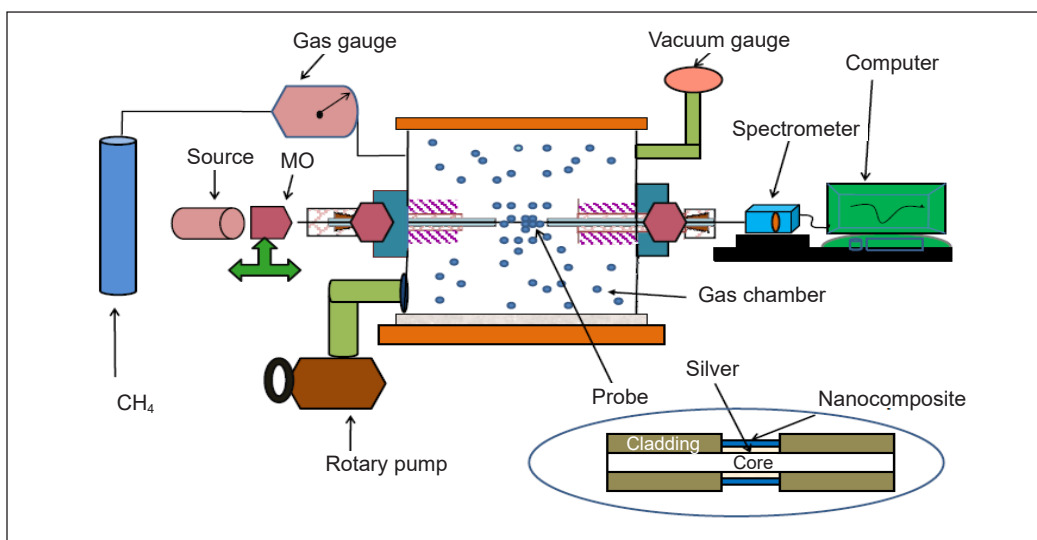


Figure 12. Schematic illustration of the SPR sensor used to detect methane gas (Mishra et al., 2015)

al., 2014). Recent examples include ITO nanocrystals (Kim et al., 2015). An equivalent strategy may be employed for CH₄ sensing, where the CO₂ characteristic band could be matched by adjusting the plasmon absorption strength via the Sn doping ratio. Additionally, including nanoparticles (AuNP) introduces a distinct type of surface plasmon resonance in metallic oxide-related detecting surfaces, particularly for high-temperature optical sensors (Ohodnicki et al., 2014). Furthermore, when exposed to CH₄, metal oxides can directly alter the optical absorbance of the metal oxide layer (Kamal et al., 2021).

Cavity Ring-down Spectroscopy

Cavity ring-down absorption spectroscopy (CRDS) technology was pioneered in 1988. Since then, a wide range of experimental modifications to CRDS spectroscopy have been developed, particularly over the last decade (Paldus & Kachanov, 2005). Foltynowicz et al. (2008) have comprehensively reviewed cavity-enhanced methods and their comparative efficacy. CRDS has become a popular method for analyzing the optical absorbance of atoms, particles, and infrared substances.

Continuous wave CRDS has been employed to investigate C–H overtone absorptions in methane, particularly focusing on wavelengths around 1.3 μm, using a slit jet expansion technique (Hippler & Quack, 2002). Research within this wavelength range has also been conducted under low-pressure and room-temperature conditions. While measurements of the absorption cross section (σ) strongly correlate with earlier spectroscopic findings, the detection limits are less favorable in the shorter wavelength band. It is attributed to the significantly lower magnitudes of σ observed at wavelengths near 1.33 μm compared to the CH₄ 2ν₃ overtone absorption band at 1.66 μm (Fawcett et al., 2002).

The CRDS approach relies on determining the duration for which radiation remains trapped within an optical resonator. This resonator typically consists of two highly reflective mirrors ($R > 99.995\%$). When a pulsed laser beam, lasting approximately 50 ns, is presented into the cavities, each mirror reflection results in a fraction $(1 - R)$ of the circulating radiation being released. In contrast, the remaining portion is mirrored again into the cavity. Figure 13 illustrates the operational mechanism of the CRDS method.

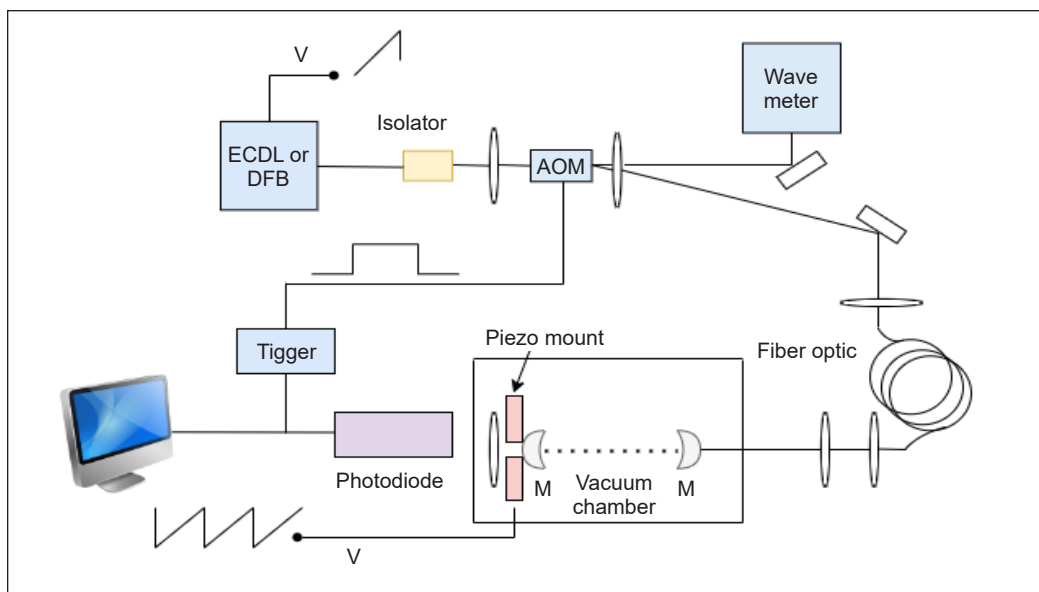


Figure 13. Illustration of Cavity Ring-Down Spectroscopy method. Here, AOM is an acoustic optic modulator; DFB is a distributed feedback laser; M is a mirror; and ECDL is an external cavity diode laser

A photomultiplier tube is employed for radiation detection behind the output mirror, while a digital oscilloscope monitors the output signal. When the cavity is filled with an absorbing substance, and the laser pulse reaches the wavelength of the absorbing gas, its decay time is reduced. Initially, the radiation decay time is determined with the empty cavity, and after that, the measurement is repeated with the addition of an absorber. Equation 4 expresses the time when the radiation (t) in the cavity disappears (Kwaśny & Bombalska, 2023).

$$\tau = \frac{L}{c[1 - R] + \alpha L} \quad [4]$$

Where L is the cavity length, R is the mirror's reflectance, and α is the coefficient of absorption.

Many CRDS method variants have been employed to find methane with ppb sensitivity (Lang et al., 2016). Numerous CRDS strategies are being used nowadays. Table 5 lists the most widely used CRDS approaches.

Table 5
Mostly used CRDS techniques

Method	Elements	Reference
Pulsed CRDS	Laser pulses are employed	He & Orr, 2000
Continuous Wave CRDS	Continuous action lasers	Romanini et al., 1997
Cavity Enhanced Absorption Spectroscopy	Consists of inserting a beam of radiation into the optical cavity off-axis	Pipino, 1999
Evanescent CRDS	Makes use of the vanishing wave principle	Atherton et al., 2004
Ring-Down Spectral Photography	With spectral decay photography	Hamilton & Orr-Ewing, 2011

COMPARISON OF PERFORMANCES

Table 6 summarizes the performance characteristics of the optical fiber instruments utilized for methane detection. The comparison of various optical fiber sensors for methane detection reveals significant differences in their performance, sensitivity, detection limits, and response times. The SnO₂/Graphene offers a broad detection range of 0 to 55%, with a detection limit of approximately 1.0%. However, the table does not mention any specific remarks or response times for this sensor, leaving questions about its practicality for real-time applications.

Table 6
Overview of the several types of optical fiber sensors used to detect methane (Adapted from Allsop & Neal, 2021)

Substance for discerning perception	Sensitivity (nm/%)	Detection limit (%)	Range (%)	Remarks	Reference
SnO ₂ /Graphene	-	~ 1.0	0 – 55	Not stated	Zhang et al., 2017
Pt/ZnO	0.01	~ 0.15	0 – 100	Regeneration, 1 s of response time	Allsop et al., 2018
Graphene+Ag	0.34	~ 0.1	0 – 3.5	Regeneration, 50 s and 160 s of response time	Wei et al., 2016
Graphene+CNTs and PMMA	1000	~ 0.0007	0 – 0.01	Not stated	Mishra et al., 2015
Cryptophane A	-1.99	~ 0.2	0 – 3.5	Not stated	Liu et al., 2018
Cryptophane A	2.5	~ 0.2	0 – 3.5	Regeneration, 60 s and 180 s of response time	Yang et al., 2017
Cryptophane A	6.39	~ 0.015	0 – 3.5	Not stated	Liu et al., 2019
Cryptophane E	1.272	~ 0.02	0 – 5	Not stated	Wang et al., 2021
Cryptophane E	4.6	~ 0.04	0 – 3	Regeneration, 60 s and 180 s of response time	Liu et al., 2020
Cryptophane E	- 1.6	~ 0.06	0 – 5	5 min of response time	Zhang et al., 2015

In contrast, the Pt/ZnO sensor provides a sensitivity of 0.01 nm/% and a detection limit of 0.15%, covering a wide operational range from 0 to 100%. Notably, it features fast regeneration with a response time of just one second, making it ideal for scenarios requiring immediate feedback. The Graphene + Ag offers moderate sensitivity at 0.34 nm/% with a detection limit of around 0.1%, but it operates within a narrower range of 0 to 3.5%. It supports regeneration but with longer response times of 50 to 160 s, making it less suitable for applications needing rapid response.

The Graphene + CNTs with PMMA sensor stands out with the highest sensitivity in the group, at 1000 nm/%, and a detection limit as low as 0.0007%. However, this sensor's operational range is extremely limited, from 0 to 0.01%, making it more appropriate for detecting trace-level methane concentrations. The performance of Cryptophane A varies significantly across studies, with sensitivity ranging from -1.99 to 6.39 nm/% and detection limits between 0.015% and 0.2%. Its operational range is generally constrained to 0 to 3.5%. Some variants, like the one reported by Yang et al. (2017), feature regeneration with response times of 60 to 180 s, making it suitable for continuous monitoring with moderate sensitivity.

The Cryptophane E sensors also exhibit diverse performance metrics, with sensitivity ranging from -1.6 to 4.6 nm/% and detection limits between 0.02% and 0.06%. Their operational ranges vary from 0 to 3% or 0 to 5%, depending on the specific study. While one version (Liu et al., 2020) offers regeneration with response times of 60 to 180 s, another (Zhang et al., 2015) demonstrates a much longer response time of five minutes, suggesting variability in recovery efficiency.

In summary, each sensor presents trade-offs between sensitivity, range, and response time. The Graphene + CNTs with PMMA sensor excels in detecting very low methane concentrations but is limited by its narrow range. Pt/ZnO offers the fastest response and widest range, making it ideal for dynamic environments. Meanwhile, Cryptophane A and Cryptophane E provide moderate sensitivity with some variants supporting regeneration, though their response times vary significantly. These insights suggest that selecting the appropriate sensor depends on the specific requirements of the application, such as detection precision, response speed, or operational range.

RECENT RESEARCH DEVELOPMENTS OF OPTICAL SENSORS

Several studies have focused on improving optical methane sensors. In recent years, infrared methane detection technology has gained popularity due to its numerous advantages, including longevity, high reliability, wide applicability, and precise detection capabilities (Yu et al., 2014). Among various laser-based methane detection techniques, photoacoustic spectroscopy has emerged as particularly promising. It has demonstrated its ability, more effectively than established methods such as Cavity Ring-down spectroscopy, differential

spectroscopy, or higher-frequency modulation techniques, to serve several distinct applications such as commercial surveillance, healthcare (e.g., breath analysis for disease diagnosis), and atmospheric and ecological studies. An optical correlator that matches gas absorption lines offers significantly improved selectivity for methane detection. In optical gas sensors that utilize laser absorption spectroscopy, photoacoustic spectroscopy, optical resonators (cavities), and multi-pass gas cells are foundational components (Mikołajczyk et al., 2016). TDLAS stands out as the most advanced, versatile, and efficient optical technique for gas detection (McManus, 2010). This method enables both in-person and remote measurements to be conducted.

Iseki et al. (2000) developed a compact remote methane sensor utilizing a 1.65 μm InGaAsP distributed feedback laser. It is intended to be a man-portable, long-path absorbance lidar that can reach up to 10 meters using a topographical target. Scanning the laser light is a simple way for an operator to look for gas leaks. Dong et al. (2007) proposed a cavity-enhanced method for a Fabry-Pérot cavity (FPC) sensor to increase the precision of gas measurements. The method comprised scanning the cavity length at each laser frequency to record the transmission maxima of the cavity modes. After integrating the new approach, it was discovered that the FPC sensor could detect methane with a sensitivity of 0.7–2.9 parts per million by mass (ppm-m).

An optical fiber-based methane sensor based on stannic oxide doped with graphene was studied by Zhang et al. (2017). Thin graphene-doped tin oxide coatings were put on side-polished optical fibers to create the sensor, and a wavelength of 1550 nm was chosen as the optical spectrum's light source. The optical fibers' output light intensities were measured using various methane concentrations. The refractive index and SnO₂ conductivity rose in parallel with the methane concentration. As a result, the absorption coefficient dropped, and the output light intensity improved. The results demonstrated that adding graphene-doped SnO₂ enhanced the sensor's sensitivity, repeatability, output light intensity, and dependability.

Tombez et al. (2017) developed a tiny, affordable, and IR-adjustable diode-laser absorption spectroscope with silicon at chip-scale photonics integrated for flexible gas sensors. With an uncooled InGaAs detection technique equipped with a high-contrast index silicon waveguide at the nanoscale, the authors analyzed ambient methane using near-IR (1650 nm) light from a laser with distributed feedback, achieving a sub-100 ppm-v limit of detection. An easy, inexpensive, and modest all-fiber methane sensor was created by Ismaeel et al. (2019). It is made up of two fiber Bragg gratings and an optical fiber with a D-shaped cross-section. The Teflon layer covering the fiber was the most important development in this work, which was doped with cryptophane, a substance that prefers methane gas. With a reaction time of 4 s, the sensor reached an impressive sensitivity (0.16 nm/ppm-m).

Recently, there has been a study on a potential technology called hollow-core photonic crystal fiber, where a more effective light-gas interaction is made possible by the gas being firmly filled into the hollow core (Xie et al., 2016). HC-PBF-based photothermal spectroscopy enables the detection of various gases, including CH₄, H₂S, CO₂, CO, and NH₃, among others. However, it is worth noting that the length of the HC-PBF can influence the sensor's sensitivity and reaction time. Additionally, a recent development involves utilizing UAVs with remotely operated methane detectors, offering a promising solution for detecting natural gas leakage in pipelines (Hollenbeck et al., 2021).

COMMERCIAL APPLICATIONS OF OPTICAL-BASED METHANE SENSORS

Optical fiber-based methane sensors have become increasingly popular due to their high sensitivity, fast response times, and immunity to electromagnetic interference. These sensors capitalize on the interaction between methane molecules and light traveling through optical fibers, providing benefits such as remote sensing, multiplexing, and suitability for challenging environments. This review delves into the practical applications of optical fiber-based methane sensors in commercial settings, showcasing their versatility across different industries. It also underscores recent sensor design and performance innovations, demonstrating the ongoing advancements in this field.

In the oil and gas sector, optical fiber-based methane sensors have emerged as valuable tools for leak detection and emissions monitoring in upstream, midstream, and downstream operations. According to Collins et al. (2022), distributed optical fiber sensors enable continuous monitoring of methane concentrations along pipelines and wellheads, providing real-time data for early leak detection and localization. Integrating optical fibers into existing infrastructure offers a cost-effective solution for enhancing safety protocols and minimizing environmental impact.

Environmental monitoring applications of optical fiber-based methane sensors encompass a wide range of scenarios, including landfill gas management, agricultural emissions, and ecosystem research. As highlighted by Butt et al. (2022), distributed optical fiber sensing technology enables spatially resolved monitoring of methane emissions from landfills, facilitating the optimization of gas collection systems and the assessment of emission mitigation strategies. Similarly, optical fiber-based sensors provide valuable insights into methane production from livestock activities and manure management practices in agricultural settings.

Optical fiber-based methane sensors also find applications in industrial process control and quality assurance, particularly in chemical synthesis, fermentation, and biogas production processes. Fiber-optic sensing platforms offer high sensitivity and multiplexing capabilities, enabling real-time monitoring of methane concentrations in reactors and

bioreactors. They facilitate process optimization, yield maximization, and product quality assurance, contributing to operational efficiency and cost savings in industrial manufacturing.

The commercialization of optical fiber-based methane sensors is poised for continued growth, driven by advancements in sensor technology, miniaturization, and integration with data analytics platforms. Moreover, integrating optical fiber sensing networks with artificial intelligence algorithms holds promise for autonomous monitoring systems and predictive maintenance strategies, opening new avenues for commercial applications in smart cities, industrial automation, and environmental monitoring.

CONCLUSION

This study has reviewed recent advancements in optical-based techniques for methane detection. Detecting even the smallest methane leaks is highlighted due to the potential explosions and environmental impact risks. Spectroscopic methods can provide both qualitative and quantitative assessments of methane levels. In addition, highly specific and sensitive methodologies are available, enabling accurate determination of methane concentrations. Unfortunately, the available spectroscopic instruments are primarily designed for laboratory use, resulting in higher operational costs and limited suitability for point-of-care analysis. Additionally, these instruments are not conducive to real-time monitoring. Given the escalating concerns regarding greenhouse gas emissions, industries must accurately track the temporal variations in methane concentrations to gain comprehensive insights into these emissions. A reliable, real-time measurement system is imperative for facilitating efficient management of greenhouse gas emissions and establishing a responsive underground mine ventilation system.

Nonetheless, Tunable Diode Laser Absorption Spectroscopy (TDLAS) emerges as a portable spectroscopic technique that can be deployed directly at the site of environmental pollution. TDLAS is further enhanced through its integration with fiber optics, enabling distributed sensing and monitoring of diverse gases. It includes open paths, gas cells, evanescent fields, and microstructure fiber-optic sensors. Optical fiber-based methane measurement stands out as a unique approach for sensing methane gas concentrations, particularly in industrial settings such as the mining sector.

Moreover, current techniques either require human intervention or exhibit significant time delays in accurately measuring gas concentrations within the target area. Future research endeavors in distributed optical fiber-based sensing techniques, particularly those employing sequential multi-cells, should prioritize developing and evaluating resilient and effective gas sensors capable of accurately measuring gas concentrations in challenging environments.

ACKNOWLEDGMENTS

The authors sincerely thank the Universiti Malaysia Pahang Al-Sultan Abdullah (UMPSA), Malaysia, for supporting and providing research funds for this project (PDU233203). Additionally, the authors would like to sincerely thank the Faculty of Electrical and Electronics Engineering Technology, UMPSA, Malaysia, for providing access to a few facilities.

REFERENCES

- Abb, M., Wang, Y., Papasimakis, N., De Groot, C. H., & Muskens, O. L. (2014). Surface-enhanced infrared spectroscopy using metal oxide plasmonic antenna arrays. *Nano Letters*, *14*(1), 346–352. <https://doi.org/10.1021/nl404115g>
- Agius, C., Brenon, M., Dill, W. G., Kelly, P., Klausmeyer, U., McManama, K., Pogorelsky, A., & Zalogine, A. S. (2000). The impact of the IECEx scheme on the global availability of explosion protected apparatus-update 2000 (parts IV-VII). In *Conference Record of the 2000 IEEE Industry Applications Conference. Thirty-Fifth IAS Annual Meeting and World Conference on Industrial Applications of Electrical Energy (Cat. No. 00CH37129)* (Vol. 4, pp. 2844-2851). IEEE Publishing. <https://doi.org/10.1109/IAS.2000.883225>
- Allsop, T., & Neal, R. (2021). A review: Application and implementation of optic fibre sensors for gas detection. *Sensors*, *21*(20), Article 6755. <https://doi.org/10.3390/s21206755>
- Allsop, T., Kundrat, V., Kalli, K., Lee, G. B., Neal, R., Bond, P., Shi, B., Sullivan, J., Culverhouse, P., & Webb, D. J. (2018). Methane detection scheme based upon the changing optical constants of a zinc oxide/platinum matrix created by a redox reaction and their effect upon surface plasmons. *Sensors and Actuators B: Chemical*, *255*, 843–853. <https://doi.org/10.1016/j.snb.2017.08.058>
- Atherton, K., Yu, H., Stewart, G., & Culshaw, B. (2004). Gas detection with fibre amplifiers by intra-cavity and cavity ring-down absorption. *Measurement Science and Technology*, *15*, 1621–1628.
- Bachu, S. (2017). Analysis of gas leakage occurrence along wells in Alberta, Canada, from a GHG perspective – Gas migration outside well casing. *International Journal of Greenhouse Gas Control*, *61*, 146–154. <https://doi.org/10.1016/j.ijggc.2017.04.003>
- Beckwith, P. H., Brown, C. E., Danagher, D. J., Smith, D. R., & Reid, J. (1987). High sensitivity detection of transient infrared absorption using tunable diode lasers. *Applied Optics*, *26*(13), Article 2643. <https://doi.org/10.1364/AO.26.002643>
- Bito, K., Okuno, M., Kano, H., Leproux, P., Couderc, V., & Hamaguchi, H. (2013). Three-pulse multiplex coherent anti-Stokes/Stokes Raman scattering (CARS/CSRS) microspectroscopy using a white-light laser source. *Chemical Physics*, *419*, 156–162. <https://doi.org/10.1016/j.chemphys.2013.02.007>
- Butt, M. A., Voronkov, G. S., Grakhova, E. P., Kutluyarov, R. V., Kazanskiy, N. L., & Khonina, S. N. (2022). Environmental monitoring: A comprehensive review on optical waveguide and fiber-based sensors. *Biosensors*, *12*(11), Article 1038. <https://doi.org/10.3390/bios12111038>

- Caumon, M. C., Robert, P., Laverret, E., Tarantola, A., Randi, A., Pironon, J., Dubessy, J., & Girard, J. P. (2014). Determination of methane content in NaCl–H₂O fluid inclusions by Raman spectroscopy. Calibration and application to the external part of the Central Alps (Switzerland). *Chemical Geology*, 378–379, 52–61. <https://doi.org/10.1016/j.chemgeo.2014.03.016>
- Collins, W., Orbach, R., Bailey, M., Biraud, S., Coddington, I., DiCarlo, D., Peischl, J., Radhakrishnan, A., & Schimel, D. (2022). Monitoring methane emissions from oil and gas operations. *Optics Express*, 30(14), Article 24326. <https://doi.org/10.1364/OE.464421>
- Dong, L., Yin, W., Ma, W., Zhang, L., & Jia, S. (2007). High-sensitivity, large dynamic range, auto-calibration methane optical sensor using a short confocal Fabry–Perot cavity. *Sensors and Actuators B: Chemical*, 127(2), 350–357. <https://doi.org/10.1016/j.snb.2007.04.030>
- Fawcett, B. L., Parkes, A. M., Shallcross, D. E., & Orr-Ewing, A. J. (2002). Trace detection of methane using continuous wave cavity ring-down spectroscopy at 1.65 μm . *Physical Chemistry Chemical Physics*, 4(24), 5960–5965. <https://doi.org/10.1039/B208486B>
- Foltynowicz, A., Schmidt, F. M., Ma, W., & Axner, O. (2008). Noise-immune cavity-enhanced optical heterodyne molecular spectroscopy: Current status and future potential. *Applied Physics B*, 92(3), Article 313. <https://doi.org/10.1007/s00340-008-3126-z>
- Formisano, V., Atreya, S., Encrenaz, T., Ignatiev, N., & Giuranna, M. (2004). Detection of methane in the atmosphere of Mars. *Science*, 306(5702), 1758–1761. <https://doi.org/10.1126/science.1101732>
- Gao, Q., Zhang, Y., Yu, J., Wu, S., Zhang, Z., Zheng, F., Lou, X., & Guo, W. (2013). Tunable multi-mode diode laser absorption spectroscopy for methane detection. *Sensors and Actuators A: Physical*, 199, 106–110. <https://doi.org/10.1016/j.sna.2013.05.012>
- Gardiner, T., Mead, M. I., Garcelon, S., Robinson, R., Swann, N., Hansford, G. M., Woods, P. T., & Jones, R. L. (2010). A lightweight near-infrared spectrometer for the detection of trace atmospheric species. *Review of Scientific Instruments*, 81(8), Article 083102. <https://doi.org/10.1063/1.3455827>
- Gurlit, W., Zimmermann, R., Giesemann, C., Fernholz, T., Ebert, V., Wolfrum, J., Platt, U., & Burrows, J. P. (2005). Lightweight diode laser spectrometer CHILD (Compact High-altitude In-situ Laser Diode) for balloonborne measurements of water vapor and methane. *Applied Optics*, 44(1), Article 91. <https://doi.org/10.1364/AO.44.000091>
- Hamilton, D. J., & Orr-Ewing, A. J. (2011). A quantum cascade laser-based optical feedback cavity-enhanced absorption spectrometer for the simultaneous measurement of CH₄ and N₂O in air. *Applied Physics B*, 102(4), 879–890. <https://doi.org/10.1007/s00340-010-4259-4>
- Hansuld, E. M., & Briens, L. (2014). A review of monitoring methods for pharmaceutical wet granulation. *International Journal of Pharmaceutics*, 472(1–2), 192–201. <https://doi.org/10.1016/j.ijpharm.2014.06.027>
- He, Y., & Orr, B. J. (2000). Ringdown and cavity-enhanced absorption spectroscopy using a continuous-wave tunable diode laser and a rapidly swept optical cavity. *Chemical Physics Letters*, 319(1–2), 131–137. [https://doi.org/10.1016/S0009-2614\(00\)00107-X](https://doi.org/10.1016/S0009-2614(00)00107-X)
- Hennig, O., Strzoda, R., Mágóri, E., Chemisky, E., Tump, C., Fleischer, M., Meixner, H., & Eisele, I. (2003). Hand-held unit for simultaneous detection of methane and ethane based on NIR-absorption

- spectroscopy. *Sensors and Actuators B: Chemical*, 95(1–3), 151–156. [https://doi.org/10.1016/S0925-4005\(03\)00399-X](https://doi.org/10.1016/S0925-4005(03)00399-X)
- Hester, K. C., Dunk, R. M., White, S. N., Brewer, P. G., Peltzer, E. T., & Sloan, E. D. (2007). Gas hydrate measurements at Hydrate Ridge using Raman spectroscopy. *Geochimica et Cosmochimica Acta*, 71(12), 2947–2959. <https://doi.org/10.1016/j.gca.2007.03.032>
- Hippler, M., & Quack, M. (2002). High-resolution Fourier transform infrared and cw-diode laser cavity ringdown spectroscopy of the $\nu_2+\nu_3$ band of methane near 7510 cm^{-1} in slit jet expansions and at room temperature. *The Journal of Chemical Physics*, 116(14), 6045–6055. <https://doi.org/10.1063/1.1433505>
- Hodgkinson, J., & Pride, R. D. (2010). Methane-specific gas detectors: The effect of natural gas composition. *Measurement Science and Technology*, 21(10), Article 105103. <https://doi.org/10.1088/0957-0233/21/10/105103>
- Hodgkinson, J., & Tatam, R. P. (2013). Optical gas sensing: A review. *Measurement Science and Technology*, 24(1), Article 012004. <https://doi.org/10.1088/0957-0233/24/1/012004>
- Hodgkinson, J., Shan, Q., & Pride, R. D. (2006). Detection of a simulated gas leak in a wind tunnel. *Measurement Science and Technology*, 17(6), 1586–1593. <https://doi.org/10.1088/0957-0233/17/6/041>
- Hollenbeck, D., Zulevic, D., & Chen, Y. (2021). Advanced leak detection and quantification of methane emissions using sUAS. *Drones*, 5(4), Article 117. <https://doi.org/10.3390/drones5040117>
- Homola, J., & Piliarik, M. (2006). *Surface Plasmon Resonance (SPR) sensors*. Springer.
- Hong, T., Culp, J. T., Kim, K. J., Devkota, J., Sun, C., & Ohodnicki, P. R. (2020). State-of-the-art of methane sensing materials: A review and perspectives. *TrAC Trends in Analytical Chemistry*, 125, Article 115820. <https://doi.org/10.1016/j.trac.2020.115820>
- Ingraffea, A. R., Wawrzynek, P. A., Santoro, R., & Wells, M. (2020). Reported methane emissions from active oil and gas wells in Pennsylvania, 2014–2018. *Environmental Science & Technology*, 54(9), 5783–5789. <https://doi.org/10.1021/acs.est.0c00863>
- Iseki, T., Tai, H., & Kimura, K. (2000). A portable remote methane sensor using a tunable diode laser. *Measurement Science and Technology*, 11(6), 594–602. <https://doi.org/10.1088/0957-0233/11/6/302>
- Ismael, R., Beaton, A., Donko, A., Talataisong, W., Lee, T., Brotin, T., Beresna, M., Mowlem, M., & Brambilla, G. (2019). High sensitivity all-fibre methane sensor with gas permeable teflon/cryptophane-a membrane. In *The European Conference on Lasers and Electro-Optics* (p. ch_6_5). Optica Publishing Group.
- Jaramillo, P., Griffin, W. M., & Matthews, H. S. (2008). Comparative analysis of the production costs and life-cycle GHG emissions of FT liquid fuels from coal and natural gas. *Environmental Science & Technology*, 42(20), 7559–7565. <https://doi.org/10.1021/es8002074>
- Kamal, D. A. M., Ibrahim, S. F., Kamal, H., Kashim, M. I. A. M., & Mokhtar, M. H. (2021). Physicochemical and medicinal properties of Tualang, Gelam and Kelulut Honeys: A comprehensive review. *Nutrients*, 13(1), Article 197. <https://doi.org/10.3390/nu13010197>
- Kamieniak, J., Randviir, E. P., & Banks, C. E. (2015). The latest developments in the analytical sensing of methane. *TrAC Trends in Analytical Chemistry*, 73, 146–157. <https://doi.org/10.1016/j.trac.2015.04.030>

- Kannath, A., Hodgkinson, J., Gillard, R. G., Riley, R. J., & Tatam, R. P. (2011). A VCSEL based system for on-site monitoring of low level methane emission. In *Vertical-Cavity Surface-Emitting Lasers XV* (Vol. 7952, pp. 99-107). SPIE. <https://doi.org/10.1117/12.874513>
- Kim, K. J., Chong, X., Kreider, P. B., Ma, G., Ohodnicki, P. R., Baltrus, J. P., Wang, A. X., & Chang, C. H. (2015). Plasmonics-enhanced metal–organic framework nanoporous films for highly sensitive near-infrared absorption. *Journal of Materials Chemistry C*, 3(12), 2763–2767. <https://doi.org/10.1039/C4TC02846E>
- Kwaśny, M., & Bombalska, A. (2023). Optical methods of methane detection. *Sensors*, 23(5), Article 2834. <https://doi.org/10.3390/s23052834>
- Lang, N., Macherius, U., Wiese, M., Zimmermann, H., Röpcke, J., & Van Helden, J. H. (2016). Sensitive CH₄ detection applying quantum cascade laser based optical feedback cavity-enhanced absorption spectroscopy. *Optics Express*, 24(6), Article A536. <https://doi.org/10.1364/OE.24.00A536>
- Lawrence, N. (2006). Analytical detection methodologies for methane and related hydrocarbons. *Talanta*, 69(2), 385–392. <https://doi.org/10.1016/j.talanta.2005.10.005>
- Liu, H., Wang, H., Chen, C., Zhang, W., Bai, B., Chen, C., Zhang, Y., & Shao, Q. (2020). High sensitive methane sensor based on twin-core photonic crystal fiber with compound film-coated side-holes. *Optical and Quantum Electronics*, 52(2), Article 81. <https://doi.org/10.1007/s11082-020-2198-9>
- Liu, H., Wang, M., Wang, Q., Li, H., Ding, Y., & Zhu, C. (2018). Simultaneous measurement of hydrogen and methane based on PCF-SPR structure with compound film-coated side-holes. *Optical Fiber Technology*, 45, 1–7. <https://doi.org/10.1016/j.yofte.2018.05.007>
- Liu, H., Zhang, Y., Chen, C., Bai, B., Shao, Q., Wang, H., Zhang, W., Chen, C., & Tang, S. (2019). Transverse-stress compensated methane sensor based on long-period grating in photonic crystal fiber. *IEEE Access*, 7, 175522–175530. <https://doi.org/10.1109/ACCESS.2019.2951133>
- McDermitt, D., Burba, G., Xu, L., Anderson, T., Komissarov, A., Riensche, B., Schedlbauer, J., Starr, G., Zona, D., Oechel, W., Oberbauer, S., & Hastings, S. (2011). A new low-power, open-path instrument for measuring methane flux by eddy covariance. *Applied Physics B*, 102(2), 391–405. <https://doi.org/10.1007/s00340-010-4307-0>
- McManus, J. B. (2010). Application of quantum cascade lasers to high-precision atmospheric trace gas measurements. *Optical Engineering*, 49(11), Article 111124. <https://doi.org/10.1117/1.3498782>
- McManus, J. B., Shorter, J. H., Nelson, D. D., Zahniser, M. S., Glenn, D. E., & McGovern, R. M. (2008). Pulsed quantum cascade laser instrument with compact design for rapid, high sensitivity measurements of trace gases in air. *Applied Physics B*, 92(3), Article 387. <https://doi.org/10.1007/s00340-008-3129-9>
- Mikołajczyk, J., Wojtas, J., Bielecki, Z., Stacewicz, T., Szabra, D., Magryta, P., Prokopiuk, A., Tkacz, A., & Panek, M. (2016). System of optoelectronic sensors for breath analysis. *Metrology and Measurement Systems*, 23(3), 481–489. <https://doi.org/10.1515/mms-2016-0030>
- Mishra, S. K., Tripathi, S. N., Choudhary, V., & Gupta, B. D. (2015). Surface plasmon resonance-based fiber optic methane gas sensor utilizing graphene-carbon nanotubes-poly(methyl methacrylate) hybrid nanocomposite. *Plasmonics*, 10(5), 1147–1157. <https://doi.org/10.1007/s11468-015-9914-5>

- Ohodnicki Jr., P. R., Brown, T. D., Holcomb, G. R., Tyleczak, J., Schultz, A. M., & Baltrus, J. P. (2014). High temperature optical sensing of gas and temperature using AU-nanoparticle incorporated oxides. *Sensors and Actuators B: Chemical*, 202, 489–499. <https://doi.org/10.1016/j.snb.2014.04.106>
- Olmer, N., Comer, B., Roy, B., Mao, X., & Rutherford, D. (2019, November 25). *Greenhouse gas emissions from global shipping, 2013–2015 Detailed Methodology*. <https://www.theicct.org/publications/GHG-emissions-globalshipping-2013-2015>
- Paldus, B. A., & Kachanov, A. A. (2005). An historical overview of cavity-enhanced methods. *Canadian Journal of Physics*, 83(10), 975–999. <https://doi.org/10.1139/p05-054>
- Pipino, A. C. R. (1999). Ultrasensitive surface spectroscopy with a miniature optical resonator. *Physical Review Letters*, 83(15), 3093–3096. <https://doi.org/10.1103/PhysRevLett.83.3093>
- Pyun, S. H., Cho, J., Davidson, D. F., & Hanson, R. K. (2011). Interference-free mid-IR laser absorption detection of methane. *Measurement Science and Technology*, 22(2), Article 025303. <https://doi.org/10.1088/0957-0233/22/2/025303>
- Richard, E. C., Kelly, K. K., Winkler, R. H., Wilson, R., Thompson, T. L., McLaughlin, R. J., Schmeltekopf, A. L., & Tuck, A. F. (2002). A fast-response near-infrared tunable diode laser absorption spectrometer for in situ measurements of CH₄ in the upper troposphere and lower stratosphere. *Applied Physics B: Lasers and Optics*, 75(2–3), 183–194. <https://doi.org/10.1007/s00340-002-0935-3>
- Romanini, D., Kachanov, A. A., & Stoeckel, F. (1997). Diode laser cavity ring down spectroscopy. *Chemical Physics Letters*, 270(5–6), 538–545. [https://doi.org/10.1016/S0009-2614\(97\)00406-5](https://doi.org/10.1016/S0009-2614(97)00406-5)
- Rothman, L. S., Gordon, I. E., Barbe, A., Benner, D. C., Bernath, P. F., Birk, M., Boudon, V., Brown, L. R., Campargue, A., Champion, J.-P., Chance, K., Coudert, L. H., Dana, V., Devi, V. M., Fally, S., Flaud, J.-M., Gamache, R. R., Goldman, A., Jacquemart, D., ... & Vander Auwera, J. (2009). The HITRAN 2008 molecular spectroscopic database. *Journal of Quantitative Spectroscopy and Radiative Transfer*, 110(9–10), 533–572. <https://doi.org/10.1016/j.jqsrt.2009.02.013>
- Schlücker, S. (2014). Surface-enhanced Raman spectroscopy: Concepts and chemical applications. *Angewandte Chemie International Edition*, 53(19), 4756–4795. <https://doi.org/10.1002/anie.201205748>
- Shao, L., Fang, B., Zheng, F., Qiu, X., He, Q., Wei, J., Li, C., & Zhao, W. (2019). Simultaneous detection of atmospheric CO and CH₄ based on TDLAS using a single 2.3 μm DFB laser. *Spectrochimica Acta Part A: Molecular and Biomolecular Spectroscopy*, 222, Article 117118. <https://doi.org/10.1016/j.saa.2019.05.023>
- Shemshad, J., Aminossadati, S. M., & Kizil, M. S. (2012). A review of developments in near infrared methane detection based on tunable diode laser. *Sensors and Actuators B: Chemical*, 171–172, 77–92. <https://doi.org/10.1016/j.snb.2012.06.018>
- Stocker, T. F., Dahe, Q., Plattner, G. K., Tignor, M. B., Allen, S. K., Boschung, J., Nauels, A., Xia, Y., Bex, V., & Midgley, P. (2014). *Climate change 2013: The physical science basis*. Cambridge University Press.
- Tiemann, M. (2007). Porous metal oxides as gas sensors. *Chemistry – A European Journal*, 13(30), 8376–8388. <https://doi.org/10.1002/chem.200700927>

- Tombez, L., Zhang, E. J., Orcutt, J. S., Kamapurkar, S., & Green, W. M. J. (2017). Methane absorption spectroscopy on a silicon photonic chip. *Optica*, 4(11), Article 1322. <https://doi.org/10.1364/OPTICA.4.001322>
- Tran, M. K., & Fowler, M. (2020). A review of lithium-ion battery fault diagnostic algorithms: Current progress and future challenges. *Algorithms*, 13(3), Article 62. <https://doi.org/10.3390/a13030062>
- Turner, A. J., Frankenberg, C., & Kort, E. A. (2019). Interpreting contemporary trends in atmospheric methane. *Proceedings of the National Academy of Sciences*, 116(8), 2805–2813. <https://doi.org/10.1073/pnas.1814297116>
- Vargas-Rodríguez, E., & Rutt, H. N. (2009). Design of CO, CO₂ and CH₄ gas sensors based on correlation spectroscopy using a Fabry–Perot interferometer. *Sensors and Actuators B: Chemical*, 137(2), 410–419. <https://doi.org/10.1016/j.snb.2009.01.013>
- Vasiliev, A. A., Pislakov, A. V., Sokolov, A. V., Polovko, O. V., Samotaev, N. N., Kujawski, W., Rozicka, A., Guarnieri, V., & Lorencelli, L. (2014). Gas sensor system for the determination of methane in water. *Procedia Engineering*, 87, 1445–1448. <https://doi.org/10.1016/j.proeng.2014.11.721>
- Wang, X., & Wolfbeis, O. S. (2016). Fiber-optic chemical sensors and biosensors (2013–2015). *Analytical Chemistry*, 88(1), 203–227. <https://doi.org/10.1021/acs.analchem.5b04298>
- Wang, Z., Gao, P., Liu, S., & Chen, X. (2021). A reflective methane concentration sensor based on biconvex cone photonic crystal fiber. *Optik*, 241, Article 166983. <https://doi.org/10.1016/j.ijleo.2021.166983>
- Wei, T., Wu, H., Dong, L., Cui, R., & Jia, S. (2021). Palm-sized methane TDLAS sensor based on a mini-multi-pass cell and a quartz tuning fork as a thermal detector. *Optics Express*, 29(8), Article 12357. <https://doi.org/10.1364/OE.423217>
- Wei, W., Nong, J., Zhang, G., Tang, L., Jiang, X., Chen, N., Luo, S., Lan, G., & Zhu, Y. (2016). Graphene-based long-period fiber grating surface plasmon resonance sensor for high-sensitivity gas sensing. *Sensors*, 17(12), Article 2. <https://doi.org/10.3390/s17010002>
- Wild, K. (2000). Gas quality measurement: A gas control revolution? *Gas Engineering and Management*, 40, 12–14.
- Wisn, J., Chesnaux, R., Werring, J., Wendling, G., Baudron, P., & Barbecot, F. (2020). A portrait of wellbore leakage in northeastern British Columbia, Canada. *Proceedings of the National Academy of Sciences*, 117(2), 913–922. <https://doi.org/10.1073/pnas.1817929116>
- Xie, S., Pennetta, R., & Russell, P. St. J. (2016). Self-alignment of glass fiber nanospikes by optomechanical back-action in hollow-core photonic crystal fiber. *Optica*, 3(3), Article 277. <https://doi.org/10.1364/OPTICA.3.000277>
- Yang, J., Che, X., Shen, R., Wang, C., Li, X., & Chen, W. (2017). High-sensitivity photonic crystal fiber long-period grating methane sensor with cryptophane-A-6Me absorbed on a PAA-CNTs/PAH nanofilm. *Optics Express*, 25(17), Article 20258. <https://doi.org/10.1364/OE.25.020258>
- Yu, X., Lv, R. H., Song, F., Zheng, C. T., & Wang, Y. D. (2014). Pocket-sized nondispersive infrared methane detection device using two-parameter temperature compensation. *Spectroscopy Letters*, 47(1), 30–37. <https://doi.org/10.1080/00387010.2013.780082>

- Zhang, J. Y., Ding, E. J., Xu, S. C., Li, Z. H., Wang, X. X., & Song, F. (2017). Sensitization of an optical fiber methane sensor with graphene. *Optical Fiber Technology*, 37, 26–29. <https://doi.org/10.1016/j.yofte.2017.06.011>
- Zhang, Y., Zhao, Y., & Wang, Q. (2015). Measurement of methane concentration with cryptophane E infiltrated photonic crystal microcavity. *Sensors and Actuators B: Chemical*, 209, 431–437. <https://doi.org/10.1016/j.snb.2014.12.002>

Case Study

Carbon Emission from Transportation in Higher Learning Institutions: A Case Study at Universiti Tun Hussein Onn Malaysia

Khairunmarhanis Zekefli¹, Aeslina Abdul Kadir^{1*}, Amir Detho¹ and Mohd Ikhmal Haqem Hassan²

¹Faculty of Civil Engineering and Built Environment, Universiti Tun Hussein Onn Malaysia, Batu Pahat, 86400, Malaysia

²Department of Engineering, Faculty of Civil Engineering and Life Sciences, Universiti Selangor, 45600 Bestari Jaya, Selangor, Malaysia

ABSTRACT

The carbon emissions stemming from transportation within the campus environment pose a significant challenge to mitigating climate change and environmental degradation. At Universiti Tun Hussein Onn Malaysia (UTHM), transportation, particularly by staff and students, has been identified as the primary contributor to greenhouse gas emissions. This study aims to assess the total carbon emissions from transportation at UTHM and analyze trends over three consecutive years (2021 to 2023). Data were obtained from the Traffic Unit of the Security Department, encompassing vehicle counts and traffic surveys conducted across five roads within the UTHM Campus. The findings revealed a concerning escalation in carbon emissions over the study period. In 2021, transportation activities accounted for 947.64 tCO₂e, which surged to 1568.42 tCO₂e in 2022 and further increased to 1679.88 tCO₂e in 2023. Notably, Persiaran Tun Ghazali Shafie emerged as a hotspot area for carbon emissions in 2023, experiencing a staggering 95.76% rise

compared to 2021, with recorded emissions of 610 tCO₂e. The average carbon emissions across the five surveyed roads in 2023 soared by 73.84% compared to 2021, indicating a persistent upward trajectory in emissions. These findings underscore the urgent need for sustained carbon emissions monitoring and mitigation efforts at UTHM. Continuous assessment by UTHM authorities is imperative to identify

ARTICLE INFO

Article history:

Received: 20 February 2024

Accepted: 03 September 2024

Published: 25 October 2024

DOI: <https://doi.org/10.47836/pjst.32.6.20>

E-mail addresses:

cf200226@student.uthm.edu.my (Khairunmarhanis Zekefli)

aeslina@uthm.edu.my (Aeslina Abdul Kadir)

amirdetho@gmail.com (Amir Detho)

haqem@unisel.edu.my (Mohd Ikhmal Haqem Hassan)

* Corresponding author

and implement effective strategies for curbing carbon emissions within the campus environment. UTHM can be pivotal in fostering a more sustainable and environmentally responsible campus community by prioritizing emission reduction initiatives.

Keywords: Carbon emission, climate change, greenhouse gas emissions, sustainability, transportation

INTRODUCTION

Carbon emissions are a significant issue in universities with a large population and expansive campuses. Due to the size of these campuses, automobiles are often necessary for transportation between different locations. Additionally, the various activities within the university, such as teaching, learning, residential living, and administrative tasks, require a considerable amount of energy for lighting, cooling, and running appliances. Furthermore, the frequent movement of vehicles within the campus leads to the consumption of fossil fuel energy and subsequent carbon dioxide emissions (Abdul-Azeez & Ho, 2015).

The type of vehicle, type of fossil fuel, and travel distance are the main factors influencing the most daily and annual carbon emissions in universities (Zakaria et al., 2021). Universities are typically bustling with students, faculty, and staff commuting to and from the campus. If most individuals use personal vehicles, they can contribute to carbon emissions. Similarly, university-owned vehicles, such as shuttle buses and maintenance trucks, also contribute to emissions.

Achieving the reduction of carbon emissions from transportation use in university campuses by encouraging low carbon emissions through the involvement of the universities may be beneficial in achieving transportation sustainability within the campus as a remedy to the current phenomenon of global warming (Abdul-Azeez & Ho, 2015). This approach will help mitigate global warming and reduce global environmental threats. Additionally, it will enable the sharing of experiences among different university campuses. It is essential to assess the current emissions levels and identify the sources contributing to them to implement effective strategies and mitigation measures to reduce greenhouse gas emissions.

The study aims to determine UTHM students' thoughts about the cycling facilities on campus, emphasizing promoting active transportation to reduce pollution and congestion traffic. An online survey was distributed via social media during the pandemic (COVID-19) to 328 respondents and analyzed using SPSS software. The findings showed that while some bicycle facilities are seen to be very vital, they perform poorly, especially when it comes to having the wrong kind of cycling paths and not adequate lighting at night (Zaperi & Termida, 2022).

Daily activities on university campuses release greenhouse gases that add to the growing amount of carbon dioxide in the air. The mode of transportation, type of fuel, and travel distance are significant factors that have a crucial impact on daily and annual

CO₂ emissions (Holmatov et al., 2019). According to (Azeez & Ho, 2015), the primary contributor to CO₂ emissions in a university setting is the vehicles used for commuting on the campus and transporting goods and equipment. These emissions are found to be equivalent to the national average carbon emissions. In other words, the carbon footprint from transportation activities within a large university campus is significant and comparable to the average emissions across the nation (Gui et al., 2019).

The author investigated how three public institutions in Malaysia listed in the UI GreenMetric 2021 World University Ranking were implementing green campus activities. Senior representatives were interviewed, and it revealed that although these universities have implemented a number of green projects, they still face many challenges. Nevertheless, there are ways to advance these initiatives, highlighting the critical responsibilities that communities and university administration have in accomplishing the SDGs and promoting sustainable practices in the future (Muhiddin et al., 2023).

The author examines the energy performance metrics for buildings owned by academic faculty members based on three years of monthly energy consumption data. FPTV exhibited the highest energy and carbon footprint consumption (4,266.95 MWh and 2,961.26 tCO₂e), resulting in the highest energy index (161.47 kWh/m²/year). Conversely, the energy indices for FPTP and FKAAB were lower at (60.21 kWh/m²/year and 63.86 kWh/m²/year, respectively, compared to the overall UTHM buildings. Energy usage was significantly reduced by 36%, saving RM 1,063,874.19 in billing charges between 2015 and 2017 by implementing energy conservation strategies. It emphasizes the significance of setting energy-saving measures to lower energy expenses and carbon footprints (Abdullah et al., 2022).

College campuses can inspire and lead the way in implementing plans to reduce emissions on a larger scale because they can serve as positive examples for society (Adenle & Alshuwaikhat, 2017). The transportation of faculty and students to and from campus is a significant cause of greenhouse gas emissions (Yañez et al., 2020). The main obstacle to achieving sustainability goals in a university is the type of vehicles used by the campus community. To create an effective plan for campus sustainability, we need to consider how often vehicles are used, how far they travel, and the prevalence of private and heavy vehicles (Zakaria et al., 2021).

The author addresses Malaysia's plan to adopt electric buses (EBs) to reduce transportation-related greenhouse gas emissions in this paper. EB technologies were introduced in Putrajaya, Melaka and Sarawak. Moreover, a general framework for EB life cycle evaluations is offered, emphasizing the effects on the environment and economy and guiding future research on charging infrastructure needs (Al-Ogaili et al., 2021).

Therefore, this study analyzed carbon emissions from transportation at UTHM, Malaysia, to identify suitable mitigation strategies for effectively addressing carbon emissions.

This study's primary objective was to evaluate and examine the total carbon emissions from transportation within UTHM over three years, from 2021 to 2023. This analysis aims to provide a foundation for implementing effective mitigation strategies to reduce total carbon emissions, promote sustainability within the campus environment, and mitigate the strategies. UTHM should put a number of CO₂ mitigation techniques into practice, such as upgrading the infrastructure for bicyclists and pedestrians, promoting public transport and ridesharing, and improving public transportation by increasing the availability of shuttle buses and providing incentives. Higher learning institutions should switch to hybrid or electric vehicle models and promote the usage of low-emission vehicles. Additionally, the carbon emissions on campus should be greatly reduced by implementing smart traffic management systems, promoting remote learning and working initiatives, and establishing continuous emissions monitoring and evaluation.

MATERIALS AND METHODS

Study Area and Sample Size

The target population for this study comprises the campus community of Universiti Tun Hussein Onn Malaysia (UTHM). The primary data collected focuses on the number of vehicles staff and students use at UTHM's Main Campus. The total population of staff and students at the UTHM Main Campus is 34,010. This study considers several variables, including the number of vehicles, the method of commuting (bus, car, or motorcycle), the fuel used (petrol or diesel), and the annual travel distance.

Sampling and Sources of Data Collection

This study was carried out by taking a sample of the number of vehicles used by staff and students in UTHM Main Campus, including cars, motorcycles, and buses. Two methods were applied in this study to obtain the sample data. The first method involved requesting three-year statistical data on the number of vehicles registered in UTHM Main Campus from the Traffic Unit Security Department. The statistical data showed the records of the number of cars and motorcycles registered in UTHM Main Campus for 2021, 2022, and 2023. The numbers of vehicles recorded were referred to as the number of vehicle stickers that had been registered. The second method involved conducting a traffic count survey to collect the number of vehicles that traveled in and out of the area of UTHM Main Campus for the year 2023. The data was collected using different modes of transportation that students and staff use on UTHM's Main Campus. Data were collected within five different roads in UTHM Main Campus, which were at Persiaran Tun Dr Ismail Persiaran Tun Tan Siew Tin, Jalan Kemajuan, Persiaran Tun Ghaffar Baba, and Persiaran Tun Ghazali to investigate carbon emissions caused by transportation usage in UTHM Main Campus.

Calculation of CO₂ Emissions

The carbon footprint formula by the UI Green Method was used to evaluate the data for carbon emission value, as shown in Equation 1 (Ishak et al., 2022). Based on Equation 1, the total travel distance used for each vehicle mode was 2.7 km, considering each road that students and staff used in UTHM daily. The number of 240 in the equation is the number of working days per year. The carbon emission values for 2021 to 2023 are determined by multiplying the road distance traveled by each vehicle with its corresponding CO₂ emission factor. In this study, the emission factors for each mode of transportation are detailed in Table 1.

$$CO_2 = \frac{NV \times 2 \times TD \times WD}{100} \times EF \quad [1]$$

Where NV refers to the Number of Vehicles in the University; TD refers to the Approximate Travel Distance of a Vehicle Each Day Inside Campus (in kilometers); WD refers to the number of working days per year; and EF refers to the Emission Factor.

Table 1
Emission factor for each mode of transportation

Mode of transportation	Emission Factor	Unit	References
Car (petrol)	0.02	tCO ₂ e/km	https://www.gov.uk/government/organisations/department-for-environment-food-rural-affairs
Motorcycle (petrol)	0.01	tCO ₂ e/km	https://www.gov.uk/government/organisations/department-for-environment-food-rural-affairs
Bus (diesel)	0.01	tCO ₂ e/km	https://www.gov.uk/government/organisations/department-for-environment-food-rural-affairs

Data Analysis

This study analyzed carbon emissions by examining data on road distance, commuting modes, and the number of vehicles. This data was evaluated and converted into carbon emissions to compare emission trends.

RESULTS AND DISCUSSION

Number of Vehicles Registered in UTHM Campus

The statistical data regarding the number of vehicles, including cars and motorcycles, was obtained from the Traffic Unit of the Security Department at UTHM Campus. As depicted in Figure 1, the trend for the number of vehicles registered by staff, students, and individuals at the UTHM Campus has consistently increased over the years. This increasing trend can significantly impact the overall carbon emissions within the UTHM Campus.

Carbon Emissions (tCO₂e) of Vehicles

The data for vehicles registered by staff, students, and individuals had been converted into carbon emissions. Based on the observations in this study, the average distance traveled by car, motorcycle, or bus within UTHM Campus is 2.7 km, considering that not all places or roads in UTHM are accessible to vehicles. Consequently, the estimated carbon dioxide (CO₂) emissions in UTHM Campus, contributed by cars, motorcycles, and buses, were calculated using Equation 1.

The estimated activity data were determined by multiplying the number of vehicles registered in the UTHM Campus by the average distance traveled by car, motorcycle, or bus. For the experimental data, the estimated activity data were calculated by multiplying the number of vehicles that traveled within the UTHM Campus by the average distance traveled by these vehicles, which was 2.7 km. Subsequently, both sets of estimated activity data, obtained from statistical and experimental sources, were multiplied by the emission factor.

The total overall carbon emissions for vehicles registered, including staff, students, and individuals at UTHM Campus, were calculated and presented in a bar chart in Figure 2, respectively. Based on Figure 2,

the higher CO₂ emissions were in 2023, 6.86% higher than CO₂ emissions in 2022 and 55.74% higher than CO₂ emissions in 2021, with a difference of 111.46 tCO₂e. The value of CO₂ emissions each year in UTHM Campus for data vehicles registered by staff, students, and individuals increases according to the data for the number of vehicles registered. By comparison, there was an increasing trend of CO₂ emissions from vehicles from 2021 until 2023. This data can be compared to previous studies in which the trend of carbon emissions of vehicles registered in UTHM seems to be decreasing (Audu, 2018; Termida et al., 2022).

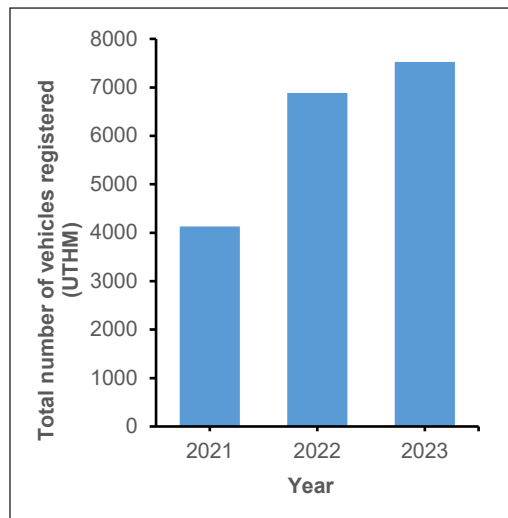


Figure 1. Total number of vehicles registered in UTHM

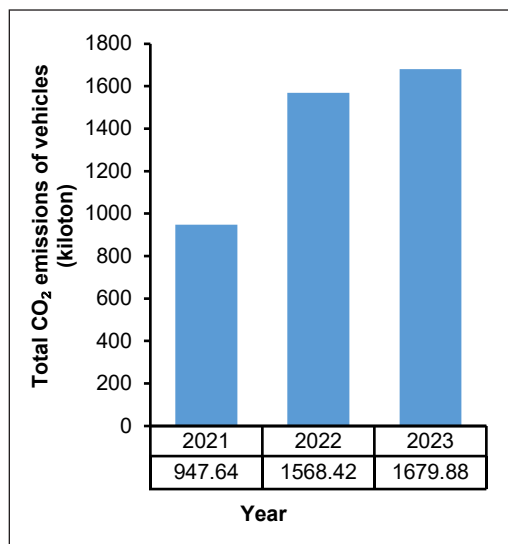


Figure 2. Total CO₂ emissions of vehicles (tCO₂e)

Traffic Survey Data Collection

A survey was conducted to record the number of vehicles traveling in and out of UTHM's Main Campus during peak working hours: 7:30 a.m. to 8:30 a.m., 1:00 p.m. to 2:00 p.m., and 5:00 p.m. to 6:00 p.m. This survey focused on five main roads within UTHM to target hotspot areas of carbon emissions. The total number of vehicles that traveled through UTHM's Main Campus was documented and presented in a bar chart, as shown in Figure 3.

According to Figure 3, the number of vehicles students and staff travel at UTHM Campus varies yearly. 2023, there was a significant increase in students and staff commuting compared to 2021. In 2023, the roads with the highest vehicle traffic, in order, were Persiaran Tun Ghaffar Baba, Persiaran Tun Dr Ismail, Persiaran Tun Ghazali Shafie, Jalan Kemajuan, and Persiaran Tun Tan Siew Sin, with Persiaran Tun Ghaffar Baba recording the highest number of vehicles. In 2023, Persiaran Tun Ghazali Shafie recorded the highest vehicle traffic by staff and students at the UTHM Campus, followed closely by Persiaran Tun Dr Ismail. The vehicle traffic on Persiaran Tun Ghazali Shafie saw a 92% increase compared to 2021, resulting in a difference of 1699 tCO₂e. Post-COVID-19, UTHM revised the route plan to a one-way system to facilitate easier mobility for students and staff and to reduce accidents in certain areas caused by route confusion.

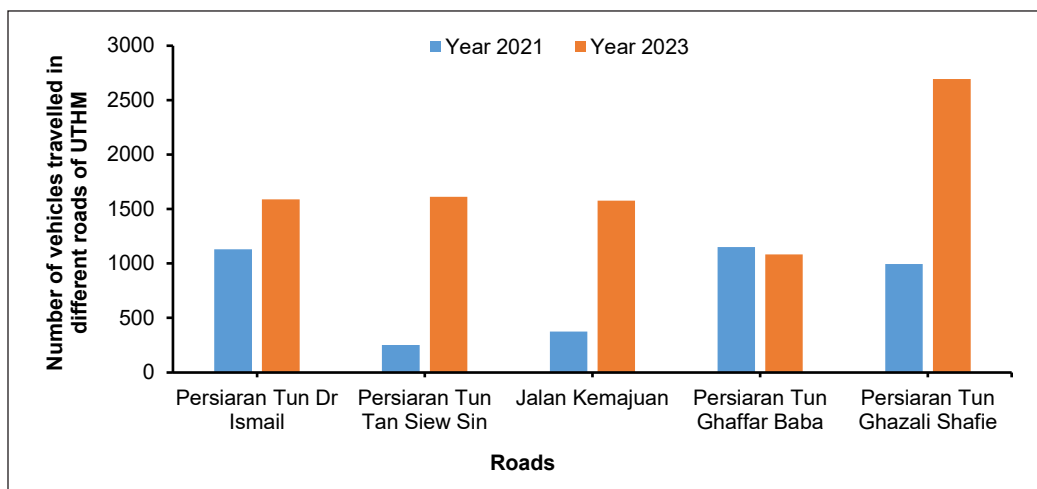


Figure 3. Total number of vehicles traveled on various roads within UTHM

Carbon Emissions (tCO₂e) by Vehicle Travelled in UTHM Campus

Based on traffic count survey data, the values have been converted to CO₂ emissions using the formula in Equation 1. The CO₂ emissions data for vehicles traveling on five different roads within UTHM's Main Campus are presented in Figure 4.

According to Figure 4, the ranking of the highest CO₂ emissions for each road in 2021 was as follows: Persiaran Tun Dr Ismail, Persiaran Tun Ghaffar Baba, Persiaran Tun



Figure 4. Total CO₂ emissions of vehicles traveled on five different roads in UTHM Campus (tCO₂e)

Ghazali Shafie, followed by Jalan Kemajuan and Persiaran Tun Tan Siew Sin. For 2023, the ranking changed from Persiaran Tun Ghazali Shafie, Jalan Kemajuan, Persiaran Tun Dr Ismail, Persiaran Tun Tan Siew Sin, and Persiaran Tun Ghaffar Baba.

The road with the highest carbon emissions values in 2023 was Persiaran Tun Ghazali Shafie, recording a value of 610 tCO₂e, representing an increase of 95.76% compared to 2021 with a difference of 395 tCO₂e. Similarly, the lowest carbon emission values belonged to Persiaran Tun Ghaffar Baba, with a value of 13.45% lower than in 2021, with a difference of 36 tCO₂e. The average value of carbon emissions for five different roads in 2023 was 1947 tCO₂e. By comparison, the average of emissions for 2023 was 73.84% higher than the average of CO₂ emissions in 2021. Hence, there was an increasing trend of carbon emissions between 2021 and 2023. By observation, the number of vehicle values change reflects the emissions levels over the two years. The greater the number of vehicles from staff and students in the UTHM Campus, the higher the values of carbon emissions.

Based on the carbon emissions values for each main road in UTHM Campus for the year 2023, the hotspot area for carbon emission production in UTHM Campus was identified to be on Persiaran Tun Ghazali Shafie, with the highest carbon emission value of 610 tCO₂e. This road serves as the primary thoroughfare for entering and exiting the UTHM Campus, making it the most frequently traveled route.

CONCLUSION

This study examined the total carbon emissions from transportation within the UTHM campus over three years (2021-2023). The analysis revealed that the number of registered vehicles and vehicles traveling on campus increased yearly, correlating with the rising number of students and staff. In 2023, the total registered vehicles reached 7,527, and

vehicles traveled amounted to 8,554 units, resulting in the highest carbon emissions of 1,679.88 tCO₂e for registered vehicles and 2,161.60 tCO₂e for vehicles traveled. The trend of increasing vehicles and CO₂ emissions was evident, rising from 947.64 tCO₂e in 2021 to 1,568.42 tCO₂e in 2022 and 1,679.88 tCO₂e in 2023.

A detailed analysis of five main roads within the campus identified Persiaran Tun Ghazali Shafie as a significant hotspot for carbon emissions in 2023, with a notable increase of 95.76% compared to 2021, recording 610 tCO₂e. The average carbon emissions across the five roads increased by 73.84% from 2021 to 2023, indicating a rising emission trend. The study successfully achieved its objectives and provided a comprehensive baseline for future research. It highlighted the need for effective CO₂ mitigation strategies, recommending enhancements in infrastructure for bicyclists and pedestrians, promoting public transport and ridesharing, increasing the availability of shuttle buses, and incentivizing low-emission vehicle usage.

Future research should expand to assess other sources of greenhouse gas emissions within the university and explore more effective CO₂ reduction options in campus transportation. This study serves as a reference for developing strategies to mitigate carbon emissions and promote sustainability within the campus environment.

ACKNOWLEDGMENTS

This research was supported by the UTHM Publisher's Office via Publication Fund E15216, Universiti Tun Hussein Onn Malaysia (UTHM), Batu Pahat, Johor, for providing the tools and facilities needed for this research.

REFERENCES

- Abdul-Azeez, I. A., & Ho, C. S. (2015). Realizing low carbon emission in the university campus towards energy sustainability. *Open Journal of Energy Efficiency*, 4(02), 15-27. <https://doi.org/10.4236/ojee.2015.42002>
- Abdullah, M. K., Usman, A. M., & Dasin, D. Y. (2022). Determination of energy efficiency indicators for academic faculty building in UTHM Malaysia. *African Journal of Earth and Environmental Sciences*, 3(2), 1060-1073.
- Adenle, Y. A., & Alshuwaikhat, H. M. (2017). Spatial estimation and visualization of CO₂ emissions for campus sustainability: The case of King Abdullah University of Science and Technology (KAUST), Saudi Arabia. *Sustainability*, 9(11), 1-15. <https://doi.org/10.3390/su9112124>
- Al-Ogaili, A. S., Al-Shetwi, A. Q., Sudhakar Babu, T., Hoon, Y., Abdullah, M. A., Alhasan, A., & Al-Sharaa, A. (2021). Electric buses in Malaysia: Policies, innovations, technologies and life cycle evaluations. *Sustainability*, 13(21), Article 11577. <https://doi.org/10.3390/su132111577>
- Audu, Y. (2018). *Evaluation of carbon dioxide absorption capacity and biomass accumulation of sub-urban plants in Universiti Tun Hussein Onn Malaysia (UTHM)* [Doctoral dissertation]. Universiti Tun Hussein Onn Malaysia. <http://eprints.uthm.edu.my/id/eprint/308>

- Gui, F., Ren, S., Zhao, Y., Zhou, J., Xie, Z., Xu, C., & Zhu, F. (2019). Activity-based allocation and optimization for carbon footprint and cost in product lifecycle. *Journal of Cleaner Production*, 236, Article 117627. <https://doi.org/10.1016/j.jclepro.2019.117627>
- Holmatov, B., Hoekstra, A. Y., & Krol, M. S. (2019). Land, water and carbon footprints of circular bioenergy production systems. *Renewable and Sustainable Energy Reviews*, 111, 224-235. <https://doi.org/10.1016/j.rser.2019.04.085>
- Ishak, S. Z., Ibrahim, N. A. S., Kamaluddin, N. A., & Dhokhikah, Y. (2022). Vehicle Kilometers Traveled (VKT) for campus population: Case study of UiTM main campus. *Environment-Behaviour Proceedings Journal*, 7(SI9), 619-624. <https://doi.org/10.21834/ebpj.v7iSI9.4315>
- Muhiddin, A. A. M., Isa, H. M., Sakip, S. R. M., Nor, O. M., & Sedhu, D. S. (2023). Green campus implementation in the Malaysian public universities: Challenges and solutions. *Planning Malaysia*, 21(1), 274–298. <https://doi.org/10.21837/pm.v21i25.1239>
- Termida, N. A., Zaperi, N. H., Daniel, B. D., Endrayana, D. B., & Hardini, P. (2022). Subjective factors influencing students to use bicycle on campus: A case study in Universiti Tun Hussein Onn Malaysia. *International Journal of Sustainable Construction Engineering and Technology*, 13(4), 121-133.
- Yañez, P., Sinha, A., & Vásquez, M. (2019). Carbon footprint estimation in a university campus: Evaluation and insights. *Sustainability*, 12(1), 1-15. <https://doi.org/10.3390/su12010181>
- Zakaria, N. F. F., Yazid, M. R. M., & Yaacob, N. F. F. (2021). Quantifying carbon emission from campus transportation: A case study in Universiti Kebangsaan Malaysia. In *IOP Conference Series: Materials Science and Engineering* (Vol. 1101, No. 1, p. 012011). IOP Publishing. <https://doi.org/10.1088/1757-899X/1101/1/012011>
- Zaperi, N. H., & Termida, N. A. (2022). Students' perceptions on bicycle facilities in campus. A case study at Universiti Tun Hussein Onn Malaysia, Johor. In *IOP Conference Series: Earth and Environmental Science* (Vol. 1022, No. 1, p. 012027). IOP Publishing. <https://doi.org/10.1088/1755-1315/1022/1/012027>

Physiological Behavior of Rubber Plants (*Hevea Brasilliensis*) to Different Soil Moisture Conditions

Rohaizad Mislan¹, Zulkefly Sulaiman^{1*}, Siti Nor Akmar Abdullah², Mohd Razi Ismail¹, Sarker Mohammad Rezaul Karim¹, Mohd Aswad Abdul Wahab³ and Aizat Shamin Noran⁴

¹Department of Crop Science, Faculty of Agriculture, Universiti Putra Malaysia, 43400 UPM Serdang, Selangor, Malaysia

²Institute of Plantation Studies, Universiti Putra Malaysia, 43400 UPM Serdang, Selangor, Malaysia

³Department of Plant Protection, Faculty of Agriculture, Universiti Putra Malaysia, 43400 UPM Serdang, Selangor, Malaysia

⁴Production Development Division, Rubber Research Institute of Malaysia, Malaysian Rubber Board, 47000, Sg. Buloh, Selangor, Malaysia

ABSTRACT

Drought conditions can severely impact rubber (*Hevea brasiliensis*) plantations, leading to economic loss in Malaysia. The study aimed to assess the impact of varying soil moisture levels on the physiological characteristics of five latex timber clones (LTCs) of rubber, with the goal of identifying the most suitable clone for specific soil moisture conditions. These conditions include (1) field capacity, (2) 75% available water (AW), (3) 50% AW, (4) 25% AW, and (5) wilting point, with the ultimate objective of optimizing cultivation methods and fostering sustainable rubber production in Malaysia. The five clones under investigation include RRIM3001, RRIM2025, RRIM2001, RRIM928, and PB350. Leaf chlorophyll content, stomatal conductance, and net photosynthesis were measured 4 and 8

months after treatment (MAT). The findings indicated significant effects of moisture stress on various physiological attributes, including total chlorophyll content, relative chlorophyll content, stomatal conductance, and net photosynthesis rate. At 4 and 8 MATs, the clones subjected to field capacity exhibited the highest values for these physiological characteristics, followed by those exposed to 75% available water, with the lowest values observed at the wilting

ARTICLE INFO

Article history:

Received: 22 September 2023

Accepted: 01 February 2024

Published: 25 October 2024

DOI: <https://doi.org/10.47836/pjst.32.6.21>

E-mail addresses:

rohaizadmislal@gmail.com (Rohaizad Mislan)

zulkefly@upm.edu.my (Zulkefly Sulaiman)

snaa@upm.edu.my (Siti Nor Akmar Abdullah)

razi@upm.edu.my (Mohd Razi Ismail)

sarker.mohammad@upm.edu.my (Sarker Mohammad Rezaul Karim)

mohdaswad@upm.edu.my (Mohd Aswad Abdul Wahab)

aizat@lgm.gov.my (Aizat Shamin Noran)

* Corresponding author

point. RRIM3001 consistently exhibited the highest total chlorophyll content, stomatal conductance, and net photosynthesis among the clones at both sampling dates. The highest net photosynthesis was observed in the RRIM3001 clone under field capacity conditions. Furthermore, a significant positive correlation was identified between total chlorophyll and relative chlorophyll contents, as well as between net photosynthesis and stomatal conductance. These findings carry practical implications for water management during the initial growth phase of rubber seedlings and for replanting initiatives in rubber plantations.

Keywords: Chlorophyll content, *Hevea brasiliensis*, latex timber clones, net photosynthesis, soil moisture regimes, stomatal conductance, volumetric soil water content

INTRODUCTION

Rubber (*Hevea brasiliensis*) is a significant economic crop in Malaysia, contributing to the country's agricultural sector and foreign exchange earnings. The success of rubber cultivation depends on various factors, including soil moisture, which plays a crucial role in plant growth, development, and productivity. Understanding the physiological adaptations of rubber clones to different soil moisture regimes is essential for optimizing cultivation practices and ensuring sustainable rubber production in Malaysia (Mislan et al., 2020; Mokhatar et al., 2011). Malaysia experiences variable rainfall patterns throughout the year, leading to fluctuating soil moisture conditions. By studying the physiological adaptations of different rubber clones to different soil moisture regimes, we can identify the most suitable moisture conditions for maximizing rubber growth and yield. Drought is a significant environmental stressor that affects rubber cultivation, particularly in regions with water scarcity or seasonal dry spells. By examining the physiological responses of rubber clones to reduced soil moisture, we can identify the mechanisms and traits associated with drought tolerance. This information can be used to develop improved rubber clones that are more resilient to water scarcity, reducing yield losses and ensuring the sustainability of rubber production in drought-prone areas (Cahyo et al., 2022).

Limitations in soil moisture elicit a range of plant responses, from recently elucidated acoustic signals to intricate physiological alterations (Waqas et al., 2023). The physiological changes are interconnected and influence overall plant performance, especially in chlorophyll contents, photosynthetic rate, and stomatal conductance in rubber clones in response to different soil moisture regimes. Investigating these interactions provides insights into the underlying mechanisms governing the physiological adaptations of the rubber clones (Kunjet et al., 2013). Understanding how different moisture regimes affect key physiological processes, such as chlorophyll content, photosynthesis, and stomatal regulation, enables us to comprehensively assess the impact of soil moisture on rubber plant physiology and productivity (Wang, 2014).

Climate change poses significant challenges to agricultural systems worldwide, including rubber cultivation. Alterations in precipitation patterns, temperature regimes, and extreme weather events can profoundly affect soil moisture dynamics. By studying the physiological adaptations of rubber clones under different soil moisture regimes, we can anticipate and prepare for potential future changes in climate (Jacob et al., 2022). With these ends in view, the research was undertaken with the following objectives – to assess the impact of varying soil moisture regimes on the physiological responses of five rubber clones, to identify the best-adapted rubber clones to different soil moisture levels, and to determine the optimal soil moisture conditions for maximizing rubber growth and yield. The research aims to identify the most suitable clones for specific soil moisture regimes, ensuring sustainable and efficient rubber production in Malaysia.

MATERIALS AND METHODS

Location and Treatments

The experiment was conducted under simulated water stress environments in a shed house at Ladang 2, Faculty of Agriculture, Universiti Putra Malaysia (3°20' N, 101°420' E, 31 m elevation). Five latex timber clone (LTC) seedlings (budded plant) aged from 4 to 5 months with 4 leaves whorls, e.g., RRIM3001, RRIM2025, RRIM2001, RRIM928 and PB350, were used as plant materials and Munchong soil series (typic hapludox/haplic ferralsol) was used as a planting media in pots. Agronomic practices, including fertilization, weed removal, and pest control, were applied to sustain the seedlings as recommended by the Malaysia Rubber Board (Malaysian Rubber Board, 2009). The soil moisture treatments included are (1) moisture at field capacity (FC), (2) 75% available water (AW), (3) 50% AW, iv) 25% AW, and (4) moisture at wilting point (WP).

Development of Munchong Soil Series Curve

Soil samples were collected from Ladang 10, Taman Pertanian, UPM, using 7.6 cm diameter and 4.0 cm depth double core rings. Water Retention Analysis determined the soil moisture content of the Munchong soil series following Teh and Jamal (2006), and the Munchong soil water retention curve was developed (Figure 1). Collected samples were divided into five equal portions and were saturated with water for 24 hours on porous plates. These samples were placed

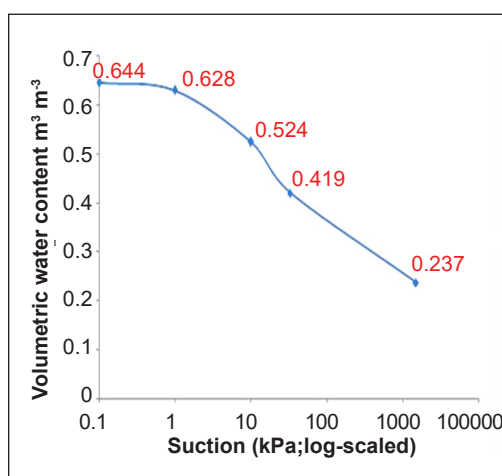


Figure 1. Munchong series soil water retention curve

inside the corresponding pressure chambers of a Pressure Membrane Chamber apparatus and connected to the outflow hub. Pressure heads ranging from 0 kPa to 1500 kPa were adjusted. The air pressure was applied uniformly until equilibrium (4–7 days) was attained, signifying no further water outflow. Afterward, air pressure was released gradually, and the samples were weighed. Oven drying at 105°C for 24 hours yielded the dry weights. Moisture content under various pressures was determined using wet and dry weights.

Bulk density was also assessed using Teh and Jamal's (2006) method (Equation 1).

$$\text{Bulk density} = \frac{D_w \text{ (gm)}}{R_v \text{ (cm}^3\text{)}} \quad [1]$$

Where D_w = Dry weight of the soil; and R_v = Ring volume.

The final moisture percentage was calculated using Equations 2 and 3.

$$\% \text{ Moisture (v/v)} = \% \text{ moisture (dry basis)} \times \text{bulk density of soil (g cm}^{-3}\text{)} \quad [2]$$

$$\text{Moisture (\%)} = \frac{W_d - D_d \text{ (g)}}{D_d - D \text{ (g)}} \times 100 \quad [3]$$

$$\% \text{ Moisture content (w/w)} = \text{Dry Basis (\%)}$$

$$\% \text{ Moisture content (v/v)} = \text{Moisture (\%)} \times B_d \text{ (g cm}^{-3}\text{)}$$

Where W_d = Wet weight of the soil with dish; D_d = Dry weight of the soil with dish; B_d = Bulk density of soil; and D = Dish weight.

The experiment was replicated four times, and average moisture values were plotted on a log scale of volumetric water content (Y-axis) against soil suctions (X-axis) at different pressures (e.g., 0 kPa, 1 kPa, 10 kPa, 33 kPa, and 1500 kPa), as suggested by Teh and Jamal (2006). Moisture at 33 kPa (0.419) represented field capacity (FC), and at 1500 kPa (0.237) indicated a wilting point (WP).

Determination of Other Treatments [% Available Water (AW)]

i) 50% AW = (moisture at FC – moisture WP) \times 0.50 + moisture at WP = 0.328 m³ m⁻³

ii) 75% AW = (moisture at FC – moisture at WP) \times 0.75 + moisture at WP = 0.3735 m³ m⁻³

iii) 25% AW = (moisture at FC – moisture at WP) \times 0.25 + moisture at WP = 0.2825 m³ m⁻³

Estimation of Total Chlorophyll Content

Chlorophyll contents were measured at 4 and 8 MAT according to the method described by Witham et al. (1986). Sample rubber leaves were cut and put in a water bucket to prevent the desiccation of leaves, and then they were brought into the laboratory. The fresh leaf was cut into pieces with scissors and weighed on a digital balance of 200 mg. The fresh weight of the sample was recorded, and samples were then transferred into a plastic vial

containing 20 ml of 80% acetone. The vial was kept in the dark for 72 hours. The absorbance was recorded at 645nm and 663nm wavelengths using the light spectrophotometer (UV-3101P, Labomed Inc, USA). Chlorophyll content was calculated and expressed as mg g⁻¹ of plant leaf tissue with Equation 4.

$$\text{Total chlorophyll (mg g}^{-1}\text{ fresh leaf)} = \frac{20.2 (A_{645}) - 8.02 (A_{663})}{1000} \times \frac{V}{W} \quad [4]$$

Where A_{645} = Absorbance of the solution at 645 nm; A_{663} = Absorbance of the solution at 663 nm; V = Volume of the solution in mL; and W = Weight of fresh sample in gram.

Relative chlorophyll content (leaf greenness) was estimated using the ratio of transmitted red light and NIR (Near-infrared) light emitted by a red and an NIR LED, respectively, through the leaf. Transmitted red light through a leaf is inversely related to the chlorophyll content because chlorophylls absorb red light efficiently (Taiz et al., 2015). Relative chlorophyll content was estimated by Yamamoto et al. (2002) by monitoring the SPAD index using a Chlorophyll meter (SPAD-502, Konica-Minolta Corp, Japan). After calibration of the meter, the sample leaves were placed under the sensor, and the readings were recorded by pressing the sensor gently on the leaf surface. Data were taken from four fully expanded and matured leaves of the clones randomly selected per treatment.

Measurement of Stomatal Conductance and Photosynthetic Rate

The stomatal conductance and photosynthesis rates in rubber plants were measured using a LI-6400 Porometer and a portable open gas exchange system with an Infrared Gas Analyzer. On sunny days, three uppermost fully expanded and matured leaves were selected from different angles for each treatment at 4 and 8 MATs (months after treatments). Stomatal conductance was assessed by the LI-6400 Porometer, which quantifies the rate of vapor diffusion through the stomata, yielding values in molH₂O m⁻²s⁻¹. Simultaneously, the rate of photosynthesis (μmolCO₂ m⁻²s⁻¹) was determined using the LI-6400 gas exchange system within a 6400-02B LED light source chamber. These measurements provide valuable insights into the physiological responses of the plants under varying conditions, contributing to a comprehensive understanding of their performance and adaptation mechanisms.

Statistical Analysis

A two-factorial experiment consisting of 25 treatment combinations (5 LTCs × 5 soil moisture regimes) was conducted and was arranged in a randomized complete block design with four replications. The overall effects of soil moisture regimes and LTCs were determined by means of a two-way analysis of variance as per Gomez and Gomez (1984). The correlation between total chlorophyll and relative chlorophyll contents was determined. The data were subjected to statistical analysis using the SPSS Statistical Program. Analysis

of variance was done to see the significant difference between the treatments, and the Studentised T-test was used to compare the means at 5% probability ($P \leq 0.05$).

RESULTS AND DISCUSSION

Effects on Chlorophyll Contents

The chlorophyll content of leaf samples from five different latex timber clones (LTCs) was significantly influenced by varying soil moisture regimes, as illustrated in Figures 2 and 3. Among these selected clones, RRIM3001 displayed the highest total chlorophyll content, registering at 3.50 mg g^{-1} , a significant 9.14%, 17.14%, 10.86%, and 8.57% higher compared to RRIM2025, RRIM2001, RRIM928, and PB350, respectively.

The interaction effects of soil moisture regimes on total chlorophyll content were highly significant ($P \leq 0.0001$), revealing distinct responses across LTCs in *H. brasiliensis* seedlings at 4 and 8 months after treatment (MAT) (Table 1). Generally, the highest total chlorophyll content was recorded under field capacity (FC) moisture conditions (4.72 mg g^{-1}), followed by 75% available water (4.01 mg g^{-1}), with the lowest values noted under wilting point (WP) conditions (1.97 mg g^{-1}). Soil moisture stress was observed to decrease the total chlorophyll content, as depicted in Figure 3. A parallel effect of soil moisture regimes was observed in rubber leaves' relative chlorophyll content (SPAD index) (Figures 4 and 5). Clone RRIM3001 displayed the highest leaf relative chlorophyll content (56.91) compared to RRIM2001, RRIM928, and PB350. No significant difference was found between RRIM3001 (56.91) and

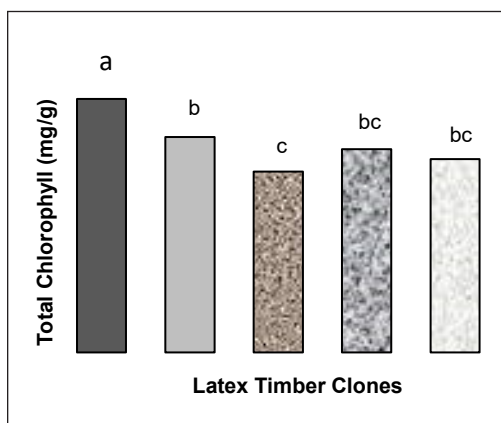


Figure 2. Total chlorophyll content (mg g^{-1}) extracted from leaf in five LTCs of *H. brasiliensis* seedlings. Note. Data are the average of two sampling dates crossing over five soil moisture regimes. At each LTC, the means with the same letters are not significantly different by the LSD at $\alpha = 0.05$. LTC = Latex timber clone

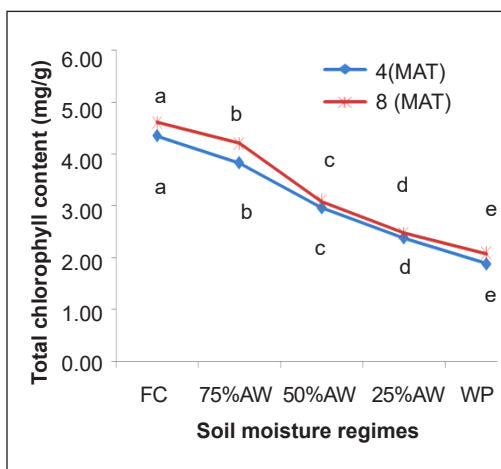


Figure 3. Total chlorophyll content (mg g^{-1}) extracted from the leaf as affected by different soil moisture regimes at 4 (blue) and 8 (red) MATs. Note. Data are the average of five LTCs. At each soil moisture regime, means with the same letters at a particular sampling date are not significantly different by the LSD at $\alpha = 0.05$. MAT = Months after treatment, FC = Field capacity, AW = Available water, WP = Wilting point

Table 1

Total chlorophyll content extracted from leaf as affected by different soil moisture regimes in five LTCs of *H. brasiliensis*

Clones	Soil moisture regimes	Total chlorophyll content (mg g ⁻¹)	
		4 MATs	8 MATs
RRIM 3001	FC	5.19 ±0.35a	5.07 ±0.79a
	75% AW	4.92 ±0.73ab	4.39 ±0.34ac
	50% AW	3.59 ±0.41cg	2.62 ±0.26eh
	25% AW	2.76 ±0.70fj	2.17 ±0.22fh
	WP	2.17 ±0.20hj	2.11 ±0.11gh
RRIM 2025	FC	4.42 ±0.98ac	4.31 ±0.37ac
	75% AW	4.19 ±0.84ad	3.75 ±0.30cd
	50% AW	2.93 ±0.08ei	3.09 ±0.66de
	25% AW	2.46 ±0.31hj	2.82 ±0.21eg
	WP	1.84 ±0.23ij	2.00 ±0.56gh
RRIM 2001	FC	3.83 ±0.63bf	4.47 ±0.30ac
	75% AW	2.97 ±0.36ch	4.04 ±0.23bc
	50% AW	2.64 ±0.22gj	2.85 ±0.32eg
	25% AW	2.08 ±0.15hj	2.16 ±0.16fh
	WP	1.77 ±0.33j	2.16 ±0.19fh
RRIM 928	FC	4.37 ±0.43ac	4.40 ±0.12ac
	75% AW	3.91 ±0.24be	4.28 ±0.16ac
	50% AW	2.53 ±0.15gj	3.00 ±0.24df
	25% AW	2.33 ±0.24hj	2.73 ±0.31eh
	WP	1.80 ±0.21j	1.89 ±0.13h
PB 350	FC	3.92 ±0.80be	4.78 ±0.023ab
	75% AW	3.11 ±0.57dh	4.53 ±0.45ac
	50% AW	3.11 ±0.11dh	3.83 ±0.21cd
	25% AW	2.25 ±0.18hj	2.47 ±0.47eh
	WP	1.81 ±0.22j	2.21 ±0.11eh

Note. Values followed by a common letter within each column are not significantly different by the LSD at $\alpha = 0.05$. AW = Available water, FC = Field capacity, WP = Wilting point, MAT= months after transplant

RRIM2025 (55.43) concerning relative chlorophyll content at 4 and 8 MAT. The trends observed in relative chlorophyll content mirrored those in total chlorophyll content and were negatively affected by soil moisture stress (Figure 5). Specifically, at 4 MAT, FC moisture conditions exhibited the highest relative chlorophyll content (66.06), outperforming the 75% available water, 50% available water, 25% available water, and WP treatments. Similar patterns were noted at 8 MATs across the five LTCs of *H. brasiliensis* seedlings. These results underscore the significant influence of soil moisture regimes on the total and relative chlorophyll contents of rubber leaves in different LTCs. Moisture conditions at FC were associated with higher chlorophyll contents, while moisture stress conditions resulted in

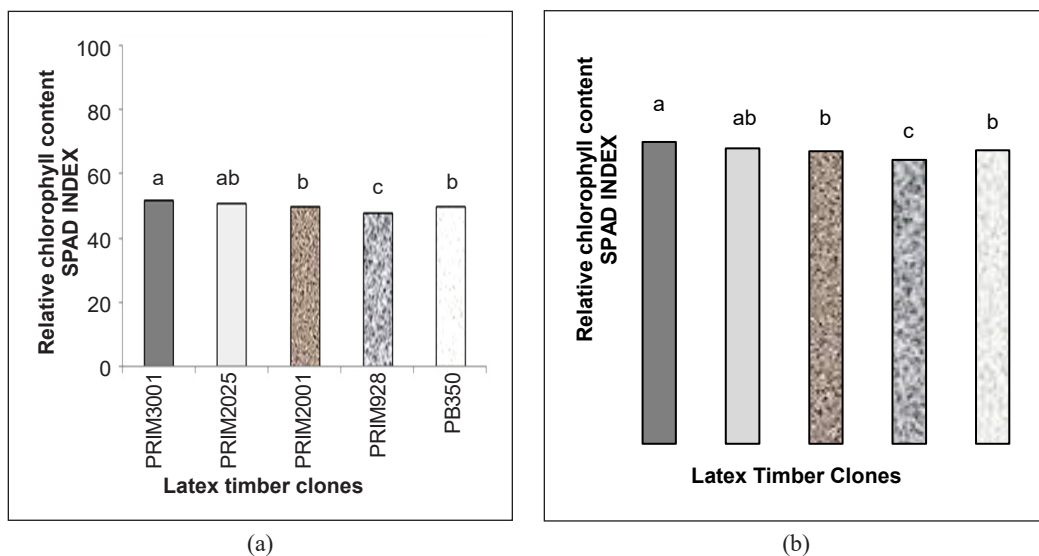


Figure 4. Relative chlorophyll content (SPAD index): (a) at 4 MAT; and (b) at 8 MAT in five LTCs of *H. brasiliensis* seedlings

Note. Values are an average of five soil moisture regimes. At each LTC, the means with the same letters are not significantly different by the LSD at $\alpha = 0.05$. MAT = Months after treatment, LTC = Latex timber clone

lower chlorophyll contents. It aligns with previous research by Wang et al. (2015), which emphasized the correlation between plant water availability and chlorophyll content.

There was a significant interaction between LTCs and moisture stresses in producing relative chlorophyll content at both 4 and 8 MATs (Table 2).

Soil moisture plays a pivotal role in various aspects of plant physiology, particularly chlorophyll production, which is indispensable for photosynthesis. Adequate soil moisture is essential for water uptake by plant roots, and water is a crucial component in chlorophyll synthesis, facilitating multiple biochemical reactions during the process (Wang et al., 2019). It also acts as a medium for transporting

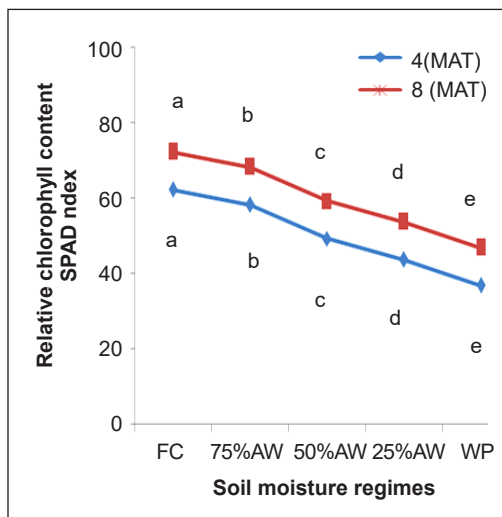


Figure 5. Relative chlorophyll content (SPAD index) at 4 MATs (blue) and 8 MATs (red) under different soil moisture regimes

Note. Values are an average of five LTCs. At each soil moisture regime, means with the same letters are not significantly different by the LSD at $\alpha = 0.05$. FC = Field capacity, AW = Available water, WP = Wilting point, MAT = Months after treatment

nutrients and minerals vital for chlorophyll production, including nitrogen (N), magnesium (Mg), and iron (Fe). These nutrients are essential for chlorophyll molecule formation, with their uptake facilitated by water movement in the soil. Chlorophyll molecules capture light energy during photosynthesis, and optimal soil moisture levels support efficient photosynthesis by maintaining turgor pressure within leaf cells. Turgor pressure, influenced by water availability, ensures proper alignment of chloroplasts within leaf cells for maximum light absorption (Li & Wang, 2021). Soil moisture levels also regulate leaf temperature through transpiration, which leads to cooling. This cooling effect helps maintain an appropriate temperature range for optimal chlorophyll synthesis and function. Additionally, soil moisture availability influences the stomatal aperture. Stomata, small

Table 2
Relative chlorophyll contents as affected by different soil moisture regimes in five LTCs of *H. brasiliensis*

Clones	Soil Moisture Regimes	Relative chlorophyll content (SPAD index)	
		4 MATs	8 MATs
RRIM3001	FC	64.45 ±0.96a	74.15 ±0.99a
	75% AW	61.20 ±1.10ac	72.20 ±1.10ab
	50% AW	50.12 ±0.25f	60.22 ±0.24f
	25% AW	44.90 ±0.73fh	55.90 ±0.74fh
	WP	37.97 ±0.76jk	47.97 ±0.75jk
RRIM2025	FC	62.40 ±0.94a-b	72.40 ±0.94ab
	75% AW	58.62 ±1.24cd	68.62 ±1.24cd
	50% AW	49.80 ±0.40f	59.80 ±0.40f
	25% AW	44.00 ±0.61hi	54.01 ±0.61hi
	WP	37.32 ±1.13k	47.33 ±1.14k
RRIM2001	FC	61.80 ±2.15ac	71.81 ±2.16ac
	75% AW	57.50 ±1.67de	67.51 ±1.68de
	50% AW	48.55 ±1.34f	58.54 ±1.34f
	25% AW	44.57 ±1.40gh	54.57 ±1.40gh
	WP	36.92 ±1.51k	47.91 ±1.51k
RRIM928	FC	60.50 ±1.10bd	59.50 ±1.09bd
	75% AW	55.07 ±1.02e	55.07 ±1.01e
	50% AW	48.02 ±1.25gj	58.02 ±1.24gj
	25% AW	41.05 ±1.90ij	51.05 ±1.89ij
	WP	35.72 ±1.85k	43.72 ±1.84k
PB350	FC	61.80 ±1.70ac	71.80 ±1.70ac
	75% AW	58.77 ±2.50cd	68.77 ±2.50cd
	50% AW	49.77 ±0.84f	59.77 ±0.84f
	25% AW	43.65 ±1.28hi	53.65 ±1.28hi
	WP	36.30 ±1.48k	36.30 ±1.48k

Note. Values followed by a common letter within each column are not significantly different by the LSD at $\alpha = 0.05$. AW = Available water, FC = Field capacity, WP = Wilting point, MAT= months after transplant

openings on the leaf surface, are responsible for gas exchange and water vapor release. In conditions of limited soil moisture, plants may close their stomata to conserve water, potentially reducing carbon dioxide availability for chlorophyll production and impacting its synthesis. Furthermore, recent findings by Swoczyna et al. (2022) highlighted the utility of chlorophyll as a potential indicator of stress conditions in plants, shedding light on its role in determining overall plant growth.

Correlation Between Total Chlorophyll Content and Relative Chlorophyll Content

The results indicated that the total chlorophyll content extracted from the leaves was significantly ($P \leq 0.0001$) correlated with the relative chlorophyll content readings obtained from the Minolta SPAD-502 device. The correlation coefficients, representing the strength and direction of the relationship, were reported as 0.74841 at 4 MATs and 0.8159 at 8 MATs.

The strength of the correlation suggests that the relative chlorophyll content readings obtained from the SPAD-502 can serve as a reliable indicator of the total chlorophyll content in rubber leaves (Jiang et al., 2017). These findings have implications for assessing the chlorophyll status of rubber leaves non-destructively and quickly using the SPAD-502 device. By measuring the relative chlorophyll content, which is strongly related to the total chlorophyll content, researchers and rubber growers can gain insights into the rubber leaves' photosynthetic activity and overall health without the need for labor-intensive and time-consuming laboratory extractions.

Effects on Stomatal Conductance

The effect of different soil moisture regimes on the stomatal conductance of five timber latex clones (LTCs) of rubber plants has been investigated. The results indicate that soil moisture regimes significantly influenced the stomatal conductance of the rubber leaves. Among the clones, RRIM2001 exhibited the highest stomatal conductance ($0.062 \text{ molH}_2\text{O m}^{-2}\text{s}^{-1}$), followed by PB350 ($0.052 \text{ molH}_2\text{O m}^{-2}\text{s}^{-1}$), while RRIM928 displayed the lowest value ($0.050 \text{ molH}_2\text{O m}^{-2}\text{s}^{-1}$) (Figure 6). It suggests that the clones responded differently to the soil moisture conditions, with RRIM2001 showing the highest stomatal conductance and RRIM928 exhibiting the lowest. Carr (2012) stated that the water relations of rubber trees are affected by drought stress, and clones differ in their susceptibility to cavitation, which occurs at xylem water potentials in the range of -1.8 to -2.0 MPa. Clone RRIM105 is capable of maintaining higher leaf water potentials than other clones because of stomatal closure, supporting its reputation for drought tolerance.

Figure 7 provides insights into the effects of various soil moisture regimes on stomatal conductance. Moisture at field capacity (FC) resulted in the highest stomatal conductance ($0.0715 \text{ molH}_2\text{O m}^{-2}\text{s}^{-1}$), followed by 75% available water (AW) ($0.0625 \text{ molH}_2\text{O m}^{-2}\text{s}^{-1}$). In contrast, the lowest stomatal conductance was observed under water stress conditions

at the wilting point (WP) ($0.0358 \text{ molH}_2\text{O m}^{-2}\text{s}^{-1}$). These results indicate that sufficient soil moisture, such as at FC, promotes higher stomatal conductance, while water deficit conditions restrict stomatal opening and reduce conductance. As a result of soil drought, leaf water potential (Ψ_L) decreases, and stomata close, which limits transpiration and photosynthesis. Manzoni et al. (2013) investigated the optimization of stomatal conductance for maximum carbon gain under dynamic soil moisture. They found that stomatal conductance is affected by changes in soil moisture. Liang et al. (2023) conducted a study on the stomatal responses of terrestrial plants to global change. They found that stomatal conductance is also sensitive to changes in soil moisture regimes.

The interaction effects of LTCs and soil moisture regimes on stomatal conductance were also significant (Table 3). Although all the LTCs showed the highest stomatal conductance under moisture at FC, the LTCs RRIM2001, RRIM2025, and PB350 only showed the second-highest stomatal conductance under soil moisture at 75% AW (Table 3). It is important to note that there were no significant differences between the five clones in terms of stomatal conductance under soil moisture at FC.

Apart from RRIM2001, there were no significant differences between the clones regarding stomatal conductance under WP conditions (Table 3). In conclusion, adequate soil moisture, such as that at field capacity, promotes higher stomatal conductance, facilitating the exchange of gases, including water vapor, between the leaf and the surrounding environment. As represented by the wilting point, water stress conditions lead to reduced

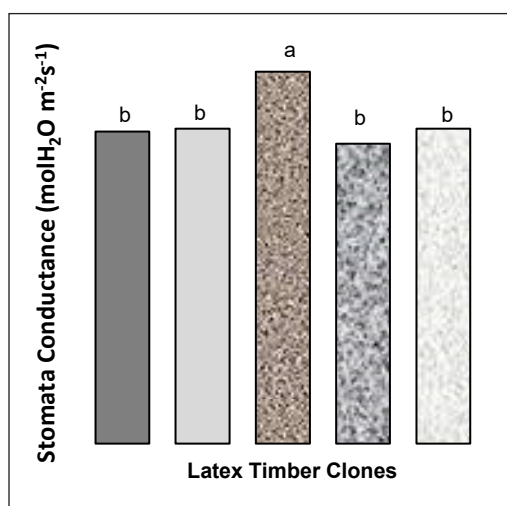


Figure 6. Stomatal conductance ($\text{molH}_2\text{O m}^{-2}\text{s}^{-1}$) in five LTCs of *H. brasiliensis* seedlings

Note. Data are the average of two sampling dates crossing over five soil moisture regimes. At each LTC, means with the same letters are not significantly different by the LSD at $\alpha = 0.05$. LTC = Latex timber clone

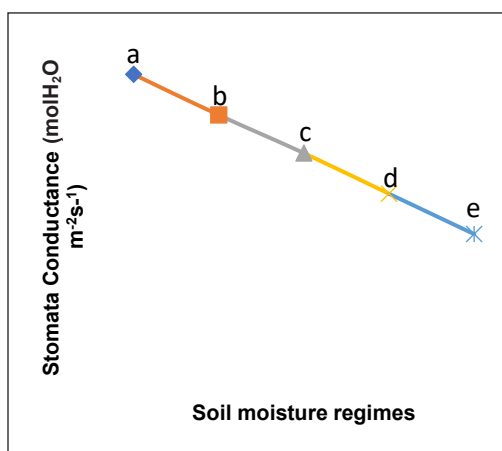


Figure 7. Stomatal conductance ($\text{molH}_2\text{O m}^{-2}\text{s}^{-1}$) as affected by different soil moisture regimes in five LTCs of *H. brasiliensis* seedlings

Note. Data are the average of two sampling dates crossing over five LTCs. At each soil moisture regime, means with the same letters are not significantly different by the LSD at $\alpha = 0.05$. LTC = Latex timber clone, FC = Field capacity, AW = Available water, WP = Wilting point

Table 3

Stomatal conductance (molH₂O m⁻²s⁻¹) and net photosynthesis rate (μmolCO₂ m⁻²s⁻¹) as affected by different soil moisture regimes in five LTCs of H. brasiliensis

Clones	Soil moisture regimes	Stomatal conductance (molH ₂ O m ⁻² s ⁻¹)	Net photosynthesis rate (μmolCO ₂ m ⁻² s ⁻¹)
RRIM3001	FC	0.0700 ±0.0040a	11.55 ±0.05a
	75% AW	0.0600 ±0.0001c	10.56 ±0.26bc
	50% AW	0.0525 ±0.0025de	7.90 ±0.03f
	25% AW	0.0420 ±0.0025f	7.45 ±0.10g
	WP	0.0350 ±0.005gh	6.18 ±0.29ij
RRIM2025	FC	0.0725 ±0.0025a	10.82 ±0.17b
	75% AW	0.0625 ±0.0025bc	10.67 ±0.11bc
	50% AW	0.0525 ±0.0025de	7.62 ±0.21fg
	25% AW	0.0420 ±0.0025f	7.35 ±0.21g
	WP	0.0320 ±0.0025h	6.03 ±0.20ij
RRIM2001	FC	0.0725 ±0.0025a	10.60 ±0.20bc
	75% AW	0.0675 ±0.0025ab	9.96 ±0.09de
	50% AW	0.0625 ±0.0025bc	7.34 ±0.06g
	25% AW	0.0570 ±0.0047cd	6.68 ±0.04h
	WP	0.0500 ±0.004e	5.21 ±0.04k
RRIM928	FC	0.0700 ±0.0001a	10.70 ±0.15b
	75% AW	0.0600 ±0.0001c	9.61 ±0.04cf
	50% AW	0.0500 ±0.0001e	6.67 ±0.04h
	25% AW	0.0400 ±0.0001fg	5.89 ±0.03j
	WP	0.0300 ±0.0001h	2.31 ±0.09m
PB350	FC	0.0725 ±0.0025a	10.70 ±0.11b
	75% AW	0.0625 ±0.0025bc	10.30 ±0.06cd
	50% AW	0.0525 ±0.0025de	6.34 ±0.01hi
	25% AW	0.0420 ±0.0025f	6.10 ±0.21ij
	WP	0.0320 ±0.0025h	4.69 ±0.04l

Note. Data are the average of two sampling dates. Values followed by a common letter within each column are not significantly different by the LSD at α = 0.05. LTC = Latex timber clone, AW = Available water, FC = Field capacity, WP = Wilting point

stomatal conductance, indicating a restriction in gas exchange and potential water loss prevention by the plants. The variations observed among the different LTCs suggest that each clone possesses a distinct response to soil moisture conditions. Praba et al. (2009) opined that soil moisture stress can affect plants' osmotic adjustment and photosynthetic activity in rice and wheat. Stomata respond to soil moisture content compared to leaf water status, and the plants respond to biochemicals for triggering low water availability. The stomatal conductance was higher in clones with better moisture access, hinting at their potential for better photosynthesis compared to those in drier conditions.

Effects on Net Photosynthesis Rate

The findings indicate that both factors, e.g., LTCs and soil moisture regimes, significantly influenced the net photosynthesis rate. Figure 8 demonstrates the variations in net photosynthesis rate among different LTCs. The rubber clone, RRIM3001, exhibited the highest net photosynthesis rate ($8.728 \mu\text{molCO}_2\text{m}^{-2}\text{s}^{-1}$), which was significantly higher than the other clones (RRIM2025, RRIM2001, PB350, and RRIM928). RRIM928 recorded the lowest net photosynthesis rate of $7.036 \mu\text{molCO}_2\text{m}^{-2}\text{s}^{-1}$. These results suggest variations in the photosynthetic capacity among the different clones, with RRIM3001 displaying the highest rate and RRIM928 exhibiting the lowest. Sterling et al. (2019) noted variations in photosynthetic rate in different rubber clones. They recorded that the clones FX4098, FDR4575, MDF180, GU198 and FDR5788 represent genotypes with the best photosynthetic performance (greater photosynthetic rates and better ability of the photosynthetic apparatus to capture, use and dissipate light energy). Carr (2012) also noted similar differences in the rubber clones with respect to their net photosynthetic rates.

The highest photosynthesis rate was observed under soil moisture at field capacity (FC) ($10.874 \mu\text{molCO}_2\text{m}^{-2}\text{s}^{-1}$), followed by 75% available water (AW) ($10.220 \mu\text{molCO}_2\text{m}^{-2}\text{s}^{-1}$). At the same time, the lowest value was recorded under water stress conditions (wilting point, WP) ($4.884 \mu\text{molCO}_2\text{m}^{-2}\text{s}^{-1}$) (Figure 9). These findings indicate that optimal soil moisture conditions, such as those at FC, promote higher net photosynthesis rates, while water deficit conditions restrict photosynthetic activity and result in lower rates. Santos et al. (2019) observed that physiological mechanisms responsible for tolerance to and recuperating from drought conditions in four rubber clones include changes in growth patterns and biomass allocation, diminishing stomatal conductance, and CO_2 assimilation rate.

The interaction between the LTCs and soil moisture regimes was significant, indicating that the response of net photosynthesis rate to moisture regimes varied among different clones (Table 3). Specifically, the rubber clone RRIM3001 exhibited the significantly highest net photosynthesis rate ($11.55 \mu\text{molCO}_2\text{m}^{-2}\text{s}^{-1}$ when subjected to soil moisture at FC. However, the clone, RRIM2001 treated with FC and 75% AW, did not significantly differ in net photosynthesis rate. On the other hand, RRIM928 displayed the lowest net photosynthesis rate ($2.31 \mu\text{molCO}_2 \text{m}^2\text{s}^{-1}$) when subjected to WP conditions. In conclusion, the LTCs and soil moisture regimes significantly affect rubber plants' net photosynthesis rate. Optimal soil moisture conditions, particularly those at field capacity, promote higher photosynthetic rates, while water stress conditions restrict photosynthetic activity.

These findings highlight the importance of proper soil moisture management in rubber plantations to optimize photosynthetic efficiency. Maintaining favorable soil moisture levels, especially around field capacity, ensures adequate water availability and promotes optimal net photosynthesis rates. Considering the specific moisture requirements of different clones, implementing appropriate irrigation strategies and water conservation practices

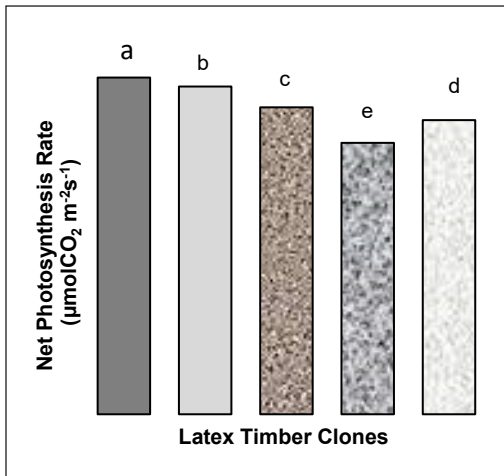


Figure 8. Net photosynthesis rate ($\mu\text{molCO}_2 \text{ m}^{-2}\text{s}^{-1}$) in five LTCs of *H. brasiliensis* seedlings
Note. Data are the average of two sampling dates crossing over five soil moisture regimes. At each LTC, means with the same letters are not significantly different by the LSD at $\alpha = 0.05$. LTC = Latex timber clone

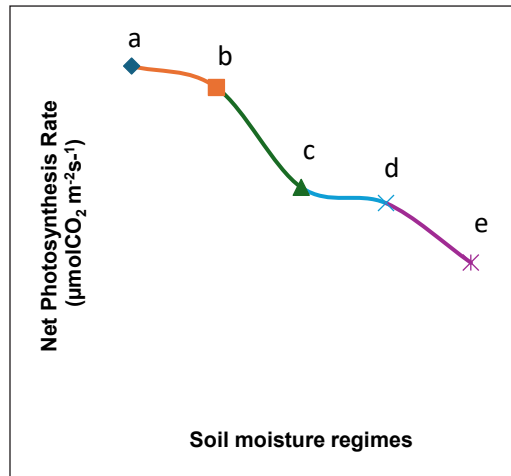


Figure 9. Net photosynthesis rate ($\mu\text{molCO}_2 \text{ m}^{-2}\text{s}^{-1}$) under different soil moisture regimes
Note. Data are the average of two sampling dates crossing over five LTCs. At each soil moisture regime, means with dissimilar letters are significantly different by the LSD at $\alpha = 0.05$. LTC = Latex timber clone

can contribute to improved photosynthetic performance and overall plant productivity. Generally, chlorophyll measurements relate, directly or indirectly, to all stages of light-dependent photosynthetic reactions, including photolysis of water, electron transport, pH gradient formation across the thylakoid membrane, and ATP synthesis and thus the general bioenergetic condition of the photosynthetic machinery (Bernat et al., 2012).

It is noted that soil moisture directly affects water availability in rubber plants. Sufficient soil moisture ensures an adequate water supply to the plant roots, allowing for efficient nutrient uptake and transport to the leaves. Water is a crucial component for photosynthesis, as it serves as the medium for various metabolic reactions and as a source of electrons in light-dependent reactions. Therefore, optimal soil moisture levels are essential for maintaining high net photosynthesis rates. Soil moisture conditions also have a significant impact on stomatal conductance, which is related to gas exchange, allowing for the uptake of carbon dioxide (CO_2) needed for photosynthesis and the release of oxygen (O_2) produced during the process. In a study, Sterling et al. (2019) investigated the comprehensive effects of atmosphere and soil drying on the stomatal behavior of different plant types. They found that high vapor pressure deficit and low soil water content limit the stomatal conductance of plants, which in turn affects the net photosynthesis rate. When soil moisture is limited, plants close their stomata partially or completely to reduce water loss through transpiration.

However, stomatal closure also restricts the entry of CO_2 , leading to a decline in net photosynthesis rates. Soil moisture influences leaf turgor pressure; the pressure water exerts

within the plant cells. Sufficient soil moisture maintains optimal turgor pressure, ensuring that plant cells are adequately hydrated and able to maintain their structural integrity. Leaf cells with optimal turgor pressure are more efficient in capturing and utilizing light energy for photosynthesis. In contrast, water stress conditions can reduce turgor pressure, resulting in cellular damage, decreased photosynthetic capacity, and lower net photosynthesis rates. Figure 10 provides insights into the influences of different LTCs and soil moisture conditions on the relatively healthy appearance of rubber leaves.

Soil moisture affects the rubber plants' availability and uptake of essential nutrients. Adequate soil moisture levels facilitate the movement of nutrients in the soil solution, making them accessible to the plant roots. Nutrients such as nitrogen, phosphorus, and potassium are crucial for various physiological processes, including photosynthesis. When soil moisture is limited, nutrient uptake and transport may be hindered, leading to nutrient deficiencies and reduced photosynthetic activity. The net photosynthesis rate followed a similar pattern exhibited in chlorophyll contents and stomatal conductance, i.e., the clones with more water available showed higher rates than those experiencing moisture stress.

Notably, RRIM3001 stood out among the clones by consistently showing higher chlorophyll content, better stomatal conductance, and higher net photosynthesis rates across various soil moisture levels. Compared to RRIM2025, RRIM2001, RRIM928, and PB350, RRIM3001 demonstrated a more robust and adaptable response to changes in soil moisture. Even under different moisture conditions, RRIM3001 maintained superior physiological performance, indicating its better ability to handle varying water availability compared to the other studied clones.

The study highlighted that sufficient soil moisture is crucial for optimal physiological performance in rubber plants. The differences in how clones responded to varying moisture levels emphasize the potential for selecting or developing clones better suited to specific moisture conditions, which could significantly contribute to sustainable rubber production methods.

The suggestion to maintain soil moisture at field capacity could significantly influence rubber plantation practices by enhancing plant health and productivity. However, achieving and maintaining this optimal moisture level might pose challenges in different environments. Environmental factors like irregular rainfall patterns or high temperatures could make it challenging to sustain field capacity consistently. Implementing irrigation systems might help regulate moisture levels, but this could raise concerns about water availability and management, especially in regions prone to water scarcity. Therefore, balancing the need for optimal moisture with the practicality and sustainability of water usage in diverse environmental conditions would be crucial in implementing this recommendation in rubber plantations.



Figure 10. Effects of different soil moisture conditions on the leaf-appearance of five TLCs of *H. brasiliensis* Note. It is obvious that the healthy appearance and dark green color were observed under the soil moisture at field capacity and at 75% available water, and it decreased with an increase in soil moisture stresses. At the top of each plate, the name of each latex timber clone (black) is given. FC = Field capacity, AW = Available water, WP = Wilting point

Correlation Between Stomatal Conductance and Net Photosynthesis Rate

A significant positive correlation (coefficient of correlation = 0.829) between the net photosynthesis rate and stomatal conductance of rubber leaves under different soil moisture regimes is noticed. As stomatal conductance increases, the net photosynthesis rate increases, indicating a positive relationship between these two variables. These results highlight the importance of stomatal conductance in regulating the photosynthetic activity of rubber leaves and emphasize the role of soil moisture in influencing this relationship.

The study found correlations between different measurements. For example, photosynthesis and stomatal conductance were also lower when chlorophyll levels were lower. It suggests that when plants lack water, multiple aspects of their health and functioning are affected together. Understanding these connections can help future research by guiding scientists to focus on improving multiple factors at once, like finding rubber clones that can handle water stress better while keeping their chlorophyll levels up. In practical terms, this knowledge might help select or develop rubber plants more resilient to water shortages, ensuring better growth and productivity in rubber farms.

Certain cultural practices should be implemented to mitigate the impacts of soil moisture stress on the rubber clones. These practices may include implementing efficient irrigation methods to maintain optimal soil moisture levels, especially during critical

growth stages (Somjan & Sadude, 2008). It was found that irrigation caused marked leaf-shedding in some groups of rubber trees, which reduced the production of new leaves by about 10-20% compared to trees that were not irrigated. The study also found that sufficient irrigation eliminated foliar injury and resulted in a high photosynthetic rate. Mulching the soil surface to reduce evaporation and maintain soil moisture is helpful to combat the negative effects of soil moisture stresses (Shen et al., 2019). The study found that mulching with organic materials improved soil moisture retention and reduced soil temperature, improving rubber plant growth and yield. The mulching also reduced weed growth and soil erosion, contributing to the rubber plants' overall health.

The study specifically investigated the effect of rubber wood biochar as a mulching material and found that it significantly increased the height, stem diameter, and biomass of the rubber plants compared to the control treatment without mulch. Applying organic matter or compost to improve soil structure and water-holding capacity will also reduce the impact of soil moisture stresses (Bhadha et al., 2017). The study found that applying organic waste materials, such as compost, improved soil fertility and structure, promoting root growth of the rubber trees. The study also found that the organic amendments increased the soil's water-holding capacity, which contributed to the improved growth of the rubber trees. By implementing these cultural practices, it may be possible to minimize the negative effects of moisture stress on rubber plantations, leading to improved chlorophyll production, stomatal conductance, net photosynthesis rate and overall plant health.

CONCLUSION

The study highlighted that keeping the soil well-watered, especially when growing rubber plants, improves their health and productivity. So, when planting new rubber trees, it is essential to ensure they have enough water for better growth. Also, choosing a rubber clone, like RRIM3001, which can handle different water levels well, could be a good idea for replanting in rubber farms. It means paying attention to how much water these plants need and adjusting irrigation methods accordingly during replanting to get the best results. Maintaining soil moisture at field capacity is important to ensure optimal rubber clone performance. Giving the right amount of water at the right times can help grow healthier and more productive rubber plants in Malaysia.

The discovery that RRIM3001 performed well even when there was less water in the soil is crucial for regions facing water scarcity in rubber production. This finding suggests that RRIM3001 could be a valuable choice for areas with limited water resources. Cultivating this specific clone might help regions with low water availability, as it showed better resilience to soil moisture deficits. The implication is that by selecting and focusing on clones like RRIM3001, rubber cultivation practices in water-scarce areas could become more sustainable, potentially reducing the impact of water shortages on rubber production in Malaysia.

Furthermore, the SPAD meter offers an advantage by providing a quick and non-destructive way to measure relative chlorophyll content in rubber plants. This device allows for on-the-spot assessment without damaging the plants, offering immediate feedback on their health. Its use enables efficient monitoring across a plantation, aiding in identifying areas or specific plants needing attention due to lower chlorophyll levels. This quick assessment facilitates targeted resource allocation, directing efforts like irrigation or nutrient application precisely where needed. Ultimately, the SPAD meter's utilization supports timely interventions, optimizing resource allocation and enhancing overall crop health assessment in rubber plantations.

ACKNOWLEDGEMENTS

The authors thank Universiti Putra Malaysia for providing the facilities to carry out the research. We gratefully acknowledge all the laboratory assistants of Universiti Putra Malaysia, Serdang, Selangor, who graciously contributed to the success of this work.

REFERENCES

- Bernat, G., Schreiber, U., Sendtko, E., Stadnichuk, I. N., Rexroth, S., Rögner, M., & Koenig, F. (2012). Unique properties vs. common themes: The atypical cyanobacterium *Gloeobacter violaceus* PCC 7421 is capable of state transitions and blue-light-induced fluorescence quenching. *Plant and Cell Physiology*, 53(3), 528-542. <https://doi.org/10.1093/pcp/pcs009>
- Bhadha, J. H., Capasso, J. M., Khatiwada, R., Swanson, S., & LaBorde, C. (2017). Raising soil organic matter content to improve water holding capacity. *EDIS*, 2017(5), Article SL447. <https://doi.org/10.32473/edis-ss661-2017>
- Cahyo, A. N., Murti, R. H., Putra, E. T. S., Oktavia, F., Ismawanto, S., & Montoro, P. (2022). Rubber genotypes with contrasting drought factor index revealed different mechanisms for drought resistance in *Hevea brasiliensis*. *Plants*, 11(24), Article 3563. <https://doi.org/10.3390/plants11243563>
- Carr, M. K. V. (2012). The water relations of rubber (*Hevea brasiliensis*): A review. *Experimental Agriculture*, 48(2), 176 – 193. <https://doi.org/10.1017/S0014479711000901>
- Gomez, K. A., & Gomez, A. A. (1984). *Statistical procedure for agricultural research* (2nd ed.). John Wiley and Sons.
- Jacob, J., Gitz, V., Gohet, E., Kadir, A. B. S. A., Nair, L., Pinizzotto, S., Nguyen, A. N., Blagodatsky, S., Brady, M., Cerutti, P. O., Chen, B., Duchelle, A. E., Fairuzah, Z., Febbiyanti, T. R., Gay, F., Jessy, M. D., Martius, C., Matsui, M., Meybeck, A., Nouvellon, Y., ... & Wjiesuriya, W. (2022, 2-6 May). *Natural rubber contributions to adaptation to climate change* [Paper presentation]. World Forestry Congress, Seoul, Korea.
- Jiang, C., Johkan, M., Hohjo, M., Tsukagoshi, S., & Maruo, T. (2017) A correlation analysis on chlorophyll content and SPAD value in tomato leaves. *HortResearch*, 71, 37-42. <https://doi.org/1020776/S18808824-71-P37>

- Kunjet, S., Thaler, P., Gay, F., Chuntuma, P., Sangkhasila, K., & Kasemsap, P. (2013). Effects of drought and tapping for latex production on water relations of *Hevea brasiliensis* trees. *Kasetsart Journal - Natural Science*, 47(4), 506-512.
- Liang, X., Wang, D., Ye, Q., Zhang, J., Liu, M., Liu, H., Yu, K., Wang, Y., Hou, E., Zhong, B., Xu, L., Lv, T., Peng, S., Lu, H., Sicard, P., Anav, A., & Ellsworth, D. S. (2023). Stomatal responses of terrestrial plants to global change. *Nature Communications*, 14(1), Article 2188. <https://doi.org/10.1038/s41467-023-37934-7>
- Li, Y., & Wang, J. (2021). Effects of soil moisture on plant growth and development. *Journal of Plant Physiology*, 258, Article 153356.
- Malaysian Rubber Board. (2009). *Rubber plantation & processing technologies*. MRB.
- Manzoni, S., Vico, G., Palmroth, S., Porporato, A., & Katul, G. (2013). Optimization of stomatal conductance for maximum carbon gain under dynamic soil moisture. *Advances in Water Resources*, 62, 90-105. <https://doi.org/10.1016/j.advwatres.2013.09.020>
- Mislan, R., Sulaiman, Z., Noordin, W. D., Abdullah, S. N. A., Islam, M. R., Selamat, A., Samad, M., Puteh, A., & Salisu, M. A. (2020) Growth and physiological response of selected clones of rubber grown under different water frequencies. *Bangladesh Journal of Botany*, 49(2), 205-213. <https://doi.org/10.3329/bjb.v49i2.49293>
- Mokhtar, S. J., Daud, N. W., & Zamri, N. M. (2011). Evaluation of different water regimes on *Hevea brasiliensis* grown on haplic ferralsol soil at nursery stage. *International Journal of Applied Science*, 1(3), 28-33.
- Praba, M. L., Cairns, J. E., Babu, R. C., & Lafitte, H. R. (2009). Identification of physiological traits underlying cultivar differences in drought tolerance in rice and wheat. *Journal of Agronomy and Crop Science*, 195(1), 30-46. <https://doi.org/10.1111/j.1439-037X.2008.00341.x>
- Santos, J. O., Oliveira, L. E. M., Souza, T., Lopes, G. M., Coelho, V. T., & Gomes, M. P. (2019). Physiological mechanisms responsible for tolerance to, and recuperation from, drought conditions in four different rubber clones. *Industrial Crops and Products*, 141, Article 111714. <https://doi.org/10.1016/j.indcrop.2019.111714>
- Shen, Q., Ding, R., Du, T., Tong, L., & Li, S. (2019). Water use effectiveness is enhanced using film mulch through increasing transpiration and decreasing evapotranspiration. *Water*, 11(6), Article 1153. <https://doi.org/10.3390/w11061153>
- Somjan, J., & Sadudee, S. (2008). Effects of irrigation on physiological responses and latex yield of rubber trees in the year-round. *Journal of Agricultural Science*, 39, 35-39.
- Sterling, A., Rodri'guez, N., Quiceno, E., Trujillo, F., Clavijo, A., & Sua'rez-Salazar, J. C. (2019). Dynamics of photosynthetic responses in 10 rubber trees (*Hevea brasiliensis*) clones in Colombian Amazon: Implications for breeding strategies. *PLoS One*, 14(12), Article e0226254. <https://doi.org/10.1371/journal.pone.0226254>
- Swoczyna, T., Kalaji, H. M., Bussotti, F., Mojski, J., & Pollastrini, M. (2022). Environmental stress - what can we learn from chlorophyll a fluorescence analysis in woody plants? A review. *Frontiers in Plant Science*, 13, Article 1048582. <https://doi.org/10.3389/fpls.2022.1048582>

- Taiz, L., Zeiger, E., Møller, I. M., & Murphy, A. (2015). *Plant physiology and development* (6th ed.). Sinauer Associates Sunderland.
- Teh, C. B. S., & Jamal, T. (2006). *Soil physics analyses*. UPM press.
- Waqas, M., Straeten, D. V. D., & Geilfus, C. M. (2023). Plants' cry' for help through acoustic signals. *Trends in Plant Science*, 28(9), 984-986. <https://doi.org/10.1016/j.tplants.2023.05.015>
- Wang, L. F. (2014). Physiological and molecular responses to drought stress in rubber tree (*Hevea brasiliensis* Muell. Arg.). *Plant Physiology and Biochemistry*, 83, 243-249. <https://doi.org/10.1016/j.plaphy.2014.08.012>
- Wang, M., Xie, B., Fu, Y., Dong, C., Hui, L., Guanghui, L., & Liu, H. (2015). Effects of different elevated CO₂ concentrations on chlorophyll contents, gas exchange, water use efficiency, and PSII activity on C 3 and C 4 cereal crops in a closed artificial ecosystem. *Photosynthesis Research*, 126, 351-362. <https://doi.org/10.1007/s11120-015-0134-9>
- Witham, F. H., Blaydes, D. F., & Devlin, R. M. (1986). *Exercises in plant physiology* (2nd ed.). PWS Publishers.
- Yamamoto, A., Nakamura, T., Adu-Gyamfi, J. J., & Saigusa, M. (2002). Relationship between chlorophyll content in leaves of sorghum and pigeonpea determined by extraction method and by chlorophyll meter (SPAD-502). *Journal of Plant Nutrition*, 25(10), 2295-2301. <https://doi.org/10.1081/PLN-120014076>

Dehydrated Food Waste and Leftover for Trench Composting

Khalida Aziz¹, Naweedullah Amin², Vinod Kumar Nathan³, Mami Irie⁴, Irwan Syah Md. Yusoff⁵, Luqman Chuah Abdullah⁶, Amirrudin Azmi⁷ and Muhammad Heikal Ismail^{7*}

¹Department of Chemical Engineering, Faculty of Engineering, Faryab University, Maymana, 1801 Afghanistan

²Department of Zoology, Faculty Biology, Kabul University, Kart-e-Char, Kabul 1006, Afghanistan

³Department of Microbiology and Fermentation Technology, CSIR Central Food Technological Research Institute (CFTRI), Mysuru 570020 India

⁴Department of International Agricultural Development, Faculty of International Agriculture and Food Studies, Tokyo University of Agriculture, Setagaya City, Tokyo 156-8502, Japan

⁵Department of Resource Management and Consumer Studies, Faculty of Human Ecology, Universiti Putra Malaysia, 43400 UPM, Serdang, Selangor, Malaysia

⁶Department Chemical and Environmental Engineering, Faculty of Engineering, Universiti Putra Malaysia Serdang, 43400 UPM, Serdang, Selangor, Malaysia

⁷Department of Environment, Faculty of Forestry and Environment, Universiti Putra Malaysia, 43400 UPM, Serdang, Selangor, Malaysia

ABSTRACT

The growing global population has a persistently negative impact on the economy and ecology due to food waste. This topic has recently received much attention from around the world. For both homes and the food processing industry, recycling food waste is crucial to waste management. This study aims to show how dehydrated food scraps and leftovers can be used as raw materials for trench compost to enhance soil quality and reduce

leachate and greenhouse gas emissions.

The results showed that the pre-treatment and air temperature significantly affected the finished trench compost products' EC, pH, and nutrient content. Pretreated dried leftover at 80°C after trench compost was found to have the highest value of CNH, S (36.53%), and micronutrients (0.103404%) when compared to micronutrients in the final product of pre-treatment dried leftover at 80°C after trench compost that was (0.057273%). Dehydrated leftovers from trench compost were thought to have

ARTICLE INFO

Article history:

Received: 09 November 2023

Accepted: 25 March 2024

Published: 25 October 2024

DOI: <https://doi.org/10.47836/pjst.32.6.22>

E-mail addresses:

khalidaaziz143@gmail.com (Aziz Khalida)

sodes.amin123@gmail.com (Naweedullah Amin)

vinodkumar@cftri.res.in (Vinod Kumar Nathan)

mami-o@nodai.ac.jp (Mami Irie)

irwansyah@upm.edu.my (Irwan Syah Md. Yusoff)

chuah@upm.edu.my (Luqman Chuah Abdullah)

amirrudinazmi1995@gmail.com (Amirrudin Azmi)

heikal@upm.edu.my (Muhammad Heikal Ismail)

* Corresponding author

nutrient content that would improve soil quality, slow decomposition, and reduce odor, thus enabling more frequent trash collection.

Keywords: Drying, food waste, leftovers, trench composting

INTRODUCTION

Food waste is a complicated issue that can negatively impact several aspects of sustainability, including the climate, economy, and social situations (Ismail et al., 2021). For authorities in developing nations, managing food waste is the most challenging problem (Mohammed et al., 2017). Approximately one-third of the food consumed, or 1.32 billion metric tons, went missing or was wasted (Sulaiman & Ahmad, 2018). In recent years, the growing amount of food waste in Malaysia has brought many problems that affect the country's solid waste management system (W. J. Lim et al., 2016). Growing amounts of solid waste, including that produced by homes, businesses, and farms, are being dumped in unhygienic landfills, endangering the public's health and environment (Chhandama et al., 2022; Sharma et al., 2022).

The primary constituents of food waste consist of fruits and vegetables, accounting for 79% of the total, with fish and meat following at 8%, noodles and rice at 5%, bread and other baked goods at 6%, and dairy products at 2%. Food waste is recognized as a key method for energy recovery and composting on a global scale, given that it often contains proteins (15%–25%), lipids (13%–30%), and carbohydrates (41%–62%) as its main components. (Slopiecka et al., 2022). The critical technical parameters that define the characteristics of food waste include the water content (74%–90%), carbon-to-nitrogen ratio (C/N ratio) ranging from 14.7 to 36.4, total solids content (TS) between 17% and 29%, and volatile solid content (VS) ranging from 17% to 26%. (Lelicińska-Serafin et al., 2023).

The water content of food waste is one of the more important factors because it breaks down quickly, along with agricultural waste. These days, drying techniques are used by both developed and developing countries to decrease their reliance on fossil fuels, improve the efficiency of urban food waste, and clean up waste sites (Pilnáček et al., 2021). Food waste's high water and nutrient content makes it easy to decompose into high-quality compost. Food waste can be used to make bio-compost, improve soil fertility, and make up for an organic matter deficit (S. L. Lim et al., 2016). However, using organic waste with a high moisture content during the composting process eventually results in major issues like increased emissions of greenhouse gases, leachate, and odor (Ahmed & Gupta, 2010).

Dehydrated food waste has become more manageable in terms of food waste management as environmental pollution is becoming more widely recognized (Wang et al., 2018). The most crucial factors for dewatering food waste and reducing the overall mass of waste can be achieved within the constraints of the waste management plan by using drying

techniques to lower the mass of water in food waste (Noori et al., 2022). The increased moisture content during the composting process promotes the growth of bacteria, yeasts, and mold, as well as the production of leachate and odor that is harmful to the environment. They offer several benefits because dehydrated organic materials are light, low moisture content, odorless, and biologically inert. Due to its high quality and low moisture content, dehydrated food waste is more acceptable for storage and transportation than innovative recycling techniques like anaerobic digestion or composting (Ayilara et al., 2020).

Composting involves removing and reusing organic material to change the soil's composition and structure (Keng et al., 2020). Various composting methods are available to turn organic waste into fertilizer (Li et al., 2013). Food waste is broken down using worms in a process called vermicomposting. By maintaining the vitality and health of the soil, this technique helps rural agricultural areas (Gong et al., 2018). Vermicomposting encourages the growth and spread of advantageous microorganisms in the soil ecosystem by supplying nutrients and improving soil aeration (Karmegam et al., 2021). Additionally, if food is scarce, too wet or dry, or the bin is overheated, this method could result in the large-scale or small-scale death of worms (Yatoo et al., 2021).

Anaerobic digestion is also a requirement to produce bokashi compost. Most fertilizer is used for rice bran, rapeseed meal, rice husks, sugar molasses, and water. The Bokashi method uses effective microorganisms to ferment feedstocks. The degradation process is facilitated and expedited using Effective Microorganisms (EM). The breakdown of organic material occurs over two to four weeks. This process's result can be used to feed and rehydrate the soil (Filho, 2022). It needs to be consistently supplemented with Bokashi bran or another EM inoculation to be effective. Odor issues could arise if this process is not appropriately managed (Lew et al., 2021).

Composting in trenches or pits is another method for managing organic waste (Taiwo, 2014). This inexpensive method only needs raw materials like kitchen scraps or other wastes like leaves and grass clippings. After that, there will not be any further expenses for the compost area because the soil will naturally begin to compost. Composting is typically done in a garden, which makes it easier for the compost to be transferred to established plants (Paritosh et al., 2017). Trench composting is a recommended approach for processing dehydrated food waste. Unlike compost piles, trench composting does not necessitate monitoring moisture levels, aeration, or sifting (<https://compost.bc.ca/>).

The study aims to examine the effects of leftovers and dry food waste in the final product to improve soil quality in terms of pH, EC, and nutrient concentrations. The collected samples underwent a five-minute pre-treatment using distilled hot water. The leftovers were then exposed to hot air drying at three distinct temperatures (80, 90, and 100°C). After that, leftovers and dried food waste were combined with garden soil in a 5/3 ratio to create trench compost, which was then stored in a compost box for four weeks.

The results will lead to a good consensus on reconfiguring solid waste management since the most recent food waste treatment policy emphasizes waste production reduction and less recycling (Ravindran & Jaiswal, 2016).

MATERIALS AND METHODS

Material

The material used in this research is food waste and leftovers. Food waste was obtained from different sources, as indicated in Figure 1(a) from the Sri Serdang community; various food wastes included vegetables like onion peeled, cucumber, spinach, tomatoes, lettuce, and fruits like banana peels, papaya, apple cores, and orange that were not properly consumed, also the leftovers included rice, bread, noodle, and different vegetable as indicated in Figure 1(b) obtained from Sri Kembangan restaurants. This study collected food waste and leftovers until a mass of about 100g each. The particle size of raw materials (food waste and leftovers) is 10mm, cut manually with a knife, and unusable waste materials are to be ready for pre-treatment.



(a)



(b)

Figure 1. (a) Food waste; and (b) leftovers for trench composting

Pre-treatment

The raw materials were soaked in warm water at 70°C for five minutes during the pre-treatment process. Pre-treating organic waste is expected to improve drying kinetics because the oil and unnecessary coating were removed during pre-treatment from the samples with no impurities covered, which introduced higher moisture removal.

Drying Process

Both treated and untreated food waste and leftovers were dried in a laboratory oven with constant air conditions set to 80°C, 90°C, and 100°C. The amount of moisture lost was tracked throughout the drying process.

Preparation of Trench Compost

After the drying process, dried food waste and leftovers were ground with a blender until it was changed to powder, and then mixed with garden soil at 5:3 ratios (20 g:12 g), and all mixed material composted in a plastic bin by the dimension of this tray is 30 cm (length),

10 cm (height) and 12 cm (width) (Inckel et al., 2005). The bins were kept in a room with ambient air of about 30°C for four weeks. Consequently, all samples were closed with newspaper to avoid contact with insects like flies. After the composting period, the trench compost was gathered using a 2 mm sieve tray. The tray was then stirred gently with sifted flour from side to side. The trench compost is dropped by leaving bigger particles size and tiny stones behind. The procedure was repeated until all samples were passed. This process guarantees a uniform texture of the trench compost and lowers the size of the particle from coarse to fine.

Physiochemical Analysis

Conducting a physical and chemical analysis of compost made from food scraps and leftovers is possible. The physical property analysis of the trench compost includes the pH value, total nitrogen, total sulfur, total carbon, identification of micronutrients (Cu, Ca, Mg, K, and Zn), and electric conductivity.

Liquid Extraction from Dehydrated Food Waste and Leftover Fertilizer

After trench compost, the dehydrated food waste and leftovers were subjected to a liquid extraction process with distilled water in a 1:10 (w/v) ratio and kept at room temperature for 24 hours. After that, the pH was measured with a pH meter, and EC was measured with an Electric conductivity (EC) detector.

pH Value

After being taken off, the pH meter cap was inserted into the sample solution (liquid region). The pH value was determined and noted. This procedure was completed for every sample of trench compost. Eutech Instruments provides a pH tutor bench meter for use in laboratories. The pH range was 0.00 to 14.00, with a relative accuracy 0.01. This research used the pH meter to determine the potential hydrogen of trench compost (Jones, 2001).

Electric Conductivity (EC)

Distilled water was used to clean the EC detector before use. The EC detector was then calibrated, and the reading was recorded. Before using the EC detector addition, the national samples were thoroughly cleaned with distilled water after recording the EC reading. This step was carried out for all trench compost samples. The electrical conductivity is determined at room temperature, validated in solutions of 1.0, 0.1, and 0.01 D KCl (aq). The measured electrical conductivities were within 0.5% of the values used as a standard (Gong et al., 2018). This research used an EC detector to detect the electric conductivity of soil and trench compost samples.

Determination of CHNS

The final product of dried food waste and leftover after trench compost was used to calculate the percentages of carbon (C), Sulphur (S), hydrogen (H), and nitrogen (N). The elemental analysis was performed using a flashed model I 112 with helium gas as the carrier gas, and the ultimate analysis was performed according to ASTM standards (ASTM M373-02) (Thompson, 2008). The CHNS machine (FLASHEA1112 SERIES) determined a sample's nitrogen, hydrogen, and sulfur levels. It typically operates at high temperatures, eliminating components from the sample.

Analysis of Macro and Micro-elements

For concertation of Cu, K, Ca, Mg, and Zn, the samples of (dehydrated food waste and leftovers after trench compost) were sent to the Analytical Laboratory 2, UPM Faculty of Agriculture, to be analyzed in an Atomic Absorption Spectrophotometer. The samples were sent in liquid form and extracted using the Dilute Double Acid (DDA) method. The DDA extraction procedure from the solid started by mixing with a 0.05 standard solution of hydrochloric acid (HCl) and a 0.025 standard solution of Sulfuric acid (H₂SO₄) (Mylavarapu et al., 2014). First, a 5.0 g sample was weighed and placed into a falcon tube. Afterward, 25 mL of DDA extracting reagent was added into the tube and shaken for 15 minutes at 180 rpm using an end-to-end shaker. Then, the solution was filtered with filter paper. The filtered sample was collected in a 50mL plastic vial and sent to an Atomic Absorption Spectrophotometer (AAS). Dilution (10×) using distilled water for the nutrients can be conducted. The Autoanalyzer machine is used to conduct soil and trench compost environmental analyses, and its design is based on the segmentation of an air bubble stream continuously running.

RESULTS AND DISCUSSION

Compost Soil Properties

The composition of compost in the soil can have a significant impact on the soil's physiochemical properties, nutrient availability, and plant growth. Composting strategically on deteriorated urban soils may have a beneficial influence on the soil's quality.

Physicochemical Analysis of Trench Compost

Figures 2(a) and 2(b) show the final product of dehydrated food waste and leftovers after the composting period. The trench compost was collected to analyze the changes in the physicochemical characteristics of several parameters, such as pH, electrical conductivity (EC), total carbon (TC), total hydrogen (TH), total nitrogen (TN), total Sulphur (TS), and micronutrients (Zinc, Calcium, Potassium, Copper, and Magnesium).

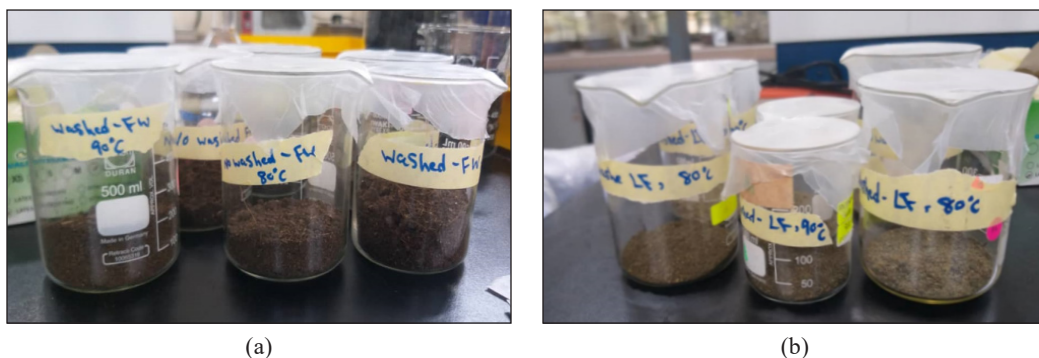


Figure 2. Harvested product from dehydrated food waste for: (a) food waste; and (b) leftovers after trench compost

Determination of pH and Electroconductivity (EC)

Figures 3 and 4 display the pH value in the final product for dried food waste and leftovers at various temperatures. The results showed that the pre-treatment and air temperature had a significant impact on the pH and EC of the final products (bio-compost). At 80°C, the pH of dried food waste pretreated was 5.72, whereas the pH of food waste that had not been pretreated was 5.61 at the same temperature. The pH value for pretreated dried food waste at 100°C after the compost was 5.47, while for non-pretreated food waste at the same temperature was 5.25.

The samples that dried at a high temperature had a lower pH value in the final product. However, pre-treatment had a positive impact because the pretreated sample had a higher pH value than the non-pretreated sample. The final dried food waste product had a high electrical conductivity value. Pre-treatment and air temperature appear to have a major impact as well. Pretreated food waste exhibited a greater electro-conductivity range of

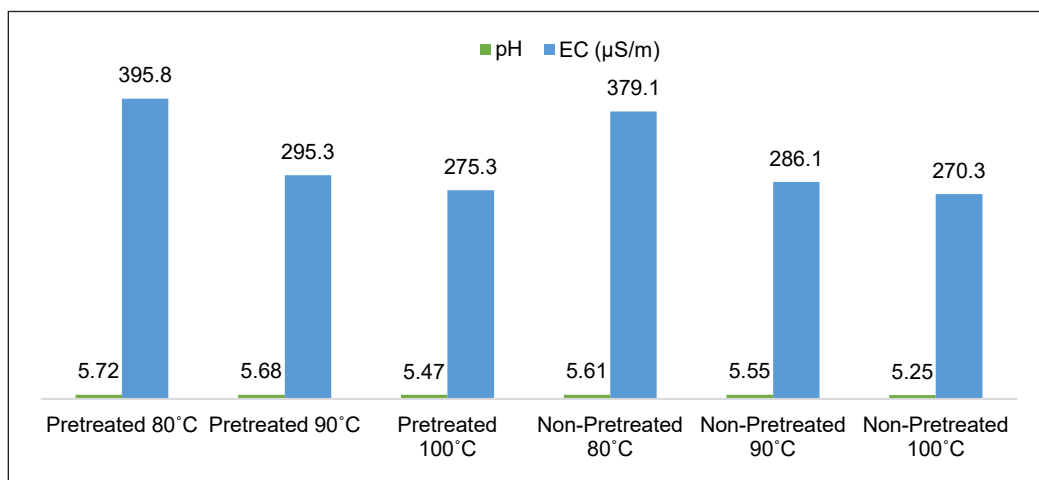


Figure 3. The electrical conductivity and pH of dehydrated food waste in the final product

275.3–395.8 $\mu\text{S}/\text{cm}$ compared to non-pretreated food waste, which had a range of 270.3–379.1 $\mu\text{S}/\text{cm}$. When the temperature rises, the electrical conductivity of both pre-treated and non-pre-treated food waste decreases, as shown in Figure 3.

The pH and electrical conductivity of leftovers at various drying temperatures after finishing trench compost are shown in Figure 4. At 80°C and 90°C, the pH of pretreated dried leftovers was 5.33, while the pH of non-pretreated leftovers was 5.31 and 5.28, respectively. The pH value for pretreated dried leftovers after composting at 100°C was 5.24, while the pH value for non-pretreated leftovers at the same temperature was 5.17. However, pre-treatment had a positive impact because the pretreated sample had a higher pH value than the non-pretreated sample. Furthermore, pre-treatment leftovers had a larger electro-conductivity range of 216.6–225.1 $\mu\text{S}/\text{cm}$ than non-pretreated leftovers, which had a 164.6–180.9 $\mu\text{S}/\text{cm}$ range. Conversely, pre-treatment enhances the breakdown rates of carbohydrates, calcium, potassium, chloride, and sulfate and increases the substrate's surface area. This process releases more ions as dissolved salts and other inorganic compounds elevate the electroconductivity (Silva et al., 2020). Furthermore, thermal washing pre-treatment over an extended period degrades carbohydrates in food waste into shorter-chain components more readily digestible by bacteria (Chua et al., 2019).

According to the findings, the fertilizer was highly acidic due to naturally acidic fruits and vegetables such as tomato, carrot, and apple peel in the raw material. There were similar findings in the food waste characterization reported by (Ho & Chu, 2019). The metabolic breakdown of organic acids during the composting process can lead to an increase in pH value. This phenomenon is often attributed to the process of ammonification, where nitrogen (N) is converted into ammonium (NH_4^+) or ammonia (NH_3) (Ramli et al., 2023).

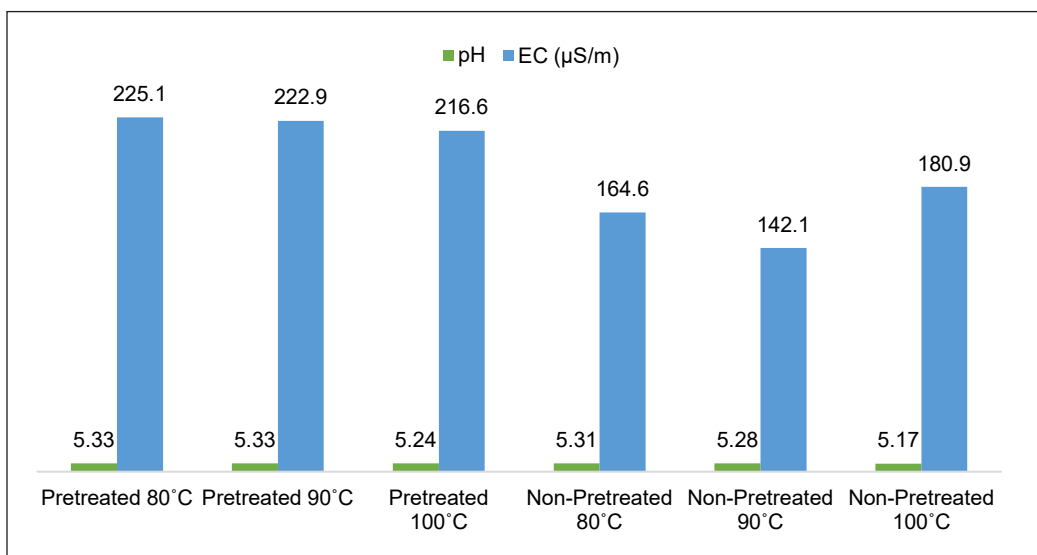


Figure 4. The electrical conductivity and pH of dehydrated leftovers in the final product

The final product will be affected if the raw material contains acidic fruits or vegetables. The pH of dehydrated organic waste fertilizer products ranges between 4.6 and 4.8, while the EC value ranges between 4.83 and 7.64 S/m. The high salt content, particularly the Na content, contributed to the high EC content of fertilizer. The sodium level of the food waste fertilizer products ranged between 0.54% and 0.67%, corresponding to the human diet (O'Connor et al., 2022). The health of plants and the proliferation of soil microorganisms are inextricably linked to soil pH. Most plants thrive in slightly acidic to neutral soils (pH 5.5–7). Blueberries are an example of a plant that thrives in acidic soils with a low pH of 4.5–5.5. Dehydrated food waste fertilizer with low pH is suitable (Schroeder et al., 2020).

Determination of Micronutrients

Micronutrients aid in plant growth and development. Crops require micronutrients such as Ca, K, Cu, Mg, manganese, and zinc. This study evaluated dehydrated food waste and leftover fertilizer products as micronutrients, as shown in Tables 1 and 2 and Figures 5 and 6.

Table 1 and Figure 5 show the micronutrient content of dried food waste fertilizer after trench composting. According to the result, air temperature and washing pre-treatment had a significant impact on the value of nutrients in the samples. The nutrient content decreased when the air temperature increased, but pretreated samples had a higher value than non-pretreated samples. Pretreated food waste at 80°C, 90°C and 100°C after trench compost recorded micronutrient Potassium (391.2, 348.5, and 220.3) mg/L, Calcium (109.8, 88.78, and 83.43) mg/L, Copper (0.98, 0.68, and 0.58) mg/L, Magnesium (58.35, 57.95, and 57.45) mg/L, and Zinc (11.4, 8.67, and 6.58) mg/L respectively. While non-pretreated food waste at same temperatures had lower value: Potassium (244.1, 205.3, and 144.5) mg/L, Calcium (69.72, 55.84, and 34.51) mg/L, Copper (0.18, 0.13, and 0.07) mg/L, Magnesium (57.22, 57.04, and 55.74) mg/L, and Zinc (6.10, 5.29, and 5.17) mg/L respectively.

According to previous research, dehydrated food waste fertilizers have a high nutritional concentration, which helps plants develop. A wide variety of plant growth-promoting microorganisms can be found in dehydrated food waste fertilizer products. Fertilizer items inoculated with the plant mutualistic *Aspergillus* sp. strain UY2015 11 improved the

Table 1

Chemical properties of dehydrated food waste fertilizer at various air temperatures

FW	Temperature (°C)	K (mg/L)	Ca (mg/L)	Cu (mg/L)	Mg (mg/L)	Zn (mg/L)
Pretreated	80	391.2*	109.8*	0.98*	58.35*	11.4*
	90	348.5	88.78	0.68	57.95	8.67
	100	220.3	83.43	0.58	57.45	6.58
Non pretreated	80	244.1	69.72	0.18	57.22	6.10
	90	205.3	55.84	0.13	57.04	5.29
	100	144.5	34.51	0.07	55.74	5.17

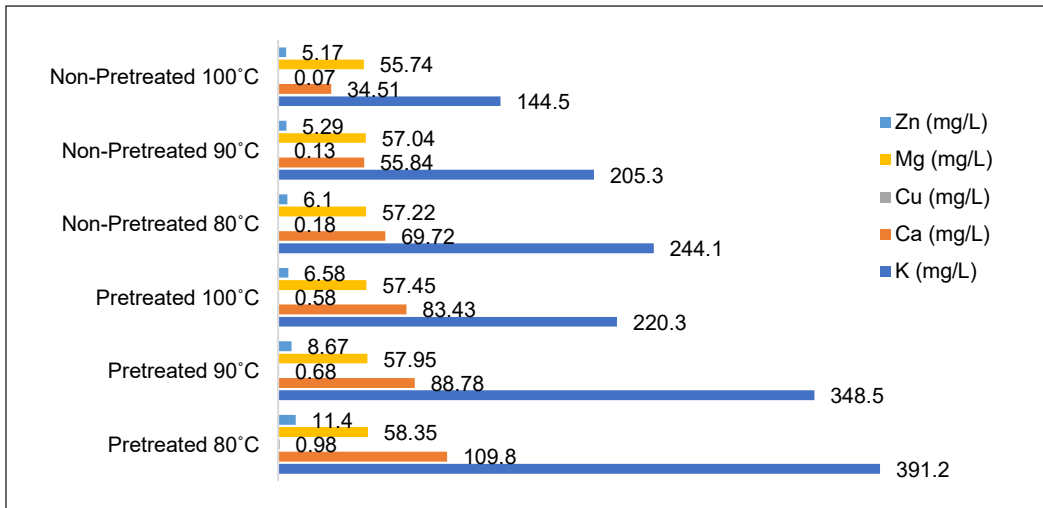


Figure 5. Micronutrients of dehydrated food waste fertilizer at various air temperatures

value of nutrients accessible in the soil. The product may also be able to prevent or treat some disorders (Liu et al., 2015). The micronutrient, made from dehydrated food waste fertilizer, increased soil respiration. Increased soil microbial activity occurs when dried food waste fertilizer items are added. Because of this, the nutrients in food waste fertilizer products were readily available for microbial respiration, as shown by substrate-induced respiration (O'Connor et al., 2022).

Dried food waste with low moisture content aids in composting by managing water content and providing an excellent input material without pathogens and with appropriate amounts of carbon and nitrogen (Sotiropoulos et al., 2015). Considering that the quantity of dry food waste recorded micronutrients are 14.2% (C), 0.42% (N), 7.1% (H), 0.02% (P), and 0.4% (K) (Han, 2017). Therefore, it is highlighted that dehydrated food waste is utilized as a source material in the composting process from food waste.

Table 2 and Figure 6 shows the Pretreated leftovers at 80°C, 90°C and 100°C after trench compost recorded micronutrient Potassium (880.1, 713.5, and 659.1) mg/L, Calcium (83.99, 72.98, and 71.38) mg/L, Copper (1.88, 1.60, and 0.95) mg/L, Magnesium (53.12, 52.76, and 52.04) mg/L, and Zinc (14.95, 13.44, and 9.26) mg/L respectively. At the same time, non-pretreated leftovers at same temperatures had lower value: Potassium (385.5, 339.9, and 329.7) mg/L, Calcium (44.18, 43.47, and 24.50) mg/L, Copper (0.94, 0.28, and 0.10) mg/L, Magnesium (51.66, 51.65, and 49.78) mg/L, and Zinc (8.74, 7.15, and 5.28) mg/L respectively. Compared to dried leftover samples after trench compost, pretreated leftovers at 80°C had the highest value of micronutrients. Based on the information provided, it can be determined that at lower temperatures, the amount of nutrients in the feedstock remains consistent compared to higher temperatures of 90°C and 100°C.

Table 2

Chemical properties of dehydrated leftover fertilizer at various air temperatures

LF	Temperature (°C)	K (mg/L)	Ca (mg/L)	Cu (mg/L)	Mg (mg/L)	Zn (mg/L)
Pretreated	80	880.1*	83.99*	1.88*	53.12*	14.95*
	90	713.5	72.98	1.60	52.76	13.44
	100	659.1	71.38	0.95	52.04	9.26
Non-pretreated	80	385.5	44.18	0.94	51.66	8.74
	90	339.9	43.47	0.28	51.65	7.15
	100	329.7	24.50	0.10	49.78	5.28

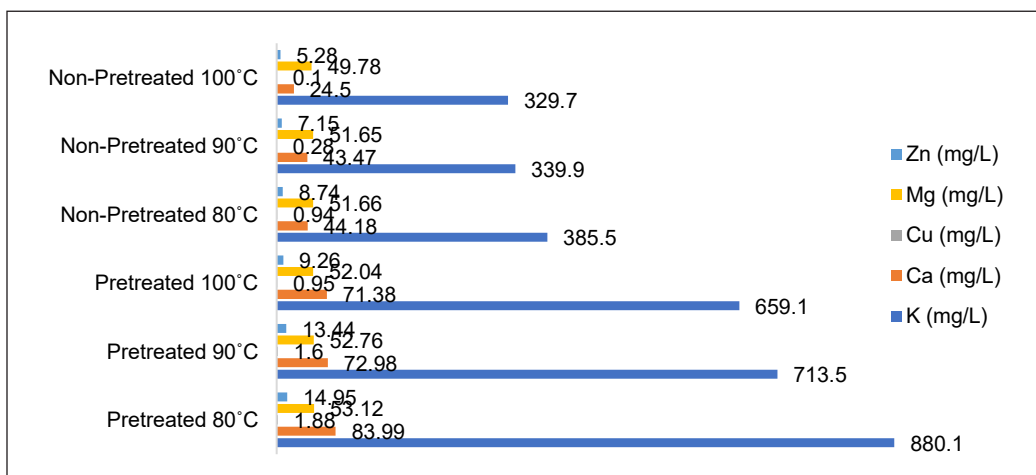


Figure 6. Micronutrients of dehydrated leftover fertilizer at various air temperatures

Determination of CHNS

Dehydrated food waste and leftovers after trench composting were analyzed using a CHNS analyzer, and the results were recorded in Tables 3 and 4, as well as Figures 7 and 8. The highest Carbon recorded was 23.76% in pretreated dry food waste at 80°C, while the lowest was 17.43% in non-pretreated dried food waste at 100°C. Also, the highest value of Nitrogen was recorded in the same sample of pretreated dried food waste at 80°C fertilizer with 1.68%, and the lowest was 1.09 for non-pretreated dried food waste at 100°C fertilizer after trench compost. Based on Table 3, Sulfur was higher in the pretreated food waste at 80°C than in pretreated and non-pretreated food waste fertilizer at 90°C and 100°C.

According to the result, the final product of dehydrated leftovers at 80°C had the highest value of CHNS: Carbon 29.54%, Hydrogen 5.12%, and Nitrogen 1.58, respectively. After composting, the Sulphur value was 0.29% for all the dried leftover samples. The air temperature and pre-treatment had a considerable impact on the nutrient content of the final product. The results show that samples dried at a higher temperature had lower C, N, and S content. The pretreated samples also had a higher nutrient content value than

the non-pretreated samples. The same result was reported in proven research when air temperatures were increased to 150–200°C; the mineralization rate from organic wastes tended to decrease dramatically (Moritsuka & Matsuoka, 2018).

As composting progressed, the nitrogen content increased while the total Carbon content decreased, resulting in a corresponding decrease in the CN ratio. Carbon is

Table 3
Determination of CHNS in dehydrated food waste fertilizer at various air temperatures

FW	Temperature (°C)	C (%)	H (%)	N (%)	S (%)
Pre-treated	80	23.76*	4.10	1.68*	0.19*
	90	23.34	4.11*	1.64	0.14
	100	20.20	4.10	1.50	0.12
Non pre-treated	80	23.74	4.11*	1.68*	0.17
	90	21.01	4.12	1.22	0.13
	100	17.43	3.98	1.09	0.12

Table 4
Determination of CHNS in dehydrated leftover fertilizer at various air temperatures

LF	Temperature (°C)	C (%)	H (%)	N (%)	S (%)
Pretreated	80	29.54*	5.12*	1.58	0.29
	90	28.36	5.10	1.26	0.29
	100	23.23	5.10	1.18	0.29
Non-pretreated	80	28.92	5.11	1.63*	0.29
	90	25.08	5.12*	1.34	0.29
	100	24.99	4.19	1.50	0.29

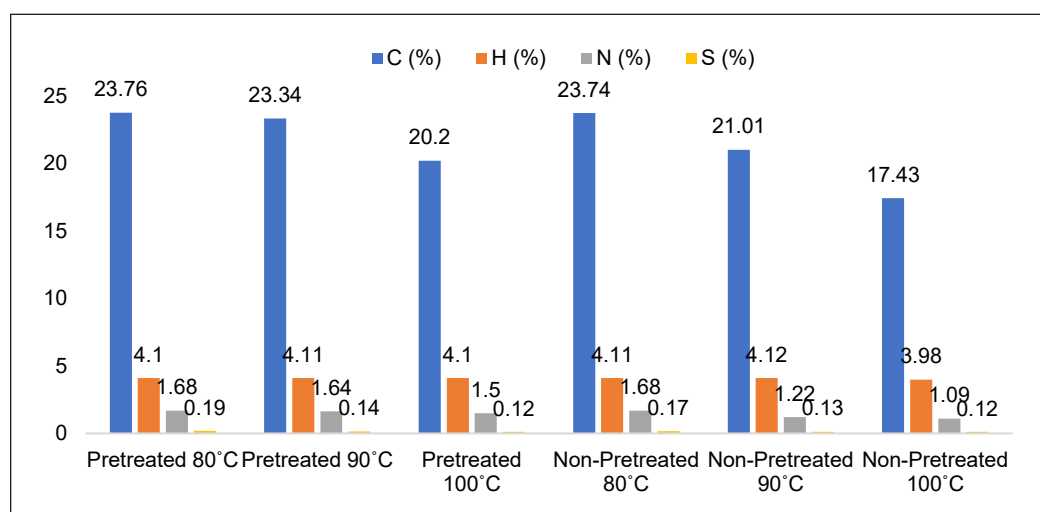


Figure 7. Value of CHNS in dehydrated food waste fertilizer at various air temperatures

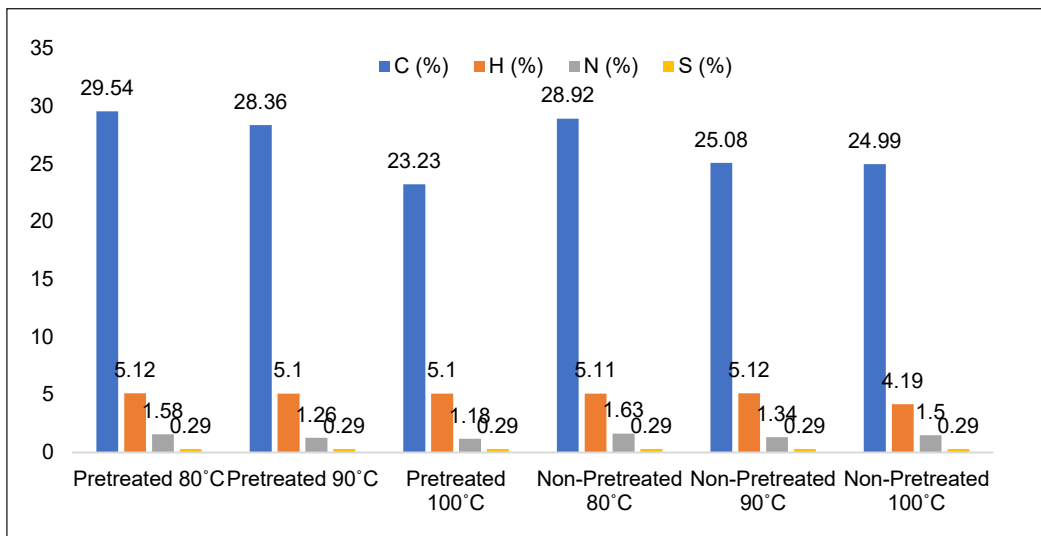


Figure 8. Value of CHNS in dehydrated leftover fertilizer at various air temperatures

the primary energy source, while nitrogen is essential for microbial population growth (Shahudin et al., 2011). Composting can increase the amount of carbon in the soil, but it is critical to use a good composting approach to preserve the carbon reserves in the soil for a long time (Beesley, 2012). Dehydrated waste before composting can help solve this problem because the bacteria will grow quickly, have the greatest biodegradation activity, and provide enough energy to heat the compost. Compared to moist compost, tobacco leaf waste composting has the highest carbon-to-nitrogen content (20.1) and can be stored for a long time (Zhao et al., 2017).

Overall, the mixture of carbon, nitrogen, and sulfur showed great promise value in the final product that can be used to improve soil quality as a fertilizer (Srivastava et al., 2011). Although the ideal C/N ratio is between 30 and 40, much research has demonstrated that a C/N ratio of less than 20 can also benefit composting. After composting, the dried food waste had a total carbon content of 31% and a Sulphur content of 0.11%, which can provide essential nutrients to plant soil (Firdaus et al., 2018).

According to the findings in Table 5 and Figure 9, pre-treatment had a substantial effect on drying time, net mass, and nutritional content for each sample. Pretreated food waste and leftovers dried more quickly than non-pre-treated samples, and samples had a lower mass value after drying due to increased moisture loss. Because the pre-treatment removed the impurity of salt and oil from the surface of the food waste and leftovers, allowing moisture from the sample slab to escape into the atmosphere. A comparison of food waste and leftovers demonstrates that all leftover samples had a higher weight value than food waste. Furthermore, the presence of salt and oil can disrupt the composting process. Salt hinders the breakdown of organic matter due to its sodium content, making it difficult for

Table 5

Comparison of the food waste and leftovers drying time, net weight after drying, and nutrient content after trench composting

Temperature	Treatment	FW Net Weight mi (g)	LF Net Weight, mi (g)	FW Time (min)	LF Time (min)	Total of CNHS FW	Total of CNHS LF
80°C	Washed	6.9	20.9	140	135	29.73	36.53
	Not washed	9	28.1	180	150	29.7	35.93
90°C	Washed	4.3	19.3	120	120	29.23	35.01
	Not washed	5.2	26	150	150	26.48	31.83
100°C	Washed	3	9.2	110	115	25.92	29.22
	Not washed	4.1	24.6	135	130	22.62	30.97

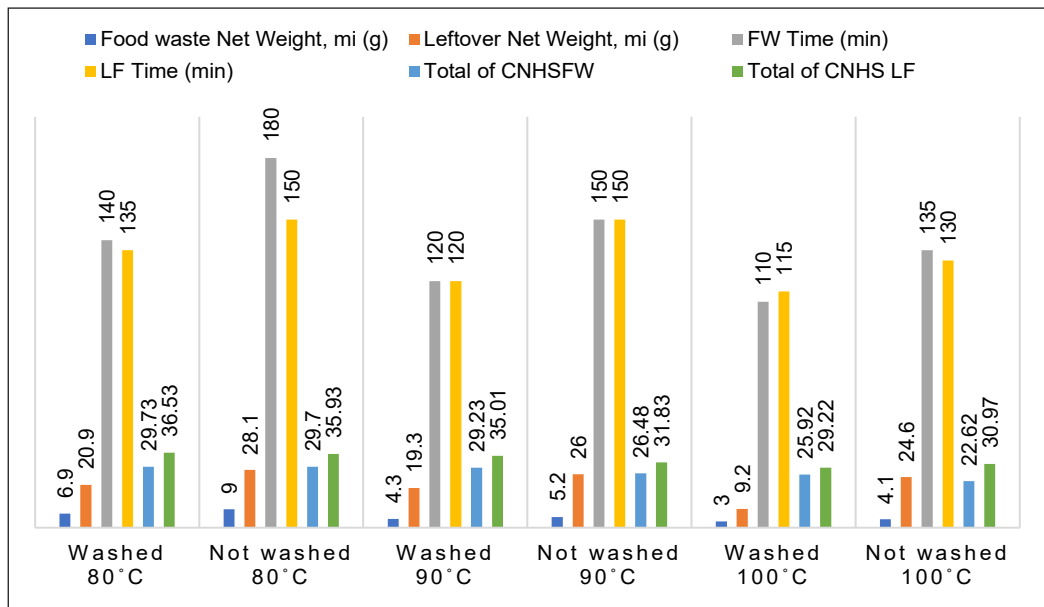


Figure 9. Comparison of the food waste and leftovers drying time, net weight after drying, and nutrient content after trench composting

beneficial microorganisms to thrive. Consequently, this can prolong the composting process and produce an unhealthy end product (Han, 2017). Additionally, oil inhibits airflow during composting, leading to water buildup within the compost (Sánchez et al., 2023).

The net weight of pre-treated leftovers after the drying process at 80°C for 135 minutes was 20.9 g, and the net weight of non-pretreated leftovers at the same temperature was 28.1 g, and it took 150 minutes to dry. The net weight of pre-treated food waste at 80°C was 6.9 g, and it took 140 minutes to dry; the non-pretreated food waste after the drying process at the same temperature was 9 g. As a result, food waste took a longer drying time than leftovers. However, leftovers had a higher net weight after drying than food waste

samples. Also, at 90°C and 100°C, food waste net weight was 4.3 g and 3 g, respectively. At the same time, The net weight of non-pretreated leftovers after drying at the same temperatures was 19.3 g and 9.2 g, which was higher than food waste. Due to food waste made up of more juicy fruits and vegetables, in this case, dried more and had a lower net weight. However, leftovers had a larger net weight after drying since they consisted of bread, rice, and noodles (O'Connor et al., 2021).

As a result, the final product of both samples was highly acidic. pH values for food waste ranged from 5.25 to 5.75, and leftovers were in the range of 5.17 to 5.33. However, the electrical conductivity of food waste was (270.3 to 395.8) S/m higher than leftover (180.9 to 225.1) S/m. Carbon, nitrogen, and sulfur are compost's three most significant elements. The resulting amount of CNHS and micronutrients in the final product of leftovers was higher than the food waste final product after trench compost.

The nutrient level of compost is directly proportional to the quality of its input material. The food waste in this study includes rotten vegetables and fruits. But leftovers included rice, bread, noodles, and a variety of vegetables and fruits. In this case, leftover final products were richer than food waste. The highest values of C, N, H, and S (36.53%) and micronutrients (K = 880.1 mg/L, Cu = 1.88 mg/L, Ca = 83.99 mg/L, Cu = 1.88 mg/L, Zn = 14.95 mg/L and Mg = 53.12 mg/L) were found in the final product of pretreated dried leftovers at 80°C. Micronutrients from food waste were lower than they were. Substance waste in the same condition resulted in a final product that contained 29.73% total CNHS and micronutrients (K = 392.2 mg/L, Cu = 0.98 mg/L, Ca = 109.8 mg/L, Zn = 11.4 mg/L and Mg = 58.35 mg/L). The nutrient content dropped significantly for sample food waste and leftovers that were dried at a higher temperature. The final product of pretreated leftovers at 80°C had the highest nutrient content than other parameters, 90°C and 100°C.

Composting source materials, such as organic waste, at high temperatures before composting might decrease dried nutritional content and delay decomposition (Khalida et al., 2022). Since raw materials are unable to decompose properly, the final product will lack the required nutritional content for plants. In this case, controlling the moisture content is a difficult task in the composting process; for composting to be successful, the moisture content of the source material must be stabilized; it should be in the optimal range of (55–65) (Chauhan et al., 2021). The nutrient contents such as Nitrogen (N), potassium (K), phosphorus (P), and many others are highly beneficial to the soil and plants. These nutrients are in adequate quantities in the original waste and can be used as raw material in composting. For instance, nitrogen is essential for leafy vegetables like Chinese kale as it ensures the growth of healthy leaves (Ramli et al., 2023). In general, the findings of this study indicate that both dehydrated food waste and leftovers from trench composting can be used as fertilizers to improve soil health and crop productivity. However, additional effort is required to optimize the application of dehydrated food waste.

CONCLUSION

In conclusion, one of the greatest ways to reduce waste management is to dehydrate food waste and leftovers according to the product. Food waste's lower moisture content can help control the water content of the organic substrate during the composting process. Furthermore, leftovers and purified dry food waste have enough nitrogen and carbon contents, are pathogen-free, and can be used as a compost feedstock. The highest values of C, N, H, and S (36.53%) were found in the final product of pretreated dried leftovers at 80°C, along with higher micronutrients. It was higher than food waste micronutrients. In contrast, the final food waste product contained micronutrients and 29.73% of total CNH under the same conditions. The nutritional value of food waste and leftovers dried at a higher temperature was lowered. The dried leftovers produced at 80°C had more nutrients than those produced at 90°C and 100°C. It is more appropriate for use as a fertilizer in this instance. This study found that the high nutrient and carbon content of dehydrated food waste and compostable residues makes them suitable for fertilizers.

ACKNOWLEDGEMENTS

The authors deeply thank the Ministry of Higher Education of Afghanistan (Higher Education Developmental Program) for supporting Khalida Aziz's study in Malaysia. The authors would also like to thank Universiti Putra Malaysia (UPM) for funding the article through the Knowledge Transfer Grant Scheme, with vote number 9437589.

REFERENCES

- Ahmed, I. I., & Gupta, A. K. (2010). Pyrolysis and gasification of food waste: Syngas characteristics and char gasification kinetics. *Applied Energy*, 87(1), 101–108. <https://doi.org/10.1016/j.apenergy.2009.08.032>
- Ayilara, M. S., Olanrewaju, O. S., Babalola, O. O., & Odeyemi, O. (2020). Waste management through composting: Challenges and potentials. *Sustainability*, 12(11), Article 4456. <https://doi.org/10.3390/su12114456>
- Beesley, L. (2012). Carbon storage and fluxes in existing and newly created urban soils. *Journal of Environmental Management*, 104, 158–165. <https://doi.org/10.1016/j.jenvman.2012.03.024>
- Chauhan, C., Dhir, A., Akram, M. U., & Salo, J. (2021). Food loss and waste in food supply chains. A systematic literature review and framework development approach. *Journal of Cleaner Production*, 295, Article 126438. <https://doi.org/10.1016/j.jclepro.2021.126438>
- Chhandama, M. V. L., Chetia, A. C., Satyan, K. B., Supongsena A., Ruatpuia, J. V., & Rokhum, S. L. (2022). Valorisation of food waste to sustainable energy and other value-added products: A review. *Bioresource Technology Reports*, 17, Article 100945. <https://doi.org/10.1016/j.biteb.2022.100945>
- Chua, G. K., Tan, F. H. Y., Chew, F. N., & Mohd-Hairul, A. R. (2019). Nutrients content of food wastes from different sources and its pre-treatment. *AIP Conference Proceedings*, 2124, Article 020031. <https://doi.org/10.1063/1.5117091>

- Filho, C. A. D. J. (2022). *Potencial tecnológico dos resíduos de uma indústria cervejeira para produção de adubo orgânico tipo Bokashi: Uma revisão* [Technological potential of waste from a brewing industry for the production of organic fertilizer in the bokashi style: A review] [Unpublish Degree]. *Universidade Federal Do Ceará Centro*.
- Firdaus, A. R. M., Samah, M. A. A., & Hamid, K. B. A. (2018). Chns analysis towards food waste in composting. *Journal CleanWAS*, 2(1), 06–10. <https://doi.org/10.26480/jcleanwas.01.2018.06.10>
- Gong, X., Cai, L., Li, S., Chang, S. X., Sun, X., & An, Z. (2018). Bamboo biochar amendment improves the growth and reproduction of *Eisenia fetida* and the quality of green waste vermicompost. *Ecotoxicology and Environmental Safety*, 156, 197–204. <https://doi.org/10.1016/j.ecoenv.2018.03.023>
- Han, D. H. (2017). A recycling method of food waste by drying and fuelizing. *Journal of Engineering and Applied Sciences*, 12(14), 3599–3603. <https://doi.org/10.3923/jeasci.2017.3599.3603>
- Ho, K. S., & Chu, L. M. (2019). Characterization of food waste from different sources in Hong Kong. *Journal of the Air and Waste Management Association*, 69(3), 277–288. <https://doi.org/10.1080/10962247.2018.1526138>
- Inckel, M., Smet, P. D., Tersmette, T., & Veldkamp, T. (2005). *The preparation and use of compost*. Agromisa Foundation.
- Ismail, M. H., Lik, H. C., Routray, W., & Woo, M. W. (2021). Determining the effect of pre-treatment in rice noodle quality subjected to dehydration through hierarchical scoring. *Processes*, 9(8), Article 1309. <https://doi.org/10.3390/pr9081309>
- Jones, J. B. (2001). *Laboratory Guide for conducting soil tests and plant analysis*. CRC.
- Karmegam, N., Jayakumar, M., Govarthanan, M., Kumar, P., Ravindran, B., & Biruntha, M. (2021). Precomposting and green manure amendment for effective vermitransformation of hazardous coir industrial waste into enriched vermicompost. *Bioresource Technology*, 319, Article 124136. <https://doi.org/10.1016/j.biortech.2020.124136>
- Keng, Z. X., Chong, S., Ng, C. G., Ridzuan, N. I., Hanson, S., Pan, G. T., Lau, P. L., Supramaniam, C. V., Singh, A., Chin, C. F., & Lam, H. L. (2020). Community-scale composting for food waste : A life-cycle assessment- supported case study. *Journal of Cleaner Production*, 261, Article 121220. <https://doi.org/10.1016/j.jclepro.2020.121220>
- Khalida, A., Arumugam, V., Abdullah, L. C., & Abd, L. (2022). Dehydrated food waste for composting : An overview. *Pertanika Journal of Science & Technology* 30(4), 2933–2960. <https://doi.org/10.47836/pjst.30.4.33>
- Lew, P. S., Nik Ibrahim, N. N. L., Kamarudin, S., Thamrin, N. M., & Misnan, M. F. (2021). Optimization of bokashi-composting process using effective microorganisms-1 in smart composting bin. *Sensors*, 21(8), Article 2847. <https://doi.org/10.3390/s21082847>
- Lelicińska-Serafin, K., Manczarski, P., & Rolewicz-Kalińska, A. (2023). An insight into post-consumer food waste characteristics as the key to an organic recycling method selection in a circular economy. *Energies*, 16(4), Article 1735. <https://doi.org/10.3390/en16041735>

- Lim, S. L., Lee, L. H., & Wu, T. Y. (2016). Sustainability of using composting and vermicomposting technologies for organic solid waste biotransformation: Recent overview, greenhouse gases emissions and economic analysis. *Journal of Cleaner Production*, *111*, 262–278. <https://doi.org/10.1016/j.jclepro.2015.08.083>
- Lim, W. J., Chin, N. L., Yusof, A. Y., Yahya, A., & Tee, T. P. (2016). Food waste handling in Malaysia and comparison with other Asian countries. *International Food Research Journal*, *23*(Suppl), S1–S6.
- Liu, L., Sun, C., Liu, S., Chai, R., Huang, W., Liu, X., Tang, C., & Zhang, Y. (2015). Bioorganic fertilizer enhances soil suppressive capacity against bacterial wilt of tomato. *PlosOne*, *10*(4), Article e0121304. <https://doi.org/10.1371/journal.pone.0121304>
- Li, Z., Lu, H., Ren, L., & He, L. (2013). Experimental and modeling approaches for food waste composting: A review. *Chemosphere*, *93*(7), 1247–1257. <https://doi.org/10.1016/j.chemosphere.2013.06.064>
- Mohammed, M., Ozbay, I., Karademir, A., & Isleyen, M. (2017). Pre-treatment and utilization of food waste as energy source by bio-drying process. *Energy Procedia*, *128*, 100–107. <https://doi.org/10.1016/j.egypro.2017.09.021>
- Moritsuka, N., & Matsuoka, K. (2018). An overview of the effects of heat treatments on the quality of organic wastes as a nitrogen fertilizer. In Amanullah & S. Fahad (Eds.) *Nitrogen in Agriculture Updates* (pp. 53–72). IntechOpen. <http://dx.doi.org/10.5772/68163>
- Mylavarapu, R., Obreza, T., Morgan, K., Hochmuth, G., Nair, V., & Wright, A. (2014). Extraction of soil nutrients using mehlich-3 reagent for acid-mineral soils of florida. *Edis*, *2014*(7), Article 620. <https://doi.org/10.32473/edis-ss620-2014>
- Noori, A. W., Royen, M. J., Medved'ová, A., & Haydary, J. (2022). Drying of food waste for potential use as animal feed. *Sustainability*, *14*(10), Article 5849. <https://doi.org/10.3390/su14105849>
- O'Connor, J., Hoang, S. A., Bradney, L., Rinklebe, J., Kirkham, M. B., & Bolan, N. S. (2022). Value of dehydrated food waste fertiliser products in increasing soil health and crop productivity. *Environmental Research*, *204*(Part A), Article 111927. <https://doi.org/10.1016/j.envres.2021.111927>
- Paritosh, K., Kushwaha, S. K., Yadav, M., Pareek, N., Chawade, A., & Vivekanand, V. (2017). Food waste to energy: An overview of sustainable approaches for food waste management and nutrient recycling. *BioMed research international*, *2017*(1), Article 2370927. <https://doi.org/10.1155/2017/2370927>
- Ramli, N. H., Hisham, N. E. B., & Baharulrazi, N. (2023). The effectiveness of rice husk ash as additive in palm oilbased compost in enhancing the nitrogen uptake by *Brassica oleracea* var. *alboglabra* L. (Chinese Kale) plant. *Pertanika Journal of Tropical Agricultural Science*, *46*(1), 215–328. <https://doi.org/10.47836/pjtas.46.1.17>
- Ravindran, R., & Jaiswal, A. K. (2016). Exploitation of food industry waste for high-value products. *Trends in Biotechnology*, *34*(1), 58–69. <https://doi.org/10.1016/j.tibtech.2015.10.008>
- Sánchez, A., Artola, A., Barrera, R., Gea, T., Font, X., & Moral-Vico, A. J. (2023). Composting of food wastes for soil amendment. In S. Al Arni, S. Chakraborty, Y. C. Ho, W. J. Lau, & R. Natarajan (Eds.), *Advanced Technologies for Solid, Liquid, and Gas Waste Treatment* (pp. 1–22). CRC Press.
- Schroeder, J. T., Labuzetta, A. L., & Trabold, T. A. (2020). Assessment of dehydration as a commercial-scale food waste valorization strategy. *Sustainability*, *12*(15), Article 5959. <https://doi.org/10.3390/SU12155959>

- Shahudin, Z., Basri, N. E. A., Zain, S. M., Afida, N., Basri, H., & Mat, S. (2011). Performance evaluation of composter bins for food waste at the Universiti Kebangsaan Malaysia. *Australian Journal of Basic and Applied Sciences*, 5(7), 1107–1113.
- Sharma, A., Kuthiala, T., Thakur, K., Thatai, K. S., Singh, G., Kumar, P., & Arya, S. K. (2022). Kitchen waste: Sustainable bioconversion to value-added product and economic challenges. *Biomass Conversion and Biorefinery*, 2022, Article 13399. <https://doi.org/10.1007/s13399-022-02473-6>
- Silva, G. V. D., Machado, B. A. S., Oliveira, W. P. D., Silva, C. F. G. D., Quadros, C. P. D., Druzian, J. I., Souza Ferreira, E. D., & Umsza-Guez, M. A. (2020). Effect of drying methods on bioactive compounds and antioxidant capacity in grape skin residues from the new hybrid variety “BRS Magna.” *Molecules*, 25(16), Article 3701. <https://doi.org/10.3390/molecules25163701>
- Slopiecka, K., Liberti, F., Massoli, S., Bartocci, P., & Fantozzi, F. (2022). Chemical and physical characterization of food waste to improve its use in anaerobic digestion plants. *Energy Nexus*, 5, Article 100049. <https://doi.org/10.1016/j.nexus.2022.100049>
- Srivastava, P. K., Singh, P. C., Gupta, M., Sinha, A., Vaish, A., Shukla, A., Singh, N., & Tewari, S. K. (2011). Influence of earthworm culture on fertilization potential and biological activities of vermicomposts prepared from different plant wastes. *Journal of Plant Nutrition and Soil Science*, 174, 420–429. <https://doi.org/10.1002/jpln.201000174>
- Sulaiman, N. F. A. R., & Ahmad, A. (2018). Save the food for a better future: A discussion on food wastage in Malaysia. *International Journal of Law, Government and Communication*, 3(10), 12–21.
- Sotiropoulos, A., Malamis, D., & Loizidou, M. (2015). Dehydration of domestic food waste at source as an alternative approach for food waste management. *Waste and Biomass Valorization*, 6, 167–176 <https://doi.org/10.1007/s12649-014-9343-2>
- Taiwo, A. M. (2014). *Composting as a sustainable waste management technique in developing countries*. *Journal of Environmental Science and Technology*, 4(2), 93–102. <https://doi.org/10.3923/jest.2011.93.102>
- Thompson, M. (2008). *Amc technical briefs* (Analytical Methods Committee AMCTB No. 29). The Royal Society of Chemistry. <chrome-extension://efaidnbmnnnnibpcajpcglclefindmkaj/https://www.rsc.org/globalassets/03-membership-community/connect-with-others/through-interests/divisions/analytical-division/amc/expert-working-groups/instrumental-analysis-expert-working-group/chns-elemental.pdf>
- Wang, H. O., Fu, Q. Q., Chen, S. J., Hu, Z. C., & Xie, H. X. (2018). Effect of hot-water blanching pretreatment on drying characteristics and product qualities for the novel integrated freeze-drying of apple slices. *Journal of Food Quality*, 2018(1), Article 1347513. <https://doi.org/10.1155/2018/1347513>
- Yatoo, A. M., Ali, M. N., Baba, Z. A., & Hassan, B. (2021). Sustainable management of diseases and pests in crops by vermicompost and vermicompost tea: A review. *Agronomy for Sustainable Development*, 41(1), Article 7. <https://doi.org/10.1007/s13593-020-00657-w>
- Zhao, G. H., Yu, Y. L., Zhou, X. T., Lu, B. Y., Li, Z. M., & Feng, Y. J. (2017). Effects of drying pretreatment and particle size adjustment on the composting process of discarded flue-cured tobacco leaves. *Waste Management and Research*, 35(5), 534–540. <https://doi.org/10.1177/0734242X17690448>

Review Article

A Systematic Review of Aquatic Organism Antimicrobial Peptides

Li Ting Lee¹, Arnold Ang¹, Ibrahim Mahmood², Ahmed AbdulKareem Najm³, Adura Mohd Adnan¹, Shazrul Fazry^{3,4} and Douglas Law^{1,5*}

¹Faculty of Health and Life Sciences, Inti International University, Persiaran Perdana BBN Putra Nilai, 71800, Nilai, Negeri Sembilan, Malaysia

²Al Rafidain University College, 9c74+prq, Baghdad, Baghdad Governorate, 46036, Iraq

³Department of Food Sciences, Faculty of Science and Technology, Universiti Kebangsaan Malaysia, 43600, Bangi, Selangor Darul Ehsan, Malaysia

⁴Chini Lake Research Centre, Faculty of Science and Technology, Universiti Kebangsaan Malaysia, 43600, Bangi, Selangor Darul Ehsan, Malaysia

⁵ENIAC, Centro Universitario de Excelencia. R. Força Pública, 89, Centro Guarulhos-SP, 07012-030, Brazil

ABSTRACT

Antimicrobial peptides (AMPs), sourced from various organisms, including aquatic life, are promising alternatives to combat antibiotic resistance. Their investigation is essential amid global antibiotic resistance concerns. The invaluable impact of antibiotics on human health, having saved numerous lives, is currently at risk. The growing global incidence of antibiotic-resistant bacteria poses a serious challenge to their ability to effectively treat various illnesses. This situation demands immediate attention and the exploration of alternative medical solutions. One of the most promising alternatives to antibiotics is antimicrobial peptides (AMPs), which can treat bacterial infections, particularly those brought by multi-drug-resistant pathogens. With a particular focus on their antimicrobial

properties, this systematic review aims to evaluate and classify recent AMPs isolated from aquatic organisms. This review advances knowledge of these aquatic life-derived AMPs' potential as alternatives to conventional antibiotics by examining their unique antibacterial characteristics and modes of action. A systematic review of articles published in English between 2014 and 2024 was carried out in the Science Direct, PubMed NCBI and Google Scholar

ARTICLE INFO

Article history:

Received: 10 December 2023

Accepted: 10 July 2024

Published: 25 October 2024

DOI: <https://doi.org/10.47836/pjst.32.6.23>

E-mail addresses:

i20018708@student.newinti.edu.my (Li Ting Lee)

i19017161@student.newinti.edu.my (Arnold Ang)

ibrahim_m_mahdy@yahoo.com (Ibrahim Mahmood)

ahmad_aljemeely@yahoo.com (Ahmed AbdulKareem Najm)

adura.mohdadnan@newinti.edu.my (Adura Mohd Adnan)

shazrul@ukm.edu.my (Shazrul Fazry)

douglas.law@gmail.com (Douglas Law)

* Corresponding author

databases using keywords and inclusion and exclusion criteria. A total of 33 potential AMPs isolated from aquatic organisms had been reported, and 21 of the AMPs were reported to have functional antimicrobial activities. Continuous research and study of natural substances, particularly AMPs, remain critical in pursuing alternatives to conventional antibiotics for effective treatments in combating antibiotic resistance. Therefore, ongoing research holds significant importance in identifying and harnessing the potential of AMPs for future medical applications.

Keywords: Antibiotics, antimicrobial peptides, aquatic life, human health, microbes

INTRODUCTION

The aquatic environment makes up more than 70% of the planet's surface. It is a habitat for such a variety of chemicals and serves as a vast supply of possible therapeutic agents. Although it is well known that the aquatic environment is one of the richest sources of antimicrobial peptides, little is known about this ecosystem. Fish, mollusks and even sponges that live in the ocean produce a variety of AMPs with various structures and purposes. These peptides frequently have strong antibacterial properties on viruses, fungi, and even bacteria (Semreen et al., 2018; Pelle et al., 2020; Peng et al., 2012; Vitali, 2018).

Antibiotics are not only often used but also misused worldwide. The effectiveness of antibiotics, which have revolutionized medicine and saved millions of lives, used in treatment for certain kinds of disease, is in jeopardy due to the increasing rise of resistant bacteria worldwide. After the first batch of patients were treated using an antibiotic for several decades, bacterial infections have again become a danger in the world (Subramaniam et al., 2020). The bacterial microbiome that typically resides in the gut is crucial to health. In areas like the vagina and gut, antibiotics frequently kill beneficial flora and result in opportunistic infections. 50% of antibiotic prescriptions for illnesses are thought to be unneeded (Sepulveda & Wilson, 2019). Studies have indicated that between 30% and 50% of the time, treatment indications, agent selections, or antibiotic medication duration need to be more accurate.

One of the most promising alternatives to antibiotics is antimicrobial peptides (AMPs), which can treat bacterial infections, particularly those brought on by multidrug-resistant pathogens (Rima et al., 2021; Xuan et al., 2023). AMPs are defined as a class of small peptides ranging from 10 to 50 amino acids, which play an important part in the immune systems of various organisms (Huan et al., 2020). These bioactive compounds pose the first line of defense for the host organism against bacteria, viruses, and fungi (Moretta et al., 2021). When used against several kinds of bacteria, yeasts, fungi, viruses, and parasites, natural AMPs have robust and broad-spectrum activity, exhibiting bacteriostatic, microbicidal, and cytolytic capabilities (Moretta et al., 2021). They have broad-spectrum activity and can kill Gram-positive and Gram-negative bacteria, which is particularly

useful given the increasing prevalence of antibiotic-resistant bacteria (Zasloff, 2002). Besides their antibacterial properties, these AMPs have also exhibited other properties such as anticancer, anti-fungal as well as antiviral properties, which genuinely shows their diversity and versatility in becoming the future of alternative medication to treat illnesses and diseases (Huan et al., 2020; Uddin et al., 2021).

MATERIALS AND METHODS

This study aims to systematically review recent research on AMPs derived from aquatic organisms, emphasizing their antimicrobial activities and mode of action. The preferred reporting items for systematic reviews and meta-analysis (PRISMA) method will be applied to this study. From this systematic review, we aim to delve into the question: Are naturally occurring antimicrobial peptides derived from fish viable against human pathogenic bacteria? Could modifications on these peptides lead to better antibacterial properties than naturally occurring ones?

Search Strategy

Google Scholar, Science Direct, Frontiers and PubMed NCBI are the four electronic databases used and searched in July 2023. Boolean operators ('AND,' 'OR') were used in the advanced search to combine words or phrases. The following MeSH (Medical Subject Headings) keywords or phrases were used: "antimicrobial peptides" AND "aquatic organism" OR "fish" OR "marine life" AND "microbes" AND "antibiotic resistance". Truncations, brackets, and quotation marks were used for an advanced search whenever possible.

Eligibility Criteria

A series of eligibility criteria were determined by the authors to ensure the quality of the studies reviewed: (1) the papers must be either a research paper or a review paper (systematic review, literature review, scope review) curated and published in the English language between 2014 and 2023, (2) the research scope of the papers should involve antimicrobial peptides derived from aquatic organism which show antibacterial properties. Studies that included synthesized peptides or peptides with no antibacterial properties and derived from sources other than marine life were excluded, and (3) the design and quality of the studies will also be appraised. Any studies that have failed the quality appraisal will be excluded from this review.

Search Outcomes

Figure 1 shows the PRISMA flow diagram. Figure 1 shows that 952 studies were found using the four electronic databases. There were still 952 studies remaining after excluding

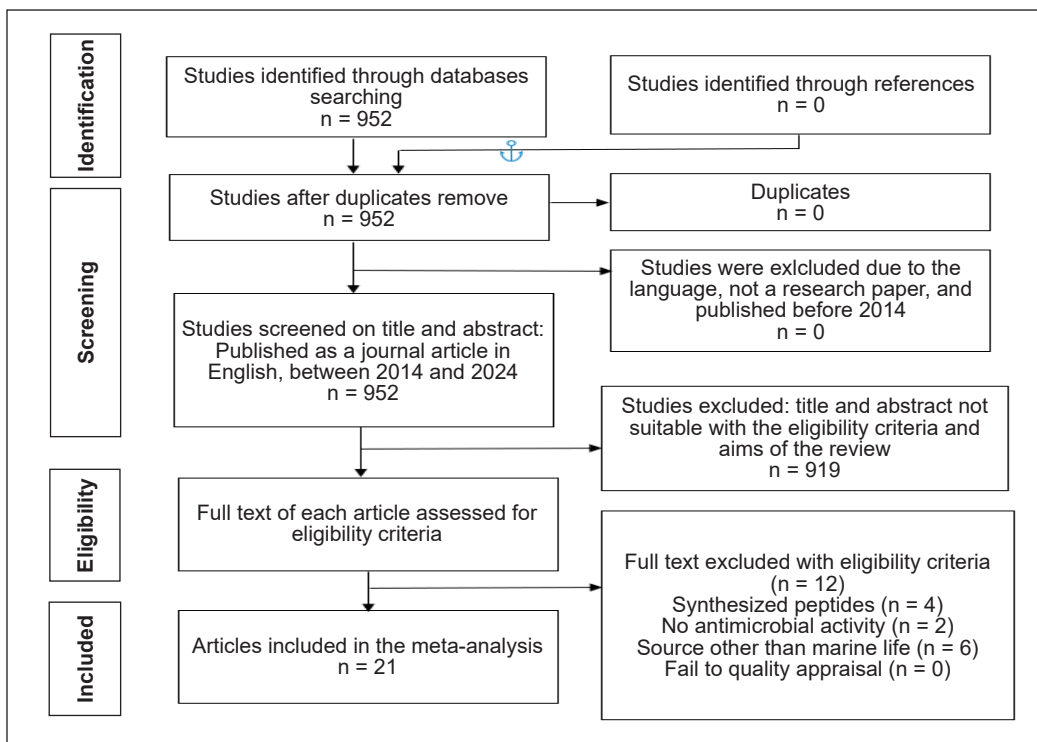


Figure 1. PRISMA flow diagram of antimicrobial peptides derived from aquatic organisms on microbes

the duplicate research and non-scientific manuscripts during the study period between 2014-2024 and excluding languages other than English.

Data Extraction and Quality Appraisal

The authors used a multiple-assessment approach to identify, screen, and choose studies using PRISMA guidelines with frequent iterations of the screening, analysis, and synthesized processes (Moher et al., 2009). To assess the consistency and dependability of studies, the authors also carried out the quality appraisal approach used in the current study (Moher et al., 2009; Walsh & Downe, 2006). The articles were evaluated using Russell and Gregory’s (2003) Guide for Evaluating Qualitative Research Studies. The observational and clinical studies were assessed using the Evidence-based Practice Centers (EPCs), the Scientific Resource Centre, and the Agency for Healthcare Research and Quality’s (AHRQ) Methods Guide for Medical Test Reviews, which made the evaluation methods consistent (Chang et al., 2012; Munn et al., 2015). According to Walsh and Downe (2006), articles were labeled as embodying high bias or risk if they met less than 70% of the assessment criteria. A summary of the included articles was presented in Table 1, which shows the reference and year of study, study objective, study methodology, biological sample used, and main findings.

Table 1
Summary of the reported aquatic organism's antimicrobial peptide from the reviewed studies

Study Objective	Methods	Biological Sample	Main Findings	Activity	References	Effects
To identify and analyze the antimicrobial peptide dromidin, which was extracted from the hemolymph of the sea crab <i>Dromia dehaani</i> , and to investigate its antibacterial properties for potential new medicinal uses.	Experimental method using ESI-MS analysis	Species: Hemolymph of marine crab <i>Dromia dehaani</i>	This study used the hemolymph of the sea crab <i>Dromia dehaani</i> to isolate and characterize the new antibacterial peptide known as Dromidin. Researchers established the existence of Dromidin utilizing various analytical methods, including ESI-MS analysis, which showed a molecular weight of 513.0 Da. These results support its importance as an antibacterial agent and advance our knowledge of bioactive marine chemicals with potential use in pathogen defense.	Antimicrobial Activity	Anbuhezian et al., 2018	Confirmed antibacterial activity against bacterial pathogens
To produce recombinant antimicrobial proteins from the marine diatom <i>Phaeodactylum tricornutum</i> (S-thanatin and bovine lactoferricin) and test their efficiency against gram-negative bacteria, particularly <i>E. cloacae</i> and <i>V. natriegens</i> .	Experimental method using antimicrobial activity assays and Western Blot	Species: Lysate of the marine diatom <i>Phaeodactylum tricornutum</i>	<i>Phaeodactylum tricornutum</i> , a sea diatom genetically altered to generate the powerful antimicrobial proteins S-thanatin and bLFcin, offers a remedy for antibiotic resistance. These microalgae successfully defeat gram-negative bacteria like <i>V. natriegens</i> and <i>E. cloacae</i> . The strain that expressed bLFcin had the most efficacy, promising a natural antibiotic substitute for bacterial infections and antimicrobial resistance.	Antimicrobial Activity	Baiden et al., 2023	Confirmed antibacterial activity towards gram-negative bacteria
Identify and assess antimicrobial peptides (AMPs) in rockfish <i>Sebastes marmoratus</i> for potential therapeutic application in aquaculture.	Analysis of liver transcriptome and real-time quantitative PCR (RT-qPCR) for AMP identification and expression profiling	<i>Sebastes marmoratus</i>	6 AMPs were identified, with LEAP-2 and Moronecidin showing broad-spectrum antimicrobial activity against aquatic pathogens without cytotoxicity, suggesting their potential as therapeutic agents in aquaculture to combat pathogenic infections.	Antimicrobial Activity	Bo et al., 2019	Confirmed antibacterial activity against aquatic pathogens

Table 1 (continue)

Study Objective	Methods	Biological Sample	Main Findings	Activity	References	Effects
To investigate the interaction between bacteria and a newly created mutant peptide termed Cnd-m3a produced from the Antarctic icefish <i>Chionodraco hamatus</i> , as well as its potential as a treatment for human diseases.	The experimental method involves isolation and identification using transmission electron microscopy (TEM), fluorescent probe assays, and in vitro assays.	Species: Antarctic icefish <i>Chionodraco hamatus</i> , from which the initial Cnd peptide and its mutant derivative Cnd-m3a were isolated	The effective creation of the mutant peptide Cnd-m3a has increased antibacterial action against human infections and improved selectivity against prokaryotic cells. The study also emphasizes how Cnd-m3a interacts with <i>Psychrobacter</i> sp. (TAD1), an Antarctic bacterium, and its capacity to pierce the outer membrane of bacteria like <i>E. coli</i> and <i>Psychrobacter</i> sp. Furthermore, Cnd-m3a demonstrated limited cytotoxic and hemolytic effects on human cells but strong antibacterial activity against a subset of Gram-negative human pathogens, highlighting its potential as a platform for creating a novel therapeutic drug.	Antimicrobial Activity	Buonocore et al., 2019	increased antibacterial activity against pathogens and improved selectivity against prokaryotic cells
Examine the antibacterial activity, immune system function, aquaculture uses, and anti-infective medication properties of the Ct-20534 antimicrobial peptide found in the Triton snail <i>Charonia tritonis</i> .	Experimental Method: Real-time fluorescence quantitative PCR (qPCR)	Species: Giant Triton snail <i>Charonia tritonis</i> ,	<i>Charonia tritonis</i> highly expresses the antimicrobial peptide gene Ct-20534 in the proboscis. It inhibits <i>S. aureus</i> and other Gram-positive and Gram-negative bacteria. These peptides are essential for the snail's immune system and could be used in aquaculture to create anti-infective drugs, which would be advantageous for the aquaculture industry.	Antimicrobial Activity	(Cen et al., 2023)	Confirmed antibacterial activity against gram-positive and negative bacteria
Characterize a novel antimicrobial peptide (AMP) derived from histone H2A in the mud crab <i>Scylla paramamosain</i>	Sequence analysis of histone H2A from <i>Scylla paramamosain</i> Extract: Histone H2A	Species: <i>Scylla paramamosain</i> Extract: Histone H2A	A 38-amino acid peptide named Sphistin was identified as an AMP with high antimicrobial activity against various pathogens, including important aquatic pathogens. Sphistin exhibited typical AMP features and exerted antimicrobial effects by disrupting bacterial cell membranes without cytotoxicity to crab haemolymphs	Antimicrobial Activity	(Chen et al., 2015)	Confirmed antibacterial activity

Table 1 (continue)

Study Objective	Methods	Biological Sample	Main Findings	Activity	References	Effects
To discover gut microbiome-derived antimicrobial peptides (AMPs) in zebrafish, targeting resistant bacteria such as <i>K. pneumoniae</i> , <i>P. aeruginosa</i> , <i>S. aureus</i> , <i>E. coli</i> , and <i>B. cereus</i> , and assess their therapeutic potential and binding characteristics using metagenomics, molecular modeling, and bioinformatics.	Experimental Method: nanoLC-Metagenomics, metabolic modeling (docking and dynamics)	Gut microbiome of zebrafish	or mammalian cells. This discovery introduces Sphistin as a potential aquaculture and veterinary medicine application candidate. The study successfully identified prospective AMPs using the zebrafish gut microbiota. One in particular, "MPPYLHEIQPHTASNCQTELVKLVKL," showed promise due to its hydrophobic characteristics and stable binding to a target protein. These results present a novel method for creating AMPs that are effective against extremely resistant bacterial species.	Antimicrobial Activity	(Gayathri et al., 2021)	Confirmed antibacterial activity against bacterial pathogens
To identify and study antimicrobial peptides (AMPs) in the Cuban freshwater snail <i>Pomacea poeyana</i> , including their chemical synthesis, structural analysis, effects on viral infections and cell toxicity, and antimicrobial activity against human pathogens.	Experimental Method: nanoLC-ESI-MS-MS technology and CD spectra analysis.	Cuban freshwater snail <i>Pomacea poeyana</i>	The study found two promising antimicrobial peptides (Pom-1 and Pom-2) in the Cuban freshwater snail <i>Pomacea poeyana</i> . Pom-1 showed potent antibacterial effects, while it had no antifungal activity. It also had low toxicity to human macrophages, making it a candidate for human antimicrobial use. Additionally, Pom-1 had a modest impact on HIV-1 infection and slightly inhibited the Zika virus.	Antimicrobial Activity	(García et al., 2023)	Confirmed antibacterial activity for Pom-1 against bacterial pathogens

Table 1 (continue)

Study Objective	Methods	Biological Sample	Main Findings	Activity	References	Effects
To characterize two antimicrobial peptides derived from histone I (LcHI) in <i>Larimichthys crocea</i>	Bioinformatics analysis, tissue distribution analysis, phylogenetic analysis, and scanning electron microscopy (SEM)	<i>Larimichthys crocea</i>	LcHI-derived peptides (LcHI-1 and LcHI-2) exhibit antimicrobial activity, forming α -helix structures and damaging bacterial membranes. LcHI expression increases in response to Cryptocaryon irritans infection, suggesting a role in the immune response and potential for disease control strategies.	Antimicrobial Activity	(Ma et al., 2023)	Increased antibacterial activity of derived peptides
To discuss the anticancer properties of fish species <i>Anabas testudineus</i> antimicrobial peptides (AMPs). It specifically aims to find and assess these AMPs' effectiveness against the MCF7 and MDA-MB-231 breast cancer cell lines.	Experimental Method: Cytotoxicity Assay, that is, MTT Assay, examining gene expression (p53, BAX, BCL-2), caspase-3 activation, and conducting docking analysis and immunoprecipitation.	<i>Anabas testudineus</i> contains antimicrobial peptides (AMPs)	This study isolated two antimicrobial peptides (AtMP1 and AtMP2) with cytotoxic action against breast cancer cell lines from <i>Anabas testudineus</i> mucus. These peptides caused cell cycle arrest and apoptosis by upregulating p53, and expressing the pro-apoptotic BAX gene, downregulating the anti-apoptotic BCL-2 gene, and activating caspase-3. Their association with target proteins was supported by computational analysis and immunoprecipitation, indicating their potential as cancer treatments.	Anticancer and Antimicrobial Activity	(Najm et al., 2021)	Confirmed antibacterial activity against bacterial pathogens
To examine and characterize SaRpAMP, an antimicrobial peptide isolated from the skin of <i>Silurus asotus</i> , a freshwater fish. The objective is to understand its structure, antibacterial activity, and mechanism of action.	Experimental Method: Primary structure analysis, cDNA cloning, secondary structure analysis, 3D modeling and antimicrobial activity testing.	Species: <i>Silurus asotus</i>	The research discovered an antimicrobial peptide with strong antibacterial activity and an amphiphilic structure, in the skin of <i>Silurus asotus</i> . SaRpAMP, the first generated from the C-terminal region of 60S ribosomal protein L27, interacts with bacterial membranes and may disrupt them, showing promise for battling bacterial infections.	Antimicrobial Activity	(Oh et al., 2020)	Confirmed antibacterial activity against bacterial pathogens

Table 1 (continue)

Study Objective	Methods	Biological Sample	Main Findings	Activity	References	Effects
To find, describe, and investigate the potential of antimicrobial peptides (AMPs) from the skin mucus of the African catfish (<i>Clarias gariepinus</i>) as prospective substitutes for conventional antibiotics in a variety of applications.	Experimental Method: C (18) Solid-Phase Extraction (Purification), Agar Well Diffusion method, broth-dilution method, Sephadex G-25 gel filtration and Orbitrap Fusion Lumos Tribrid Mass Spectrometry (peptide identification)	Species: African Catfish (<i>Clarias gariepinus</i>)	Both <i>S. aureus</i> and <i>E. coli</i> were resistant to the antibacterial properties of the skin mucus from African catfish. With the lowest Minimum Inhibitory Concentration (MIC), the catfish from Lake Albert displayed the highest activity level. Seven brief AMPs with excellent antibacterial ratings and amphipathic properties were discovered through mass spectrometry investigation. These AMPs have the potential to replace conventional antibiotics in a variety of industries, but further investigation is required to determine how safe they are.	Antimicrobial Activity	(Okella et al., 2021)	Confirmed antibacterial activity against bacterial pathogens
To investigate the expression, structure, interactions with membranes, biological effects, safety for mammalian cells, and antibacterial drug potential of trimetozine.	Experimental Methods: rtPCR, Circular dichroism spectroscopy, Fluorescence assays, Membrane studies, antimicrobial activity assessments, Cytotoxicity assays	Species: Antarctic fish <i>Trematomus bernacchii</i> , from which the AMP Trimetozine was identified and characterized	To demonstrate that trimetozine is an effective antibacterial peptide with the potential to become a novel therapeutic candidate. Through a carpet-like process, it demonstrates activity against a variety of pathogens, including Gram-negative bacteria. Trimetozine is comparable to other AMPs from Antarctic fishes in terms of its minimum inhibitory concentration (MIC) and minimum bactericidal concentration (MBC) values against bacteria. Trimetozine is a possible option for further therapeutic development because it does not exhibit hemolytic or cytotoxic effects against mammalian cells at effective dosages against bacteria.	Antimicrobial Activity	(Pelle et al., 2020)	Confirmed antibacterial activity against bacterial pathogens

Table 1 (continue)

Study Objective	Methods	Biological Sample	Main Findings	Activity	References	Effects
To evaluate the bioinformatics characterization and antimicrobial role of two piscidin (Pi) peptides identified from the transcriptome of Channa striatus.	Bioinformatics analysis; gene expression analysis with immune stimulants; antibiogram assay; minimum inhibitory concentration (MIC) and antibiofilm assays; flow cytometry analysis; scanning electron microscopy (SEM) imaging	Transcriptome of striped murrel <i>Channa striatus</i>	The study identified two antimicrobial peptides, CsRG12 and CsLC11, from CsPi. Gene expression analysis revealed induced expression patterns of CsPi with immune stimulants. CsRG12 and CsLC11 exhibited activity against multi-drug-resistant pathogens <i>S. aureus</i> and <i>B. cereus</i> , disrupting bacterial membrane formation as observed via flow cytometry and SEM imaging. These findings suggest CsPi's involvement in innate immunity and potential for therapeutic development in aquaculture biotechnology.	Antimicrobial Activity	(Raju et al., 2020)	Confirmed antibacterial activity
To investigate Anisakis marine parasitic worm-derived antimicrobial peptides (anisaxins) for their efficacy as bactericidal agents, especially against multi-drug-resistant Gram-negative bacteria, while understanding their mechanism of action and selectivity against bacteria with minimal harm to human peripheral blood mononuclear cells (HPBMCs).	Experimental Method: solid-state NMR (ssNMR), molecular dynamics (MD) simulations (investigate peptide's mode of action) Atomic force microscopy and flow cytometry (membrane permeabilization and cytotoxicity)	Species: <i>Nematode Anisakis</i> Extract: anisaxins	The study discovered anisaxins, novel antimicrobial peptides made by the marine parasite <i>Anisakis</i> that have strong bactericidal action, especially against Gram-negative bacteria that are multi-drug resistant. Anisaxins interact with bacterial membranes, producing lipid extraction and membrane bulging, which kills the bacteria by preventing cell division. These peptides do not cause much cytotoxicity in human cells, which is significant since they suggest they will make good candidates for future antimicrobial medication development during antibiotic resistance.	Antimicrobial Activity	(Rončević et al., 2022)	Confirmed antibacterial activity against bacterial pathogens

Table 1 (continue)

Study Objective	Methods	Biological Sample	Main Findings	Activity	References	Effects
To characterize two piscidin-like antimicrobial peptides (LjPL-3 and LjPL-2) isolated from Japanese sea bass (Lateolabrax japonicus) and investigate their role in the innate immune response, particularly their antimicrobial activity and modulation of immune cell functions.	Isolation and characterization of LjPL-3 and LjPL-2 from Japanese sea bass; examination of their expression, antimicrobial activity, and immune modulation.	Species: Japanese sea bass (<i>Lateolabrax japonicus</i>) Extract: LjPL-3 and LjPL-2	LjPL-3 and LjPL-2, isolated from Japanese sea bass, exhibit differential tissue expression and are upregulated after <i>Vibrio harveyi</i> infection. They display distinct antimicrobial spectra, while treatment decreases inflammatory cytokine production and enhances immune cell functions. LjPL-2 shows bacterial killing capability in monocytes/macrophages, and administration enhances fish survival post-infection, reducing bacterial burden.	Antimicrobial Activity	(Wu et al., 2023)	Increased antibacterial activity against aquatic pathogens
Investigate the antimicrobial activity of moricin-like peptides (MLPs) from <i>Antheraea pernyi</i> against <i>Vibrio</i> pathogens in aquatic animals, particularly sea cucumbers.	Bioinformatics analysis, heterologous expression using the AnpeNPV bacmid system, and purification from <i>A. pernyi</i> pupae	Species: <i>A. pernyi</i> Extract: rAnpe-MLP1	Recombinant Anpe-MLP1 exhibited antimicrobial activity against gram-positive <i>Staphylococcus aureus</i> , gram-negative <i>Escherichia coli</i> , and three <i>Vibrio</i> species. It effectively inhibited wild-type <i>Vibrio</i> fluvialis infections in sea cucumbers, suggesting its potential as a novel anti-infective agent for aquaculture.	Antimicrobial Activity	(Ye et al., 2024)	Confirmed antibacterial activity against aquatic pathogens
To identify novel antimicrobial peptides (AMPs) derived from subunits of Tegillarca granosa hemoglobin (Hb) and evaluate their antibacterial activity against various bacteria strains	Bioinformatics prediction, synthetic synthesis of peptides, minimum inhibitory concentration (MIC) assays	Species: <i>Tegillarca granosa</i> Extract: mTgHbP7	A mutant <i>T. granosa</i> hemoglobin peptide (mTgHbP7) exhibited significant antibacterial activity against <i>Vibrio alginolyticus</i> , <i>V. parahaemolyticus</i> , and <i>Escherichia coli</i> . mTgHbP7 demonstrated an α -helical structure, characteristic of bactericidal AMPs, and exhibited no cytotoxicity to mammalian cells, even at high concentrations. These findings offer insights into the potential of mollusk hemoglobin-derived AMPs for developing antimicrobial agents.	Antimicrobial Activity	(Zheng et al., 2022)	Increased antibacterial activity of the modified peptide

RESULT AND DISCUSSION

After screening the titles and abstracts, 922 of these articles were removed as they were published before 2014 (Figure 1). Studies with titles and abstracts unsuitable for the review's eligibility criteria and aims are also excluded. A total of 34 journal articles were evaluated, and 12 were disqualified because they contained synthesized peptides (n=4), lacked anticancer or antimicrobial effects (n=2), or came from sources other than aquatic life (n=6).

Antimicrobial Peptides from Aquatic Organism

The reviewed papers show the types, modes of action, potential benefits and the sources of the derived AMPs. The presence of AMPs among all aquatic organisms shows that they provide a first barrier of protection against a multitude of microbial pathogens (Baiden et al., 2023; Buonocore et al., 2019; Cen et al., 2023; García et al., 2020), with hundreds of AMPs being discovered and identified from both plants and animals (Najm, 2021). Among the identified AMPs, most sources come from marine life, including fish, crustaceans, and marine plants (Anbuechian et al., 2018; Baiden et al., 2023; García-Beltrán et al., 2023). It is due to the living conditions that contain a lot of free-floating microbes that also harbor potential pathogenic microorganisms, resulting in the need for high amounts of AMPs to protect marine life against infections and disease (Najm et al., 2021).

From this systematic review, a total of 18 aquatic life species including fish, aquatic plants, and nematodes, were reported to produce AMPs based on in-vitro study results, including *Danio rerio* (Gayathri et al., 2021), *Phaeodactylum tricornutum* (Anbuechian et al., 2018), *Sebastiscus marmoratus* (Bo et al., 2019), *Chionodraco hamatus* (Buonocore et al., 2019), *Charonia tritonis* (Cen et al., 2023), *Scylla paramamosain* (Chen et al., 2015), *Pomacea poeyana* (García et al., 2020), *Larimichthys crocea* (Ma et al., 2023), *Anabas testudineus* (Najm et al., 2021), *Silurus asotus* (Oh et al., 2020), *Clarias gariepinus* (Okella et al., 2021), *Trematomus bernacchii* (Pelle et al., 2020), *Channa striatus* (Raju et al., 2020), *Nematode anisakis* (Rončević et al., 2022), *Lateolabrax japonicus* (Wu et al., 2023), *Antheraea pernyi* (Ye et al., 2024), *Tegillarca granosa* (Zheng et al., 2022).

Classification of AMPs

One of the most promising antibiotic alternatives is antimicrobial peptides, which can treat bacterial infections, particularly those brought on by multi-drug-resistant pathogens (Rima et al., 2021). AMPs, also known as host defense peptides (HDPs), are a component of the innate immune response in all kinds of life (Ganz, 2002). Various organisms naturally create them as a defense mechanism against pathogens, including bacteria, viruses, and fungi that invade the body (Zasloff, 2007). The antibacterial activity of AMPs is broad-spectrum, making them useful against a variety of pathogens. They can damage an organism's cell

membrane, causing it to lyse or burst open, which kills the creature. It led to a big discovery and one of the potential antibiotic replacements.

AMPs have been categorized according to several factors, including their origin, structure, method of action, and amino acid makeup. These divisions aid in designing and developing new medicinal drugs to fight infectious diseases and understanding the diversity and complexity of AMPs (Hafeez et al., 2021). Figure 2 shows the classification of AMPs based on their biological activity, sources/origin, and the difference between natural and synthetic antimicrobial peptides.

Based on their origin, antimicrobial peptides from marine life can be divided into different groups. This classification distinguishes different marine AMP sources. For example, fish-derived AMPs come from *Tilapia* species, while mollusk-derived AMPs are obtained from marine creatures like sea hares and snails (Peng et al., 2012). The biodiversity-rich sponges also produce AMPs that are generated from them, and marine algae contribute to this classification by creating AMPs that have antibacterial capabilities. These peptides are available from different marine sources in different numbers and with different properties.

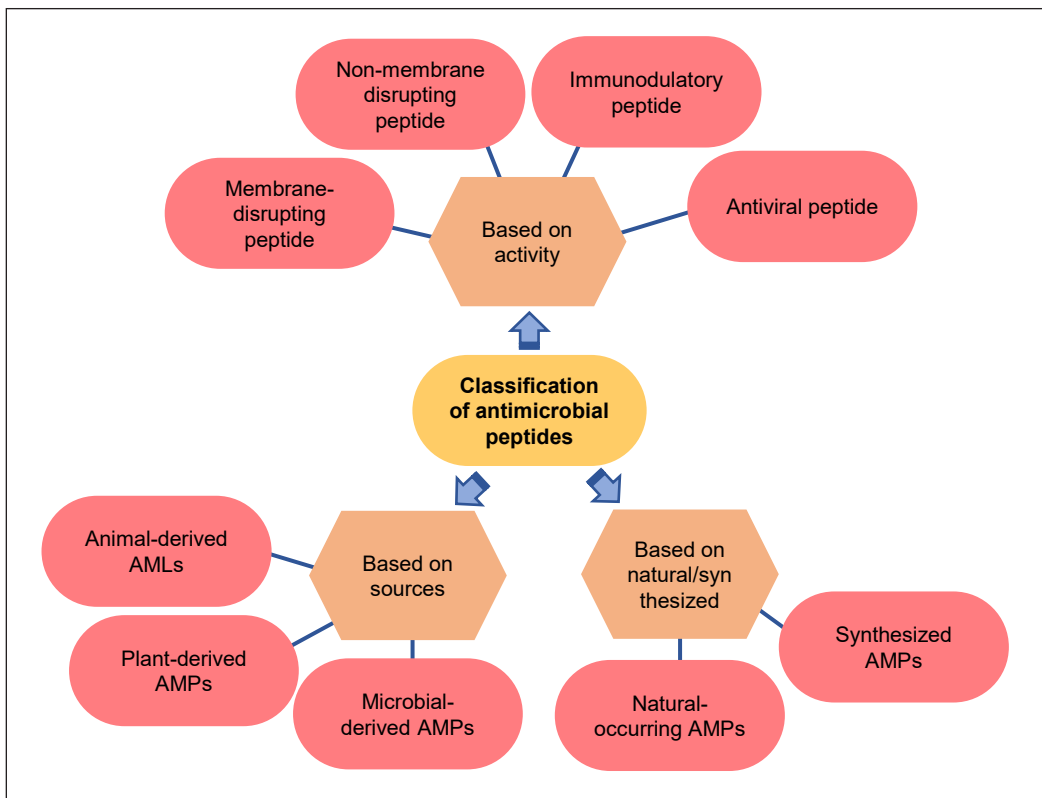


Figure 2. Classification of AMPs based on their biological activity, sources/origin, and the difference between natural and synthetic antimicrobial peptides

Marine-derived AMPs are categorized using a structure-based approach that considers their structural characteristics. As with Magainin, linear AMPs have a straightforward, linear structure without disulfide links. Contrarily, cyclic AMPs like pardaxin frequently create a cyclic or ring structure due to disulfide bonds. Like LL-37, several AMPs have a mostly helical secondary structure, whereas tachyplesin adopts a β -sheet shape. These structural differences shed light on the actions they might take (Falanga et al., 2016).

Another classification takes into account how AMPs work, that is, their mode of action. Some peptides are particularly recognized for rupturing the membranes of bacterial cells, which causes cell lysis and bacterial death; this refers to membrane-disrupting AMPs. Others exert their impact differently, like interfering with intracellular functions, which refers to non-membrane-disrupting AMPs (Semreen et al., 2018). It is crucial to understand their primary mechanisms of action to evaluate their prospective applications and therapeutic use.

The origin of AMPs is another way to classify them, with natural AMPs coming straight from marine species. As opposed to their natural counterparts, synthetic AMPs are created and produced based on their structures and characteristics to improve their activity, stability, or other characteristics (Lei et al., 2019). These modifications, intended to improve activity, stability, or other desired qualities, may involve changes to the peptide's sequence, amino acid content, or structural features. Through the customization of these artificial analogs, scientists can adjust their biological characteristics to tackle certain issues like cancer treatment or resistance to antibiotics (Wang et al., 2023). It will be referred to as synthetic analog classification. Synthesized AMPs are created in a laboratory, but naturally occurring AMPs are created by living things as a part of their natural defensive mechanism. Synthesized AMPs may function more effectively as therapeutic agents if they possess particular qualities, such as improved potency or selectivity. It has also been found that synthesized AMPs are generally more stable and possess a longer half-life as compared to naturally occurring AMPs (Baharin et al., 2021; Büyükkiraz & Kesmen, 2022; Lei et al., 2019). This characteristic highlights the potential superiority of synthetic AMPs in therapeutic settings, providing increased durability and longevity.

Mode of Actions Towards Microbes

AMPs exert their effects by compromising the integrity of the bacterial cell membrane or impeding vital cellular functions, including protein synthesis and DNA replication. The precise manner of action differs depending on the particular peptide and the target microorganism (Lei et al., 2019). As will be covered below in Figure 3, they can affect microorganisms in a variety of ways.

The breakdown of the microbial cell membrane is one frequent method. As AMPs insert into membranes, they can create pores or channels, causing intracellular contents to spill,

ultimately causing microbial death (Lei et al., 2019). Certain AMPs can also prevent the synthesis of proteins by attaching to ribosomes during the termination of translation, interfering with the synthesis of proteins (Huan et al., 2020). Inhibiting bacterial growth and proliferation may result from this. They can even prevent DNA and RNA synthesis by attaching to bacterial genomes (Huan et al., 2020).

By activating or inhibiting immune cells, other AMPs can modify the immunological response and increase the clearance of infections. For instance, some AMPs can activate macrophages, which are important immune cells in phagocytosis and the eradication of invasive microbes (Mahlapuu et al., 2016).

The production of pro-inflammatory cytokines can be inhibited by other AMPs, which can lessen tissue damage and encourage healing when an infection is present (Méndez-Samperio, 2013).

Also, it has been demonstrated that some AMPs can dislodge biofilms, which are intricate colonies of microorganisms that are challenging to treat with conventional antibiotics. Biofilms can develop on surfaces like medical implants and are linked to persistent illnesses that are challenging to treat. Certain AMPs have been discovered to prevent biofilms' development or damage the matrix that binds them together, which causes the biofilm to break down and makes bacteria more vulnerable to antimicrobial agents (Batoni et al., 2016).

Moreover, some AMPs have anti-inflammatory properties that may lessen tissue damage and encourage healing when an infection is present. Although inflammation plays a crucial role in the immune response and is a typical reaction to infection, it can also cause tissue damage and increase the severity of the illness. It has been discovered that some AMPs have anti-inflammatory properties that can aid in reducing tissue damage and encouraging recovery (Luo & Song, 2021).

In conclusion, AMPs are a variety of chemicals that affect bacteria in a variety of ways. One reason AMPs are efficient against a variety of microbes and can potentially be an important weapon in the fight against antimicrobial resistance is their capacity to function through numerous routes (Luo & Song, 2021).

Figure 4 shows the different modes of action via electrostatic interactions used by AMPs towards the bacterial membranes' inhibition of bacterial growth, which prevents

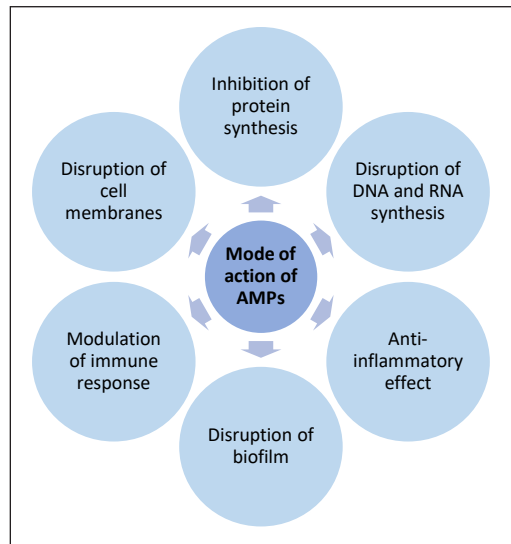


Figure 3. Different types of modes of action of antimicrobial peptides towards microbes

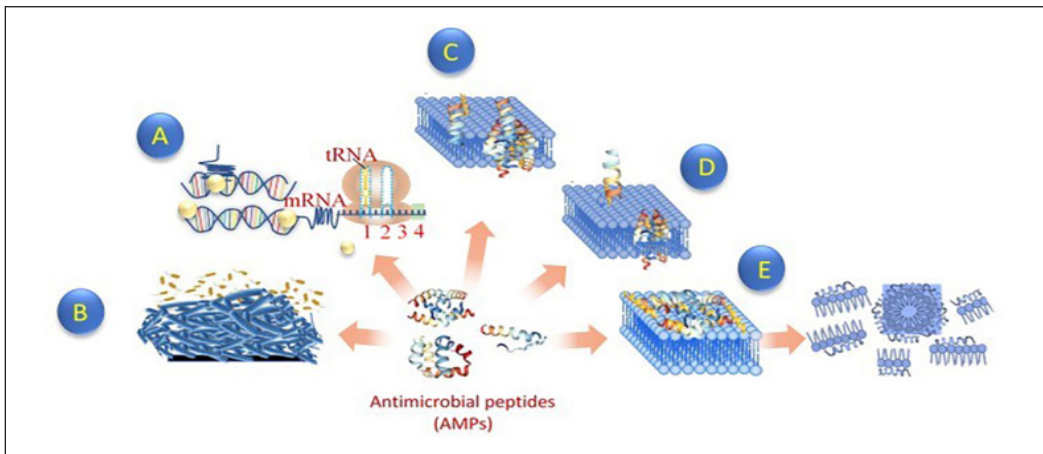


Figure 4. Mode of actions of AMPs against microbes (Mba & Nweze, 2022)

the host bacteria from developing resistance against the AMPs. Based on the type of AMP, they are able to disrupt intercellular processes such as protein synthesis, which alters enzymatic and cell signaling activities, as seen in (A). Some AMPs possess the ability to disrupt biofilm formation, as seen in (B), which is one of the defense mechanisms of some bacteria. As for AMPs that disrupt the bacterial membrane, there are three categories of modes of action that have been identified, with the first being the Barrel-stave model, as seen in (C), where the AMPs aggregate together to form a tube and are arranged parallel to the phospholipid bilayer to form a channel. The Toroidal pore model (D) acts similarly to the Barrel-stave model, where the AMPs are arranged parallel to the phospholipid bilayer to form a channel, with the difference being that with the Toroidal pore model, there are no lateral interactions between the peptides in the formation of the channel. Finally, for the Carpet model (E), the AMPs are scattered throughout the bacterial membrane like a carpet and, at a high enough concentration, will exhibit a detergent-like behavior where sections of the phospholipid bilayer are pulled away in a globular shape (Mba & Nweze, 2022).

Antibacterial, Antiviral, and Anti-Inflammatory Activities of Marine-derived Peptides

Antibacterial peptides from marine life have a variety of biological functions with exceptional promise for therapeutic uses. Because of their antibacterial, antiviral, and anti-inflammatory properties, they can defend against a variety of health risks (Kang et al., 2015).

Antibacterial Activity

These peptides are skilled at locating and damaging bacterial cell membranes, eliminating pathogenic bacteria. Peptides from the marine environment have demonstrated notable antibacterial activity in their natural forms and as-synthesized analogs.

For instance, the natural antibacterial peptides AtMP1 and AtMP2, produced in the epidermal mucus of the *Anabas testudineus* fish, have shown stronger antibacterial activity against both gram-positive and gram-negative pathogenic bacteria than conventional antibiotics (Najm et al., 2021).

In addition to naturally occurring peptides, synthetic analogs inspired by their marine counterparts were also created. A notable example of a synthetic peptide with potent antibacterial properties derived from AtMP1 is AtMP5, which showed significant improvements in antibacterial properties compared to its original counterpart (Law et al., 2023). These synthetic counterparts serve as an example of how technological advancements might harness the power of peptides originating from marine sources and improve those compounds' efficacy against a variety of bacterial diseases (Hallock et al., 2003).

Antiviral Activity

Some peptides of marine origins may prohibit viruses from replicating and infecting host cells. Figure 5 shows the horseshoe crab *Tachypleus tridentatus* peptide tachyplesin, a marine antimicrobial cell-penetrating peptide, as an anti-HBV agent, exhibits antiviral action against a variety of viruses, including HIV and the herpes simplex virus (Narula et al., 2023). Enfuvirtide has played a key role in the management of HIV infections by obstructing the virus's entry into immune cells and limiting its capacity to spread infection. The natural antiviral properties of marine peptides inspired it. The success of these synthetic antiviral medications demonstrates the important role that marine-derived peptides play in creating treatments for some of the most difficult viral illnesses (Narula et al., 2023).

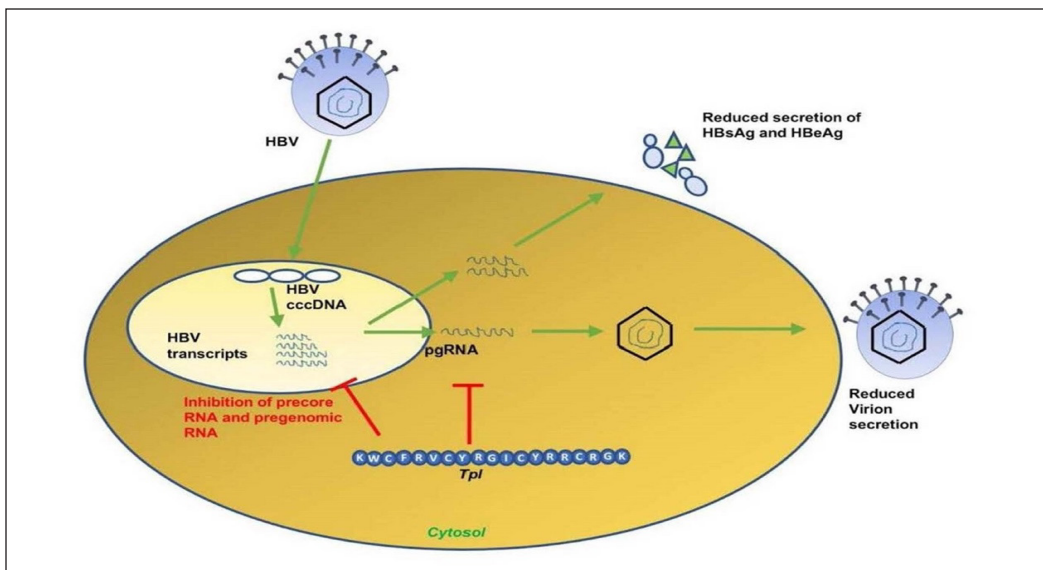


Figure 5. Tpl's anti-HBV efficacy at non-cytotoxic dosages demonstrates a potent therapeutic peptide for HBV (Narula et al., 2023)

These findings emphasize the value of investigating diverse marine life for potential remedies to problems with world health and the value of comprehending the mechanisms underlying these extraordinary antiviral marine peptides.

Anti-inflammatory Activities

Many peptides of marine origins are anti-inflammatory, reducing inflammation and its associated discomfort. In the blood of marine species, a peptide called Hemorphin has antibacterial and anti-inflammatory properties. Controlling the immune response can reduce inflammation, making it useful for future anti-inflammatory drugs (Nyberg et al., 2013). Such peptides may facilitate the creation of brand-new anti-inflammatory medications.

Hemorphin's combined abilities to fight bacterial threats and reduce inflammation highlight its potential importance in creating new anti-inflammatory medications (Nyberg et al., 2013). Researchers trying to discover these peptides' medicinal potential remain fascinated by the marine environment and its tremendous variety.

Studies of AMPs on Therapeutic Research

Studies demonstrate the effects of AMPs on microorganisms. Most AMPs found in marine invertebrates, such as arthropods, mollusks, and cnidarians, are cationic and hydrophobic, and they specifically target vital elements of microbial cell walls and membranes. It dictates the range of activity of these AMPs. For AMPs from marine invertebrates, a wide variety of modes of action have been reported and discussed in detail for several families. For instance, mollusk defensins bind to lipid II, the precursor of peptidoglycan, and are primarily effective against Gram-positive bacteria. Both mollusk bactericidal/permeability-increasing protein (BPI) and arthropod anti-lipopolysaccharide factors (ALFs), which are mostly active against Gram-negative bacteria, bind to lipopolysaccharide (LPS). Lastly, the exclusively anti-fungal crustacean PvHCt permeabilizes the fungal plasma membrane (Destoumieux-Garzón et al., 2016).

In another research shown in Figure 6, the antimicrobial peptide in the epidermal mucus of *Anabus testudineus*, a sturdy freshwater fish, was tested in its microbial activity. Both epidermal mucus and streptomycin have antibacterial effects on pathogenic bacteria, such as *P. aeruginosa*, *E. coli*, *B. subtilis*, and *B. cereus*, which have undergone triplicate. It was revealed that EM has a lower MIC (62.5 g/mL) than streptomycin (125 g/mL) for inhibiting the development of *P. aeruginosa* and *E. coli*. Bivariate analysis was performed in the correlation analysis, which produced significant results ($p < 0.01$) between EM and the control (streptomycin) for the pathogens *E. coli* and *P. aeruginosa*. This finding corroborated the findings of Wei et al. (2010), who discovered that *P. aeruginosa* and other Gram-negative bacteria are more susceptible to the antibacterial effects of snakehead fish.

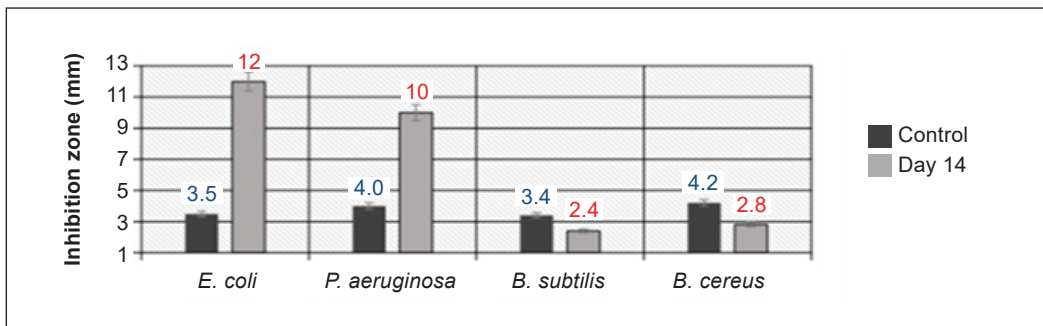


Figure 6. The sample used as a control included streptomycin and was undergone triplicate (Najm et al., 2021)

It might aid both species' capacity to endure in contaminated water (Najm et al., 2021). Further research on the naturally occurring peptides via modification has also shown that modifying AMPs can increase antibacterial activity, such as AtMP5 (Law et al., 2023). Besides that, both studies have found that the AMPs derived from the *Anabas testudineus* fish have the ability to function as an antiproliferative agent against breast cancer cells, thus also categorizing the peptides as having dual activities, namely antibacterial and anticancer (Law et al., 2023; Najm et al., 2021).

Therapeutics

Antimicrobial peptides (AMPs) have been studied extensively for their potential therapeutic applications. In addition to their direct antimicrobial activity, AMPs have been found to have a range of other biological properties, including anti-inflammatory, wound healing, and immunomodulatory effects. These properties make AMPs attractive candidates for developing novel therapeutics (Giuliani et al., 2007).

It takes a multidisciplinary team effort involving cooperation between biotechnology businesses, academics, and marine science experts to develop synthetic marine-derived AMPs for therapeutic reasons. It entails creating artificial replicas of the natural peptides while guaranteeing their bioavailability, stability, and efficient delivery to the infection site. Some examples of AMP-derived therapeutics have been developed or are in various stages of development. Pexiganan: It is a synthetic version of the frog skin peptide magainin. Pexiganan is used to treat diabetic foot ulcers caused by bacterial infections. It works by disrupting bacterial membranes and is effective against a variety of Gram-positive and Gram-negative bacteria (Lipsky et al., 2008). Besides Pexiganan, there is also Brilacidin, a synthetic AMP with broad-spectrum activity against bacteria, viruses, and fungi. Brilacidin is being developed to treat infections, including acute bacterial skin and skin structure infections, oral mucositis, and inflammatory bowel disease (Brilacidin). More AMP-based treatments will likely become available as research in this area continues.

Future Potential of Antimicrobial Peptides

Future research should include medium to long-term randomized clinical trials to confirm the effect of peptides on disease and test their efficacy in increasing resistance to chronic diseases. As a result, additional research is needed to link the benefits of AMP, its peptidomimetics, and antibiotics to drug resistance reduction (Cipolari et al., 2020). Fish-derived AMPs have been proposed as a future therapeutic strategy (Chee et al., 2019). Further and continuous research into synthesizing and characterizing these peptides is critical to ensuring their efficacy and usability. AMPs derived from fish have shown promise as therapeutic strategies. Recent research into *in-silico* modifications of these AMPs has also shown promising results with increased antibacterial activity as well as increased robustness and stability, which needs to be further studied to fully take advantage of these natural resources in the battle against antibiotic resistance (Law et al., 2023).

In-silico predictions and modifications of AMPs are at the forefront of AMP modification due to their ability to accurately predict how the changes in peptide sequence affect the structure, net charge, hydrophobicity as well as stability of the peptide (Law et al., 2023). One of the biggest open-source AMP databases, known as the Collection of Antimicrobial Peptides (CAMP), is commonly used for the identification and prediction of AMPs used in peptide modifications (Law et al., 2023; Najm et al., 2021; Waghu & Idicula-Thomas, 2019).

Limitations

Antimicrobial peptides (AMPs) have been shown to have great potential as therapeutics. However, several concerns must be addressed before they can be utilized for human therapies. One such concern is their toxicity, as excessive amounts of certain AMPs can harm mammalian cells. For example, melittin in bee venom shows high hemolytic effects at high concentrations (Jenssen et al., 2006).

Another concern would be the specialization of AMPs towards a specific pathogen. As AMPs are able to target a wide range of microorganisms, it must be seen that the AMPs are built to target a specific pathogen instead of random targeting of microorganisms, which could adversely affect the natural microbiota, leading to unforeseen problems (Lazzaro et al., 2020). The stability of the AMPs also poses a concern as they can easily be broken down by enzymes and proteases within the body or even environmental factors such as temperature and pH, which would lead to a decrease in their therapeutic potency (Tortorella et al., 2023).

The cost of research and development and industrial manufacturing poses a concern within the medicinal industry due to the specificity of the amino-acid sequence buildup and storage of the AMPs, which would be costly to build and maintain a framework of machinery and downstream processing procedures. It would limit the availability and affordability of the AMPs or even make it financially unviable for large-scale manufacturing

(Jenssen et al., 2006). Moreover, there have also been discoveries showing that some microbes have developed defense mechanisms against AMPs, which has reduced the efficacy of the AMPs, much like how microbes have developed resistance towards conventional antibiotics. Therefore, much more research is needed to be performed on the modification of naturally-derived AMPs to counter such resistance from microbes in order to increase their efficacy and shelf life (Jenssen et al., 2006)

These concerns and limitations must be considered, and steps taken to overcome them to fully utilize the promising potential of AMPs in therapeutics. From this review study, ongoing research is being carried out to overcome these hurdles and maximize the potential of AMPs for therapeutic uses. Some AMPs derived from marine organisms might be key to addressing these concerns. As marine life adapts to its ever-changing environments, researchers are able to gain insights into how nature is adapting these AMPs to suit the environment. In summary, research into AMPs derived from marine animals holds an untapped source of potential for overcoming existing limitations and concerns surrounding antibiotic resistance.

CONCLUSION

This systematic review examined 952 research articles on antimicrobial peptides from marine species and thoroughly summarized the field's current understanding. Twenty-one articles were carefully analyzed, and the results showed a notable distribution between review journals and in-vitro studies: 11 articles were devoted to in-vitro investigations, and 10 articles were added to the discussion by providing in-depth reviews of antimicrobial peptides in aquatic organisms.

The comprehensive review of these compounds showcases the types, mode of action, and prospective advantages of antimicrobial peptides (AMPs) generated from marine species. With hundreds of AMPs found in plant and animal sources, their presence provides an essential first line of defense against microbial infections in a wide spectrum of marine organisms. The abundance of AMPs in these creatures, primarily derived from marine life such as fish, crabs, and marine plants, is a reaction to the harsh living conditions marked by a multitude of free-floating bacteria and potentially harmful microorganisms.

The systematic review highlights 12 aquatic species, such as *Phaeodactylum tricornutum* (Anbuchezeian et al., 2018), *Chionodraco hamatus* (Buonocore et al., 2019), *Charonia tritonis* (Cen et al., 2023), *Pomacea poeyana* (García et al., 2020), *Danio rerio* (Gayathri et al., 2021), *Anabas testudineus* (Najm et al., 2021), *Silurus asotus* (Oh et al., 2020), *Clarias gariepinus* (Okella et al., 2021), *Trematomus bernacchii* (Pelle et al., 2020), and *Nematode anisakis* (Rončević et al., 2022). It is reported to produce AMPs based on in-vitro studies, emphasizing the promising potential of marine-derived AMPs for developing novel and effective antimicrobial agents.

Although effective antimicrobial drugs have been developed thanks to advances in synthetic peptide design, more study is essential to discovering new peptides and improving our comprehension of their actions. The results of this systematic review highlight the need for continuing research into and utilization of the enormous potential of synthetic antimicrobial peptides derived from the rich and diverse marine ecosystem. They also highlight the significance of marine life as a source of inspiration for creative antimicrobial solutions.

ACKNOWLEDGEMENT

This work is supported by Malaysia Ministry of Higher Education (MOHE) under FRGS grant: FRGS/1/2022/STG01/INTI/02/3 and FRGS/1/2023/STG01/UKM/02/5

REFERENCES

- Anbuchejian, R., Ravichandran, S., Karthick Rajan, D., Tilivi, S., & Prabha Devi, S. (2018). Identification and functional characterization of antimicrobial peptide from the marine crab *Dromia dehaani*. *Microbial Pathogenesis*, *125*, 60–65. <https://doi.org/https://doi.org/10.1016/j.micpath.2018.08.056>
- Baiden, N., Gandini, C., Goddard, P., & Sayanova, O. (2023). Heterologous expression of antimicrobial peptides S-thanatin and bovine lactoferricin in the marine diatom *Phaeodactylum tricornutum* enhances native antimicrobial activity against Gram-negative bacteria. *Algal Research*, *69*, Article 102927. <https://doi.org/10.1016/j.algal.2022.102927>
- Batoni, G., Maisetta, G., & Esin, S. (2016). Antimicrobial peptides and their interaction with biofilms of medically relevant bacteria. *Biochimica et Biophysica Acta (BBA) - Biomembranes*, *1858*(5), 1044-1060. <https://doi.org/10.1016/j.bbamem.2015.10.013>
- Bo, J., Yang, Y., Zheng, R., Fang, C., Jiang, Y., Liu, J., Chen, M., Hong, F., Bailey C. Segner, H., & Wang, K. (2019). Antimicrobial activity and mechanisms of multiple antimicrobial peptides isolated from rockfish *Sebastes marmoratus*. *Fish & Shellfish Immunology*, *93*, 1007-1017. <https://doi.org/10.1016/j.fsi.2019.08.054>
- Buonocore, F., Picchietti, S., Porcelli, F., Della Pelle, G., Olivieri, C., Poerio, E., Bugli, F., Menchinelli, G., Sanguinetti, M., Bresciani, A., Gennari, N., Taddei, A. R., Fausto, A. M., & Scapigliati, G. (2019). Fish-derived antimicrobial peptides: Activity of a chionodracine mutant against bacterial models and human bacterial pathogens. *Developmental & Comparative Immunology*, *96*, 9–17. <https://doi.org/10.1016/j.dci.2019.02.012>
- Büyükkiraz, M. E., & Kesmen, Z. (2022). Antimicrobial peptides (AMPs): A promising class of antimicrobial compounds. *Journal of Applied Microbiology*, *132*(3), 1573-1596. <https://doi.org/10.1111/jam.15314>
- Cen, X., Liu, B., Zhang, G., Liu, H., Yao, G., He, M., & Liu, W. (2023). Antimicrobial peptide in giant *Triton* snail *Charonia tritonis*: mRNA profiles for tissues and its potential antibacterial activity. *Fish & Shellfish Immunology*, *136*, Article 108734. <https://doi.org/https://doi.org/10.1016/j.fsi.2023.108734>
- Chang, S. M., Matchar, D. B., Smetana, G. W., & Umscheid, C. A. (Eds.). (2012). *Methods guide for medical test reviews*. Agency for Healthcare Research and Quality.

- Chee, P. Y., Mang, M., Lau, E. S., Tan, L. T. H., He, Y. W., Lee, W. L., Pusparajah, P., Chan, K., Lee, L., & Goh, B. H. (2019). Epinecidin-1, an antimicrobial peptide derived from grouper (*Epinephelus coioides*): Pharmacological activities and applications. *Frontiers in microbiology*, *10*, Article 2631. <https://doi.org/10.3389%2Ffmicb.2019.02631>
- Chen, B., Fan, D. Q., Zhu, K. X., Shan, Z. G., Chen, F. Y., Hou, L., Cai, L., & Wang, K. J. (2015). Mechanism study on a new antimicrobial peptide Sphistin derived from the N-terminus of crab histone H2A identified in haemolymphs of *Scylla paramamosain*. *Fish & Shellfish Immunology*, *47*(2), 833–846. <https://doi.org/10.1016/j.fsi.2015.10.010>.
- Cipolari, O. C., de Oliveira Neto, X. A., & Conceição, K. (2020). Fish bioactive peptides: A systematic review focused on sting and skin. *Aquaculture*, *515*, Article 734598. <https://doi.org/10.1016/j.aquaculture.2019.734598>
- Destoumieux-Garzón, D., Rosa, R. D., Schmitt, P., Barreto, C., Vidal-Dupirol, J., Mitta, G., Gueguen, Y., & Bachere, E. (2016). Antimicrobial peptides in marine invertebrate health and disease. *Philosophical Transactions of the Royal Society B: Biological Sciences*, *371*(1695), Article 20150300. <https://doi.org/10.1098%2Frstb.2015.0300>
- Falanga, A., Lombardi, L., Franci, G., Vitiello, M., Iovene, M. R., Morelli, G., Galdiero, M., & Galdiero, S. (2016). Marine antimicrobial peptides: Nature provides templates for the design of novel compounds against pathogenic bacteria. *International Journal of Molecular Sciences*, *17*(5), Article 785. <https://doi.org/10.3390/ijms17050785>
- Ganz, T. (2002). Antimicrobial polypeptides in host defense of the respiratory tract. *The Journal of Clinical Investigation*, *109*(6), 693–697. <https://doi.org/10.1172/JCI15218>
- García-Beltrán, J. M., Arizcun, M., & Chaves-Pozo, E. (2023). Antimicrobial peptides from photosynthetic marine organisms with potential application in aquaculture. *Marine Drugs*, *21*(5), Article 290. [https://doi.org/10.3390/md21\(5\),290.1050290](https://doi.org/10.3390/md21(5),290.1050290)
- Gayathri, K. V., Aishwarya, S., Kumar, P. S., Rajendran, U. R., & Gunasekaran, K. (2021). Metabolic and molecular modelling of zebrafish gut biome to unravel antimicrobial peptides through metagenomics. *Microbial Pathogenesis*, *154*, Article 104862. <https://doi.org/10.1016/j.micpath.2021.104862>
- Giuliani, A., Pirri, G., & Nicoletto, S. (2007). Antimicrobial peptides: An overview of a promising class of therapeutics. *Central European Journal of Biology*, *2*(1), 1–33. <https://doi.org/10.2478/s11535-007-0010-5>
- Hafeez, A. B., Jiang, X., Bergen, P. J., & Zhu, Y. (2021). Antimicrobial peptides: An update on classifications and databases. *International Journal of Molecular Sciences*, *22*(21), Article 11691. <https://doi.org/10.3390/ijms222111691>
- Hallock, K. J., Lee, D. K., & Ramamoorthy, A. (2003). MSI-78, an analogue of the magainin antimicrobial peptides, disrupts lipid bilayer structure via positive curvature strain. *Biophysical Journal*, *84*(5), 3052–3060. [https://doi.org/10.1016/S0006-3495\(03\)70031-9](https://doi.org/10.1016/S0006-3495(03)70031-9)
- Huan, Y., Kong, Q., Mou, H., & Yi, H. (2020). Antimicrobial peptides: Classification, design, application and research progress in multiple fields. *Frontiers in Microbiology*, *11*, Article 2259. <https://doi.org/10.3389/fmicb.2020.582779>

- Jenssen, H., Hamill, P., & Hancock, R. E. (2006). Peptide antimicrobial agents. *Clinical Microbiology Reviews*, 19(3), 491-511. <https://doi.org/10.1128%2FCMR.00056-05>
- Kang, H. K., Seo, C. H., & Park, Y. (2015). Marine peptides and their anti-infective activities. *Marine Drugs*, 13(1), 618-654. <https://doi.org/10.3390/md13010618>
- Law, D., Najm, A. A., Chong, J. X., K'ng, J. Z., Amran, M., Ching, H. L., Wong, R. R., Leong, M. H., Mahdi, I. M., & Fazry, S. (2023). In silico identification and in vitro assessment of a potential anti-breast cancer activity of antimicrobial peptide retrieved from the ATMP1 anabas testudineus fish peptide. *PeerJ*, 11, Article e15651. <https://doi.org/10.7717/peerj.15651>
- Lazzaro, B. P., Zasloff, M., & Rolff, J. (2020). Antimicrobial peptides: Application informed by evolution. *Science*, 368(6490), Article eaau5480. <https://doi.org/10.1126/science.aau5480>
- Lei, J., Sun, L., Huang, S., Zhu, C., Li, P., He, J., Mackey, V., Coy, D. H., & He, Q. (2019). The antimicrobial peptides and their potential clinical applications. *American Journal of Translational Research*, 11(7), Article 3919
- Lipsky, B. A., Holroyd, K. J., & Zasloff, M. (2008). Topical versus systemic antimicrobial therapy for treating mildly infected diabetic foot ulcers: A randomized, controlled, double-blinded, multicenter trial of pexiganan cream. *Clinical Infectious Diseases*, 47(12), 1537-1545. <https://doi.org/10.1086/593186>.
- Luo, Y., & Song, Y. (2021). Mechanism of antimicrobial peptides: Antimicrobial, anti-inflammatory and antibiofilm activities. *International Journal of Molecular Sciences*, 22(21), Article 11404. <https://doi.org/10.3390/ijms222111401>
- Ma, H., Yang, L., Tian, Z., Zhu, L., Peng, J., Fu, P., Xiu, J., & Guo, G. (2023). Antimicrobial peptide AMP-17 exerts anti-Candida albicans effects through ROS-mediated apoptosis and necrosis. *International Microbiology*, 26(1), 81-90. <https://doi.org/10.1007/s10123-022-00274-5>.
- Mahlpuu, M., Håkansson, J., Ringstad, L., & Björn, C. (2016). Antimicrobial peptides: An emerging category of therapeutic agents. *Frontiers in Cellular and Infection Microbiology*, 6, Article 235805. <https://doi.org/10.3389/fcimb.2016.00194>
- Mba, I. E., & Nweze, E. I. (2022). Antimicrobial peptides therapy: An emerging alternative for treating drug-resistant bacteria. *The Yale Journal of Biology and Medicine*, 95(4), 445-463.
- Méndez-Samperio, P. (2013). Recent advances in the field of antimicrobial peptides in inflammatory diseases. *Advanced Biomedical Research*, 2(1), Article 50. <https://doi.org/10.4103/2277-9175.114192>
- Moher, D., Liberati, A., Tetzlaff, J., & Altman, D. G. (2009). Preferred reporting items for systematic reviews and meta-analyses: The PRISMA statement. *BMJ*, 339, Article b2535. <https://doi.org/10.1136/bmj.b2535>
- Moretta, A., Scieuzo, C., Petrone, A. M., Salvia, R., Manniello, M. D., Franco, A., Lucchetti, D., Vassallo, A., Vogel, H., Sgambato, A., & Falabella, P. (2021). Antimicrobial peptides: A new hope in biomedical and pharmaceutical fields. *Frontiers in Cellular and Infection Microbiology*, 11, Article 668632. <https://doi.org/10.3389/fcimb.2021.668632>
- Munn, Z., Moola, S., Lisy, K., Riitano, D., & Tufanaru, C. (2015). Methodological guidance for systematic reviews of observational epidemiological studies reporting prevalence and cumulative incidence data. *International Journal of Evidence-based Healthcare*, 13(3), 147-153. <https://doi.org/10.1097/xeb.0000000000000054>

- Najm, A. A. K., Azfaralariff, A., Dyari, H. R. E., Othman, B. A., Shahid, M., Khalili, N., Law, D., Alwi, S. S. S., & Fazry, S. (2021). Anti-breast cancer synthetic peptides derived from the *Anabas testudineus* skin mucus fractions. *Scientific Reports*, *11*(1), Article 23182. <https://doi.org/10.1038/s41598-021-02007-6>
- Narula, P., Kiruthika, S., Chowdhari, S., Vivekanandan, P., & Chugh, A. (2023). Inhibition of hepatitis B virus (HBV) by Tachyplesin, a marine antimicrobial cell-penetrating peptide. *Pharmaceutics*, *15*(2), Article 672. <https://doi.org/10.3390/pharmaceutics15020672>
- Nyberg, F., Carlsson, A., & Hallberg, M. (2013). Casomorphins/Hemorhins. In A. J. Kastin (Ed.) *Handbook of Biologically Active Peptides* (pp. 1550–1555). Academi Press. <https://doi.org/10.1016/b978-0-12-385095-9.00211-6>
- Oh, H. Y., Go, H. J., & Park, N. G. (2020). Identification and characterization of SaRpAMP, a 60S ribosomal protein L27-derived antimicrobial peptide from amur catfish, *Silurus asotus*. *Fish & Shellfish Immunology*, *106*, 480–490. <https://doi.org/https://doi.org/10.1016/j.fsi.2020.06.038>
- Okella, H., Ikiriza, H., Ochwo, S., Ajayi, C. O., Ndekezi, C., Nkamwesiga, J., Kaggwa, B., Aber, J., Mtewa, A. G., Koffi, T. K., Odongo, S., Vertommen, D., Kato, C. D., & Ogwang, P. E. (2021). Identification of antimicrobial peptides isolated from the skin mucus of *African Catfish, Clarias gariepinus* (Burchell, 1822). *Frontiers in Microbiology*, *12*, Article 794631. <https://doi.org/10.3389/fmicb.2021.794631>
- Pelle, G. D., Perà, G., Belardinelli, M. C., Gerdol, M., Felli, M., Crognale, S., Scapigliati, G., Ceccacci, F., Buonocore, F., & Porcelli, F. (2020). Trematocine, a novel antimicrobial peptide from the antarctic fish *Trematomus bernacchii*: Identification and biological activity. *Antibiotics*, *9*(2), Article 66. <https://doi.org/10.3390/antibiotics9020066>.
- Peng, K. C., Lee, S. H., Hour, A. L., Pan, C. Y., Lee, L. H., & Chen, J. Y. (2012). Five different piscidins from *Nile tilapia, Oreochromis Niloticus*: Analysis of their expressions and biological functions. *PLoSOne*, *7*(11), Article e50263. <https://doi.org/10.1371/journal.pone.0050263>
- Raju, V. S., Sarkar, P., Pachaiappan, R., Paray, B. A., Al-Sadoon, M. K., & Arockiaraj, J. (2020). Defense involvement of piscidin from striped murrel *Channa striatus* and its peptides CsRG12 and CsLC11 involvement in an antimicrobial and antibiofilm activity. *Fish & Shellfish Immunology*, *99*, 368–378. <https://doi.org/10.1016/j.fsi.2020.02.027>
- Rima, M., Fajloun, Z., Sabatier, J. M., Bechinger, B., & Naas, T. (2021). Antimicrobial peptides: A potent alternative to antibiotics. *Antibiotics*, *10*(9), Article 1095. <https://doi.org/10.3390/antibiotics10091095>
- Rončević, T., Gerdol, M., Mardirossian, M., Maleš, M., Cvjetan, S., Benincasa, M., Maravić, A., Gajski, G., Krc, L., Aviani, I., Hrabar, J., Trumbić, Ž., Derks, M., Pallavicini, A., Weingarth, M., Zoranić, L., Tossi, A., & Mladineo, I. (2022). Anisaxins, helical antimicrobial peptides from marine parasites, kill resistant bacteria by lipid extraction and membrane disruption. *Acta Biomaterialia*, *146*, 131–144. <https://doi.org/https://doi.org/10.1016/j.actbio.2022.04.025>
- Russell, C. K., & Gregory, D. M. (2003). Evaluation of qualitative research studies. *Evidence-Based Nursing*, *6*(2), 36–40. <https://doi.org/10.1136/ebn.6.2.36>
- Semreen, M. H., El-Gamal, M. I., Abdin, S., Alkhazraji, H., Kamal, L., Hammad, S., El-Awady, F., Waleed, D., & Kourbaj, L. (2018). Recent updates of marine antimicrobial peptides. *Saudi Pharmaceutical Journal*, *26*(3), 396–409. <https://doi.org/10.1016/j.jsps.2018.01.001>

- Sepulveda, J., & Wilson, M. (2019). *The use and abuse of antibiotics*. Institute for Global Health Sciences. <https://globalhealthsciences.ucsf.edu/news/use-and-abuse-antibiotics>
- Subramaniam, G., Yew, X. Y., & Sivasamugham, L. A. (2020). Antibacterial activity of *Cymbopogon citratus* against clinically important bacteria. *South African Journal of Chemical Engineering*, *34*, 26–30. <https://doi.org/10.1016/j.sajce.2020.05.010>
- Tortorella, A., Leone, L., Lombardi, A., Pizzo, E., Bosso, A., Winter, R., Petraccone, L., Del Vecchio, P., & Oliva, R. (2023). The impact of N-glycosylation on the properties of the antimicrobial peptide LL-III. *Scientific Reports*, *13*(1), Article 3733. <https://doi.org/10.1038/s41598-023-29984-0>
- Uddin, T. M., Chakraborty, A. J., Khusro, A., Zidan, B. R., Mitra, S., Emran, T. B., Dhama, K., Ripon, Md. K., Gajdács, M., Sahibzada, M. U., Hossain, M. J., & Koirala, N. (2021). Antibiotic resistance in microbes: History, mechanisms, therapeutic strategies and future prospects. *Journal of Infection and Public Health*, *14*(12), 1750–1766. <https://doi.org/10.1016/j.jiph.2021.10.020>
- Vitali, A. (2018). Antimicrobial peptides derived from marine sponges. *American Journal of Clinical Microbiology and Antimicrobials*, *1*(1), Article 1006.
- Waghu, F. H., & Idicula-Thomas, S. (2019). Collection of antimicrobial peptides database and its derivatives: Applications and beyond. *Protein Science*, *29*(1), 36-42 <https://doi.org/10.1002/pro.3714>
- Walsh, D., & Downe, S. (2006). Appraising the quality of qualitative research. *Midwifery*, *22*(2), 108–119. <https://doi.org/10.1016/j.midw.2005.05.004>
- Wang, S., Fan, L., Pan, H., Li, Y., Qiu, Y., & Lu, Y. (2023). Antimicrobial peptides from marine animals: Sources, structures, mechanisms and the potential for drug development. *Frontiers in Marine Science*, *9*, Article 1112595. <https://doi.org/10.3389/fmars.2022.1112595>
- Wei, O. Y., Xavier, R., & Marimuthu, K. (2010). Screening of antibacterial activity of mucus extract of snakehead fish, *Channa striatus* (Bloch). *European Review for Medical and Pharmacological Sciences*, *14*(8), 675–681.
- Wu, Y., Wang, H., & Chu, P. K. (2023). Enhancing macrophages to combat intracellular bacteria. *The Innovation Life*, *1*(2), 100027-100028. <https://doi.org/10.59717/j.xinn-life.2023.100027>
- Xuan, J., Feng, W., Wang, J., Wang, R., Zhang, B., Bo, L., Chen, Z. S., Yang, H., & Sun, L. (2023). Antimicrobial peptides for combating drug-resistant bacterial infections. *Drug Resistance Updates*, *68*, Article 100954. <https://doi.org/10.1016/j.drug.2023.100954>
- Ye, Z., Fu, L., Li, S., Chen, Z., Ouyang, J., Shang, X., Liu, Y., Gao, L., & Wang, Y. (2024). Synergistic collaboration between AMPs and non-direct antimicrobial cationic peptides. *Nature Communications*, *15*(1), Article 7319. <https://doi.org/10.1038/s41467-024-51730-x>
- Zasloff, M. (2002). Antimicrobial peptides of multicellular organisms. *Nature*, *415*(6870), 389–395. <https://doi.org/10.1038/415389a>
- Zheng, X., Yuan, C., Zhang, Y., Zha, S., Mao, F., & Bao, Y. (2022). Prediction and characterization of a novel hemoglobin-derived mutant peptide (mTgHbP7) from *Tegillarca granosa*. *Fish & Shellfish Immunology*, *125*, 84-89. <https://doi.org/10.1016/j.fsi.2022.05.007>

Application of GIS for Monitoring Firefly Population Abundance (*Pteroptyx tener*) and the Influence of Abiotic Factors

Nurhafizul Abu Seri and Azimah Abd Rahman*

Geoinformatic Unit, Geography Section, School of Humanities, Universiti Sains Malaysia, 11800 USM, Pulau Pinang, Malaysia

ABSTRACT

This study focuses on the *Pteroptyx tener* species in the Sepetang River, Malaysia, aiming to evaluate the firefly's abundance and explore its correlation with various biotic and abiotic parameters. The study was conducted over six months, from November 2021 to April 2022, utilizing Geographic Information System (GIS) software to apply hotspot mapping and Inverse Distance Weighting (IDW) analysis to elucidate the spatial distribution of firefly populations. A total of 111,615 individuals were recorded, with a particular focus on this firefly species' presence on their display trees. Hotspot analysis showed that Station 6, located at the mouth of a river with dense mangroves, hosted 55,723 fireflies (50.01%). In contrast, Stations 9 and 10, near ponds and shrimp settlements, recorded 517–723 fireflies (0.65% and 0.46%). Pearson's correlation coefficient (r) unveiled a statistically significant positive correlation ($r = 0.88$, $p < 0.05$) between wind speed and the abundance of firefly populations within the Sepetang River. However, no statistically significant correlation ($p > 0.05$) was found between firefly abundance and various other abiotic parameters, including relative humidity (RH), air temperature, tide level, pH, electrical conductivity (EC), salinity, total dissolved solids (TDS), and water clarity. Thus, the results revealed the preference for fireflies due to the availability of vegetation, wind speed and minimal disturbance in this area. In conclusion, this study's information significantly adds to our understanding of these interesting insects and their complicated relationships in nature.

It underscores the importance of preserving their habitats and ecosystems.

ARTICLE INFO

Article history:

Received: 24 January 2024

Accepted: 10 June 2024

Published: 25 October 2024

DOI: <https://doi.org/10.47836/pjst.32.6.24>

E-mail addresses:

nurhafizul.abuseri97@gmail.com (Nurhafizul Abu Seri)

azimahrahman@usm.my (Azimah Abd Rahman)

* Corresponding author

Keywords: Abiotic parameters, Geographic Information System (GIS), insect population, Inverse Distance Weighting (IDW), Pearson's correlation coefficient (r), *Pteroptyx tener* species

INTRODUCTION

Geographic Information System (GIS) is a computer-based platform facilitating the collection, storage, analysis, and visualization of spatial data, integrating diverse sources like satellite imagery, maps, surveys, and non-spatial data. Through this integration, GIS offers a comprehensive perspective of specific geographic areas, serving as a powerful tool for comprehending and managing intricate spatial relationships within the environment (Tu & Hoang, 2023). Recently, the advancement of information availability and tools for information management has facilitated the development of geographically based databases essential for protecting biodiversity, and the operation of many conservation programs is inherently spatial (Malavasi, 2020). GIS plays a pivotal role in biodiversity monitoring, allowing targeted surveys and tracking species and habitat distribution changes over time (Rocchini et al., 2016).

In contrast, international research has shown a more widespread use of GIS to examine the relationships between insect species and their environments. Studies on various insect populations, such as the spotted borer, African oil palm weevil, anuran species, insect pests, termites, aphids, and others (Kokila et al., 2021; Lubis et al., 2023; Keinath et al., 2023; Roy et al., 2020; Ozsahin et al., 2022; Du et al., 2020) have extensively employed GIS to investigate the influence of biotic (living) and abiotic (non-living) parameters on their distribution, behavior, and abundance. These international studies have showcased the diverse applications of GIS in entomological research, highlighting its effectiveness in analyzing complex ecological patterns, understanding habitat preferences, and predicting species responses to environmental changes. Through the comprehensive integration of GIS, researchers have uncovered valuable insights into the intricate relationships between insects and their surrounding ecosystems, contributing to the advancement of ecological knowledge and conservation strategies on a global scale.

GIS and its related technologies are indispensable for informed decision-making, particularly in addressing the spatial aspects relevant to biodiversity (Mileti et al., 2024). Balaman (2019) explained that GIS is useful for gathering, documenting, storing, analyzing, presenting, and managing spatial and geographic data utilizing interactive maps. Also, creating web GIS tools to map and describe habitats and biodiversity, particularly the future distribution of species, can play an important role in conservation planning (Obeidavi et al., 2019). Additionally, regarding commercialization, GIS output maps that include clear captions and grouping of various colors and patterns make it simpler to visualize the geographic information. It makes inexperienced GIS users comfortable using the application (Paramasivam, 2019). A wide spectrum of specialized fields, such as geology, geomorphology, geography, geophysics, hydrology, hydrogeology, environmental science, oceanography, meteorology, and atmospheric science, heavily rely on geospatial data to grapple with complex Earth-related dilemmas.

Some of these predicaments would be exceptionally arduous to tackle without integrating GIS (Zhou, 2021).

In Malaysia, despite its potential, the utilization of GIS applications has been relatively limited. For example, a study by Idris et al. (2021) focused on assessing firefly habitats. This study integrated GIS with remote sensing techniques, allowing researchers to comprehensively analyze various landscape factors that affect firefly populations. Using GIS tools, the researchers could map the distribution of firefly habitats, discern the influence of different landscape elements on their populations, and propose effective conservation strategies to protect these vulnerable species. This study provided valuable information on the ecological requirements of fireflies and highlighted the importance of preserving their habitats. The study conducted by Poukin et al. (2023) only used ArcGIS 9.3 to delineate and map sampling stations within their designated study area.

The documentation of Congregating Firefly Zones (CFZs) in Malaysia, as outlined in the study by Wong (2022), demonstrates the importance of GIS in understanding the spatial distribution of firefly populations. GIS was utilized to accurately map the locations of these CFZs along rivers, providing valuable spatial data for conservation planning and management. Moreover, the study's emphasis on conducting in-depth research on firefly species diversity aligns with GIS's role in facilitating data collection, analysis, and visualization. GIS can help researchers identify areas with high biodiversity and prioritize conservation efforts accordingly. Additionally, the Selangor Declaration on the Conservation of Fireflies highlights the critical role of protecting firefly habitats, a task that GIS can support through spatial analysis of habitat threats and identifying priority conservation areas.

The lack of a GIS approach to collect biodiversity data poses a significant challenge to efficient conservation efforts, particularly in monitoring firefly populations in Malaysia. This limitation hampers the ability to collect accurate and comprehensive data, essential to understanding firefly populations and implementing effective conservation strategies. Therefore, this research aims (1) to assess the spatial distribution of firefly population abundance, (2) to map the Inverse Distance Weighting (IDW) and firefly population abundance correlation using GIS tools, and (3) to analyze the influence of abiotic factors on the firefly population abundance.

MATERIALS AND METHODS

Study Area

Figure 1 shows the location of Kuala Sepetang (Sepetang Estuary) in the Larut, Matang, and Selama districts of Perak, Malaysia. Sepetang Estuary is located at coordinates 4°50'26"N 100°37'42"E and is a rapidly developing fishing village. The length of the Sepetang River is approximately 32 km, while the catchment area is about 189 km². It was also one of

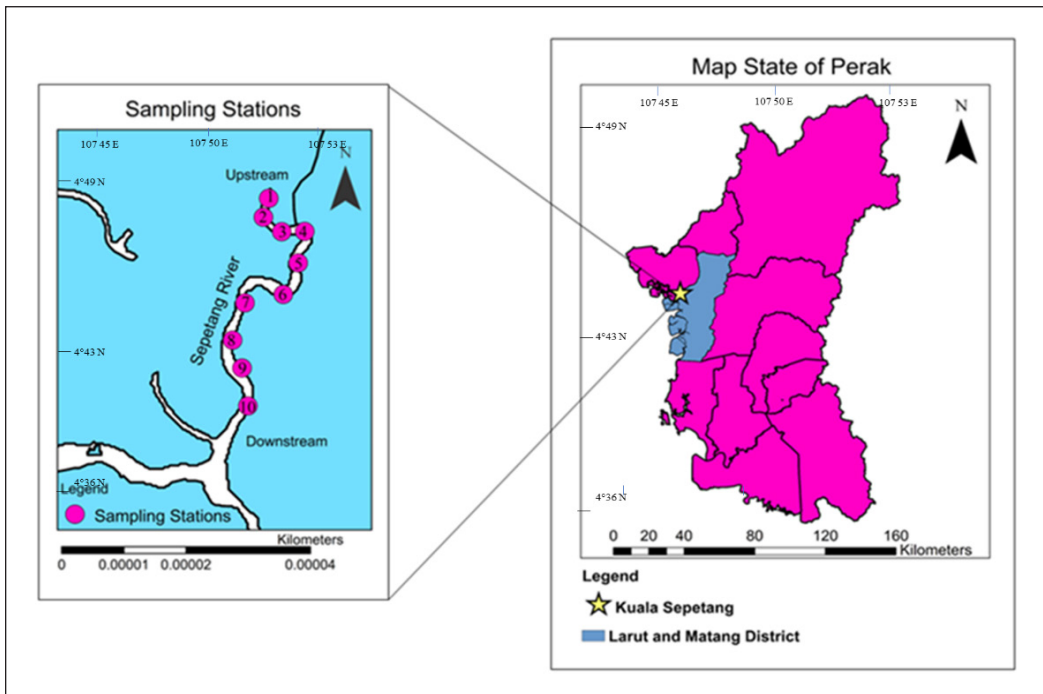


Figure 1. The sampling stations (SS1–SS10) along the Sepetang River

Malaysia’s Congregating Firefly Zones (CFZs), which aims to protect the firefly colonies of the river, especially *Pteroptyx tener* (Wong & Yeap, 2012).

The Methodology

During a six-month continuous monitoring period at the Sepetang River, the most active activity of fireflies was observed flashing their lights between 19:35 and 22:00 MST, persisting even during heavy rain. The study area experiences a tropical climate characterized by abundant rainfall from October to January, which constitutes the rainy season. In contrast, the period between February and September represents the hottest months in this region. Consequently, the sampling activities were conducted during two distinct seasons: the rainy season (November 2021 to December 2021) and the dry season (January to April 2022), starting from 5:30 p.m. to 9:00 p.m.

The selection of sampling stations was based on the presence of firefly colonies observed on the display trees, which were marked using a handheld Altimeter GPS+ attached to an iPhone X, version 4.7.3. Table 1 lists abiotic parameters and the units and instruments used during field studies. Rapid on-site day and night sampling assessment also ensured systematic data collection of fireflies, vegetation, and insect mimics. The use of rapid assessments is also crucial to avoiding loss of data and misinformation. The applied rapid assessment was adapted from the work of Jusoh et al. (2011).

Table 1
Abiotic parameters, units, instruments, and notable features

Abiotic Parameter	Measurement	Unit	Instruments
Electrical Conductivity	MicroSiemens per centimeter	$\mu\text{S}/\text{cm}$	Hach SensION 5 waterproof conductivity meter and conductivity probe
Total Dissolved Solids	MicroSiemens per centimeter	ppm	Hach SensION 5 waterproof conductivity meter and conductivity probe
Water Salinity	MicroSiemens per thousand	ppt	Hach SensION 5 waterproof conductivity meter and conductivity probe
Potential of Hydrogen	MicroSiemens per centimeter	pH	Hach SENSION1 Waterproof Ph/mV meter electrode
Clarity/Turbidity	Nephelometric Turbidity Units	NTU	Hach 2100P portable turbidimeter
Wind Speed	Meters per second	knots	Smart Sensor Mini Anemometer with an LCD digital display
Air Temperature	Celcius	$^{\circ}\text{C}$	Benetech GM1361+ humidity temperature meter
Relative Humidity	Percentage	%	Benetech GM1361+ humidity temperature meter
Tide Level	Meters	m	Tideschart application (Developer: 7th Gear)

Visual Counting

The visual counting method was chosen over alternative techniques since it is fast and low-cost (Jusoh et al., 2010a), particularly in field studies where real-time observations are crucial. Two trained observers were tasked with implementing this method, as Jusoh et al. (2010a) suggested, to mitigate potential visual biases stemming from variations in visual acuity or observer habits. Furthermore, the reliability of visual counting can be enhanced through validation by different observers conducting repeated observations, ensuring the accuracy of data collection.

The study implemented several measures to minimize the likelihood of overestimation. First and foremost, extensive training was provided to the observers involved in the counting process. This training focused on developing a standardized approach to identify and distinguish individual fireflies, considering their unique flashing patterns and behaviors. Additionally, rigorous training sessions were conducted to enhance the observers' visual acuity and consistency in counting. Moreover, the study established specific observation periods during the counting. This temporal restriction was intended to ensure the counts were made within a defined time frame, reducing the chances of overcounting due to repetitive observations of the same fireflies.

Regular assessments were also conducted to monitor observer performance and minimize potential biases that might lead to inaccurate counting. These assessments aimed to identify any variations or discrepancies in the counting process, allowing immediate corrective actions to be taken. While manual counting presents certain limitations and

potential concerns, the study took proactive measures to justify its use as a reliable estimation method. The rigorous training, standardized counting protocols, and careful monitoring of the counting process were all critical components in ensuring the accuracy and validity of the population estimations for *Pteroptyx tener*.

Sweep-netting

The sweep net technique used in this study complies with ethical guidelines for firefly conservation in many ways. First, it is non-invasive, allowing researchers to capture adult fireflies for species identification and taxonomic studies without harming them or their habitat and does not require continuous daily monitoring. This approach is important to minimize any adverse effects on the fireflies and their environment during data collection. Sweep net sampling is efficient for estimating the presence and abundance of species in the field and remains the best approach (Edde, 2022). Second, sweep nets have proven efficient in species identification, allowing researchers to accurately study the physical characteristics of various firefly species and their flicker patterns. This method also minimizes errors by accurately identifying captured specimens, such as *Pteroptyx tener*, in this study, thus maintaining the specificity of the data collected. Furthermore, sweep-netting also assisted in estimating the abundance and population density of adult fireflies in our research area. This data was valuable for understanding population abundance and monitoring changes over time.

Spatial and Non-spatial Data Analysis Techniques

Spatial and non-spatial data analysis techniques played a crucial role in the study. The hotspot analysis required prior geocoding, involving deriving firefly distribution coordinates using sampling stations and vegetation coordinates in the study area. Utilizing Google Earth and the Earth Point tool for geocoding, which is essential for changing location descriptors into specific Earth positions, facilitated the application of hotspot analysis, resulting in a comprehensive hotspot map.

Additionally, the study employed Inverse Distance Weighted Interpolation (IDW) within ArcGIS version 10.3 for mapping abiotic parameters from sampling stations. IDW operates on the principle that proximate items share more similarities than distant ones, considering the localized impact of each measured location. This technique assigns higher weights to points nearest the forecast location, gradually decreases as distance increases and provides a detailed spatial representation of abiotic parameters in the study area.

Pearson Correlation Coefficient (r)

Pearson's correlation coefficient measures the strength and direction of a linear relationship between two variables (Obilor & Amadi, 2018). Ranging from -1 to +1 for continuous data,

a value approaching +1 signifies a perfect positive relationship, while a value nearing -1 indicates a perfect negative correlation. A value of 0 implies no correlation between the two variables. The technique is more precise and accessible for interpretation than just looking at the R-value. Table 2 interprets Pearson’s correlation coefficient (r), and Table 3 indicates its strength and direction for the variables.

Table 2
Correlation type between two variables with interpretation of the Pearson’s correlation coefficient (r) (Turney, 2022)

Pearson correlation coefficient (r)	Correlation type	Interpretation
Between 0 and 1	Positive correlation	All the variables change in the same direction when one variable changes
0	No correlation	The variables have no relationship
Between 0 and -1	Negative correlation	All the variables change in the opposite direction when one variable changes.

Table 3
Pearson’s correlation coefficient (r) strength and direction (Turney, 2022)

Pearson correlation coefficient (r) value	Strength	Direction
> .5	Strong	Positive
Between .3 and .5	Moderate	Positive
Between 0 and .3	Weak	Positive
0	None	None
Between 0 and -.3	Weak	Negative
Between -.3 and -.5	Moderate	Negative
< -.5	Strong	Negative

RESULTS AND DISCUSSION

Total Population Abundance of *Pteroptyx tener* Along the Sepetang River

Table 4 presents the findings from a six-month monitoring period (November 2021 to April 2022) at ten sampling stations along the Sepetang River, focusing on the population abundance of *Pteroptyx tener*. A total of 111,615 individuals were collected, revealing significant variations in abundance levels across the sampling stations and months. SS6 showed the highest SE ± Mean (16417.11 ± 496.25), while SS10 had the lowest (155.17 ± 3.73). Notably, January 2022 exhibited the highest SE ± Mean (4265.17 ± 2692.30), indicating greater variability, while November 2021 had the lowest (2082.07 ± 1319.40). The mean firefly count on November 21 was 13,194, with a moderate SE, suggesting reasonable precision. December 2021 maintained a mean count of 15,631, with an increased SE, indicating greater variability. January 2022 had the highest SE ± Mean (26923 fireflies, 4265.17 ± 2692.30), signifying a larger range of variance. February and March 2022 had

intermediate SE ± Mean values (21,701 and 16,793 fireflies, respectively), and April 2022 showed a mean count of 17,373 with an SE of 2616.29 ± 1737.30 (Table 4).

Figure 2 shows a hotspot map that displays the total firefly abundance over a six-month monitoring period at ten Sepetang River sampling stations. Consistent with prior research by Jusoh et al. (2010a), this study supports the observation that the Sepetang River is a major hotspot for *Pteroptyx* fireflies. Station 6, strategically located in the river’s mouth bar with clustered mangrove trees, exhibited exceptionally bright flashing patterns, hosting 55,723 fireflies, representing 50.01% of the total (Table 4). This unique setup suggests the fireflies’ preference for this area. Mouth bars, formed by sediment accumulation at river mouths, can serve as suitable firefly habitats depending on vegetation availability, water quality, and minimal disturbances. The presence of mangrove trees and other aquatic plants in mouth bars creates favorable conditions for fireflies, as their larvae thrive in moist, semi-aquatic environments. Studies by Fu et al. (2005; 2006) indicate that semi-aquatic larvae inhabit soil and leaf litter along riverbanks, occasionally transitioning to water environments for foraging.

Table 4
Cumulative number, mean value, and standard error of *Pteroptyx tener* along the Sepetang River

Sampling Station	Nov-21	Dec-21	Jan-22	Feb-22	Mar-22	Apr-22	Total Per Station	SE ± Mean
SS1	72	87	118	65	70	190	602	180.17 ± 8.17
SS2	115	88	327	425	336	458	1749	526.74 ± 13.03
SS3	799	1101	1095	1244	901	1239	6379	1866.37 ± 43.80
SS4	831	1099	1642	1829	1303	1574	8278	2434.37 ± 34.12
SS5	2233	4952	6120	6207	2573	3038	25123	7481.78 ± 151.78
SS6	7250	6238	14242	9845	9023	9125	55723	16417.11 ± 496.25
SS7	1292	1510	3175	1666	2260	1351	11254	3338.48 ± 123.05
SS8	418	319	100	200	109	121	1267	385.63 ± 11.63
SS9	116	182	73	121	105	126	723	212.96 ± 3.70
SS10	68	55	31	99	113	151	517	155.17 ± 3.73
Total Per Month	13194	15631	26923	21701	16793	17373	111615	-
SE ± Mean	2082.07 ± 1319.40	2094.17 ± 1563.10	4265.17 ± 2692.30	3102.82 ± 2170.10	2600.10 ± 1679.30	2616.29 ± 1737.30	-	-

Lewis et al. (2020) assumed that because the larval stage of fireflies spends months to years either underwater or in soil, excessive pesticide concentrations in water and soil may be particularly damaging to aquatic fireflies (such as *Aquatica* and *Sclerotia*). It might also damage *Pteroptyx* firefly larvae, known to lodge among the roots of riparian mangrove trees and in the vegetation behind adult display trees or soil (such as terrestrial fireflies *Lampyrus*, *Photinus*, and *Photuris*). Firefly eggs are deposited in soil, moss, or decaying wood; pupae develop underground or on tree trunks and may be exposed. Meanwhile, aquatic larvae in various settings exhibit diverse behaviors, including bottom-dwelling and back-swimming (Ho et al., 2010; Vaz, Guerrazzi et al., 2021).

SS5, with the highest firefly count ranging from 11,254 to 25,123 individuals, represents a notable hotspot, constituting 22.55% of the total population (Table 4). This increase in activity is attributed to the concealed and darker environments of SS5 and SS6, strategically positioned away from human activity and light sources. Vaz, Manes et al. (2021) support this, stating that fireflies prefer darker areas, highlighting light pollution as a potential threat. In contrast, SS9 and SS10, close to potential disturbances like shrimp ponds and human settlements, recorded only 517–723 individuals, constituting 0.65% and 0.46%, respectively. Hazmi and Sagaff (2017) noted the detrimental effects of pollutants from shrimp ponds on fireflies, indicating a connection between habitat disruption and firefly abundance.

In the Rembau-Linggi estuary, Peninsular Malaysia, the growing number of oil palm plantations has encroached on the riverbank area, affecting the breeding of fireflies *Pteroptyx tener*. It is challenging because riverbank mangrove forests have transformed into agricultural, aquaculture, and urbanization zones (Jusoh & Hashim, 2012). This transformation is exacerbated by the economic benefits associated with firefly ecotourism, which encourages human activities that endanger firefly habitats in Malaysia, such as in Sepetang Estuary and Rembau-Linggi (Jusoh et al., 2010a; Jusoh et al., 2010b). As a result, many riverine firefly species will face extinction because of this practice. Broad areas of mangrove banks along riverbanks have been cleared in

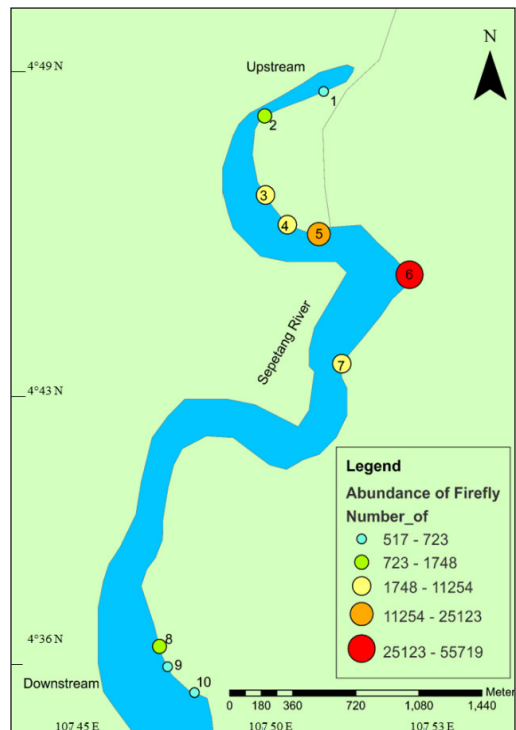


Figure 2. Firefly hotspot map along the Sepetang River

Southeast Asia for oil palm plantations, shrimp farms, or flood mitigation. This region was rendered unsuitable for the growth and reproduction of *Pteroptyx* firefly larvae and their snail prey larvae (Jusoh et al., 2010b; Jusoh & Hashim, 2012; Khoo et al., 2012; Thancharoen, 2012; Wong & Yeap, 2012). It has been reported that influences from anthropogenic, rapid, and extensive urbanization, industrialization, and ecotourism have jeopardized the mangrove habitat that *Pteroptyx* fireflies live on (Prasertkul, 2018; Sartsanga et al., 2018; Wong & Yeap, 2012).

The study emphasizes that stations with high firefly abundance, like SS5 and SS6, are likely to maintain their populations due to factors such as habitat quality, protection from disturbances, habitat continuity, pollution levels, and past habitat degradation. Human settlements and land use changes, including mangrove conversion to shrimp ponds, negatively impact stations like SS1, SS2, SS3, SS8, SS9, and SS10. Converting mangrove forests for economic gains, driven by firefly ecotourism, threatens firefly habitats, leading to potential extinction. SS5 and SS6, located away from anthropogenic activities, exemplify the negative impacts of rapid urbanization, industrialization, and ecotourism on mangrove habitats.

Observing the highest total population in January 2022 (26,923 individuals) aligns with seasonal patterns and favorable climate conditions. January likely represents a peak mating season for *Pteroptyx tener*, as reported by Ho et al. (2010). The study also considers the impact of weather conditions, with wet and dark nights favoring firefly activity, while dry seasons may decrease their activity. The temporal variations in precipitation levels, alternating between rainy and dry periods, influence firefly behavior. The lowest abundance in November 2021 (13,194 individuals) corresponds to the end of the breeding period, in line with Koken et al.'s (2022) findings on the breeding period of *Photinus immigrans*. This pattern suggests that the breeding period for *Pteroptyx tener* in the Sepetang River spans from mid-June to early November (Figure 3).

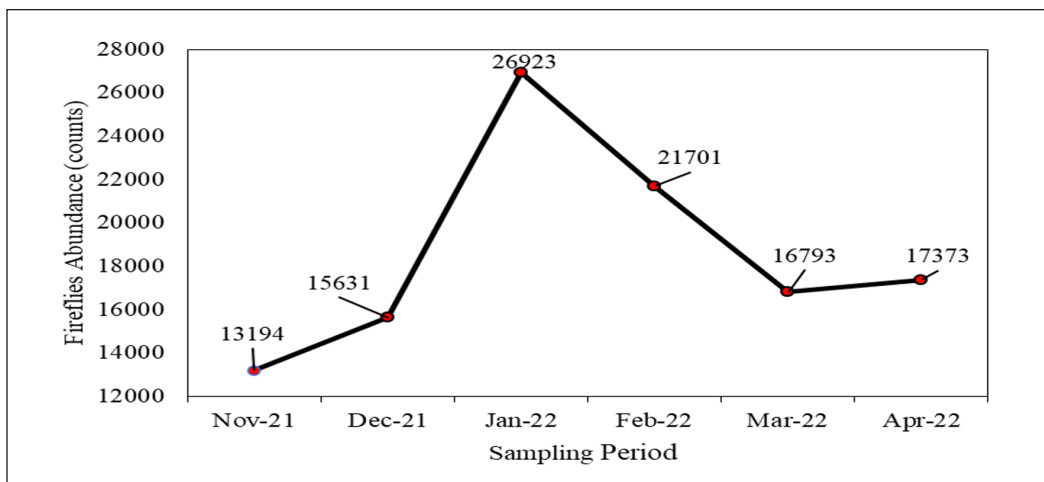


Figure 3. The abundance of fireflies recorded monthly at 10 sampling stations along the Sepetang River

Firefly Population Abundance and Abiotic Influences

Human activities along the Sepetang River, including physical changes, settlements, and commercial areas, have led to water deterioration, with the Water Quality Index indicating 59% pollution and classifying the river in the class III category (Hazmi & Sagaff, 2017). Long-term surveys reveal declines in glowworm and mangrove firefly populations due to water quality deterioration (Atkins et al., 2017; Jusoh & Hashim, 2012; Khoo et al., 2014). Hazmi and Sagaff (2017) also stated that the deterioration of water quality would cause the number of fireflies to decrease and the population's extinction. The population of fireflies is closely linked to water quality in their habitats, as they deposit their eggs in crevices or loose soil on the ground in tidal floodplains of rivers (Faudzi et al., 2021). For example, Abdullah et al. (2020) found that the lowest abundance of fireflies in Sungai Raan, Miri, Sarawak, was related to the river's location in the center of a fishing village, where domestic activities and fishing vessels create anthropogenic pressure on the river. In contrast, a healthy mangrove environment, like Sungai Niah, supported the largest firefly populations.

Hazmi and Sagaff (2017) emphasize the vulnerability of fireflies to environmental changes and their dependence on factors like water quality. The decline, though not as extreme as in other regions, raises concerns about potential extinction. Global instances of insect population decline, such as a 76% decrease in flying insect biomass in German protected areas (Hallmann et al., 2017) and a 50% reduction in European grassland butterfly populations (Van Swaay et al., 2013), underscore the severity of the issue. River water pollution in Japan has similarly led to a decline in firefly populations (Ohba & Wong, 2004).

Moreover, firefly numbers decrease due to changes in river water quality caused by pollution, diesel consumption, and development around firefly habitats (Jusoh et al., 2010b). Mangrove areas, like Kuala Sepetang, suffer from poor waste disposal, further impacting water quality. Herbicides and pesticides from nearby agricultural areas contribute to river pollution (Asyraf et al., 2013). The correlation analysis indicates a significant positive relationship between wind speed and firefly abundance, highlighting the impact of abiotic factors on firefly populations, while other parameters show less statistically significant correlations (Table 5). Figure 4 visually represents the correlation between various abiotic parameters and fireflies' abundance.

The study reveals a non-significant relationship between RH and the firefly population at Sepetang River sampling stations ($r = -0.53$, $p = 0.28$) (Table 5). It contradicts Norela et al.'s (2017) findings yet aligns with Abdullah et al. (2020), who reported a weak, non-significant correlation in other rivers. The highest RH at SS1, SS2, and SS3 did not correspond to high firefly abundance, supporting the conclusion that RH does not influence Sepetang River firefly abundance (Figure 5).

While RH is vital in firefly ecology, influencing breeding and mating, its role is complex. Studies by Axmacher et al. (2009), Fazal et al. (2012), Kaiser et al. (2017), and

Table 5
Values of the Pearson correlation coefficient (r) analysis of abiotic parameters

Parameters	Correlation	r value	p Value
Relative Humidity	None	-0.53	0.28
Air Temperature	None	0.38	0.46
Wind Speed	Positive	0.88	0.02
Tide Level	None	0.48	0.34
pH	None	-0.57	0.24
Electrical Conductivity	None	-0.42	0.40
Salinity	None	0.71	0.12
TDS	None	-0.18	0.73
Water Clarity	None	-0.43	0.39

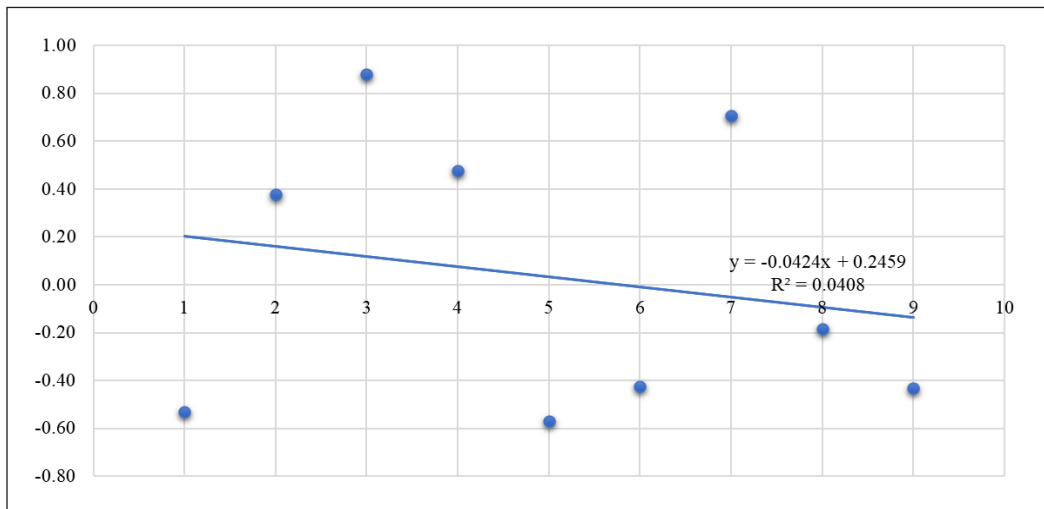


Figure 4. The correlation between various abiotic parameters (relative humidity, air temperature, wind speed, tide level, pH, EC, salinity, TDS, and water clarity) and fireflies' abundance

Cheng et al. (2020) highlight its relevance. However, the connection between RH and firefly numbers is intricate and context-dependent, varying across environments. Considering various determinants like habitat quality, light pollution, predation dynamics, and pesticide use, caution is warranted in interpreting correlations between RH and firefly abundance. Globally, RH alone is unlikely to be the primary factor affecting firefly populations; instead, a complex interplay of ecological factors shapes their abundance.

The correlation between fireflies and water pH was strongly negative and statistically significant ($r = -0.57$, $p = 0.24$) (Table 5). This finding aligns with Faudzi et al.'s (2021) discovery in Sungai Cherating, Malaysia, indicating that pH is not correlated with firefly populations. Shahara et al. (2017) also found no significant relationships between TDS, temperature, RH, wind speed, water salinity, conductivity, and firefly populations at Bernam

River, Selangor. Abdullah et al. (2021) supported the lack of significant differences in pH between sampling stations in the Rembau River. The study, spanning rainy and dry seasons, noted lower pH during the rainy season due to increased H_2CO_3 formation. Referring to Figure 6, sampling stations SS5 and SS6, with suitable water pH, had the highest firefly abundance. The river water pH across all stations was around 5.70, with temperatures ranging from 28°C to 31°C, suitable for tropical mangrove forests. Robertson-Bryan (2004) highlighted the preference of estuarine-dwelling species for pH levels between 6.5 and 8.5. Marine organisms will struggle to survive if the pH rises or falls below 5.0 or above 9.0. The pH value of water is one of the main predictors for determining the level of water pollution, such as eutrophication and water degradation (Feng et al., 2017). Along the Sepetang River, the pH was acidic, approaching neutral, ranging between 5.61 and 5.95. pH impacts various chemical processes in aquatic environments, including acid-base reactions, solubility reactions, oxidation-reduction reactions, and complexation (Saalidong et al., 2022).

The firefly population in Sungai Sepetang shows a positive correlation with salinity ($r = -0.71$), although this correlation is not statistically significant ($p = 0.12$). The average salinity of freshwater from the river is 0.5 ppt or less, falling within the mesohaline range (6.99 ppt) considered normal for organism survival. Elevated salinity beyond tolerance ranges can impact stress, reproduction, and survival rates (Palmer et al., 2008). Salinity influences

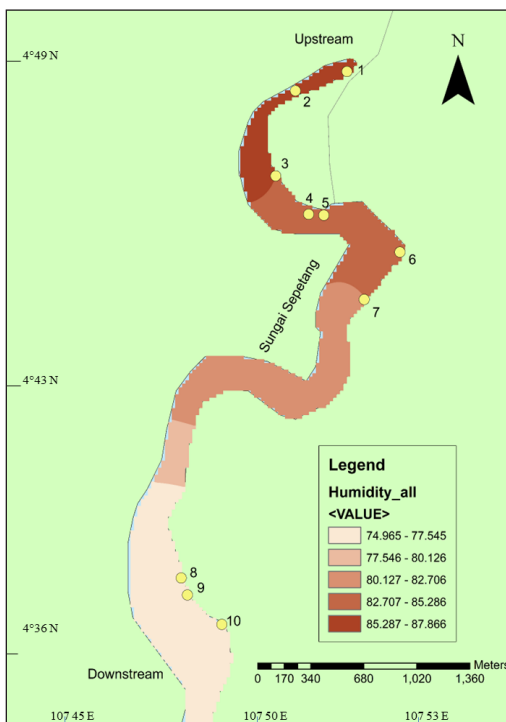


Figure 5. Average of relative humidity

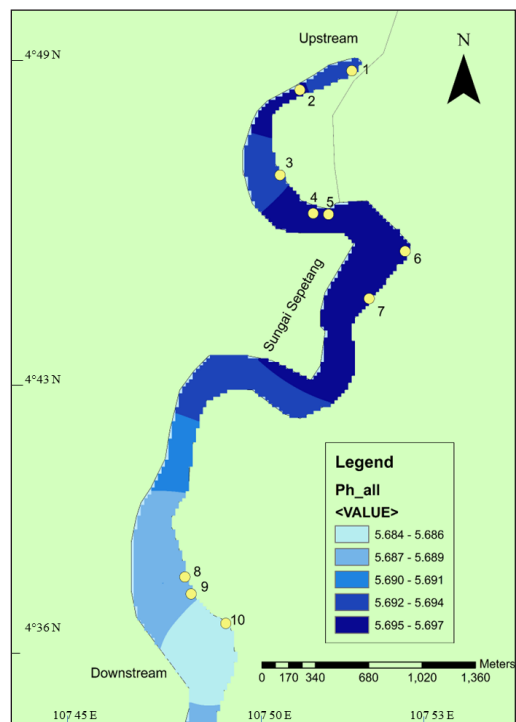


Figure 6. Average pH level

water density, increasing dissolved salt concentration and higher density (Corbett, 2007). The conductivity of the Sepetang River (28.63 s/cm) falls within the normal freshwater range, influenced by its clay-type soil. Mangroves in the area with high salinity tolerance remain unaffected by moderate temperature (31.8°C) and salinity conditions (6.99 ppt) (Figure 7).

Mangroves are plants with a high tolerance to salinity, tidal variations, temperature, and moisture growing in the intertidal zone (Tokan et al., 2018; Yahya et al., 2020). Therefore, the conditions of temperature (31.8°C) and salinity (6.99 ppt), which are not extreme in Sungai Sepetang, do not affect the condition of mangrove trees in the area. The humidity there is also very high, 97.12% and is very suitable for mangrove plants that display trees by fireflies. Changes in the salinity reading of the river water may be due to the difference in the measurement time concerning the tide. The populations of fireflies in the Selangor and Rembau rivers are unaffected by water salinity, according to Khoo et al. (2012) and Asri et al. (2021). Salinity levels are relatively lower in freshwater systems like rivers compared to marine or ocean environments.

Adult fireflies, with a terrestrial life stage, spend most of their lives in terrestrial habitats, exhibiting ecological behaviors primarily terrestrial in nature. Their reproductive behaviors near riverine locales emphasize the importance of water quality for firefly populations. The study underscores the ecological nuances of terrestrial habitats, diurnal navigation toward arboreal sustenance, and orchestration of nocturnal mating behaviors near riverine locales as key determinants of firefly population abundance. Monitoring the salinity levels of the Sungai Sepetang River is crucial due to its role as a water source for the mangrove forest ecosystem, impacting ecotourism and local economic growth in the future. Salinity levels across sampling stations, divided into oligohaline and mesohaline, are suitable for fireflies, as observed in mesohaline stations (SS5 and SS6) with high abundance, contrasting with mesohaline stations (SS4, SS7, SS8, SS9, and SS10) exhibiting lower firefly abundance.

In Malaysian rivers like Sepetang, Rembau, and Chukai, an increase in insect abundance is linked to decreased salinity levels, which are crucial for larval growth and firefly survival. Maintaining optimal salinity is essential, as it affects the soil where fireflies lay eggs and larvae develop (Abdullah et al., 2019). Asri et al. (2021) found peak firefly populations in downstream river zones with ideal salinity. Conversely, in the Selangor River, an increase in salinity negatively impacted firefly populations in *Sonneratia caseolaris* along the riverbanks (Khoo et al., 2012).

Pteroptyx tener larvae inhabit the upper soil horizon/organic layer, which is washed regularly by the tidal river. They spend most of their time hunting their host (*Cyclotropis carinata*; Assimineidae) in this zone. Importantly, their eggs and pupae, which reside in the upper soil layers, might be used as effective environmental health indicators. Living at a higher soil horizon makes them highly susceptible to water and soil quality changes

(Cheng et al., 2020). Non-synchronous fireflies, such as *Pteroptyx bearni*, *Pteroptyx valida*, and *Pteroptyx gelasina*, are typically encountered in waters with higher salinity and species such as *Rhizophora*, *Aviccenia*, *Sonneratia alba*, and *Excoecaria*. In contrast, *Pteroptyx tener* and *Pteroptyx malaccae* are synchronous fireflies that inhabit brackish waters where *Sonneratia caseolaris*, *Gluta renghas*, *Talipariti*, and *Barringtonia* were found (Wong, 2022).

The wind speed showed a highly strong positive correlation ($r = 0.88$) with the population of fireflies and a significant positive relationship at ($p = 0.02$) (Table 5). The observed correlation with wind speed implies that it plays a significant role in shaping the abundance of fireflies. Fireflies are small, delicate insects, and wind conditions can influence their ability to fly. High wind speeds can make it difficult for fireflies to engage in mating displays and aerial activities. Therefore, they may be more active and abundant on nights with calmer winds. It is the same as the results obtained by Asri et al. (2021), where, temporally, the wind speed showed a significant negative relationship with the abundance of fireflies ($F = 6.72$, $p < 0.05$).

Fireflies rely on their bioluminescent flashes for communication and mating. Wind can disrupt these signals, making it difficult for fireflies to locate and communicate with potential mates. Calm nights with lower wind speeds are likely more conducive to successful firefly mating displays, which can lead to higher population abundances. For insects to engage in flight activity (in the case of *Pityophthorus juglandis*), moderately high temperature and moderate wind speed conditions are required. When the temperature was about 30°C, and the wind speed was approximately 2 km/h, male and female *Pityophthorus juglandis* flew the most due to the following second-order interactions between the factors (Chen & Seybold, 2014).

When the wind speed can affect a firefly species (*Pteroptyx valida*) larger than *Pteroptyx tener*, which is approximately 11.0 ± 0.02 mm in length (Jaikla et al., 2020), it is expected that this study discovered wind speed to affect *Pteroptyx tener*. Adult males of *Pteroptyx valida* were smaller than females, averaging 10.1 ± 0.04 mm and

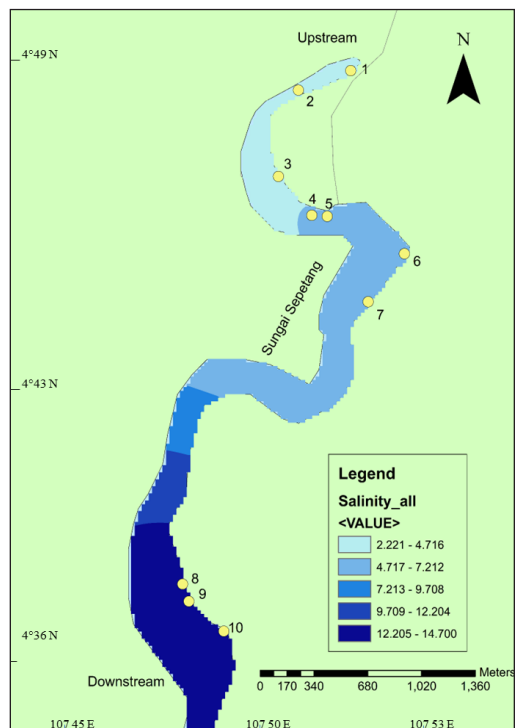


Figure 7. Average salinity level

11.4 ± 0.10 mm, respectively (Jaikla et al., 2020). On the other hand, the *Pteroptyx tener* is comparatively smaller, with males measuring between 5391.411 µm or 5.39 mm and 5391.130 µm or 5.39 mm in length. In contrast, females are larger, ranging from 6861.083 µm or 6.86 mm to 6858.535 µm or 6.86 mm, surpassing the length of adult males.

Wind speed impacts *Pteroptyx tener* fireflies in the Sepetang River as they fly in search of mates. Small (5–7 mm), the *Pteroptyx tener* is easily carried by moving air (Gatehouse, 1997). Wang et al. (2007) stated that wind, rain, and colder weather cause a drop in firefly luminous activity. According to Abdullah et al. (2019), the population number of fireflies in the Rembau River has been affected by wind speed. In addition, there is a strong negative correlation between wind speed and the diversity and number of insects in the Sepetang and Chukai rivers.

Jaikla et al. (2020) conducted a study on the impact of wind speed and direction on the horizontal distribution of *Pteroptyx* species in Thailand. According to the findings, the firefly species prefer to be perched on tree branches facing away from the direction of the strongest winds in Surat Thani, Phetchaburi, Krabi and Nakhon Si Thammarat. More than 45° on either side of the wind direction is where 85% of these firefly species are perched. 13.1% of the fireflies fell within 45° of the current wind direction on either side, while 1.9% fell upwind. Wind speed has a large impact on the temporal variation of the firefly. Additionally, variations in wind speed were found to cause variations in the size of the firefly population in Rembau River, Negeri Sembilan (Abdullah et al., 2019; Asri et al., 2021). This finding may be related to exposure to the Southwest monsoon, which winds up to 15 knots stronger than those in the Sepetang and Chukai rivers (Asri et al., 2021).

Sampling stations with high wind speeds are at SS7, SS8, SS9, and SS10, which are directly proportional to the relatively low firefly population recorded in this area. SS1-SS6 are among the stations that consistently record a higher population abundance of fireflies compared to other stations (Figure 8). Additionally, a bubble graph was included to support the IDW map results of the relationship between the abundance of fireflies and abiotic parameters (Figure 9).

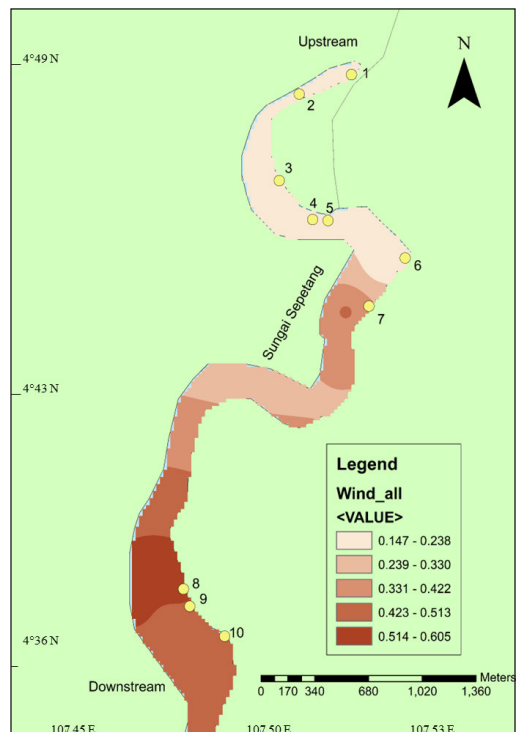


Figure 8. Average wind speed

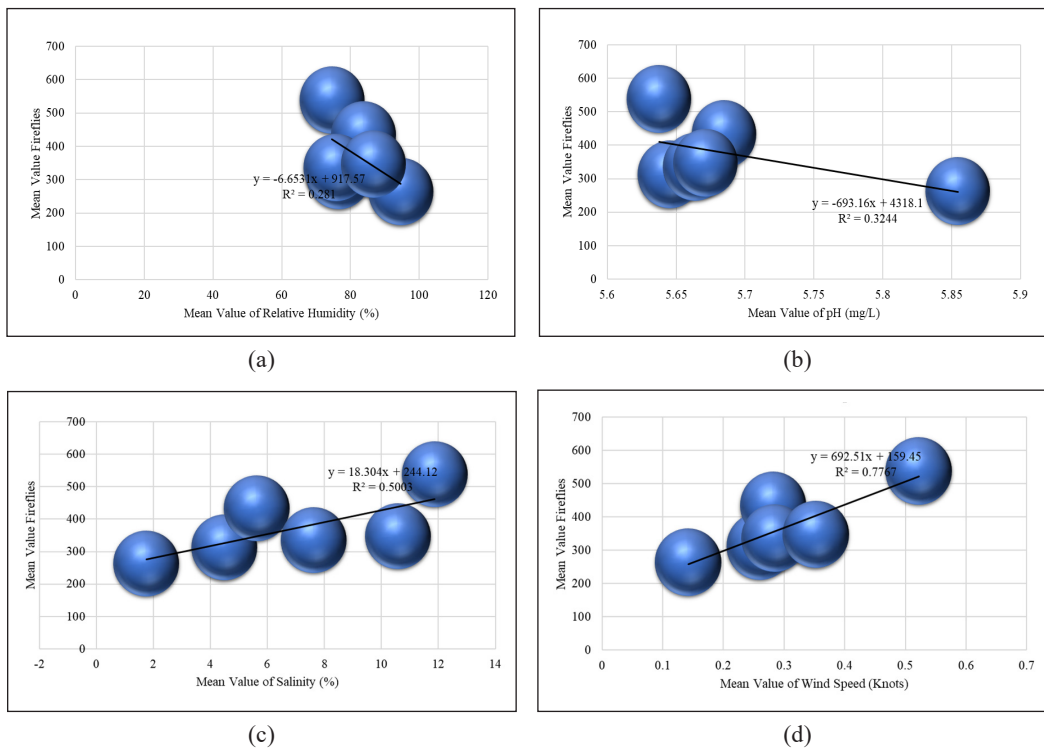


Figure 9. The connection between the mean abundance of fireflies and (a) relative humidity, (b) pH, (c) salinity and (d) wind speed

The results of the TDS and fireflies' population reveal a weak negative correlation ($r = -0.18$), lacking statistical significance ($p = 0.73$) (Table 5). Existing scientific research minimally connects TDS to firefly populations, with studies emphasizing more prominent threats like habitat destruction, light pollution, pesticide use, and climate change. In freshwater, TDS is generally low (<500 ppm), with seawater and brackish water concentrations ranging between 500 to 30,000 and 30 to 40,000, respectively (Moran, 2018). Sepetang River's low TDS concentration, below 500 ppm, fosters an ideal environment for aquatic life, particularly firefly larvae reliant on tiny snails as a food source (Peng et al., 2020).

TDS primarily denotes the concentration of dissolved ions, with firefly larvae being aquatic and exposed to TDS levels in their habitats. While firefly larvae adapt to various freshwater environments, they are less tolerant of highly saline waters. Excess TDS, often due to human activities, threatens aquatic organisms (Caedo-Argüelles et al., 2013). Abdullah et al. (2020) found no statistically significant correlation between TDS and fireflies in the Niah and Raan Rivers. Similarly, Shahara et al. (2017) observed a weak and non-significant correlation between fireflies and abiotic factors, including TDS, in the Bernam River, Selangor.

TDS concentrations in the study consistently remained below 500 ppm (Figure 10), with no significant differences among stations. This observation explains the absence of an effect of TDS on firefly population abundance. The indirect and less significant relationship between TDS and firefly abundance in adult fireflies is influenced by courtship, mating, and reproduction factors. Adult fireflies, primarily terrestrial during their short-lived stage, allocate energy to these activities, making them less directly impacted by TDS levels in water (Angelini et al., 2010).

The firefly population in the Sepetang River shows a moderately negative correlation with water clarity ($r = -0.43$), but this relationship is not statistically significant ($p = 0.39$) (Table 5). Water clarity, measured at 38.93 NTU, is suitable

for living organisms, although it may conceal parasites like *Cryptosporidium*. Changes in water clarity, induced by factors like suspended solids, wind-induced sediment re-dispersion, and rainfall, can indirectly impact firefly populations (Stevenson & Bravo, 2019; Booth et al., 2000). The survival rate of flying insects (Caddisflies) is not significantly different when their larvae are exposed to varied levels of water clarity at either water temperature. That is, the water clarity level does not affect the life of flying insects (Suzuki et al., 2018).

While water clarity and turbidity may not directly affect adult fireflies, variations in these parameters can indirectly influence firefly populations by altering the abundance and distribution of prey species. Fireflies in the Sepetang River may have adapted to the specific water quality conditions, with some species being more tolerant to changes in clarity and turbidity. Excessive turbidity in watersheds can indicate the presence of organic and inorganic materials, posing concerns such as increased algal growth or sediment suspension. Continuous monitoring of turbidity is crucial due to its potential detrimental effects on ecosystems. However, in the Sepetang River, the absence of abnormally strong wind conditions mitigated noticeable cloudiness in the water, reducing any potential effect on firefly abundance (Gillett & Marchiori, 2019; Smith & Davis-Colley, 2001).

The study suggests that firefly larvae may thrive in suitable habitats despite variations in water clarity, such as submerged vegetation or debris, offering protection and food

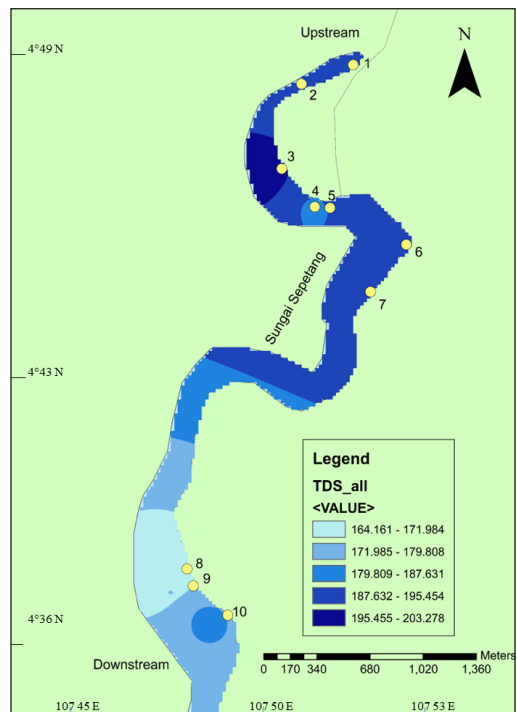


Figure 10. Average of TDS

sources. Short-term variations in water quality, including turbidity, may be tolerated by firefly populations, but prolonged periods of poor water quality can have a more pronounced negative impact. The lack of a consistent correlation between water clarity and firefly abundance, as shown in the IDW map (Figure 11), indicates that changes in water clarity do not consistently predict variations in firefly populations.

Firefly population and air temperature are also moderately but positively correlated ($r = 0.38$) without a statistically significant relationship ($p = 0.46$) (Table 5). Abdullah et al. (2021) also stated that there was no statistical significance between the sampling station and the temperature ($F = 0.814$, $p > 0.05$). Fireflies and air temperature were also correlated moderately but positively correlated ($r = 0.38$) without a statistically significant relationship ($p = 0.46$). According to (Khoo et al., 2012), for three years (2006 to 2008), the average monthly temperature and RH, which are constant and only slightly fluctuate, do not appear to alter the trend of an increasing adult firefly population. Findings by Rabha et al. (2021) suggest that the species is active on hot days due to a “hot effect” and may disappear during winter due to a “cold effect.” The average temperature of 29.33°C obtained from this study indicates that it does not exceed 34°C. According to Rabha et al. (2021), temperatures above this threshold, with even slight increases, likely signify the denaturation of the enzyme luciferase, which catalyzes the light-producing reaction in fireflies.

The report given by Abdullah et al. (2019) also showed that temperature and RH were not significantly correlated with the insect community. Like what Mahadimenakbar et al. (2018) discovered, parameters such as air temperature, RH, wind speed, and light intensity did not exhibit unusual patterns. The highest and medium air temperature was recorded at SS4-SS10, while SS5 and SS6 also included these two stations as hotspot areas and recorded the highest overall population abundance of fireflies. It shows that there is no difference and that the effect of air temperature on the firefly population is not significant (Figure 12). Furthermore, it was shown that the density of firefly larvae was higher in sago plantations than in palm oil plantations, which may be related to the cooler, more humid,

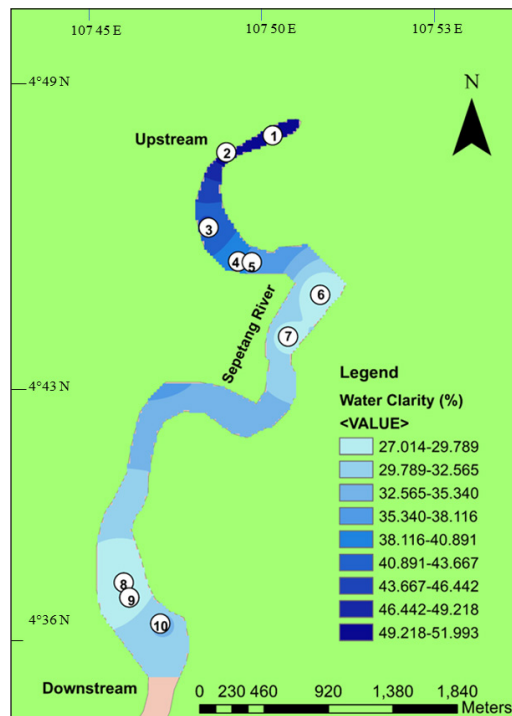


Figure 11. Average of water clarity

and shaded environment near the sago patch. The soil temperature in the orchard is also substantially higher at a depth of 5 cm than in the sago patch and oil palm plantation (Kirton et al., 2006).

The Sepetang River’s electrical conductivity (EC) of 28.63 s/cm falls within the normal freshwater range (0-1,500 $\mu\text{s}/\text{cm}$), serving as a reliable baseline for salinity and TDS estimates (Fondriest Environmental, 2014). Firefly species, known for their adaptability to various climates, can thrive in diverse geographic regions with varying temperature regimes (Faust, 2004; Usener & Cognato, 2005; Lloyd, 2008; Nada & Ballantyne, 2018). The study’s average temperature of 29.33°C is below the critical threshold of 34°C for enzyme luciferase denaturation in fireflies, as Rabha et al. (2021) suggested. A moderate negative correlation ($r = -0.42$) and non-significant relationship ($p = 0.40$) between EC and firefly population indicate a healthy river environment. The EC value (47.72 $\mu\text{S}/\text{cm}$) is relatively low, typical for freshwater habitats, contrasting with saline or brackish environments—mangrove ecosystems, usually saline, host firefly species adapted to slightly higher EC levels.

Water temperature significantly influences conductivity, causing daily fluctuations, with warmer water exhibiting higher conductivity (Fondriest Environmental, 2014). Though water flow changes can affect conductivity and potentially impact firefly habitats, the study suggests that daily temperature-related changes might not immediately and profoundly affect adult fireflies. Research findings indicate stable conductivity levels during the monitored period, with no extreme temperature, salinity, or TDS changes. The absence of a correlation between EC and firefly population abundance, emphasized by the IDW map analysis, underscores their relationship’s non-linear and complex nature (Figure 13).

The firefly population in the Sepetang River shows a moderately positive but statistically insignificant correlation with tidal levels ($r = 0.48$, $p = 0.34$) (Table 5) (Angelini et al., 2010). It implies that changes in tidal levels do not significantly impact the abundance of fireflies in the river. The study emphasizes the importance of further research into the relationship between firefly abundance and tidal levels, cautioning against taking the current findings for granted. While firefly larvae adapt to varying water levels,

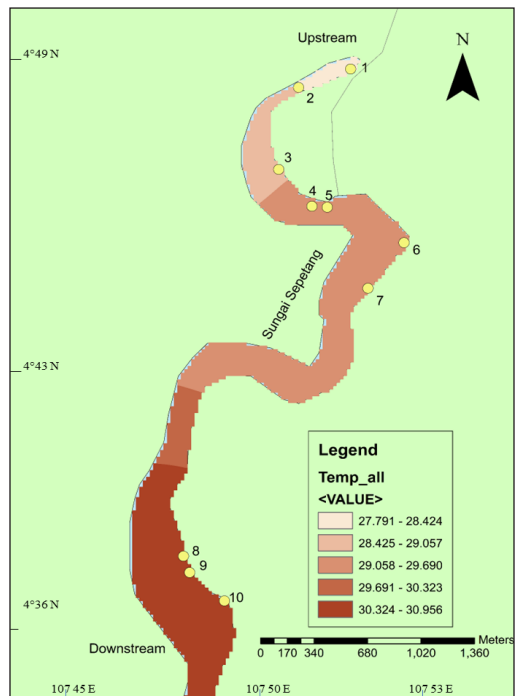


Figure 12. Average of air temperature in the river water sample

adults primarily rely on terrestrial habitats for their activities (McHugh & Liebherr, 2009; Reed et al., 2020; Riley et al., 2021). Tidal levels, which primarily affect aquatic environments, may have a limited direct impact on adult fireflies. Firefly larvae are known to be resilient to tidal fluctuations if suitable aquatic habitats are available (Angelini et al., 2010).

The consistent and predictable tide levels observed in the Sepetang River, influenced by gravitational forces from the moon and sun, suggest that fireflies have adapted to these environmental conditions. This adaptation is likely due to certain environmental factors supporting the reproduction and survival of firefly larvae, as they deposit their eggs in damp habitats (Angelini et al., 2010). Fireflies may adapt their breeding behavior based on tide levels to meet specific environmental

requirements, such as moisture levels and food availability. It further emphasizes the ecological nuances influencing firefly populations in the Sepetang River area.

Tide levels are primarily influenced by the gravitational forces exerted by the moon and sun, resulting in a tidal cycle. The tidal cycle exhibits variability and is not uniformly consistent monthly. Tides are influenced by multiple elements, such as the positioning of the moon and sun, and can lead to variations in water levels. The study's results indicate a consistent and predictable tide level in the Sepetang River area, and the fireflies have adapted; accordingly, certain environmental conditions in the area likely support the reproduction and survival of their larvae. Fireflies frequently deposit their eggs in damp habitats, and their larvae may require a specific environment for growth. Fireflies may adapt their breeding behavior to align with a specific tide level if it provides a favorable habitat. These modifications may arise due to the need for ideal moisture levels, the availability of food, or other ecological considerations. Fireflies are predominantly found in terrestrial ecosystems, such as grasslands and forests, rather than aquatic tidal environments. However, if fireflies were to adapt to a tidal-influenced environment, it would likely be due to biological factors that result in consistently higher tide levels than the average monthly tide level. A bubble graph was also included to support the IDW map results of the relationship between the abundance of fireflies and abiotic parameters (Figure 14).

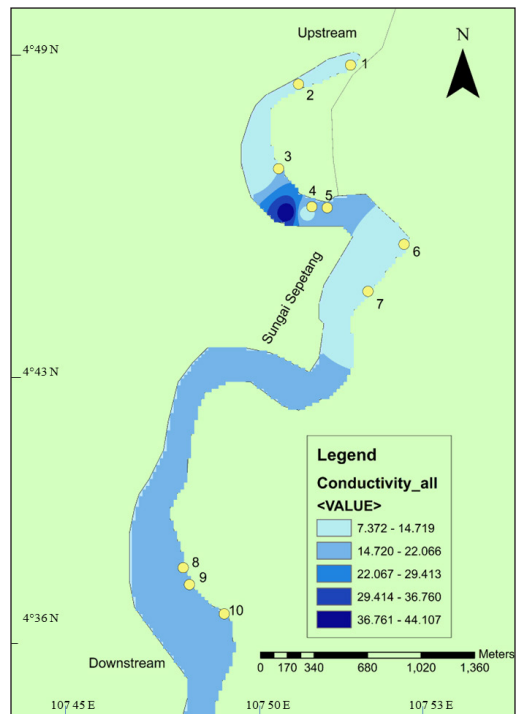


Figure 13. Average of electrical conductivity

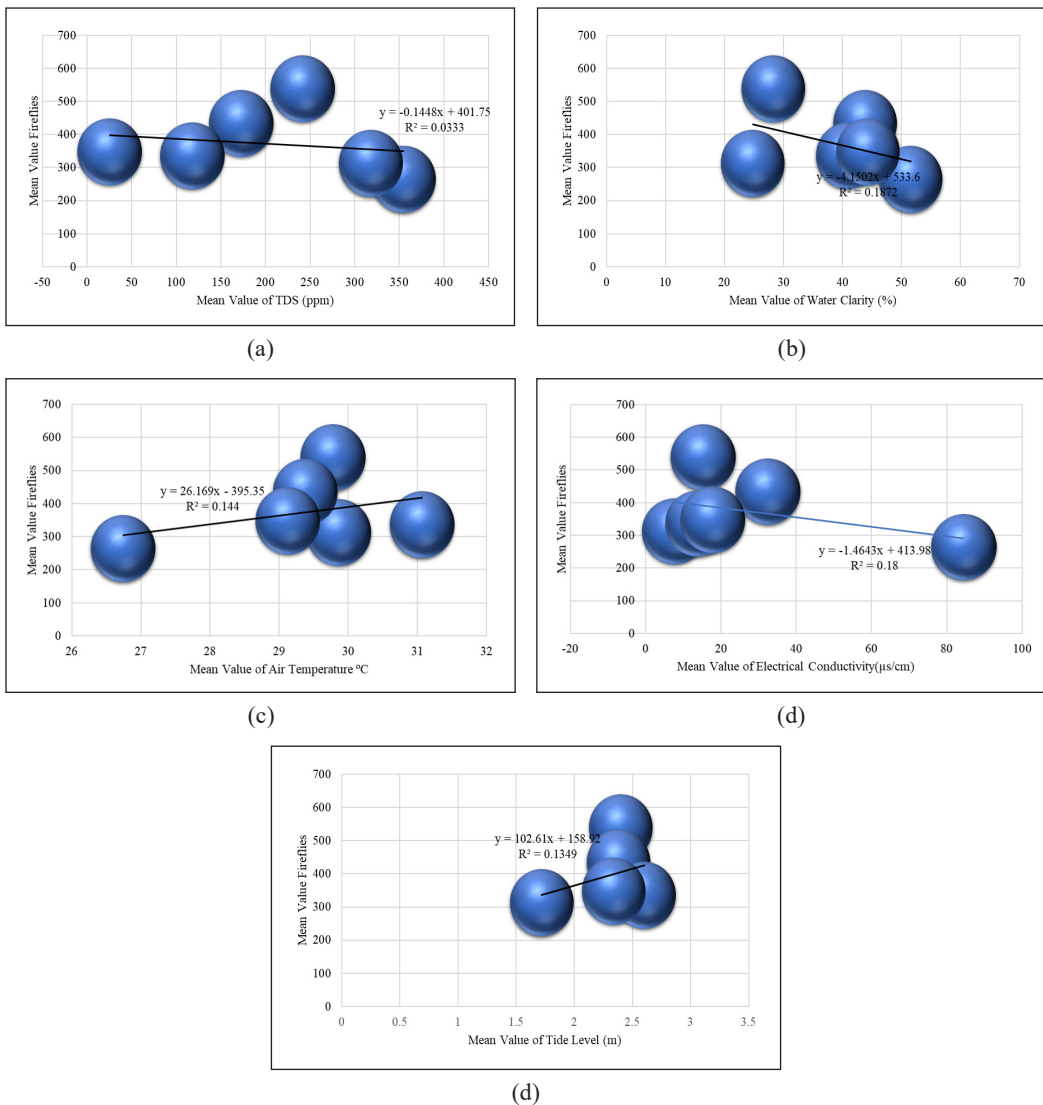


Figure 14. The connection between the mean abundance of fireflies and (a) TDS, (b) water clarity, (c) air temperature, (d) electrical conductivity and (e) tide level

CONCLUSION

The statistically significant positive correlation between wind speed and firefly abundance highlights the importance of considering specific abiotic factors in understanding the dynamics of firefly populations. However, the lack of statistically significant correlations between firefly abundance and other abiotic parameters, such as RH, air temperature, tide level, pH, EC, salinity, TDS, and water clarity, suggests the need for further investigation into the complex relationships between these parameters and firefly population dynamics. These findings contribute significantly to understanding firefly ecology and emphasize

the complex interplay between abiotic factors in their habitat selection and population dynamics. This study highlights the importance of preserving the Sepetang River mangrove ecosystem. It underscores the need for extended research efforts to uncover the intricacies of firefly behavior and their delicate ecological interactions. This study suggested that future studies should include a more extended sampling period (a year or more that consists of all seasonal factors) to monitor fireflies' abiotic parameters and optimize data collection. Focus should also be given to including other abiotic parameters such as vegetation suitability, vegetation health, insecticides contained in the vegetation, prey of firefly larvae (mangrove snail: *Cyclotropis carunculata*), artificial light pollution, light intensity, air quality, climatology, and soil quality (water level in soil) along the Sepetang River. However, for the long-term survival of the fireflies that live along the Sepetang River, they should be protected by focusing on ecological, physical, and biological aspects, including protecting all species of vegetation that occupy the area.

Our study differentiates our research methodology using GIS software, specifically ArcGIS version 10.3. These advanced tools facilitate detailed spatial analysis, particularly through hotspot mapping and IDW analysis, thereby improving our understanding of firefly population distribution. On the other hand, previous studies either rely solely on GPS data or do not incorporate direct mapping methodology (Shahara et al., 2017; Asri et al., 2021), potentially limiting the accuracy and comprehensiveness of their spatial analysis. Our study offers a comprehensive view of the spatial distribution of firefly populations, which is significant for conservation efforts and understanding habitat preferences. While certain previous studies investigated specific aspects such as habitat modification or the influence of abiotic factors on firefly populations (Abdullah et al., 2021; Faudzi et al., 2021; Jusoh & Hashim, 2012), our research introduces a new dimension through its emphasis on spatial analysis.

While previous studies covered various rivers and estuaries across various regions, providing a broader understanding of firefly ecology in Malaysia (Abdullah et al., 2019; Abdullah et al., 2020; Wong, 2022), our study focused on a specific geographic area. This concentration may limit the generalizability of our findings compared to studies covering different regions. However, the depth of spatial analysis facilitated by GIS techniques mitigates this limitation. Similar to several previous studies, our research explores the correlation between environmental factors and firefly abundance, yielding valuable insights into the ecological determinants of firefly populations. However, while previous studies examined a variety of environmental variables, our study focused primarily on spatial distribution and may not delve into specific ecological interactions that affect firefly populations.

Our study and previous research underscore the importance of certain vegetation types as habitats for fireflies, enriching our understanding of species preferences and ecosystem

associations. However, while our study provides valuable insight into habitat preference through spatial analysis, it may not offer detailed information on species diversity and ecological interactions because it explicitly focuses on these aspects. Our research greatly contributes to the field by leveraging GIS techniques for spatial analysis, thereby providing detailed insights into firefly population distribution. However, to achieve a comprehensive understanding of firefly ecology, integrating findings from previous studies investigating diverse dimensions such as habitat modification, species diversity, and ecological interactions is desirable.

ACKNOWLEDGEMENT

This research was financed by the Ministry of Higher Education Malaysia under the Fundamental Research Grant Scheme with project code FRGS/1/2020/SS0/USM/02/6.

REFERENCES

- Abdullah, N. A., Asri, L. N., Husin, S. M., Shukor, A. M., Darbis, N. D. A., Ismail, K., Agustar, H. K., Sulaiman, N., & Hazmi, I. R. (2021). Influence of physico chemical characteristics of rembau river, peninsular Malaysia, on congregating *Pteroptyx* fireflies. *Environmental Monitoring and Assessment*, 193(10), Article 634. <https://doi.org/10.1007/s10661-021-09426-y>
- Abdullah, N. A., Radzi, S., Asri, L. N., Idris, N. S., Husin, S., Sulaiman, A., Khamis, S., Sulaiman, N., & Hazmi, I. R. (2019). Insect community in riparian zones of Sungai Sepetang, Sungai Rembau and Sungai Chukai of Peninsular Malaysia. *Biodiversity Data Journal*, 7, Article e35679. <https://doi.org/10.3897/BDJ.7.e35679>
- Abdullah, N. A., Asri, L. N., Radzi, S. N. F., Musbah, M., Hazmi, I. R., & Sulaiman, N. (2020). Abiotic factors influencing diversity and abundance of congregating fireflies (Coleoptera: Lampyridae) in Miri, Sarawak, Malaysia. *Oriental Insects*, 55(2), 149-164. <https://doi.org/10.1080/00305316.2020.1757529>
- Angelin, J. A., Jehamalar, E. E., Das, S. S. M., & Kumar, S. P. (2010). Effect of salinity on the distribution of aquatic insects of Manakudy estuary, Kanyakumari district. *Journal of Basic and Applied Biology*, 4, 91-97.
- Asri, L. N., Abdullah, N. A., Sulaiman, A., Asri, M. H. M., Norela, S., Satiman, E. M. F. E. N., Husin, S. M., Shukor, A. M., & Darbis, N. D. A. (2021). Abundance and species composition of synchronous flashing firefly at Sungai Rembau, Negeri Sembilan, Malaysia. *International Journal of Tropical Insect Science*, 41, 1095-1106. <https://doi.org/10.1007/s42690-020-00295-5>
- Asyraf, M. K. M., Nor'Aini, Y., & Suraiyati, R. (2013, October 29-31). Rivers, lakes, and swamps: Sustainable approach towards ecotourism. In *Proceedings of the 3rd Regional Conference on Tourism Research* (pp. 29-31). Langkawi, Malaysia.
- Atkins, V., Bell, D., Bowker, A., Charig, M., Crew, J., Dale, M., Hickmott, B., Payne, B., Pendleton, D., Pendleton, T., Robinson, M., Wollen, K., Woodell, B., & Tyler, J. (2017). The status of the glow-worm *Lampyris noctiluca* L. (Coleoptera: Lampyridae) in England. *Lampyrid*, 4, 20-35.
- Axmacher, J. C., Brehm, G., Hemp, A., Tünste, H., Lyaruu, H. V., Müller-Hohenstein, K., & Fiedler, K. (2009). Determinants of diversity in afro-tropical herbivorous insects (Lepidoptera: Geometridae): Plant

- diversity, vegetation structure or abiotic factors? *Journal of Biogeography*, 36(2), 337-349. <https://doi.org/10.1111/j.1365-2699.2008.01997.x>
- Balaman, Ş. Y. (2019). Modeling and optimization approaches in design and management of biomass-based production chains. In *Decision-making for Biomass-Based Production Chains* (pp. 185-236). Academic Press. <https://doi.org/10.1016/B978-0-12-814278-3.00007-8>
- Booth, J., Miller, R., McKee, B., & Leathers, R. (2000). Wind-induced bottom sediment resuspension in a microtidal coastal environment. *Continental Shelf Research*, 20(7), 785-806. [https://doi.org/10.1016/S0278-4343\(00\)00002-9](https://doi.org/10.1016/S0278-4343(00)00002-9)
- Chen, Y., & Seybold, S. J. (2014). Crepuscular flight activity of an invasive insect governed by interacting abiotic factors. *PLoS ONE*, 9(8), Article e105945. <https://doi.org/10.1371/journal.pone.0105945>.
- Cheng, S., Munian, K., Sek-Aun, T., Faidi, M. A., & Ishak, S. F. (2020). Mitochondrial DNA diversity and gene flow in Southeast Asian populations of the synchronously flashing firefly, *Pteroptyx tener* Olivier (Coleoptera: Lampyridae). *Oriental Insects*, 54(2), 175-196. <https://doi.org/10.1080/00305316.2019.1600594>.
- Corbett, C. A. (2007). Colored Dissolved Organic Matter (CDOM) Workshop summary. *Reports*. 2. https://digitalcommons.usf.edu/basgp_report/2
- Du, C., Chen, J., Jiang, L., & Qiao, G. (2020). High correlation of species diversity patterns between specialist herbivorous insects and their specific hosts. *Journal of Biogeography*, 47(6), 1232-1245. <https://doi.org/10.1111/jbi.13816>
- Edde, P. A. (2022). Field crop arthropod pests of economic importance. *Academic Press*. <https://doi.org/10.1016/B978-0-12-818621-3.00002-1>
- Faudzi, R., Abas, A., Othman, N. W., & Mazlan, S. M. (2021). Effect of water quality on the abundance of firefly populations at Cherating River, Pahang, Malaysia. *EnvironmentAsia*, 14(1), 69-79. <https://doi.org/10.14456/ea.2021.8>
- Faust, L. F. (2004). Fireflies as a catalyst for science education. *Integrative and Comparative Biology*, 44(3), 264-265. <https://doi.org/10.1093/icb/44.3.264>
- Fazal, S., Manzoor, F., & Abdul-Sattar, A. (2012). Impact of abiotic factors on insect diversity of at Lawrence Garden, Lahore. *Pakistan Journal of Science*, 64(2), 127-132.
- Feng, Z., Su, B., Xiao, D. D., & Ye, L. Y. (2017). Study on pH value and its variation characteristics of the main rivers into Dianchi lake under the anthropogenic and natural processes, Yunnan, China. *Journal of Information and Optimization Sciences*, 38(7), 1197-1210. <https://doi.org/10.1080/02522667.2017.1367501>
- Fondriest Environmental. (2014). Conductivity, salinity and total dissolved solids. <https://www.fondriest.com/environmental-measurements/parameters/waterquality/conductivity-salinity-tds/>
- Fu, X., Nobuyoshi, O., Vencl, F. V., & Lei, C. (2005). Structure, behavior, and the life cycle of an aquatic firefly, *Luciola substriata*, in China. *The Canadian Entomologist*, 137, 83-90. <https://doi.org/10.4039/n04-022>.
- Fu, X., Nobuyoshi, O., Vencl, F. V., & Lei, C. (2006). Life cycle and behaviour of the aquatic firefly *Luciola leii* (Coleoptera: Lampyridae) from Mainland China. *Canadian Entomologist*, 138(6), 860-870. <https://doi.org/10.4039/n05-093>

- Gatehouse, A. G. (1997). Behavior and ecological genetics of wind-borne migration by insects. *Annual Review of Entomology*, 42(1), 475-502. <https://doi.org/10.1146/annurev.ento.42.1.475>
- Gillett, D., & Marchiori, A. (2019). A low-cost continuous turbidity monitor. *Sensors*, 19(14), 3039. <https://doi.org/10.3390/s19143039>
- Hallmann, C. A., Sorg, M., Jongejans, E., Siepel, H., Hofland, N., Schwan, H., Stenmans, W., Müller, A., Sumser, H., Hörrren, T., Goulson, D., & de Kroon, H. (2017). More than 75 percent decline over 27 years in total flying insect biomass in protected areas. *PLoS one*, 12(10), Article e0185809. <https://doi.org/10.1371/journal.pone.0185809>
- Hazmi, I. R., & Sagaff, S. A. S. (2017). Fireflies population and the aquaculture industry (Coleoptera: Lampyridae) of the Sungai Sepetang, Kampung Dew, Perak, Malaysia. *Serangga*, 22(2), 217-237.
- Ho, J. Z., Chiang, P. H., Wu, C. H., & Yang, P. S. (2010). Life cycle of the aquatic firefly *Luciola ficta* (Coleoptera: Lampyridae). *Journal of Asia-Pacific Entomology*, 13(3), 189-196. <https://doi.org/10.1016/j.aspen.2010.03.007>
- Idris, N. S., Mustapha, M. A., Sulaiman, N., Khamis, S., Husin, S. M., & Darbis, N. D. A. (2021). The dynamics of landscape changes surrounding a firefly ecotourism area. *Global Ecology and Conservation*, 29, Article e01741. <https://doi.org/10.1016/j.gecco.2021.e01741>
- Jaikla, S., Lewis, S. M., Thancharoen, A., & Pinkaew, N. (2020). Distribution, abundance, and habitat characteristics of the congregating firefly, *Pteroptyx Olivier* (Coleoptera: Lampyridae) in Thailand. *Journal of Asia-Pacific Biodiversity*, 13(3), 358-366. <https://doi.org/10.1016/j.japb.2020.05.002>
- Jusoh, W. F. A. W., Hashim, N. R., & Ibrahim, Z. Z. (2010a). Firefly distribution and abundance on mangrove vegetation assemblages in Sepetang estuary, Peninsular Malaysia. *Wetlands Ecology and Management*, 18(3), 367-373. <https://doi.org/10.1007/s11273-009-9172-4>.
- Jusoh, W. F. A. W., Hashim, N. R., & Ibrahim, Z. Z. (2010b). Distribution and abundance of *Pteroptyx* fireflies in Rembau-Linggi estuary, Peninsular Malaysia. *Environment Asia*, 3(special issue), 56-60.
- Jusoh, W. F. A., Hashim, N. R., & Wong, C. H. (2011). Zonation of firefly species and their display trees along Kerteh River, Terengganu. *Serangga*, 16(2), 59-66.
- Kaiser, L., Ode, P., van Nouhuys, S., Calatayud, P. A., Colazza, S., Cortesero, A. M., Thiel, A., & van Baaren, J. (2017). The plant as a habitat for entomophagous insects. *Advances in Botanical Research*, 18, 179-223. <https://doi.org/10.1016/bs.abr.2016.09.006>
- Keinath, S., Onandia, G., Griesbaum, F., & Rödel, M. O. (2023). Effects of urbanization, biotic and abiotic factors on aquatic insect diversity in urban ponds. *Frontiers in Ecology and Evolution*, 11, Article 1121400. <https://doi.org/10.3389/fevo.2023.1121400>
- Khoo, V., Nada, B., & Kirton, L. (2014, July 14-18). Conservation of the Selangor River population of *Pteroptyx tener* in Malaysia: Results of seven years of monitoring. In *International Firefly Symposium 2014*. Florida, USA.
- Khoo, V., Nada, B., Kirton, L. G., & Phon, C. K. (2012). Monitoring the population of the firefly *Pteroptyx tener* along the Selangor River, Malaysia for conservation and sustainable ecotourism. *Lampyrid*, 2, 162-173.

- Kirton, L. G., Nada, B., Tan, S. A., Ang, L. H., Tang, L. K., Hui, T. F., & Ho, W. M. (2006). The Kampung Kuantan firefly project: A preliminary assessment of the habitat requirements of *Pteroptyx tener* (Coleoptera: Lampyridae). *Highlights of FRIM's non IRPA projects. Forest Research Institute Malaysia, Malaysia*.
- Koken, M., Guzmán-Álvarez, J. R., Gil-Tapetado, D., Romo Bedate, M. A., Laurent, G., Rubio, L. E., Comas, S. R., Wolfler, N., Verfaillie, F., & De Cock, R. (2022). Quick spreading of populations of an exotic firefly throughout Spain and their recent arrival in the French Pyrenees. *Insects*, *13*(2), Article 148.
- Kokila, R., Balasubramanian, B., Meenambigai, K., Alagirisamy, K., Kumar, A., Kamyab, H., Ydav, K. K., & Nareshkumar, A. (2021). A GIS-based tool for the analysis of the distribution and abundance of *Chilo sacchariphagus indicus* under the influence of biotic and abiotic factors. *Environmental Technology & Innovation*, *21*, Article 101357. <https://doi.org/10.1016/j.eti.2021.101357>
- Lewis, S. M., Wong, C. H., Owens, A., Fallon, C., Jepsen, S., Thancharoen, A., Wu, C., De Cock, R., Novák, M., López-Palafox, T., Khoo, V., & Reed, J. M. (2020). A global perspective on firefly extinction threats. *BioScience*, *70*(2), 157-167. <https://doi.org/10.1093/biosci/biz157>
- Lloyd, J. E. (2008). Fireflies (Coleoptera: Lampyridae). In J. L. Capinera (Ed.), *Encyclopedia of Entomology* (pp. 1429–1452). Springer. <https://doi.org/10.1007/0-306-48380-7>
- Lubis, F. I., Agustin, I., Putra, G. I. S., Mailisa, I., Taufiq, Rahmah, S., Damayani, C. P. & Rudiansyah (2023). Male inflorescences, natural enemies, and climate as biotic and abiotic factors on population *Elaeidobius kamerunicus* at three soil types. In *IOP Conference Series: Earth and Environmental Science* (Vol. 1208, No. 1, p. 012007). IOP Publishing. <https://doi.org/10.1088/1755-1315/1208/1/012007>
- Mahadimenakbar, M. D., Jeperi, S. R., Fiffy Hanisdah, S., & Bagul, A. H. B. P. (2018). Notes on congregating fireflies (Coleoptera, Lampyridae) of Binsulok River, Sabah. *Journal of Tropical Biology and Conservation*, *15*, 155-162.
- Malavasi, M. (2020). The map of biodiversity mapping. *Biological Conservation*, *252*, Article 108843. <https://doi.org/10.1016/j.biocon.2020.108843>.
- , J. V., & Liebherr, J. K. (2009). Coleoptera:(beetles, weevils, fireflies). In *Encyclopedia of insects* (pp. 183-201). Academic Press. <https://doi.org/10.1016/B978-0-12-374144-8.00062-X>.
- Mileti, F. A., Russo, D., Fraissinet, M., Langella, G., Ferraro, G., & Terribile, F. (2024). Supporting the planning and management of biodiversity through the development of a geospatial decision support system. *Land Degradation & Development*, *35*(5), 1837-1849. <https://doi.org/10.1002/ldr.5024>
- Moran, S. (2018). *An applied guide to water and effluent treatment plant design*. Elsevier. <https://doi.org/10.1016/B978-0-12-811309-7.00023-0>
- Nada, B., & Ballantyne, L. A. (2018). A new species of *Pygoluciola* Wittmer with unusual abdominal configuration, from lowland dipterocarp forest in peninsular Malaysia (Coleoptera Lampyridae: Luciolinae). *Zootaxa*, *4455*(2), 343-362. <https://doi.org/10.11646/zootaxa.4455.2.5>
- Norela, S., Loo, M. C., & Abdullah, M. (2017). Association between the firefly population and some biotic and abiotic factors along the Sungai Sepetang river banks at Kampung Dew. *Malayan Nature Journal*, *69*(3), 110-118.

- Obeidavi, Z., Rangzan, K., Kabolizade, M., & Mirzaei, R. (2019). A web-based GIS system for wildlife species: A case study from Khouzesan Province, Iran. *Environmental Science and Pollution Research*, 26(16), 16026-16039. <https://doi.org/10.1007/s11356-019-04616-1>
- Obilor, E. I., & Amadi, E. C. (2018). Test for significance of Pearson's correlation coefficient. *International Journal of Innovative Mathematics, Statistics & Energy Policies*, 6(1), 11-23.
- Ohba, N., & Wong, C. H. (2004). External morphology and ecological study of the firefly, *Pteroptyx tener* at Kampong Kuantan, Selangor, Malaysia. *Science Report of Yokosuka City Museum*, 51, 1-33.
- Ozsahin, E., Ozdes, M., Smith, A. C., & Yang, D. (2022). Remote sensing and GIS-based suitability mapping of termite habitat in the African Savanna: A case study of the Lowveld in Kruger national park. *Land*, 11(6), Article 803. <https://doi.org/10.3390/land11060803>
- Palmer, T. A., Montagna, P. A., & Kalke, R. D. (2008). Benthic indicators of the initial effect of opening a channel. *Environmental Bioindicators*, 3(3-4), 205-206. <https://doi.org/10.1080/15555270802551776>
- Paramasivam, C. R. (2019). Merits and demerits of GIS and geostatistical techniques. In V. Senapathi, P. M. Viswanathan & S. Y. Chung (Eds.), *GIS and Geostatistical Techniques for Groundwater Science Book* (pp. 17-21). Elsevier. <https://doi.org/10.1016/B978-0-12-815413-7.00002-X>
- Peng, J., Kumar, K., Gross, M., Kunetz, T., & Wen, Z. (2020). Removal of total dissolved solids from wastewater using a revolving algal biofilm reactor. *Water Environment Research*, 92(5), 766-778. <https://doi.org/10.1002/wer.1273>
- Poukin, E., Mahadimenakbar, M. D., & Mohamed, M. (2023) The seasonal monsoon variations and the climatic effects on the abundance of fireflies (Coleoptera: Lampyridae) at Klias River, Beaufort, Sabah, East Malaysia. *Serangga*, 28(2),78-97.
- Prasertkul, T. (2018). Characteristics of *Pteroptyx* firefly congregations in a human dominated habitat. *Journal of Insect Behavior*, 31(4), 436-457. <https://doi.org/10.1007/s10905-018-9687-8>
- Rabha, M. M., Sharma, U., & Barua, A. G. (2021). Light from a firefly at temperatures considerably higher and lower than normal. *Scientific Reports*, 11(1), Article 12498. <https://doi.org/10.1038/s41598-021-91839-3>
- Reed, J. M., Nguyen, A., Owens, A. C., & Lewis, S. M. (2020). Linking the seven forms of rarity to extinction threats and risk factors: An assessment of North American fireflies. *Biodiversity and Conservation*, 29, 57-75. <https://doi.org/10.1007/s10531-019-01869-7>
- Riley, W. B., Rosa, S. P., & da Silveira, L. F. L. (2021). A comprehensive review and call for studies on firefly larvae. *PeerJ*, 9, Article e12121. <https://doi.org/10.7717/peerj.12121>
- Robertson-Bryan, I. (2004). *pH requirements of freshwater aquatic life* (pp. 1-13). Technical Memorandum, Robertson Bryan, Inc.
- Rocchini, D., Boyd, D. S., Féret, J. B., Foody, G. M., He, K. S., Lausch, A., Nagendra, H., Wegmann, M., & Pettorelli, N. (2016). Satellite remote sensing to monitor species diversity: Potential and pitfalls. *Remote Sensing in Ecology and Conservation*, 2(1), 25-36. <https://doi.org/10.1002/rse2.9>
- Roy, S., Barooah, A. K., Ahmed, K. Z., Baruah, R. D., Prasad, A. K., & Mukhopadhyay, A. (2020). Impact of climate change on tea pest status in northeast India and effective plans for mitigation. *Acta Ecologica Sinica*, 40(6), 432-442. <https://doi.org/10.1016/j.chnaes.2019.08.003>

- Saalidong, B. M., Aram, S. A., Otu, S., & Lartey, P. O. (2022). Examining the dynamics of the relationship between water pH and other water quality parameters in ground and surface water systems. *PlosOne*, 17(1), Article e0262117. <https://doi.org/10.1371/journal.pone.0262117>
- Sartsanga, C., Swatdipong, A., & Sriboonlert, A. (2018). Distribution of the fireflygenus *Pteroptyx Olivier* and a new record of *Pteroptyx asymmetria* Ballantyne (Coleoptera: Lampyridae: Luciolinae) in Thailand. *The Coleopterists Bulletin*, 72(1), 171-183. <https://doi.org/10.1649/0010-065X-72.1.171>
- Shahara, A., Nura, A. M. R., Maimon, A., & Norela, S. (2017). Assessment of firefly abundance at a new ecotourism site of Sungai Bernam, Selangor, Malaysia. *Malayan Nature Journal*, 69(2), 67-74.
- Smith, D., & Davis-Colley, R. (2001). Turbidity suspended sediment and water clarity. *Journal of the American Water Resources Association*, 37, 1085-1101. <https://doi.org/10.1111/j.1752-1688.2001.tb03624.x>
- Stevenson, M., & Bravo, C. (2019). Advanced turbidity prediction for operational water supply planning. *Decision Support Systems*, 119, 72-84. <https://doi.org/10.1016/j.dss.2019.02.009>
- Suzuki, J., Imamura, M., Nakano, D., Yamamoto, R., & Fujita, M. (2018). Effects of water turbidity and different temperatures on oxidative stress in caddisfly (*Stenopsyche marmorata*) larvae. *Science of the Total Environment*, 630, 1078-1085. <https://doi.org/10.1016/j.scitotenv.2018.02.286>
- Thancharoen, A. (2012). Well managed firefly tourism: A good tool for firefly conservation in Thailand. *Lampyrid*, 2, 142-148.
- Tokan, M. K., Imakulata, M. M., Neolaka, Y. A., & Kusuma, H. S. (2018). Species diversity and vertical distribution of arboreal organisms on the Paradiso mangrove environment of Kupang Bay, East Nusa Tenggara, Indonesia. *Asian Journal of Agriculture and Biology*, 6(4), 535-542.
- Tu, T. T., & Hoang, H. Y. (2023). Applications of Geographic Information System (GIS) in environmental management. *Scientific Collection*, (154), 397-402.
- Turney, S. (2022). *Pearson correlation coefficient (r): Guide & examples*. Scribbr. correlation-coefficient/.
- Usener, J. L., & Cognato, A. I. (2005). Patterns of mitochondrial diversity among desert firefly populations (Lampyridae: *Microphotus octarthrus* Fall). *The Coleopterists Bulletin*, 59(3), 361-367. <https://doi.org/10.1649/796.1>
- Van Swaay, C., van Strien, A., Harpke, A., Fontaine, B., Stefanescu, C., Roy, D., Kühn, E., Önuao, E., Regan, E., Švitra, G., Prokofev, I., Heliölä, J., Settele, J., Pettersson, L., Botham, M., Musche, M., Titeux, N., Cornish, N., Leopold, P., ... & Warren, M. (2013). *The European grassland butterfly indicator: 1990–2011*. EEA Technical Reports. <https://doi.org/10.2800/89760>
- Vaz, S., Guerrazzi, M. C., Rocha, M., Faust, L., Khattar, G., Mermudes, J., & da Silveira, L. F. L. (2021). On the intertidal firefly genus *Micronaspis Green*, 1948, with a new species and a phylogeny of *Cratomorphini* based on adult and larval traits (Coleoptera: Lampyridae). *Zoologischer Anzeiger*, 292, 64-91. <https://doi.org/10.1016/j.jcz.2021.01.00>
- Vaz, S., Manes, S., Gama-Maia, D., Silveira, L., Mattos, G., Paiva, P. C., Figueirido, M., & Lorini, M. L. (2021). Light pollution is the fastest growing potential threat to firefly conservation in the Atlantic Forest hotspot. *Insect Conservation and Diversity*, 14(2), 211-224. <https://doi.org/10.1111/icad.12481>

- Wang, Y., Fu, X., Lei, C., Jeng, M. L., & Nobuyoshi, O. (2007). Biological characteristics of the terrestrial firefly *Pyrocoelia pectoralis* (Coleoptera: Lampyridae). *The Coleopterists Bulletin*, 61(1), 85-93. <https://doi.org/10.1649/907.1>
- Wong, C. H. (2022). *Congregating Firefly Zones (CFZ) in Malaysia: Conservation of mangrove congregating fireflies*. (MNS Conservation Publication No. 20). Malaysian Nature Society.
- Wong, C. H., & Yeap, C. A. (2012). Conservation of congregating firefly zones (CFZs) in Peninsular Malaysia. *Lampyrid*, 2, 174-187.
- Yahya, N., Idris, I., Rosli, N. S., & Bachok, Z. (2020). Mangrove-associated bivalves in Southeast Asia: A review. *Regional Studies in Marine Science*, 38, Article 101382. <https://doi.org/10.1016/j.rsma.2020.101382>
- Zhou, W. (2021). GIS for earth sciences. In D. Alderton & S. A. Elias (Eds.), *Encyclopedia of Geology* (pp. 281-293). Academic Press. <https://doi.org/10.1016/B978-0-08-102908-4.00018-7>

Secure Data Aggregation and Transmission System for Wireless Body Area Networks Using Twofish Symmetric Key Generation

Insozhan Nagasundharamoorthi^{1*}, Prabhu Venkatesan² and Parthasarathy Velusamy³

¹Department of Computer Science & Engineering, VelTech Multi Tech Dr. Rangarajan Dr. Sakunthala Engineering College, Tamil Nadu 600062, India

²Department of Electronics and Communication Engineering, VelTech Multi Tech Dr. Rangarajan Dr. Sakunthala Engineering College, Tamil Nadu 600062, India

³Department of Computer Science Engineering, Karpagam Academy of Higher Education (Deemed to be University), Tamil Nadu 641021, India

ABSTRACT

Nowadays, Wireless Body Area Networks (WBANs) are mostly used in the healthcare industry. They represent a portable, inexpensive network that exhibition adaptability. The data developed using WBAN devices is vulnerable to transmission-related internal and external attacks; nevertheless, this vulnerability arises due to resource restrictions; by employing data aggregation technologies to conduct statistical analyses of medical data while protecting patient privacy, medical professionals can enhance the precision of diagnoses and assist medical insurance firms in selecting optimal plans for their clients. Maintaining the confidentiality and integrity of sensitive health information becomes more stimulating at the stages of aggregation and transmission due to security issues. This study proposes a novel method, Twofish Symmetric Key Generation (TFSKG), combined into a Secure Data Aggregation (SDA) and transmission system intended for WBANs. The Twofish technique is animatedly employed to make the secure symmetric keys chosen for its robust encryption capabilities. These keys are used to encrypt and decrypt aggregated health data through transmission. The proposed TFSKG-SDA method implements effective algorithms for aggregating data to safeguard end-to-end privacy and preserve data accuracy while

reducing bandwidth consumption. Thus, for improved performance, an innovative genetic algorithm for data security is presented in this study. This paper introduces TFSKG-SDA, a system that, by employing rigorous simulation testing, enhances security protocols, resistance against recognized threats, and data transmission

ARTICLE INFO

Article history:

Received: 07 February 2024

Accepted: 01 August 2024

Published: 25 October 2024

DOI: <https://doi.org/10.47836/pjst.32.6.25>

E-mail addresses:

insozhann@gmail.com (Insozhan Nagasundharamoorthi)

prabhu.cvj@gmail.com (Prabhu Venkatesan)

sarathy.vp@gmail.com (Parthasarathy Velusamy)

* Corresponding author

efficacy in the context of resource-constrained WBANs. We assess the encryption strength, computational cost, and communication efficiency of the TFSKG- SDA method to prove its significance to real-world healthcare applications.

Keywords: Data privacy, medical data, secure data aggregation, transmission system, Twofish symmetric key generation, wireless body area network

INTRODUCTION

The development of technology for wireless communication in recent years has transported unique ways that incorporate wireless networking and modern healthcare monitoring (Salem et al., 2020). Significant progress in healthcare has been made possible due to these growths. WBANs are advanced for personalized treatment, real-time monitoring of health, and analysis. The transmission system is vital to WBAN, as it simplifies the dependable and efficient transfer of physical data within the human body. Wireless Body Area Networks (WBAN) make it easy for small, energy-efficient sensor nodes to communicate with one another and the rest of the human body with the help of transmission technology. This dangerous network of sensor nodes is essential for the quick and correct delivery of health-related data to researchers, doctors, and patients. Repeated assembly of important health comprehensions like temperature, heart rate, and other physical parameters facilitates the unrestricted exchange of serious information. Because of these aspects' substantial impact on data transmission latency, energy consumption, and reliability, researchers in this area have focused on transmission system design and efficiency.

Van Dam presented the WBAN conception in 2001 as a result of progress in low-energy devices and the Internet of Things (IoT) (<https://www.geeksforgeeks.org/wireless-body-area-network/>). Biosensor nodes devoted to the human body should be used in the WBAN network to enhance patient care and overall life excellence. Combining biosensor–implanted nodes may offer physical data, including blood pressure, blood glucose, ECG and EEG parameters. With technical development, the WBAN has become a vital implement for slightly monitoring patients' health. The IoT simplifies the sample collection, storage, processing, and transmission of essential health data in hospital IT systems (Tseng et al., 2019). Medical devices using wireless networks can track vital signs, such as respiration rate (RR) (Santos et al., 2020), pulse, heart rate (HR), temperature (T), blood pressure (BP) (Wang et al., 2019), electrocardiogram (ECG) (Abualsaud et al., 2018), electroencephalogram (EEG) (Hu et al., 2016), electromyogram (EMG) (He et al., 2017) an anonymous authentication for WBAN (Subramani et al., 2023) fog-based data aggregation Scheme for WBANs (Liu et al., 2021) and other health-related variables. These devices depend on healthcare cost management, public health, and hospital congestion expectations.

Physical indicator data transmitted overhead from wearables or biosensors is more probable to be overhead, interrupted, or altered during transmission because the data is

transmitted across open channels prior to data aggregation. Additionally, manipulated health-related data may cause clinicians to make incorrect conclusions. Worse, it could result in medical mishaps that deteriorate a patient's condition. If health insurance companies colluded to increase premiums, the patient would suffer. A person looking for coverage may allow many insurance providers to review their medical information to obtain the best possible health insurance rate. For this reason, the patient may want access to the sensitive data gathered by medical sensors to be restricted to authorized individuals and anonymous to one another. As a result, preserving patient privacy when aggregating medical data while achieving anonymity across multiple approved recipients is crucial and challenging.

The issues of fine-grained access, multiple recipient anonymity, and data privacy aggregation can currently be solved using a variety of cryptographic algorithms. However, these solutions only address a fraction of these issues and do not solve all three simultaneously. Two viable options to address the three security concerns in WBAN mentioned above are attribute-based encryption (Hu et al., 2016) and broadcast encryption. However, these techniques typically involve lengthy ciphertexts, private keys, public parameters, and some laborious processes. IoT body sensors and other low-energy wearable devices are not suited for many attribute-based encryption methods and broadcast encryption techniques now in use. On the other hand, more problems with efficiency or data security occur when these methods are coupled with data aggregation. For example, complex computations can lead to communication latency problems and recipient information may be exposed due to attributes in attribute-based encryption systems, among other issues.

The proposed TFSKG-SDA system is important as it provides a robust encryption framework that protects the security and integrity of patient information while preventing illegal access and modification. Utilizing Twofish, a well-known cryptographic technique known for its strength and dependability, the system generates a secure communication channel across wireless body area networks, promoting confidence and compliance with severe privacy rules. In addition, the system's improved data aggregation approaches progress network performance, permitting more accurate and timely medical data processing. Lastly, this new explanation not only progresses the security of wireless healthcare systems but also assists in better patient care outcomes by allowing the safe and fast transmission of essential medical information.

The primary contribution to this study is:

- To develop a novel method to overcome these difficulties by developing the combination of Twofish Symmetric Key Generation (TFSKG) into a Secure Data Aggregation (SDA) and transmission system established for WBANs
- Secure symmetric keys can be generated by dynamically employing the Twofish algorithm, renowned for its robust encryption capabilities. These keys are crucial

for transferring aggregated health data securely because they provide encryption and decryption.

- The proposed system uses outstanding data aggregation algorithms to reduce bandwidth usage without sacrificing data accuracy. Through rigorous simulations and performance evaluations, TFSKG-SDA improves security measures, resilience against common attacks, and data transmission efficiency in the resource-constrained setting of WBANs
- Assessing the TFSKG-SDA system's encryption strength, computational overhead, and communication efficiency proves its applicability to practical healthcare applications.

LITERATURE SURVEY

Zhong et al. (2022) conducted extensive and in-depth research on the demands and challenges of WBANs. They focused on WBAN standards and issues after first carefully examining WBAN applications. An original aspect of the article was its investigation of WBAN data transfer standards and technology. A brief discussion of the significance, features, and mitigation of energy usage in the WBAN was provided. The article is overly cursory, and the mention of security and privacy issues is one of its shortcomings. By implementing artificial intelligence algorithms and protocols that progress the speed and lower the energy consumption of the WBAN, this study seeks to address this gap. It also categorizes dissimilar types of attacks and highlights common security problems in WBANs.

Dynamic capability testing in numerous WBAN scenarios was given by Thippun et al. (2023). The use of IEEE 802.15.4 low-power sensor nodes in establishing a WBAN allowed this to be achieved. The experimental results show that the packet delivery ratio (PDR), which measures the reliability of WBAN connections, is affected by several significant elements. The findings demonstrate that the diverse environment testbed can impact network performance for WBAN data transmission. The study recommends that to achieve a Packet Delivery Ratio (PDR) of more than 90% and excellent network reliability in all test situations, a packet interval length longer than 15 ms is essential.

Azees et al. (2021). While protecting patients' and physicians' privacy, the recommended anonymous authentication technique aids in confirming the credibility of both parties. Although cryptographic encryption systems like AES and DES guarantee privacy, the challenges related to key sharing and key size significantly hinder the achievement of suitable security levels. Therefore, associated with other existing encryption algorithms, this study's efficient affine cipher-based encryption method needs a reduced key size and proposes a high level of privacy. To ensure its suggestions provide more protection, the security analysis of the recommended work shows how strong its security is against a variation of harmful security risks. For WBAN with limited resources, Subramani et al.

(2022) provide a computationally efficient privacy-preserving anonymous authentication technique. It also protects sensor physical security and biological information (BI) confidentiality and provides WBAN users conditional privacy.

With the energy constraints of tiny wireless sensors in mind, Wang et al. (2020) generated a physiological data transmission system that is dependable and efficient. They consider a particular WBAN scenario aimed at building an adaptive power control system and allotting time slots to improve total energy efficiency for performing health monitoring duties. They used a Markov decision process (MDP) to express the maximizing problem with latency and the energy budget restrictions of the sensors. According to the random oracle model, Kumar (2020) established the security of the anonymous authentication technique for wireless body area networks. Here, we cryptanalyze this system and develop an attack model that illustrates a key replacement assault that preserves client anonymity by having the adversary substitute a user's public key with a predetermined value. As a result, this method is unreliable and insufficient for creating a safe wireless band network.

Kaleem and Devarajan (2023) proposed WBAN utilizing data transmission techniques based on prediction. This method uses anticipated rather than actual sensor values while maintaining the same level of data quality. The quantity of data transferred between the base station and sensor nodes is being minimized. It is still very difficult to accurately forecast results within a given error margin. Most of the time, the base station will adjust the transmission settings using a prediction model, lowering the quantity of data provided to the sink. Despite having a lower computing cost and a faster recall path, this model performs better than its predecessors.

Mehmood et al. (2020) suggested a communication method based on trust to guarantee the dependability and confidentiality of WBAN. A cooperative communication approach guarantees dependability and a cryptography method protects privacy. For IoT devices, Mathews and Jose (2024) proposed a number of lightweight cryptographic (LWC) protocols and offered a thoughtful investigation into present ubiquitous ciphers. Also, the paper evaluates the security of numerous newly proposed hybrid homomorphic LWC and lightweight (LW) block ciphers.

In this work, Khan et al. (2022) proposed an actual and safe architecture for ABEs by outsourcing compound encryption and decryption tasks. We present a workable substitute for expensive pairing procedures using elliptic curve scalar point multiplication as the core technology for Attribute-Based Encryption (ABE). It also supports the verifiability of outsourced medical data and attribute/user revocation. The recommended technique using the selective-set security model is considered secure under the elliptic curve decisional Diffie-Hellman (ECDDH) assumption. Moreover, this method is appropriate and effective for access control in eHealth smart societies. This efficiency is proven by performance calculations and top scores obtained using the fuzzy logic-based EDAS (Evaluation based on Distance from Average Solution) approach.

The Mobile Agent-Based Data Aggregation (DA) method for WBANs was established by Mehmood et al. (2022) and is a dependable energy conservation technique. Cluster heads are appointed when the network has been separated into groups according to the approach. The base station then sends a mobile agent to collect data from these cluster heads. If problems compromise network performance with the present route, the scheme swiftly progresses to a backup approach.

Two software agents are introduced in a fog node by Mohapatra et al. (2022): the Software agent for Blockchain Formation and Monitoring (SAB), which implements a blockchain security framework, and the Software agent for Network Formation and Monitoring (SAN), which oversees and manages the Internet of Things device network. They use group key sharing with three different AES versions (128, 192, and 256) to enable encrypted communication within blockchain blocks. An approved IoT device uses a proof of work (PoW) based on AES 128 for block addition. Additionally, the blockchain uses SHA 256 for hashing. The experiment considers three systems, System 1, System 2, and System 3, with varying design parameter choices.

Shyja et al. (2023) discussed a link quality and energy effectual optimal clustering-multipath (LEOC-MP) system's primary goals are to ensure node-to-node link quality, extend network life, and compute high-performing cluster heads to ensure reliable multipath data transfer. This project was completed in three stages. First, an effective simplified clustering method for data collection from body sensors is obtainable based on an enhanced pelican optimization (ICO) algorithm. Numerous design restrictions are applied to node rank computation, energy efficiency, network quality, path loss, distance, and delay.

Kumar and Chand (2020) suggested creating a cutting-edge, publicly verifiable, secure, and effective cloud-based IoMT smart healthcare system. The system innovation secures data transfer via an escrow-free identity-based aggregate signcryption (EF-IDASC) approach, which is also suggested in this paper. The proposed EF-IDASC approach aggregates and encrypts medical data gathered from multiple implanted sensors on the patient's body. The data is then sent via a smartphone to a medical cloud server. Kumar and Chand (2021) created the identity-based anonymous authentication and key agreement (IBAACA) protocol for cloud-assisted WBANs to ensure user anonymity and enable mutual authentication. Based on the widely accepted computational Diffie-Hellman assumption and the random oracle model, our security analysis shows that this IBAACA approach is provably secure and satisfies the relevant security requirements.

Anh et al. (2023) developed multiple-input multiple-output (MIMO) systems based on a cell-free architecture incorporating multiple access points (APs) supporting numerous sensors simultaneously. They suggest a novel system model in which sensors are dispersed throughout the body and communicate directly with APs, as opposed to via a coordinator. The transmission power control method for uplink data development takes into account

minimizing interference generated by several sensors transmitting signals simultaneously to improve the system's spectrum efficiency.

Limitations of the Existing System

- The available bandwidth for communication in WBANs is frequently constrained, resulting in data transmission rate constraints. Transferring enormous amounts of data, such as high-resolution medical images or continuous streaming of high-frequency physiological signals, can be a considerable difficulty.
- The human body is a complex medium that can induce signal attenuation and interference. Tissues, organs, and bodily fluids can degrade signals and shorten the effective communication range. Furthermore, interference from nearby electronic devices and rival wireless networks might lower connection dependability.
- WBAN devices frequently operate on batteries, so energy consumption is an important consideration. The energy required for wireless data transmission is substantial, and finding the sweet spot between efficient energy use and dependable connection is no easy feat.
- Because the human body is always changing, so can the placement and movement of any devices implanted or connected to it. Due to its dynamic nature, assembly quality could fluctuate, leading to communication interruptions or decreased reliability, particularly in active or mobile environments.

MATERIALS AND METHODS

The proposed system model uses the combination of TFSKG-SDA and WBAN transmission. Twofish algorithm dynamically generated secure symmetric keys, well-known for its strong encryption capabilities. These keys ensure end-to-end confidentiality by encrypting and decrypting aggregated health data while it is transmitted. By using effective data aggregation techniques, the proposed method reduces bandwidth consumption without sacrificing data accuracy. Simulations and performance testing have displayed that our TFSKG-SDA solution improves data transmission efficiency, security, and resilience against common attacks in resource-constrained WBANs. There are practical healthcare uses for the TFSKG-SDA system, as displayed by an inspection of its computational overhead, communication efficiency, and encryption strength.

The proposed TFSKG-SDA system provides a robust encryption way to preserve the security and integrity of sensitive information, which is mainly important in healthcare applications. By employing Twofish, known for its powerful cryptographic properties, the explanation reduces the risks connected with data breaches. It progresses the efficiency of data aggregation processes, optimizing network speed while adhering to high-security values. The security and dependability of communication channels for transmitting medical

data are enhanced by this new method, suggestively improving the safety of wireless body area networks.

System Model

Our proposed TFSKG-SDA model uses four main dissimilar entities: trusted authority (TA), wearable devices, multiple data users (the receivers), and cloud server (CS). Figure 1 displays the proposed diagram.

(i) Trusted Authority:

Its responsibilities include launching the system overall, supplying data users with necessary authentication and organizational services, and offering wearables equipped with Internet of Things sensors.

(ii) Cloud Server:

Our system’s cloud server collects and stores data with ample storage capacity and robust processing power.

(iii) Wearable devices:

Wearable devices collect data in real-time by observing vital signs like heart rate and blood pressure using a network of Internet of Things (IoT) sensors. Doctors can then utilize the encrypted data for future diagnostic purposes by sending it to a server over the Internet.

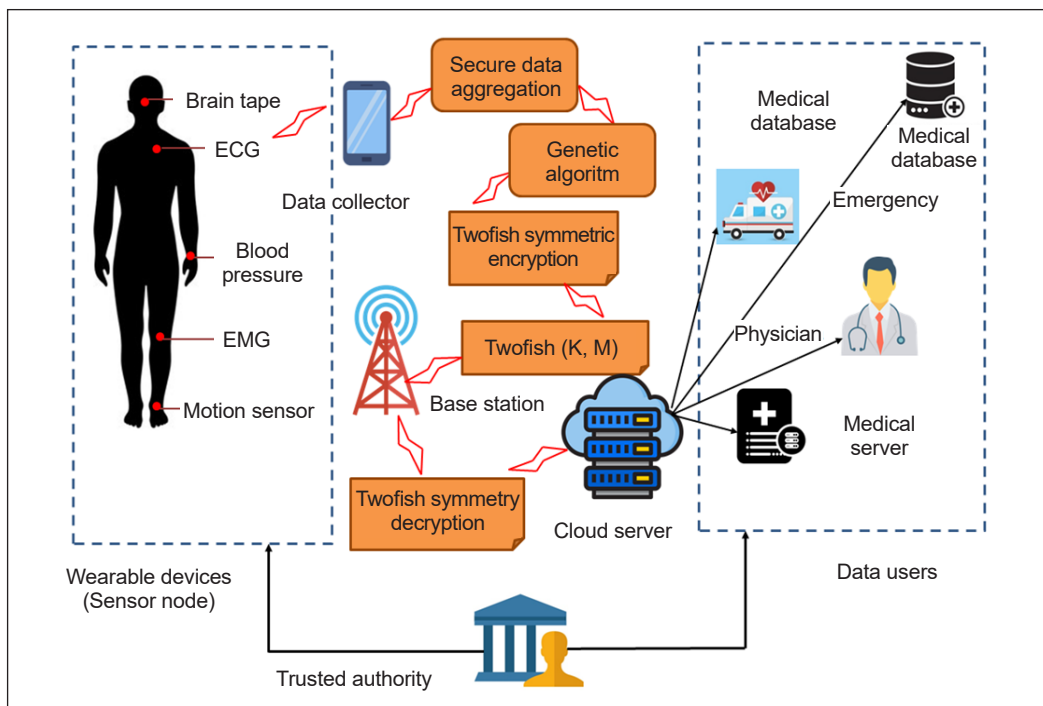


Figure 1. The proposed technique of TFSKG-SDA

(iv) Multiple Data Users:

They function as data recipients. Data users, such as doctors and medical facilities, receive the encrypted version of the patient's aggregated data from the cloud server for a specific duration. Subsequently, with the decryption key still in their possession, they retrieve the plaintext of this aggregated data.

System Configuration

A TA sets up the system's public parameters at this stage.

$pk \leftarrow Setup(1^k)$: The public key $pk = (po, PO, GP)$ for the entire system is retrieved by the trustworthy authority executing the Setup procedure by entering k , where $GP = \langle PO \rangle$ is an additive cyclic group of prime order po produced by a generator PO . The element H_0 was randomly selected for group G . Furthermore, it selects a cryptographic hash function

$H_1 : \{0,1\}^* \rightarrow Z_{po}$. In addition, it selects two random values $u_1, u_2 \in Z_{po}$ to compute $GP_1 = u_1 PO$ and $GP_2 = u_2 H_0$. Table 1 shows notations and descriptions of the proposed method.

Twofish Symmetric Key Generation

The National Institute of Standards and Technology's AES design standards follow the Twofish symmetric block cipher, which utilizes a single key and a predefined block configuration to process 128-bit input messages. There are three different key length options: 128 bits, 192 bits, or 256 bits. Because of its flexible form and sturdy keys, it stands out. It is fast on both hardware and software, efficient, and performs well across a range of systems. And lastly, it works well for stream ciphering (Zhang & Dong, 2022; Rane, 2016). The 16-iteration Feistel network is the basis of Twofish's main functionality. Before starting the input whitening procedure, Twofish divides the 128-bit plaintext into four 32-bit block words called W_0, W_1, W_2 , and W_3 . Subsequently, XOR combines each word with four additional 32-bit words (K_0, K_1, K_2 , and K_3). The outputs of the whitening procedure are given into the modules and F function (Apoorva, 2013). The Fixed Maximum Distance Separable (MDS) matrix and the Twofish directive function F conform to the same mathematical code. Each of the four S-boxes in this function has an 8-bit input, an 8-bit output, and five operational components. It also involves four dependent keys. 232

Table 1

Describes the main notations in the proposed method

Notations	Description
M_e	Message
C_t	The current time of sent message
$Sig(BS_n)$	Signature of Base station
h	Hash function
k_{id}	Sensor node's identity
PU_K	Public key
C_{kid}	A certificate was issued to identify the sensor node
c_e	Certificate expiration time

is added modularly to a simple 32-bit mixing process known as the pseudo-Hadamard transform. Twofish does further output whitening after 16 cycles.

As displayed in Figure 2, the XOR operation is replaced with a new operation in every cycle of the Twofish algorithm. This innovative approach involves the utilization of multi-state tables and dynamic block sizes, characterized by their intricate design and rapid retrieval speeds, leading to enhanced computational efficiency. The fundamental elements constituting the foundation of the

Twofish algorithm includes:

i. Feistel: The fundamental approach, initially introduced by Horst in the DES algorithm, can be employed to transform any function F into a permutation within a block cipher. This process involves generating two blocks from the input block, followed by the repeated execution of identical procedures.

ii. Confusion and Diffusion:

In 1949, Shannon introduced encryption methods that incorporate both confusion and diffusion. Confusion is introduced through the replacement approach, intensifying the complexity of the relationship between the ciphertext and the key to enhance the challenge of deciphering the plaintext. Also, diffusion employs the permutation approach (Geetha et al., 2022; Kareem et al., 2020) to elevate the statistical intricacy between the plaintext and ciphertext.

Algorithm 1

pseudocode for the Twofish algorithm

Pseudo code for Twofish algorithm:

- 1 Initialize:
Set the encryption algorithm="two fish"

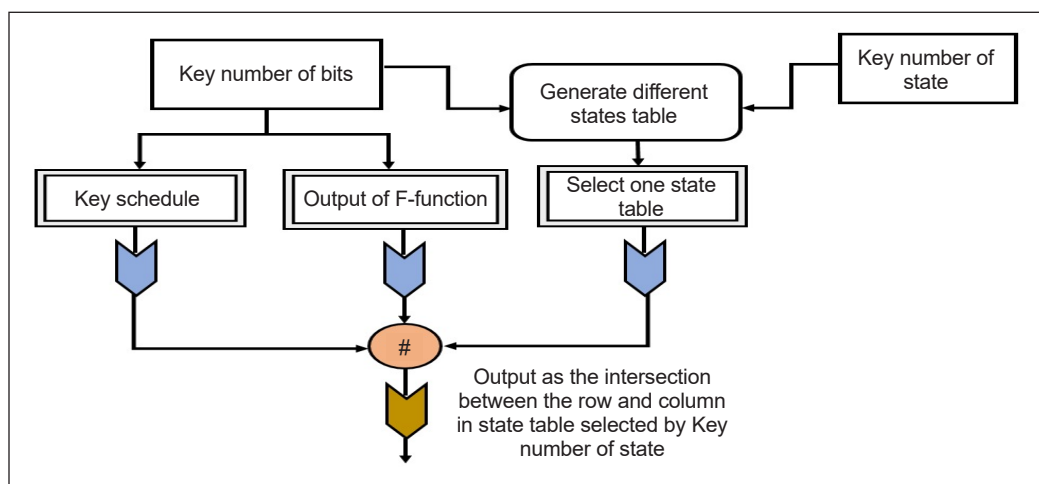


Figure 2. Workflow of the Twofish algorithm

```

crypt.put _Crypt Algorithm (“two fish”);
crypt.put _CipherMode (“ebc”);
// Electronic code block (EBC)
2 The length of the key can be 128,192,256.
Crypt.put _KeyLength (256);
3 Crypt.put _Padding scheme (0);
4 Crypt.put _Encoding Mode (“hex”);
5 String Hex =“000102030405060708090A0B0C0D0E0F”
Crypt.Set EncodedIV (Hex,”hex”);
6 String keyHex=00102030405060708090A0B0C0D0E0F1011112131415161
71819A1B1C1D1E1F
Crypt.SetEncodedKey (keyHex,”hex”);
7 Encrypt a string....
The input string is 44 ANSI characteristics (i.e.44 bytes),so
the output should be 48 bytes (a multiple of 16)
System.out.println (encStr);
8 Finally, decrypt:
String decStr =crypt.decryptStringENC (encStr);
System.out.println (decStr);

```

iii. Substitution Boxes (S-Box) and MDS Matrices: Driven by a table and with adjustable input and output sizes, the S-box functions as a non-linear replacement. An algorithm or a random technique can be used to generate it. Twofish uses two predetermined 8-by-8-bit permutations, including the necessary components, to generate four different S-boxes. A composite vector of 32 bits is formed through a linear mapping of two fields, ‘a’ and ‘b,’ with components expressed as $(a + b)$. This method is utilized to ascertain the MDS code for a specified field. The MDS matrix, a 4×4 transformation matrix, provides diffusion. Multiplication of four-byte vectors in the GF (28) matrix is achieved by the irreducible polynomial $x^4 + x^6 + x^5 + x^3 + 1$.

iv. Pseudo-Hadamard Transforms (PHT): The PHT encourages dispersion due to its inherent mixing capability. To illustrate, let us consider two inputs, denoted as ‘a’ and ‘b.’ The following is a description of the 32-bit PHT:

v. Whitening: It is crucial to employ XOR operations on plaintext and key components before and after the initial round to enhance the key’s defense against potential attacks.

Functions Used in Twofish

1. Function F. Function F is an important component that modifies the 128-bit plaintext post-whitening in the Twofish Feistel network. It is a significant and interdependent role.

Three important parameters—round number (r), determining subkey selection, and two words (P0, P1)—are requisite for properly executing this function. Before entering the g function, R1 undergoes an 8-bit left rotation, yielding T1, while R0 is directly fed into the g function to generate T0. Combining two words from the expanded key forms a Piling-up Hash Table (PHT) using the resulting outputs T0 and T1. Synopsis of the F function Equations 1 to 4 are as follows.

$$T_0 = g(R_0) \tag{1}$$

$$T_1 = g(ROL(R_1, 8)) \tag{2}$$

$$F_0 = (T_0 + T_1 + K_{2r+8}) \bmod 2^{32} \tag{3}$$

$$F_1 = (T_0 + 2T_1 + K_{2r+9}) \bmod 2^{32} \tag{4}$$

2. Function g. The fundamental component of the Twofish algorithm is its core function, ‘g,’ which is essential to organizing inputs into four bytes per word, each consisting of 32 bits. Subsequently, the S-box is employed to process each byte, and the MDS matrix combines the four S-box outputs, resulting in a 32-bit output. A brief explanation of the g function Equations 5 to 8 as follows.

$$x_i = \lfloor X / 2^{8i} \rfloor \bmod 2^8 \quad i = 0, \dots, 3 \tag{5}$$

$$y_i = s_i[x_i] \quad I = 0, \dots, 3 \tag{6}$$

$$\begin{pmatrix} z_0 \\ z_1 \\ z_2 \\ z_3 \end{pmatrix} = \begin{pmatrix} \square & \square & \square & \square \\ MDS \\ \square & \square & \square & \square \end{pmatrix} \cdot \begin{pmatrix} y_0 \\ y_1 \\ y_2 \\ y_3 \end{pmatrix} \tag{7}$$

$$Z = \sum_{i=0}^3 z_i \cdot 2^{8i} \tag{8}$$

Z represents the outcome of the function g, and s_i denotes the S-boxes influenced by the key. Performing addition in GF (2⁸) is equivalent to the exclusive OR (XOR) operation on the bytes. Thus, this can be considered the “inherent” mapping. Algorithm 1 shows the pseudocode for the Twofish algorithm.

Secure Data Aggregation

In this step, we will describe the operation of the suggested data aggregation system. A wearable implant gathers physiological data from the user and employs the

AHEncrypt method to generate a verified homomorphic ciphertext based on this data. $CT(M',T) \leftarrow AHEncrypt(pk,sk_w,M',T,PCL)$: Using the public parameters pk , the private key sk_w of the wearable device, the sensed data M' and time t , and the public key list PCL of the doctor users serving as receivers as inputs, the algorithm runs as follows:

- 1) It selects $k_r \in Z_p$ at random and computes $B_i = k_t.H_0 + sk_w.p_i$ for $p_i \in PCL$;
- 2) $p_i \in PCL$ creates a polynomial with a degree $|PCL| - 1$, specifically, Equation 9 relates to polynomial interpolation.

$$f_i(y) = \prod_{j=1, j \neq i}^{|PCL|} \frac{y - y_j}{y_i - y_j} = \sum_{j=0}^{|PCL|-1} b_{i,j} y_j \text{ mod } p \tag{9}$$

Where the number of doctor users' public keys in the PCL - is indicated by $y_i = H_1(sk_w, p_i)$ and $|PCL|$.

- 3) $f_i(y)$ are computed, after all. Once the necessary corrections are identified, these polynomial coefficients are employed in the computation process. Given Equation 10, this could be related to ciphertexts in cryptographic contexts.

$$CT_i = \sum_{j=1}^{|PCL|} b_{j,i} B_j \quad (i = 0, \dots, |PCL| - 1) \tag{10}$$

- 4) After that, it computes. U_1 and U_2 are the results of Equations 11 and 12, potentially representing an output value related to a cryptographic operation, computation, or message encoding.

$$U_1 = M'PO + k_r H_0 \tag{11}$$

$$U_2 = sk_w.M'.G_1 + H_0 + k_t + GP_2 \tag{12}$$

- 5) The ultimate homomorphic ciphertext generated by Equation 13.

$$CT(M, T) = (CT_0, \dots, CT_{|PCL|-1}, U_1, U_2) \tag{13}$$

In addition, Equation 14 shows for each CT_i .

$$CT_i = \sum_{j=1}^{|PCL|} b_{j,i} B_j = \sum_{j=1}^{|PCL|} b_{j,i} (k_t H_0 + sk_w.p_i) \tag{14}$$

$$= k_r \cdot \left[\sum_{j=1}^{|PCL|} b_{j,i} H_0 \right] + \left[sk_w \cdot \sum_{j=1}^{|PCL|} b_{j,i} p_i \right]$$

With a constant PCL receiver set, computing CT_i simply requires one addition and multiplication operation, as known from the CT_i computation method.

A wearable device requires real-time data observation and uploading to a cloud server. As such, ciphertexts $CT(M_j, j)$ will be sent to the cloud server when $j \in TimeIndex$ needs them. Afterward, the wearable device's data is kept on the cloud server as a Time Series Data Table.

Obtaining a patient's pathology data from time T_1 to time T_n is as simple as sending a request to a cloud server. In the given time range (T_1 to T_n), the cloud server must gather the sensed data from the wearable device using the approved aggregation technique.

Equations 15 to 18 show that it decodes the ciphertexts of the detected data $CT(M_1, T_1), \dots, CT(M_n, T_n)$ as $(CT_{i,0}, \dots, CT_{i|PCL|}, V_{i,1}, V_{i,2})$ for $i \in [1, n]$ after receiving them. The aggregate is then computed.

$$\mathcal{E}T_0 = \sum_{j=1}^n CT_{j,0} = a_{0,0} \sum_{j=1}^n B_{j,0} + \dots + a_{|PCL|,0} \sum_{j=1}^n B_{j|PCL|} \tag{15}$$

$$\mathcal{E}T_i = \sum_{j=1}^n CT_{j,i}, \quad i = \dots, |PCL| - 1 \tag{16}$$

$$\mathcal{U}_1 = \sum_{j=1}^n U_{j,1} = \sum_{j=1}^n M_j P + \sum_{j=1}^n k_j H_0 \tag{17}$$

$$\mathcal{U}_2 = \sum_{j=1}^n U_{j,2} = s \cdot \sum_{j=1}^n M_j G_1 + nH_0 + \sum_{j=1}^n k_j G_2 \tag{18}$$

The j -th ciphertext, B_j matches the B_i . Let us assume $M = \sum_{j=1}^n M_j$ and $K = \sum_{j=1}^n k_j$. The combined result then has the structure shown in Equation 19.

$$CT_{M,t[1,n]} = (\mathcal{E}T_0, \dots, \mathcal{E}T_{|PCL|-1}, \mathcal{U}_1, \mathcal{U}_2) \tag{19}$$

Data Protection Using Genetic Algorithm (GA)

The genetic algorithm (GA) is a well-known and widely used optimization method that draws inspiration from natural selection. By modeling the search for solution space after an environmental process, the GA takes into account the Darwinian theory of species evolution. Each member of a GA population—a chromosome—stands for a possible answer to the problem. The objective function serves to define the problem that is being solved. The value that symbolizes the quality of an individual is assigned to them based on how well they fit the objective function. One important metric is this number, which is called the individual's fitness. Highly esteemed people are more likely to be chosen for the next generation. The three operators in GAs are selection, crossover, and mutation. In selection, individuals are chosen based on their fitness values from the previous generation. In crossover, two individuals are chosen to exchange parts of themselves. Mutation involves randomly changing the values

of specific genes. In this paper, we study approaches to strengthen the data protection mechanisms of WBANs by including Genetic Algorithms (GAs) in its transmission system. Genetic algorithms have successfully optimized complicated problems by drawing on genetics and natural selection concepts. Data transmission efficiency and security in WBANs are the focus of this research, which aims to use their adaptive and evolutionary characteristics.

Mathematical Modelling of Genetic Algorithm

Equation 20 shows that W denotes the provisional data, updated in accordance with operational procedures, and x is the plaintext subjected to an XOR operation with k , which is the produced key's value.

$$W = x \oplus k \quad [20]$$

Equation 21 performed mutation values assigned to the indexes of the data array.

$$W_1 = M.T \quad [21]$$

W_1^{c1} and W_1^{c2} signifying four bits each form the entire 8 bits of data, equivalent to W_2 shown in Equation 22.

$$W_2 = W_1 C_1 \rightarrow W_1 \overset{\square}{C}_1 \quad [22]$$

The following step in Equation 23 shows that a crossover operation is carried out following the division of the data into two halves. When the values on the right and left sides are switched, W_3 results.

$$W_3 = W_1 \overset{\square}{C}_2 \rightarrow W_1 \overset{\square}{C}_1 \quad [23]$$

The W_3 short-term produced cipher is replaced with S-box values and assigned to W_4 shown in Equation 24.

$$W_4 = W_3 \rightarrow S_{box} \quad [24]$$

Now,

$$W_5 = W_4 \rightarrow A \min o_{Acid} \quad [25]$$

Additional amino acid coding values over the W_4 created data will equal to W_5 shown in Equation 25.

Using Equation 26, which recognizes "0" as "A" and "1" as "B," the resulting strings of A's and B's equal Z6, the ciphertext.

$$W_6 = W_5 \rightarrow String_{Mapping} \quad [26]$$

Transmission Security

Using the $HDec(pk, p_w, sk_w, CT_{M,T[1,n]})$ algorithm, the doctor user decrypts the aggregated findings $CT_{M,T[1,n]}$ that he receives from the cloud server.

$M \leftarrow AHDec(pk, p_w, sk_w, CT_{M,T[1,n]})$. The public parameters P_k wearable device, public key, p_w doctor user private key, sk_w and aggregated output $CT_{M,T[1,n]}$ are the inputs.

- 1) To compute $y_i = H(sk_i, p_w)$, it utilizes its private key sk_i .
- 2) After that, Equation 27 calculates W .

$$W = \text{CT}_0 + \sum_{j=1}^{|PCL|} y_i^j \text{CT}_j \tag{27}$$

- 3) The aggregated plaintext is then producing Equation 28.

$$M = \log_{PO}(\text{U}_1 - W + n.sk_i.p_w) \tag{28}$$

- 4) Finally, Equation 29 can be used to verify the retrieved plaintext's correctness.

$$\text{U}_2 = M.u_1.p_w + n.H_0 + u_2 \left(\sum_{j=1}^n k_j.H_0 \right) \tag{29}$$

Where $(\sum_{j=1}^n k_j.H_0) = W - n.sk_i.p_w$.

Advantages of the Proposed Method

- Twofish is a symmetric key block cypher recognized for its strong security. It proposes strong encryption. Because of its high level of encryption, data transmitted over a wireless body area network is protected from tampering and unauthorized access.
- TFSKG progresses key generation efficiency, which is important for secure communication in wireless band networks. By ensuring cryptographic keys are created swiftly and securely, efficient key generation lowers the possibility of key compromise and improves system security as a whole.
- Twofish has been considered to withstand a range of cryptographic attacks, such as linear and dissimilarity cryptanalysis. Because of this resistance, the security system is more resilient and complete, and it is more problematic for attackers to take advantage of encryption algorithm flaws.
- Within the WBAN, SDA lets efficient data aggregation. SDA lets information be analyzed and transmitted rapidly while preserving security and privacy by safeguarding that collective data is private and immutable

The choice of the TFSKG method for obtaining WBAN data is sufficient because of its many features. To initiate, Twofish is well-known for its strong security features, which

provide extreme encryption strength and resilience to different cryptographic attacks. Its symmetric key creation development authorizes data to only be decrypted by authorized parties with the exact key, increasing the secrecy and integrity of data transmission inside WBAN. Furthermore, Twofish is impeccable for WBANs due to its capability to handle short data packets regularly encountered in healthcare monitoring performances. Its nearer encryption and decryption methods reduce computing costs, declaring that real-time data transfer performance and latency are not negatively impacted, which is well-known in healthcare circumstances. Also, the evolutionary algorithm simplifies key management and distribution by regularly generating and growing cryptographic keys based on predefined parameters such as randomness and entropy. It lowers the overhead of manual key management, confirming smooth operation and scalability in large-scale WBAN allocations.

RESULTS

With a 2.4 GHz ISM band operation, 2 MHz bandwidth, and 0 dBm of transmission power, our wireless signal can be detected using IEEE 802.15.4 values. This setup was implemented so that our entire university could contribute to the RSSI dataset. Each of the four MICAz Mote modules has a 2.4 GHz ZigBee transceiver and an ATmega128L low-power MCU, and the housing can hold two AA 1.5-volt batteries. The individual has ten chip antennas placed thoughtfully on their left arm, right arm, chest, left finger, right front pocket, left front pocket, right hip pocket, and left hip pocket. Several simulation configurations are listed in Table 2 and were taken into consideration for the research.

A packet was sent from each antenna at intervals of 0.1 seconds during 150 seconds in each experimental session to measure the Received Signal Strength Indicators (RSSIs) at the remaining nine antennas. We used a combination of indoor and outdoor settings to experiment. The participant performed a variety of poses and movements, including sitting for 20 seconds, standing up for 20 seconds, standing motionless for 20 seconds, turning about for 20 seconds in a room, walking for 30 seconds in a hallway and 40 seconds outside, sitting down, and sitting motionless for 20 seconds outside. Genetic algorithm with Markov decision process (GA-MDP) (Roy et al., 2021), Multiple-input multiple-output (MIMO) (Anh et al., 2023), hospital-centered wireless body area network (HCWBAN) (Dangi et al., 2020), compensation adaptive sampling algorithm and resuscitation adaptive sampling algorithm (RASA -CASA) (Lee & Lee, 2017), convolutional neural network, and long-short-term memory network (CNN-LSTM) (Paulraj & Baburaj, 2023) are using the existing systems used in research.

Table 2
Analysed simulation parameters

Simulation metric	Values
Simulator	MATLAB R2020b
Type of channel	Wireless
Number of nodes	300
Simulation time	150 s
Energy	10 Joule
MAC type	802.5.4

Performance Metrics

The classifier’s performance is assessed statistically utilizing the subsequent performance evaluation metrics:

Efficiency Rate Analysis

The efficiency rate measures how efficiently and optimally data are transmitted within the network. It assesses the system’s ability to transmit information with minimal energy consumption, low latency, and high throughput, ensuring reliable communication between wearable devices within the body area network.

The efficiency rate analysis of the TFSKG-SDA Method is displayed in Figure 3 and Table 3, among other existing models. The graph shows how the efficiency rate was maintained while efficiency was increased using the WBAN approach. The efficiency rate for 50 nodes of the TFSKG-SDA model is 91.213%, while the efficiency rates for the MIMO, HCWBAN, GA-MDP, RASA-CASA, and CNN-LSTM models are 79.920%,

Table 3
Efficiency rate analysis for TFSKG-SDA method

Number of nodes	MIMO	HCWBAN	GA-MDP	RASA-CASA	CNN-LSTM	TFSKG-SDA
50	79.920	87.627	85.324	82.636	90.524	91.213
100	78.563	86.536	84.213	81.425	89.526	91.062
150	78.924	86.927	84.738	81.927	89.725	91.727
200	79.314	87.324	85.029	82.415	90.324	92.526
250	78.314	86.314	83.827	80.029	89.042	92.827
300	79.625	88.526	85.121	83.627	90.121	92.313

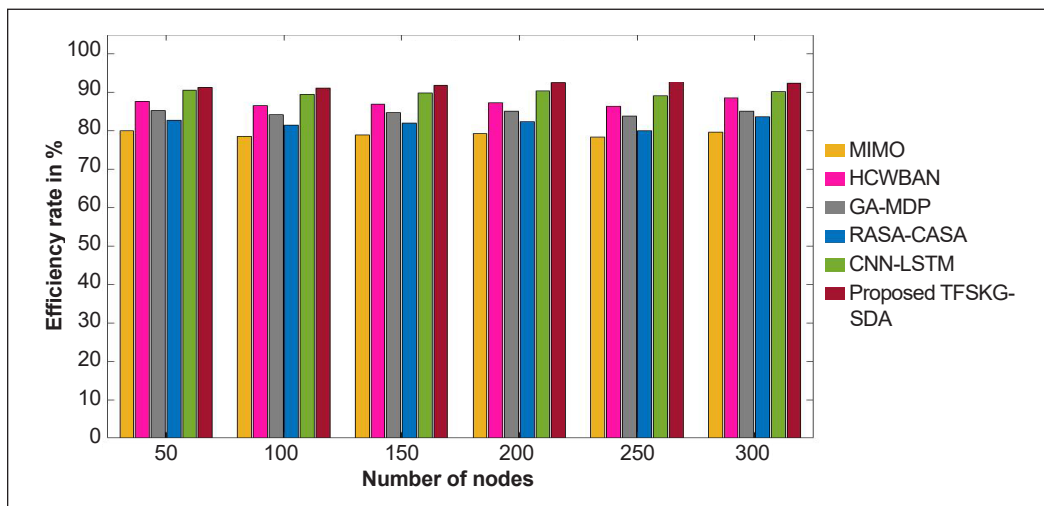


Figure 3. Efficiency rate analysis for TFSKG-SDA method

87.627%, 85.324%, 82.636%, and 90.524%, respectively. With different data quantities, however, the TFSKG-SDA model fared better. In comparison, the efficiency rates of the MIMO, HCWBAN, GA-MDP, RASA-CASA, and CNN-LSTM models are 79.625%, 88.526%, 85.121%, 83.627%, and 90.121%, respectively while the TFSKG-SDA model has a 92.313% efficiency rate under 300 nodes.

Encryption Time Analysis

The quantity of time needed to secure and encrypt data before it is transferred wirelessly over the network is referred to as the encryption time. This process involves applying cryptographic algorithms to transform the information into a coded format, ensuring privacy and security during communication between devices within the body area network. Encryption time is essential in maintaining the confidentiality of sensitive health-related data transmitted over the wireless network.

Figure 4 and Table 4 illustrate an encryption time comparison of the TFSKG-SDA Technique with other known models. According to the data, the TFSKG-SDA strategy

Table 4
Encryption time analysis for TFSKG-SDA method

Number of nodes	MIMO	HCWBAN	GA-MDP	RASA-CASA	CNN-LSTM	TFSKG-SDA
50	78.425	74.625	69.425	61.728	55.324	51.029
100	77.314	72.425	66.928	60.415	53.425	51.314
150	78.672	75.432	70.627	62.983	56.827	51.816
200	77.927	73.029	67.972	61.324	54.029	52.314
250	78.425	75.213	71.234	63.272	57.324	52.716
300	76.827	73.526	65.324	59.324	53.726	52.526

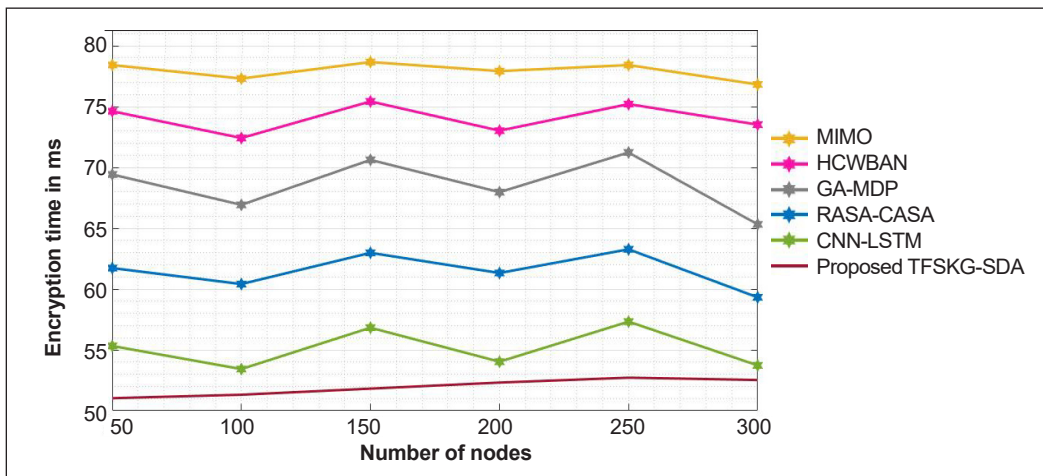


Figure 4. Encryption time analysis for TFSKG-SDA method

outperformed all other tactics. For example, the proposed TFSKG-SDA strategy took just 51.029 ms to encrypt 50 nodes, whereas other current approaches such as MIMO, HCWBAN, GA-MDP, RASA-CASA, and CNN-LSTM took 78.425 ms, 74.625 ms, 69.425 ms, 61.728 ms, and 55.324 ms, respectively. Similarly, the proposed TFSKG-SDA strategy takes 52.526ms to encrypt 300 nodes, whereas existing techniques such as MIMO, HCWBAN, GA-MDP, RASA-CASA, and CNN-LSTM take 76.827 ms, 73.526 ms, 65.324 ms, 59.324 ms, and 53.726 ms, respectively for encryption.

Decryption Time Analysis

“Decryption time” is the duration necessary for the recipient of a transmission to decipher encrypted material. Efficient decryption plays a critical role in the timely and secure transmission of sensitive health information in the context of wearable and implanted medical devices, or WBANs. The decryption time influences the overall communication latency and is critical in ensuring these networks’ real-time monitoring and management of health-related data.

Table 5
Decryption time analysis for the TFSKG-SDA method

Number of nodes	MIMO	HCWBAN	GA-MDP	RASA-CASA	CNN-LSTM	TFSKG-SDA
50	321.72	171.02	272.72	211.82	142.72	112.62
100	332.92	179.52	279.52	218.82	148.76	123.82
150	361.02	195.61	292.52	242.72	164.92	119.72
200	358.62	186.42	286.72	239.71	157.52	126.52
250	342.72	181.52	281.76	231.82	151.02	139.62
300	372.82	199.81	296.42	263.82	165.72	131.62

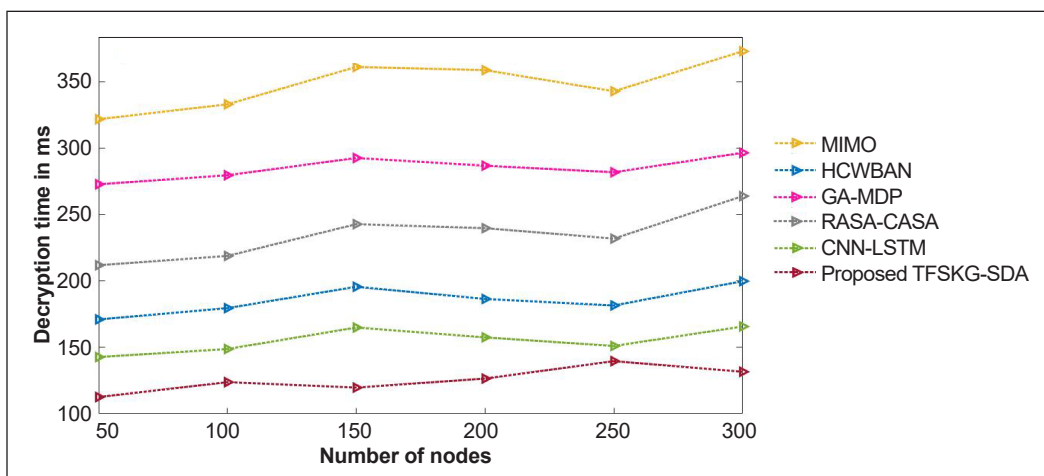


Figure 5 Decryption time analysis for TFSKG-SDA method

The results of the decryption time analysis, comparing the TFSKG-SDA Method to several established models, are displayed in Figure 5 and Table 5. Based on the statistics, the TFSKG-SDA strategy outperformed all other tactics. The suggested TFSKG-SDA strategy, for example, required just 112.62 ms to decrypt 50 nodes, whereas MIMO, HCWBAN, GA-MDP, RASA-CASA, and CNN-LSTM have taken 321.72 ms, 171.025 ms, 272.72 ms, 211.82 ms, and 142.72 ms, respectively. Similarly, the proposed TFSKG-SDA method decrypts 300 nodes in 131.62 ms, while existing approaches such as MIMO, HCWBAN, GA-MDP, RASA-CASA, and CNN-LSTM require 372.82 ms, 199.816 ms, 296.42 ms, 263.82 ms, and 165.72 ms, respectively for decryption.

Packet Delivery Ratio (PDR) Analysis

PDR is defined as Equation 30.

$$\text{Packet Delivery Ratio} = \frac{\text{data}_{DS}(\text{Total packets received by sink})}{\text{data}_{SL}(\text{Total packets sent by LMUs})} \quad [30]$$

Without present strategies, the Local Monitoring Units (LMUs) would determine packet transmission using a routing protocol on their own. Classically, this protocol needs numerous control signals from the network to determine the best course of action for each state.

The PDR analysis of the TFSKG-SDA Method with other existing models is shown in Figure 6 and Table 6. The graph shows how the WBAN strategy improves efficiency while maintaining PDR. In comparison to the MIMO, HCWBAN, GA-MDP, RASA-CASA, and CNN-LSTM models, which have PDR of 82.728%, 62.029%, 69.516%, 77.435%, and 66.019%, respectively, the TFSKG-SDA model has a PDR of 89.026% for 50 nodes. The TFSKG-SDA model, on the other hand, fared better with different data sizes. Under 300 nodes, the TFSKG-SDA model has a PDR of 94.726%, whereas the MIMO, HCWBAN, GA-MDP, RASA-CASA, and CNN-LSTM models have a PDR of 88.829%, 65.324%, 75.726%, 81.028%, and 67.324%, respectively.

Table 6
Packet delivery ratio analysis for the TFSKG-SDA method

Number of nodes	MIMO	HCWBAN	GA-MDP	RASA-CASA	CNN-LSTM	TFSKG-SDA
50	82.728	62.029	69.516	77.435	66.019	89.026
100	86.826	65.873	72.928	79.435	67.728	90.627
150	84.536	64.782	71.425	78.536	66.415	91.425
200	83.928	63.526	70.616	77.825	66.314	92.725
250	87.452	64.324	73.724	80.627	68.524	93.672
300	88.829	65.324	75.726	81.028	67.324	94.726

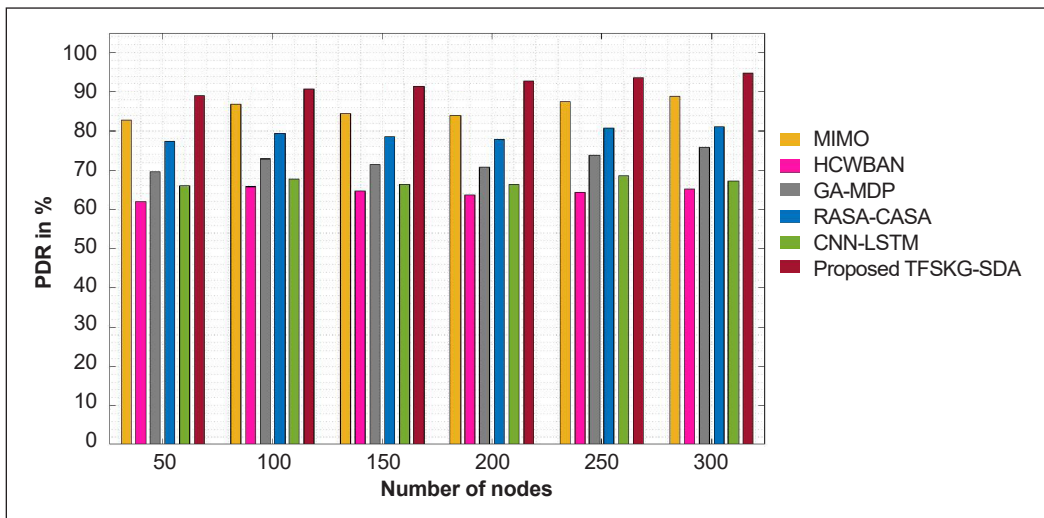


Figure 6. Packet delivery ratio analysis for the TFSKG-SDA method

Accuracy Analysis

Accuracy (ACC): The precision was designed by dividing the total number of examples by the sum of the true positives (TP) and true negatives (TN) (Equation 31).

$$Accuracy = \frac{TP + TN}{TP + TN + FP + FN} \tag{31}$$

TP denotes successfully predicted data labels corresponding to the actual data. FP, on the other hand, refers to incorrectly expected negative data labels assigned to the incorrect category of image labels. TN is an abbreviation for expected negative sample data sets. FN signifies positive data labels that were mistakenly predicted.

Figure 7 and Table 7 depict the accuracy of the study of the TFSKG-SDA Method in comparison with other existing models. The graph illustrates how the WBAN method increased efficacy without sacrificing accuracy. The TFSKG-SDA model exhibits a PDR of 92.424% for 50 nodes, surpassing the accuracy values of 75.052%, 82.728%, 89.314%,

Table 7
Accuracy analysis for TFSKG-SDA method

Number of nodes	MIMO	HCWBAN	GA-MDP	RASA-CASA	CNN-LSTM	TFSKG-SDA
50	75.052	82.728	89.314	87.029	79.324	92.424
100	77.025	84.324	90.827	87.526	81.526	92.827
150	76.324	83.926	90.423	88.524	80.728	93.627
200	78.425	86.625	90.072	88.927	82.526	94.536
250	77.526	85.728	91.252	87.062	81.829	94.972
300	76.762	83.526	89.738	87.425	79.627	95.536

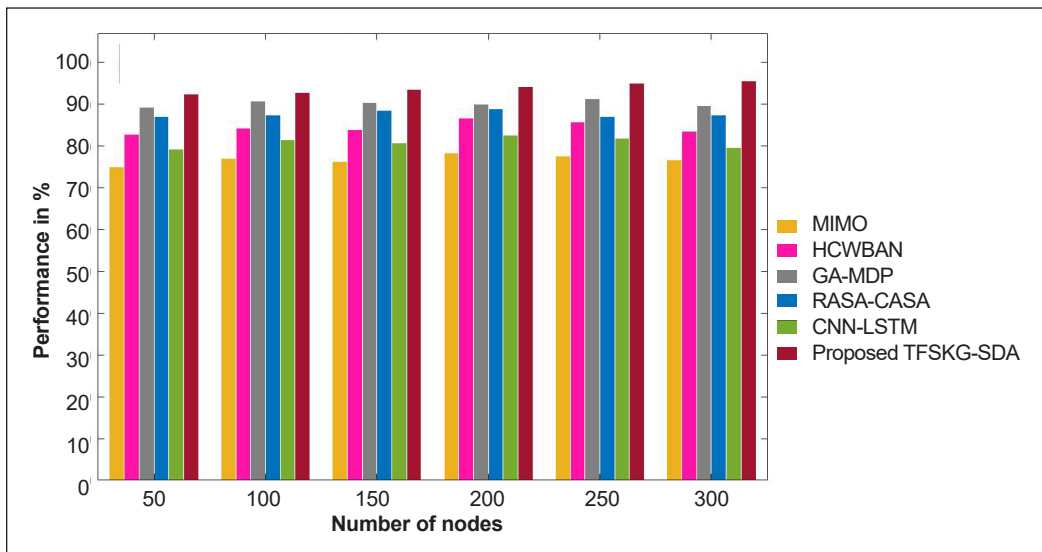


Figure 7. Accuracy analysis for TFSKG-SDA method

87.029%, and 79.324% for the MIMO, HCWBAN, GA-MDP, RASA-CASA, and CNN-LSTM models. Notably, with varying data sizes, the TFSKG-SDA model outperformed its counterparts in contrast to the MIMO, HCWBAN, GA-MDP, RASA-CASA, and CNN-LSTM models, which demonstrated accuracy values of 76.762%, 83.526%, 89.738%, 87.425%, and 79.627%, respectively, the TFSKG-SDA model achieved an accuracy of 95.536% under 300 nodes.

DISCUSSION

In WBANs, the suggested Secure Data Aggregation and Transmission System with TFSKG showed strong performance in guaranteeing data integrity and secrecy. Employment can obtain a reliable technique for aggregating private health data by efficiently decreasing possible security risks throughout the aggregation procedure. The encryption method was accomplished estimably in terms of encryption time and competence rate. The encryption algorithm professionally protected the secrecy of the cooperative data, preventing illegal access during communication. The security mechanisms are vital in preserving the integrity and privacy of sensitive medical data shared via WBANs, addressing significant apprehensions in healthcare data management and communication.

CONCLUSION

In conclusion, TFSKG-SDA and transmission have expressive WBAN data privacy and security. The Twofish algorithm, known for its robust encryption method, assists in protecting sensitive data being moved through networks by providing an extra layer of

security against probable threats and illegal access. When considering WBANs, these improvements are even more important, as the transmission of medical data must be secure and uninterrupted for healthcare treatments to be both rapid and operative. The primary limitation is the probable computational overhead associated with the Twofish encryption procedure, which could influence real-time data transmission frequently in resource-constrained circumstances. Also, managing symmetric keys for encryption labels is problematic for key distribution and security management, mainly in large-scale network installations. Despite these limitations, the system significantly develops healthcare data security by preservative privacy and integrity, resulting in better patient care results in WBAN. As the use of WBANs becomes progressively common in healthcare and other industries, the necessity of strong security measures cannot be stressed. By providing a dependable and effective method of preserving sensitive data throughout its lifecycle, the Twofish method in research proposed an accurate explanation for the problems faced by security threats in WBANs. As a result, an innovative genetic algorithm for data security is proposed for increased performance in this work. Our proposed framework, the TFSKG-SDA method, performs an outstanding accuracy of 95.536%. Future WBAN communication dependability assessments should be made using extra performance metrics. Implementation will also be recommended to prioritize network performance and energy efficiency. Finally, radio propagation models with computed path loss coefficients in wireless band situations will be discussed.

ACKNOWLEDGEMENTS

The authors thank VelTech Multi Tech Dr. Rangarajan Dr. Sakunthalal Engineering College, Tamil Nadu, India, for providing facilities and testing for this research. The authors would also like thank all the reviewers for their helpful comments and suggestions during the research's execution. The authors greatly appreciate their generosity with their time.

REFERENCES

- Abualsaud, K., Mohamed, A., Khattab, T., Yaacoub, E., Hasna, M., & Guizani, M. (2018). Classification for imperfect EEG epileptic seizure in IoT applications: A comparative study. In *2018 14th International Wireless Communications & Mobile Computing Conference (IWCMC)* (pp. 364-369). IEEE Publishing. <https://doi.org/10.1109/IWCMC.2018.8450279>
- Anh, B. T., Quoc, D. D., & Hiep, P. T. (2023). Optimizing transmission power for uplink data in cell-free wireless body area networks. In *2023 IEEE Statistical Signal Processing Workshop (SSP)* (pp. 275-279). IEEE Publishing. <https://doi.org/10.1109/SSP53291.2023.10208084>
- Apoorva, Y. K. (2013). Comparative study of different symmetric key cryptography algorithms. *International Journal of Application or Innovation in Engineering & Management*, 2(7), 10-15. <https://doi.org/10.4236/jis.2020.113009>

- Azees, M., Vijayakumar, P., Karuppiyah, M., & Nayyar, A. (2021). An efficient anonymous authentication and confidentiality preservation schemes for secure communications in wireless body area networks. *Wireless Network*, 27(3), 2119–2130. <https://doi.org/10.1007/s11276-021-02560-y>
- Dangi, K. G., Bhagat, A., & Panda, S. P. (2020). Emergency vital data packet transmission in hospital centered wireless body area network. *Procedia Computer Science*, 171, 2563-2571. <https://doi.org/10.1016/j.procs.2020.04.278>
- Geetha, B. T., Mohan, P., Mayuri, A. V. R., Jackulin, T., Aldo Stalin, J. L., & Anitha, V. (2022). Pigeon inspired optimization with encryption based secure medical image management system. *Computational Intelligence and Neuroscience*, 2022(1), Article 2243827. <https://doi.org/10.1155/2022/2243827>
- He, D., Zeadally, S., Kumar, M., & Lee, J. H. (2017). Anonymous authentication for wireless body area networks with provable security, *IEEE Systems Journal*, 11(4), 2590-2601. <https://doi.org/10.1109/JSYST.2016.2544805>
- Hu, C., Li, H., Huo, Y., Xiang, T., & Liao, X. (2016). Secure and efficient data communication protocol for wireless body area networks. *IEEE Transactions on Multi-Scale Computing Systems*, 2(2), 94-107. <https://doi.org/10.1109/TMSCS.2016.2525997>
- Kaleem, M., & Devarajan, G. G. (2023). Wireless body area networks utilizing data transmission techniques based on prediction. In *2023 10th International Conference on Computing for Sustainable Global Development (INDIACom)* (pp. 1586-1591). IEEE Publishing.
- Kareem, S. M., & Rahma, A. M. S. (2020). A novel approach for the development of the Twofish algorithm based on multi-level key space. *Journal of Information Security and Applications*, 50, Article 102410. <https://doi.org/10.1016/j.jisa.2019.102410>
- Khan, S., Iqbal, W., Waheed, A., Mehmood, G., Khan, S., Zareei, M., & Biswal, R. R. (2022). An efficient and secure revocation-enabled attribute-based access control for eHealth in smart society. *Sensors*, 22(1), Article 336. <https://doi.org/10.3390/s22010336>
- Kumar, M., & Chand, S. (2020). A secure and efficient cloud-centric internet-of-medical-things-enabled smart healthcare system with public verifiability. *IEEE Internet of Things Journal*, 7(10), 10650-10659. <https://doi.org/10.1109/JIOT.2020.3006523>
- Kumar, M., & Chand, S. (2021). A lightweight cloud-assisted identity-based anonymous authentication and key agreement protocol for secure wireless body area network. In *IEEE Systems Journal*, 15(2), 2779-2786. <https://doi.org/10.1109/JSYST.2020.2990749>
- Kumar, M., (2020). Cryptanalysis and improvement of anonymous authentication for wireless body area networks with provable security. *Cryptology ePrint Archive*. <https://eprint.iacr.org/2020/936>
- Lee, C., & Lee, J. (2017). Harvesting and energy aware adaptive sampling algorithm for guaranteeing self-sustainability in wireless sensor networks. In *2017 International Conference on Information Networking (ICOIN)* (pp. 57-62). IEEE Publishing. <https://doi.org/10.1109/ICOIN.2017.7899475>
- Liu, Q., Mkongwa, K. G., & Zhang, C. (2021). Performance issues in wireless body area networks for the healthcare application: A survey and future prospects. *SN Applied Sciences*, 3(2), Article 155. <https://doi.org/10.1007/s42452-020-04058-2>

- Mathews, R., & Jose, D. V. (2024). Hybrid homomorphic-asymmetric lightweight cryptosystem for securing smart devices: A review. *Transactions on Emerging Telecommunications Technologies*, 35(1), Article e4866. <https://doi.org/10.1002/ett.4866>.
- Mehmood, G., Khan, M. Z., Fayaz, M., Faisal, M., Rahman, H. U., & Gwak, J. (2022). An energy-efficient mobile agent-based data aggregation scheme for wireless body area networks. *Computers, Materials & Continua*, 70(3), 5929-5948. <https://doi.org/10.32604/cmc.2022.020546>
- Mehmood, G., Khan, M. Z., Waheed, A., Zareei, M., & Mohamed, E. M. (2020). A trust-based energy-efficient and reliable communication scheme (trust-based ERCS) for remote patient monitoring in wireless body area networks. *IEEE Access*, 8, 131397-131413. <https://doi.org/10.1109/ACCESS.2020.3007405>
- Mohapatra, D., Kumar, S., Bhoi., Jena, K. K., Nayak, S. N., Singh, A., (2022). A blockchain security scheme to support fog-based internet of things. *Microprocessors and Microsystems*, 89, Article 104455. <https://doi.org/10.1016/j.micpro.2022.104455>
- Paulraj, D., & Baburaj, E. (2023). Admission control policy and key agreement based on anonymous identity in cloud computing. *Journal of Cloud Computing: Advances, Systems and Applications*, 12(1), 1-18. <https://doi.org/10.1186/s13677-023-00446-2>
- Rane, D. D. (2016). Superiority of twofish over blowfish. *International Journal of scientific research and management*, 4(11), 4744-4746. <https://doi.org/10.18535/ijstrm/v4i11.01>
- Roy, M., Chowdhury, C., & Aslam, N. (2021). Designing GA based effective transmission strategies for intra-wban communication. *Biomedical Signal Processing and Control*, 70, Article 102944. <https://doi.org/10.1016/j.bspc.2021.102944>
- Salem, O., Alsubhi, K., Mehaoua, A., & Boutaba, R. (2020). Markov models for anomaly detection in wireless body area networks for secure health monitoring. *IEEE Journal on Selected Areas in Communications*, 39(2), 526-540. <https://doi.org/10.1109/JSAC.2020.3020602>.
- Santos, M. A., Munoz, R., Olivares, R., Rebouças Filho, P. P., Del Ser, J., & de Albuquerque, V. H. C. (2020). Online heart monitoring systems on the internet of health things environments: A survey, a reference model and an outlook. *Information Fusion*, 53, 222-239. <https://doi.org/10.1016/j.inffus.2019.06.004>
- Shyja, V., Irine., Ranganathan, G., & Bindhu., V. (2023). Link quality and energy efficient optimal simplified cluster-based routing scheme to enhance lifetime for wireless body area networks. *Nano Communication Networks*, 37, Article 100465. <https://doi.org/10.1016/j.nancom.2023.100465>.
- Subramani, J., Azees, M., Rajasekaran, A. S., & Al-Turjman, F. (2023). EPF-FDA: Efficient pairing free and confidentiality preserving fog-based data aggregation scheme for WBANs. *IEEE Instrumentation & Measurement Magazine*, 26(8), 10-16. <https://doi.org/10.1109/MIM.2023.10292620>
- Subramani, J., Maria, A., Rajasekaran, A.S., and Al-Turjman, F. (2022). Lightweight privacy and confidentiality preserving anonymous authentication scheme for WBANs. *IEEE Transactions on Industrial Informatics*, 18(5), 484-3491. <https://doi.org/10.1109/TII.2021.3097759>
- Thippun, P., Sasiwat, Y., Buranapanichkit, D., Booranawong, A., Jindapetch, N., & Saito, H. (2023). Implementation and experimental evaluation of dynamic capabilities in wireless body area networks: Different setting parameters and environments. *Journal of Engineering and Applied Science*, 70(1), Article 1. <https://doi.org/10.1186/s44147-022-00171-8>

- Tseng, T. W., Wu, C. T., & Lai, F. (2019). Threat analysis for wearable health devices and environment monitoring internet of things integration system. *IEEE Access*, 7, 144983-144994. <https://doi.org/10.1109/ACCESS.2019.2946081>
- Wang, C., Qin, Y., Jin, H., Kim, I., Vergara, J. D. G., Dong, C., Jiang, Y., Zhou, Q., Li, J., He, Z., Zou, Z., Zheng, L. R., Wu, X., & Wang, Y. (2019). A low power cardiovascular healthcare system with cross-layer optimization from sensing patch to cloud platform. *IEEE Transactions on Biomedical Circuits and Systems*, 13(2), 314-329. <https://doi.org/10.1109/TBCAS.2019.2892334>
- Wang, L., Zhang, G., Li, J., & Lin, G. (2020). Joint optimization of power control and time slot allocation for wireless body area networks via deep reinforcement learning. *Wireless Networks*, 26, 4507-4516. <https://doi.org/10.1007/s11276-020-02353-9>
- Zhang, J., & Dong, C. (2022). Secure and lightweight data aggregation scheme for anonymous multi-receivers in WBAN. *IEEE Transactions on Network Science and Engineering*, 10(1), 81-91. <https://doi.org/10.1109/TNSE.2022.3205044>
- Zhong, L., He, S., Lin, J., Wu, J., Li, X., Pang, Y., & Li, Z. (2022). Technological requirements and challenges in wireless body area networks for health monitoring: A comprehensive survey. *Sensors*, 22(9), Article 3539. <https://doi.org/10.3390/s22093539>

**REFEREES FOR THE PERTANIKA
JOURNAL OF SCIENCE & TECHNOLOGY**

Vol. 32 (6) Oct. 2024

The Editorial Board of the Pertanika Journal of Science and Technology wishes to thank the following:

Ab Al-hadi Ab Rahman
(UTM, Malaysia)

Hosam M. Saleh
(EAEA, Egypt)

Ahmad Razif Muhammad
(UKM, Malaysia)

Irfan Ahmed Shaikh
(SAU, Pakistan)

Ali Kadhun M. Al-Qurabat
(University of Babylon, Iraq)

Iskandar Ishak
(UPM, Malaysia)

AM Abdelghany
(NRC, Egypt)

Jafar Ahmad Abed Alzubi
(BAU, Jordan)

Azees Maria
(VIT-AP, India)

Javad Seyedmohammadi
(AREEO, Iran)

Aziah Khamis
(UTeM, Malaysia)

Jyoti Chaubey
(MNIT, India)

Bin Wang
(ZJOU, China)

K. V. Ramana Rao
(ICAR, India)

Brij Bhooshan Gupta
(Asia University, Taiwan)

Kada Bouchouicha
(URERMS, Algeria)

Chengathir Selvi
(MEPCOENG, India)

Ke Feng
(Imperial College London, UK)

Everaldo Silvino dos Santos
(UFRN, Brazil)

Khuzaimah Zailani
(UPM, Malaysia)

Ghufran Redzwan
(UM, Malaysia)

Lindah Roziani Jamru
(UMS, Malaysia)

Ghulam Rasool
(HHU, China)

Mahadimenakbar Mohd. Dawood
(UMS, Malaysia)

Gulzar Mehmood
(UoM, Pakistan)

Mahender Kumar
(JNU, India)

Han Xiuyou
(DLUT, China)

Malgorzata Worwag
(CUT, Poland)

Hazrul Abdul Hamid
(USM, Malaysia)

Manikandan Ramachandran
(SASTRA University, India)

Herryawan Ryadi Eziwar Dyari
(UKM, Malaysia)

Md Amzad Hossain
(JUST, Bangladesh)

Moovendhan Meivelu
(SIMATS, India)

Muhammad Idzdihar Idris
(UTeM, Malaysia)

Muhammad Nasir Bashir
(Yonsei university, Korea)

Muhammad Waqas
(HGU, Germany)

Muhd Danish Daniel Abdullah
(UMT, Malaysia)

Mustabshirha Gul
(BZU, Pakistan)

Muzneena Ahmad Mustapha
(UKM, Malaysia)

Nadeem Sarwar
(Bahria University, Pakistan)

Nageswara Lalam
(NETL, USA)

Nazlin Hanie Abdullah
(UNISEL, Malaysia)

Nor Hanuni Ramli
(UMP, Malaysia)

Noramalina Abdullah
(USM, Malaysia)

Pankaj Kumar Gupta
(UWaterloo, Canada)

Qin Zhihao
(CAAS, China)

Ramya Kumanayake
(KDU, Sri Lanka)

Razali Ngah
(UTM, Malaysia)

Sandeep Pattnaik
(IITB, India)

Setiyo Gunawan
(ITS, Indonesia)

Shulin Zhuang
(Zhejiang University, China)

Syam Krishnan
(QUT, Australia)

Tan Chye Lih
(UNIMAP, Malaysia)

Teerapong Panboonyuen
(Chulalongkorn University, Thailand)

Wasana Suyotha
(PSU, Thailand)

Winy Routray
(NITRKL, India)

AREEO – Agricultural Research, Education and Extension Organization
BAU – Al-Balqa' Applied University
BZU – Bahauddin Zakariya University
CAAS – Chinese Academy of Agricultural Sciences
CUT – Czestochowa University of Technology
DLUT – Dalian University of Technology
EAEA – Egyptian Atomic Energy Authority
HGU – Hochschule Geisenheim University
HHU – Hohai University
ICAR – Central Institute of Agricultural Engineering
IITB – Indian Institute of Technology Bhubaneswar
ITS – Institut Teknologi Sepuluh Nopember
JNU – Jawaharlal Nehru University
JUST – Jashore University of Science and Technology
KDU – Kotelawala Defence University
MEPCOENG – Mepco Schlenk Engineering College
MNIT – Malaviya National Institute of Technology
NETL – National Energy Technology Laboratory
NITRKL – National Institute of Technology Rourkela
NRC – National Research Center

PSU – Prince of Songkla University
QUT – Queensland University of Technology
SAU – Sindh Agriculture University
SIMATS – Saveetha Institute of Medical and Technical Sciences
UFRN – Federal University of Rio Grande do Norte
UKM – Universiti Kebangsaan Malaysia
UMP – Universiti Malaysia Pahang
UMS – Universiti Malaysia Sabah
UMT – Universiti Malaysia Terengganu
UNIMAP – Universiti Malaysia Perlis
UNISEL – Universiti Selangor
UoM – University of Malakand
UPM – Universiti Putra Malaysia
URERMS – Saharan Renewable Energy Research Unit
USM – Universiti Sains Malaysia
UTeM – Universiti Teknikal Malaysia Melaka
UTM – Universiti Teknologi Malaysia
UWaterloo – University of Waterloo
VIT-AP – Vellore Institute of Technology - Andhra Pradesh
ZIOU – Zhejiang Ocean University

While every effort has been made to include a complete list of referees for the period stated above, however if any name(s) have been omitted unintentionally or spelt incorrectly, please notify the Chief Executive Editor, *Pertanika* Journals at executive_editor.pertanika@upm.edu.my

Any inclusion or exclusion of name(s) on this page does not commit the *Pertanika* Editorial Office, nor the UPM Press or the university to provide any liability for whatsoever reason.

Assessment of Nitrate Reduction by Microbes in Artificial Groundwater Medium <i>Preeti Thakur and Pammi Gauba</i>	2753
<i>Review Article</i>	
A Comprehensive Review of State-of-the-art Optical Methods for Methane Gas Detection <i>Sayma Khandaker, Nurulain Shaipuzaman, Md Mahmudul Hasan, Mohd Amir Shahlan Mohd Aspar and Hadi Manap</i>	2769
<i>Case Study</i>	
Carbon Emission from Transportation in Higher Learning Institutions: A Case Study at Universiti Tun Hussein Onn Malaysia <i>Khairunmarhanis Zekefli, Aeslina Abdul Kadir, Amir Detho and Mohd Ikhmal Haqem Hassan</i>	2797
Physiological Behavior of Rubber Plants (<i>Hevea Brasiliensis</i>) to Different Soil Moisture Conditions <i>Rohaizad Mislan, Zulkefly Sulaiman, Siti Nor Akmar Abdullah, Mohd Razi Ismail, Sarker Mohammad Rezaul Karim, Mohd Aswad Abdul Wahab and Aizat Shamin Noran</i>	2807
Dehydrated Food Waste and Leftover for Trench Composting <i>Khalida Aziz, Naweedullah Amin, Vinod Kumar Nathan, Mami Irie, Irwan Syah Md. Yusoff, Luqman Chuah Abdullah, Amirrudin Azmi and Muhammad Heikal Ismail</i>	2827
<i>Review Article</i>	
A Systematic Review of Aquatic Organism Antimicrobial Peptides <i>Li Ting Lee, Arnold Ang, Ibrahim Mahmood, Ahmed AbdulKareem Najm, Adura Mohd Adnan, Shazrul Fazry and Douglas Law</i>	2847
Application of GIS for Monitoring Firefly Population Abundance (<i>Pteroptyx tener</i>) and the Influence of Abiotic Factors <i>Nurhafizul Abu Seri and Azimah Abd Rahman</i>	2873
Secure Data Aggregation and Transmission System for Wireless Body Area Networks Using Twofish Symmetric Key Generation <i>Insozhan Nagasundharamoorthi, Prabhu Venkatesan and Parthasarathy Velusamy</i>	2903

Low-temperature Deposited Highly Sensitive Integrated All-solid Electrodes for Electrochemical pH Detection <i>Norhidayatul Hikmee Mahzan, Shaiful Bakhtiar Hashim, Rosalena Irma Alip, Zuhani Ismail Khan and Sukreen Hana Herman</i>	2561
Design an Agricultural Soil and Environment Monitoring System Based on IoT <i>Bayu Rima Aditya, Elis Hernawati, Tedi Gunawan and Pramuko Aji</i>	2575
Analysis of Soil Viability Monitoring System for In-house Plantation Growth Using an Internet of Things Approach <i>Spoorthi Singh, Utkarsh Ojha, Prashant M Prabhu, Poothi Rohan Reddi and Shivashankar Hiremath</i>	2591
Evaluating Convolutional Neural Network Architecture for Historical Topographic Hardcopy Maps Analysis: A Study on Training and Validation Accuracy Variation <i>Saiful Anuar Jaafar, Abdul Rauf Abdul Rasam and Norizan Mat Diah</i>	2609
A Comprehensive Analysis of a Framework for Rebalancing Imbalanced Medical Data Using an Ensemble-based Classifier <i>Jafhate Edward, Marshima Mohd Rosli and Ali Seman</i>	2631
Improved Early Detection of Tube Leaks Faults in Pulverised Coal-fired Boiler Using Deep Feed Forward Neural Network <i>Abdul Munir Abdul Karim, Yasir Mohd Mustafah and Zainol Arifin Zainal Abidin</i>	2655
A Framework for Prioritising the Performance Criteria of Natural Fibre Composite Materials: Incorporation of CRITIC-TOPSIS Method <i>Mohd Hidayat Ab Rahman, Siti Mariam Abdul Rahman, Ridhwan Jumaidin and Jamaluddin Mahmud</i>	2679
Machine Learning and Remote Sensing Applications for Assessing Land Use and Land Cover Changes for Under-monitored Basin <i>Muhammad Amiruddin Zulkifli, Jacqueline Isabella Anak Gisen, Syarifuddin Misbari, Shairul Rohaziawati Samat and Qian Yu</i>	2699
Variation and Forecasting of Land Surface Temperature in Malaysia <i>Munawar Munawar, Rhysa McNeil, Rohana Jani, Edwar M Nur and Don McNeil</i>	2723
The Application of Smart Drip Irrigation System for Precision Farming <i>Suhardi, Bambang Marhaenanto and Bayu Taruna Widjaja Putra</i>	2737

Foreword <i>Mohd Sapuan Salit</i>	i
Performance Comparison of Seed Generation Techniques of Stimulated Brillouin Scattering-based Microwave Photonics Amplifier and Filter <i>Shahad Khudhair Abbas, Noran Azizan Cholan, Mohd Saiful Dzulkefly Zan, Mohd Adzir Mahdi, Makhfudzah Mokhtar and Zuraidah Zan</i>	2405
Bernoulli Distillation System (BDS) for Bioethanol Sorghum Stalk Purification <i>Djoko Wahyudi, Wignyanto, Yusuf Hendrawan and Nurkholis Hamidi</i>	2421
Spectroscopic Analysis of Chrysotile Asbestos and its Environmental Resistance in Asbestos Cement Waste Products <i>Gergely Zoltán Macher, Fanni Károly, Christopher Teh Boon Sung, Dóra Beke, András Torma and Szilveszter Gergely</i>	2441
<i>Review Article</i>	
State-of-the-Art Probabilistic Solar Power Forecasting: A Structured Review <i>Noor Hasliza Abdul Rahman, Shahril Irwan Sulaiman, Mohamad Zhafran Hussin, Muhammad Asraf Hairuddin, Ezril Hisham Mat Saat and Nur Dalila Khirul Ashar</i>	2459
Prediction of Temperature Variability on Power Transmission Line Parameters Using Intelligent Approaches <i>Ashfaq Ahmad, Iqra Javed, Changan Zhu, Muhammad Babar Rasheed, Muhammad Waqar Akram, Muhammad Wisal Khan, Umair Ghazanfar, Waseem Nazar, Syed Baqar Hussain and Amber Sultan</i>	2489
Isolation and Screening of Indigenous Filamentous Fungi Producing Ligninolytic, Cellulolytic and Hemicellulolytic Enzymes from Decomposed Oil Palm Frond <i>Ahmad Fariz Nicholas, Hasliza Abu Hassim, Mohd Huzairi Mohd Zainudin, Zunita Zakaria, Mohd Termizi Yusof, Mohd Nazri Md Nayan and Amirul Faiz Mohd Azmi</i>	2511
Chemical Composition of Acid Soluble Collagen (ASC) Isolated from Indonesia Local “Kacang” Goat Skin (<i>Capra aegagrus hocus</i>) <i>Dita Prameswari Trenggono Putri, Rina Wahyuningsih, Rusman, Nurliyani and Yuny Erwanto</i>	2541



Pertanika Editorial Office, Journal Division,
Putra Science Park,
1st Floor, IDEA Tower II,
UPM-MTDC Center,
Universiti Putra Malaysia,
43400 UPM Serdang,
Selangor Darul Ehsan
Malaysia

<http://www.pertanika.upm.edu.my>
Email: executive_editor.pertanika@upm.edu.my
Tel. No.: +603- 9769 1622

PENERBIT
UPM
UNIVERSITI PUTRA MALAYSIA
PRESS

<http://www.penerbit.upm.edu.my>
Email: penerbit@upm.edu.my
Tel. No.: +603- 9769 8851

